



HAL
open science

Physical modelling of cell and tissue mechanics applied to single cell spreading, cancerous budding and cell extrusion

Mathieu Dedenon

► **To cite this version:**

Mathieu Dedenon. Physical modelling of cell and tissue mechanics applied to single cell spreading, cancerous budding and cell extrusion. Other [cond-mat.other]. Sorbonne Université, 2021. English. NNT: 2021SORUS038 . tel-03483186

HAL Id: tel-03483186

<https://theses.hal.science/tel-03483186>

Submitted on 16 Dec 2021

HAL is a multi-disciplinary open access archive for the deposit and dissemination of scientific research documents, whether they are published or not. The documents may come from teaching and research institutions in France or abroad, or from public or private research centers.

L'archive ouverte pluridisciplinaire **HAL**, est destinée au dépôt et à la diffusion de documents scientifiques de niveau recherche, publiés ou non, émanant des établissements d'enseignement et de recherche français ou étrangers, des laboratoires publics ou privés.

**THÈSE DE DOCTORAT
DE SORBONNE UNIVERSITÉ**

Spécialité : Physique

École doctorale n°564: Physique en Île-de-France

réalisée

au laboratoire Physico-Chimie Curie

sous la direction de Pierre SENS

présentée par

Mathieu DEDENON

pour obtenir le grade de :

DOCTEUR DE SORBONNE UNIVERSITÉ

Sujet de la thèse :

**Description physique de mécanique cellulaire et tissulaire
appliquée à l'étalement de cellules uniques, le
bourgeoisement cancéreux et l'extrusion cellulaire**

soutenue le 29 Juin 2021

devant le jury composé de :

Mme Ana-Suncana SMITH	Rapportrice
M. Ulrich SCHWARZ	Rapporteur
Mme Alice NICOLAS	Examinatrice
M. Raphaël VOITURIEZ	Examineur
M. Danijela Matic VIGNJEVIC	Invitée
M. Philippe Marcq	Invité
M. Pierre SENS	Directeur de thèse

Abstract

During this PhD, I studied different phenomena pertaining to the mechanics of cells and tissues. The first project describes lamellipodial initiation during cell spreading. The model introduces a coupling between membrane curvature and cortical actin orientation, that generates substrate tractions by friction. A full wetting transition exists when edge curvature, actin orientation and tractions enter into a positive feed-back loop. A bi-stable transition allows a polar nucleation. The second project is an experimental collaboration that studies the way Cancer-Associated Fibroblasts (CAFs) cells could reshape tumours. CAFs surrounding a cluster of Cancer Cells (CCs) assemble a contractile ring to end up on top of CCs, and sometimes build a 3D bud through a shear stress. We use an elasto-plastic model for CAFs, compared with CAF closure dynamics and tractions. We combine vertex and continuous mechanical models to describe the CC monolayer shape, until the appearance of rearrangements. Finally, we describe the mechanical stability of buds by combining elasticity with plastic rearrangements. The last project reports preliminary results on the mechanics of cell extrusion in an epithelial monolayer under compression. Using the same vertex model, we look at the mechanical properties able to drive the basal-to-lateral and lateral-to-apical transitions. Then, we search for a mechanical instability on a minimal 3-cell system, and identify conditions that favour extrusion.

Acknowledgements

So, this is the end. After almost four years on track, trying, failing, doing, worrying, thinking, trying again! It is a truism to say that a PhD makes you evolve a lot, but it is especially true in my case. Although it remained invisible for almost three years, such a large incubation time have been necessary to start to digest the huge literature of biomechanics. The process is not finished but the association of ideas comes much more easily.

In that regard, the fourth year of my PhD has been absolutely essential and I am really grateful for Sorbonne Université and the Physico-Chimie lab at Curie institute to have provided me an extra-funding (3+6 months). I also thank Pierre to have kept his calm and positivity in this choppy time to compensate my fears (the extension time followed the series 1 – 3 – 1 – 3 – 4 – 6 – 8 – 9 months) and to have spontaneously encouraged for extensions when needed. I also thank the doctoral school from SU with Maria Chamarro and Nadine Yassine, who have been very sympathetic to deal with all those changes and temporal uncertainties.

At a more personal level, I would like to thank Pierre in priority for the great human management. It could have been very hard in many places of science, but a posteriori the Curie lab was really exceptional for me. He always put the good boundaries to not fall into "science overload", something on which I could fall easily. The project trajectories have been quite chaotic, with some big moments of frustration when fighting for months without achieving anything, but I am sincerely convinced that I owe him a lot on the fact that I "survived" this PhD.

Similarly, I strongly believe that the initiation of the experimental collaboration with Danijela, Jorge and Carlos after one and a half years has been critically positive. Beyond the beautiful features of the experimental system and the rich biological context, the interaction with real-world data has been a huge respiration and I am grateful to Pierre and Danijela for having initiating this. Pierre has been remarkably perceptive when jumping on the opportunity, since this project became the major one in the end, to replace the not-working (at the time) extrusion project. Although coarse-grained theoretical models have their own interest, to spend an entire PhD in biophysics inside an abstract space without much interactions with experiments looks quite unappealing a posteriori. Indeed, despite the big troubles on the modelling aspects, this is the part of the PhD that I enjoyed the most because it contained the highest phenomenological richness. So of course, I am grateful to Danijela, Jorge and Carlos for our great exchanges. It was not always easy to understand each other, and we struggled on our side to adopt the good modelling strategy that could be well suited for your experimental data, but I just keep great interactions and a fantastic system to explore decorated by great biological questions. I hope that the experimental paper will be published in a great journal, it deserves it!

I also thanks Philippe for having struggled with us on this extrusion project. It looked fuzzy and blocked for a very long time but I think the time spent on the discrete equations have been useful in the end to build some intuition. Although the current state is still not entirely satisfying, I personally learned a lot on a technical point of view and in terms of project management.

Moreover, it is a pleasure to thank Alice Nicolas and Raphaël Voituriez for having accepted to be jury members, as well as Ana-Suncana Smith and Ulrich Schwarz to read and evaluate this (hopefully not too) heavy technical manuscript. I hope the PhD defense will be rewarding for all of us.

Finally, it has been great to exchange with my TAC members Andrew and Pascal: they brought an independent and kind supervision at moments of big doubts, especially at the beginning. The

positivity of your feed-backs and reports have been very valuable to attenuate my internal worries so thank you for that.

Before my PhD, I received the mentorship of an exceptional human and researcher: Asmaa Abada from LPT at Orsay. Her support has played an important role in my trajectory up to this PhD in Curie institute and I thank her for that.

Now regarding the lab life, I must say that the interactions with colleagues have been a great source of joy and stress release. I am particularly grateful to Thomas for the open discussions in front of herbal tea after a long day, as well as Michele who is always happy to discuss about diverse topics! It was also a pleasure to be around such accomplished scientists as Jean-François, Jacques et Françoise to catch a tiny fraction of their exceptional experience.

Now comes the (many) great team mates who have been fantastic social integrators throughout the years, starting with the seniors Carles and Rémy when offices were not renovated yet, followed by Efe the Great, Gert-Jan, Jean-Patrick, Louis, Niladri, Sami, Sergio, Victor and the survivors Amit, Ander, Romain and Sam. Beyond the team, many people put a lot of effort into the integration of reserved people, and I am grateful to Thanh, Anne-Marie, Joanna, Majdouline, Tommaso, Oleg, Alicia, Koceila, Kotryna, John, Elie, Maud, Lucie, Laura, Dureen, Lorena... among others.

Enfin, je vais parler en français pour remercier mes proches.

D'abord mes parents qui justifient à eux seuls ma présence en doctorat grâce à leur éducation exceptionnelle et leur soutien continu. J'aurais tellement aimé soutenir cette thèse devant mon père parti bien trop tôt, mais la vie est parfois déchirante et il faut savoir absorber les pertes les plus tragiques. Je dédis ce travail à mon père, à ma mère et à ma soeur, qui ont constitué le noyau familial qui a rendu tout cela possible.

Je pense également à ma famille, mes grands-parents, marraine, oncles, tantes, cousins dont j'ai hâte de retrouver les visages en cette journée de "retour à la vie", et à mon grand-père parti également il y a peu que j'aurais aimé inviter à la soutenance. Je salue aussi la mémoire de Thomas dont la sensibilité était un peu trop forte pour ce monde, ainsi que ses parents, son frère, sa femme et sa fille.

Enfin j'adresse une pensée à Cyril, Emilien, Jérémie ainsi que mon cousin Eric, qui m'ont apporté ces dernières années une véritable soupape de compression vis-à-vis de certaines normes socio-culturelles citadines et scientifiques, et je les en remercie. De même, Mohammed, Jacky et Ilham ainsi que toute la classe de L2 P furent de précieuses rencontres au sein de cette délabrée mais vivante université d'Orsay.

Contents

Abstract	i
Acknowledgements	iii
Foreword	ix
1 Lamellipodium initiation	1
1.1 Introduction: actin, cortex and cell spreading	1
1.1.1 Actin filament assembly, networking and the polymerization motor	1
1.1.2 The actin cortex, liposomes and network rheology	2
1.1.3 Stages of <i>in vitro</i> cell spreading	5
1.1.4 Molecular clutch and adaptor proteins	8
1.2 Model: The adherent cortical vesicle	10
1.2.1 A polarization vector field for cortical orientation	12
1.2.2 A Frank energy coupling membrane shape and actin orientation	12
1.2.3 Membrane mechanics and cell spreading	14
1.2.4 Traction force generation and leading edge advancement	15
1.3 Results: The adherent cortical vesicle	18
1.3.1 Mechanical response in Fourier space	18
1.3.2 Toy model: cortical membrane wetting a wedge	19
1.3.3 Adhesion of a cortex-free vesicle	21
1.3.4 Spreading of the cortical vesicle	24
1.4 Discussion and conclusion	27
1.4.1 Mechanical feed-back loop and lamellipodium initiation	27
1.4.2 Adhesion-dependent versus adhesion-independent lamellipodial growth	29
1.4.3 Conclusion	30
2 2D side vertex model	33
2.1 Introduction: tissue modelling	33
2.1.1 Epithelial tissues	33
2.1.2 Continuous mechanics	35
2.1.3 Vertex models	36
2.2 Model: 2D bubbly vertex model	40
2.2.1 Presentation of the framework: 2D side vertex model	40
2.2.2 Uniform 2D epithelial monolayer	40
2.2.3 External compression	42
2.2.4 Flatness limit for apical interface	43
2.2.5 Parameter estimates	44
2.3 Model: Non-uniform tissue mechanics	44
2.3.1 Force balance equations	44
2.3.2 Discrete linear perturbation	45
2.3.3 Continuous approximation	46
2.3.4 Boundary relaxation	47
2.3.5 Bubbly vs polygonal mechanical response	48

2.3.6	Connexion to 2D incompressible elasticity	50
3	Cancerous budding	53
3.1	Introduction: tumour budding, gap closure and experimental system	53
3.1.1	The biological context: tumour budding and cancer-associated fibroblasts . .	53
3.1.2	Epithelial gap closure: purse-string and leader migration	54
3.1.3	Presentation of the <i>in vitro</i> experimental system	58
3.1.4	Quantitative characterisation of the system	58
3.2	Model: experimental constraints on CAF dynamics and tissue mechanics	63
3.2.1	Pillar compression	65
3.2.2	CAF closure dynamics	67
3.2.3	CAF rheology and traction localization	70
3.2.4	Localized deformation: rim	72
3.3	Model: CC rheology	75
3.3.1	CAF-free region	77
3.3.2	CAF-covered region with tissue viscosity	78
3.3.3	Boundary conditions	79
3.3.4	Numerical scheme for the boundary value problem	81
3.3.5	CAF closure limit	81
3.4	Model: vertex framework for CC monolayer deformation	82
3.4.1	Basal tension gradient	82
3.4.2	Apical tension gradient	83
3.4.3	Linear perturbation of the vertex model	84
3.4.4	Cluster region free of CAFs	85
3.4.5	Continuous limit in the free region	87
3.4.6	Cluster region covered by CAFs	89
3.5	Results: free CAFs pulled by contractile ring	90
3.5.1	CAF closure or stable equilibrium	90
3.5.2	Constraints on the parameters	92
3.5.3	Yield stress nature	93
3.6	Results: CAF closure and tractions for N-cadh KD	93
3.6.1	cluster s33	96
3.6.2	cluster s34	97
3.7	Results: CC bud stability at steady-state	98
3.7.1	Experimental traction analysis and bud compression	98
3.7.2	Permeation model with yield pressure	102
3.8	Results: CC cluster deformation dynamics	107
3.8.1	Rim width scaling	107
3.8.2	Results on CC shape dynamics	109
3.8.3	Early volume transfer	112
3.8.4	Rim disappearance and central amplification	113
3.8.5	Towards undeformed CAF-covered region?	115
3.8.6	Flat covered limit	116
3.8.7	Bud final area	122
4	Cell extrusion	125
4.1	Introduction to cell extrusion	127
4.1.1	The biological context	127
4.1.2	Crowding-induced cell extrusion	127
4.2	Results: weakly perturbed tissue around target cell	129
4.2.1	Extrusion and multilayering 'rule of thumb'	129
4.2.2	Enzymatic shift of model parameters	131
4.3	Results: three-cell system and spontaneous instability	134
4.3.1	Free conditions	134

4.3.2	External compression	136
5	General conclusion and perspectives	141
5.1	Lamellipodial initiation	141
5.2	Cancerous budding and cell extrusion	142
5.3	Outlook	143
A	French report	145
A.1	Initiation d'un lamellipode	145
A.1.1	Modèle: la vésicule corticale adhérente 2D	145
A.1.2	Résultats: transitions d'étalement	147
A.1.3	Conclusion	149
A.2	Modèle de "vertex" 2D en vue de côté	149
A.3	Bourgeonnement cancéreux	153
A.3.1	Présentation du système expérimental	153
A.3.2	Modèle: contraintes expérimentales et mécanique des tissus	155
A.3.3	Résultats: fermeture des FACs et tractions sans N-cadhérines	158
A.3.4	Résultats: stabilité des bourgeons cancéreux	159
A.3.5	Résultats: dynamique de déformation des amas de CCs	161
A.4	Extrusion cellulaire	163
A.4.1	Résultats: critère énergétique naïf	164
A.4.2	Résultats: décalage enzymatique des paramètres	165
A.4.3	Résultats: système à trois cellules sous compression et instabilités	166
	Bibliography	169

Foreword

"In an honest search for knowledge, you quite often have to abide by ignorance for an indefinite period..."

E. Schrödinger, *Nature and the Greeks*

Biophysics is an old field of science where interdisciplinarity between biology and physics have been used for very different purposes. One uses specific tools from experimental physics (X-ray crystallography, fluorescent/phase/neutron/electron microscopy, laser traps, etc...) to describe some properties of biological elements like the atomic structure, protein interactions and localization, or mechanical response to external force. Thanks to the possibility of many new quantitative insights on cell behaviours like multi-fluorescent channels, those techniques have been coupled to a rich variety of *in vitro* environments like substrate gels, adhesion patterns, or microfluidic devices to explore different cell responses. This may be called "technical/experimental biophysics".

Another purpose of biophysics deals with the understanding of the role played by physical interactions in the biological phenomena. Among many others: the protein aggregation in the context of soft matter physics, electro-osmotic effects in cells and tissues, the mechanical interplay between migrating cells and their matrix environment, and extensions to physiology with organ rheology and tissue repair. This may be called "phenomenological biophysics".

Finally, a last direction of biophysics often named "physics inspired by biology" does not necessarily target a directed understanding of biological effects but uses some biological phenomena as an inspiration to adapt existing theoretical frameworks (or create new ones) to the out-of-equilibrium situation of living systems. A classical example is the field of active matter, but it also applies to the exploration of some mechanisms which are less likely encountered in the inanimate world of physics due to lower elemental complexity. When accurate biological details are explicitly introduced in a theoretical model, one may talk about "quantitative" modelling, whereas the search for generic mechanisms which are robust to various microscopic behaviours may be called "qualitative" modelling. Precisely, this distinction fixes the boundary between "phenomenological biophysics" and "physics inspired by biology". This "biology inspired by physics" has also been important from an historical perspective, where analogies with purely physical systems have been used. Classical examples are:

- the work of D'Arcy Thompson [1] expressing simple but powerful analogies from physics and mathematics to describe the shape of biological structures, in particular the famous analogy between cell monolayers and foams,
- the popular science book "What is Life?", written by the physicist E. Schrödinger during Second World War [2], who proposed an aperiodic crystal with different covalent bond configurations to encode biological information and stimulated the discovery of DNA helical structure, among a strong generational influence,
- more recently, the liquid droplet model for the mechanics of suspended and adhered cells [3, 4]. Despite its simplicity, this PhD thesis will use extensively its assumptions of a uniform and incompressible bag delimited by a constant surface tension.

The theoretical work which have been performed during this PhD can be associated with the third category of "physics inspired by biology" and more precisely the "qualitative modelling" approach, targeting three biological phenomena in the sub-fields of cell and tissue biomechanics:

- the emergence of thin sheet protrusions along the periphery of single cells spreading on a solid substrate, called *lamellipodia*,
- the appearance of collective buds in the context of cancer and how the mechanics applied by the stromal cells surrounding a tumour can generate localized clusters invading the body, a phenomenon called *tumour budding*.
- the elimination of living cells from cell monolayers that is central for tissue homeostasis, named *cell extrusion*, and its connexion to the mechanical compression induced by proliferative cells.

All these phenomena are embedded in the Animalia kingdom, for multicellular eukaryotic organisms able to move but unable to produce their own nutrients.

The first and third projects are purely theoretical whereas the second one involves an experimental collaboration with the team of D. Vignjevic from another lab of the Curie institute (UMR 144), on an *in vitro* assay to mimic a tumour and its micro-environment. This naturally organizes the thesis in four chapters:

- the first one describes the project of lamellipodial initiation, separated into an introduction on actin cytoskeleton and cell spreading, followed by a model description, to finish with the main results and a discussion,
- a second one describes the discrete mechanical framework (2D side vertex model) common to the two last projects on tissue mechanics, separated into an introduction, a presentation of the model for uniform tissues, and the derivation of the general mechanical equations,
- a third one presents the theoretical and quantitative analysis for the project on cancerous budding, separated into an introduction on the biological context and the *in vitro* experimental system, followed by a description of the modelling assumptions and their compatibility with experimental constraints, half of results when cancerous clusters can be considered uniform, to finish with the other half of results for the heterogeneous evolution of the monolayer shape,
- and the last one describes the project of cell extrusion, separated into an introduction on the phenomenon and preliminary results, when target cells in a monolayer are transformed, and when a three-cell system is compressed.

Although the second and third projects share phenomenological similarities and both deal with tissue mechanics, the first one remains at a single cell level and can be considered independent. Therefore, we did not attempt to artificially converge the three projects under a global theme for the thesis. Similarly, the challenge of integrating those different phenomena into a general introduction of cell and tissue biomechanics has not been considered reasonable: many aspects like single cell rheology or single/collective cell migration are only superficially touched and do not appear particularly relevant for our three projects. Since we only deal with coarse-grained modelling approaches, the choice of three separated introductions should be enough to introduce the relevant knowledge from the literature specific to each project.

Chapter 1

Lamellipodium initiation

The goal of this project is to propose a minimal model of the transition between the cortical actin of a suspended cell and the lamellipodial protrusion of a spreading cell on flat *in vitro* substrates, with focus on the mechanical coupling between the peripheral actin filament orientation and the plasma membrane curvature at the cell edge. Before the model presentation and results, the main phenomena involved in the system are introduced, without any hope for exhaustivity. For a more synthetic presentation, a pre-print of the research article is available on ArXiv (ID=1906.02559).

1.1 Introduction: actin, cortex and cell spreading

1.1.1 Actin filament assembly, networking and the polymerization motor

The assembly of actin filaments from non-covalent binding of monomers is regulated by the concentration of available subunits. Whereas an unpolarized filament would elongate above a critical concentration¹ $c^* \equiv k_{\text{off}}/k_{\text{on}}$ and shrink below this value, the actin globular protein possesses minus (pointed) and plus (barbed) ends which distinguishes the growth rate on both sides. Moreover, ATP can bind to actin monomers to transform the passive polymerization into an active process, with a change of reaction rates for ATP- or ADP-bound actin and different critical concentrations c_+^* and c_-^* for plus and minus ends, respectively. ATP-bound actin monomers tend to polymerize at plus ends and transform into ADP-bound actin over time, giving a linear history along filaments with depolymerizing ADP-bound actin at minus ends. This leads to a richer dynamics as shown on Fig. 1.1b:

- for $c < c_+^*$, both filament ends shrink.
- for $c_+^* < c < c_-^*$, the minus end shrinks whereas the plus end grows and gives an overall increase of filament length (as if the depolymerized monomers on one side were transferred to polymerize the other side), a phenomenon named treadmilling.
- for $c < c_-^*$, both filament ends grow.

Because of the high plasticity required for cell morphogenetic changes, the actin cytoskeleton has evolved around a pool of interacting proteins called Actin-Binding Proteins (ABPs) that perform structural, signalling and mechanical functions. This rich eco-system has evolved to achieve specific network organizations, for branched filaments nucleated by the Arp2/3 complex (Fig. 1.1c, top) or bundles nucleated by formins (Fig. 1.1c, bottom), both stabilized by cross-linking proteins like filamin, α -actinin or fimbrin. The polymerization dynamics of actin filaments is regulated by nucleators (Fig. 1.1a) and their upstream signalling activators (WASP, WAVE, WH2 or NPF), capping and severing proteins (Fig. 1.1a) to control the filament length distribution, stabilizing proteins (tropomyosin) to increase filament durability before degradation, whereas the couple profilin/cofilin controls the pool of available monomers. Finally, two functional groups of ABPs are

¹The polymerization reaction can be written for a n -sized filament reacting with one monomer: $[n] + [1] \rightleftharpoons [n+1]$ with on-rate k_{on} and off-rate k_{off} .

not represented on the sketch of (Fig. 1.1c): the Membrane-to-Cortex Attachment (MCA) proteins ezrin, radixin and moesin ensure a stable linkage between the plasma membrane and the underneath cytoskeleton, except for localized disruptions generating blebs (Fig. 1.1d, bottom), whereas myosin motors can generate forces along actin filaments (myosin II mini-filaments) or directly from the cell surface (myosin I).

A critical property of actin filaments for their role in cell morphogenetic processes, also common to microtubules, is their ability to perform mechanical work against a load when they polymerize or unpolymerize². This is called the actin polymerization motor when it pushes the load (reviews [6], [7]) and possesses a pulling counterpart associated to actin depolymerization.

Depending on the system, this load can be the plasma membrane itself (Fig. 1.1c), a solid bead or a bacterial wall [8]. The first mechanical model of this effect was based on thermal fluctuations of the boundary close to the polymerizing filament embedded in a stiff actin network, called the "Brownian ratchet model" [5]. The observations of motile bacteria *Listeria monocytogenes* pushed by an actin comet tail in infected cells [9] provided too small fluctuations of the bacterial wall to account for the estimated forces (review [10]). Three years later, the same authors proposed the "Elastic Brownian ratchet" based on filament bending by thermal fluctuations, efficient for small filaments to avoid buckling (at ~ 100 nm) and optimised for a specific angle close to the Arp2/3-dependent (top of Fig. 1.1c) branched network (review [10]). Although both models seem reasonable for actin filaments polymerizing against the plasma membrane, they rely on the stiffness of the supporting network, an assumption that cannot be assumed in general except for saturated cross-linking protein concentration. Indeed, models at the network level have shown that growth rate could be independent from load force thanks to an increase in density, when new filaments polymerize from existing filaments (auto-catalytic model) contrarily to de novo filament polymerization (nucleation model) ([11], review [7]). Nevertheless, others mechanisms for polymerization forces can be expected from formin nucleators [12] or myosin I motors when filaments are anchored to the wall ([13], review [7]). Finally contrarily to a naive initial thought, capping proteins seem necessary for an efficient force transmission [9], to prevent the appearance of long filaments that are inefficient for protrusive forces.

In suspended cells, the actin polymerization motor pushes against the plasma membrane to generate dynamic protrusions that can be analysed with the most recent detection techniques [14]: pseudopodia with local sheets of branched networks (Fig. 1.1d, top) or filopodia for a bundle architecture (Fig. 1.1d, middle).

In addition to the pushing capability of actin networks, a contractile behaviour can emerge at the collective level by the incorporation of myosin motors. This contractile ability is tackled by stress fibres (parallel bundle) connecting adhesion clusters and by the actomyosin cortex underneath the plasma membrane with largely isotropic network orientation in membrane plane. For example, it is essential at the end of cell division (cytokinesis) with ring constriction to separate daughter cells[15].

1.1.2 The actin cortex, liposomes and network rheology

The actin cortex is a thin layer of F-actin network attached to the plasma membrane by proteic linkers (reviews [19, 20, 21]), whose thickness can be as small as 100 – 200 nm for HeLa cells [22] and up to few microns for oocytes [20]. The main function of this cytoskeletal network present around the cell periphery is, on one hand, to resist elastically the external mechanical perturbations that could damage the cell [23], and on the other hand to orchestrate the required shape changes of cell migration, cell division or developmental morphogenesis at the tissue scale (review [20]). Those

²According to a general thermodynamic argument applied to unpolarized filaments (for simplicity), the modified critical concentration of actin monomers under a compressive force F is $c^*(F) = c^*(0) \exp F\delta/k_B T$ and promotes depolymerization, where $\delta = 2.7$ nm is the length added by one subunit. Filament growth stops at the stall force $F_{\text{stall}}(c) = (k_B T/\delta) \log(k_{\text{on}}c/k_{\text{off}})$. With a cell monomer concentration of the order of 10 μM and $c^* \simeq 0.1$ μM , one gets $F_{\text{stall}} \simeq 1 - 10$ pN [5].

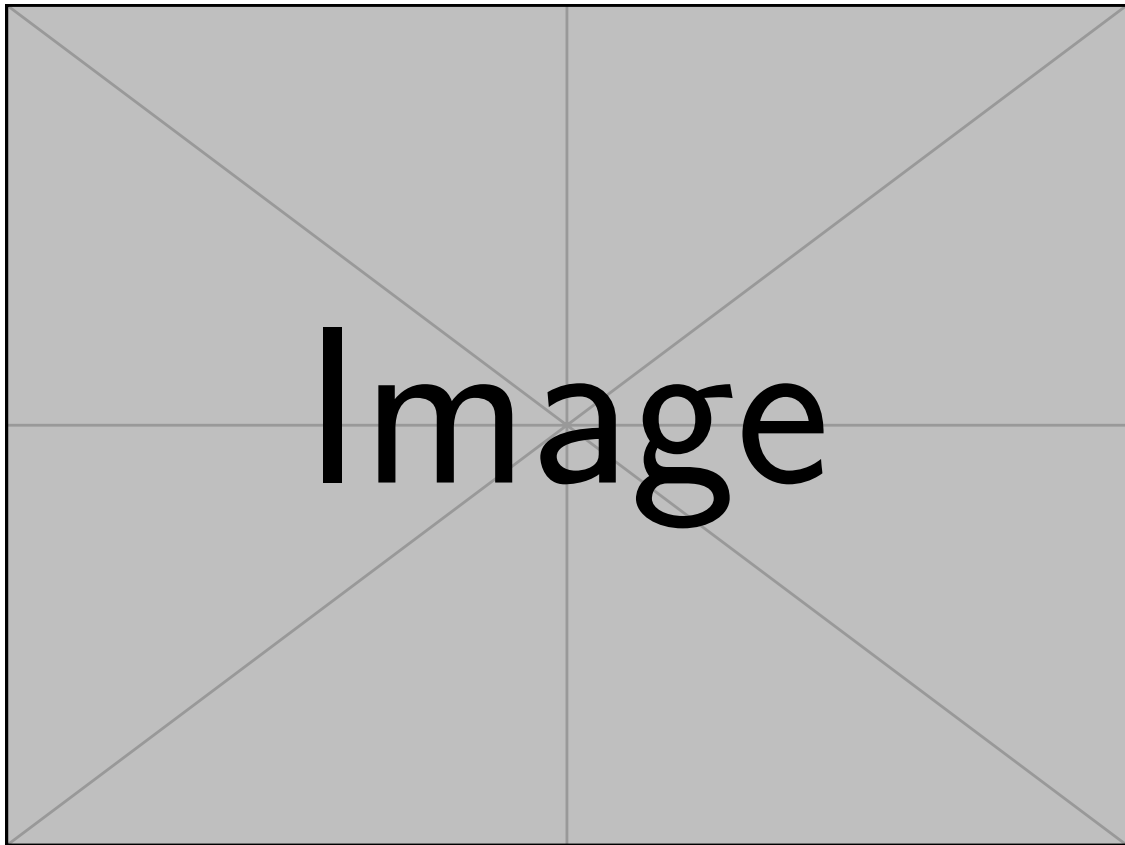


Figure 1.1: **(a)**: Actin filament can assemble spontaneously or through proteic nucleators. The Arp2/3 complex creates new branches on existing filaments with a characteristic angle of 70 degrees, Spire initiates filament growth by minus end stabilization, and the Formin family facilitates polymerization at the plus end. Several families of actin-binding proteins can sever filaments, cap one end or cross-link filaments. From [16]. **(b)**: Filament growth rate as a function of available monomer concentration with the two critical concentrations at plus and minus ends. Treadmilling (plus end growth and minus end shrinkage) occurs at intermediary concentration. From [17]. **(c)**: Sketch representing the organization of bundled (filopodia-like) and branched actin networks (cortex and lamellipodia-like) at the cell periphery. Assembly is promoted by membrane-associated factors whereas disassembly and monomer recycling occurs towards the cell center. This network polarization analogous to filamentous treadmilling and controlled by many proteic factors is maintained dynamically. It requires the permanent renewal of actin filaments with a tight control of available monomer concentration (profilin/cofilin balance). From [18]. **(d)**: High resolution 3D live microscopy and motif detection tools allow a classification of cell surface morphology: pseudopodia on dendritic cells (top), filopodia on HBEC cells (middle) and blebs on MV3 melanoma cells. The characteristic flatness of pseudopodia on suspended cells make them analogous to the lamellipodia of adherent cells. From [14].

ambivalent properties are performed at the price of a high structural, dynamical and mechanical complexity that are still poorly understood, in addition to a lack of universality for a cortical "identity" among cell types and phenotypes, as well as the potential integration to cytoplasmic cytoskeleton for global cell mechanical resistance (review [24]).

The cortex contains two subpopulations of actin filaments polymerized through Arp2/3 or formins that constantly renew with a turnover time of few tens of seconds [25, 26] and a typical network mesh size of ~ 100 nm in the tangential membrane plane [27]. Since this permanent actin renewal does not perturb the well-defined cortical thickness [22] and actin nucleation factors are activated at the plasma membrane (review [28]), some kind of treadmill process transverse to the membrane plane (at the network scale) may occur³ (Fig. 1.1c). A submembranous network of spectrin-like proteins parallel to the plasma membrane, initially discovered in erythrocytes, is also considered to be part of the actin cortex [30] to stiffen the cell surface, and may connect it to microtubules and intermediate filaments through plectin binding [31]. In addition to the many ABPs that are common to actin networks (see the previous section), the presence of myosin motors generates a cortical rest tension which is a core property of the cortex (figure Fig. 1.2a). In case of actomyosin contractility gradients, cortical flows can be used for polarity factors transportation during embryogenesis [32] or single cell migration [33]. Another functional example is the local disruption of the membrane-to-cortex attachment (Fig. 1.2b) generating blebs in dividing cells (the inflating membrane driven by hydrostatic pressure difference), a mechanism used to compensate for the mechanical instability that comes from fluctuations in cortical tension to avoid asymmetric division [15].

This active tension γ_c usually dominates the plasma membrane tension γ_m and is balanced by the hydrostatic pressure difference in a spherical suspended cell (Fig. 1.2c), with typical values $\gamma_c = 10 - 1000$ pN/ μm [23, 34, 35], whereas $\gamma_m = 1 - 100$ pN/ μm ([36, 34], review [37]). This simple description is known as the liquid cell droplet model [23], with surface tension encapsulating an homogeneous incompressible cytosol. The overall cell tension $T_{\text{cell}} = T + \gamma$ can be measured by the micro-pipette aspiration technique [38] or AFM indentation for adherent cells [35], which can also estimate the cortical elastic modulus at ~ 1 kPa [39]. Although myosin II minifilaments are presented as the main drivers of cortical rest tension (review [19]), there is evidence for some tension added by myosin I motors⁴ anchored to the PM [38], as well as a contribution from end-tracking crosslinkers in case of depolymerization (review [20]) and filament population length that affects network connectivity [35]. Finally, the cortex-to-membrane attachment may affect the cortical tension T , cell stiffness and membrane tension either mechanically or indirectly through signalling events [41].

Although easily detectable by actin fluorescent labelling as shown on figure Fig. 1.2d, the resolution limits have prevented for many years the exploration of the cortical properties, and only the most recent techniques of the past decade are starting to highlight some key features: the thickness [22], the turnover dynamics [25], the architecture evolution [42], the actin filament length distribution [43], the network patterns (vortices, asters or stars) [39] and the membrane protein confinement⁵.

In parallel to *in vivo* progress, several minimal systems able to discover new cortical properties or mimic existing ones have dealt with *in vitro* actin networks. They can be embedded in a fluid

³For a typical cortical thickness $h \sim 100$ nm and a turnover time $\tau \sim 10$ s, one can build a characteristic retrograde velocity $v_r = h/\tau$ associated to the cortex, with an order of magnitude ~ 10 nm/s similar to the lamellipodial retrograde flow [29].

⁴Tether pulling experiments also showed the role played by myosin I motors in membrane-to-cortex attachment (Fig. 1.2a), with net decrease of tether force in myosin I KO cells [40].

⁵This illustrates the picket fence model for plasma membrane proteic organization (in replacement of the fluid mosaic model), where submembranous filament clusters attached provide an ordered micro-environment that limits in-plane diffusivity [27, 44].

next to an open surface to study their rheology [45], the role of molecular motors [46, 47], the cross-linking proteins [48, 49] and the emergence of contractility [50]. Starting from standard rheological properties of entangled polymer networks, elastic resistance to quick deformations (solid-like) and viscous response to slow deformations (liquid-like) by filament rearrangements, the combination of cross-linking proteins and/or molecular motors can generate rich behaviours. Network fluidization by myosin II is observed without cross-linkers [46] whereas the addition of filamin generates the opposite behaviour [47]. Moreover, F-actin networks with filamin but without myosin show softening (stiffening) at low (high) cross-linking concentration upon large shear deformations [48], and only reaches physiological elasticity with a pre-stress [49]. The crucial contractile property of the actin cortex can be reproduced *in vitro* above a threshold myosin II concentration and at intermediate cross-linker concentration [50]. Finally, under compression load, the network first stiffens but softens by filament buckling above a critical stress [45].

Actin networks can also grow next to a closed surface coated with polymerization activators, like a bead [8], a liposome [51, 52, 53], or a water droplet surrounded by oil [54]. Actin networks outside unilamellar vesicles can reproduce filopodial protrusions with only Arp2/3 nucleators in vesicles [51] and perform shell polarization (symmetry breaking) for large myosin II concentration and intermediate capping protein concentration [52]. For inside systems, symmetry breaking also occurs for cortical water droplets embedded in water [54] whereas cortical vesicles can produce endocytotic-like membrane fission events [53].

To handle this remarkable active material exhibiting elastic [45], viscous [32, 55], and poro-elastic [56] behaviour while constantly renewed, many different models have been proposed. Due to the natural separation of scales between cortical thickness $h \sim 100$ nm and cell radius $R \sim 10$ μ m, some models describe the actomyosin cortex as a surface [57, 32, 58, 59, 60] in a thin film approximation, within the framework of active gel theory (review [61]) or active surfaces for complex geometries [62, 59]. Only few models consider explicitly the direction normal to the plasma membrane plane [8, 63].

A continuous framework have been applied to several experimental systems, with a deformation field for an elastic description [8], a velocity field for a viscous description [32], eventually coupled to a filament density field [63], or an orientation field in the active gel framework ([57] and review [61]). More sophisticated models relying on numerical simulations (Fig. 1.2e) have also been performed, to describe filament orientation in network treadmilling [64], cortical contractility linked to network architecture [35], stress dissipation under cortical flows [65], or vesicle shapes under polymerization forces [60].

1.1.3 Stages of *in vitro* cell spreading

In the literature, cell spreading designates a precise *in vitro* phenomenon of suspended cells in a culture fluid adhering on a solid substrate, with a characteristic expansion of their contact area. After the beginning of cell culture in the fifties, single adhered cells has quickly been recognized as a privileged system to understand some cell morphogenetic changes [68] and its sensitivity to substrate specificity called haptotaxis [69], the directed motion of cells towards regions of higher adhesion. Although some *in vivo* cellular events share similarities with cell spreading, like leukocytes adhering on the endothelial wall of blood vessels, the large amount of research results on this topic concerns *in vitro* observations⁶.

⁶Interestingly, despite a massive literature, cell spreading does not seem recognized as a proper biological phenomenon except in the context of T cell activation [70], probably because the experimental conditions are far from the environment of living organisms. As a consequence, very few review papers or monographs exist to synthesize the many observations made over decades on this ubiquitous aspect of cell culture. Moreover, even if cell culture on plates have been immensely useful for the understanding of cell migration, cell proliferation, cell fate, cell mechanosensitivity and cytoskeletal regulators, a lot of factors remain uncontrolled and weaken the scientific robustness of some results, making comparisons between different experimental assays difficult. For example, in the study of Lam Hui et al [70], the addition of serum in the growth medium affects the adhesion clustering and the spreading dynamics anisotropy.

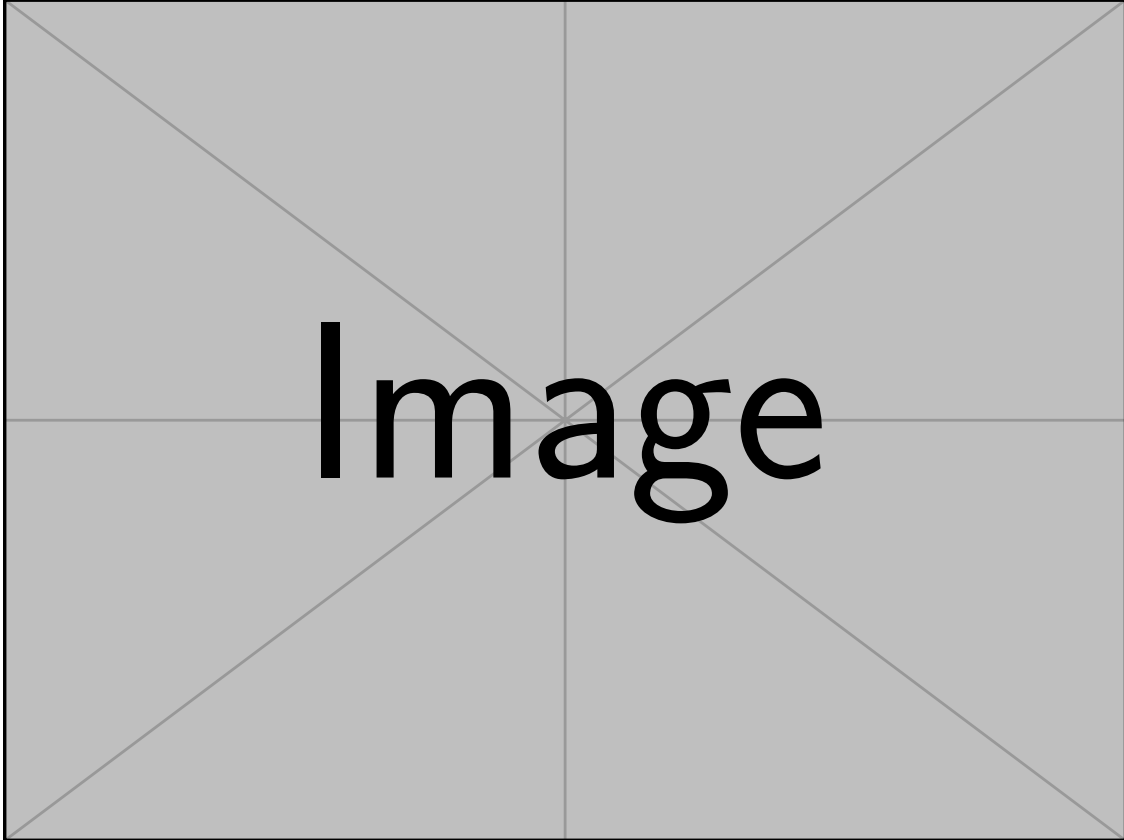


Figure 1.2: **(a)**: Minimal sketch of the actomyosin cortex underneath the plasma membrane, showing membrane-to-cortex attachments (ERM proteins, myosin I, etc...), myosin II minifilaments, polymerizing actin filaments and cross-linking proteins. The molecular motor activity (large black arrows) builds a large scale contractility responsible for a pre-stressed state with active tension (gray arrows). From [21]. **(b)**: Time-lapse image series of a bleb expansion and retraction on an HeLa cell. The cortex first detaches from the plasma membrane, which cannot support the pressure difference anymore (c), and then reassembles along the bleb surface to drive its size reduction. The scale bar is $5\ \mu\text{m}$. From [22]. **(c)**: Sketch of a suspended cell with the actin cortex (gray) and the plasma membrane (black). The inset shows the decomposition of the cell tension into cortical (T) and membrane (γ) tensions, with $\gamma \ll T$ in general. At mechanical equilibrium, the Laplace force balance relates inside (P_{in}) and outside (P_{out}) hydrostatic pressures to twice the tension T divided by the cell radius R . From [66]. **(d)**: Fluorescent image of a dividing *Drosophila* S2 cell with the actin cortex (red) and duplicated DNA (blue). The depletion of moesin destabilizes the cortex and leads to cell division failure. The scale bar is $10\ \mu\text{m}$. From [67]. **(e)**: Top view of an *in silico* actomyosin cortex with actin filaments (red), myosin II minifilaments (blue) and cross-linkers (green). The cortical tension is sensitive to the filament length distribution and inversely correlated to thickness during the cell cycle. From [35].

After an initial contact phase where the glycocalyx reorganizes under non specific adhesion and adhesion receptors are activated to bind specifically to substrate ligands, the spreading cell undergoes a sequence of characteristic shape changes [71]. At the beginning, the cell surface is largely folded whereas the edge of the ventral part is rich in filopodial protrusions: this is the so-called P_0 phase for fibroblast spreading [72]. Later on (few minutes), the membrane folds forming a membrane surface reservoir progressively disappear (Fig. 1.3b) whereas a thin lamellipodial sheet forms at the contact edge [73]. This membrane unfolding generates an increase of plasma membrane tension that triggers sequences of exocytotic bursts to prevent membrane lysis, ensuring a roughly constant PM tension upon cell spreading after the initial phase of surface buffer (folds) depletion [74, 75], as in keratocyte migration [76]. In addition to these active effects, passive invaginations called vacuole-like dilations can form (review [77] and [78]) to participate in the maintenance of the cell surface integrity. For some cells, the contact area increases first linearly with time [79] in a phase called P_1 before a slowing-down during the so-called phase P_2 [72]. Mouse embryonic fibroblasts generate traction forces on the substrate early in spreading, but a sharp increase in magnitude occurs at the beginning of the P_2 phase (Fig. 1.3c), probably related to the assembly of contractile stress fibres connecting the mature focal contacts.

For some cells, a clear shape distinction between the cell body and the lamellipodium is visible after few minutes (Fig. 1.3b,e). However, other cells tend to have higher shape continuity (Fig. 1.3f) and it is difficult to extrapolate a generality from the few side pictures available in the literature. According to the published literature that I explored, there is no much data showing at a high acquisition rate the precise shape transition associated to the lamellipodium initiation. Without any strong technical limitation for the experimental investigation of this question, we hope it will be tackled in the near future. From the more usual top view, cell spreading can be classified according to the lamellipodial structure [80]:

- isotropic if a single protrusion advances at a similar rate for any polar angle around the cell center for few minutes, eventually followed by anisotropic perturbations of the leading edge at later times (Fig. 1.3a, right),
- anisotropic when several localized protrusions can be distinguished along the leading edge and break the global angular pseudo-symmetry of isotropic spreading (Fig. 1.3a, left),

After the fast spreading of the phase named P_1 (observed only for isotropic cases), fibroblasts shift to slower anisotropic dynamics in the phase P_2 (Fig. 1.3a,c), characterized by periodic edge contractions and adhesion clusters maturation [81, 72].

Then, the spreading cell can either establish a front-rear polarity and start to migrate [82], or continue to increase its contact area for hours with the assembly of contractile stress fibres between mature adhesion complexes⁷ until a stationary state is reached. Those generic behaviours are largely cell-type dependent since the spreading dynamics of T cells reaches a stationary contact area after only two minutes [70], with a fitting curve scaling like an hyperbolic tangent function, in agreement with a model where spreading is proposed to be driven by shear-stress dependent actin polymerization [85].

The later stage tends to polarize the cell shape along principal directions defined by stress fibres, giving a finger-like appearance to those un motile cells (Fig. 1.3d). Indeed, an analogy with liquid fingering instability has been proposed for the transition between P_1 and P_2 in isotropic spreading [86].

For the former stage in which a transition from cell spreading to cell motility occurs, the use of a minimal system of cell fragments or cytoplasts⁸ has shown experimentally [87, 88] and theoretically [89] that a generic mechanism of spontaneous symmetry breaking could establish a front-rear

⁷Those mature adhesion complexes named focal adhesions are presented as stiffness sensors since their growth seems to depend on the pulling force applied by stress fibres and substrate elasticity (reviews [83, 84]).

⁸They consist in keratocytes deprived of their body, leaving only a membrane bilayer enclosing a network of actin and myosin II minifilaments. Other elements like signalling proteins or adaptor proteins at the membrane surface are not considered to be essential for the migration transition.

polarity and cell motility. It only requires an anisotropic localization of myosin II minifilaments or actin flow reorientation and has been applied to entire keratocytes [82], either spontaneously or through drug injection to perturb actin or myosin II. The establishment of this front-rear polarity occurs without any directional cue (chemotaxis, haptotaxis, durotaxis, etc...) and does not rely on specific biochemical pathways, whereas other elements controlling cell polarization - like Golgi positioning or micro-tubule orientation - could also induce this spontaneous transition from spreading to motility. Interestingly, some cells like neutrophils establish a cell front before the cell rear, but others like fibroblasts trigger rear retraction before to drive cell migration [90]. A spontaneous symmetry breaking is also observed for *in vitro* cell systems under geometric confinement, for single cells along linear stripes [91] or 2-3 cells on circular patches starting a persistent rotation [92].

All those stages are very sensitive to the experimental preparation of coated ECM ligands, in particular their surface density and their nanoscale organisation which can be random or clustered [93]. However, different cell types on substrates functionalized with different ligands have no impact on the initial spreading dynamics⁹ since the observed rate of contact area increase is quantitatively very similar [96, 79]. Of course, different integrin dimers have affinity for different ECM ligands and initiate potentially different signalling pathways, but this result illustrates the generic physical mechanisms involved in early cell spreading. Note that the out-in signalling associated to initial cell adhesion to ECM ligands can drive various responses able to affect morphogenetic events: for example, the total F-actin mass of cultured hepatocytes increases by a factor 20 for high ECM ligands after 30 minutes of cell attachment [96], and did not require new actin protein synthesis. This indicates a strong activation of actin polymerization that modulates the initial spreading dynamics, according to observations based on dose-dependent addition of latrunculin-A. Finally, the perturbation of myosin II motors activity by inhibitory drugs (blebbistatin, Y27632) is cell type-dependent: it decreases the area expansion rate but does not significantly affect the final spreading area on T cells [70], whereas fibroblasts have higher spreading rate and final area upon myosin II inhibition [97].

1.1.4 Molecular clutch and adaptor proteins

The lamellipodium is a thin protrusion at the leading front of cells adhered to a flat substrate, made of a thin layer of a dense actin network enclosed by the plasma membrane, with two sub-populations of branched filaments mediated by Arp2/3 nucleation and linear filaments polymerized through formins [99]. This network has a very polarized structure, with most filaments oriented parallel to the substrate and their barbed ends (fastest polymerisation side) pointing towards the cell periphery (Fig. 1.4a), giving a roughly flat structure [100] with an usual thickness of 100 – 200 nm as it can be appreciated on Fig. 1.4b. At the leading edge, the actin network has a characteristic branched organisation with short filaments (called a dendritic network), a signature of Arp2/3 polymerisation which can be directly observed thanks to electron microscopy [99]. Formally speaking, lamellipodia do not contain myosin II minifilaments which are localized in the underlying region called the lamella [29], as shown on Fig. 1.4a. The contractile activity of the myosin motors pulls on the lamellipodial actin, which generates a retrograde flow of F-actin towards the cell center of the order of 1 – 100 nm/s [29, 97], with the additional help of membrane tension at the cell edge when actin polymerization is stalled. After the initiation at the cell periphery, retractions of the lamellipodium alternate with expansion phases [72] that are related to the transient coupling between adhesion complexes and the actin filaments, as well as the transport of myosin activators (MLCK) through the retrograde flow [81].

The actin retrograde flow interacts with the transient adhesion complexes through adaptor proteins like talin and vinculin, which generate traction forces (Fig. 1.4b) in a mechanism called the

⁹An old research article [94] claimed an early disruption of the actin cortex on the contact part of the cell that helps for area expansion by a bleb-like mechanism, but recent experiments seem incompatible with this statement: they justify the early spreading dynamics by a viscous-like dissipation coming from the actin cortex in the adhesive region [79, 95]. However, this mechanism may be compatible with T cell spreading [70].

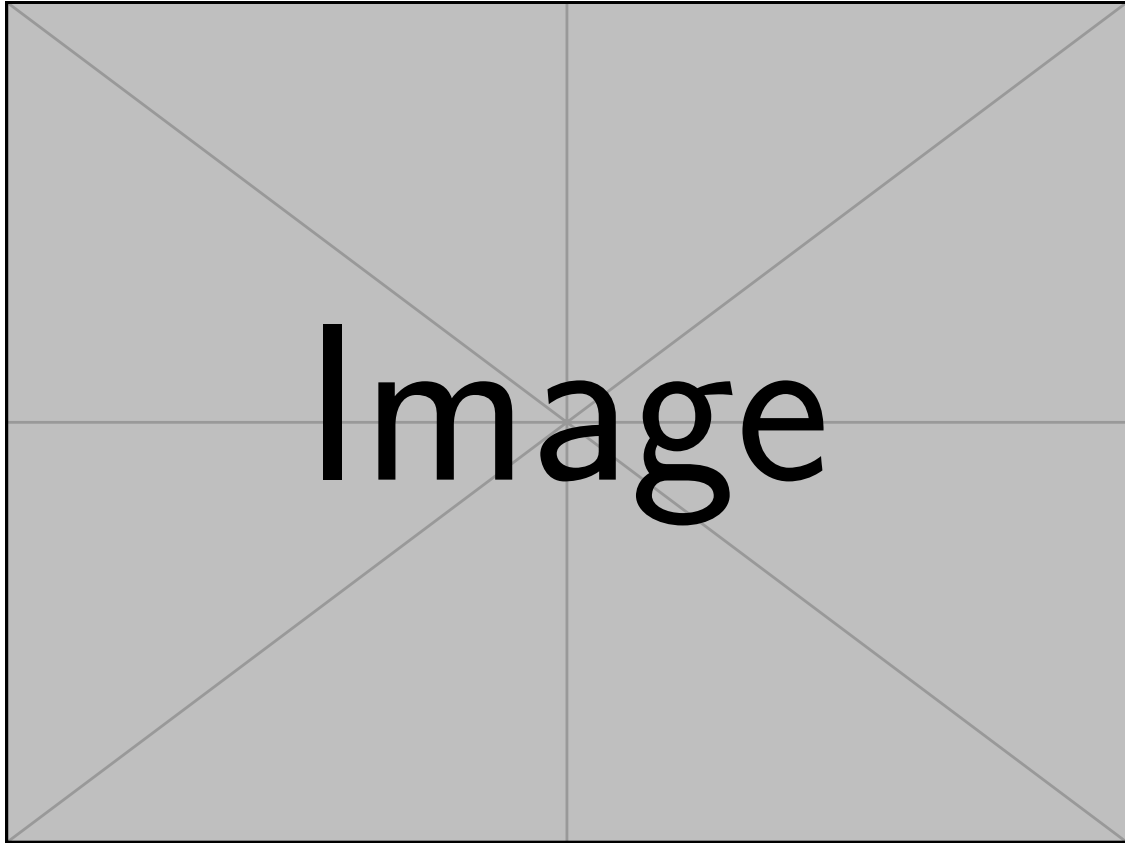


Figure 1.3: **(a)**: 3D representation of the cell edge dynamics for various angles, showing the anisotropic (left) and isotropic (right) classification. For the former, there are stochastic-like transient extension steps. For the later, there is a smooth extension before the appearance of similar but longer extension steps. From [80]. **(b)**: 3D reconstruction of a mouse embryonic fibroblast early spreading in the P_1 phase. Four membrane folds are visible in bright and decrease in size from left to right. The initiation time corresponds to the beginning of P_1 . From [75]. **(c)**: Total traction force generated by mouse embryonic fibroblasts upon cell spreading, measured by micro-pillar pattern deflection. A weak force of the order of 100 nN is generated during the initial (P_0) and early (P_1) phases of spreading, but a 5-fold increase occurs at the beginning of the late spreading phase (P_2). This probably indicates the assembly of stress fibres that exert contractile forces, transmitted to the substrate by their connexion to matured adhesion clusters (focal contacts). From [72]. **(d)**: F-actin fluorescent image of a mouse embryonic fibroblast, spread on a glass coverslip coated with fibronectin 90 minutes after cell attachment. Mature focal adhesions are developed at the cell periphery and are connected two-by-two by clearly visible stress fibres. There is a clear shape anisotropy in this late spreading stage. The scale bar is 10 μm . From [97]. **(e)**: Electron micrograph of a *Xenopus* endothelial cell in early spreading stage. One clearly distinguishes a thin protrusion at the cell edge with membrane ruffles, generating a sharp transition with the cell body shape. From [94]. **(f)**: Scanning electron microscope image of a mouse embryonic fibroblast in early spreading stage. There is no clear discontinuity between the cell body and the cell periphery, contrarily to (e). From [98].

"molecular clutch" (reviews [101, 102]) illustrated on Fig. 1.4c. The clutch corresponds to a transient mechanical link between bound adhesion receptors and the actin cytoskeleton. When the clutch is disengaged, the edge dynamics v_e is regulated by a balance between the polymerization rate v_p and the retrograde flow v_r such that $v_e = v_p - v_r$. This assumes a close proximity between the polymerizing filaments and the plasma membrane, where a sufficiently high membrane tension γ_m can stall the protrusion growth ($v_e = 0$) with the inverse relationship $v_p \propto 1/\gamma_m$ [103]. When the clutch is engaged, the linkage generates traction forces on the substrate (Fig. 1.4b) and reduces the retrograde flow¹⁰, making the leading edge protrude. Following [105] and neglecting the friction between unbound adhesion receptors and actin filaments, the horizontal force balance on an F-actin slice of size l and thickness h leads to $\zeta v_r l = \gamma_c + \gamma_m C_m h$, where γ_c is the myosin-dependent tension coming from the lamella, γ_m is the membrane tension, C_m is the membrane curvature, and ζ the actin-receptor friction coefficient (it contains the density of bonds). In principle, one should split the friction coefficient ζ in two components: one specific to the actin-substrate interaction ζ_{specific} , and the other for generic friction sources $\zeta_{\text{unspecific}}$ (other actin filaments, membrane-bound proteins) such that $\zeta = \zeta_{\text{specific}} + \zeta_{\text{unspecific}}$. This equation shows that both myosin contractility in the lamella and membrane tension at the tip contribute as sources of retrograde flow. The polymerization rate v_p is independently regulated by diffusion-limited transport of actin monomers, capping proteins and nucleator activators density at the leading edge. A stochastic approach for the molecular clutch modelling leads to various theoretical behaviours like a biphasic friction law and a stick-slip regime [104], both being observed experimentally depending on the substrate stiffness [106, 107].

Talin can bind to both actin and integrin receptors and its stretching opens cryptic sites for vinculin binding [108]. When integrins are bound to ECM ligands, the talin connexion allows force transmission to the substrate [109], and those traction forces are enhanced when active vinculins are recruited. The mechanosensitivity of the molecular clutch controls the maturation of adhesion complexes and generates a hierarchy of adhesion maturation away from the lamellipodial edge ([110, 111] and reviews [101, 102]). Whereas some integrin receptors are recruited at the cell periphery to produce new nascent adhesions, the "old" adhesions are transported away to mature into focal contacts, connected by actomyosin stress fibres (Fig. 1.4d).

1.2 Model: The adherent cortical vesicle

Starting from a roughly spherical shape in suspension, a cell spreading on a solid substrate needs to face important shape changes, in particular in the transition region between the adherent surface and the free one where the curvature is maximal. This shape evolution should affect the cellular cortex, known to be a major regulator of cell shape. Later on, many cells develop one or several flat membrane protrusions at their contact edge called the lamellipodia, filled with a branched actin network where filaments are oriented horizontally in average. We expect a "continuous" transition between the actin cortex and the lamellipodia, in the sense that the former progressively adapts to the nearby substrate and transforms its cytoskeletal network from a cortical structure to a lamellipodial one. A straightforward distinction between the two structures is the filament orientation, both isotropic in the membrane plane [87, 27] but strongly aligned in the horizontal direction for lamellipodia [115], whereas cortical filaments tend to be oriented parallel to the membrane [27]. The membrane tension likely contributes to the flatness of well-developed lamellipodia [116]. Since the architecture of the actin network is influenced by the geometry of the membrane from which it grows [8], but also affects the polymerization forces that modulate the shape [117], we clearly expect a coupling between shape evolution and actin cytoskeleton reorganization upon spreading. Despite a large interest for lamellipodium structure and dynamics [118, 119, 120, 121], the mechanisms involved in lamellipodium initiation and how it depends on the mechanical interactions between the plasma membrane, the actin network and the cell-substrate adhesions remain weakly understood. The goal of this work is to propose a minimal model of cell spreading with a mechanism for the

¹⁰It can be described as a stochastic binding/unbinding at the proteic level [104] or as a friction-like force at the mesoscopic scale [105] (mean-field approach).

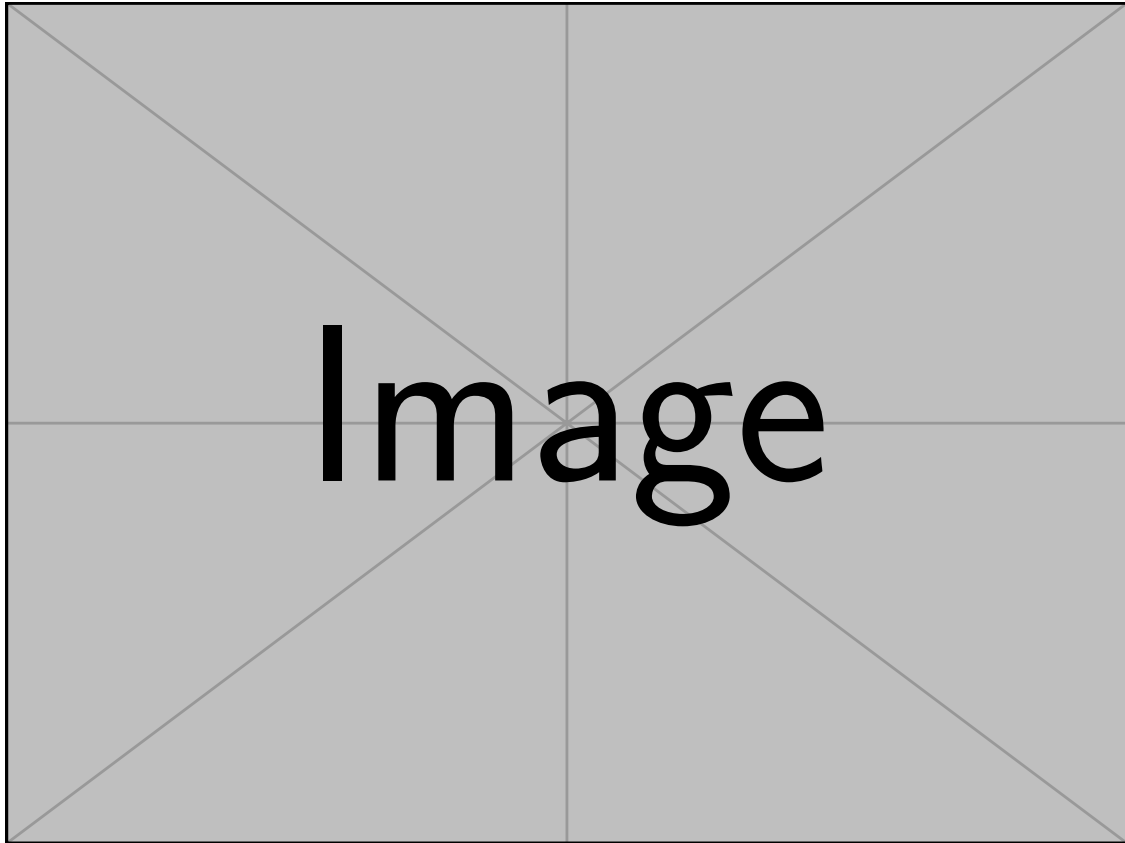


Figure 1.4: **(a)**: Quantitative fluorescent speckle microscopy of F-actin turnover in a migrating kidney cell. Polymerization (red) is dominant at the cell edge, whereas the highest depolymerization rate (green) is observed beneath. The growth rate is small in the lamella, and its boundary with the lamellipodium is defined as the second local maximum of net assembly. From [29]. **(b)**: Time-lapse of a spreading mouse embryonic fibroblast with a plasma membrane tag. Traction forces (color) are generated mostly behind the lamellipodium, with a slight out-of-plane component. The edge advances between 30 and 40 minutes but stops until 60 minutes when tractions increase, as expected by the molecular clutch model. From [112]. **(c)**: The molecular clutch model proposes that membrane tension essentially stalls actin polymerization (top), whereas the F-actin retrograde flow (driven by myosin contractility in the lamella) is reduced by transient connexion to nascent adhesions, resulting in slight front advancement (middle). The actin-integrin engagement through talin and vinculin generates traction forces on the substrate that promotes adhesion maturation and enhances both traction and forward edge motion (bottom). From [113] (license Creative Commons). **(d)**: Sketch of a migrating cell showing its structural polarity, with the lamellipodium and filopodia at the leading edge (red/brown) and nascent adhesions (blue points) underneath, whereas focal adhesions (blue rectangles) are localized from the lamella to the cell rear. Adapted from [114].

lamellipodium initiation based on this dialogue between cell shape and actin filament organization (Fig. 1.5).

1.2.1 A polarization vector field for cortical orientation

To this aim, one introduces a polarization field \vec{p} that consists of a mesoscopic average of individual filament orientation vectors \vec{p}_f over the side cortical plane (see Fig. 1.5a). By convention, the \vec{p}_f arrow is defined from the plus (barbed) end to the minus (pointed) end. Without precise knowledge of the cortical structure normal to the membrane, there is some ambiguity regarding the choice of the mesoscopic volume V_m over which \vec{p} is defined according to $\vec{p} \equiv \sum_{f \in V_m} \vec{p}_f$: it can contain the full network thickness, a slice of filaments close to the plasma membrane or be defined by a characteristic height combining the polymerization elongation rate $v_p \sim 1 - 10 \text{ nm/s}$ and the renewal time $\tau \sim 10 - 100 \text{ s}$ ($h = v_p \tau \sim 10 - 1000 \text{ nm}$). The polarization field \vec{p} is defined along a differential surface S that corresponds to the coarse-grained plasma membrane surface (elimination of high frequency fluctuations), which can be assimilated to a cellular surface of negligible thickness.

Since polymerization nucleators are activated by specific proteins (WASP, N-WASP, SCAR/WAVE, cortactin, ...) located at the plasma membrane (reviews [122, 123]), one expects a natural radial-like polarization where minus (depolymerizing) ends are located towards the cell center whereas plus (polymerizing) ends face the cell surface. This specific filament organization can be directly observed with electron microscopy, for example in the comet tail near the surface of *Listeria monocytogenes* where polymerization activators are expressed [124]. Without any preferred direction in the membrane tangential plane [27], the mesoscopic polarization vector \vec{p} is oriented normal to the membrane plane, towards the cell center (Fig. 1.5a). By stalling the pushing force from polymerizing filaments, the plasma membrane tension is expected to generate a permanent retrograde flow whose direction is tackled by the polymerization vector field \vec{p} , akin to network-scale treadmilling. However, note that the low cortical thickness makes hard to have direct experimental evidence for this normal actin flow, contrarily to measured turnover rates in the membrane plane [25]. One needs to extrapolate from the large scale retrograde flow observed at the tip of lamellipodia [29] from the known membrane localization of active polymerization nucleators.

However, no direct experimental evidence seems to confirm this normal actin flow for the cortex as the low thickness only gives access to tangential turnover rates [25], and

1.2.2 A Frank energy coupling membrane shape and actin orientation

In case of high membrane curvature (normal plane), adjacent retrograde flows need to deviate from the normal direction because of internal stress gradients. This tends to locally realign the polarization field, an observation that can be described using the visco-elastic cortical model from the active polar gel framework (review [125]). Since our modelling aims at preserving this effect without the introduction of complicated mathematics connecting the polarization field, the velocity field, the visco-elastic stress with the plasma membrane shape and mechanics, we propose a generic approach where a simple alignment of the local polarization field \vec{p} occurs for high membrane curvature (Fig. 1.5b).

In addition to this alignment effect, it is natural to expect symmetric reconfiguration of actin filaments with respect to the normal direction \vec{n} . This makes the normal orientation $\vec{p} = \vec{n}$ robust to fluctuations: a deviation from this preferred polarization develops a reaction force (as represented by little springs in Fig. 1.5b). For a spherical-like membrane containing an internal cortex, a local increase of curvature (concave) will generate compression costs by retrograde flow convergence in favour of a shift away from normal cortical orientation, whereas a negative curvature (convex) should stretch the cortex to favour a convergent shift from normal direction. We assume the physical description to be symmetric in (Gaussian) curvature sign and thus describe those stress-induced orientation shifts as a local alignment effect of the polarization field. This generic mechanism maps to the correct behaviour in the two situations by competition with normal anchoring, while remaining technically simple.

To account for both effects, normal membrane anchoring and local flow alignment in high curvature regions, we write an effective elastic energy density over the cell surface inspired by the Frank's energy of nematic liquid crystals [126, 127] and normal growth of actin shells on spherical beads [8]: actin flow alignment translates into a term proportional to the quadratic trace of the vector field surface gradient¹¹ $\propto (\text{Tr} \nabla_S \vec{p}(S))^2$, whereas the preferred normal orientation corresponds to an hookean energy cost $\propto |\vec{p}(S) - \vec{p}(S) \cdot \vec{n}(S)|^2 \equiv |\vec{p}_t|^2$. $S = (s_1, s_2)$ symbolizes a set of surface coordinates and $\vec{n}(S)$ is the normal vector to the membrane tangential plane. The summation of these local contributions to the mechanics of the entire cell cortex leads to the cortical energy over the cell surface:

$$E_{\text{cortex 3D}} = \frac{1}{2} \oint dS \left\{ k_\alpha |\vec{p}_t|^2 + \kappa_c (\text{Tr} \nabla_S \vec{p}(S))^2 \right\} \quad (1.1)$$

k_α is the anchoring stiffness and κ_c is an alignment coefficient that will be interpreted as an effective bending rigidity.

To limit the technical complexity of the approach, we only consider the membrane side plane as sketch in (Fig. 1.5) and do not take into account the ortho-radial direction (along the cell edge) of an axi-symmetric cell, which corresponds to a "2D" system invariant in the transverse direction with mirror symmetry. This approximation remains valid for a "3D" cell as long as the transverse edge curvature of the side plane is much larger than the contact edge curvature (in the orthoradial direction). Moreover, the analogy with nematic liquid crystals and its director field [126] is pursued by imposing a unit amplitude to the polarization field \vec{p}

$$|\vec{p}| = 1 \quad (1.2)$$

Although some interesting effects may contribute to the cortical energy through a term $\propto |\vec{p}|^2$, for example the impact of myosin II contractility that likely affects negatively the polarization field amplitude¹², we postpone this more sophisticated treatment to a future work. Indeed to describe this cortex-to-lamellipodium transition, we chose to only consider the coupling between network orientation and membrane geometry, without explicitly describing the complex interactions between the cortical entities of this mean field level description: concentration of motors and cross-linkers, cortical height, concentration of polymerization and depolymerization factors, concentration of monomers, etc...

Therefore, the cortical energy becomes only a function of the curvilinear abscissa s along the cell "line" interface, oriented by a local tangential vector $\vec{t}(s)$ and a local normal vector $\vec{n}(s)$. The deviation from the normal orientation can be represented by the scalar angular field $\theta(s)$ (see Fig. 1.5b), that will replace the unitary vector field $\vec{p}(s)$. $\theta(s)$ is defined positive when the tangential component of $\vec{p}(s)$ is towards increasing s . The previous assumptions greatly simplify the expression of the flow alignment term and the normal anchoring term, now expressed as a function of the orientation field $\theta(s)$ and the local curvature $C(s)$: one can easily show that $|\partial_s \vec{p}|^2 = [C(s) - \partial_s \theta(s)]^2$ whereas $|\vec{p}_t|^2 = [\sin \theta(s)]^2$. This explicitly shows the coupling between the membrane shape and the cortical orientation, meaning that a reorganization of the cortex mechanically affects the membrane whereas a shape change modifies the network architecture. A final assumption asks for weak deviations from normal anchoring to eliminate the non linearity of the field equations: $|\theta(s)| \ll 1$. One gets the final expression for the cortical energy (per unit of transverse length)

$$E_{\text{cortex 2D}} \simeq \frac{1}{2} \int ds \left\{ k_\alpha \theta^2(s) + \kappa_c [C(s) - \partial_s \theta(s)]^2 \right\} \quad (1.3)$$

¹¹This term corresponds exactly to the one constant model for the 2D director theory of a nematic shell [127].

¹²A network of filaments with normal average orientation can be almost tangential to the membrane plane (weak amplitude), or reach a configuration where all filaments are aligned along the normal direction (maximal amplitude). A local increase of myosin II activity that enhances network contractility is then expected to reduce the polarization field amplitude, providing a negative sign to the coefficient in the term $\propto |\vec{p}|^2$. This degree of freedom that may couple the polarization field to the myosin II concentration is not taken into account by our minimal model.

This elastic interfacial energy has a ground state with vanishing costs only for an open surface with a flat shape and normal anchoring, i.e. for $\theta(s) = 0$ and $C(s) = 0$. However if the surface is closed, a curvature necessarily exists and the two terms are antagonist: the cortical energy cannot vanish and a characteristic relaxation length $\lambda_c \equiv \sqrt{\kappa_c/k_\alpha}$ separates regions where alignment dominates from regions with normal anchoring. Indeed for a spherical cell in suspension, the radial symmetry imposes a normal orientation along the full contour ($\theta(s) = 0$) and the energy density becomes quadratic in the curvature $C(s)$. Thus, the alignment coefficient κ_c is interpreted as an effective bending rigidity for the actin cortex¹³.

1.2.3 Membrane mechanics and cell spreading

At the cell level, cell spreading involves shape changes (surface extension and curvature increase) that cost mechanical energy, whereas the extension of the adherent area generates a gain in adhesion energy. Those generic features have inspired a fertile analogy between cell spreading and liquid wetting [4, 86] but limited by different dissipation dynamics [79, 95] and additional spreading force [85]. A liquid droplet that wets a solid substrate reaches mechanical equilibrium when the Young-Dupré horizontal force balance $\gamma(1 + \cos \phi) = \epsilon$ is satisfied (see Fig. 1.5), with γ the liquid-gas surface tension and ϵ the adhesion energy density (review [128]). Depending on the ratio ϵ/γ , the liquid droplet can be in a state of dewetting ($\epsilon = 0$, $\phi = \pi$), full wetting ($\epsilon \geq 2\gamma$, $\phi = 0$), or partial wetting ($0 < \epsilon < 2\gamma$, $0 < \phi < \pi$). Those states will guide us as a transition pattern towards the emergence of a lamellipodium during cell spreading, within the quasi-static approximation. Even if the cell spreading is inherently a dynamical problem, we propose to describe the cell system with the use of static methods to obtain mechanical force balance through an energy minimization, and get the quasi-equilibrium states of a minimal cell. For *in vitro* experiments, the so-called isotropic spreading is often observed [80, 72] and one expects the cell to have an axial symmetry of rotation. Here, we study the spreading of a two-dimensional cell. Our conclusions are relevant to the spreading of three-dimensional cells in the limit where the radius of the adhered area is much larger than the radius of curvature of the cell edge. This is always the case in practice for a cell with well developed lamellipodia.

To account for the mechanical cost of cell shape changes, we use the classical Helfrich model [129] for the plasma membrane curvature energy, function of the mean curvature H and the gaussian curvature K and parametrized by two bending rigidities κ , $\bar{\kappa}$ and a spontaneous curvature C_{sp} :

$$E_H = \oint dS \left\{ \frac{1}{2} \kappa (2H - C_{\text{sp}})^2 + \bar{\kappa} K \right\} \quad (1.4)$$

The Gauss-Bonnet theorem relates the surface integral of the gaussian curvature to a topological invariant (the number of holes in the surface): for a closed surface without holes, this term only gives a constant proportional to $\bar{\kappa}$ and can be ignored for a spreading cell. In addition, the cell tension γ which combines membrane and cortical tensions is assumed constant all over the process and contributes to the free energy density by the constant γ . The plasma membrane tension has been shown to be regulated by membrane folds release [130] and exocytotic bursts during cell spreading to remain essentially constant [75]. Many regulations are possible on cortical tension, especially in cell spreading through integrin signalling or activation of mechano-sensitive channels by temporary membrane tension increase [131, 132], and a correct phenomenological law accounting for those effects would require an explicit description of additional elements (channels, pumps, ionic and signalling protein concentrations, etc..) that will darken the general effect we are searching for. Thus, the assumption of constant cell tension is a reasonable hypothesis in our minimal framework.

¹³Over a differential surface, the surface gradient of the normal vector $\vec{n}(S)$ is equal to (minus) the second fundamental form $\Pi(S) = -\nabla_S \vec{n}(S)$ such that its trace is twice the mean curvature H [127]. If the polarization vector field $\vec{p}(S)$ is oriented along the normal direction, the flow alignment term of the 3D cortical energy Eq. 1.1 $\propto (\text{Tr} \nabla_S \vec{p}(S))^2$ becomes $\propto (2H)^2$ and the bending rigidity interpretation for κ_c remains valid in 3D.

Cell adhesion is a complicated problem that relies on receptor activation, clustering and recycling, single ligand-receptor binding, membrane mechanics and connexion to the cytoskeleton [133]. Nevertheless, the free diffusive receptors provide a 2D osmotic pressure that acts as a constant adhesion energy density ϵ [134], at least in early cell spreading before the maturation of adhesion complexes and saturation of bound receptors. This contributes to the mechanical energy by a term $-\epsilon A_c$ where $A_c \equiv \pi L^2$ (Fig. 1.5) is the area of contact with the substrate.

To complete the spreading mechanics, a constraint on cell volume or a cytoplasmic rheological behaviour must be added. Even if some recent experiments have observed a decrease of cell volume upon spreading [135, 136], we choose to consider a fix volume for simplicity and are confident that our central results, based on a localized mechanism, are insensitive to this global constraint. This introduces a energy density $-\Delta P(V - V_0)$ with the Lagrange multiplier technique, where ΔP is the hydrostatic pressure difference with the environment, V is the cell volume and V_0 the target volume of the cell. From a thermodynamic point of view, the ensemble we use for cell spreading corresponds to the following assumptions over the system's accessible states: constant surface tension, constant adhesion energy density and constant volume, exactly like a wetting liquid droplet with negligible evaporation. The combination of the different energetic terms describes the spreading of a cell-like vesicle¹⁴ [137, 138]. If one adds the contribution from the 2D cortical energy Eq. 1.3 and transforms the energy Eq. 1.4 for a 2D vesicle [139], one obtains the total energy per unit of transverse length of a 2D cortical vesicle with adherent length $2L$ an target area A_0 :

$$E_{\text{tot}} = \frac{1}{2} \int ds \left\{ \kappa [C(s)]^2 + 2\gamma + k_\alpha \theta^2(s) + \kappa_c [C(s) - \partial_s \theta(s)]^2 \right\} - 2\epsilon L - \Delta P(A - A_0) \quad (1.5)$$

Contrarily to the 3D membrane mechanical energy Eq. 1.4, the spontaneous curvature C_{sp} is ignored. Although at first there is no formal reason to do so, we can eliminate it for two reasons. First, it doesn't have any active role in cell spreading and this reduces the number of free parameters. Second, we plan to describe a 2D system for which the spontaneous curvature does not enter into the membrane shape equations¹⁵ [139], which makes spontaneous curvature irrelevant in 2D. The second argument is wrong in 3D and only the first one can be used to simplify the analysis.

In addition to the cortical length $\lambda_c \equiv \sqrt{\kappa_c/k_\alpha}$, the membrane mechanics is controlled by the length $\lambda \equiv \sqrt{\kappa/\gamma}$. If this length is much smaller than the typical vesicle size, a separation of scales allows to describe approximately the spreading vesicle as a wetting droplet (see Fig. 1.5), characterized by an infinite curvature at the contact edge in the side plane. However, the presence of the cortical layer can modify this scaling by renormalizing the effective cell bending rigidity ($\kappa_{\text{cell}} = \kappa + \kappa_c$) in some situations described in the following chapter.

1.2.4 Traction force generation and leading edge advancement

Finally, the last ingredient of our model comes from the interaction between the cortical flow and the substrate, on the basal part of the cell locally adhered to ECM ligands by integrin receptors. Since the highest curvature of a spreading cell develops at the contact edge (see Fig. 1.5), the cortical energy Eq. 1.5 favours an alignment configuration in this local region. On the contrary, the cortical orientation remains normal near the center (Fig. 1.5) both because of symmetry and basal flatness. To connect the two regions with conflicting orientations, a relaxation of the polarization field occurs on a scale λ_c and forces a non-normal flow on the adherent region (as sketched in Fig. 1.5c). At a smaller scale, nascent adhesion complexes transiently connect to actin filaments thanks to adaptors proteins: talin first [109], followed by vinculin [108] during early cell spreading, whereas many other proteins accumulate upon adhesion maturation into focal contacts at the stage

¹⁴For a normal giant unilamellar vesicle, spreading on a flat substrate occurs at a fixed surface area (approximately inextensible membrane) that prevents any full wetting transition, and a fixed pressure difference or a fixed volume depending on the environmental osmolarity [137].

¹⁵The integration of the cross-term $C(s)C_{\text{sp}}$ along a closed line gives a shape-independent constant because the curvature is equal to the differential of the tangential shape angle $\psi(s)$ ($C(s) = d\psi(s)/ds$), whereas the quadratic term C_{sp}^2 can be absorbed in the arbitrary definition of the zero-point energy.

of late cell spreading. Indeed, traction forces generated on the substrate by early spreading cells are observed for the first tens of minutes¹⁶ for mouse embryonic fibroblasts [72] or endothelial cells [140]. In the same time range, the inhibition of talin expression prevents the generation of traction forces by cells on the substrate [141], showing the fast linkage between the actin cytoskeleton and bound adhesion receptors. At the mesoscopic scale, we propose to describe those traction forces as a frictional interaction between the actin retrograde flow v_r and adhesion complexes, which produces a net horizontal force (per unit surface) only if filaments have a non-normal orientation on the basal part of the spreading cell (see Fig. 1.5c). Therefore, we integrate all the stress contributions coming from the horizontal projections of the actin flows, from the central region ($s = 0$) up to the contact edge ($s = L$) to get the total force per unit of transverse length on the substrate f_s :

$$f_s = 2\xi v_r \int_0^L ds \sin \theta(s) \equiv 2\epsilon_s \quad (1.6)$$

The factor of 2 comes from the mirror symmetry of the spreading cell (Fig. 1.5d). The friction coefficient ξ is a mesoscopic parameter that emerges from the stochastic interactions of bound receptors with actin filaments [104, 142], dependent on linkers (lineic) density ρ_l , the effective stiffness of the complex k_l and the rate of detachment from the cytoskeleton k_{off} : $\xi \equiv \rho_l k_l k_{\text{off}}$. Note that this substrate-cytoskeleton interaction should also generate a torque on actin filaments that can be shown to renormalise the anchoring stiffness k_α .

This friction force f_s establishes cortical tension gradients on the ventral part of the cell as $\partial_x \gamma_{xx} = \xi v_r \sin \theta$ under the thin film approximation. If the orientation field θ remains localized at the cell periphery ($\lambda_c \ll L$) and vanishes at center, one expects the cortical tension to also relax at its natural value γ since the spreading time ~ 10 min let the cortex relax. The friction forces generates a tension drop at $x = L$ with $\gamma_{xx}(L) - \gamma = \epsilon_s$, with $\theta < 0$ by convention. On the other hand, there is no source of tension gradient on the non-adherent cortical region and the local tension balance can be written as an effective Young-Dupré equation at the leading edge (Fig. 1.5d), where the ventral tension component γ is replaced by $\gamma_{xx}(L)$. In this picture, the horizontal tension balance is equivalent to adding a supplementary adhesion energy density equal to ϵ_s in magnitude¹⁷. One gets the effective Young-Dupré equation of the spreading cortical vesicle:

$$\partial_L E_{\text{tot}} = \epsilon - \epsilon_f \int_0^L \frac{ds}{L_0} \sin \theta(s) \quad (1.7)$$

The frictional adhesion parameter $\epsilon_f \equiv \xi v_r L_0$ contains a generic length L_0 related to the 2D cell incompressibility. The minus sign in the equation only comes from the conventions used for s (positive here) and $\theta(s)$ (negative here), but the friction force promotes adhesion as does the generic term ϵ . They are resisted by $-\partial_L E_{\text{tot}}$, the generalized tension projection from the cortical vesicle that replaces the term $\gamma(1 + \cos \phi_{\text{eff}})$ of a normal liquid droplet, adding the effects of membrane rigidity κ and cortical elasticity through k_α and κ_c . Note that the energy E_{tot} only contains the constant cortical tension γ whereas the local cortical gradients are described separately.

This minimal description naturally asks for model extensions that remain technically challenging, to treat the interplay between the membrane mechanics and the actin flow, contractility, architecture and polymerization.

¹⁶Later on, a sharp transition occurs with the assembly of stress fibres and focal contacts, producing a 5-fold increase of traction forces [72].

¹⁷A more advanced analysis treats the tangential cortical flows coming from the substrate friction f_s , using a viscous rheology $\gamma_{xx} = 2\eta \partial_x v_x$. One can show that the tension drop at $x = L$ remains of the order of ϵ_s if dissipation is localized at the edge and $k_\alpha \ll \gamma$. In the next section, we will show that the constraint $k_\alpha \ll \gamma$ corresponds to the parametric region where interesting things happen.

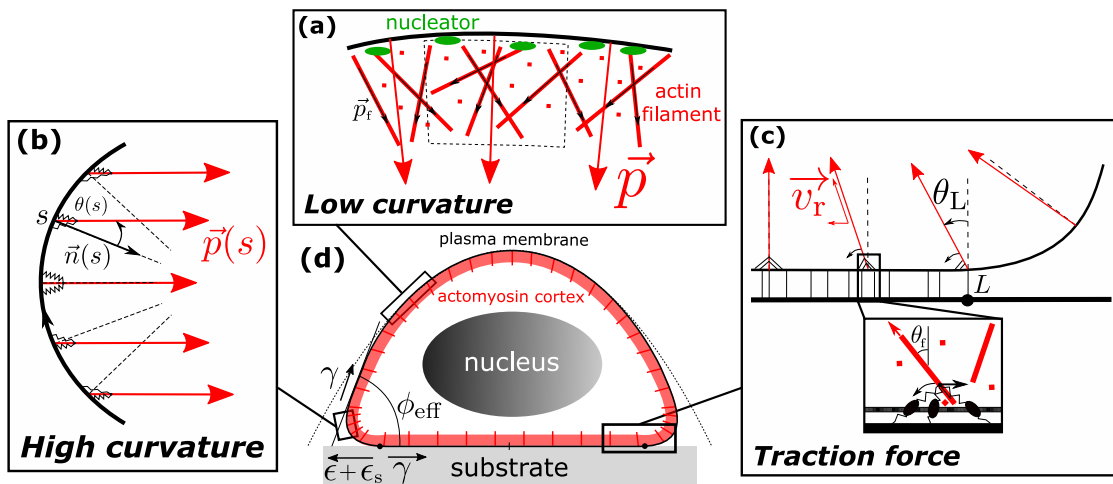


Figure 1.5: **(a)**: The actin cortex underneath the plasma membrane is described thanks to a polarization field \vec{p} as the mesoscopic average of individual filament polarization \vec{p}_i over the volume V_m : $\vec{p} \equiv \sum_{f \in V_m} \vec{p}_i$. At the filament population scale, the permanent actin polymerization induced by activators at the plasma membrane favours the proximity of plus (barbed) ends, and the absence of privileged direction in the tangential plane orient \vec{p} along the membrane normal direction \vec{n} when its curvature remains small. The membrane force resisting the polymerization force of actin filaments builds a retrograde flow following \vec{p} . **(b)**: In regions of high curvature like the edge of a spreading cell, the orientation of the polarization field $\vec{p}(s)$ (at the curvilinear abscissa s) deviates from the membrane's normal vector $\vec{n}(s)$ by an angle $\theta(s)$, to release the mechanical stress associated to gradients of actin retrograde flow. The cell shape is described by membrane mechanics, and must therefore be coupled to the cortical architecture. The polarization field $\vec{p}(s)$ is represented by "mesoscopic" filaments (red arrows) sampling the cortical orientation along the cell surface. Importantly, the transient cortex-to-membrane anchoring, assumed uniform, generates a reaction force towards normal orientation (black springs attached to the pseudo-filaments). **(c)**: The antagonist effects between flow alignment and normal anchoring propagate the deviation from the region of highest curvature to the flat adherent region (point L). The interaction of the actin retrograde flow (velocity v_r) with adhesion complexes attached to the substrate builds a net traction force, proportional to the horizontal projection of the flow. We assume that the filamentous network is sufficiently connected to transmit those traction forces to the cell edge and enhance spreading. **(d)**: Sketch of a spreading cell over a rigid substrate made of a membrane, a nucleus and an actin cortex with "mesoscopic" filaments representing the polarization field \vec{p} along the cell contour. The large scale orientation of the actin filaments is normal to the membrane (a) at the top and bottom of the cell, whereas the high curvature of the contact edge facilitates flow alignment (b). In analogy with liquid wetting, the cell contour makes an effective contact angle ϕ_{eff} with the substrate, which defines a force balance akin to Young-Dupr e equation between cell tension γ , adhesion strength ϵ and traction force density ϵ_s . The cell has a contact area (length) of radius (semi-size) L in 3D (2D).

1.3 Results: The adherent cortical vesicle

The two important equations of the last section, describing the spreading of a (2D) cortical vesicle, are the following:

$$E_{\text{tot}} = \frac{1}{2} \oint ds \left\{ \kappa [C(s)]^2 + 2\gamma + k_\alpha \theta^2(s) + \kappa_c [C(s) - \partial_s \theta(s)]^2 \right\} - 2\epsilon L - \Delta P (A - A_0) \quad (1.8)$$

$$\partial_L E_{\text{tot}} = \epsilon - \epsilon_f \int_0^L \frac{ds}{\sqrt{A_0}} \sin \theta(s) \quad (1.9)$$

It contains the membrane, cortical and adhesion energies with the (2D) incompressibility constraint, and the generalized Young-Dupré horizontal force balance supplemented by the transmission of traction forces to the leading edge extension through a frictional effective adhesion.

Before presenting the results obtained for the spreading of a cortical vesicle, we briefly discuss the Fourier spectrum for the perturbation of a flat membrane and or it differs from a simple membrane, then study the toy model of a cortical membrane wetting on a wedge to introduce the effect of the frictional adhesion on a simple geometry, and finally describe the spreading of a cortex-free vesicle to introduce some technical tools and facilitate the transition to the full problem.

1.3.1 Mechanical response in Fourier space

A natural way to understand the effects of the cortical terms in the energy Eq. 1.8 is to perform a Fourier transform on a weakly perturbed shape, freely embedded in a neutral fluid. Using the Monge representation and abscissa x for position indexation, $h(x)$ represents the membrane displacement with respect to the flat reference state and $\theta(x)$ the cortical deviation angle from the normal direction (vertical here). Weak deformations means $|h'(x)| \ll 1$ and $|\theta(x)| \ll 1$. Under those hypotheses, the energy reads up to quadratic order:

$$E_{\text{free}} = \frac{1}{2} \int dx \left\{ \kappa [h''(x)]^2 + \gamma [h'(x)]^2 + k_\alpha [\theta(x)]^2 + \kappa_c [h''(x) - \theta'(x)]^2 \right\} \quad (1.10)$$

From this energy, one may identify relevant length scales for the membrane deformation (λ) and the cortex orientation (λ_c) and dimensionless parameters (e and α) according to:

$$\lambda = \sqrt{\frac{\kappa}{\gamma}} \quad , \quad \lambda_c = \sqrt{\frac{\kappa_c}{k_\alpha}} = \lambda \sqrt{\frac{e}{\alpha}} \quad \text{with} \quad e = \frac{\kappa_c}{\kappa} \quad , \quad \alpha = \frac{k_\alpha}{\gamma} \quad (1.11)$$

The functional minimization in h and θ leads to the coupled equations

$$\lambda^2 (1 + e) h^{(4)}(x) - h''(x) - e \lambda^2 \theta^{(3)}(x) = 0 \quad (1.12)$$

$$\alpha \theta(x) + e \lambda^2 [h^{(3)}(x) - \theta''(x)] = 0 \quad (1.13)$$

Using Parseval's theorem, with the Fourier transforms defined as $h(x) = \frac{1}{\sqrt{2\pi}} \int dq e^{iqx} h_q$ and $\theta(x) = \frac{1}{\sqrt{2\pi}} \int dq e^{iqx} \theta_q$, the energy Eq. 1.10 reads

$$E_{\text{free}} = \frac{\gamma}{2} \int dq \left\{ \lambda^2 (1 + e) q^4 |h_q|^2 + q^2 |h_q|^2 + \alpha |\theta_q|^2 + \lambda^2 e q^2 (|\theta_q|^2 - 2iq h_q \theta_q^*) \right\} \quad (1.14)$$

The translation in Fourier space of the second equilibrium equation Eq. 1.12 gives $\theta_q = \frac{e \lambda^2 q^3}{\alpha + e(\lambda q)^2} i h_q$, such that the energy becomes in terms of the mode-dependent stiffness K_q

$$E_{\text{free}} \equiv \frac{1}{2} \int dq K_q |h_q|^2 \quad \text{with} \quad \frac{K_q}{\gamma} = \lambda^2 q^4 + q^2 + \alpha e \frac{\lambda^2 q^4}{\alpha + e(\lambda q)^2} \quad (1.15)$$

In the absence of cortex ($e = 0$, $\theta(x) = 0$), $K_q/\gamma = \lambda^2 q^4 + q^2$ as for a simple membrane: its mechanical response is dominated by bending rigidity at length scales smaller than λ and by the

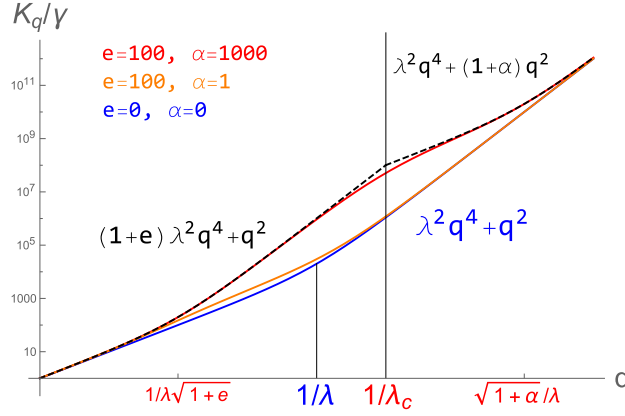


Figure 1.6: Log-Log plot of the linear elastic response of a cortical membrane to small deformations, quantified by the mode-dependent stiffness K_q of Eq. 1.15 in Fourier space. The pure membrane response is shown in blue, with a crossover between a tension-dominated response ($K_q \simeq \gamma q^2$) at low q ($\lambda q \ll 1$) and bending rigidity-dominated response ($K_q \simeq \kappa q^4$) at high q ($\lambda q \gg 1$). The limit of high anchoring $\alpha \gg 1$ is shown in red, and the limit of low anchoring in orange. The asymptotic regimes with effective rigidity $K_q \simeq \kappa(1+e)$ for $\lambda_c q < 1$ and effective “tension” $K_q \simeq \gamma(1+\alpha)$ for $\lambda_c q > 1$ are shown as dashed lines.

membrane tension at scales $1/q \gg \lambda$. As shown in Fig. 1.6, the cortex modifies the membrane properties at intermediate length scales between $\lambda/\sqrt{1+\alpha}$ and $\lambda/\sqrt{1+e}$ with a bending-dominated response $\sim \lambda^2(1+e)q^4$ for $\lambda_c q < 1$ and a tension-like response $\sim \gamma(1+\alpha)q^2$ for $\lambda_c q > 1$. Note that despite the tension-like response for $\lambda_c q > 1$, the parameter $\gamma_{\text{eff}} = \gamma(1+\alpha)$ cannot be interpreted as an effective tension because the cortical response lacks the first component of $\gamma(1+h'^2/2)$ acting on the unperturbed shape. On the other hand, the parameter $\kappa_{\text{eff}} = \kappa(1+e)$ correctly represents the concept of an effective bending rigidity and appears to be useful to describe the coupling between cortex orientation and membrane shape.

In the limit of free anchoring ($\alpha = 0$), the cortex is free to adapt to any shape deformation, controlled by $\theta'(x) = h''(x)$, and the response is that of a pure membrane $K_q/\gamma = \lambda^2 q^4 + q^2$, illustrated on Fig. 1.6 by the collapse of the orange curve on the blue one. As already discussed in the previous chapter, this large scale adaptation to membrane shape is only possible for open interfaces.

1.3.2 Toy model: cortical membrane wetting a wedge

To understand the properties of the equations Eq. 1.8, we studied a simple problem of a membrane with cortex wetting a wedge (see Fig. 1.7a). The wedge is parametrised by an angle ψ , small enough so that the membrane shape can be described by its height $h(x)$ using the Monge representation with $|h'(x)| \ll 1$, as in Eq. 1.10. The membrane has a free segment not touching the wedge if $|x| < L$ and a segment in contact with the wedge substrate for $|x| > L$, defining the penetration length L . From Eq. 1.10, the quadratic energy of the cortical membrane is:

$$E_{\text{wedge}} = \frac{1}{2} \int_0^L dx \left\{ \kappa (h'')^2 + \gamma (h')^2 + k_\alpha \theta^2 + \kappa_c (h'' - \theta')^2 \right\} \quad (1.16)$$

$$+ \frac{1}{2} \int_L^D dx \left\{ k_\alpha \theta^2 + \kappa_c (\theta')^2 \right\} + \gamma L + \gamma (D-L) \left(1 + \frac{\psi^2}{2} \right) \quad (1.17)$$

where $D \rightarrow +\infty$ is the (irrelevant) location of the adhered membrane edge. The minimization of the energy functional Eq. 1.16 with respect to the fields $h(x)$ and $\theta(x)$ leads to coupled linear equations Eq. 1.12 for the free membrane segment ($|x| < L$), which can be solved analytically. The shape and cortex orientation of the adhered membrane segment ($|x| > L$) satisfies $h(x) \simeq \psi x$ and $\lambda_c \theta''(x) - \theta(x) = 0$. The latter equation gives an exponential decay of cortical reorientation $\theta(x) = \theta_L e^{-(|x|-L)/\lambda_c}$, where the cortex orientation at the edge of the adhered region θ_L is an integration constant.

The solutions of Eq. 1.12, which involve six integration constants, must be supplemented by boundary conditions to close the problem. Mirror symmetry at $x = 0$ imposes $h'(0) = 0$, $h'''(0) = 0$, $\theta(0) = 0$. Continuity of the membrane shape at $x = L$ imposes $h(L) = \psi L$ and $h'(L) = \psi$. The last boundary condition is that of torque balance between actin filaments at $x = L$, which reads

$$(\theta' - h'')|_{x=L^-} = (\theta')|_{x=L^+} \quad (1.18)$$

where L^- and L^+ denote the free and adhered side of the boundary, respectively, and with $h''(x) = 0$ for $x > L$.

Once the membrane shape and the cortex orientation field are determined, the elastic energy E_{wedge} can be obtained, and the force balance equation¹⁸ $-\partial_L E_{\text{wedge}} = \epsilon + \epsilon_f \int_{\text{adh}} ds \sin \theta(s)$ can be solved to determine the equilibrium penetration length L^* .

Pure membrane without cortex

Without cortex, the free membrane is controlled by the equation $\lambda^2 h^{(4)}(x) = h''(x)$ with a solution parametrized by adhesion length L and membrane length λ :

$$h(x|L, \lambda) = \psi \left[L + \lambda \frac{\cosh(x/\lambda) - \cosh(L/\lambda)}{\sinh(L/\lambda)} \right] \quad (1.19)$$

The elastic energy associated to this configuration is $E_{\text{free}} = \frac{\psi^2}{2} \sqrt{\kappa \gamma} \coth(L/\lambda)$. It goes to infinity when $L \rightarrow 0$ since the curvature becomes infinite, whereas it relaxes to a constant when the membrane is largely de-adhered from the wedge ($L \gg \lambda$), and composed of two straight segments connected around $x = L$ by a curved region of curvature $\sim \psi/\lambda$. The equilibrium adherent length L^* is obtained by a force balance between membrane restoring force $f_m = -\partial_L E_{\text{wedge}}$ and adhesion $\epsilon(1 + \frac{\psi^2}{2})$, such that

$$L^* = \lambda \operatorname{arcsinh} \left(\frac{\psi}{\sqrt{2\bar{\epsilon} + \psi^2(\bar{\epsilon} - 1)}} \right), \quad \bar{\epsilon} \equiv \epsilon/\gamma \quad (1.20)$$

This equation exhibits a de-wetting transition; the system possesses a finite wetting state only if the condition $2\bar{\epsilon} + \psi^2(\bar{\epsilon} - 1) > 0$ is verified, equivalent to $\epsilon > \frac{\psi^2}{2 + \psi^2} \gamma$. If the adhesion energy density is smaller than this threshold value, the membrane does not wet the wedge.

Membrane with cortex

The traction force on the adherent part may be written as $f_t \simeq -\epsilon_f \int_L^\infty dx (1 + \frac{\psi^2}{2}) \theta(x) = -\epsilon_f \lambda \sqrt{e/\alpha} \theta_L (1 + \frac{\psi^2}{2})$ in the limit $\theta \ll 1$; hence, the force balance between the restoring force $f_{\text{mc}} = -\partial_L E_{\text{wedge}}$, adhesion $\epsilon(1 + \frac{\psi^2}{2})$ and the traction force f_t gives the equilibrium adherent length L^* :

$$f_{\text{mc}} - \left(\epsilon + \epsilon_f \lambda \sqrt{\frac{e}{\alpha}} \theta_L \right) \left(1 + \frac{\psi^2}{2} \right) |_{L=L^*} = 0 \quad (1.21)$$

where the cortex orientation angle at the adhering edge θ_L can be shown to be always positive. The traction force thus amounts to a supplementary adhesion strength which acts to reduce L^* . This is illustrated in Fig. 1.7c, where the cortical membrane restoring force, possessing the same asymptotic behaviour as a pure membrane, can be seen to diverge when $L \rightarrow 0$ as the curvature at $x = 0$ diverges in this limit, whereas the traction force in green increases the adhesion strength in black, which reduces the equilibrium length L^* and enhances membrane's wetting on the wedge.

A graph of the membrane profile $h(x)$ along the wedge is given on Fig. 1.7b. In the absence of traction force, the cortex essentially increases the rigidity of the membrane and thereby reduces the penetration inside the wedge (it increases the penetration length). Including the traction force generated by cortex reorganisation increases the adhesion force and enhances the membrane penetration inside the wedge. This can improve penetration beyond that of a pure membrane if the traction force amplitude ϵ_f is strong enough.

¹⁸There is a sign difference compared to the equation Eq. 1.8 because the problem is reversed: the orientation field is positive and the adhesion region is at high x values.

Supplementary results for a membrane wetting a wedge are shown on Fig. 1.7d,e,f. The equilibrium length L^* is expressed as a function of the reduced anchoring coefficient $\alpha \equiv k_\alpha/\gamma$ and the reduced cortical bending rigidity $e \equiv \kappa_c/\kappa$. Decreasing α promotes filament reorientation, increases the traction force, and favours wetting. In the limit $\alpha \rightarrow 0$, a complete parallel alignment of the cortex orientation is obtained, fixed by the angle of the wedge $\theta(x) = \psi$. In this limit, cortex reorientation propagates to infinity ($\lambda_c \rightarrow \infty$), yielding a diverging traction force able to compensate for the infinite wedge curvature at center, to generate full wetting: $L^* \rightarrow 0$. Increasing e at fixed α may show a non-monotonic behaviour. For $e \rightarrow 0$, the membrane is decoupled from the cortex and the wetting length is that of a pure membrane. As e increases, cortical bending rigidity may decrease adhesion (increase of the penetration length L^*), but a further increase of e allows for cortex reorientation and the appearance of a traction force able to dominate the rigidity effect of the cortex so that it increases wetting (decrease of L^*). When e becomes infinite, the cortical orientation adapts perfectly to the shape and one recovers the global alignment that produces an infinite traction force, and again $L^* \rightarrow 0$.

Finally, the supplementary adhesion provided by the traction force can trigger a stability transition according to Fig. 1.7f: when non-specific adhesion should imply a non-adhered state of the pure membrane, it is possible to find one stable and one unstable equilibria in a narrow region of the parameter space $(e, \alpha, \epsilon_f \lambda/\gamma)$, such that a perturbation around the stable solution could drive a de-wetting transition ($L^* \rightarrow \infty$).

1.3.3 Adhesion of a cortex-free vesicle

Now we describe in details the spreading properties of a simple membrane without cortex. Unlike previous work on the adhesion of vesicles [137, 139, 138], which are passive membrane bags with a fixed area, the membrane of living cells is not isolated. It exchanges area with cytoplasmic membrane reservoirs by way of exocytosis/endocytosis and regulate other membrane invaginations located at the cell surface ([75, 78] and review [77]). In this case, rather than fixed area, a fixed membrane tension is more appropriate.

The regulation of cellular volume during cell spreading is a rich scientific question that remains at a preliminary stage both experimentally and theoretically [135, 136]. Here, we choose to consider that the cell volume remains constant. One reason for this assumption is simplicity; the other natural thermodynamic ensemble would be an object under constant pressure, but this does not yield stable states even for non-adhering cells if the membrane tension is fixed. Short of choosing a particular, and rather arbitrary relationship between pressure and volume, we thus adopt the fixed volume ensemble.

Assessment of the shape parametrization

The force balance equation describing cell spreading Eq. 1.8 requires the computation of the shape of the adhering cell, which can be obtained through a functional minimisation of the cell's elastic energy Eq. 1.8. Owing the strong cell deformation accompanying spreading, this must be done numerically: this is tractable for a pure membrane without cortex, but becomes much more involved when the shape is coupled to the cortical orientation field θ . To simplify the technical description, we use a shape parametrization approach justified by the length scale separation between the membrane scale λ and the vesicle size [138], where the cell shape is decomposed into three distinct regions: a flat adhered zone of length L , a highly curved edge with a constant radius of curvature R_e and opening angle ψ_e , and a spherical cap of curvature C_0 (see Fig. 1.8a). Continuity of the interface position and slope leaves three independent parameters: L , R_e and C_0 .

Calling \mathcal{L}_0 and \mathcal{L}_e the arc-lengths of the spherical cap and the curved edge, and A the area of the object, the system's energy reads:

$$E(L, C_0, R_e, \Delta P|\kappa, \gamma, \epsilon) = \frac{\kappa}{2} \left(\frac{\mathcal{L}_e}{R_e^2} + C_0^2 \mathcal{L}_0 \right) + \gamma(L + \mathcal{L}_e + \mathcal{L}_0) - \Delta P(A - A_0) - \epsilon L \equiv E_m - \epsilon L \quad (1.22)$$

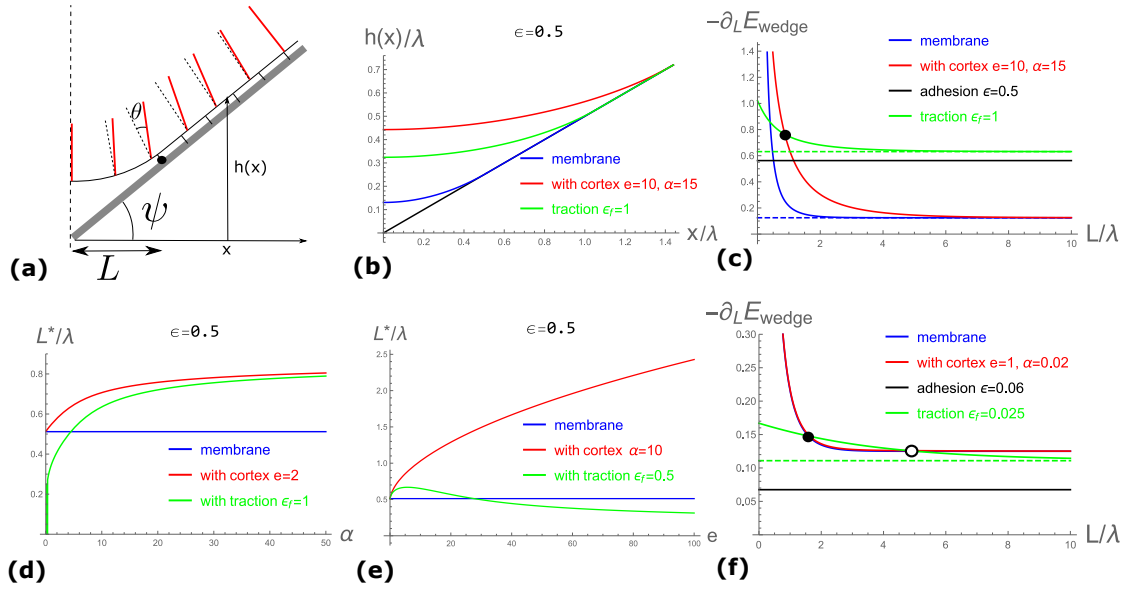


Figure 1.7: *Wetting of a wedge.* Blue curves correspond to a pure membrane, red curves to a membrane with a cortex, and green curves to a membrane with cortex exerting traction forces on the substrate. Inclination $\psi = 0.5$. **(a)**: A membrane adhering on a wedge with a small inclination (excessive to facilitate visualisation) of angle ψ and an actin cortex underneath described by the orientation angle field $\theta(x)$. There is an implicit mirror symmetry across $x = 0$ and all quantities are expressed per unit of transverse length when necessary. **(b)**: Membrane profile along the wedge for a pure membrane, a membrane with a cortex without traction force, and including the traction force. The cortex rigidifies the membrane whereas the traction force improves wetting on the wedge. **(c)**: Restoring force ($\partial_L E_{\text{wedge}}$ - red), constant non-specific adhesion force (ϵ - black) and full adhesion force containing the traction force (green). **(d)**: Equilibrium penetration length L^* as a function of α with $e = 2$. The cortex rigidifies the membrane and reduces the wedge penetration, whereas the addition of traction forces enhances it. The limit $\alpha \rightarrow 0$ corresponds to a global alignment of the orientation field over the infinite adherent region, providing an infinite traction force towards total wedge penetration. **(e)**: L^* as a function of e with $\alpha = 10$. On one hand, the limit $e \rightarrow 0$ corresponds to a decoupling between shape and orientation fields, with normal anchoring not contributing to traction force generation, such that only the membrane elasticity and adhesion energy density contribute. On the other hand, the limit $e \rightarrow +\infty$ means a "perfect match" between shape and orientation with global alignment, producing an infinite traction force able to drive a total wedge penetration. **(f)**: Graphical representation of force balance with the appearance of bistability in a narrow region of parameter space. Stable and unstable solutions are represented by black and white dots respectively. An adequate perturbation around the stable equilibrium may trigger a dewetting transition with full membrane detachment from the wedge ($L \rightarrow +\infty$).

where the energy (per unit of transverse length) and lengths can be written in units γL_0 and L_0 respectively, with $A_0 \equiv L_0^2$ the total area, assumed constant. ΔP is a Lagrange multiplier corresponding to the pressure difference between the inside and outside of the vesicle and enforcing constant area: $\bar{A} = 1$. In the following, the symbol $\bar{\cdot}$ will denote a dimensionless parameter: $\bar{\lambda} \equiv \lambda/L_0$ and $\bar{\epsilon} \equiv \epsilon/\gamma$.

Equilibrium shapes for a given adhered length L are obtained by solving the algebraic equations $\partial_{C_0} E = \partial_{R_e} E = \partial_{\Delta P} E = 0$ to obtain $C_0(L)$, $R_e(L)$ and $\Delta P(L)$. Plugging these expressions back into Eq. 1.22 yields the membrane restoring force $\partial_L E_m(L)$. Its variation with the adhesion length L calculated from this parametrization agrees well with the one calculated numerically using a shooting algorithm (see Fig. 1.8b). In particular, it shows that the non-monotonic behaviour of the restoring force, indeed due to bending rigidity, is not an artefact from the parametrization. Force balance at the adhesion edge reads $\partial_L E_m(L) = \epsilon$. The equilibrium edge radius of curvature R_e also agrees well with its theoretical value obtained from torque balance at the contact point ($s = L$), given by $1/R_e = \sqrt{2\epsilon/\kappa}$ [139] or $1/\bar{R}_e = \sqrt{2\bar{\epsilon}/\bar{\lambda}}$ (Fig. 1.8c-d). We thus conclude that our geometric parametrization is reasonable and allows us to simplify the study of a bound vesicle without losing much information about its equilibrium state.

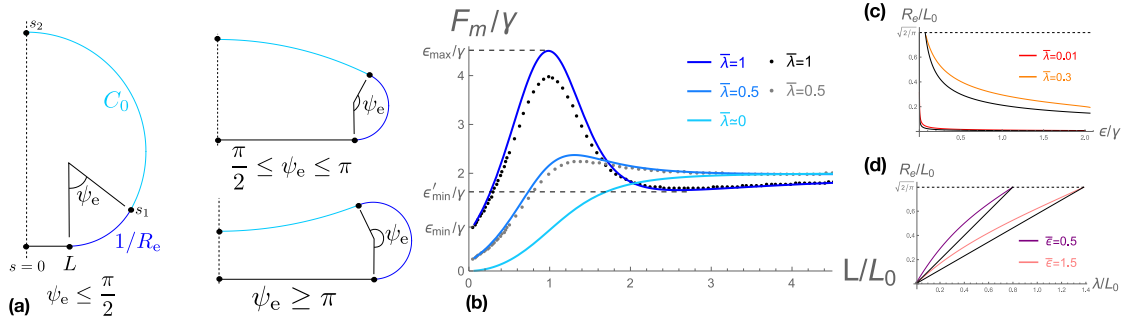


Figure 1.8: **(a)**: Vesicle parametrization with an adherent length L , a contact curvature $1/R_e$ for $L < s < s_1$ and a spherical cap of curvature C_0 between $s_1 < s < s_2$, where s is the curvilinear coordinate whose origin is localized at the center of the adherent region. Three characteristic shapes classified by the edge opening angle ψ_e are shown. **(b-d)**: Comparison between the results given by the shape parametrization (color) and exact numerical solution (black or gray) for **(b)** Membrane restoring force $\partial_L E_m \equiv F_m$ as a function of L with threshold values $\{\epsilon_{\min}, \epsilon'_{\min}, \epsilon_{\max}\}$, and contact radius of curvature R_e **(c)** as a function of ϵ and **(d)** as a function of λ .

Vesicle adhesion equilibrium and phase diagram

The force balance $\partial_L E_m = \epsilon$ can be solved graphically for given parameters λ and ϵ by finding the intersection point $\{L^*(\lambda, \epsilon), \epsilon\}$ of the curve $\partial_L E_m(L)$ with the straight line ϵ , as shown in Fig. 1.9a. If the bending rigidity is negligible ($\lambda \rightarrow 0$), the problem is equivalent to the wetting of a small liquid droplet (for which gravity can be neglected): the wetting transition is continuous for $\epsilon \geq 0$, and a transition to full-wetting appears at $\epsilon = 2\gamma$, as predicted by the Young-Dupré relation $\gamma(1 + \cos \phi) = \epsilon$. However, if $\lambda \neq 0$, the restoring force exhibits qualitatively different features, as shown in Fig. 1.8b and Fig. 1.9a. A minimum value of the adhesion energy is required to initiate the adhesion transition¹⁹ [137, 139]: a small deformation expansion around the circular shape yields $\epsilon_{\min} = \pi\kappa/(4L_0^2)$. Moreover, the membrane restoring force may exhibit a maximum at finite adhesion length L_{\max} (defined on Fig. 1.9a). Inspection of the vesicular shapes as a function of ϵ (see insets in Fig. 1.9a), shows that the maximum of the membrane restoring force corresponds to shapes where $\psi_e \simeq \pi$ ($C_0 \simeq 0$). This is followed by a local minimum for larger L (see Fig. 1.8b), and the restoring force $\partial_L E_m \rightarrow 2\gamma$ in the limit $L \rightarrow \infty$. Note that due to the analytical expression of the incompressibility constraint on the area, one formally allows non-physical shapes that cross themselves. They appear to minimize the energy Eq. 1.22 beyond a threshold adhered length $L_{h=0}$, for which the vesicle's central height h vanishes (see Fig. 1.9a). We find $L_{h=0} \sim 200$ when $\lambda/L_0 = 10^{-2}$ and $L_{h=0} \sim 4$ when $\lambda/L_0 = 1$. Implementing steric constraints could solve this problem and lead to a "final" shape with a flat central section of vanishing area flanked by two droplets at the edges. This is not required here since we are interested in the transition to full adhesion, defined by the adhesion threshold $\epsilon > \epsilon_{\max}$ that do not rely on shapes with $h < 0$ (see below). For a spreading cell, the nucleus stiffness would resist further decrease of central height when it reaches the nuclear size [143]. This is not to be incorporated in the model to remain minimal: the important results are independent from this effect, believed to be important only for high spreading states.

Fig. 1.9b presents the vesicular adhesion phase diagram on parameter space $\{\lambda/L_0, \epsilon/\gamma\}$, where six different phases are present. Three of them possess a single state: Non-adherent vesicles (N) if $\epsilon < \epsilon_{\min} = \pi\kappa/(4L_0^2)$, Partial adhesion (P) if $\epsilon_{\min} < \epsilon < \epsilon'_{\min}$, and Full adhesion (F) if $\epsilon > \epsilon_{\max}$. The three other phases define bistable regions with one unstable state ($\partial_L^2 E_m < 0$) and two "stable" states. In phase (BS0), for $\epsilon'_{\min} < \epsilon < \epsilon_{\min}$ where ϵ'_{\min} is defined as the local minimum of the membrane resisting force (Fig. 1.8b), one stable state is non-adhered and the other is partially

¹⁹Although the 2D transitions are independent of the spontaneous curvature parameter C_{sp} [139], one can realize that the exact 2D invariant $\oint ds C(s)$ is shape-dependent in the parametrization framework. This makes the adhesion transition artificially dependent on C_{sp} and shouldn't be trusted quantitatively. For example, according to [139] the correct adhesion threshold seems to differ by a factor of 2: $\epsilon_{\min} = \pi\kappa/(2L_0^2)$.

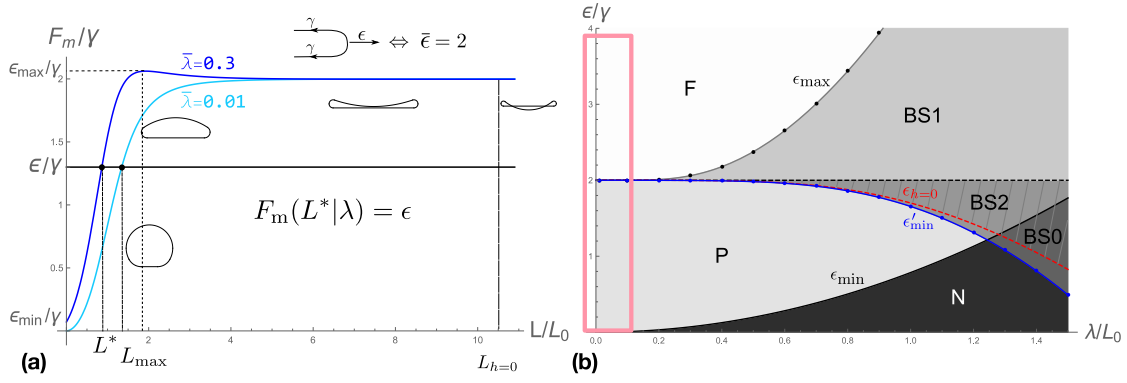


Figure 1.9: **(a)**: Graphical resolution of the equilibrium shape by equating the adhesion strength ϵ to the restoring membrane force $\partial_L E_m \equiv F_m$. The threshold adhesion energy density required to initiate vesicle spreading ϵ_{\min} , and the maximum restoring force ϵ_{\max} are shown in the case $\bar{\lambda} = 0.3$ where there are clearly visible. **(b)**: Phase diagram of a planar adhering vesicle at fixed area as a function of the dimensionless membrane scale (λ/L_0) and adhesion strength ϵ/γ . The transition from Non-adhered (N) to Partial adhesion (P) is given by $\epsilon_{\min} = \pi\kappa/(4L_0^2)$. A Full adhesion state (F) with $L \rightarrow \infty$ exists if $\epsilon > 2\gamma$, and is the unique "equilibrium" state if $\epsilon > \epsilon_{\max}(\lambda)$. (BS1) is a region where there is bistability between partial and full adhesion. (BS2) is a region where there is bistability between two partial adhesion states, for $\epsilon'_{\min} < \epsilon < 2\gamma$, where ϵ'_{\min} is defined on Fig. 1.8b. The shaded grey region for $\epsilon_{h=0} < \epsilon < 2\gamma$ is a region where the physical shape crosses itself (unphysical) and where additional steric constraints would need to be implemented. This includes the bistable region (BS0) where there is bistability between non-adhered and partially adhered states. The pink square represents a physiological range of parameters for our system of interest, a cortex-free cell identified to a giant unilamellar vesicle connected to a membrane reservoir.

adhered. In phase (BS1), for $2\gamma < \epsilon < \epsilon_{\max}$, one stable state is partially adhered and the other is fully adhered. Finally in phase (BS2), for $\text{Max}[\epsilon_{\min}, \epsilon'_{\min}] < \epsilon < 2\gamma$, the two stable state are partially adhered. Note that the dashed region of the phase diagram between the curves $\epsilon = 2\gamma$ and $\epsilon = \epsilon_{h=0}$ indicates that one partially adhesive state is unphysical, with negative central height.

The description of the phase diagram above has been introduced for completeness, but the details regarding the non-monotonic force-extension curve (Fig. 1.9a) that generates bistability are probably sensitive to our choice of thermodynamic ensemble (constant 2D-volume and constant membrane tension). On Fig. 1.9 b, the expected range of physiological parameters, shown as a pink square, is confined to small values of $\bar{\lambda} = \lambda/L_0$: for a fictitious cortex-free cell akin to a giant uni-lamellar vesicle connected to a membrane reservoir, $\lambda \sim 100$ nm and $L_0 \sim 10$ μm such that $\bar{\lambda} \sim 10^{-3}$. For such parameters, the adhesion phase diagram is fairly simple, with only partial and full spreading states, and can be used as a good basis to evaluate the feedback between cortex orientation and cell spreading.

1.3.4 Spreading of the cortical vesicle

After the study of a toy model designed for the linearisation thanks to a weakly inclined wedge, penetrated by a flat cortical membrane, and the assessment of a shape parametrization that mimics quite well the non linear differential equations of a vesicle spreading (in our "cell" ensemble), the previous tool can be re-used for the full system of a cortical vesicle. As a reminder, the spreading equilibrium states are described by the minimization of the total free energy subjected to area incompressibility

$$E_{\text{tot}} = \frac{1}{2} \int ds \left\{ \kappa [C(s)]^2 + 2\gamma + k_\alpha \theta^2(s) + \kappa_c [C(s) - \partial_s \theta(s)]^2 \right\} - 2\epsilon L - \Delta P (A - A_0) \quad (1.23)$$

, supplemented by a generalized Young-Dupré force balance between the cortical membrane restoring force, the adhesion energy density and the traction force generated by the coupling between the non-vertical cortical flow of the adherent region with the adhesion complexes, akin to a friction

force at the mesoscopic scale [105]

$$\partial_L E_{\text{tot}} = \epsilon - \epsilon_f \int_0^L \frac{ds}{\sqrt{A_0}} \sin \theta(s) \quad (1.24)$$

With axial symmetry, only the half-cell defined by the central axis of symmetry needs to be considered.

Parameter estimates

The mechanical parameters of the model $\{\kappa, \gamma, \epsilon, \kappa_c, k_\alpha, \epsilon_f\}$ and the cell size L_0 can be estimated for physiological conditions. One expects $\kappa \sim 10 - 25k_B T$ [144], $\gamma \sim 10^{-5} - 10^{-3} \text{ N/m}$ [34], such that $\lambda \lesssim 100 \text{ nm}$, $\epsilon \sim 10^{-5} \text{ N/m}$ [145, 79], and $\kappa_c \sim 200 - 1000k_B T$ [145]. Choosing a characteristic cell size $L_0 \sim 10 \mu\text{m}$, we fix the dimensionless membrane length scale to the small value $\bar{\lambda} \equiv \lambda/L_0 = 10^{-2}$ and the dimensionless cortex rigidity to a large value $e \equiv \kappa_c/\kappa = 10^2$. The reduced adhesion strength $\bar{\epsilon} \equiv \epsilon/\gamma \sim 10^{-2} - 1$ is expected to be around 0.1 or less.

The "anchoring strength" $\alpha = k_\alpha/\gamma$ is considered as a control parameter because it is difficult to estimate from current data, since it depends on the coupling between actin filaments and the membrane at the molecular scale, but also on the cortex structure (and hence is not strictly independent of κ_c). At the scaling level, the anchoring stiffness should satisfy $k_\alpha \simeq k_a l_a^2 \rho_a$, where $k_a \sim 1 - 10 \text{ pN/nm}$ is a stiffness of membrane-actin anchors, $l_a \sim 3 - 10 \text{ nm}$ is their characteristic length, and $\rho_a \sim 10^2 - 10^3/\mu\text{m}^2$ is the 2D density of anchoring points on the tangential plane. This gives a broad range $k_\alpha \sim 10^{-6} - 10^{-3} \text{ N/m}$, or $\alpha \sim 10^{-3} - 10^2$.

The maximal traction force density is of order $\epsilon_f \simeq \rho_l k_l v_r / k_{\text{off}}$, where ρ_l is the density of ligand between actin and the substrate, k_l their stiffness, k_{off} their unbinding rate and v_r the actin retrograde flow velocity [104]. With $\rho_l \sim 10/\mu\text{m}^2$, $k_l \sim 1 \text{ pN/nm}$, $k_{\text{off}} \sim 0.1 - 1/\text{s}$ and $v_r \sim 1 - 10 \text{ nm/s}$, we find $\epsilon_f \sim 10 - 10^3 \text{ Pa}$, which agrees well with the typical traction force density measured in spreading cells [140, 72], and $\bar{\epsilon}_f \sim 10^{-1} - 10^2$.

Equilibrium cortical orientation for given shape

The shape and cortical orientation of a spreading cell can be obtained for a given adherent length L by minimizing the cell's mechanical energy Eq. 1.23 with respect to the local curvature $C(s)$ and cortical orientation $\theta(s)$. As sketched in Fig. 1.10a, we parametrize the cell shape by a flat region for $0 \leq s \leq L$, an edge of constant curvature C_e for $L \leq s \leq s_1$, and a spherical cap of curvature C_0 for $s_1 \leq s \leq s_2$. The segmentation of the curvature field $C(s)$ by geometric variables facilitates the energy minimization and gives a differential equation for the local cortex orientation, as in Eq. 1.12 with $\partial_s C = 0$:

$$\lambda_c^2 \partial_s^2 \theta(s) = \theta(s) \quad (1.25)$$

The equilibrium polarization field is obtained with appropriate boundary condition of torque balance - continuity of $(\partial_s \theta - C)$ - at curvature discontinuities ($s = L$ and $s = s_1$), and normal cortical orientation at the cell centre imposed by axial symmetry ($\theta(0) = \theta(s_2) = 0$). The energy resulting from the injection of the equilibrium polarization field into Eq. 1.23 is minimised with respect to the geometric variables C_e and C_0 for a given L .

Representative cortical profiles are shown in Fig. 1.10b. Cortex reorientation (deviation from the normal direction) is maximal near the cell edge ($s = L$) where curvature gradients are large. It decays over the length scale $\lambda_c \equiv \lambda \sqrt{e/\alpha}$ (Eq. 1.25). For large L , the maximal reorientation θ_L and the curvature of the edge C_e can be approximately obtained by requiring that the curvature saturates at the inverse length scale $C_e \approx \sqrt{2\gamma/\kappa_{\text{eff}}(C_e)}$, where $\kappa_{\text{eff}}(C_e)$ is a scale dependent effective bending rigidity that decreases upon cortex reorientation, itself increasing with the curvature (as in Eq. 1.15, see S.I.). This leads to the asymptotes $\lambda C_e \approx \sqrt{2/(1+e)}$ and $|\theta_L| \approx 1/\sqrt{2\alpha}$ for strong anchoring $\alpha \gg 1$ that makes reorientation weak and localized, whereas the opposite occurs for weak anchoring $\alpha \ll 1$ since $\lambda C_e \approx \sqrt{2}$ and $\theta_L \approx -\pi/2$, see Fig. 1.10b,c.

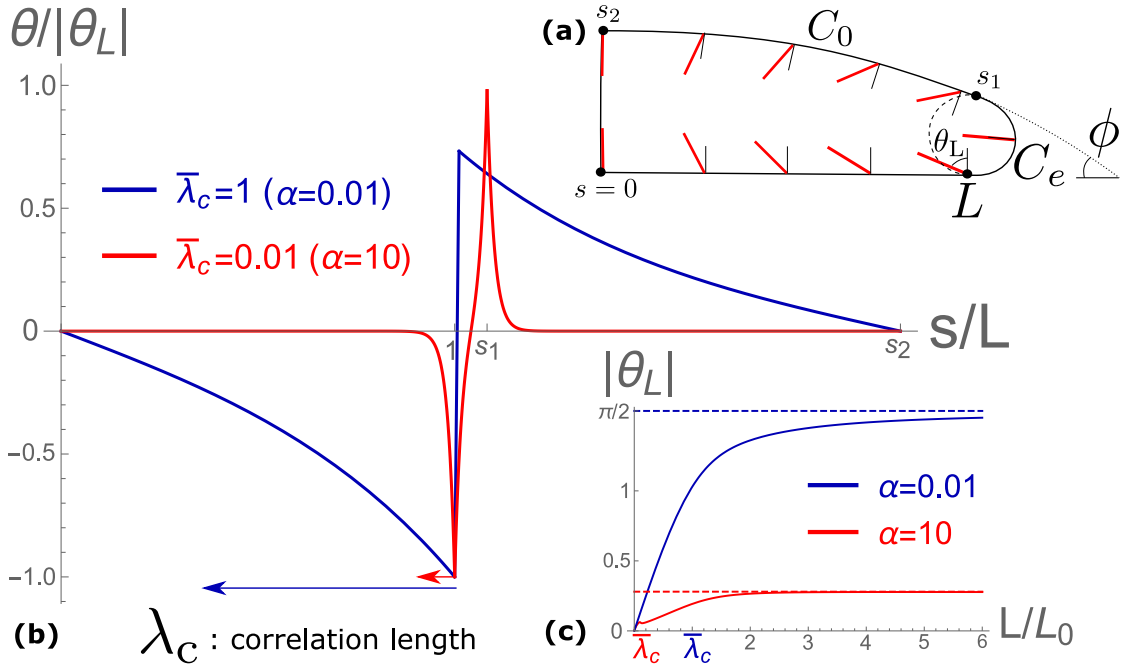


Figure 1.10: (a): Sketch of a cortical vesicle with parametrization of the membrane shape given by an adherent length L ($0 < s < L$), an edge curvature C_e ($L < s < s_1$) and a cap curvature C_0 ($s_1 < s < s_2$), with an illustrative cortical orientation profile. The alignment occurs in the region of highest curvature and induces a non-zero deviation at contact point $s = L$ of angle θ_L , here negative in the adopted convention. A vesicle of negligible bending rigidity would form a contact angle ϕ with the substrate and spread as a liquid droplet. (b): Normalized orientation field θ along the cell membrane as a function of arc-length s for weak (orange) and strong (red) anchoring, which shows the strong differences of relaxation scale, controlled by the correlation length λ_c . The geometric variables $C_0(L)$ and $C_e(L)$ have been minimized for a fixed adherent length $L = 1.8L_0$. (c): Cortical reorientation amplitude at contact point $|\theta_L|$ as a function of L for the situation described in (b). In addition to scale relaxation, a weak anchoring (orange) generates a strong deviation from the normal direction, up to $\pi/2$ in the limit $\alpha \rightarrow 0$. Parameters are $\bar{\lambda} = 10^{-2}$ and $e = 100$.

The addition of a cortical layer to the spreading vesicle (previous section) adds one special feature. The system of a cortical membrane penetrating a wedge (previous section) already illustrated the increase of the effective bending rigidity of the interface to hinder penetration at low membrane curvature, and an increase of the traction force due to filament reorientation to promote penetration at high curvature (Fig. 1.7e). Nevertheless, it was only partially representative of the cortical effects mostly because of the interface was naturally open, whereas the cortex belongs to a close surface during cell spreading. In particular, this impedes the "perfect" flow alignment ($\partial_s \theta(s) \sim C(s)$) when the anchoring rigidity k_α vanishes because of conflicting orientations. In that case, whereas the filaments preferentially align near the edge region of high curvature, the axial symmetry and the flatness of the contact region forces a vertical orientation. Since the limit $\alpha \rightarrow 0$ corresponds to a far propagation of the orientation field ($\lambda_c \rightarrow +\infty$), the vertical flow at the center can induce alignment costs for the cortical energy that can be relaxed by a spreading extension: the resisting tension $\partial_L E_{\text{tot}}$ is reduced. In general, the associated increase of adherent length L is weak and does not drive any transition.

Spreading states and stability transitions

To get the full spreading equilibrium state and in particular the equilibrium adherent length L^* , the solution of Eq. 1.25 is injected into Eq. 1.23 (deprived of the adhesion term), function of variables L , C_0 , C_e and ΔP , and minimized with respect to C_0 , C_e and ΔP to obtain their dependency on L and finally get a mono-variable energy $E_{\text{mech}}(L)$. Its derivative gives the cortical membrane resisting force $F_{\text{m}\oplus\text{c}}$, balanced by the adhesion force and the frictional traction force according to Eq. 1.24. This horizontal force balance equation is solved graphically on Fig. 1.11a

by representing the membrane restoring force, and effective adhesion force as a function of the adherent length L . For a vesicle without cortex, the total adhesion force ϵ is constant and the restoring force increases to the value 2γ , with the full wetting condition $\epsilon > 2\gamma$ (for $\bar{\lambda} \ll 1$). With cortex, the restoring force is modified in the strong anchoring regime, due to an effectively more rigid membrane ($\lambda_{\text{eff}} = \lambda\sqrt{1+e}$). It may possibly overshoot (non-monotonic), but it saturates at the same value 2γ . The traction force, on the other hand, increases to a value corresponding to the maximal reorientation of the cortex θ_L discussed above and shown in Fig. 1.10c. The total effective adhesion force $\epsilon + f_f$ includes the integrated traction force f_f , which in the limit $L \gg \lambda_c$, reads $f_f^\infty \sim \epsilon_f \lambda_c |\theta_L|$. Hence, full wetting is possible when the friction parameter ϵ_f exceeds a threshold given by $\epsilon + f_f^\infty \gtrsim 2\gamma$, with the following asymptotes in the strong and weak anchoring regimes:

$$\epsilon_f = \frac{2\gamma - \epsilon}{\lambda\sqrt{e}} g(\alpha) \quad , \quad g(\alpha) \sim \begin{cases} \sqrt{\alpha}, & \text{if } \alpha \ll 1 \\ \alpha, & \text{if } \alpha \gg 1 \end{cases} . \quad (1.26)$$

The full spreading transition is summarized on a phase diagram in Fig. 1.11b relating the threshold values of traction force amplitude ϵ_f to the anchoring rigidity α , in excellent agreement with the scaling law Eq. 1.26.

Another important characteristics of the traction force is the way it reaches the saturation value. For strong anchoring, the traction force density propagates a short distance $\lambda_c \ll L_0$ away from the cell edge, and the total traction force saturates together with the edge curvature, corresponding to $L \sim L_0$. For weak anchoring, and as long as $L < \lambda_c$, cortex reorientation propagates over the entire adhered region, and the net traction force scales linear with the adhered length: $f_f \sim \frac{\pi}{4} \epsilon_f L$ (for full cortex reorientation: $\theta_L \simeq \pi/2$). Crudely assuming that the membrane restoring force also scales linearly with the adhered length for small length: $F_{\text{m}\oplus\text{c}} \sim \gamma L/L_0$, the force balance could admit two stationary solutions, one stable and one unstable, if the traction force increases slower than the restoring one with the adhered length. This behaviour, illustrated on Fig. 1.11, should occur if $\bar{\epsilon}_f = \epsilon_f L_0/\gamma < 1$. This simple argument, confirmed by numerical calculations, predicts that the phase diagram contains a region of bistability in the low anchoring regime, where a partial spreading state coexists with the full spreading state, see Fig. 1.11.

Finally a last specificity of this coupling between orientation, shape and traction is the appearance of two orientation "domains" represented on the phase diagram in Fig. 1.11b. For strong anchoring ($\alpha \gg 1$), cortical reorientation is small ($\theta_L \simeq 1/\sqrt{2\alpha}$) and localized ($\lambda_c \ll L_0$), whereas it becomes large ($\theta_L \lesssim 1/\sqrt{2\alpha}$) and extended over the ventral part of the cell ($\lambda_c \sim L_0$). For a cell to extend lamellipodia, either isotropically or by anisotropic nucleation events (bi-stability regime), we claim that it requires both a full-wetting transition and a large reorientation at the leading edge. Those criteria are largely met in the region of physiologically accessible parameters (pink frame on Fig. 1.11b), and the full spreading regime with small reorientation (strong anchoring) but large traction force amplitude is likely not physiologically relevant.

1.4 Discussion and conclusion

1.4.1 Mechanical feed-back loop and lamellipodium initiation

In summary, we propose that there exists a mechanical feedback loop between the membrane curvature, cytoskeleton structure and traction force at the edge of spreading cells. High curvature drives actin filaments to orient parallel to the substrate, which increases the traction force, promotes cell spreading and increases back the edge curvature. We argue that this corresponds to the initiation of a lamellipodium, the thin and flat protrusion of oriented actin filaments found at the edge of many spreading and crawling cells.

The model relies on three important assumptions. First, if the tension of the cell membrane remains fixed (regulated) during the process, this can lead to a finite contact area with the substrate at equilibrium, or to a state of full (unbounded) spreading. Thus, we assume that the transition between those equilibrium states can indicate a likelihood for lamellipodial protrusion, and that the inherent dynamical features of cell spreading can be ignored to perform a quasi-static description.

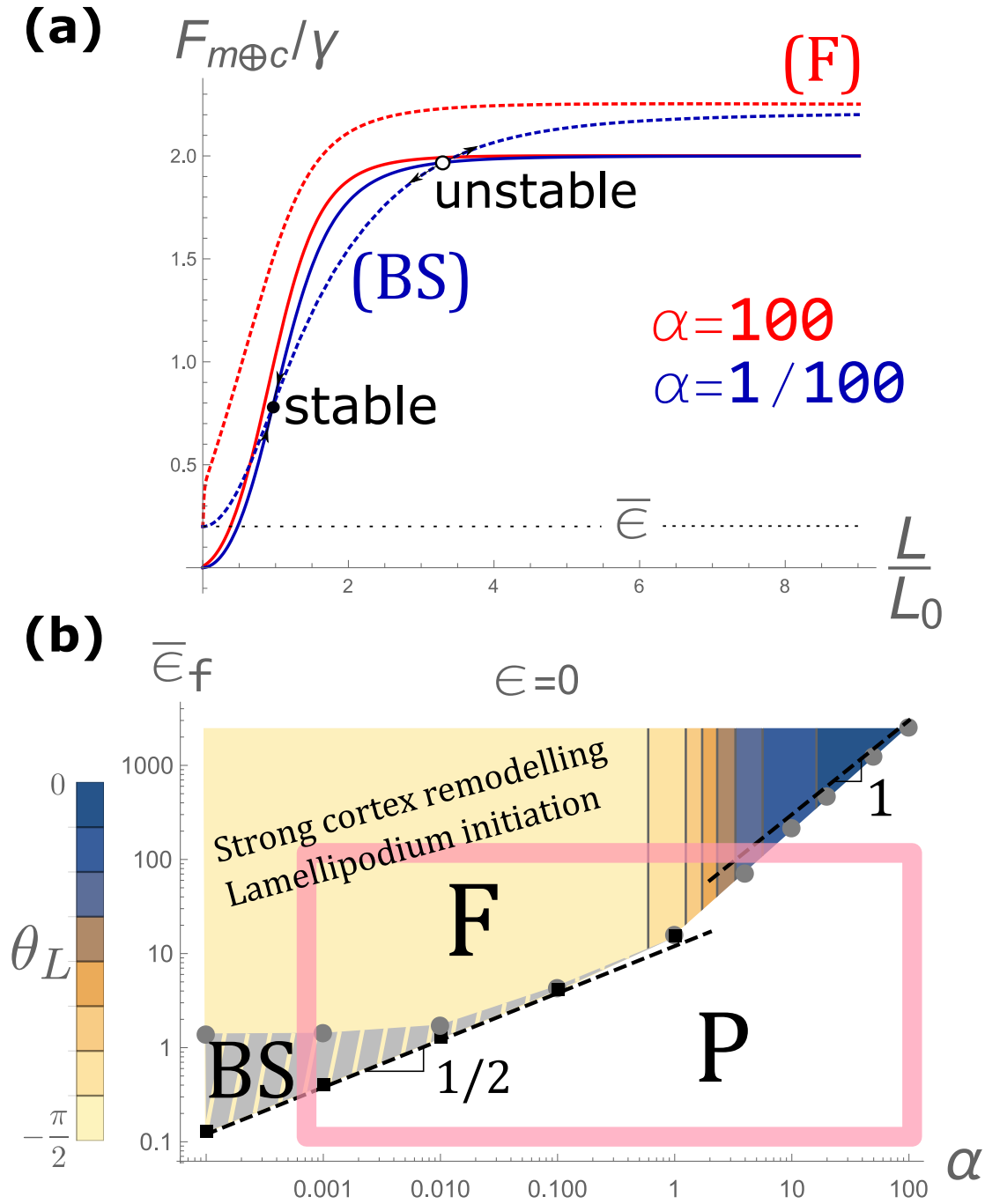


Figure 1.11: **(a)**: Graphical resolution of the force balance equation Eq. 1.24. The restoring force (solid lines), the passive adhesion force (dotted line) and the total traction force (dashed lines) are shown as a function of the adhered length L for weak (blue) and strong (red) anchoring. Equilibrium states (P) correspond to the forces being equal, and Full spreading (F) to the case when there is no solution as shown for strong anchoring ($\bar{\epsilon}_f = 2750$). For weak anchoring, the system might show bi-stability (BS), with a (meta)stable and an unstable solution leading to full spreading ($\bar{\epsilon}_f = 1.3$). Parameter values are: $\bar{\lambda} = 0.01$, $e = 100$ and $\bar{\epsilon} = 0.2$. **(b)**: Phase diagram in the $\alpha, \bar{\epsilon}_f (= \epsilon_f L_0 / \gamma)$ parametric space for negligible non-specific adhesion ($\epsilon \ll \gamma$), delimiting the three systems phases in white (P), gray (BS) and beige-blue (F). The full spreading region contains a quantification of the cortex reorientation angle at the edge θ_L ($-\pi/2$ means horizontal). Its large value for small anchoring parameter α is indicative of lamellipodial initiation. The scaling behaviour predicted by Eq. 1.26 is also confirmed (dashed lines). The pink frame delimits the physiological accessible range of parameters.

Second, we make a generic mechanical coupling between the mesoscopic actin cortex orientation and the large scale membrane curvature. This is tackled by two antagonist effects that are necessarily in competition on a closed surface: normal anchoring and local flow alignment. Third, the transient connexion of actin filaments to the substrate - through adaptor proteins and bound adhesive receptors - and their polymerization against the plasma membrane generates a frictional traction force, transmitted to the leading edge by mechanical propagation. As clearly shown in the results (Fig. 1.11b), we assume those tractions to be essential for the appearance of lamellipodia, with the observational consequence that any disruption of the actin-substrate connexion should suppress lamellipodial protrusions. Of course, the model does not intend to describe the precise protrusion shape and how it evolves in later spreading stages.

Our "lamellipodial" transition is mostly controlled by two parameters (see Fig. 1.11b): the ratio of traction force of a fully oriented lamellipodium over the membrane tension $\bar{\epsilon}_f = \epsilon_f L_0 / \gamma$, and the ratio of the cortex anchoring stiffness over tension $\alpha = k_\alpha / \gamma$. The range of physiological values for these parameters corresponds to the region in the phase space where interesting things happen, like large cortex reorientation or the transition between partial and full spreading (lamellipodium initiation), with the possible coexistence of the two states when lamellipodium initiation is a nucleation event (Fig. 1.11b). Our model predicts that relatively weak variations of intracellular and extracellular parameters may modulate the cell spreading behaviour. It constitutes a possible mechanism for spontaneous symmetry breaking, establishing a front-rear polarity followed by cell migration, as observed along 1D stripes [91].

The importance of cell edge curvature for lamellipodium initiation has been confirmed experimentally [118]: cells spreading on square adhesive patterns generate protrusions on the edges (regions of highest curvature). Contrarily to our model that only deals with curvature along the radial direction, this experimental result is associated with orthoradial curvature. However, the generic aspect of our theoretical feed-back loop between geometry, orientation and tractions could also be applied along this direction with similar features. Before a future investigation of the 3D axi-symmetric model extension to prove that shape fluctuations of the cell leading edge can indeed nucleate local protrusions (with a transition analogous to "bistability"), the extrapolation of our findings looks natural. This project extension may justify the experimental observation of isotropic versus anisotropic spreading modes [80], with either a unique lamellipodium or multiple local protrusions. For instance, this model extrapolation predicts that decreasing the traction force parameter ϵ_f should trigger a transition from isotropic spreading ("full spreading") to anisotropic spreading ("bistability") (Fig. 1.11b). This transition has indeed been observed for endothelial cells upon reduction of the the substrate ligand density [140].

1.4.2 Adhesion-dependent versus adhesion-independent lamellipodial growth

At early spreading stage, the adhesion complexes only involve few clustered integrins and primarily bind talin, a known activator of integrins [146] that triggers out-in signalling, followed by other adaptor proteins like paxillin, vinculin, α -actinin or FAK [147]. Since talin can bind both integrin and actin, this allows a first cytoskeleton-substrate connexion that transmits cell-generated tractions to the substrate [109]. Indeed, the depletion of talin on spreading fibroblasts [141] shows two important features. First as expected, those cells strongly reduce their substrate tractions (at early spreading stage) and tend to detach after ~ 20 min because integrins have not been activated, making cell-substrate adhesion probably weakly specific. Second, a lamellipodial protrusion can still be observed before cell detachment. This challenges our prediction that a disruption of actin-substrate connexion should suppress lamellipodial protrusions ($\epsilon_f = 0$), except if an unknown linker could replace talin or if unspecific source of friction (actin/plasma membrane) could sustain a significant amount of traction.

In fact, the biological literature has largely focused on the biochemical aspects of the actin polymerization motor, seen as the driver of lamellipodium initiation [148] through upstream small G

protein Rac signalling [149, 150]. This ignores the actin-substrate interaction, exemplified by the molecular clutch model (reviews [123, 101, 102]). Indeed, Rac has also been shown to stimulate the formation of nascent adhesions at the leading edge [151], which makes a distinction between adhesion-dependent and independent modes not straightforward a priori. Moreover, the precise role of NPFs N-WASP and WAVE do not look completely elucidated (review [123]): whereas WAVE isoforms are seen as the dominant activators of actin polymerization at the leading edge, N-WASP can also play a role in some cell types (MDCK cells but not fibroblasts). But contrarily to N-WASP, naturally auto-inhibited and directly activated by GTPases Cdc42 and Rac, WAVE activation is not a straightforward downstream target for those GTPases.

At downstream level, the lamellipodial inhibition induced by capping protein knock-down on melanoma cells [152] also suggests an adhesion-independent scenario, because capping activity restricts the distribution of filament lengths and avoids buckling at the leading edge: it then converts individual filament pushing into network-scaled protrusive force.

Neutrophil migration adds an interesting feature [153]. The authors observe a compensatory mechanism that allow neutrophils to migrate despite losing their substrate adhesion, upon inhibition of integrin or talin expression. Contrarily to fibroblasts that need an adhesion "clutch" mechanism to migrate efficiently, neutrophils seem able to compensate for the loss of adhesion by increasing their actin polymerization rate at the leading edge, resulting in similar protruding velocities with or without adhesion (Fig. 1.12a). They also claim that the lack of substrate bounds give more flexibility to the plasma membrane and favours higher leading edge extension, although some feedback control on filament growth could also provide a load-independent protrusion rate as in the auto-catalytic model [11]. Those results tend to favour the traction-independent lamellipodium initiation scenario.

Another primary target to test the traction-dependent scenario is vinculin, an adaptor protein recruited at adhesion complexes with talin that can also bind Arp2/3 independently from actin [154]. It can bind both actin and talin by stretch-dependent opening of talin cryptic sites [108]. Contrarily to the previously described talin knock-out, old results on spreading cells lacking vinculin [155] have shown the absence of lamellipodia with a strong reduction of cytoskeleton-integrin stiffness. In the control case, the F9 carcinoma cells used in this study exhibit a local lamellipodium corresponding to anisotropic cell spreading (Fig. 1.12b). Moreover, the localization of vinculin at the tip of lamellipodia [149] may indicate a correlation between vinculin recruitment at nascent adhesions and protrusion growth. Surprisingly, vinculin knock-out in another cell type (mouse embryonic fibroblasts) do not suppress lamellipodia and the injection of constitutively active vinculin tails shows anti-localization with lamellipodial protrusions [156]. With the same cell type, another group find the opposite result with lamellipodium inhibition under vinculin knock-out [154]. In addition to vinculin, inhibition of the protease calpain eliminates isotropic lamellipodia from 3T3 fibroblasts, replaced by anisotropic or no protrusion and less spreading [157]. Interestingly, the authors find an increase of ezrin (a cortex-to-membrane attachment protein) expression, that could be connected to an increase of our anchoring cortical stiffness k_{alpha} (in agreement with Fig. 1.11b), or may perturb the protruding machinery at the leading edge in the traction-independent picture.

To distinguish between traction-dependent and traction-independent scenarios, some elementary thought experiments can be imagined. For example, nano-patterning with non-adhesive bridges separating parallel lines [158] seems to show no spreading rate difference between the two regions. Another possibility could be a stiff material surrounding a spreading cell that blocks leading edge extension on half cell height (Fig. 1.12c). Injection of constitutively activated Rac1 proteins may then induce a traction-independent protrusion along the top surface of the surrounding material (treated to be adhesion independent) if the polymerization-driven scenario is likely to occur.

1.4.3 Conclusion

In terms of theoretical biophysics, there are two main strategies: one is to study an experimentally controlled system and propose a model that appears consistent with the observations, another

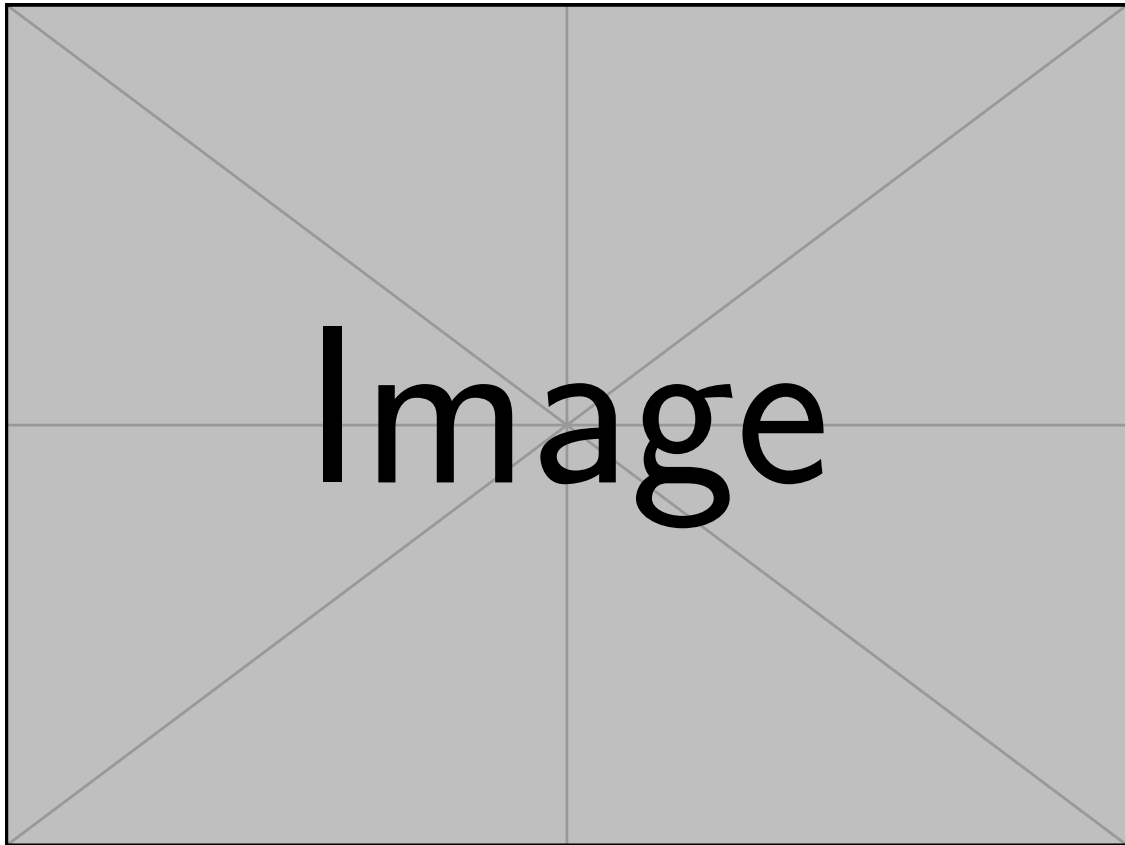


Figure 1.12: **(a)**: Sketch of adhesion-dependent and adhesion-independent mechanisms for leading edge advancement. When actin filaments are bound to substrate through adhesion receptors and adaptor proteins (top), the myosin-II dependent retrograde flow is cancelled and actin polymerisation pushing force drives front advance. If the clutch is disengaged (middle) and actin experiences a friction-like force with the substrate, the retrograde flow increases but is counterbalanced by an increased polymerization rate at the tip, with similar protrusion growth rate. If no adhesion components are available, the retrograde flow is maximal but is again compensated by higher polymerization rate, leaving the protrusion growth rate unchanged. This adaptation is observed on migrating neutrophils but knock-out of integrin or talin seem to prevent fibroblast migration, and asks for the relevant mechanisms in various cell types and morphological phenomena where actin is implicated. From [153]. **(b)**: Experiment with carcinoma F9 cells in wild-type conditions (top) that exhibit filopodia and a localized lamellipodium (arrowheads), and vinculin-deficient cells (bottom) that only protrude filopodia (arrow). This tend to indicate the importance of actin-substrate connexion for lamellipodia generation, in contrast to other results with different cell types ([141]). Both images correspond to 10 min after initial cell-substrate attachment and scale bar is 10 μm . Modified from [155]. **(c)**: Sketch illustrating a thought experiment where a spreading cell is prevented from extending a leading edge by a stiff material, with a thickness smaller than cell height. In case of traction-independent scenario, activation of active rac1 (blue) may trigger the initiation of a "lamellipodial" protrusion along the top surface of the stiff material. It can also provide evidence for the importance of edge curvature on local filament alignment and its impact on the membrane deformation amplitude.

is to use experimental phenomenology as an inspiration and design minimal models to emphasize theoretical mechanisms. Here, we are more concerned with the second strategy, although it remains useful to test the compatibility of the model with the available literature.

This motivates the highlight on two different views of actin protrusions, relying either on the biochemistry of actin polymerization or on the mechanics of the traction-driven lamellipodia through the use of a "molecular-clutch" mechanism. In the last decades, the dense and diverse literature that have been accumulated on the topic makes hard any trial to make a theoretical model compatible with the "state of the art". The strong evidences showing the controllability of lamellipodia upon Rac expression/inactivation are rarely put in regard with the actin-substrate link, whereas ambivalent results exist between the emergence of lamellipodia and specific actin-substrate adaptors like vinculin [155, 154] or talin [141].

Even in the traction-independent scenario, our model still remains valuable for the transition between the cortical architecture and the parallel organization in the mature protrusion. Indeed, a robust alignment of actin filaments is expected at the cell periphery, in a feed-back loop manner with the edge curvature. Since the total polymerization force exerted on the membrane tip should be higher when the network is coherently oriented, compared to a randomly organized one, the amplitude of our orientation field deviation at the edge (θ_L) may nonetheless be connected to the lamellipodial extension. Some indirect effect from the substrate connexion, the torque applied on actin filaments, may also contribute to the edge reorientation. A higher resolution model able to tackle the coupling between plasma membrane and actin network is still lacking, and would be greatly beneficial to test the robustness of phenomenological models for the coupling between network polarization, polymerization and plasma membrane resistance. Finally, a better experimental quantification of the cortical reorganization at early stages of cell spreading, in terms of thickness, myosin density or actin reorientation would be of great use for a better theoretical characterization.

Chapter 2

2D side vertex model

The next two projects involve the theoretical description of epithelial monolayer mechanics: this part II is dedicated to the presentation of the discrete cell framework used for that purpose. It consists in a 2D vertex model but projected on the transverse plane (xz), contrarily to the majority of vertex models that deals with the apical plane of monolayers (xy) that is easily accessible to microscopic imaging. We consider constant polar tensions on all cell interfaces and assume that hydrostatic pressure difference between adjacent cells or cell and lumen is equilibrated by interfacial curvature (Laplace law). Hence the so-called 2D bubbly vertex model.

A first chapter introduces the various tissue models used for epithelial monolayer mechanics. A second presents the 2D bubbly vertex model and the uniform tissue state associated to mechanical equilibrium. A last chapter deals with the linear perturbation theory for the mechanical response of an heterogeneous tissue, both at "cell" level with discrete equations and at "tissue" level with a continuous approximation.

2.1 Introduction: tissue modelling

2.1.1 Epithelial tissues

The standard tissue classification used for multicellular organisms comprises epithelial, nervous, connective and muscle tissues. Epithelia are cellular tissues covering the external body surface and internal or external cavities associated to organs. They can organize into monolayers or multilayers of cells (Fig. 2.1a), with one side proximal to the connective tissue on which the deepest layer is anchored thanks to a basal lamina. This asymmetry between different cell sides is robustly achieved at the biochemical level to define an apical interface in contact with the organ lumen, a lateral interface for cell-cell contact and a basal interface anchored to the basal lamina (Fig. 2.1b,c). Epithelia have several functions:

- act as a protective barrier to avoid pathogens, toxins, unwanted cell invasion or mechanical damage like skin,
- gland secretion like mucus secretion in the trachea,
- transcellular transport for gas exchange in lung, nutrient absorption in intestine (Fig. 2.1b) or filtration in kidney,
- sensing of environmental signals like the sound waves detected by hear cells.

Specialized apical domains are present on several tissues, like micro-villi to increase the exchange surface (Fig. 2.1c), stereocilia for the detection of sound frequency, and cilia to transport extracellular fluids or bodies. They can be filled with actin (micro-villi and stereocilia) or microtubules (cilia).

Apical domains and various epithelial junctions are essential for the integrity of these differentiated tissues (Fig. 2.1b). To perform their barrier function, epithelia possess tight junctions at the

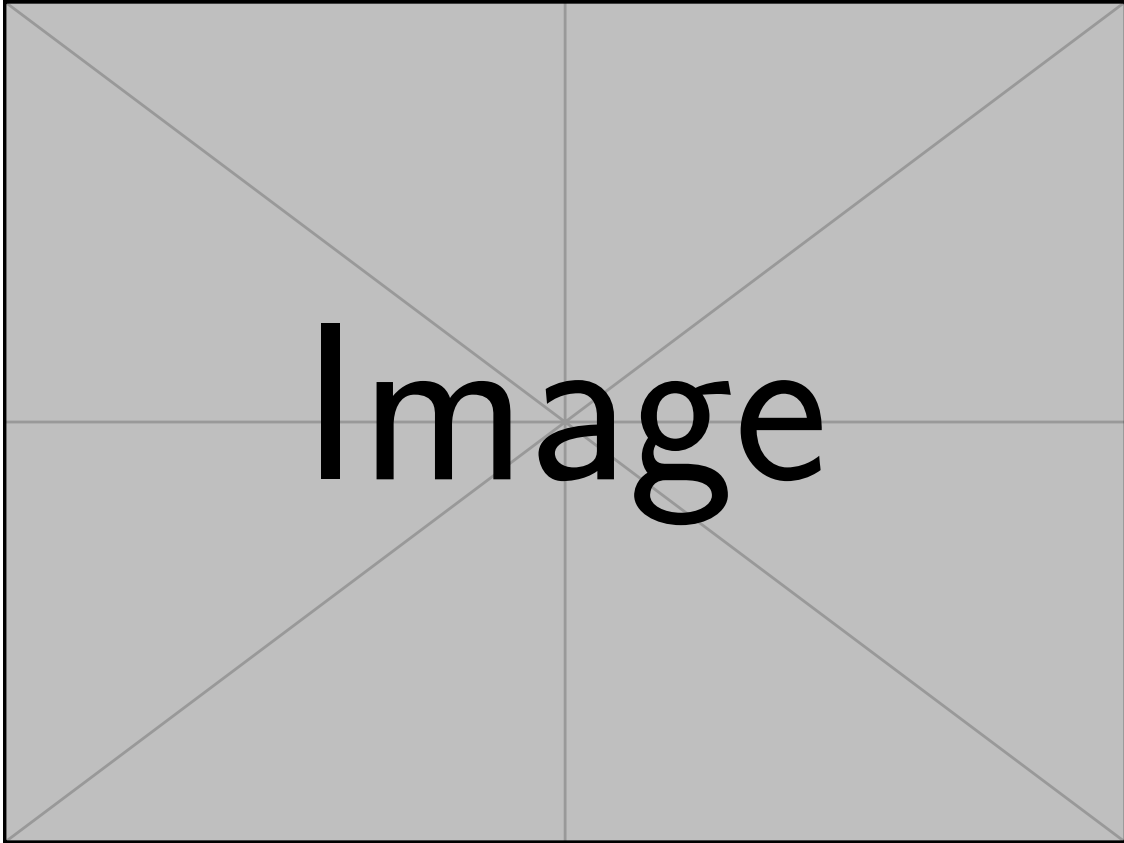


Figure 2.1: **(a)**: Classification of epithelial tissues as observed in cytology, in terms of layer (simple/stratified) and cell shape (squamous/cuboidal/columnar). Special cases are simple tissues with pseudostratified appearance, keratinized surfaces and transitional layer organization. From [159] (license Creative Commons). **(b)**: Canonical sketch of epithelial junctions for cell-cell and cell-matrix adhesion, connected either to intermediate filaments or actin. This is valid in the context of monolayers since stratified epithelia have "internal" cells disconnected from the lumen or the Extra-Cellular Matrix (ECM) that seem to not possess tight junctions (skin). At the bottom of the epithelial tissue, the ECM is structured into a thin layer of fibers (laminin, collagen) called the basement membrane or basal lamina. Adapted from [160] (license Creative Commons). **(c)**: Super-resolution image of mouse intestinal epithelium. On the apical side, micro-villi (red) increase the surface of exchange to absorb nutrients. The scale bar represents $5\ \mu\text{m}$. From [161]. **(d)**: Confocal microscopic image of MDCK II monolayer showing polygonal cell packing to cover the surface. From [162].

apex which prevent unwanted leakage of substances from the lumen to the organ interior, and can also selectively transport ions (paracellular). Gap junctions perform the opposite task to facilitate intercellular communication, either to synchronize a global response (heart), transmit a chemical signal or to "prepare" the neighbours for cell death (extrusion). Adherens junctions and desmosomes maintain the tissue mechanical integrity through cell-cell adhesions of the cadherin family, connecting the cellular cytoskeletons (actin and intermediate filaments) together. Adherens junctions are enriched in myosin II to assemble a contractile belt, essential for morphogenetic changes involving cell apical constriction [163]. Finally, adhesion complexes on the basal interface ensure the epithelial anchorage to the Extra-Cellular Matrix (ECM), thanks to binders of the integrin family. Whereas focal adhesions linked by stress fibers are also expressed on migrating cells in the stroma, hemi-desmosomes are only present in epithelia. They can have a major role on tissue integrity since a desmosomal mutation leads to the blistering effect on human skin [164].

Below, we focus only on epithelia that form a single layer. To act as a barrier and cover surfaces, cell-cell interfaces in epithelial monolayers tend to arrange into polygonal networks (Fig. 2.1d). Although a purely hexagonal lattice is sufficient for full covering, observations on real tissues show more complex distributions with a significant fraction of pentagons and heptagons (Fig. 2.1d and Fig. 2.3a).

To describe biological tissues theoretically, there are two main approaches:

- a tissue-scale approach where one uses some experimentally accessible field variables (velocity field, cell number density, orientation field) that are connected to stress tensors through constitutive equations within the framework of continuous mechanics [165]. Tissue rheology is generally chosen to be fluid, elastic or visco-elastic.
- a discrete approach where individual cells are explicitly modelled in a simple manner, eventually related to tissue scale features by bottom-up convergence to the continuous approach. Vertex models are the most popular descriptions ([166], review [167]), often applied to epithelial monolayers within the horizontal plane as in Fig. 2.1d.

In parallel, the microscopic constraints naturally favour models in the horizontal plane (xy) with surface-like properties. For some specific systems, the transverse plane (xz) appears more appropriate whereas 3D vertex models have started to be developed recently [168, 169, 170].

2.1.2 Continuous mechanics

When dealing with cell monolayers containing thousands of cells, it is natural to average out the detailed properties at the single cell level and study the spatio-temporal evolution at the tissue scale. In particular, the small height-to-width aspect ratio of tissue monolayers make them particularly suitable for planar continuous approaches with surface-like properties.

For the study of morphological changes in tissues, which is particularly relevant in developmental biology ([171] and thesis [172]), one can try to map epithelial mechanics into the framework of surface mechanics. For example, the villi structures in animal intestine, folds on the surface epithelium that increase the total surface of nutrient exchange, can be described within the framework of continuum elasticity (Fig. 2.2a). The shape instability develops because higher cell division rate is assumed in valleys (curvature-sensitive). Spatial localization of "villi" occurs because of the coupled mechanics for the cell monolayer covering the stromal tissue, with length fixed by the ratio of epithelial-to-stromal elastic moduli. More generally, a systematic framework known as the mechanics of "active surfaces" [173] has been developed recently to identify how cell inner activity can add new morphological features and new classes of systems to the "passive" theory of surfaces. In opposition to the tissue-scale approach, one can start from an explicit description of single cells (see next section) but apply a continuous limit when studying the relaxation of relevant quantities on scales larger than cell width ([174, 170] and thesis [172]) to obtain effective continuous models that can be compared to standard mechanics of surfaces or ropes.

For systems that remain in a fixed geometry like the widely-studied epithelial monolayers on flat substrates [175, 176, 177], the framework of planar continuous mechanics is sufficient. One needs to define a material rheology that relates the tissue stress to the strain (elastic), the strain rate (viscous) or a combination of both (visco-elastic) (reviews [165, 61]). This is usually presented on a rheological diagram as in (Fig. 2.2b), where cell-cell adhesions and their integration to cytoskeleton confer elasticity to the monolayer, with an active force driving cell migration and resisted by substrate sliding. Nonetheless, many dissipative processes tend to rearrange cell inner components so that a viscous rheology is often considered more appropriate for tissue stress on usual experimental times of hours [178, 176, 177]: the plane stress tensor then reads $\gamma_{\alpha\beta} = -P\delta_{\alpha\beta} + \eta(\partial_\alpha v_\beta + \partial_\beta v_\alpha)$. Depending on cell type and experimental conditions, epithelia can grow by cell division or shrink by cell apoptosis with effective rate $k_d - k_a$, or be at confluence with fixed density ρ_H . This saturated density associated to contact inhibition of growth is often named homeostatic density, and defines an homeostatic pressure P_H for a given constitutive equation $P(\rho)$ [179]. Then, confluence is captured by an expansion around ρ_H for the growth rate, and enters into the local incompressibility equation relating density field ρ and velocity field \vec{v}

$$\partial_t \rho + \vec{\nabla} \cdot [\rho \vec{v}] = -\frac{\rho}{\tau} \left(\frac{\rho}{\rho_H} - 1 \right) \quad (2.1)$$

The system is closed with local force balance $\partial_\beta \gamma_{\alpha\beta} = T_\alpha$ where T is the substrate traction containing active migration stress and sliding friction as in Fig. 2.2b. The coupling between pressure field, velocity field and density field can lead to a rich phenomenology when active terms are introduced, like mechanical waves that tend to disappear if activity is cancelled [175, 178], as shown theoretically on Fig. 2.2c over a fixed spatial domain.

Finally in addition to geometry, stress, velocity and density, a last property of cells that can be incorporated into a field description is the cell polarization through the vector \vec{p} [178, 176, 177]. This corresponds to a coarse-grained measure of the front-rear polarity in migrating cells, with active traction stress $T_\alpha = -T_0 p_\alpha$ and active tension¹ $\gamma_{\alpha\beta}[\text{active}] \propto p_\alpha p_\beta$ as shown on Fig. 2.2d. Then, the mechanical cost associated to orientation gradients naturally localizes polarized cells at the tissue periphery on a width L_c whereas the tissue core remains unpolarized (Fig. 2.2d). Cell orientation can be critical for the tissue behaviour, exemplified by nematic fibroblasts confined on linear stripes (Fig. 2.2e): above a critical width of the stripe, cells align non vertically at the center and the induced mechanical constraints on the boundaries generate a spontaneous shear flow. Thus, the continuous mechanics approach relies on a combination of field equations for stress, velocity, density and orientation. The active terms specific to living systems often appear to be crucial, and are directly responsible for the rich phenomenology that have been merely touched here.

2.1.3 Vertex models

The 2D vertex model in the horizontal plane deals with straight cell-cell junctions that intersect at vertices (Fig. 2.3a). The positions of the later, noted $\{\vec{x}_i(t)\}$, are the degrees of freedom used to define the tissue state at given time t . Several topological transitions can occur in the junctional network like the so-called T1 transition: two neighbour cells loose their shared interface and allow transverse cells to assemble a new shared interface by network reconfiguration. Cells can also disappear in a T2 transition, whereas some explicit rules need to be introduced to model cell division.

Each vertex position evolves according to the force balance $\zeta d_t \vec{x}_i = \vec{F}_i$ with a generic friction coefficient ζ , where the force is derived from a energy function E such that $\vec{F}_i = -\partial E / \partial \vec{r}_i$. Using cell index α and vertex index i, j for interface (i, j) of length l_{ij} , the total energy function of the

¹One usually writes an active tension $\gamma_{\alpha\beta}[\text{active}]$ proportional to the nematic tensor $Q_{\alpha\beta} = p_\alpha p_\beta - (1/2)\delta_{\alpha\beta}$ in 2D, but the isotropic part can also be absorbed by the pressure field so that $\gamma_{\alpha\beta}[\text{active}] \propto p_\alpha p_\beta$.

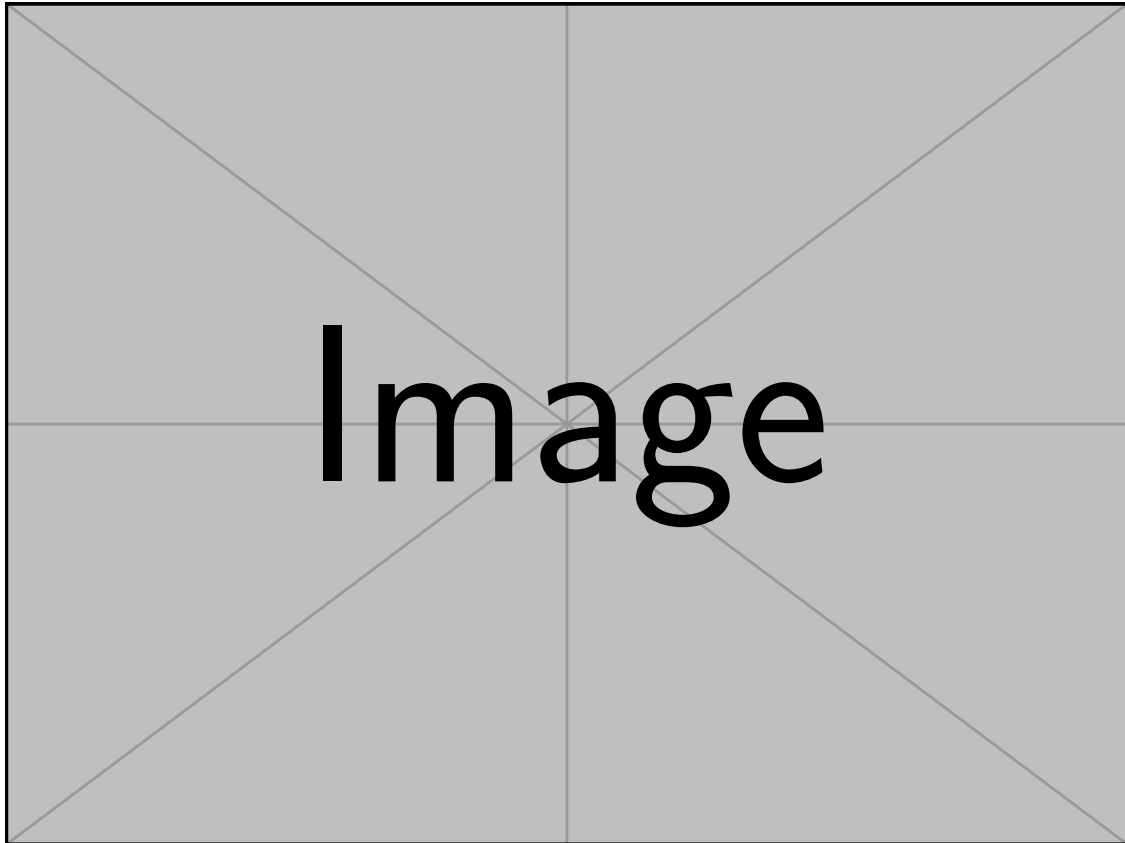


Figure 2.2: **(a)**: Theoretical simulation of an epithelial surface representing intestinal villi, with elastic rheology and coupling to an elastic stroma on the bottom. The shape instability relies on curvature-sensitive cell divisions. From [180]. **(b)**: Simple rheological diagram for an epithelial monolayer on flat substrate, with elastic cells (spring) able to generate active forces (red arrow) in addition to passive slippery friction (dashpot). From [175]. **(c)**: Kymograph of tissue density with a travelling wave for $t < 200$. Beyond $t = 200$, a numerical "knock-down" is applied by a decrease of active parameters and the wave is lost. From [178]. **(d)**: Sketch of a spreading monolayer with viscous rheology, described theoretically through velocity field v_α and polarization field p_α . One has viscous stress with polar active tension $\gamma_{\alpha\beta} = \eta(\partial_\alpha v_\beta + \partial_\beta v_\alpha) - \zeta p_\alpha p_\beta$ (red arrows), slippage on substrate with stress $\sigma = \xi v_\alpha$ (purple arrows) and active tractions generated by peripheral cells $\sigma = -T_0 p_\alpha$ (blue arrows). Polarization is localized at the periphery over the nematic length L_C . From [177]. **(e)**: Monolayer of fibroblasts confined on a linear stripe with nematic orientation (left). Cells remain aligned vertically for a small stripe width, whereas symmetry breaking occurs above a critical width (right). From [176].

tissue typically looks like[166, 181]

$$E(\{\vec{x}_i\}) = \frac{1}{2} \sum_{\alpha} \left\{ K_{\alpha} [A_{\alpha} - A_0]^2 + \Lambda_{\alpha} P_{\alpha}^2 \right\} + \sum_{\langle i,j \rangle} \Gamma_{ij} l_{ij} \quad (2.2)$$

The first term simply represents an elastic resistance to surface area change (away from rest value A_0) with modulus K_{α} , and can be associated to cell volume conservation when cell height response is decoupled from planar mechanics. The second term corresponds to a ring-like contractility along the perimeter whereas the third term represents junctional tensions Γ_{ij} (not necessarily positive due to cell-cell adhesion). The junctional sum on the third term is sometimes replaced by a sum over cell perimeter [181]: because only forces are physically relevant, the last two terms can be combined to get a term $\propto (P_{\alpha} - P_0)^2$ with effective rest perimeter $P_0 \sim -\Gamma/\Lambda$.

For some epithelial tissues, the assumption of straight cell-cell junctions cannot be assumed and the framework needs to be modified to account for the interfacial curvature generated by a pressure difference on neighbour cells, as predicted by Laplace law [182]. The properties of the two models are similar but the bubbly model can account for external boundary forces on finite systems more naturally, because it treats both point and line forces (Fig. 2.3b).

Other discrete models do not use vertex positions as degrees of freedom, but define a cell center position $\vec{X}_i(t)$ and build the tissue network thanks to a Voronoi tessellation [183, 184]. Those so-called self-propelled Voronoi models propose an hybrid approach between the 2D vertex model and self-propelled particle models [185], to account for tissue confluence as well as cell migration. This is exemplified by circular confinement of monolayers where spontaneous rotation can be observed (Fig. 2.3c).

One very important property that can be studied with those discrete models is the rigidity transition, when a material goes from a fluid to solid behaviour because the energetic cost for rearrangements cannot be overpassed. Contrarily to self-propelled particles where jamming occurs at a critical packing density [185], confluent tissues can rigidify at a fixed density [181, 184]. It is predicted for both vertex [181] and self-propelled Voronoi [184] models to depend on the relative strength of contractility and cell-cell adhesion (Γ/Λ as in Eq. 2.2).

Beyond 2D models in the horizontal plane, some biological systems naturally ask for a description in the transverse plane (xz) like ventral furrow formation during drosophila gastrulation (Fig. 2.3d). This class of 2D models assumes invariance along the Oy axis and is used to study tissue folding ([186, 171], thesis [172] and review [167]). A similar energy function can be defined with area elasticity and junctional tensions for apical, lateral and basal interfaces. Out-of-plane tissue deformation with respect to the horizontal plane has also been studied within the usual vertex model framework [174]. Those discrete models are suitable for a continuous limit over surface mechanics for plane sheet perturbation [174] or transverse monolayer folding ([170] and thesis [172]).

Finally, a complete 3D description can be used with a generalization of Eq. 2.2 when both plane and out-of-plane deformations matter [169, 170]. For a uniform tissue with hexagonal packing, a simple energetic calculation defines an equilibrium shape with cell shape varying from squamous to columnar aspect ratio depending on parameters, through a competition between apical ring contractility, cell-cell/basal adhesion and bulk elasticity [168]. If the monolayer is not forced to adhere on a rigid flat substrate, an apico-basal polarization of tensions can favour a tubular shape [168, 170]. When some transformed cells lose their polarity with similar tensions on apical and basal sides, pancreatic tubes are observed to be deformed either inwards or outwards depending on their diameter [170]. Indeed, such a generic observation can be recapitulated with 3D vertex models simulations (Fig. 2.3e) and confirms the robustness of this framework.

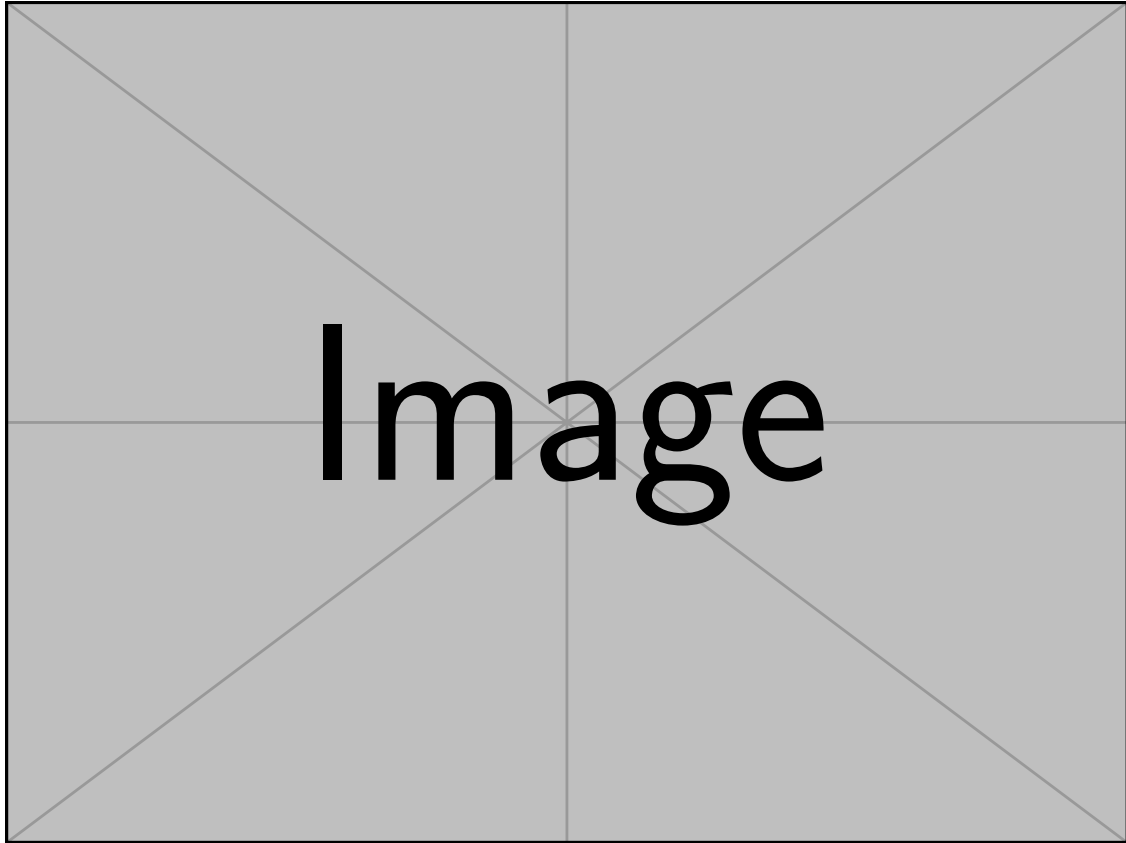


Figure 2.3: **(a)**: 2D vertex model in horizontal plane (xy) describing the dynamics of point vertices connecting cell-cell interfaces, assumed to be straight. This defines a geometric network with various polygonal sizes, more frequently pentagons, hexagons and heptagons. An energy function penalizes deviations from a target area and target perimeter whereas heterogeneous tensions on cell-cell interfaces add a contractile property. From [166]. **(b)**: Bubbly vertex model with curved cell-cell interfaces. Compared to (a), it takes into account the Laplace law when a pressure difference exists between neighbour cells and curves the interface. From [182]. **(c)**: Self-propelled Voronoi model able to describe both cell migration and network rearrangements, thanks to a Voronoi tessellation of cell position variables $\{\vec{X}_i\}$. Here, it describes the spontaneous rotational migration under circular confinement. From [183]. **(d)**: 2D vertex model in the transverse plane (xz) applied to ventral furrow formation in drosophila gastrulation. From [171]. **(e)**: 3D vertex model with constant apical, lateral, basal tensions and cell incompressibility for the description of pancreatic tubular epithelium (left). The figure shows a simulation of exophytic deformation in ductal neoplasia. From [170].

2.2 Model: 2D bubbly vertex model

2.2.1 Presentation of the framework: 2D side vertex model

Although many theoretical descriptions assume straight interfaces for epithelial cells, mechanical consistency and some experimental observations confirm the requirement of curved interfaces, either along the tissue plane like in drosophila pupa [182] or when one deals with their vertical shape as shown on Fig. 2.4a (thesis [162]).

For two homogeneous media separated by a thin interface under constant surface tension, the pressure difference is balanced by the product of tension and curvature (Laplace's law). For epithelial cells possessing interfaces with a lumen (apical), a matrix (basal) and neighbour cells (lateral), the polarized regulation of cortical actomyosin contractility, the cell-cell and cell-matrix adhesion strength w and eventual stress fibres contribute to overall interfacial tensions Γ as

$$\begin{aligned}\Gamma_a &\sim \Gamma_{\text{cortex,a}} \\ \Gamma_b &\sim \Gamma_{\text{cortex,b}} + \gamma_{\text{stress fibers}} - w_{\text{integrins}} \\ \Gamma_l &\sim 2\Gamma_{\text{cortex,l}} - w_{\text{cadherins}}\end{aligned}$$

Note that the apico-basal polarity can be responsible for different actomyosin expressions to get $\Gamma_{\text{cortex,a}} \neq \Gamma_{\text{cortex,b}}$ even without contributions from cell-substrate adhesion or stress fibres as observed in [170]. At the cell scale, Γ_l is not precisely an interfacial tension since it corresponds to the combination of two cell surfaces between the cell interior and interstitial fluid; one may talk about "wall" tension [187]. For a tissue not anchored to a solid matrix, this asymmetry would generate a spontaneous curvature, essential for the formation and maturation of epithelial tubes. Since our model is interested in specific cell shape transitions for a monolayer attached to a substrate, we do not allow tissue detachment and assumes infinite substrate rigidity to uncouple the mechanics of the two materials in contact.

Moreover, we consider the cell volume to remain constant under any shape configuration change (incompressibility hypothesis²). Finally, the assumption of constant tensions is central in this model and appears as a rude zero-th order approximation, meaning for example that a variation of interfacial sizes would not alter the actomyosin activity or modify cortical thickness/tension. Without specific information on epithelial cell shape regulation and the interplay with tensions on the experimental side, we adopt the simplest assumption and take Γ_a , Γ_b and Γ_l as model parameters. In particular for adhesion processes (integrins on basal region or cadherins on cell-cell contacts), we consider an ensemble with constant receptor density such that the energy density w is independent from the size of the interface. This minimal model with polar tensions is called "transverse bubbly vertex model".

This theoretical description is technically challenging in 3D because it requires cell shapes to adapt to incompatible constraints from uniform curvature and polygonal vertex positioning. To reduce this technical complexity that appears inessential for the physical mechanisms involved, we have focused so far on a "2D" system which consists in a lateral projection (xz plane) of an epithelial monolayer with invariance along transverse direction (Oy). Hence the use of Γ for line tensions, whereas the condition of incompressibility becomes a constraint on projected area $A \sim lh = A_0$, where l is cell width and h is cell height.

2.2.2 Uniform 2D epithelial monolayer

For a uniform tissue, the pressure equilibrates between cells and only the apical interface is curved (see Fig. 2.4b). For uniform pressure and tension, local force balance shows that the apical

²If one wants to relax this assumption, it is necessary to introduce compression costs like $K P \Delta V / 2$, with a constitutive law $P(V|...)$ for pressure. Moreover, internal cell structures like nucleus or cytoskeleton should prevent shape deformations like $l \rightarrow 0$ and $h \rightarrow 0$, where l is cell width and h is cell height. [168] proposed terms like A/l^2 , B/h^2 for 3D cells.

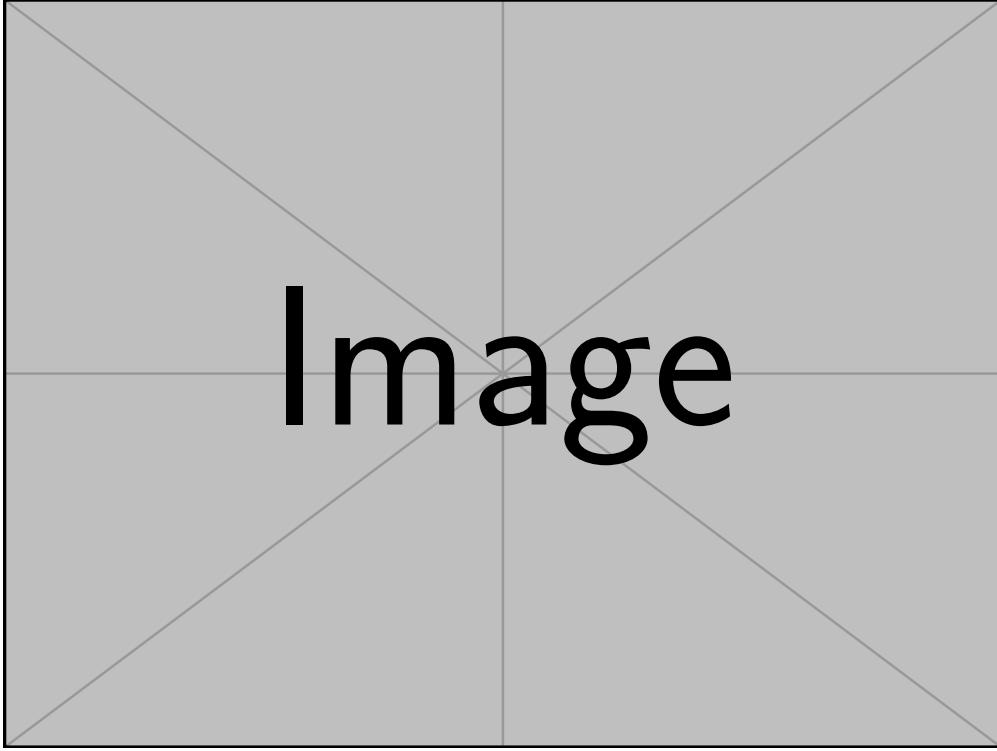


Figure 2.4: **(a)**: Transverse fluorescent image of MDCK cells showing a net curvature of apical interfaces. From thesis [162]. **(b)**: 2D cell in a uniform monolayer with curved apical interface. Its geometry is parametrized according to a polygonal skeleton defined by vertices of height h and width l whereas the curved part has a deviation angle ψ with horizontal and a radius of curvature R . One variable can be eliminated thanks to $l = 2R \sin \psi$. Note that $\psi < \pi/2$ to prevent any overlap of neighbour cells. **(c)**: Parameter domain on which the uniform state exists in the plane ($\alpha \equiv \Gamma_a/\Gamma_1, \beta \equiv \Gamma_b/\Gamma_1$). Γ_a is assumed positive because it corresponds to a cortical tension, which requires Γ_1 positive for stability, but Γ_b can be negative. For the limit case of the polygonal model ($\Gamma_a \gg \Gamma_1$), the domain boundary is indicated by a dashed line.

interface has a circular shape, parametrized by a deviation angle ψ and a radius of curvature R . The cell width l becomes $l = 2R \sin \psi$ whereas the apical interfacial length is $2R\psi$. The non-zero apical curvature also adds a cap projected area $R^2 [\psi - \cos \psi \sin \psi]$ to the rectangular base. Thus, the interfacial energy of one cell reads

$$E_{\text{cell}} = \Gamma_a 2R\psi + \Gamma_b 2R \sin \psi + \Gamma_1 h - P(2Rh \sin \psi + R^2 [\psi - \cos \psi \sin \psi] - A_0) \quad (2.3)$$

where P is the Lagrange multiplier for area conservation, physically representing the pressure difference between the cell interior and the external fluid medium.

The equilibrium configuration corresponds to a minimum of the energy Eq. 2.3 with respect to variables ψ , R , h and P . Using the geometrical relation $l = 2R \sin \psi$, one gets

$$\left\{ \begin{array}{l} \psi^* = \arcsin\left(\frac{\Gamma_1}{2\Gamma_a}\right) \\ l^* = \sqrt{A_0} \frac{2\Gamma_1}{\sqrt{\Gamma_1 \left(4\Gamma_b + \sqrt{4\Gamma_a^2 - \Gamma_1^2}\right) + 4\Gamma_a^2 \arcsin\left(\frac{\Gamma_1}{2\Gamma_a}\right)}} \\ h^* = \sqrt{A_0} \frac{2\Gamma_b + \sqrt{4\Gamma_a^2 - \Gamma_1^2}}{\sqrt{\Gamma_1 \left(4\Gamma_b + \sqrt{4\Gamma_a^2 - \Gamma_1^2}\right) + 4\Gamma_a^2 \arcsin\left(\frac{\Gamma_1}{2\Gamma_a}\right)}} \\ R^* = \Gamma_a l^* / \Gamma_1 \\ P^* = \Gamma_a / R^* \end{array} \right. \quad (2.4)$$

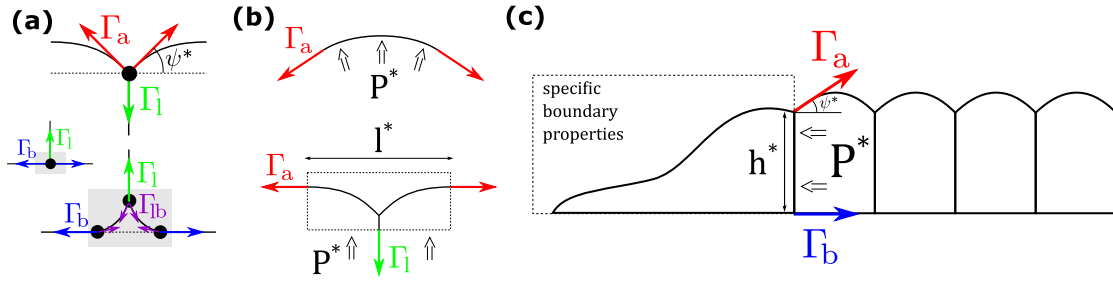


Figure 2.5: **(a)**: Point force balance on apical (top) and basal (bottom) vertices. The uniformity automatically ensures horizontal force balance while a vertical projection gives $2\Gamma_a \sin(\psi^*) = \Gamma_1$. Although the basal vertex force balance requires a new interfacial tension Γ_{1b} in principle (bottom), we neglect this interstitial region (gray rectangle) and replace it by a unique basal point thanks to some substrate anchoring. **(b)**: Laplace pressure balance reads $P^* = \Gamma_a/R^*$ where P^* is the pressure difference between cell and lumen (top). This pressure is resisted vertically by lateral tension through $P^*l^* = \Gamma_1$ (bottom). **(c)**: A last equation is necessary to obtain an equilibrium shape, and it corresponds to an horizontal force balance combining tension projections (the lateral tension does not contribute) and pressure difference P^* between cells and lumen. This is performed on a test box defined between tissue boundary and any lateral interface, sufficiently deep in the tissue to ignore any boundary effect and assume uniformity. Note that this result is completely independent from any specific mechanism generated by peripheral cells, like lamellipodial activity and/or high traction forces on substrate.

One can show that all energy derivatives (with respect to ψ , R , h and P) can be correctly interpreted as mechanical force balance equations: vertical apical vertex force balance (Fig. 2.5a, top), Laplace's law (Fig. 2.5b) and horizontal force balance (Fig. 2.5c), with the incompressibility constraint $A = A_0$. A combination of the geometric relation $l = 2R \sin \psi$ and the vertical apical vertex force balance leads to $P^*l^* = \Gamma_1$, interpreted as a vertical force balance on a test box of cell width size centred on the lateral interface (Fig. 2.5a, bottom). The representation of Fig. 2.5a (top) does not consider the situation with $\Gamma_a, \Gamma_1 < 0$: indeed this is excluded because the apical tension is only driven by actomyosin contractility and should be positive at steady-state. Thus one has $\Gamma_a, \Gamma_1 > 0$ but Γ_b can be positive or negative. Nonetheless, some parameter values are not allowed because the equilibrium shape is ill-defined (imaginary value). The domain region in which equilibrium is well-defined corresponds to $2\Gamma_a > \Gamma_1$ (vertical apical force balance) and $2\Gamma_b + \sqrt{4\Gamma_a^2 - \Gamma_1^2} > 0$ (positive height) (see Fig. 2.4c).

Rigorously speaking, when $\Gamma_b > 0$ the force balance at basal vertices (Fig. 2.5a, bottom right) should be determined according to an interstitial region without contact with cell-cell or cell-substrate contact, adding a supplementary interfacial tension Γ_{1b} . We overcome this inessential complexity by ignoring the interstitial region, and replace it by a single basal vertex on which is applied basal and lateral tensions independently of the sign of Γ_b . The cost to pay is an ill-defined vertical force balance (Fig. 2.5a, bottom left) that we consider to be automatically fulfilled thanks to rigid adhesion bonds, which prevents any cell detachment.

These parameter restrictions allow to use $\Gamma_1\sqrt{A_0}$ as the energy unit with $\sqrt{A_0}$ as the natural length unit. We therefore introduce the notation $\alpha \equiv \Gamma_a/\Gamma_1$ and $\beta \equiv \Gamma_b/\Gamma_1$.

2.2.3 External compression

If an external operator applies a compressive force F on a uniform tissue along horizontal axis, it is straightforward to describe the new equilibrium shape by using an extension of the horizontal force balance (Fig. 2.5c), showing that the precise compression technique has no effect on the deep tissue shape as long as the boundary effects are damped on a finite size. The equilibrium occurs when

$$Ph = \Gamma_b + F + \Gamma_a \cos \psi^* \quad (2.5)$$

The other force balance equations stay unchanged so ψ^* has the same equilibrium value, but R , h , l and P are perturbed according to a shift in the parameter $\Gamma_b \mapsto \Gamma_b + F$ for equilibrium equations Eq. 2.4. Note that F and Γ have the same dimension in 2D but F is a force per unit transverse length (y direction) in 3D.

This external compression can be controlled by a stretching device [188], where MDCK cells are deposited on a pre-stressed elastic membrane and then compressed by the release of prior tension after confluency. This is expected to reproduce more physiological conditions in which a local over-proliferation should trigger cell extrusion to maintain homeostatic epithelial cell density. Therefore, the compressive force F can also effectively represent the effect of dividing cells without describing explicitly the change in cell number.

It is instructive to make the analogy with a 2D incompressible material with rheology $\sigma_{xx} = -P + \frac{1}{2}E\partial_x u_x$, $\sigma_{zz} = -P + \frac{1}{2}E\partial_z u_z$, where the application of an external pressure P_{ext} (along the horizontal or vertical direction) generates a height deformation $\delta h = \pm h P_{\text{ext}}/E$. For horizontal compression, one puts $F = P_{\text{ext}}h$ in Eq. 2.5, and thanks to area incompressibility and vertical force balance $Pl = \Gamma_1$, one obtains the equilibrium state $h^*[P_{\text{ext}}]$. It is then linearized with respect to the free equilibrium h^* (Eq. 2.4) to obtain an equivalent Young modulus by comparison with elastic formula. For vertical compression, $F = 0$ in Eq. 2.5 but the vertical force balance becomes $(P - P_{\text{ext}})l = \Gamma_1$. One can easily show that the equivalent Young modulus is identical in both cases, with typical scaling $E_{\text{eff}} \sim \Gamma_1/\sqrt{A_0}$ (per unit of transverse unit) and exact formula

$$E_{\text{eff}} = \frac{2\Gamma_1 A_0}{l^*(2A_0 - h^*l^*)} \quad (2.6)$$

2.2.4 Flatness limit for apical interface

An instructive limit is $\Gamma_a \gg \Gamma_1$ when the apical interface flattens ($\psi^* \rightarrow 0$), which reproduces the polygonal cell shape assumption of many models: this is the (2D transverse) polygonal vertex model ([186, 171] and thesis [172]). In that case, the cell energy becomes

$$E_{\text{cell}} = (\Gamma_a + \Gamma_b)l + \Gamma_1 h - P(hl - A_0) \quad (2.7)$$

and the equilibrium point corresponds to³

$$\begin{cases} l^* &= \sqrt{A_0} \sqrt{\frac{\Gamma_1}{\Gamma_a + \Gamma_b}} \\ h^* &= \sqrt{A_0} \sqrt{\frac{\Gamma_a + \Gamma_b}{\Gamma_1}} \\ P^* &= \frac{1}{\sqrt{A_0}} \sqrt{\Gamma_1(\Gamma_a + \Gamma_b)} \end{cases} \quad (2.8)$$

If one writes⁴ area constraint $h = A_0/l$ and rewrite cell energy Eq. 2.7 as a function of l , the second derivative leads to

$$\frac{d^2 E}{dl^2} = \frac{2\Gamma_1 A_0}{l^3} \quad (2.9)$$

Therefore the solution Eq. 2.8 will be a stable equilibrium only if $\Gamma_1 > 0$. One can show that this stability condition is preserved for the bubbly model. Recalling the notation $\alpha \equiv \Gamma_a/\Gamma_1$ and

³One can easily show that the limit $\Gamma_a \gg \Gamma_1$ applied to the expressions Eq. 2.4 gives an equivalent result.

⁴It is also possible to compute the bordered Hessian matrix for variables l , h and P : the determinant is equal to $-2h^*\Gamma_1$ at the fixed point. A necessary and sufficient criterion for stability of a 3-variables constrained problem (minimum of the energy) is to have a negative determinant, which requires $\Gamma_1 > 0$ since h^* is positive definite. Note that from the perspective of the bubbly model, $\Gamma_1 > 0$ is equivalent to $\Gamma_a > 0$ according to apical vertex force balance.

apical α	basal β	Epithelial Tissue	Technique	Ref.
1.25	–	MDCK II	AFM indentation on apical interface	[41]
1.3 – 1.4	–	MDCK II	vertex tension inference (xz)	[162]
0.54	0.39	pancreatic tube (wild-type)	relative pMLC fluorescence	[170]
0.69	0.24	pancreatic tube (transformed)	relative pMLC fluorescence	[170]

Table 2.1: Parameter values for α and β using either relative myosin fluorescence on apical and basal interfaces with cell aspect ratio matching, or AFM microscopy to reconstruct the apical shape and extract an apical angle.

$\beta \equiv \Gamma_b/\Gamma_l$ and the use of $\sqrt{A_0}$ as the length unit, the energy Eq. 2.3 becomes in dimensionless format

$$\hat{E}_{\text{cell}} = (\alpha + \beta)l + h - P(lh - 1), \quad \text{for } \psi \rightarrow 0 \quad (2.10)$$

The minimal energy per cell is straightforwardly $\hat{E}_{\text{cell}}^* = 2\sqrt{\alpha + \beta}$. Importantly, the parameter domain on which the equilibrium shape is well-defined corresponds to $\alpha + \beta > 0$ for the polygonal description, with the constraint $\alpha \gg 1$.

If one wants to apply a compressive force at the periphery of the tissue, one simply needs to use the equation Eq. 2.5 with ($\psi^* \rightarrow 0$).

From now all expressions will be given in this set of adimensionalized variables and parameters if the contrary is not mentioned, and the symbol $\hat{\cdot}$ will be considered implicit.

2.2.5 Parameter estimates

Interestingly, the measurement of apical height variation through AFM indentation allows to compute an estimation for the parameter α . Indeed, the report [41] gives for a normal MDCK cell a width $l \simeq 20 \mu\text{m}$ and additional height $\Delta h \simeq 2 \mu\text{m}$, from Fig. 2g. Assuming a weak pressure difference with deviation angle $\psi \ll 1$, the geometry gives $4\Delta h \simeq l\psi$ and one gets $\psi^* \simeq 0.4\text{rad} \simeq 23\text{deg}$. Moreover, vertical force balance on apical vertex $2\alpha\psi^* \simeq 1$ leads to $\alpha \simeq 1.25$.

Another test is the elastic resistance to in-plane (uniaxial) stretching, as performed in [189] for a suspended MDCK monolayer maintaining its apico-basal polarity. In normal conditions, they obtain a Young modulus $E_{\text{WT}} \simeq 20 \text{ kPa}$ whereas treatment with actin polymerization or myosin inhibitor (Latruncunlin B and Y27632) generates a two-fold decrease. However, a cadherin inhibitor (EDTA) has a much stronger effect since $E_{\text{EDTA}} \simeq 1 \text{ kPa}$ with higher tendency for material failure at high strain. After translation from 2D to 3D quantities, the vertex model predicts an effective Young modulus $E_{\text{theo}} \sim \gamma_l/l^*$ at linear order in strain: with typical values of lateral surface tension $\gamma_l \sim 10^{-4} - 10^{-3} \text{ N/m}$ and $l^* \sim 10 \mu\text{m}$, one gets $E_{\text{theo}} \sim 10 - 100 \text{ Pa}$ which is clearly not compatible with experimental values. Note that the model imposes $\gamma_l < \gamma_a$ because of apical force balance and the high tensions $\sim 10^{-2} - 10^{-1} \text{ N/m}$ necessary for $E_{\text{theo}} \sim E_{\text{exp}}$ may be considered unrealistic, although many epithelial tissues exhibit a rather flat (differentiated) apical interface [161]. It shows that the elastic resistance associated to interfacial deformation, transferred into lateral cost by cell incompressibility, is not sufficient and one must involve the cytoplasmic elasticity that ensures the epithelial mechanical integration at tissue scale (actin, intermediate filaments and microtubules).

In principle, a bulk elastic term can be added to the model such that $E_{\text{theo}} = E_{\text{interface}} + E_{\text{bulk}}$ but this additional property may not be relevant for the understanding of a precise theoretical mechanism, and could therefore be ignored to keep a minimal model.

2.3 Model: Non-uniform tissue mechanics

2.3.1 Force balance equations

When any perturbation drives a shape change away from uniform equilibrium Eq. 2.4, the cell mechanics adjust vertex and interface positions through five force balance relations, three on basal

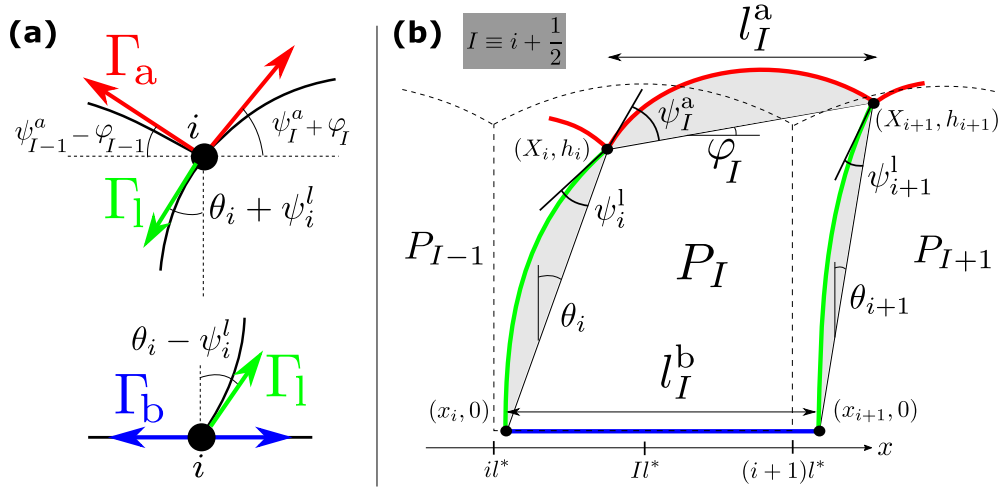


Figure 2.6: (a): Out-of-equilibrium point force balance on apical (top) and basal (bottom) vertices with uniform tensions. (b): Heterogeneous cell with curved apical (red) and lateral (green) interfaces, whereas the basal interface (blue) in contact with an undeformable substrate remains flat. One distinguishes lateral properties indexed by i , like vertex positions x , X , h , vertical tilt angle θ and lateral angle ψ^l , and cellular properties indexed by $I \equiv i + 1/2$, like apical and basal cell widths $l^a \equiv X_{i+1} - X_i$, $l^b \equiv x_{i+1} - x_i$, pressure P , horizontal tilt angle φ and apical angle ψ^a . Angles ψ^a and ψ^l are associated to interfacial curvatures whereas θ and φ represent the vertex "skeleton" tilt from uniform state.

and apical vertices (indexed by i), one on lateral interface (indexed by i) and one on apical interface (indexed by $I \equiv (i, i + 1) \equiv i + 1/2$)

$$\left\{ \begin{array}{l} \theta_i = \psi_i^l \quad [\text{basal vertex}] \\ \psi_{I-1}^a - \varphi_{I-1} = \psi^* + \theta_i + \psi_i^l \quad [\text{apical vertex 1}] \\ \psi_I^a + \varphi_I = \psi^* - (\theta_i + \psi_i^l) \quad [\text{apical vertex 2}] \\ P_I = \alpha C_I^a \quad [\text{apical interface}] \\ P_I - P_{I-1} = C_i^l \quad [\text{lateral interface}] \end{array} \right. \quad (2.11)$$

where geometric compatibility imposes $h_i C_i^l = 2 \cos \theta_i \sin \psi_i^l$ and $(X_{i+1} - X_i) C_I^a = 2 \cos \varphi_I \sin \psi_I^a$ to fix interfacial curvatures $C_i^l \equiv 1/R_i^l$ and $C_I^a \equiv 1/R_I^a$. A last equation ensures global area incompressibility. The first three equations correspond to Fig. 2.6a: apical force balance can be expressed along the lateral tension direction to shift angles from the equilibrium deviation angle ψ^* defined through $2\alpha \sin \psi^* = 1$, whereas basal tension uniformity forces the lateral deviation angle to equilibrate the vertical tilt. To perform the distinction between dependent and independent variables, invisible in Fig. 2.6b, one proposes the use of "polygonal" variables $\{X_i, h_i, \theta_i | P_I\}$ which leads to secondary variables $\{x_i, C_i^l, \psi_i^l | C_I^a, \varphi_I, \psi_I^a\}$. With definitions $\tan \varphi_I = (h_{i+1} - h_i)/(X_{i+1} - X_i)$, $x_i = X_i - h_i \tan \theta_i$, the two previous compatibility relations $h_i C_i^l = 2 \cos \theta_i \sin \psi_i^l$, $(X_{i+1} - X_i) C_I^a = 2 \cos \varphi_I \sin \psi_I^a$, and the use of force balance equations in Eq. 2.11, one can express all secondary variables as a function of primary variables. In the end, four equations (basal vertex, apical vertex 1 and 2, area incompressibility) remain available for the four variables $\{X_i, h_i, \theta_i | P_I\}$.

2.3.2 Discrete linear perturbation

Starting from a uniform monolayer, one can perturb cell shapes in all geometric variables with linear expansion around the prior state $\{X_i = X_{i-1} + l^* + \delta X_i, h_i = h^* + \delta h_i, \theta_i = 0 + \delta \theta_i | P_I = P^* + \delta P_I\}$ and $\{x_i = X_i + \delta x_i, C_i^l = 0 + \delta C_i^l, \psi_i^l = 0 + \delta \psi_i^l | C_I^a = C^* + \delta C_I^a, \varphi_I = 0 + \delta \varphi_I, \psi_I^a = \psi^* + \delta \psi_I^a\}$, where the primary variable X will be replaced by apical length $l_I^a \equiv X_{i+1} - X_i = l^* + \delta l_I^a$. The geometric compatibility equations provide at first order $\delta x_i = \delta X_i - h^* \delta \theta_i$, $h^* \delta C_i^l = 2 \delta \psi_i^l$, $l^* \delta C_I^a = 2 \delta \psi_I^a$, and $\delta \varphi_I = (\delta h_{i+1} - \delta h_i) / l^*$, all expressed in terms of primary variables. The linearization of force

balance equations Eq. 2.11 gives

$$\left\{ \begin{array}{l} \delta\theta_i = \delta\psi_i^l \quad [\text{basal vertex}] \\ \delta\psi_{I-1}^a + \delta\psi_I^a + \delta\varphi_I - \delta\varphi_{I-1} = 0 \quad [\text{apical vertex 1}] \\ \delta\psi_{I-1}^a - \delta\psi_I^a - (\delta\varphi_{I-1} + \delta\varphi_I) = 2(\delta\theta_i + \delta\psi_i^l) \quad [\text{apical vertex 2}] \\ (l^*)^2 \delta P_I = -\delta l_I^a + 2\alpha l^* \cos \psi^* \delta\psi_I^a \quad [\text{apical interface}] \\ \delta P_I - \delta P_{I-1} = 2\delta\psi_i^l / h^* \quad [\text{lateral interface}] \end{array} \right. \quad (2.12)$$

whereas the area incompressibility closes the system of equations

$$\left[\frac{2}{l^*} - h^* \right] \delta l_I^a + \frac{l^*}{2} (\delta h_i + \delta h_{i+1}) + (l^*)^2 \frac{1 - \psi^* \cot \psi^*}{2(\sin \psi^*)^2} \delta\psi_I^a - \frac{(h^*)^2}{2} (\delta\theta_{i+1} - \delta\theta_i) - \frac{(h^*)^2}{6} (\delta\psi_{i+1}^l - \delta\psi_i^l) = 0 \quad (2.13)$$

The combination of apical vertex equations with basal constraint $\delta\psi_i^l = \delta\theta_i$ gives $\delta\psi_I^a = \delta\theta_{i+1} - \delta\theta_i$ and $\delta\varphi_I = -(\delta\theta_{i+1} + \delta\theta_i)$. The apical Laplace law in Eq. 2.12 terminates the expression of secondary variables as a function of primary ones with δl^a depending on δP and $\delta\theta$. Since $\delta\varphi$ can also be expressed as a function of δh , one gets a simple geometric equation valid at mechanical equilibrium, away from tissue boundaries and for uniform tensions:

$$\delta h_{i+1} - 2\delta h_i + \delta h_{i-1} = -l^* (\delta\theta_{i+1} - \delta\theta_{i-1}) \quad (2.14)$$

In addition, area incompressibility constraint Eq. 2.13 can be associated to apical pressure difference equation in Eq. 2.12 to obtain the equilibrium pressure deviation δP as a function of δh (at position i)

$$\frac{1}{2} (\delta P_{I-1} + \delta P_I) = -\frac{h^* (3\alpha l^* \cos \psi^* - h^*)}{3(l^*)^2 (2 - h^* l^*)} (\delta h_{i+1} - 2\delta h_i + \delta h_{i-1}) + \frac{1}{2 - h^* l^*} \delta h_i \quad (2.15)$$

In the framework of thin film continuous mechanics, this equation can be seen as a normal force balance at the free interface ($z = h$) where bulk pressure δP equilibrates a "surface tension" (Laplace law) with a new term expressing height rigidity emerging from discrete lateral interfaces.

Finally, the lateral and apical pressure difference equations in Eq. 2.12 can be combined to eliminate δP whereas $\delta\theta$ disappears thanks to Eq. 2.14. One gets an independent difference equation for the equilibrium height response to perturbation:

$$\left(3\alpha \cos \psi^* - \frac{h^*}{l^*} \right) (\delta h_{i+2} - 4\delta h_{i+1} + 6\delta h_i - 4\delta h_{i-1} + \delta h_{i-2}) = \frac{6}{(h^*)^2} (\delta h_{i+1} - 2\delta h_i + \delta h_{i-1}) \quad (2.16)$$

and an equivalent one in terms of tilt response to perturbation:

$$\left(3\alpha \cos \psi^* - \frac{h^*}{l^*} \right) (\delta\theta_{i+2} - 2\delta\theta_{i+1} + 2\delta\theta_{i-1} - \delta\theta_{i-2}) = \frac{6}{(h^*)^2} (\delta\theta_{i+1} - \delta\theta_{i-1}) \quad (2.17)$$

2.3.3 Continuous approximation

Using a central difference scheme at lowest accuracy with step size l^* and mid-grid point values obtained by the average of adjacent points⁵, one can easily transform these discrete equations into

⁵One defines cell variables indexed by $I \equiv i + 1/2$ on mid-grid points $x_I = Il^*$ and lateral variables indexed by i on points $x_i \equiv il^*$, with mid-grid averages $.I \equiv (.i + .i+1)/2$ or $.i \equiv (.I + .I-1)/2$ when necessary. Derivatives at x_i are defined as $(.I - .I-1)/l^*$ for cell variables and $(.i+1 - .i-1)/2l^*$ for lateral variables.

differential equations over continuous fields $\delta P(x)$, $\delta\theta(x)$ and $\delta h(x)$.

$$\delta\theta'(x) \simeq -\frac{1}{2}\delta h''(x) \quad (2.18)$$

$$\delta P(x) \simeq -\frac{h^*l^*}{3(2-h^*l^*)} \left(3\alpha \cos \psi^* - \frac{h^*}{l^*} \right) \delta h''(x) + \frac{1}{2-h^*l^*} \delta h(x) \equiv -\Gamma_{\text{eff}} \delta h''(x) + k_{\text{eff}} \delta h(x) \quad (2.19)$$

$$0 \simeq (h^*l^*)^2 \left(3\alpha \cos \psi^* - \frac{h^*}{l^*} \right) \delta h^{(4)}(x) - 6\delta h''(x) \Rightarrow \Gamma_{\text{eff}} \delta h^{(4)}(x) \simeq \frac{2A_0}{h^*l^*} k_{\text{eff}} \delta h''(x) \quad (2.20)$$

The mechanical interpretation of those equations in terms of continuum mechanics will be given in a next section. The pressure equation is used to define effective parameters: a surface (line) tension Γ_{eff} and stiffness k_{eff} , making a characteristic length $\lambda_{\text{eff}} \equiv \sqrt{\Gamma_{\text{eff}}/k_{\text{eff}}}$. They become in dimensional form

$$\Gamma_{\text{eff}} \equiv \frac{h^*l^*}{2A_0 - h^*l^*} \left(\Gamma_a \cos \psi^* - \Gamma_b \frac{h^*}{3l^*} \right), \quad k_{\text{eff}} \equiv \frac{\Gamma_1}{2A_0 - h^*l^*} \quad (2.21)$$

One can easily show that the effective stiffness k_{eff} is strictly positive for any tension values α , β coherent with the existence of a stable uniform equilibrium, according to Fig. 2.4b. Indeed, $2A_0 - h^*l^*$ is strictly positive because the difference $A_0 - h^*l^*$ corresponds to the apical cap area⁶ (Fig. 2.4a). For the effective surface tension, its sign is equivalent to the sign of the expression $2\alpha \cos \psi^* - \beta > 0$. It is positive for a large portion of the allowed parameter space, except for a tiny region when $\alpha \gtrsim 0.5$ and $\beta \gtrsim 0$.

In fact, the compatibility between the difference equation for height Eq. 2.16 and its differential equivalent Eq. 2.18 requires the characteristic height relaxation scale $\lambda_{\text{eff}} \sqrt{h^*l^*/(2A_0)}$ to be much larger than the cell width l^* . Thus, the continuous limit can be considered to be valid only when

$$\Lambda \equiv \left| \frac{(h^*)^2}{2A_0} \left(\alpha \cos \psi^* - \frac{h^*}{3l^*} \right) \right| \gg 1 \quad (2.22)$$

One can easily check that this is only possible if $\alpha \gg 1$. It importantly implies that the continuous limit is invalid in the region over which the effective surface tension Γ_{eff} Eq. 2.21 is negative definite, meaning that this parameter cannot be physically interpreted as a surface tension⁷ for too small α . Since the equilibrium cell aspect ratio h^*/l^* is approximately equal to $\alpha + \beta$ in the limit $\alpha \gg 1$, one gets three possible cases to verify the condition $\Lambda \gg 1$: $\beta = \alpha + o(1)$, $\beta = o(1)$ or $\beta = -\alpha + o(1)$ ($\beta = -\alpha + o(1/\alpha)$ would give $\Lambda \sim o(1)$). The first two cases generate a large cell aspect ratio ($h^*/l^* \sim \alpha$) and a continuous threshold scaling $\Lambda \sim \alpha^2$. However, a largely negative basal tension $\beta = -\alpha + o(1)$ corresponds to a finite aspect ratio ($h^*/l^* = o(1)$)⁸ with a smaller continuous threshold $\Lambda \sim \alpha$.

In this relevant limit of $\alpha \gg 1$, the cells become approximately polygonal and the two effective parameters are reduced to $\Gamma_{\text{eff}} \simeq \frac{1}{3}(2\Gamma_a - \Gamma_b)$ and $k_{\text{eff}} \simeq \Gamma_1/A_0$. Note that the effective surface tension is equal to apical cell tension (at first order) only in the third case $\beta = -\alpha + o(1)$, the two first ones containing multiplicative factors 1/3 or 2/3.

2.3.4 Boundary relaxation

Although the equilibrium tissue shape away from the boundaries is independent of boundary conditions as explained in Fig. 2.5, it is instructive to look at the exact solution for an homogeneous epithelium where mechanical properties of peripheral cells remain identical to the bulk part,

⁶However, this argument implies $k_{\text{int}} < 0$ and questions the relevance of the formal identification with the 2D incompressible elastic model from the previous paragraph.

⁷The broken continuous limit equivalently means that $\delta h_{i+1} - 2\delta h_i + \delta h_{i-1}$ cannot be reduced to $l^2 \delta h''(x)$ with $x = il^*$, such that the parameter Γ_{eff} defined through the pressure equation Eq. 2.21 cannot be reduced anymore to a surface tension (Laplace's law).

⁸ $o(1)$ is a classical mathematical notation meaning that this quantity is negligible with respect to $\alpha \gg 1$, whereas it dominates terms proportional to $1/\alpha$.

although phenomenological specificities are expected experimentally at the tissue periphery, like protrusive activity and weak epithelial phenotype (mesenchymal-like). This assumption of tissue uniformity has an important consequence on the parameter space: the peripheral basal vertex force balance must equilibrate apical and basal tensions according to $\Gamma_a \cos \phi = \Gamma_b$ (see Fig. 2.7a), which imposes the constraint $|\Gamma_b| < \Gamma_a$ on the accessible parameter space.

Contrarily to energetics of uniform tissues that ignore boundaries [168], this nicely explains why the equilibrium height of rectangular cells vanishes when $\Gamma_b \rightarrow -\Gamma_a$ ($h^* \propto \sqrt{\Gamma_a + \Gamma_b}$, see Eq. 2.8): it simply corresponds to a limit of full wetting with infinite tissue extension and vanishing thickness. However, note that the opposite limit $\Gamma_b \rightarrow \Gamma_a$ is not forbidden by energetics, in contradiction with this force balance constraint at the tissue boundary. It predicts the shrinkage of the basal interface for $\Gamma_b > \Gamma_a$ with tissue reconfiguration into a disk-like geometry (or a spheroid in 3D), although its experimental observation may be difficult due to phenotypic changes at the periphery that may locally reverse the sign of basal tension.

Compared to Fig. 2.4b, the constraint $|\Gamma_b| < \Gamma_a$ means that the domain $\beta > \alpha$ should also be considered unphysical in this assumption of overall tissue uniformity. Under these conditions, the validity of the continuous limit Eq. 2.22 can be quantified and seems to break only for $\alpha \lesssim 2$ and $\beta \gtrsim -\alpha$ (see Fig. 2.7b).

In terms of cell shapes, the peripheral cell is "special" because it has only one lateral interface and can be in mechanical equilibrium with its neighbours only with a pressure difference as shown on Fig. 2.7a. One gets cell shape perturbation localized at the tissue periphery, with exponential-like relaxation towards the geometry predicted by equations Eq. 2.18 as shown on Fig. 2.7c for tissue height, lateral tilt and cell pressure. This localization effect allows to ignore boundary effects to focus only on the bulk tissue. Note the large discrepancy between the boundary value predicted by the continuous equations and the exact one: this is partly due to non-linearities, because the maximal deformation with respect to central tissue shape is at the boundary, and also due to discrete boundary equations differing from bulk ones because the peripheral cell experiences specific forces. More generally, since the equations obtained for a perturbed cell monolayer assume tension homogeneity among the population of vertices i , any boundary where cell properties - tension or target area - have to change implies a deviation from the "bulk" equations, continuous limit or not, as can be easily checked on Fig. 2.7c for $x \sim 0-1$. This deviation will be particularly relevant for an extruding cell inserted into an homogeneous epithelium, where oncogenic-like transformations are mapped to a tension shift, or at the interface between two cell populations that define homogeneous domains (no mixing).

2.3.5 Bubbly vs polygonal mechanical response

The limit of flat apical interfaces $\alpha \gg 1$ can be computed easily as $h^* \rightarrow \sqrt{\alpha + \beta}$, $l^* \rightarrow 1/h^*$ and $\psi^* \rightarrow 0$. For example, the equilibrium height response equation Eq. 2.16 becomes

$$(2\alpha - \beta) (\delta h_{i+2} - 4\delta h_{i+1} + 6\delta h_i - 4\delta h_{i-1} + \delta h_{i-2}) = \frac{6}{\alpha + \beta} (\delta h_{i+1} - 2\delta h_i + \delta h_{i-1}) \quad (2.23)$$

However, the polygonal vertex model differs significantly from the bubbly one because of the geometric tilt on lateral tension induced by a pressure difference. When studying the uniform equilibrium configuration, this distinction is hidden because pressure is uniform.

The polygonal cell corresponds to the "skeleton" of a bubbly cell, represented on Fig. 2.6b with vertices positioned at $(x_i, 0)$, $(x_{i+1}, 0)$, (X_i, h_i) and (X_{i+1}, h_{i+1}) on cell I . Using the geometric relation $X_i = x_i + h_i \tan \theta_i$ and the area conservation to eliminate x_i and X_i variables, one can

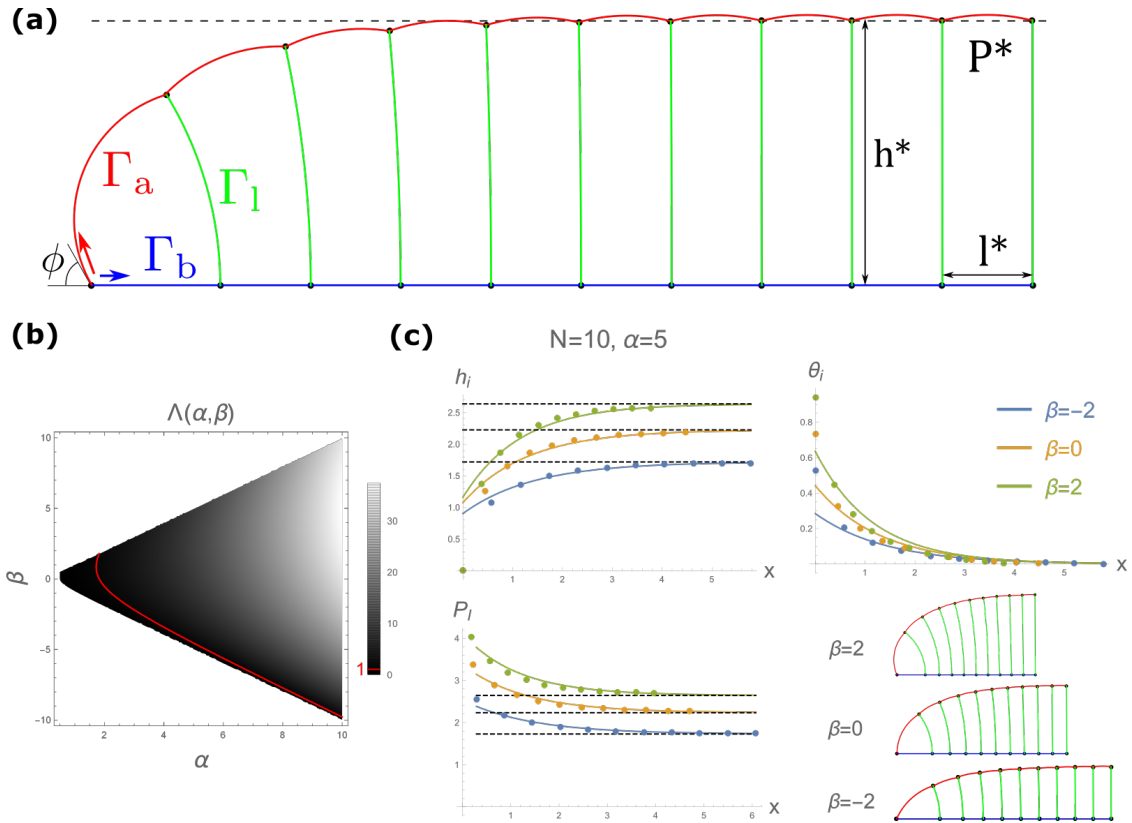


Figure 2.7: (a): Sketch of a peripheral 2D side tissue in mechanical equilibrium. Even with homogeneous mechanical properties among the entire tissue, the fact that the peripheral cell as a distinct environment (only one lateral interface) leads to a local deviation from bulk properties h^* , l^* or P^* with exponential-like relaxation. Here the basal tension is positive ($\alpha = 2$ and $\beta = 1$) but it is not required in general as long as the peripheral basal force balance $\Gamma_a \cos \phi = \Gamma_b$ is satisfied. (b): The continuous threshold Λ (Eq. 2.22) in the parameter space (α, β) restricted to a physical domain where $2\alpha > 1$, $h^* \geq 0$ and $|\beta| < \alpha$. The line $\Lambda = 1$ (red) separates two regions where the continuous limit is approximately valid ($\Lambda \gg 1$) or invalid ($\Lambda \lesssim 1$). (c): Quantification of boundary relaxation for tissue height h , lateral tilt θ and cell pressure P discrete variables (points), with $N = 10$ cells at $\alpha = 5$ for three basal tension values. For those parameters, the continuous approximation (lines) works well when the third lateral height is given (Eq. 2.16 is defined for $i \geq 2$). Dashed lines indicate asymptotic values, P^* for pressure and h^* for height, as illustrated on (a). To facilitate the comparison with the continuous equations, discrete lateral height and tilt are expressed as a function of $x_i \equiv i.l^*$ ($0 \leq i \leq 10$) whereas pressure is represented at $x_l \equiv (i + 0.5)l^*$. For each basal tension, the tissue profile is sketched as in (a).

show that the exact energy for the cell I is, as a function of h_i, θ_i

$$E_I = \alpha \sqrt{\left(\frac{2 + h_{i+1}^2 \tan \theta_{i+1} - h_i^2 \tan \theta_i}{h_i + h_{i+1}}\right)^2 + (h_{i+1} - h_i)^2} + \beta \frac{2 + h_i h_{i+1} (\tan \theta_i - \tan \theta_{i+1})}{h_i + h_{i+1}} + \frac{h_i}{2 \cos \theta_i} + \frac{h_{i+1}}{2 \cos \theta_{i+1}} \quad (2.24)$$

The tissue is in mechanical equilibrium when the derivation of total energy $E_{\text{tissue}} = \sum_I E_I$ with respect to any variable h_i, θ_i vanishes. The exact equations $\partial E_{\text{tissue}} / \partial h_i = 0$ and $\partial E_{\text{tissue}} / \partial \theta_i = 0$, corresponding to effective local force balance equations, can be linearized around the uniform state $h_i = h^* + \delta h_i$ and $\theta_i = 0 + \delta \theta_i$ exactly like the previous section:

$$\begin{aligned} 4\delta\theta_i &= -h^* (\delta h_{i+1} - \delta h_{i-1}) \\ 8\delta h_i &= 2(2\alpha \frac{h^*}{j^*} - 1)(\delta h_{i+1} - 2\delta h_i + \delta h_{i-1}) + (h^*)^3 (\delta \theta_{i+1} - \delta \theta_{i-1}) \end{aligned} \quad (2.25)$$

The independent discrete equation for height mechanical response is easily derived to get

$$\begin{aligned} 32\delta h_i + 4[(\alpha + \beta)(\beta - 3\alpha) + 2](\delta h_{i+1} - 2\delta h_i + \delta h_{i-1}) \\ + (\alpha + \beta)^2 (\delta h_{i+2} - 4\delta h_{i+1} + 6\delta h_i - 4\delta h_{i-1} + \delta h_{i-2}) = 0 \end{aligned} \quad (2.26)$$

The geometric equation coupling height and tilt perturbations is similar to the bubbly model (Eq. 2.14) and can be shown to be equivalent at least order for the continuous approximation. However, the equation for height mechanical response Eq. 2.23 is fundamentally distinct from Eq. 2.26. This is shown through the analysis of the characteristic regimes (decay, oscillations or damped oscillations) for those finite difference equations as a function of parameter space. Similarly to continuous differential equations, one uses an expansion $\delta h_i \propto \lambda^i$ to get the characteristic 4th-order polynomials in λ from bubbly (Eq. 2.23) and polygonal (Eq. 2.26) versions. Depending on the sign and amplitude of $\lambda(\alpha, \beta)$, one can obtain an "exponential" solution ($|\lambda| \geq 1$ with $\lambda > 0$), an "oscillatory" solution ($|\lambda| = 1$ with $\lambda < 0$ or complex) or a "damped oscillatory" solution ($|\lambda| \geq 1$ with $\lambda < 0$ or complex). This is summarized on Fig. 2.8: one clearly sees the absence of "damped oscillations" for the bubbly model in opposition to the polygonal one, in the flatness limit $\alpha \gg 1$. In this limit, the uniform tissue equilibrium is defined for $\alpha + \beta > 0$ which justifies the use of the parameter space $(\alpha + \beta, \alpha - \beta)$. Finally, one property unique to the bubbly model is the existence of a special parametric line $\beta = 2\alpha$ (dashed line on Fig. 2.8a) on which no characteristic length exists: the tissue mechanical response becomes global.

Note that in the full bubbly framework, for which one imposes $|\beta| < \alpha$ to satisfy force balance equations up to the tissue boundary, only the upper half-space of those diagrams become relevant and the distinction between the two models disappears: the "oscillations" regime is forbidden whereas the "damped oscillations" regime that occurs for the polygonal model (when both $\alpha - \beta \lesssim 1$ and $\alpha + \beta \lesssim 1$) is not consistent with the flat interface hypothesis ($\alpha \gg 1$) for any value of β .

2.3.6 Connexion to 2D incompressible elasticity

To understand the previous set of static field equations Eq. 2.18, it is instructive to compare them to a model of 2D incompressible elasticity under the thin film approximation. An epithelial monolayer is likely to have a transverse isotropy: the response to a longitudinal load (quantified by the Young modulus E) is isotropic in the horizontal plane ($E_x = E_y \equiv E_t$) but different along the vertical axis ($E_z \equiv E_n \neq E_t$), and requires the introduction of five independent elastic moduli $\{E_t, E_n, \nu_t, \nu_n, G_t\}$. However, it is sufficient to consider an isotropic rheology for our 2D side system because of two reasons. First, a 2D transversely isotropic material becomes a bit special when assumed incompressible, because the Young moduli $\{E_t, E_n\}$ can be shown to be identical under this condition (a property that do not concern the equivalent 3D case). Second, although the xz shear modulus G_t becomes an independent parameter in transverse isotropy, our system is under shear-free conditions and therefore one cannot determine the difference with isotropic elasticity.

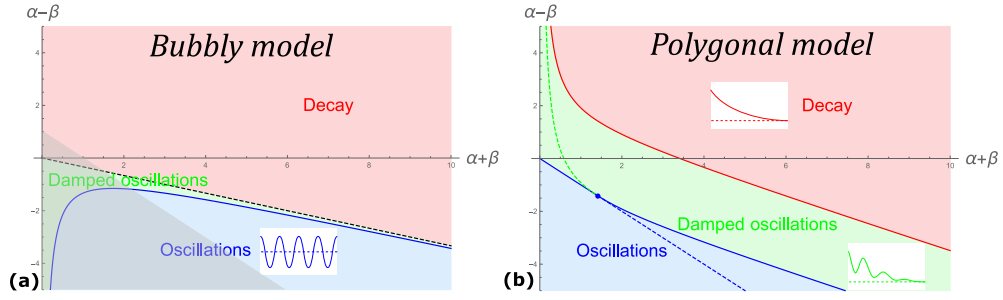


Figure 2.8: Diagram representing in parameter space ($x = \alpha + \beta, y = \alpha - \beta$) the different regimes for a tissue mechanical response to a perturbation, for the bubbly model (a) and the polygonal model (b). The flatness limit ($\alpha \gg 1$) is assumed for simplicity so that the region where both x and y are small should not be considered. The existence of uniform equilibrium requires $\alpha + \beta > 0$ ($x > 0$). The striking difference between the two diagrams is the disappearance of "damped oscillations" for the bubbly model as $\alpha \rightarrow +\infty$, contrarily to the polygonal model where a finite region remains. Moreover, one unique feature of the bubbly model is the singular limit along the line $\beta = 2\alpha$ (dashed line) for which Eq. 2.23 is reduced to $\delta h_i^{(2)} = 0$: there is no characteristic length. This only occurs on the polygonal model under the forbidden limit $\beta \rightarrow -\alpha$. Finally, another difference for the bubbly model is the apical vertex force balance that imposes $\alpha > 1/2$ ($y > 1 - x$) as represented in gray, but this limit is not compatible with prior assumptions and should be of less concern.

Thus, the rheology is defined as $\sigma_{xx} = -P + \frac{1}{2}E\partial_x u_x$, $\sigma_{zz} = -P + \frac{1}{2}E\partial_z u_z$, $\sigma_{xz} = \frac{1}{4}E(\partial_z u_x + \partial_x u_z)$ where P is a Lagrange multiplier to ensure 2D incompressibility $\partial_x u_x + \partial_z u_z = 0$. Horizontal and vertical stress balance reads

$$\partial_x \sigma_{xx} + \partial_z \sigma_{xz} = 0, \quad \partial_z \sigma_{zz} + \partial_x \sigma_{xz} = 0 \quad (2.27)$$

whereas the z boundary conditions are: no shear stress $\sigma_{xz}(x, z = 0) = \sigma_{xz}(x, z = h^*) = 0$, substrate anchorage $u_z(x, z = 0) = 0$ and Laplace pressure $\sigma_{zz}(x, z = h^*) = \gamma \delta h''(x) - k_{\text{int}} \delta h(x)$ with the definition $u_z(x, z = h^*) \equiv \delta h(x)$.

The thin film approximation corresponds to a field expansion with respect to the parameter $\epsilon \equiv h^*/L$ (up to order 2) where L is a characteristic length along the horizontal direction (tissue size):

$$\begin{aligned} u_x(x, z) &= u_0(x, z) + \epsilon u_1(x, z) + \epsilon^2 u_2(x, z) + O(\epsilon^3) \\ u_z(x, z) &= w_0(x, z) + \epsilon w_1(x, z) + \epsilon^2 w_2(x, z) + O(\epsilon^3) \\ P(x, z) &= P_0(x, z) + \epsilon P_1(x, z) + \epsilon^2 P_2(x, z) + O(\epsilon^3) \\ \delta h(x) &= \delta h_0(x) + \epsilon \delta h_1(x) + \epsilon^2 \delta h_2(x) + O(\epsilon^3) \end{aligned}$$

Then one expands local force balance equations Eq. 2.27 at each ϵ order after the transformation into dimensionless quantities $X \equiv x/L$, $U \equiv u_x/L$, $Z \equiv z/h^*$, $W \equiv u_z/h^*$, which ensures an equivalent order for $\partial_x u_x$ and $\partial_z u_z$ for incompressibility.

At zero-th order in ϵ , the horizontal stress balance is equivalent to $\partial_z^2 u_0 = 0$ whereas the vanishing shear stress at both boundaries gives $\partial_z u_0 = 0$: incompressibility and substrate anchorage then imply $w_0(x, z) = \delta h_0(x)z/h^*$. The vertical stress balance becomes $\partial_z \sigma_{zz}^0 = -\partial_z P_0 = 0$ such that Laplace pressure equation leads to

$$P_0(x) = \left[\frac{E}{2h^*} + k_{\text{int}} \right] \delta h_0(x) - \gamma \delta h_0''(x) \quad (2.28)$$

Following the same logic, the equations at first order in ϵ are shown to be identical to zero-th order: $\partial_z u_1 = 0$, $w_1(x, z) = \delta h_1(x)z/h^*$ and $\partial_z P_1 = 0$.

At second order, one can show that $\partial_z u_2(x, z) = -\delta h_0'(x)z/h^*$, $\partial_z P_2(x, z) = E\delta h_0''(x)z/(2h^*)$, whereas the horizontal stress balance fixes the horizontal propagation of zero-th order fields as it reads $-4\partial_r P_0 + E\partial_r^2 u_0 + E\partial_z^2 u_2 = 0$. With the expression of $u_2(x, z)$, this equation appears to be

equivalent to $\partial_r \sigma_{rr}^0 = 0$. Finally, using the expression for P_0 as a function of δh_0 (Eq. 2.28) leads to

$$\gamma \delta h_0^{(3)}(x) = \left[\frac{E}{h^*} + k_{\text{int}} \right] \delta h_0'(x) \quad (2.29)$$

The comparison with the continuous version of the vertex model equations (Eq. 2.18) shows that the pressure equation Eq. 2.15 corresponds to normal stress balance at the free interface, whereas the equation for height relaxation Eq. 2.16 corresponds to horizontal Stokes equation. Moreover, the geometric equation connecting height field δh and lateral tilt $\delta \theta$ (Eq. 2.14) is equivalent to no shear stress condition. Indeed, with definition $\delta \theta(x) = [u_x(x, z = h^*) - u_x(x, z = 0)]/h^*$ (coming from geometry $\tan \theta = \Delta u_x/h^*$) and second order equation $\partial_z u_2(x, z) = -\delta h_0'(x)z/h^*$, one gets a similar equation $\delta h_0''(x) = -2\delta \theta'(x)$. Finally, the parametric equivalence between the two models leads to

$$k_{\text{eff}} = \frac{E}{2h^*} + k_{\text{int}}, \quad \gamma_{\text{eff}} = \gamma, \quad \frac{2A_0}{h^*l^*} k_{\text{eff}} = \frac{E}{h^*} + k_{\text{int}} \Rightarrow k_{\text{eff}} = \frac{El^*}{2(2A_0 - h^*l^*)}, \quad k_{\text{int}} = -\frac{E}{h^*} \frac{A_0 - h^*l^*}{2A_0 - h^*l^*} \quad (2.30)$$

Note that because the cell area can be written as $A_0 = h^*l^* + A_{\text{apical}}$, k_{eff} is strictly positive (as discussed before) but the interfacial stiffness k_{int} , introduced as a necessary degree of freedom to make the comparison, is negative definite. Since the stiffness appears in the mechanical equation Eq. 2.28 only through a factor proportional to k_{eff} , the mechanics remains "natural". In the limit where the apical interface is approximately flat ($\alpha \gg 1$), $h^*l^* \simeq A_0$, one doesn't need an interfacial stiffness ($k_{\text{int}} = 0$) and $k_{\text{eff}} = E/(2h^*)$ is a purely bulk effect associated to the material Young modulus E .

Independently from the precise stress-strain constitutive equations, the assumption of an elastic rheology for the adhered epithelial monolayer is questionable. But since the vertex model do not contain dissipational properties at the cell level (cytoplasmic or interfacial viscosity) and possesses a "free" equilibrium state through interfacial energy minimization constrained by cell incompressibility, the emergent rheology must be elastic in nature.

Chapter 3

Cancerous budding

This project is a collaboration with the team leader Danijela Matic Vignjevic (UMR 144, Curie institute) and her post-docs Jorge Barbazán and Carlos Pérez-González to add some theoretical insights on an ongoing experimental project. In the context of tumour invasiveness, they designed an *in vitro* experimental set-up to study the mechanical influence of cancer-related stromal cells on the generation of cancer cell clusters. Starting from a circular monolayer of cancer cells surrounded by the stromal tissue, a key feature occurs after few hours of co-culture: the spontaneous assembly of a supracellular contractile ring in stromal cells at the tissue interface. The ring initially compresses the cancerous cluster but quickly climbs on top of it to undergo gap closure, which is reminiscent of the purse-string mechanism observed during epithelial wound healing. A fraction of cancerous clusters are weakly perturbed and let stromal cells close on top, whereas the others strongly reorganize into a 3D cluster of cancer cells. This experimental system tries to mimic on a flat substrate the *in vivo* formation of tumour buds from the primary site, and confirm the hypothesis of an active role played by cancer-related stromal cells in this important process associated to low patient prognosis. In a first chapter, the experimental system is presented within its biological context with the main quantitative results obtained. Then, the modelling approach and the theoretical assumptions are introduced, followed by a last chapter on the theoretical results and their comparison to experiments (when possible). A pre-print focused on the experimental aspects of the project is available on bioRxiv [190].

3.1 Introduction: tumour budding, gap closure and experimental system

3.1.1 The biological context: tumour budding and cancer-associated fibroblasts

Cancers often start by oncogenic transformation of individual epithelial cells followed by localized neoplasia, later transformed into a primary tumour. Later, it often gives rise to secondary cancerous sites called metastases through single or collective cancer cell invasion (review [191]). Despite the strong impact of metastasis on patient survival rate (review [192]), precise mechanisms for tumour invasion are still lacking. Even the time at which dissemination starts - early or late during tumour development - is not clearly established (review [193]). Moreover, some paradigms of cancer invasion have been recently questioned, including the requirement for Epithelial-to-Mesenchymal Transition (EMT) [194, 195], metalloproteinase-dependent basement membrane degradation [196] or the promotive effect of E-cadherin loss [197]. The EMT was initially seen as a binary transition from an epithelial phenotype to a migratory phenotype used by cancer cells to escape the primary tumour and invade the body, later followed by a reverse transition named MET (Fig. 3.1a,b) to develop malignant metastases (review [198]). In the last decade, it has been realised [199] that those transitions were more dynamic (Fig. 3.1a,b), with intermediate states (partial EMT) that share similarities with embryonic development (reviews [200, 201, 202]). The current picture attributes hybrid properties to tumour cells circulating in the bloodstream (Fig. 3.1a), often isolated with a small proportion of cell clusters [199]. Nonetheless despite being rare, those clusters have increased

metastatic potential [203, 204], higher resistance to apoptosis through E-cadherin expression [197] and EMT markers [205]. They are also mixed into an heterogeneous population with non-malignant cells [206], and emerge from the primary tumour site rather than by aggregation of single circulating cells [203, 204].

In addition to cancer cell properties, the tumour micro-environment embedded in the extra-cellular matrix (review [207]) is increasingly being recognised as an important biological and mechanical factor for the tumour fate (reviews [208, 209]). It contains Cancer-Associated-Fibroblasts (CAFs) as well as normal fibroblasts, immune cells, Tumour-Associated Macrophages (TAMs), Cancer Stem Cells (CSCs), and endothelial cells (Fig. 3.1a). CAFs emerge from the differentiation of normal fibroblasts, endothelial cells or mesenchymal stem cells among others (reviews [207, 208]), and "promote" cancer development with tumour growth by proliferative signalling and angiogenesis ([210] and review [208]), but also indirectly promotes invasiveness by basement membrane weakening [196], extra-cellular matrix alignment for directed cancer cell migration [211], fibronectin assembly [212], and enhanced survival by incorporation into invasive clusters [206]. In addition, CAFs seem able to directly promote cancer cell invasion (Fig. 3.1c) as migrating leaders [213], thanks to an heterotypic cadherin adhesion linking both cell types [214]. Although those evidences show the tumour-promoting effects of CAFs, the later can also have inhibitory effects on tumour fate [215], maybe by forming a mechanical cage confining the tumour through matrix stiffening and high cell contractility ([212] and review [209]).

At the invasive front of the primary tumour, the observation of small cell clusters embedded in the stroma have been named tumour budding (Fig. 3.1d). This histological characteristic is associated with higher metastatic potential and lower survival prognosis (reviews [216, 217]). Often discussed in the context of colo-rectal cancer, the second most lethal cancer in Europe for both men and women [218], tumour budding has been restricted to single cells or clusters of less than five cells (review [217]) but no clear mechanism has been identified to generate cancerous buds. The abundance of CAFs in the tumour micro-environment [219] and their important mechanical activity (Fig. 3.1c) asks for their role in the initiation of cancer cell invasion. This overall medical context encouraged the study of the interactions between CAFs and cancer cells, in particular under the controllable conditions of *ex vivo* approaches.

3.1.2 Epithelial gap closure: purse-string and leader migration

As described in the chapter introduction, the experimental system of a circular cluster of cancer cells surrounded by a CAF tissue (the stromal cells) presents an analogy with the biological phenomenon of wound healing. Consecutive to a skin injury, local cell death or some morphological processes during development, epithelial tissues need to close a spatial gap to keep their integrity and preserve their barrier function. Several *in vitro* systems have been designed to mimic with minimal settings the *in vivo* phenomena described above, playing with cell type, geometry or wound generation mechanism (review [221]). In particular, the generation of a circular gap can be made with cell damage through laser ablation (Fig. 3.2a, [222]) or micro-dissection knife (Fig. 3.2b, [223]), and without cell damage thanks to a PDMS stencil (Fig. 3.2c, [224, 225, 226]) or by substrate nano-patterning of non-adhesive patches (Fig. 3.2d, [227, 228, 229]). To drive gap closure, two main mechanisms have been identified as shown on Fig. 3.2e: a supracellular contractile ring (purse-string) and protrusive activity (review [221]).

Depending on the conditions, the main driving force to close the gap can be

- generic cell-scale extensions depending on tissue density for small diameters (below 20 μm) [224],
- only the purse-string [229, 228] when the wound is made non-adhesive to prevent protrusive activity at the edge, as shown on Fig. 3.2d,

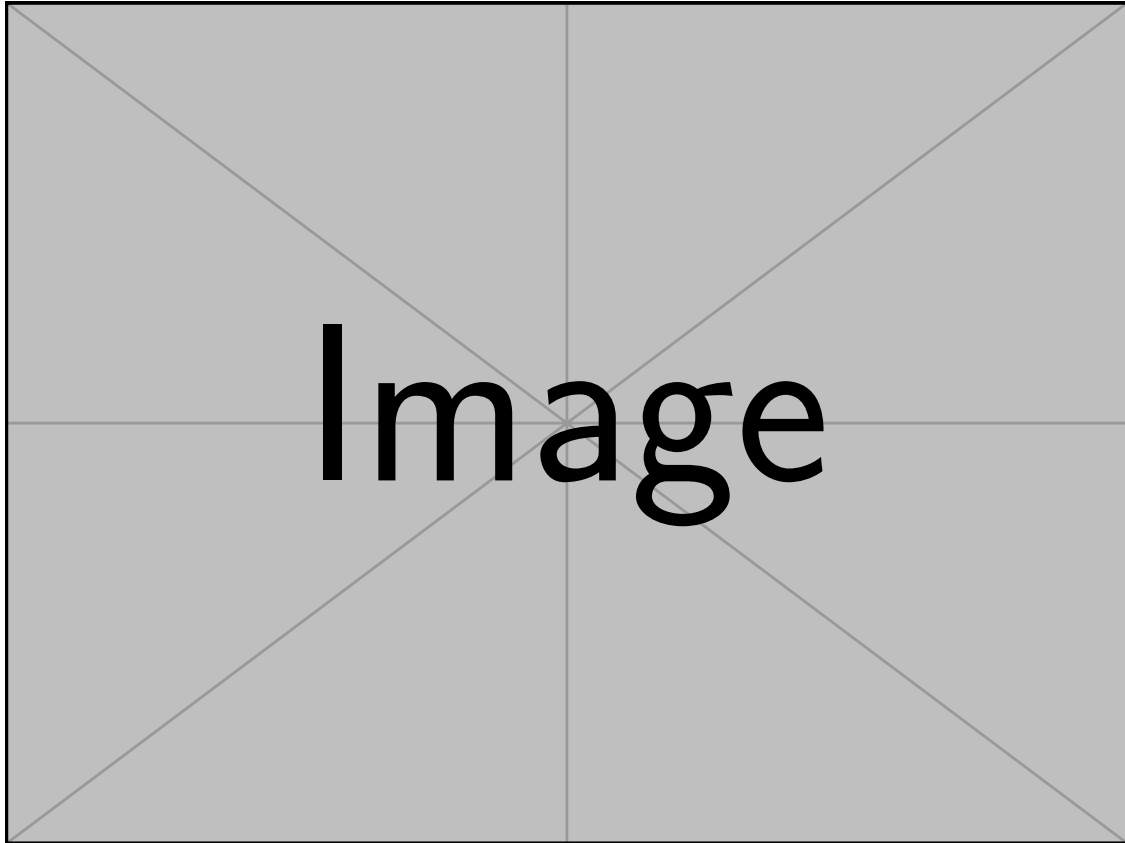


Figure 3.1: **(a)**: Sketch of the cancer invasion process from the primary tumour to the distant metastatic site, with intravasation in the bloodstream of migratory cells becoming Circulating Tumour Cells (CTCs) before their extravasation. Single invasive cells undergo an Epithelial-to-Mesenchymal Transition (EMT) to migrate in the stroma but do not necessarily lose all their epithelial characteristics (transition states EM1 and EM2/3) when they form a cluster. The tumour micro-environment is represented by Tumour-Associated Macrophages (TAMs) and Cancer-Associated Fibroblasts (CAFs). From [200]. **(b)**: Sketch of Epithelial-to-Mesenchymal and Mesenchymal-to-Epithelial transitions and the associated markers of the extreme phenotypes, showing that intermediate states (partial EMT) are possible by the loss/gain of one or several characteristics. This plasticity is believed to be essential for cancer invasion (EMT) and metastasis (MET) as shown in (a). From [201]. **(c)**: 3D spheroid culture of cancer cells (green) embedded in ECM, are pulled by CAFs (red) thanks to an heterotypic E-cadherin/N-cadherin bond. This likely promotes collective cancer invasion with CAF leaders. The scale bar is 100 μm . From [214]. **(d)**: Immunohistochemical staining (β -catenin) at the invasive front of a human colorectal cancer where tumour buds (small cell clusters) can be easily distinguished. Their observation is associated to a low survival prognosis. From [220].

- only the protrusive forces when acto-myosin cables are not distributed with sufficient regularity along the gap contour to build a significant tension (large gap diameters) and may simply help to stabilize the edge [225, 224]
- both mechanisms acting in concert as shown on Fig. 3.2e,f with expression dependent on edge curvature [226, 222].

In general, the sign of curvature is connected to the closure mechanism response (review [221]): a concave edge contour (circle-like) tends to assemble a contractile ring that drives closure through the purse-string effect, whereas protrusive forces dominate along a convex contour (Fig. 3.2e and [226, 222]). Despite this curvature sign sensitivity that would predict significant purse-string closure for circular wounds, a PDMS stencil method induces only weak unconnected actomyosin cables and closure is driven by protrusive forces on epithelial monolayers [224, 225, 226]. On the contrary, local cell damage tends to trigger a purse-string response to eliminate the dying cells in combination to protrusive activity [222], in analogy with cell extrusion [230, 231]. Interestingly, the contractile ring is localized basally after damaged-cell wound generation and transmits both normal and tangential forces to the substrate (Fig. 3.2f and [222]). The detection of a larger density of focal adhesions near the ring seems able to explain this force transmission, but contrarily to protrusive-driven closure that is inhibited on soft substrates [224], the combination with purse-string induces no dynamical change upon substrate stiffness variation [222]. Because purse-string inhibition has a small impact on closure dynamics, some complex response is expected to compensate for migratory substrate sensitivity: [222] propose that anisotropic substrate displacements generated by an heterogeneous contractile ring contractility could guide cell migration.

For gap closure over non-adhesive circular patches, where only the purse-string mechanism is involved, MDCK cells do not close for wound diameter above $\sim 120 \mu\text{m}$ [228] and cells accumulate into a 3D bulge at the edge [229], whereas keratinocytes (HaCaT cells) have a threshold diameter above $150 \mu\text{m}$ and faster dynamics [229] indicating higher ring tension. The existence of a maximal closing diameter is consistent with a curvature-dependent purse-string competing with tissue resistive tension, where a constant line tension Γ builds a 2D pressure $\Gamma.C(t)$ for an edge curvature $C(t)$. Surprisingly, the normal tractions associated to purse-string do not vanish after closure of keratinocytes [229], showing the existence of residual actomyosin contractility and elastic tissue response to transmit the tension to substrate at steady-state.

Despite the clear features understood to drive gap closure, the concept of kenotaxis [227], identified on epithelial monolayers at confluence around large non-adhesive gaps (radius of $450 \mu\text{m}$), is quite intriguing. Contrarily to expectations from migrating monolayers where tractions are protrusive (towards tissue core) at the leading edge [232], cells close to the non-adhesive edge have inward tractions (away from tissue core) in [227]. This is unexpected because this effect seems independent from edge curvature (Fig. 3.2g), and therefore cannot be explained by a purse-string mechanism even if actin accumulation is observed near the edge.

Because the apical surface of cancer cells do not express ECM ligands, our experimental system where CAFs undergo gap closure on top of CC cluster is analogous to the nano-patterning of non-adhesive patches [227, 228, 229]. However, CAFs are modified stromal cells and have to be distinguished from epithelial tissues. Indeed, gap closure for a thin layer of suspended fibroblasts embedded in collagen (as sketched on Fig. 3.2b) shows the importance of fibronectin deposition to heal the wound [223]: whereas gap closure occurs thanks to protrusive activity on a scratch assay over a 2D substrate, the suspended wound closure (3D) requires a combination of actomyosin contractility, tangential cell migration along the edge and progressive fibronectin scaffolding. Either matrix-dependent (3D) or not (2D), fibroblasts undergo wound healing with similar velocities $\sim 1 \mu\text{m/h}$.

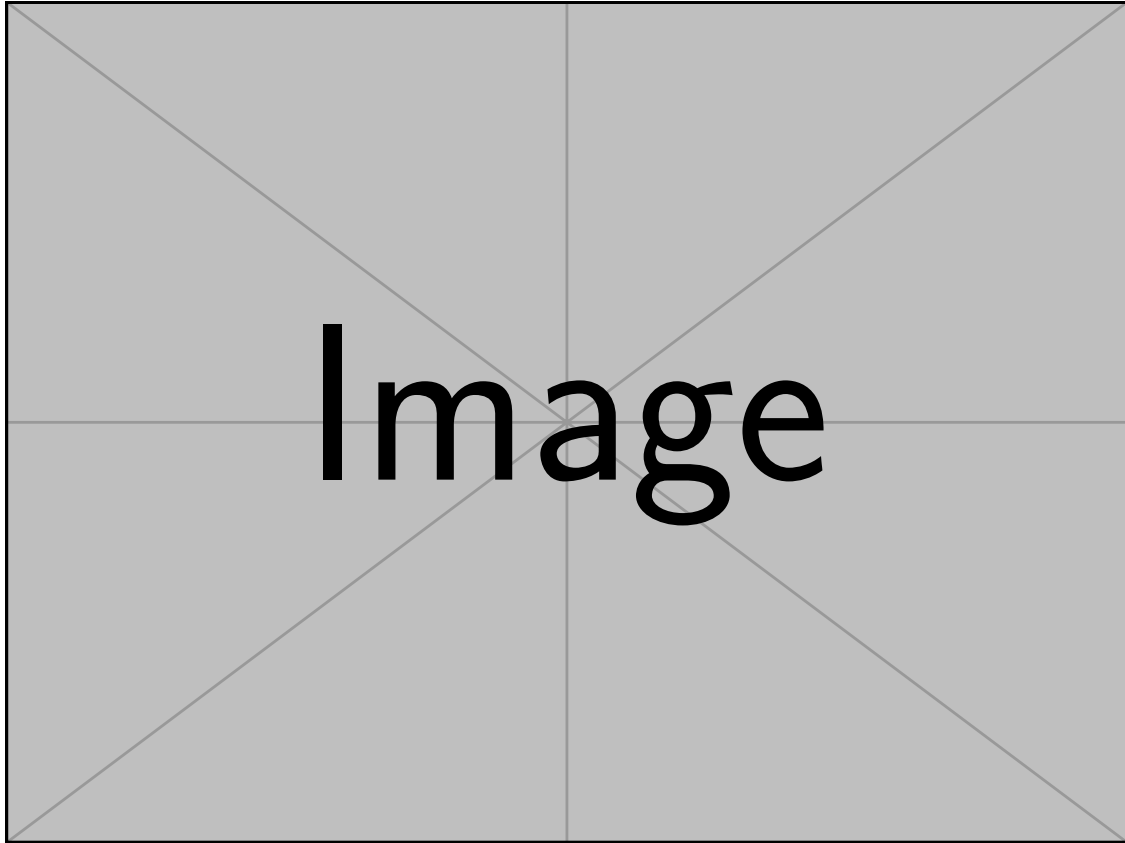


Figure 3.2: **(a)**: Sketch of the laser ablation tool used to create an epithelial wound, with the inconvenience of unprecise geometry and uncontrolled cell damage. From [222]. **(b)**: Sketch of the micro-dissection technique to make a wound in a suspended tissue. Over an adhesive substrate, scratching and other techniques applying mechanically-induced cell damage have been used with similar inconvenients to laser ablation. From [223]. **(c)**: Sketch of a PDMS stencil with a confluent monolayer around the non-adhesive pillars. The stencil is removed to create gaps chemically identical to the surrounding surface (ECM ligand absorption). This technique is more reproducible but less representative of the proper wound healing phenomenon that involves tissue damage. From [225]. **(d)**: Epithelial gap closure over a non-adhesive circular patch (white line), showing the actomyosin ring at the tissue edge where actin and myosin co-localize. From [228]. **(e)**: Sketch of the two main mechanisms driving epithelial gap closure in presence of an adhesive gap: actomyosin ring tension (red) and protrusive forces (blue). From [226]. **(f)**: Experimental kymograph of tractions normal to the gap contour, showing protrusive activity at the leading edge and in the deep tissue (red), whereas a contractile actomyosin ring assembled behind the edge pulls the substrate inwards (green). Here the gap has been obtained thanks to the laser ablation technique. Radial closure dynamics is indicated with blue dots. From [229]. **(g)**: Spatial map of vertical tractions showing an effect of kenotaxis along the non-adhesive gap contour: normal tractions oriented towards bottom side. Although protrusions should be cancelled by the non-adhesive gap at the edge and purse-string forces should pull the substrate towards the top because of curvature sign (blue), the opposite is observed (red). From [227].

3.1.3 Presentation of the *in vitro* experimental system

The Vignjevic's lab (UMR 144, Curie institute) designed a minimal *in vitro* co-culture on a 2D soft substrate to mimic the invasive front of a tumour, made of a cluster of primary Cancer Cells (CCs) surrounded by Cancer-Associated Fibroblasts (CAFs), both extracted from the same patient suffering from colo-rectal cancer¹ (Fig. 3.3a).

CCs are first deposited on a circular adhesive patch of controllable size (diameter from 100 to 400 μm) and proliferate into a confluent monolayer, without invasion away from the adherent region. Next, CAFs are added around the circular patch and form a dense and highly dynamic tissue after few hours of proliferation. Those special fibroblasts also produce and deposit some extra-cellular matrix components like collagen or fibronectin that can self-assemble into an heterogeneous scaffold (Fig. 3.3b). Then, the geometric restriction imposed by CCs start to affect the closest CAFs and seem to modify their phenotype: they align tangentially to the interface and assemble contractile actomyosin cables that progressively become mechanically active at the supracellular scale (Fig. 3.3c). This interfacial actomyosin ring first compresses the CC cluster, shown experimentally to be myosin-II dependent as expected. More surprising is the importance of fibronectin fibres (Fig. 3.3c) to stabilize the compressive ring, as their inhibition frequently leads to cycles of ring assembly and collapse without detectable CC cluster compression.

Later on, for a large number of clusters on independent experiments, the CAF layer is able to climb on top of CCs to undergo a gap closure process (Fig. 3.3d,e,f), similarly to the purse-string gap closure of epithelial monolayers over non-adhesive substrates [229]. Depending on the conditions, CAF tissue closure may be stalled by the formation of a multicellular bud of cancer cells (Fig. 3.3d), or may proceed without much CC deformation and succeed with CAFs covering entirely the CC cluster (Fig. 3.3e). The former morphology is sometimes followed by severing the bud from the main CC body, but large buds (Fig. 3.3g) oppose mechanical resistance to CAF compression and remain stable at steady-state. The appearance of unambiguous intensity deviations near the CAF ring, observed in phase contrast microscopy at intermediate time, suggests the existence of an out-of-plane CC deformation named "rim" (Fig. 3.3d,e) due to the mechanical interaction between the two tissues.

Preliminary experiments convincingly showed a significant reduction of CC budding upon N-cadherin knock-down, suggesting that transient N/E-cadherin binding between CAFs (N) and CCs (E) could be responsible for a friction-like force transmission between the two tissues and control the observed budding frequency among a population of CC clusters. Regarding the physiological context of *in vivo* tumour budding, this would suggest the importance of a specific CAF-induced shear stress on CCs. Contrarily to human cells, the same experiments performed with mouse cells still show a distinction between control and N-cadherin knock-down condition but with less robustness, indicating the importance of cell type and growing environment. Nevertheless, the production of collagen fibres and other extra-cellular matrix components by CAFs (Fig. 3.3c) - in particular between the closing tissue front and the CCs - or some unspecific CAF-CC interactions (glycocalyx) is likely to provide generic sources of friction at the mesoscopic scale. Although a simple inhibition of N-cadherin expression may not be sufficient to reduce the frequency of *in vivo* tumour budding, this CAF-CC *in vitro* system appears as a good tool to test our working hypothesis that CAF intrinsic contractility could reshape tumours through specific/unspecific mechanical interactions.

3.1.4 Quantitative characterisation of the system

Budding frequency, size and initiation

As explained in the last section, the CAF tissue closure on top of the CC cluster is driven by a contractile actomyosin ring, integrated at the supracellular level by fibronectin fibres originating from CAF deposition. It can either lead to a full covering of the cluster by the CAF tissue or

¹To reduce the possible phenotype differences associated to cell culture lines, primary cancer cells and their surrounding CAFs are extracted from patients and "conserved" in an immunodeficient environment that preserves their phenotypic landscape (PDX method), prior to *in vitro* culture, imaging and drug tests.

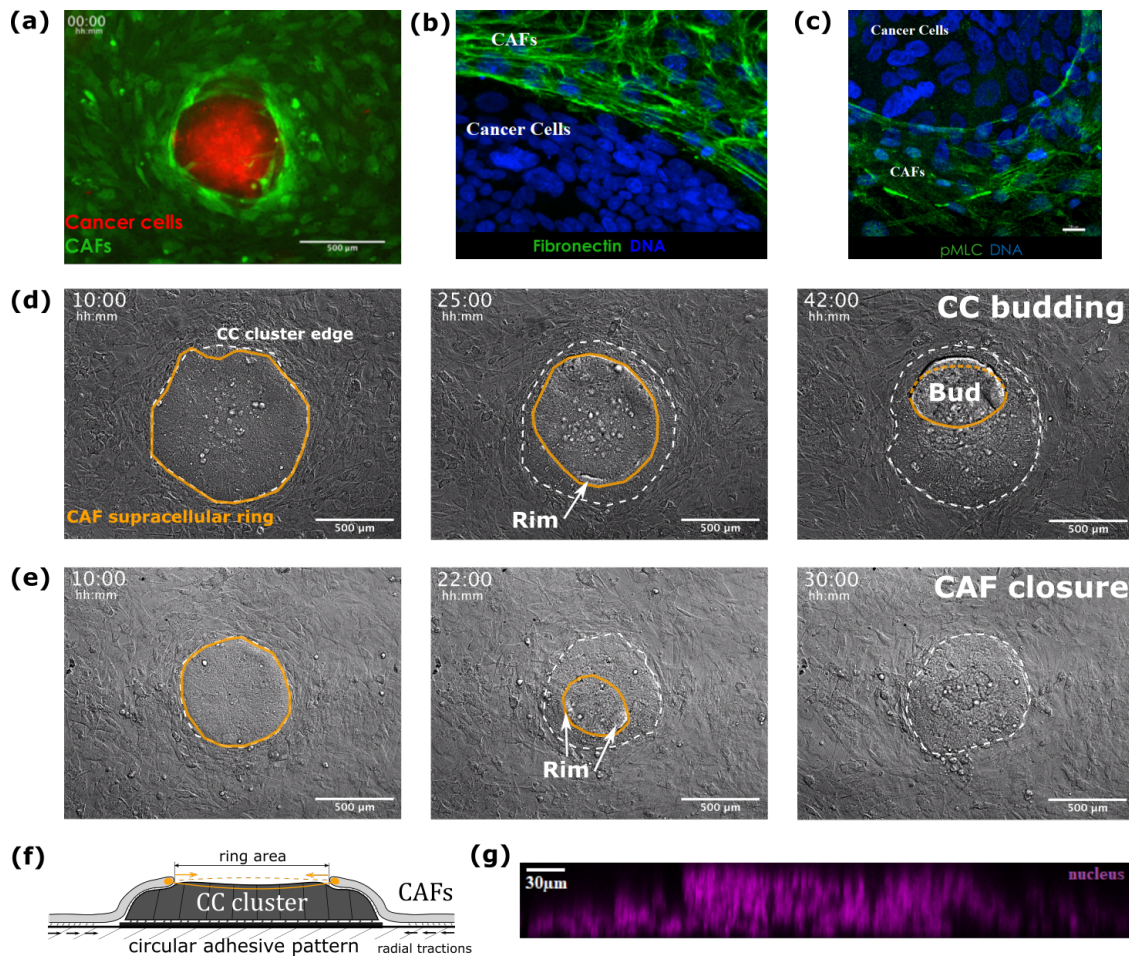


Figure 3.3: (a): Fluorescent image of a Cancer Cell (CC) cluster in red, surrounded by a confluent tissue of Cancer-Associated Fibroblasts (CAFs) in green. CCs are deposited on a circular adhesive pattern of controllable size (here the diameter is 400 μm). (b): High resolution fluorescent image of CC and CAF tissues before the CAF climbing event, with DNA (nucleus) in blue and fibronectin (matrix fibres) produced by CAFs in green. The region free of fibronectin corresponds to the CC cluster. This heterogeneous matrix scaffold is important for the tissue mechanics and is shown to stabilize the actomyosin ring (c) that assembles at the CAF-CC interface. (c): High resolution fluorescent image of CCs and CAFs with DNA (nucleus) in blue and phospho-Myosin Light Chain (pMLC) in green, indicating several actomyosin cables at the CAF tissue front. The integrity of the supracellular ring is shown experimentally to be fibronectin-dependent (b). The CAFs are already closing on top of the CC cluster, distinguishable on the top region free of PMLC. (d): Time-lapse in phase contrast microscopy of a CC cluster (dashed line) surrounded by CAFs with a contractile supracellular ring (orange line) assembled at the edge of the CAF monolayer, terminating in CC budding. CAFs initiate gap closure on top of CCs at 10 h, induce localized CC out-of-plane deformations (rim) distinguishable at 25 h. At 42 h, the system is stabilized with CAFs compressing a multicellular cancerous bud. (e): Time-lapse in phase contrast microscopy of a CC cluster (dashed line) surrounded by CAFs with a contractile supracellular ring (orange line) assembled at the edge of the CAF monolayer, terminating in CAF closure. After initially unperturbed gap closure, two localized CC out-of-plane deformations (rims) can be distinguished at 22 h, with more clarity on films. Contrarily to the previous case (c), those deformations disappear and gap closure ends up with CAF tissue covering the CC cluster beyond 30 h. (f): Sketch of the CAF-CC system seen from a side view, at an early stage before multilayering. The pulling force from the actomyosin ring (orange) deforms CCs and applies tension on the surrounding CAF tissue, confirmed by the observation of inward radial tractions on substrate (next section). (g): Confocal image of CC nuclei at steady-state showing a large bud with cylindrical-like shape, from a cluster developed on 400 μm patch diameter (top). [Courtesy of D. Vignjevic, J. Barbazán and C. Pérez-González]

accumulation of out-of-plane deformations into a multicellular bud. Since the circular adhesive patch on which CCs grow can be made of different sizes (diameter of 100, 200, 300 and 400 μm), it offers a nice set-up to study the correlation between the cluster size and the budding characteristics. Indeed, the frequency of budding phenotype appears positively correlated with the pattern size (Fig. 3.4a) except for a patch diameter of 100 μm where a different budding phenotype occurs. For such small clusters, CAFs tend to form protrusions below the CCs and destroy their substrate adhesion until the entire cluster is detached. Surprisingly, the infiltration of CAFs below the CC cluster do not occur upon N-cadherin knock-down. Another important observation is the positive correlation between the patch diameter and the final bud projective area measured from top view (Fig. 3.4b), observed after the stabilization of the system.

Finally, a crucial aspect of this composite system is to understand how the CAF and CC tissue interactions terminate in a bud for some cases and CAF closure otherwise, and in particular what controls the transition from a CC monolayer to a 3D-like structure with cells disconnected from substrate. Whereas budding is necessarily a consequence of multilayering events, it is not straightforward to assume that those events are a sufficient condition. The later case assumes that CAF closure only occurs on top of a deformable monolayer whereas budding occurs as long as multilayering events are triggered, which is the simplest working hypothesis. Indeed, preliminary data over four clusters under three different conditions are compatible with this hypothesis (Fig. 3.4c). When fibronectin knock-down condition prevents the CAF tissue from climbing on top of the CC cluster, or when N-cadherin knock-down leads to CAF closure, randomly targeted CCs remain adherent to the substrate. In the control case, some cells detach from the substrate and terminate into a bud. An alternative scenario is the possibility that multilayering events do not prevent CAF closure (Fig. 3.4d). The budding transition would then be associated to a quantitative difference in the impact of multilayering events and their ability to stall CAF closure, rather than a qualitative difference in CC tissue organization (monolayer vs multilayer) postulated on the first scenario where "bud=multilayering". Since the first scenario is compatible with preliminary data (Fig. 3.4c) and no available data exists in favour of the "bud=CAF stalled" scenario, we will only focus on the first one (Fig. 3.4d).

Thus, our central modelling assumption relies on a binary transition for the activation of a multilayering event, necessarily followed by an amplification that collects the central CCs into a final bud. Conceptually, we can then reduce the distinction between CAF closure and CC bud phenotypes to the absence or appearance of individual cell detachment from substrate. We propose to study how the mechanical interaction between closing CAFs and CC cluster can drive out-of-plane deformation of the CC monolayer and relate this to the likelihood for multilayering events.

CAF compression against micro-pillars

To quantify the amplitude of compression generated by the supracellular actomyosin ring at the CAF periphery and see if its assembly is CC dependent, our experimental collaborators replaced the CC clusters by elastic pillars. They patterned an acrylamide gel into a grid of micro-pillars and allowed CAF proliferation between them by fibronectin coating (Fig. 3.5a). Exactly like in the CAF-CC system, they observe the assembly of actomyosin cables at the interface between the CAF tissue and the pillars, applying a compression quantified by the radial pillar displacement (Fig. 3.5b). This confirms the independence of the contractile ring mechanism from CCs. Since the elastic modulus of the gel is known ($E = 11$ kPa), the measurement of the deformation gives access to a quantitative estimate of the contractile tension generated by the supracellular actomyosin ring (Fig. 3.5c,e). Moreover, the importance of fibronectin for ring stabilization and force generation is also confirmed, since experiments with fibronectin knock-down show no pillar deformation (Fig. 3.5c). Finally, the addition of blebbistatin (an inhibitory drug for myosin II) shows that the CAF compression (normal traction) on pillars is also actomyosin driven (Fig. 3.5d), as expected. More surprising is the observation of shear deformations on pillars, that produce tangential tractions also myosin dependent (Fig. 3.5d). They may average out when integrated over long times and we consider them as "noise". **Ask Jorge and Carlos what kind of magnitude is made for Fig1.5d**

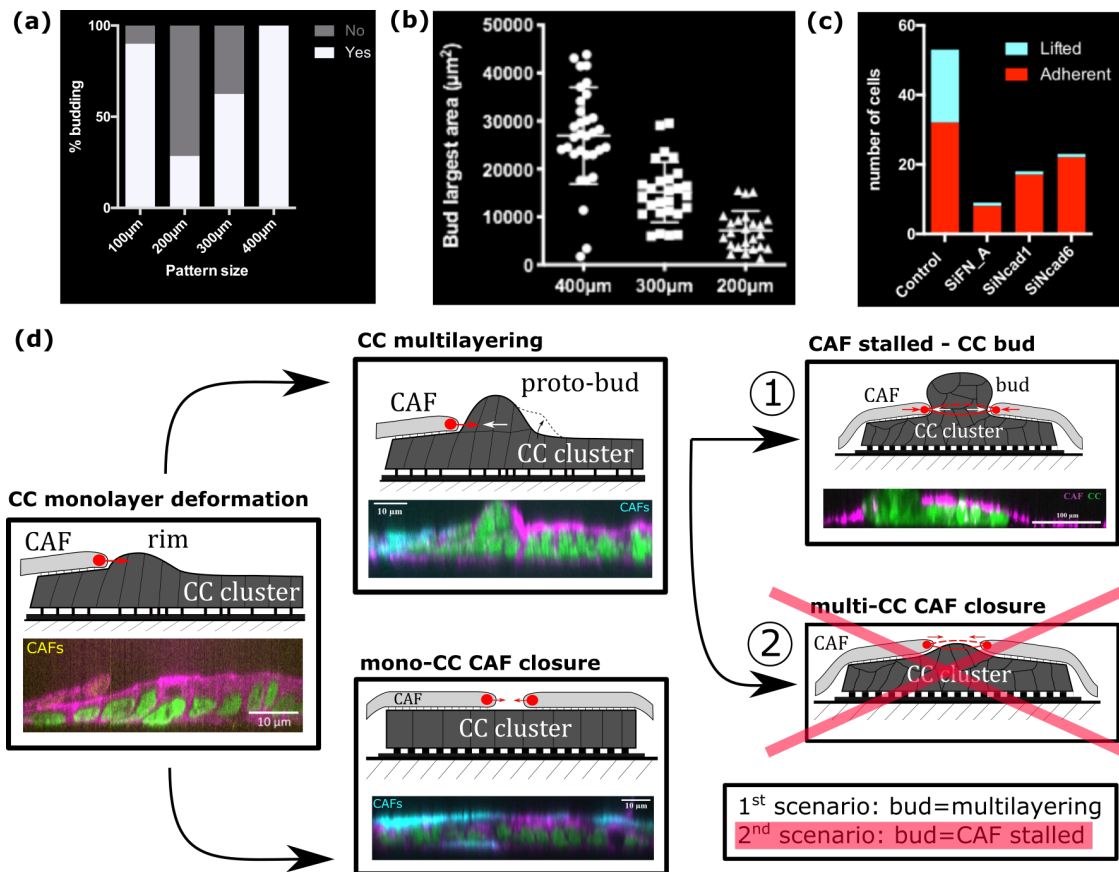


Figure 3.4: (a): Graph of the observed budding frequency as a function of the circular patch diameter, showing a positive correlation with pattern size except for the diameter of 100 µm. The latter situation corresponds to a CC cluster lifted up by CAFs penetrating below to destroy the substrate adhesions. (b): Graph of the final projected bud area observed from a top view as a function of the circular patch diameter, showing again a positive correlation with pattern size. (c): Graph showing the fraction of adherent and detached (lifted) CCs in control, fibronectin knock-down and N-cadherin knock-down conditions (preliminary data). Random targeted cells are imaged to see their substrate attachment, and only the control case shows a significant proportion of detached CCs. This favours the working hypothesis for which the difference between CC budding and CAF closure relies on the activation of multilayering events. (d): Summary of the different cluster states at different times and how multilayering is connected to budding phenotype. In a first scenario "bud=multilayering", CAF closure only occurs on top of CC monolayers and multilayering events are both necessary and sufficient to observe buds. On the second scenario, CAFs can also close on multilayered clusters and buds appear only when CAFs are mechanically stalled by CCs. The first scenario is simpler and available data (c) is compatible with it, so that we choose to ignore the second one. [Courtesy of D. Vignjevic, J. Barbazán and C. Pérez-González]

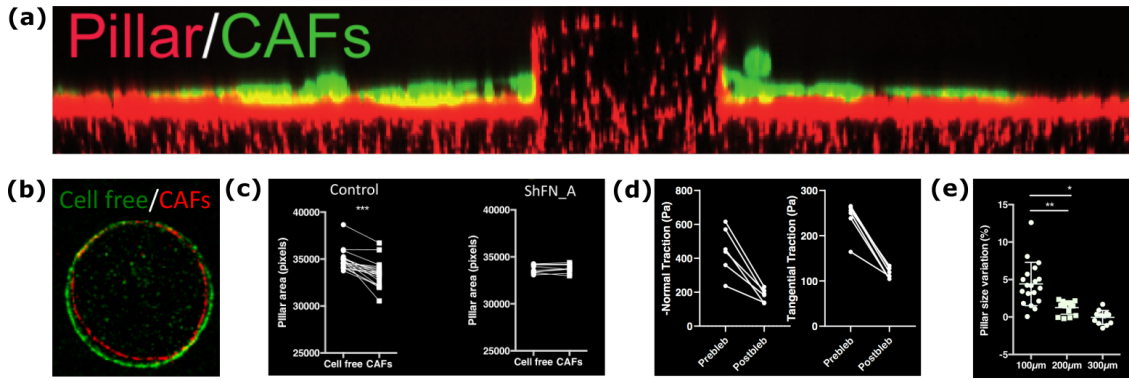


Figure 3.5: **(a)**: Side view of a fluorescent image centred on a pillar made of an acrylamide gel, coated with fibronectin (red). CAFs are deposited in the space surrounding the pillars and proliferate until a full surface coverage (green). The pillar obstacle triggers the local assembly of actomyosin cables as in the CAF-CC system. **(b)**: The CAF actomyosin cables generate a substantial inward force that compresses the pillar (red) when compared to the initial profile (green). **(c)**: In the control situation, the measurement of pillar projected area from top view shows a net decrease after CAF addition (left). The same measurement performed under conditions of fibronectin inhibition shows no pillar deformation (right), indicating the importance of fibronectin fibres for the ring stability and force generation, as in the CAF-CC system. **(d)**: Quantification of traction stresses on the pillar in the normal and tangential direction, averaged over the pillar surface in contact with CAFs. Those stresses are myosin-dependent as one expects from forces generated by actomyosin cable contractility. Non-zero tangential stress is observed with lower magnitude compared to normal ones. **(e)**: Graph of the radial pillar deformation (relative change of diameter) as a function of initial pillar diameter. This shows the reduction of stresses for larger pillars, compatible with the theoretical description of the actomyosin ring as a constant line tension. [Courtesy of D. Vignjevic, J. Barbazán and C. Pérez-González]

From a theoretical perspective, an important quantification is the dependency of compressive stress upon pillar diameter. Although the deformations are quite dispersed among a population of pillars, probably related to CAF tissue heterogeneities in ring assembly, there is a clear anti-correlation with pillar size (Fig. 3.5e).

The simplest theoretical description consistent with those data is the constant line tension hypothesis: the supracellular actomyosin ring is modelled as a contractile line with magnitude Γ , that exerts a 2D pressure Γ/R_0 on a pillar of initial radius R_0 by Laplace law. Since the pillar deformation ϵ_r is proportional to the elastic stress $\sigma_{rr} = 2E\epsilon_r/3$, the force balance applied over the pillar surface in contact with CAFs (of initial height h_0) gives straightforwardly $\epsilon_r = A/R_0$ with the constant $A \equiv 3\Gamma/(2Eh_0)$. This reproduces the observed anti-correlation (Fig. 3.5e) and gives access to the actomyosin ring line tension Γ because $E = 11$ kPa is known and h_0 can be measured (Fig. 3.5a).

Note that for a pillar diameter of $300 \mu\text{m}$, the averaged pillar compression cannot be distinguished from zero and individual pillars can even be pulled by CAFs (Fig. 3.5e). Interestingly, the rings assembled by CAFs around CC clusters of similar diameter ($\sim 300 \mu\text{m}$) are significantly contractile and drive gap closure on cluster top surface similarly to smaller (200) and higher (400) cluster diameters. Although we don't have a direct access to the tension magnitude generated by those rings when they assemble near CCs, this qualitative non-equivalence with the elastic pillar system could indicate the sensitivity of ring assembly to the environmental stiffness. Indeed, CAF tissue substrate and pillars are made of the same acrylamide gel with elastic modulus $E = 11$ kPa: the difference in ring assembly may be linked to the planar stiffness experienced by CAFs, the pillar material in one case and the cancer cells for the other system, that may be softer. The sensitivity of ring assembly to environmental stiffness has already been investigated theoretically [233]. However, the impact of curvature on contractile magnitude, with the possible existence of a critical radius as indicated on Fig. 3.5e, has not been addressed to our knowledge.

CAF tissue traction and dynamics

As already mentioned in Fig. 3.3b, the pulling force exerted by the supracellular actomyosin ring on the CAF tissue is propagated away from the CC cluster periphery, to the surrounding tissue in contact with substrate. This is confirmed by a measurement of radial inward traction forces in this out-of-cluster region (Fig. 3.6a).

A spatial average is performed on an annular region near the CC cluster edge where tractions are concentrated, shown for clusters with a diameter of 300 μm in different conditions (Fig. 3.6b). Initially, tractions are directed outward because of CAF protrusive activity near the CC cluster edge². In few hours, this "basal" tissue activity disappears, replaced by the pulling force generated by the freshly assembled actomyosin ring. The resulting inward tractions continuously increase over time until a "plateau" is reached. Since the fibronectin knock-down has been shown to alter the actomyosin ring stability and contractility amplitude, this is normal to observe a strong reduction of radial traction forces compared to normal conditions (Fig. 3.6b). The fact that tractions remain of similar magnitude upon N-cadherin knock-down indicates that the cadherin-mediated CAF-CC interaction acts as a small perturbation on CAF closure dynamics.

A richer quantitative information is obtained from spatio-temporal heat maps of traction forces like Fig. 3.6c for a 300 cluster upon N-cadherin knock-down. In normal conditions, kymographs are shown in next chapters. There is a clear pattern of inward tractions localized around the CC cluster on a ring of the order of 100 μm width, whereas outward tractions occur beyond this region. Note the complete absence of tractions behind the CC cluster.

In addition to tractions, the position of the CAF leading edge can be tracked over time to compute the gap area internal to the closing gap. The ring area dynamics is shown on Fig. 3.6d for different cluster sizes upon N-cadherin knock-down. Small clusters are observed to close in 20 – 30 hours whereas the 400 μm clusters have a saturated ring area, meaning that the CAF ring compression is stalled by a stationary CC bud. Interestingly, the averaged radial tractions seem to reach a plateau value when the gap closes (clusters 200 and 300). At first, the nature of those residual tractions is unclear. It could result from the unstopped myosin activity of a central contractile patch pulling on the surroundings [229] and/or represent the contribution from a stationary elastic deformation somehow connected to the substrate: a natural candidate would be the fibronectin scaffold produced by CAFs (Fig. 3.3b).

In a large scale window far from the leading edge, the tracking of local CAF velocity over space can be transformed into an averaged amplitude to be compared for the different conditions (Fig. 3.6e). It shows that N-cadherin inhibition does not alter the CAF mobility, whereas the reduction of fibronectin deposition, followed by a reduction of its assembly into connected fibres, slows down the resistance to CAF mobility and increases the tissue scale velocity amplitude.

Finally, spatio-temporal heat maps of radial velocity can also give valuable information, under N-cadherin knock-down conditions on a 300 cluster for Fig. 3.6f, for which CAF closure around 30 h (Fig. 3.6d). It clearly shows an inward flow associated to CAF closure (Fig. 3.6d), but transient outward flows that expand far in the tissue can also be observed, particularly after gap closure. Nevertheless, we chose to ignore those oscillatory patterns, as well as the complicated tangential flows/tractions that can be represented similarly.

3.2 Model: experimental constraints on CAF dynamics and tissue mechanics

To describe the mechanical response of the CC monolayer associated to CAF closure, that ultimately leads to full cluster coverage or cancerous budding, one can use the framework of continuum mechanics with a prior guess on the appropriate rheology, or consider the discrete CC mechanics

²Contrarily to an elastic layer bound to the substrate where inward pulling generates centripetal tractions, cells migrating towards the center generate tractions of opposite direction because of the retrograde flow.

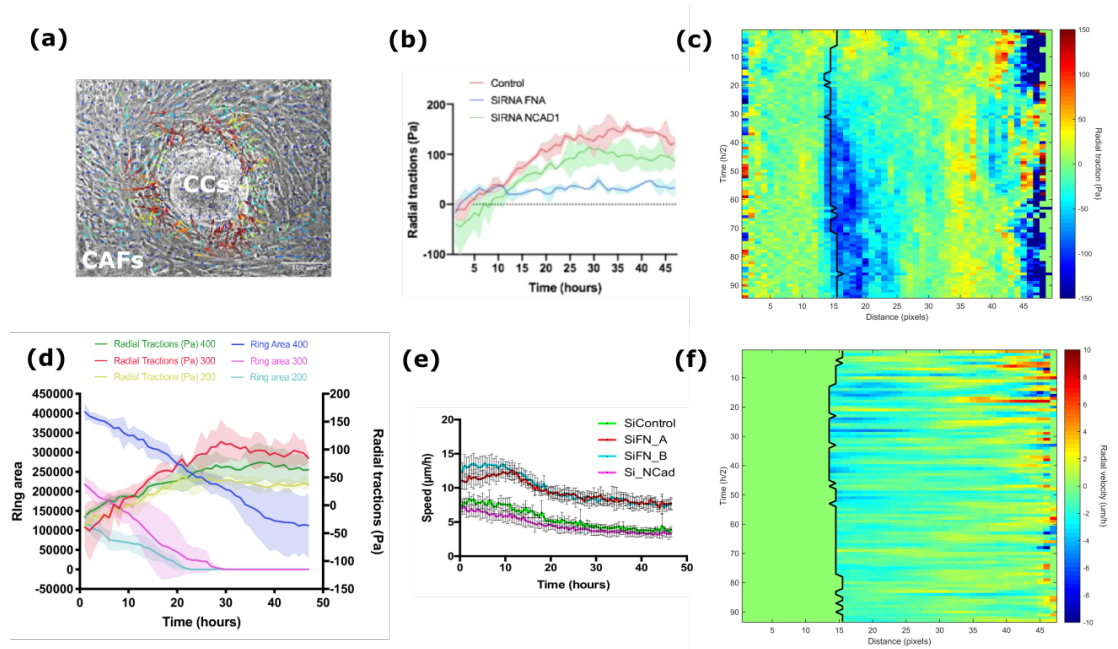


Figure 3.6: (a): Phase contrast image of a CC cluster surrounded by CAFs that have started their inward motion on top of CCs. A clear pattern of radial inward traction forces is visible, with blue (red) arrows indicating low (high) amplitude. Fourier-transform traction microscopy with finite substrate thickness is used to compute traction forces [232]. (b): Graph of the time evolution of averaged radial tractions for control case (red), fibronectin knock-down case (blue) and N-cadherin case (green) for clusters of $300\ \mu\text{m}$ diameter. The average is performed on an annular region away from the CC cluster edge (black line on (c)) with $20\ \mu\text{m}$ width. The sign convention used is positive (negative) for inward (outward) tractions. The initially negative tractions correspond to CAF protrusive activity at the CC cluster periphery. (c): Kymograph expressing the spatial distribution of radial traction stresses over time with CC cluster edge position (black line), for a cluster of $300\ \mu\text{m}$ in N-cadherin knock-down conditions. CAF closure occurs here around 30 h. No tractions are observed below the CCs, inward tractions only on a limited portion of the out-of-cluster region ($15 - 25$ pixel distance) and outward tractions beyond that part (35 pixel distance). The high values on the two borders (0 and 45 pixel distance) are considered as non-significant artefacts. 1 pixel is approximately $10\ \mu\text{m}$. (d): Graph combining the evolution of averaged radial tractions and CAF ring area dynamics for the three cluster sizes, in N-cadherin knock-down conditions. Both 200 and 300 clusters undergo CAF closure (vanishing ring area) whereas the larger cluster form a stationary bud (finite ring area). The tractions start from a negative value (outward), increase upon CAF closure (decrease of ring area) and seem to reach a plateau when the gap is closed or when the ring is stalled by a bud. (e): Evolution of the CAF velocity magnitude for different conditions (control, Fn-KD, N-cadh KD), spatially averaged over a large portion of the tissue far from the leading edge. It shows that the average CAF mobility is independent from N-cadherin homotypic interactions but strongly increases in the condition of fibronectin knock-down: the fibrous scaffold normally produced by CAFs reduce their mobility. (f): Heat map showing the CAF radial velocity field in space and time, in the region away from the CC cluster edge (black line), for a cluster of $300\ \mu\text{m}$ in N-cadherin knock-down conditions. CAF closure occurs here around 30 h. Although the inward flow (negative sign) dominates, one can distinguish alternate periods of outward flow with a pseudo-oscillatory pattern. As in (c), the high amplitudes at the border are non-significant artefacts. [Courtesy of D. Vignjevic, J. Barbazán and C. Pérez-González]

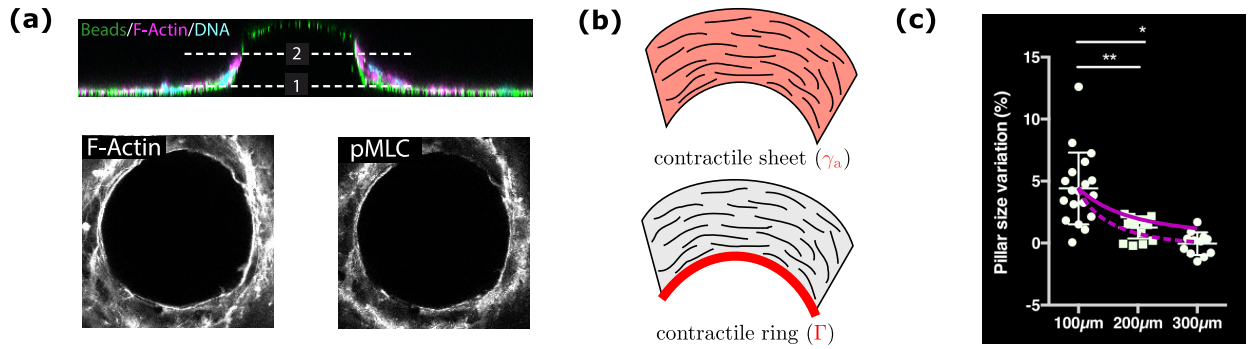


Figure 3.7: **(a)**: Side view of the CAF-pillar system (top) with visualisation of the complex material deformations: the curved region of the elastic substrate indicates pulling stress coming from the compressed pillar. Top view of the CAF tissue near the pillar obstacle (bottom) with fluorescent images showing a local enrichment in actin and myosin. **(b)**: Sketch of the two contractile structures that could be responsible for pillar compression: a contractile sheet (top) that depends on CAF intrinsic pre-stress and tangent alignment to the leading edge to build an anisotropic active tension γ_a , or a contractile ring (bottom) associated to actomyosin enrichment near the obstacle (a) that creates a line tension Γ . **(c)**: Graph of the pillar relative deformation $\epsilon_r \equiv (R_0 - R)/R_0$ as a function of initial pillar diameter $2R_0$. Scalings $\epsilon_r \propto 1/R_0$ and $\epsilon_r \propto (1/R_0)^2$ are shown in full and dashed lines respectively. A constant line tension Γ would produce a strain $\epsilon_r \propto 1/R_0$ whereas an anisotropic tension would generate a deformation independent from pillar size.

through a vertex model. Since the CAFs do not undergo major morphological changes, it is naturally described within continuum mechanics and the question of a continuous vs. discrete framework only concerns the CC cluster.

Our first central assumption is to associate the budding phenotype observed experimentally to the mechanical deformation of the CC cluster, driven by a frictional shear stress with CAF front tissue closing on top.

Our second central assumption considers the loss of basal attachment for individual cells (named "multilayering transition") as a causal transition from a deformed monolayer to a bud, so that the vertex model appears more appropriate because of its resolution able to describe cell-scale events. The major difference compared to the standard vertex model that usually assumes constant polar tensions ([186, 171] and review [167]) comes from the assumption of frictional shear stress between CAFs and CCs: it is easily described as a boundary condition $\sigma_{tn} \sim \xi(V_{CAF} - V_{CC})$ in the framework of continuum mechanics but the vertex model needs to be modified to account for this mechanical coupling on the CC apical side. Moreover, some technical aspects remain challenging in 3D, in particular regarding interfacial curvatures that introduce geometrical incompatibilities between a spherical shape (coming from uniform pressure and tension) and the polygonal skeleton of tri-cellular junctions. This has never been addressed to our knowledge ([169, 170] and review [167]) and illustrates the relative simplicity of the 2D transverse model where this issue is absent. Pragmatically, in absence of prior expertise on vertex model computation and considering that those technical aspects would artificially complexify the model without an equivalent benefit on biophysical modelling quality and insight, we started with a purely continuous approach and got inspiration from the physical phenomenon of liquid dewetting [234, 235, 236].

In addition, we tried an hybrid approach for a comparison between the continuum mechanics equations and a dynamical version of the 2D side vertex model, similar to the linear expansion theory made for static conditions (chapter 2).

3.2.1 Pillar compression

As shown in the introductory chapter (section?), CAF-induced compression is CC-independent and significantly deforms PAA elastic pillars. Although pillar deformations and CAF tissue geometry are slightly heterogeneous and anisotropic (Fig. 3.7a), we only intend to extract an order of magnitude for CAF compressive force so that an assumption of angular invariance along pillar center axis is sufficient. Importantly, actin/pMLC localization is experimentally observed at the

CAF leading edge and defines a supracellular actomyosin ring (Fig. 3.7a,b) parametrized by a line tension Γ . However, since relatively high fluorescence is also detected deeper in the tissue as a consequence of intrinsic CAF contractility, with tangent cell alignment observed along the obstacle (either pillar or CC cluster) and far away, one cannot a priori eliminate a role played by tissue orientation on the generation of CAF compression force. Even without specific actomyosin enrichment at the leading edge, this anisotropic CAF contractility could contribute to the CAF-induced pillar compression through a contractile sheet structure (Fig. 3.7b), parametrized by an active tension γ_a along the orthoradial direction.

Although both effects could add up for compression of obstacles, those mechanisms have precise geometric consequences. For a leading edge radius R , a pure ring with line tension Γ builds a compressive tension Γ/R (2D Laplace law) when applied on the pillar, whereas a pure contractile sheet described as a 2D active nematic³ applies the anisotropic tension γ_a . Formally speaking, the later merges into a line tension when this active tension is expressed on a small region of width w , such that $\gamma_a w \rightarrow \Gamma$ when $w \ll R$. Here, γ_a is related to the CAF orthoradial alignment that occurs on tissue scale ($w \gtrsim R$) and the two mechanisms are clearly different (Fig. 3.7b).

Thus, measuring the pillar deformation as a function of initial radius R_0 gives valuable information on the CAF-dependent compressive mechanism. Moreover, the complex supracellular assembly of a contractile ring mixing fibronectin, actin and myosin elements may also depend on pillar radius R_0 in principle, such that $\Gamma(R_0)$ and $\gamma_a(R_0)$.

Experiments performed on three pillar sizes show a negative correlation for relative deformation ϵ (Fig. 3.7c). A line tension independent from R_0 would predict a strain $\epsilon \propto (R_0)^{-1}$ assuming uniform cylinder compression ($\epsilon \propto \Gamma(R_0)/R_0$), a scaling that is reasonably compatible with the experimental data given the low signal-to-noise ratio. Note that this assumption tends to over-estimate the deformation amplitude for the largest pillars and a scaling $\epsilon \propto (R_0)^{-2}$ appears quantitatively better (Fig. 3.7c), but it is hard to determine if this slight difference can be considered significant or not. The absence of significant compression on pillars with 300 μm diameter seen on Fig. 3.7c could be related to a decrease of actomyosin enrichment for a ring-like structure (Γ) and/or to lower tangential alignment of CAFs for a sheet-like structure (γ_a). Since we are not aware of precise arguments to justify this geometric sensitivity, and because a robust answer would require an entire project on its own, it seems reasonable to focus on the constant line tension hypothesis which is qualitatively consistent with the data without the need for any artificial assumption: $\Gamma(R_0) = \Gamma$ and $\gamma_a = 0$.

Focusing on pillars with an initial radius $R_0 = 50 \mu\text{m}$, the relevant quantities are the final pillar radius $R = R_0(1 - \epsilon_r)$ (Fig. 3.7c), the PAA elastic modulus $E = 11 \text{ kPa}$, and the average normal stress⁴ $\sigma_{rr} = 400 \pm 200 \text{ Pa}$ exerted by CAFs over a covering surface with thickness $h_c = 30 \pm 10 \mu\text{m}$. Integrating the average normal stress over the CAF-covering thickness, the radial tension balance reads $h_c \sigma_{rr} = \Gamma/R$. With total pillar tension $h_c \sigma_{rr} \simeq (1.2 \pm 0.8) \times 10^{-2} \text{ N/m}$, a line tension $\Gamma \simeq 600 \pm 400 \text{ nN}$ is extracted. One can connect this value to the typical line tension of one stress fiber $\Gamma[\text{SF}] \sim 10 \text{ nN}$ [237], corresponding to a typical cell force dipole $\Gamma[\text{cell}] \sim 100 \text{ nN}$ that may indicate the high contractile activity of CAFs with higher tension and/or higher number of stress fibers per cell.

³One assumes an active rheology with a pre-stress tensor γ_{ij} [active] proportional to the 2D nematic tensor $Q_{ij} = p_i p_j - \frac{1}{2} \delta_{ij}$ where \vec{p} is the planar orientation field normalized to unity. Writing γ_{ij} [active] = $2\gamma_a Q_{ij}$ with orthoradial nematic orientation in polar coordinates ($p_r = 0, p_\theta = 1$), one gets $\gamma_{\theta\theta} = \gamma_a$ (pulls in orthoradial direction) and $\gamma_{rr} = -\gamma_a$ (pushes in radial direction) [176]. This traceless contribution should be distinguished from an isotropic contractile pre-stress γ_∞ used in next sections, where one would have γ_{ij} [active] = $\gamma_\infty \delta_{ij}$ in the tissue plane (review [61]).

⁴The stress quantification is inferred from measured 3D micro-bead displacements thanks to an hyper-elastic model that have been made by external collaborators of Vignjevic' team [collaborators].

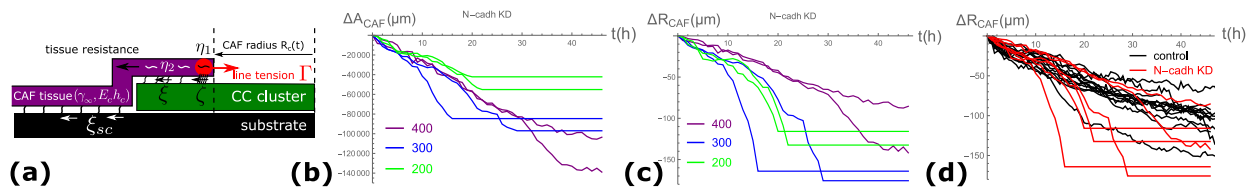


Figure 3.8: **(a)**: Sketch of the CAF tissue climbing on top of CCs with gap closure driven by line tension Γ (red). It is resisted by CAF tissue pre-stress γ_∞ or elasticity with modulus $E_c h_c$, whereas dissipation could be dominated by ring line viscosity η_1 , tissue viscosity η_2 , CAF-substrate and CAF-CC 2D friction coefficients ξ_{sc}, ξ or ring line friction ζ . **(b,c)**: Experimental CAF closure dynamics in terms of leading edge gap area (b) and leading edge radius (c) for different cluster diameters (200, 300, 400), in N-cadherin knock-down conditions. Note that contrarily to cluster diameters (200, 300), the clusters with diameter 400 undergo budding without complete CAF closure. For the closing clusters, one important feature is the quasi-linear dynamics for area change ($R_c V_c \simeq c^{\text{ste}}$). **(d)**: Dynamics of CAF leading edge radius for N-cadherin knock-down condition (red) or control (black). One can see that initial velocity is independent from the condition.

Note that this back-of-the-envelope calculation do not take into account the PAA elastic deformations coming from the CAF substrate region (as seen on Fig. 3.7a): it could renormalize the bare resistive stress $\sigma_{rr} \sim E(R_0 - R)/R_0$ (uniform cylinder compression) experienced by CAFs along the inner edge, because the surrounding material resists the pulling stresses localized near the pillar and introduces a non local stiffening effect. In addition, we couldn't consider the effect of steady-state substrate tractions T_r without available data, that would add another source of resistance to the pulling tension from the ring with mechanical coupling to the PAA substrate elasticity mentioned above. This can bias the local force balance with an effective resistive tension as $h_c \sigma_{rr} = \Gamma/R - \gamma[\text{elastic resistance}]$ such that the previous calculation likely under-estimates the ring tension: one can keep the characteristic value $\Gamma \sim 1 \mu\text{N}$.

This order of magnitude for ring line tension is in qualitative agreement with an independent estimation coming from surface integration of radial tractions in the CAF-CC system as described in a next section. Unfortunately, the precision is too low to assess if the CAF ring tension depends on the type of obstacle (CC cluster versus elastic pillar) or if only the hole size is relevant. Nevertheless, this minimal CAF-pillar system emphasizes how a high CAF-generated tension is able to mechanically compress its environment in an unspecific manner, with potential *in vivo* implications for primary tumour sites surrounded by a high concentration of CAFs.

3.2.2 CAF closure dynamics

After the assembly of a supracellular actomyosin ring around CC clusters, CAFs climb on top and close the disc-like gap. The acquisition of area dynamics for different cluster sizes and various drug conditions gives valuable constraints on the theoretical mechanisms compatible with the experimental data, an analysis already performed for *in vitro* epithelial gap closure [225, 228] without use of traction maps information. It is especially useful in N-cadh knock down conditions where CAFs have higher tendency to undergo gap closure (less budding phenotype) without detection of substrate tractions below the CC cluster (Fig?). This allows to consider the observed CC monolayer deformations (local rims) as a weak effect that can be ignored at first, to not introduce complex geometric features and treat the CC cluster as a rigid substrate (constant peripheral radius) for the CAF leading edge.

In generic terms (see Fig. 3.8a), gap closure dynamics can be analysed according to

- a driving tension $\gamma[\text{driving}]$ that pulls the tissue inwards, associated to a ring line tension Γ because a sheet anisotropic tension γ_a has been eliminated by pillar compression experiments (previous section),

- a resistive tension γ [resistance] that retains the tissue outwards, either from tissue pre-stress γ_∞ or tissue elastic modulus $E_c h_c$,
- a dissipation function D that controls the ratio of tension used for closure work and lost in the environment, either dominated by an internal effect (viscosity) as a 1D ring viscosity η_1 or a 2D CAF tissue viscosity η_2 , or an interfacial effect (dynamic friction) like ring line friction ζ , CAF-CC 2D friction ξ or CAF-substrate coefficient ξ_{sc}

which is represented by the symbolic equation for the closing edge velocity V_c

$$V_c = \frac{\gamma[\text{driving}|\Gamma] - \gamma[\text{resistance}|\gamma_\infty, E_c h_c]}{D[\text{viscosity}|\eta_1, \eta_2] + D[\text{friction}|\zeta, \xi, \xi_{sc}]} \quad (3.1)$$

If one further assumes planar incompressibility for the CAF tissue and rotational invariance around the CC cluster center, the radial velocity field reads $v_r(r) = -V_c R_c / r$ where $V_c = -dR_c/dt$, together with the radial displacement $u_r(r) = (R_c - R_0)R_c / r$ from an initial radial position corresponding to the CC cluster radius R_0 . This considerably simplifies the calculations for the different theoretical mechanisms, up to the introduction of a cut-off length R_∞ at which the tissue stress relaxes to the pre-stress value γ_∞ [225]. With Lagrange multiplier Π to ensure planar incompressibility, the CAF tissue tension can be written $\gamma_{rr} = -\Pi + 2\eta_2 \partial_r v_r + E_c h_c \partial u_r$ in the radial direction and $\gamma_{\theta\theta} = -\Pi + 2\eta_2 v_r / r + E_c h_c u_r / r$ for the orthoradial component. In addition to the interfacial frictions ξv_r and $\xi_{sc} v_r$ that build tension gradients in the CAF tissue, viscous and frictional dissipations localized along the ring generate stresses proportional to CAF velocity V_c . Using similar stress equations for a spatially extended ring over a width w , with 2D ring viscosity η_1/w , CAF-CC 2D ring friction coefficient ζ/w and anisotropic active tension $\Gamma/w = \gamma_a$, one can show that the limit of a vanishing ring width ($w \rightarrow 0$) leads to the radial tension balance $V_c[\zeta + 2\eta_1/(R_c)^2] = \Gamma/R_c - \gamma_{rr}$ at the CAF leading edge $r = R_c$ if one ignores CC cluster deformations. With initial condition $R_c(t=0) = R_0$, one can write the precise closure dynamics equation

$$V_c = \frac{\Gamma(R_c|R_0)/R_c - \gamma_\infty - E_c h_c (R_0 - R_c)/R_c}{2\eta_1/(R_c)^2 + 2\eta_2/R_c + \zeta + \xi_{sc} R_c \log[R_\infty/R_0] + \xi R_c \log[R_0/R_c]} \quad (3.2)$$

where the line tension $\Gamma(R_c|R_0) = \Gamma_0(R_0) \cdot (R_0/R_c)^x$ can a priori contains a curvature-dependent feed-back [229] that could strengthen ($x > 0$) or inhibit ($x < 0$) actomyosin contractility for smaller gap radii, and a size-dependent initial value $\Gamma_0(R_0)$.

The typical CAF velocity measured experimentally at the beginning of closure is $V_c \sim 3 \mu\text{m/h} \sim 1 \text{ nm/s}$, with CAF radius $R_c \sim 100 \mu\text{m}$, ring line tension $\Gamma \sim 1 \mu\text{N}$ from pillar compression experiments (previous section). This gives a driving tension $\Gamma/R_c \sim 10^{-2} \text{ N/m}$ and an order of magnitude for the dissipation function $D \sim 10^7 \text{ Pa s}$. With a CAF tissue height $h_c \sim 10 \mu\text{m}$ and a rim width $w \sim 1 - 10 \mu\text{m}$ to convert 1D or 2D quantities into 3D, one can extract a typical value for the different dissipation parameters when assumed to be the dominant mechanism.

- For actomyosin ring viscosity $\eta_1 \equiv \eta_3 \cdot h_c w$, one obtains $\eta_1 \sim 10^{-1} \text{ Pa s m}^2$ or equivalently $\eta_3 \sim 10^9 - 10^{10} \text{ Pa s}$. Note that the typical viscosity extracted from different visco-elastic models is found around 10^5 Pa s for suspended MDCK monolayers [189] but jump to $10^7 - 10^8 \text{ Pa s}$ for spreading MDCK monolayers [238] or 3T3 fibroblasts [176]. It remains below the estimation associated to viscous dissipation concentrated in the supracellular ring; this may easily be explained by the heavy structural differences between tissue monolayer and actomyosin ring. However, even if one assumes viscosity to be controlled by actomyosin dissipation in contractile cables (or bundles), one expects $\eta_3 \sim 10^4 - 10^7 \text{ Pa s}$ for such structures [239]. Thus, ring viscosity is unlikely to be the dominant mechanism.
- For CAF tissue viscosity $\eta_2 \equiv \eta_3 \cdot h_c$, one obtains $\eta_2 \sim 10^3 \text{ Pa s m}$ or equivalently $\eta_3 \sim 10^8 \text{ Pa s}$. Indeed, this value is compatible with estimates for spreading monolayers on substrates [238, 176].

- For ring line friction $\zeta \equiv \xi_r \cdot w$, one obtains $\zeta \sim 10^7$ Pa s or equivalently $\xi_r \sim 10^{12} - 10^{13}$ Pa s/m. This value is too large for tissue-tissue friction measured in development, as small as 10^6 Pa s/m for zebrafish embryogenesis [240] or $10^7 - 10^9$ Pa s/m near zebrafish somites [241], whereas tissue-substrate friction can reach 10^{11} Pa s/m for C2C12 monolayers on small discs [242] and $10^{11} - 10^{12}$ Pa s/m for single cell migration [243]. Gap closure of MDCK monolayers over non-adherent surfaces, also driven by a contractile ring, provide a typical value $\zeta \sim 10^5 - 10^6$ Pa s [228].
- For CAF-substrate friction ξ_{sc} and CAF-CC friction ξ , one obtains $\xi_{sc} \sim \xi \sim 10^{11}$ Pa s/m, which is compatible with monolayer slippage [242].

This naive scaling argument tends to favour CAF tissue viscosity η_2 over ring line viscosity η_1 but cannot exclude it. Friction-dominant dissipation provides values at the upper-limit of the estimations available in the literature, both for ring line friction ζ and 2D frictions ξ_{sc}, ξ . Note that CAF-CC friction ξ does not contribute to initial closure dynamics (Eq. 3.2), whereas the observation of steady-state substrate tractions is not consistent with CAF slippage on substrate $T_r = \xi_{sc} v_r$ (see next section). Therefore, we eliminate CAF-substrate friction ξ_{sc} as a potential source of dissipation in this system.

Without justification for a contractile feed-back on the actomyosin ring, dissipation dominated by ring line friction ζ is privileged, a modelling already used for epithelial gap closure [228]. For the experimentally constrained ratio Γ/ζ (Fig. 3.8b), one finds a range of $300 - 550 \mu\text{m}^2/\text{h}$ to be compared to $10 \mu\text{m}^2/\text{h}$ measured for MDCK monolayers closing on non-adhesive surface [228]. The biological structures that would be responsible for a ring line friction parameter ζ are not identified, but focal adhesions enriched along the cells that constitute the supracellular ring have already been observed on MDCK monolayers performing gap closure around laser-induced wounds[222]

Under N-cadh KD conditions, the compilation of experimental closure dynamics for different clusters in terms of area (Fig. 3.8b) or radius (Fig. 3.8c) show one important feature: the areal velocity $R_c(t)V_c(t)$ is approximately constant in time. Even if this property is weakened by a low statistical power for CAF closure phenotype ($N = 4$), the combination of CAF dynamics for all clusters show with better robustness ($N = 6 + 13$) that initial radial velocity is independent from N-cadh KD conditions (Fig. 3.8d): $V_c^0[\text{WT}] \sim V_c^0[\text{N-cadh}]$. According to Fig. 3.8b, the initial areal velocity also seems weakly dependent from cluster size ($R_0 \cdot V_c(0) \simeq c^{\text{ste}}$), despite some dispersion when one compares with the dynamical lines $R_c(t)V_c(t) \simeq c^{\text{ste}}$.

Neglecting the resisting tension, all those conditions are valid if one assumes the line tension Γ to be constant and the dissipation to be dominated by a N-cadh independent line friction ζ : $R_c(t)V_c(t) \simeq \Gamma/\zeta$. Following the previous scaling argument, dissipation could also be dominated by 2D tissue viscosity η_2 , but this choice requires a 1st order positive feed-back ($\Gamma \propto 1/R_c$) as proposed by [229]. A ring line viscosity η_1 dominant-dissipation would require a 2nd order positive feed-back to be compatible with CAF closure dynamics, whereas a CAF-substrate friction ξ_{sc} is compatible with a 1st order negative feed-back ($\Gamma \propto R_c$) but is disregarded for independent reasons as discussed above.

With better statistics, the dependency of initial velocity on cluster size R_0 , like $R_0 \cdot V_c(0) \simeq c^{\text{ste}}$, could add new constraints on the initial line tension $\Gamma_0(R_0)$. With the example $R_0 \cdot V_c(0) \simeq c^{\text{ste}}$, one would need $\Gamma_0 \propto R_0^{-2}$ for ring line viscosity η_1 , $\Gamma_0 \propto R_0^{-1}$ for tissue viscosity η_2 , $\Gamma_0 \propto (R_0)^0$ for line friction ζ and $\Gamma_0 \propto (R_0)^1$ for CAF-substrate friction ξ_{sc} .

It is clearly difficult to establish any precise scaling for the initial areal velocity $R_0 \cdot V_c(0)$ according to the available experimental data Fig. 3.8b. Still, it is interesting to mention that those scalings on initial dynamics can be compared in principle with the pillar compression experiments where one finds $\Gamma_0 \propto (R_0)^{-1,0}$. Thus, the constraint $R_0 \cdot V_c(0) \simeq c^{\text{ste}}$ would favour CAF tissue viscosity η_2 or ring line friction ζ . Everything combined, this analysis tends to favour either line friction ζ or CAF tissue viscosity η_2 as the dominant source of dissipation for CAF closure dynamics.

In addition, the important phenotypic changes between control and N-cadh KD conditions in terms of budding frequency show that CAF dynamics is dominated by a mechanism unspecific to

the N-cadherin/E-cadherin interaction (Fig. 3.8d), whereas the tissue-tissue shear stress is expected to be N-cadh dependent. In general, one expects the CAF-CC surface friction coefficient ξ , the CAF viscosity η (tissue or ring) and the line friction coefficient ζ to contain two components unspecific or specific to the N-cadherin/E-cadherin interaction (N/E)

$$\xi_{\text{tot}} = \xi[\text{unspecific}] + \xi[\text{N/E}], \quad \eta_{\text{tot}} = \eta[\text{unspecific}] + \eta[\text{N/E}], \quad \zeta_{\text{tot}} = \zeta[\text{unspecific}] + \zeta[\text{N/E}] \quad (3.3)$$

The important change for budding likelihood between control and N-cadh KD conditions is in favour of $[\text{unspecific}] \lesssim [\text{N/E}]$, whereas the similar CAF closure dynamics in both situations (Fig. 3.8d) is more compatible with $[\text{unspecific}] \gg [\text{N/E}]$. In fact, the CAF-CC surface friction cannot control CAF closure initiation because the surface of contact between the two tissues starts from zero. Then, the similar initial velocity indicates $\zeta[\text{unspecific}] \gg \zeta[\text{N/E}]$ or $\eta[\text{unspecific}] \gg \eta[\text{N/E}]$ for potential parameters controlling closure dynamics, whereas the conditional phenotype could only apply on surface friction $\xi[\text{unspecific}] \lesssim \xi[\text{N/E}]$ to drive CC cluster deformations followed by budding. If CAF closure was controlled by viscosity and if CAF-CC interaction was relying on line friction, one would also expects $\zeta[\text{unspecific}] \lesssim \zeta[\text{N/E}]$. Indeed, the spatial average of CAF velocity on the full tissue, that should depend on tissue viscosity η_2 , is unperturbed by N-cadh KD (Fig. 3.9b) which confirms the claim that $\eta[\text{unspecific}] \gg \eta[\text{N/E}]$. Note that a scenario where both CAF closure dynamics and CAF-CC interaction would be controlled by ring line friction ζ is not compatible with experimental features and one also needs specific surface friction.

Those simple arguments put some constraints on the physical mechanisms able to reproduce the observed CAF closure dynamics. The high dispersion of measurements on both pillar compression and CAF closure experiments makes hard the selection of one precise mechanism. Thus, we will consider the independent scenarios where dissipation is either dominated by ring viscosity, tissue viscosity or ring line friction:

- unspecific viscosity η_1 or η_2 with specific surface friction ξ or specific line friction ζ ,
- zero viscosity $\eta_1 = \eta_2 = 0$ but unspecific line friction ζ with specific surface friction ξ .

3.2.3 CAF rheology and traction localization

The CAF tissue that surrounds the CC cluster is composite because those cells produce ECM proteins that spontaneously assemble into a network (Fig. 3.9a). In particular, the fibronectin (Fn) fibers are shown to ensure the supracellular integrity of the actomyosin ring since Fn knock-down leads to transient ring collapses and weak cluster compression without CAF climbing transition. The importance of ECM deposition has already been acknowledged in wound healing for normal fibroblast tissues [223], where circumferential assembly at the leading edge serves as a track for gap closure. The recent discovery of Fn-dependent cell-cell adhesions on fibroblasts [244] also suggests an ECM contribution to the full tissue rheology, confirmed by higher CAF velocity in Fn knock-down conditions (Fig. 3.9b). Thus, even if CAFs could be described as a Maxwell fluid (review [61]) with viscous rheology at long times⁵, the ECM component should add tissue elasticity described by a characteristic modulus E_{Fn} . This corresponds to a Standard Linear Solid (SLS) rheological model where elastic ECM is in parallel with Maxwellian CAFs (Fig. 3.9c), approximated as a Kelvin-Voigt solid when the CAF portion becomes viscous at long times (Fig. 3.9c) compared to the relaxation time scale $\tau_{\text{CAF}} \equiv \eta_{\text{CAF}}/E_{\text{CAF}}$.

An experimental signature for this solid rheology assumption comes from two features of measured substrate tractions (Fig. 3.9d):

⁵This assumption is not necessarily appropriate because the high CAF proliferation could also trigger a jamming transition above a critical cell density and considerably reduce cell rearrangements [181]. This would make the effective viscosity so high ($\tau \equiv \eta/G \gg t_{\text{exp}}$) that the tissue would behave elastically.

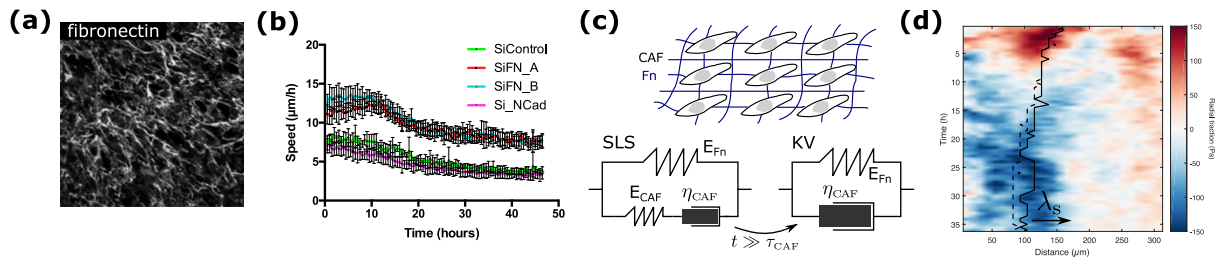


Figure 3.9: **(a)**: Fluorescence intensity of fibronectin in a confluent CAF tissue showing fibres with network-like structure. The window size is $350\ \mu\text{m}$. **(b)**: Spatial average of individual CAF velocity magnitude in the field of view far from the CC cluster, as a function of time (particle image velocimetry method). N-cadh KD doesn't significantly modify the speed when compared to control but cells under Fn KD conditions speed-up. **(c)**: Sketch of the CAF tissue composed of cells and ECM fibers (fibronectin). This corresponds to a Standard Linear Solid (SLS) rheology with ECM spring in parallel with Maxwell CAFs (spring and dashpot in series) and becomes a Kelvin-Voigt (KV) solid at long times compared to CAF relaxation scale $\tau_{\text{CAF}} \equiv \eta_{\text{CAF}}/E_{\text{CAF}}$. **(d)**: Experimental kymograph of radial substrate tractions with CC cluster peripheral radius (full black line) and CAF leading edge radius (dashed black line), corresponding to a stable bud phenotype. Outward tractions, coming presumably from CAF protrusive activity as they are mostly observed at the beginning when CAFs crawl towards the cluster periphery, are positive (red). Inward tractions, associated to the pulling forces from the actomyosin ring that are transmitted to the substrate, are negative (blue). The system stabilizes after 30 h after what both radii remain approximately constant. The tractions in the surroundings saturate over a finite spatial width λ_s , contrarily to the tractions below the CC cluster which decrease at steady-state after maximal amplitude in the range 25 – 30 h.

- the existence of significant inward tractions at steady-state, essentially at the CC cluster periphery from the CAF surrounding tissue. It occurs either for a budding phenotype where the CAF leading edge is stabilized along the bud (Fig. 3.9d), or for the closure phenotype where tractions do not dissipate after CAF covering of the CC cluster.
- the spatial localization of those inward tractions over a width λ_s of the order of $50\ \mu\text{m}$ away from the CC cluster boundary (Fig. 3.9d).

This pattern of traction saturation has already been observed for epithelial monolayers closing gaps along non-adhesive patches [229], with a similar temporal trend: outward tractions at the beginning, reversed into inward tractions when closure begins to remain at a stationary value when closure ends. Those tractions are also confined at the periphery over a finite width of the order of $10\ \mu\text{m}$.

Those steady-state radial tractions are not compatible with dynamic friction exchanged between moving cells and substrate ($T_r = \xi_{sc}v_r$) as it is often assumed for tissues spreading on substrates [243, 222, 238, 176, 242] in addition to a protrusive term directed by cell polarity \vec{p} ($T_r = T_0p_r$). It is then natural to associate inward tractions with pulling forces from the actomyosin ring that are transmitted elastically to the substrate: $T_r = Y_s u_r$ where Y_s is a phenomenological CAF-substrate stiffness and u_r represents the CAF tissue radial displacement.

If the CAF tissue rheology was fluid at steady-state with viscosity η_{CAF} , there would no characteristic length scale to localize tractions on a finite width⁶, whereas an elastic rheology with modulus E_c ensures a natural length scale E_c/Y_s for this localization feature. Indeed, this generic elastic coupling with substrate has already been proposed for circular adherent monolayers [245, 246] and relies on the tendency for focal adhesions to be over-expressed at the tissue periphery compared to the core. Under the thin film approximation, an homogeneous elastic material with Young modulus E_c , Poisson ratio ν and thickness h_c , coupled to the substrate through the stiffness Y_s , builds a localization length $\lambda_s \equiv \sqrt{E_c h_c / (Y_s (1 - \nu^2))}$ on which stress or displacement fields localize⁷. Other

⁶For example, when assuming 2D incompressibility [225], the radial velocity or displacement fields must decay as $1/r$ and therefore propagate far away from the CC cluster periphery.

⁷The limit of 3D incompressibility ($\nu \rightarrow 1/2$) poses no divergence problem but the assumption of planar incompressibility ($\nu \rightarrow 1$) that is often made in tissue mechanics [225, 176] eliminates localization because $\lambda_s \rightarrow \infty$. As discussed above, this corresponds to a decay $\propto 1/r$ for the radial velocity or displacement field.

localization scales could be introduced like the nematic correlation scale [238, 242] associated to cell alignment, but we choose to limit the complexity of the field description and ignore the polarization field. Our essential assumption of elastic substrate coupling makes λ_s appear as a natural consequence for a solid tissue.

The planar rheology associated to this elastic rheology reads

$$\begin{aligned}\gamma_{rr} &= \gamma_\infty + \frac{E_c h_c}{1 - \nu^2} [\epsilon_{rr} + \nu \epsilon_{\theta\theta}] \\ \gamma_{\theta\theta} &= \gamma_\infty + \frac{E_c h_c}{1 - \nu^2} [\epsilon_{\theta\theta} + \nu \epsilon_{rr}]\end{aligned}\quad (3.4)$$

where γ_∞ is a constant pre-stress, $\epsilon_{rr} = \partial_r u_r$ and $\epsilon_{\theta\theta} = u_r/r$ are the linear strain components for a radial displacement field u_r within rotational invariance around hole center. One defines the reference configuration (initial hole radius R_0) with respect to an absence of pre-stress. In the formal limit $h \ll \lambda_s$, one can show using a lubrication approximation [247] that radial force balance between CAF tissue planar stress gradient and radial substrate tractions $T_r(r) = Y_s u(r)$ is simply

$$\partial_r \gamma_{rr}(r) + \frac{1}{r} [\gamma_{rr}(r) - \gamma_{\theta\theta}(r)] = Y_s u(r) \quad (3.5)$$

Similarly to [229], we add a yield stress f^* [248] that captures the limited deformability of CAF-substrate linkers: they tend to break and re-attach above a critical displacement f^*/Y_s . Thus, the appropriate substrate interface rheology is chosen to be

$$T_r = Y_s u_r \quad \text{if } |T_r| < f^*, \quad T_r = -f^* \quad \text{otherwise} \quad (3.6)$$

According to the previous section, the CAF closure dynamics is compatible with dissipation dominated either by tissue viscosity $\eta_2 \equiv \eta_{\text{CAF}} h_c$ or ring line friction ζ . If the second scenario is considered, the addition of CAF viscosity will only increase the technical complexity without any physical insight. To concentrate the modelling complexity on the CC cluster deformations, we then choose to ignore CAF viscosity⁸ and use a simple elastic rheology for the surrounding region as described on Eq. 3.4.

On the contrary, a rigorous visco-elastic description is not useful for the front CAF monolayer that covers partially the CC cluster, and we assume 2D incompressibility for the closing CAF layer with planar viscosity η_2 if needed. This is not expected to add any qualitative changes. Those choices keep the fundamental features of traction saturation and localization at the cluster periphery, without the need for the technical resolution of a three boundary (leading edge, cluster periphery and infinity) spatio-temporal problem with visco-elastic rheologies.

3.2.4 Localized deformation: rim

The CC mechanical response to CAF-induced shear stress is fairly complicated, and is expected to trigger mechano-sensitive pathways that could specifically affect the cytoskeletal properties. Indeed at early stages, although a freely growing CC cluster localizes YAP in CC nuclei, YAP is observed to delocalize in cytoplasm when CAFs restrain growth by confinement: this observation may be a direct consequence of CAF compression induced by the contractile actomyosin ring [190]. The other source of CAF-induced stress is frictional shear when CAFs close on top of CCs, which could also affect YAP activity since a fluid shear stress as weak as 10^{-2} Pa has been shown to alter

⁸If one compares viscous and elastic stresses for a Kelvin-Voigt model, the viscous term is negligible for $\eta_3 \ll E_c u_r / v_r$ where u_r and v_r are characteristic amplitudes for radial displacement field and radial velocity field, respectively. As discussed in results, we expect $E_c \sim 100$ Pa whereas $u_r \sim 10 - 100 \mu\text{m}$ and $v_r \sim 1 \text{ nm/s}$. Thus, one gets $\eta_3 \ll 10^6 - 10^7$ Pa s. This is not compatible with the value found in the assumption where tissue viscosity is the dominant dissipation mechanism for CAF closure. It may indicate that CAF rheology is inherently a bi-component system and one cannot assume $\epsilon_{\text{CAF}} \sim \epsilon_{\text{Fn}}$ and $\dot{\epsilon}_{\text{CAF}} \sim \dot{\epsilon}_{\text{Fn}}$. Instead, one expects a transport of CAFs with fibronectin network stretching ($\epsilon_{\text{CAF}} \sim \epsilon_{\text{Fn}}$) but independent dissipation in CAFs ($\dot{\epsilon}_{\text{CAF}} \neq 0$ and $\dot{\epsilon}_{\text{Fn}} \simeq 0$), which corresponds to our final CAF-Fn rheology choice.

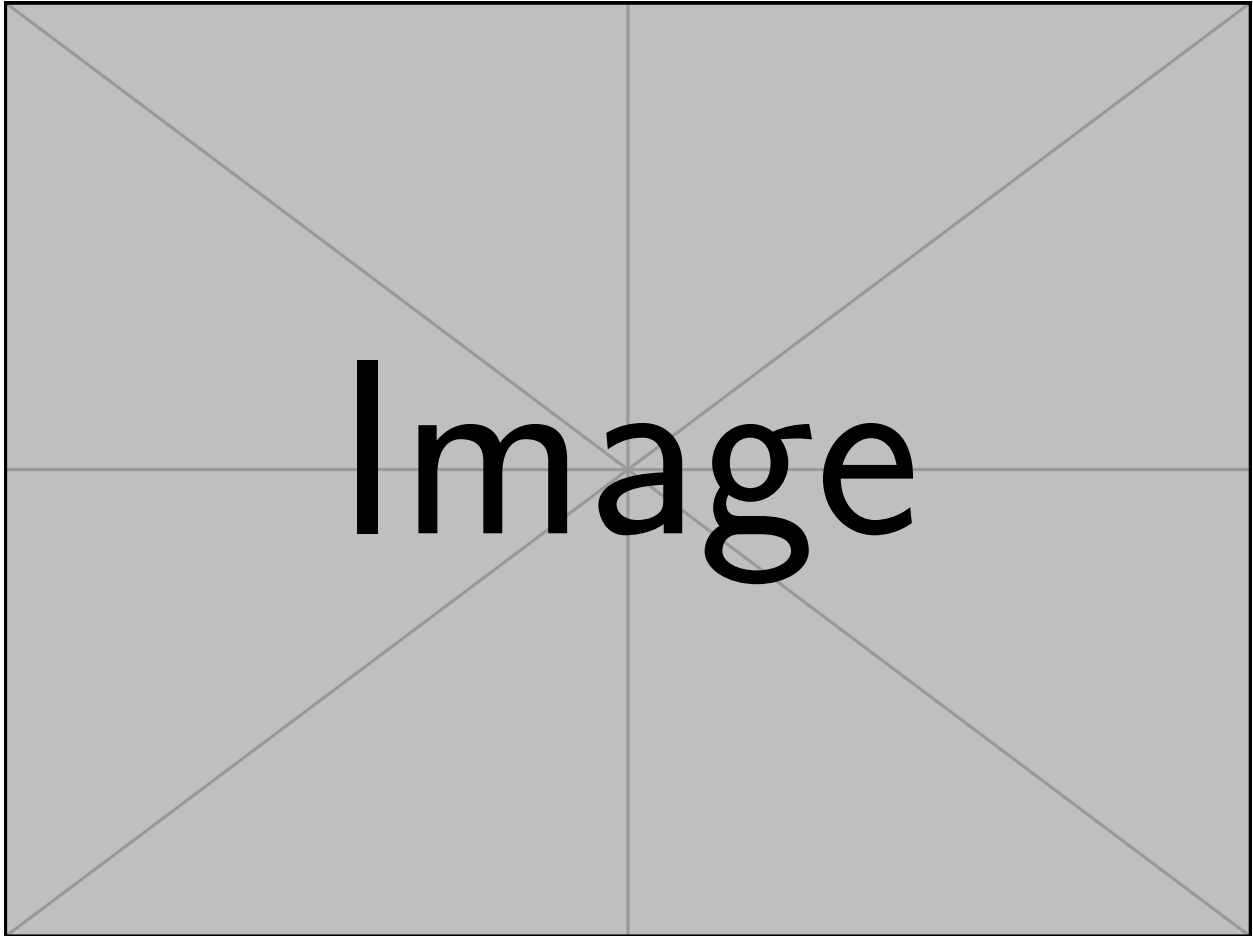


Figure 3.10: **(a)**: Phase contrast microscopy of a CC cluster partially covered by CAFs (contractile ring in orange) in top view. The shear stress between the two tissues drives a centripetal displacement of CCs that applies pressure on the uncovered region in center. As a consequence, localized out-of-plane deformations of the CC cluster are generated near the ring, called "rims". **(b)**: Localized rim observed on an unstable liquid film after nucleated dewetting. For visco-elastic liquids that can slip on the substrate, the rim width Δ saturates at a parametric length $\sqrt{h^*b}$, where h^* is the film thickness and b the slip length relating liquid viscosity η and substrate friction ξ_s : $b \equiv \eta/\xi_s$. The picture represents a PDMS film with $30 \mu\text{m}$ thickness and 4 cm window size, from [234]. **(c)**: High resolution microscopic images of the CAF-CC system in side view at experimental time $t = 24 \text{ h}$. The CAF tissue advancement along the CC cluster (towards the right side in those images) generates out-of-plane CC displacements near the actomyosin ring, when comparing the tissue thickness on covered and free regions (top). Without precise spatio-temporal imaging, it is hard to distinguish the monolayer rim (top) and a multilayer rim (proto-bud) where some cells form a second layer (bottom). The rim width Δ is of the order of $10 - 100 \mu\text{m}$. **(d)**: Kymograph of substrate tractions for a CC cluster that terminates into a stationary bud. In control case, CAFs tend to penetrate below the cluster but the robust pattern of inward tractions suggest a mechanical transmission of the stress contained in the CC cluster. Those tractions below the cluster seem to relax at steady-state, suggesting sliding friction for cluster-substrate interaction.

YAP1 expression on prostate cancer cells [249]. Although shear stresses coming from external fluid flow or tissue-tissue contact are phenomenologically distinct, it remains interesting to mention that the surface friction term $\sigma_{xz} \sim \xi V_c$ can be evaluated using its sub-dominant effect on CAF closure dynamics compared to dissipation function $D \sim 10^7$ Pa s: one gets $\sigma_{xz} \lesssim 10$ Pa. Nevertheless, the cancer cells covered by CAFs do not directly participate in the budding generation and only "transforms" the CAF shear stress into compression over the uncovered region. Without precise spatio-temporal mapping of mechano-sensitive factors like YAP, we restrict ourselves to the passive tissue mechanical response and choose to ignore those potential sources of cell heterogeneity.

After the initiation of CAF closure on top of CC clusters, it is frequent to observe localized shape variations near the actomyosin ring on confocal microscopy (Fig. 3.10a). Ignoring the angular heterogeneities associated to single clusters, those out-of-plane bulges are reminiscent of the phenomenon of liquid dewetting [234, 235, 236, 250] as represented on Fig. 3.10b, where an unstable liquid film dewets by nucleating an expanding dry hole. There is a clear localization of film deformation at the hole periphery, and this dynamical bulge is called a rim. If the liquid film is visco-elastic and can slip with respect to the substrate, one can show [235, 236] that the rim width Δ scales like $\sqrt{h^* \eta / \xi_s}$, where h^* is the initial film thickness, η the liquid shear viscosity and ξ_s the sliding friction coefficient between the film and substrate. The two dissipational parameters builds a natural length scale $b \equiv \eta / \xi_s$ called the slip length [236]. The divergent geometry of hole expansion in thin film dewetting (Fig. 3.10b) is not appropriate for comparison with the CAF-CC system, contrarily to the reverse wetting of a dielectrophoresis-induced spread film [250] that relaxes into a droplet shape: one initially observes a peripheral rim upon film retraction that let the central region unperturbed, until the deformation propagates to center and makes the rim "disappear", before converging into a spherical cap.

Contrarily to those passive polymeric liquids, the CC monolayer is expected to respond elastically to that type of mechanical perturbation: even with high rate of planar cell rearrangements (T1 transitions), the convergent flow of incompressible cells can only be sustained by single cell deformation as can be seen on Fig. 3.10c. Indeed, one can show (chapter 2) that a 2D side vertex model with incompressible cell area A_0 and polar tensions γ_a (apical), γ_l (lateral) responds to external pressure with an effective elastic modulus $E_{CC} \sim \gamma_l / \sqrt{A_0}$ and surface tension $\gamma_{CC} \sim \gamma_a$ to resist height deformations. Our 2D side vertex model ignores cytoplasmic viscosity as most vertex models (review [167]), and cannot naturally deal with cell rearrangements since the transverse direction is ignored. In the CAF-CC system, long-term velocity gradients are possible in cells, thanks to differential sources of shear stress on apical and basal interfaces for free and covered regions (Fig. 3.10c), as well as neighbour-to-neighbour cell transitions in the plane. However, we choose to remain inside the boundaries defined by our vertex model and ignore those sources of viscous dissipations, considered as secondary effects.

Even if we lack precise spatio-temporal quantification for rim dynamics, it is important to notice that the type of CC rheology and CC-substrate interaction will influence its characteristic width. A liquid film is parametrized by planar viscosity ηh^* , a solid film by elastic modulus $E h^*$, whereas film-substrate friction can be associated to a sliding friction coefficient ξ_s involving relative velocities, or a static friction coefficient Y_s involving relative displacements. Thus, one expects a parametric width $\Delta = \sqrt{h^* \eta / \xi_s}$ for a slipping liquid and $\Delta = \sqrt{E h^* / Y_s}$ for a gripping solid by connecting longitudinal and shear stresses. However, there is no parametric length scale for a slipping solid, and a dynamical rim width $\Delta(t)$ is defined according to a diffusion constant $D_s = E h^* / \xi_s$ such that $\Delta(t) \equiv \sqrt{D_s t}$. In addition, a surface tension γ introduces another length scale $\lambda \equiv \sqrt{\gamma h^* / E}$ when comparing normal stresses at the free interface. The need to consider epithelial elasticity eliminates the scenario of a slipping liquid and remain only the gripping or slipping solid assumptions. In the future, thanks to better spatio-temporal quantification of tissue out-of-plane deformations, the analogy with thin film dewetting invites to develop a new tissue rheological probe associated to rim length scaling, giving information on the "ratio" between bulk and interfacial resistance to

deformation.

Experimentally, the rim appearing on the CC cluster has a typical width of the order of $10 - 100 \mu\text{m}$ (Fig. 3.10a,c). To evaluate an order of magnitude for the effective stiffness Y_s between substrate and CCs, a simple calculation assuming discrete bond stretching over the adhered surface of a cell gives⁹ $Y_s \sim 10^{11} \text{ Pa/m}$. However, this calculation likely over-estimates the parameter Y_s because FAs are displaced under very weak forces [252] ($\sim 0.1 \text{ nN}$ per FA), whereas experimental cluster displacements up to $10 \mu\text{m}$ (Fig. 3.10d) do not seem compatible with the picture of single bond stretching. Indeed, confined clusters of keratocytes exhibit localized tractions compatible with $Y_s \sim 10^6 \text{ Pa/m}$ [246]. This low value may be related to a complex cell adhesion response hidden by the tissue scale, or cell-substrate stiffness could be dominated by substrate response as two springs in series with one much softer than the other. Knowing that the typical elastic modulus of cancer cells is $E \sim 10^2 - 10^4 \text{ Pa}$ depending on the type of cancer, the cell phenotype and the mechanical measurement probe (review [253]), the rim width Δ of a gripping solid with thickness $h^* \sim 10 \mu\text{m}$ should be between 100 nm and $100 \mu\text{m}$. On the contrary, the sliding friction coefficient ξ_s of epithelial monolayers spreading on substrates is found around $\sim 10^9 - 10^{11} \text{ Pa s/m}$ [225, 242], and the rim width Δ of a slipping solid reaches between $10 \mu\text{m}$ and 1 mm after $t \sim 10 \text{ h}$ growth (Fig. 3.10c).

Numerical evaluation cannot discriminate the slipping or gripping assumptions over the substrate. However, on control experiments, the tractions observed below the cluster are able to propagate over the full area and seem to relax at steady-state, as shown on Fig. 3.10d. Despite the low signal-to-noise ratio, this pattern is found on different clusters and suggests that the slipping scenario is more compatible with available data. Interestingly, on experiments with N-cadherin knock-down, the absence of significant tractions observed below the CC cluster provides a limit for the friction coefficient ξ_s . Calling v the characteristic magnitude of the CC velocity field associated to cluster deformation (black line on Fig. 3.10d), one expects $v \lesssim 0.1 - 1 \mu\text{m/h}$, whereas negligible tractions correspond to $\xi_s v \lesssim 10 \text{ Pa}$. This leads to $\xi_s \lesssim 10^{10} - 10^{11} \text{ Pa s/m}$, which remains in line with the expected range of values $\sim 10^9 - 10^{11} \text{ Pa s/m}$ [225, 242]. The same strategy can be applied to the gripping scenario, where the characteristic CC displacement $u \lesssim 1 - 10 \mu\text{m}$ provides $Y_s \lesssim 10^6 - 10^7 \text{ Pa/m}$: it clearly shows that the evaluation based on discrete bond stretching ($Y_s \sim 10^{11} \text{ Pa/m}$) is flawed. Thus, both experimental cases give valuable informations, on the nature and magnitude of CC-substrate mechanical interaction.

Finally, with surface tension γ of the order of typical cortical tension magnitudes $\sim 10^{-4} - 10^{-3} \text{ N/m}$ [34], one gets $\lambda \sim 0.1 - 10 \mu\text{m}$ which only adds a small contribution to rim width scaling (see next section).

To conclude, a table recapitulates the main theoretical assumptions of the model for the different sub-systems: the CAF actomyosin ring, the CAF tissue surrounding the CC cluster, the front CAF monolayer that closes on top of the CC cluster, the CC cluster itself, and CAF-substrate/CAF-CC/CC-substrate interfaces.

3.3 Model: CC rheology

As discussed in the previous chapter and summarized on Fig. 3.11, we describe the CC monolayer as an incompressible elastic material with slipping friction on both substrate (parameter ξ_s) and CAF-CC interface (parameter ξ). The closure dynamics quantified in N-cadherin knock-down conditions is compatible with: constant ring line tension Γ and ring line friction ζ , or curvature-sensitive line tension $\Gamma_t = \Gamma(R_0/R_c)$ and CAF tissue viscosity η_2 . One expects the surface friction ξ to be dependent on the specific N/E-cadherin interaction whereas the line friction ζ or tissue

⁹One can extract the effective density of bonds on an adhered cell by using a bond surface density $n_{\text{FA}} \sim 1/(20 \text{ nm})^2$ in FAs that have a typical surface $A_{\text{FA}} \sim 1 \mu\text{m}^2$ [111, 251], or 1000 bonds per FA. With 10 FAs per cell over an adhered surface of $A_{\text{cell}} \sim 100 \mu\text{m}^2$, the bond surface density becomes at cell resolution $n_b \simeq n_{\text{FA}} \cdot 10 A_{\text{FA}} / A_{\text{cell}}$ or $n_b \sim 1/(100 \text{ nm})^2$. With adhesion bond stiffness $k_b \sim 1 \text{ pN/nm}$, one gets $Y_s = k_b n_b \sim 10^{11} \text{ Pa/m}$.

sub-system	rheology (parameter)	property
CAF actomyosin ring	line tension (Γ) and line viscosity (η_1)	Γ constant or feed-back
CAF surrounding tissue	elastic ($E_c h_c$) with pre-stress (γ_∞)	3D incompressible ($\nu \rightarrow 1/2$)
CAF front monolayer	viscous (η_2)	2D incompressible
CC cluster	elastic (Eh^*) with surface tension γ	3D incompressible
CAF-substrate interface	elasto-plastic (Y_s, f^*)	$T_r = Y_s u_r$ or $T_r = -f^*$
CAF-CC interface	surface friction (ξ) or ring line friction ζ	$\sigma = \xi \Delta v_r$ or $h^* \sigma = \zeta \Delta v_r$
CC-substrate interface	sliding friction (ξ_s)	$\sigma = \xi_s v_r$

Table 3.1: Summary of the theoretical assumptions for the different elements of the model. Three scenarios are considered for CAF closure main dissipation: ring line viscosity η_1 , CAF tissue viscosity η_2 and ring line friction ζ .

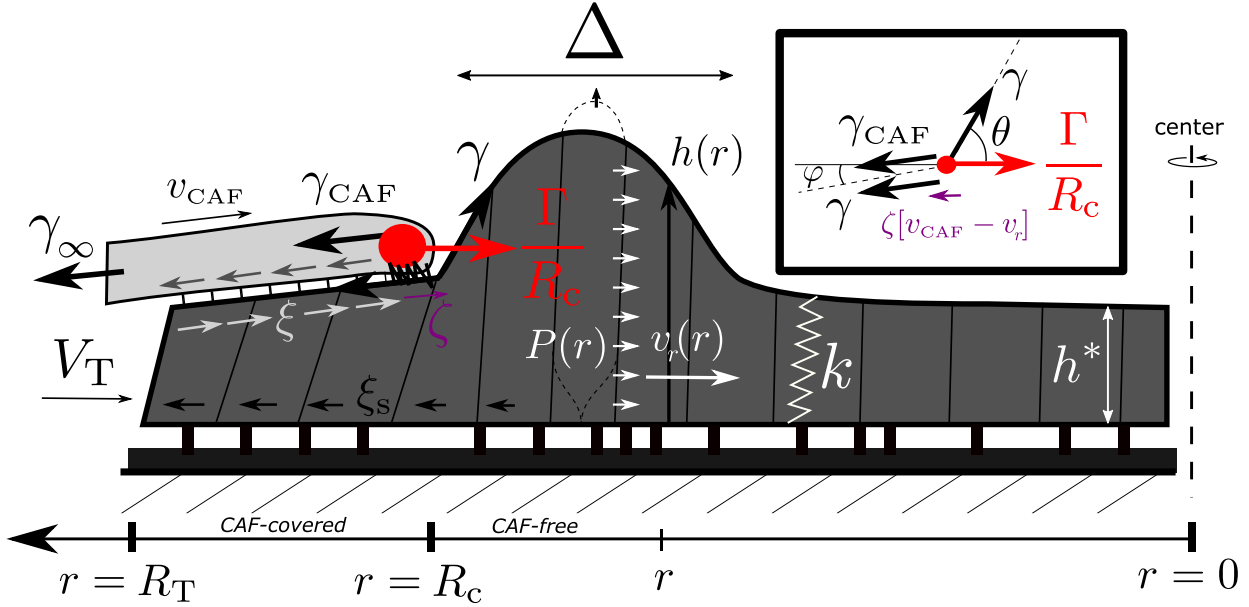


Figure 3.11: Sketch of the CC monolayer (dark gray) mechanically perturbed by the shear stress exchanged with CAFs, either localized over the covered surface with sliding friction coefficient ξ (gray arrows), or localized near the actomyosin ring (red) with line friction coefficient ζ at $r = R_c$ (purple arrow). This frictional CAF-CC mechanical interaction comes from the ring line tension Γ that drives CAF closure. It induces convergent CC displacement with radial velocity field $v_r(r)$ translated into out-of-plane deformation through height field $h(r)$, and builds tissue pressure $P(r)$ when shape deviates from its reference height h^* . The mechanical resistance to CC monolayer deformation is controlled by height stiffness k and surface tension γ . The system is rotationally invariant and cell divisions are neglected so that the CC cluster volume remains constant. One assumes CC cluster slippage over the substrate with sliding friction coefficient ξ_s (black arrows). The advancing CAFs have a tissue surface tension $\gamma_{CAF}(r)$ resisted by tension γ_∞ at the cluster periphery from the surrounding CAFs. This implies slope discontinuity at contact point $r = R_c$ by tension balance applied on a small element of actomyosin ring (box). One assumes the line friction tension to be distributed on the covered part ($r = R_c^+$). For small deformations, one has $\varphi \simeq |h'_{adh}|$ and $\theta \simeq |h'_{free}|$.

viscosity η_2 should be unspecific because initial CAF closure velocity is independent from experimental conditions. The surface friction between CAF and CC tissues builds a tension gradient on the advancing CAF monolayer, seen as a thin layer, such that the tissue tension $\gamma_{CAF}(r)$ is position-dependent.

As shown in the last part for no shear stress boundary conditions, the continuous equations for the local response mechanics of the side vertex model make a correspondence between lateral cell-cell tension and height stiffness k on one side, apical tension and surface tension γ on the other side. Because the equivalent elastic modulus associated to lateral tension E_{int} is expected to be of the order of $\sim 0.01 - 0.1$ kPa (see last part), whereas epithelial monolayers of MDCK cells or cancer cells have moduli $\sim 0.1 - 10$ kPa ([189] and review [253]), we choose to ignore the interfacial con-

tribution to height stiffness k_{int} and write $k_{\text{bulk}} \equiv k$.

As shown on Fig. 3.11, the CC cluster deformation driven by CAF-CC frictional shear is described in a model with three classes of parameters: geometrical, mechanical and dissipational.

- geometrical: reference thickness h^* , initial CC cluster radius R_0 ,
- mechanical: CC stiffness k , CC surface tension γ , CAF surrounding tension γ_∞ , actomyosin ring line tension Γ ,
- dissipative: CAF-CC friction coefficient ξ , CC-substrate friction coefficient ξ_s , ring line friction coefficient ζ , CAF tissue viscosity η_2 , and/or ring viscosity η_1 .

CAF closure makes the ring radius $R_c(t)$ change in time whereas CAF-CC friction drives the displacement of CC peripheral radius $R_T(t)$. The position-dependent CC cluster deformations are captured by height $h(r)$ and velocity $v(r)$ fields in addition to mechanical pressure $P(r)$, whereas friction builds non-uniform tension $\gamma_{\text{CAF}}(r)$ in the advancing CAF monolayer. Thus, the CAF-CC system evolves on two spatial domains: the CAF-free region ($r < R_c$) and the CAF-covered region ($R_T > r > R_c$).

3.3.1 CAF-free region

First on the free region ($r < R_c$) as defined by Fig. 3.11, we start from the stress-strain equations of a 3D incompressible material with isotropic elasticity¹⁰ under rotational invariance

$$\sigma_{rr} = -P + \frac{2E}{3}\partial_r u_r, \quad \sigma_{\theta\theta} = -P + \frac{2E}{3}\frac{u_r}{r}, \quad \sigma_{zz} = -P + \frac{2E}{3}\partial_z u_z, \quad \sigma_{rz} = \frac{E}{3}(\partial_z u_r + \partial_r u_z) \quad (3.7)$$

for radial displacement $u_r(r, z)$ and vertical displacement $u_z(r, z)$ constrained by local incompressibility $(1/r)\partial_r(ru_r) + \partial_z u_z = 0$. The free interface is parametrized with the height profile function h such that $z = h(r)$, also expressed as a perturbation around the reference monolayer thickness h^* with $h(r) \equiv h^* + \delta h(r)$. The system is closed by the boundary conditions

- $z = 0$: $u_z = 0$ and $\sigma_{rz} = \xi_s v_r$
- $z = h^*$: $\sigma_{tn} = 0$ and $\sigma_{nn} = -P_0 + \gamma h''[1 + h'^2]^{-3/2} + \gamma(h'/r)[1 + h'^2]^{-1/2}$

where t (n) represents the tangent (normal) direction at the free interface, such that the equation for σ_{nn} represents the Laplace pressure difference generated by interfacial curvature. Pressure is expanded around the reference value P_0 for a flat monolayer with $h = h^*$: $P = P_0 + \delta P$.

We perform a thin film expansion to get the approximate Stokes equations

$$h^* \partial_r \sigma_{rr} + \frac{h^*}{r} (\sigma_{rr} - \sigma_{\theta\theta}) \simeq \sigma_{rz}[z=0] - \sigma_{rz}[z=h^*], \quad \partial_z \sigma_{zz} \simeq 0 \quad (3.8)$$

with $\partial_z u_r \simeq 0$ at lowest order. Assuming a linear expansion ($h'^2 \ll 1$) that allows the approximation $\sigma_{tn} \simeq \sigma_{rz}$ and $\sigma_{nn} \simeq \sigma_{zz}$ at the free interface, one easily expresses the vertical displacement field and pressure field as a function of height perturbation field δh

$$u_z(r, z) \simeq \delta h(r) \frac{z}{h^*}, \quad \delta P(r) \simeq k \delta h(r) - \gamma \left[\delta h''(r) + \frac{\delta h'(r)}{r} \right] \quad (3.9)$$

with the introduction of the height stiffness $k \equiv 2E/(3h^*)$. Then, the radial Stokes equation becomes

$$-h^* [\delta P'(r) + k \delta h'(r)] \simeq \xi_s v_r(r) \quad (3.10)$$

¹⁰In principle, a tissue monolayer is expected to belong to the class of transversely isotropic materials. Elasticity is then characterized by five independent moduli $\{E_n, E_t, \nu_n, \nu_t, G_t\}$ for a compressible material, with $\nu_n \rightarrow 1/2$ and $\nu_t \rightarrow 1 - E_t/(2E_n)$ for an incompressible one. However, our derivation in the last part deals with a 2D side vertex model, for which the incompressible limit do not allow any distinction with a 2D isotropic material. Since our equations are inferred from this 2D side modelling and we don't want to introduce unnecessary free parameters, we limit ourselves to 3D isotropy, having in mind that the generalization can be made without technical difficulty.

with $v_r = \partial_t u_r$. Since pressure depends only on the height field (Eq. 3.9), a single Partial Differential Equation (PDE) can be obtained for the height perturbation field δh if one applies a time derivative on local incompressibility: $\partial_t \delta h + (h^*/r) \partial_r [r v_r] \simeq 0$. Using the diffusion coefficient $D_s \equiv k h^{*2} / \xi_s$ and mechanical length $\lambda \equiv \sqrt{\gamma/k}$, one finally gets the growth PDE on the CAF-free region by combination of Eq. 3.9 and Eq. 3.10

$$\partial_t \delta h \simeq D_s \frac{1}{r} \partial_r \left[2r \delta h' - \lambda^2 \left(r \delta h^{(3)} + \delta h'' - \frac{\delta h'}{r} \right) \right] \quad (3.11)$$

3.3.2 CAF-covered region with tissue viscosity

To account for the evolution of CC cluster height on the covered region, one assumes the advancing CAF monolayer to follow the free CC interface, allowing only relative displacement of the two tissues in the tangent direction \vec{t} , as in Fig. 3.11. As described in the previous chapter, we further assume 2D incompressibility for the CAF monolayer in the tangent plane, such that $v_{\text{CAF}}^t(r) \propto [r\sqrt{1+h'^2}]^{-1}$ with lagrange multiplier $\gamma_{\text{CAF}}(r)$. Despite the strict rheological incompatibility with the CAF tissue surrounding the cluster that considers 3D incompressibility for field localization, this assumption considerably simplifies the technical description on the covered region since the velocity field is already given. This is not expected to add any qualitative changes. Indeed, because the resistive effect associated to the surrounding tissue is sub-essential, we ignore the elastic contribution and consider only the CAF rest tension γ_∞ as shown on Fig. 3.11. Then, the mechanical coupling between CAFs and CCs is ensured by two effects:

1. The surface friction force between CAFs and CCs builds a tension gradient in the CAF monolayer: the CAF tension γ_{CAF} depends on space through the equation

$$\partial_s \gamma_{\text{CAF}}(s) = \xi [\vec{v}_{\text{CAF}}(s) - \vec{v}(s)] \cdot \vec{t}(s) \quad (3.12)$$

, where $s = r\sqrt{1+h'^2}$ is a curvilinear coordinate along the line defined by the CAF layer and \vec{t} its tangent vector. The normal velocity components of both CAFs and CCs should be equal by hypothesis at $z = h$: $[\vec{v}_{\text{CAF}}(s) - \vec{v}(s)] \cdot \vec{n}(s) = 0$.

2. the CAF tension γ_{CAF} adds up with CC surface tension γ to build pressure when the interface is curved, which leads to a spatially-dependent effective tension $\gamma_{\text{eff}}(s) \equiv \gamma + \gamma_{\text{CAF}}(s)$ on the cluster region covered by CAFs. More generally, the addition of tissue viscosity η_2 makes the CAF tension anisotropic, with $\gamma_{rr} = \gamma_{\text{CAF}} + 2\eta_2 \partial_r v_{\text{CAF}}(r)$ and $\gamma_{\theta\theta} = \gamma_{\text{CAF}} + 2\eta_2 v_{\text{CAF}}(r)/r$. It modifies the pressure term on the covered part according to the Laplace law generalization $\Delta \sigma_{zz} \simeq (\gamma + \gamma_{rr}) C_r + (\gamma + \gamma_{\theta\theta}) C_\theta$.

Under the thin film approximation, one can use $\vec{t} \simeq \vec{e}_r$ with $s \simeq r$ and $v_{\text{CAF}}(r) \simeq -V_c R_c / r$, following the notation of the previous chapter that calls the ring closure velocity $v_{\text{CAF}} \equiv -V_c$ at $r = R_c$. The tension gradient along the covered part simply becomes $\partial_r \gamma_{\text{CAF}} \simeq \xi [v_{\text{CAF}} - v_r]$.

Compared to the free region, the CC cluster mechanics differs on the stress boundary conditions at $z = h^*$: $\sigma_{tn} \simeq \sigma_{rz} = \xi [v_{\text{CAF}} - v_r]$ and $\sigma_{nn} \simeq \sigma_{zz} = -P_0 + (\gamma + \gamma_{rr}) \delta h'' + (\gamma + \gamma_{\theta\theta}) \delta h' / r$. Following an identical thin film expansion for the covered region, one gets

$$\delta P(r) \simeq k \delta h(r) - \{\gamma + \gamma_{\text{CAF}}(r)\} \left[\delta h''(r) + \frac{\delta h'(r)}{r} \right] - 2\eta_2 \frac{R_c V_c}{r^2} \left[\delta h''(r) - \frac{\delta h'(r)}{r} \right] \quad (3.13)$$

whereas the horizontal Stokes equation becomes

$$-h^* [\delta P'(r) + k \delta h'(r)] \simeq (\xi_s + \xi) v_r(r) - \xi v_{\text{CAF}}(r) \quad (3.14)$$

Since the CAF tension following $\partial_r \gamma_{\text{CAF}} \simeq \xi [v_{\text{CAF}} - v_r]$ contains velocity v_r that is itself related to the height perturbation field δh by horizontal stress balance (Eq. 3.14), the combination of Eq. 3.13

and Eq. 3.14 introduces non-linear order terms. Keeping only 1st order terms in δh , one gets the CAF tension on the covered part by integration

$$\begin{aligned} \gamma_{\text{CAF}}(r) = & \left\{ \gamma_{\infty} + \frac{\xi\xi_s}{\xi + \xi_s} R_c V_c \log\left(\frac{R_T}{r}\right) \right\} \left[1 - \frac{\xi h^*}{\xi + \xi_s} \left(\delta h'' + \frac{\delta h'}{r} \right) \right] \\ & + \frac{\xi h^*}{\xi + \xi_s} \left\{ 2k\delta h - \gamma \left(\delta h'' + \frac{\delta h'}{r} \right) - 2\eta_2 \frac{R_c V_c}{r^2} \left(\delta h'' - \frac{\delta h'}{r} \right) \right\} \end{aligned} \quad (3.15)$$

which translates from Eq. 3.14 into CC radial velocity

$$\begin{aligned} (\xi + \xi_s)v_r(r) \simeq & -\xi \frac{R_c V_c}{r} \left[1 - \frac{\xi_s}{\xi + \xi_s} \left(\delta h'' + \frac{\delta h'}{r} \right) \right] \\ & - 2kh^*\delta h' + h^* \left\{ \gamma + \gamma_{\infty} + \frac{\xi\xi_s}{\xi + \xi_s} R_c V_c \log\left(\frac{R_T}{r}\right) \right\} \left[\delta h^{(3)} + \frac{\delta h''}{r} - \frac{\delta h'}{r^2} \right] \\ & + 2\eta_2 h^* \frac{R_c V_c}{r^2} \left[\delta h^{(3)} - \frac{3\delta h''}{r} + \frac{3\delta h'}{r^2} \right] \end{aligned} \quad (3.16)$$

whereas pressure is reduced at 1st order to

$$\delta P(r) \simeq k\delta h(r) - \left\{ \gamma + \gamma_{\infty} + \frac{\xi\xi_s}{\xi + \xi_s} R_c V_c \log\left(\frac{R_T}{r}\right) \right\} \left[\delta h'' + \frac{\delta h'}{r} \right] - 2\eta_2 \frac{R_c V_c}{r^2} \left[\delta h'' - \frac{\delta h'}{r} \right] \quad (3.17)$$

The exact incompressibility equation reads (in eulerian representation)

$$\partial_t \delta h + \frac{h^*}{r} \partial_r [r v_r] + \frac{1}{r} \partial_r [r \delta h v_r] \simeq 0 \quad (3.18)$$

and allows an additional term compared to Eq. 3.11 because the velocity contains a 0th order term in δh from Eq. 3.14. All together, one gets the growth PDE for the CAF-covered part with effective tension length $\bar{\lambda}^2 \equiv (\gamma + \gamma_{\infty})/k$ and effective diffusion coefficient $D \equiv k(h^*)^2/(\xi + \xi_s)$

$$\begin{aligned} \frac{\partial_t \delta h}{D} \simeq & \frac{\delta h'}{r} \left\{ 2 - \frac{\bar{\lambda}^2}{r^2} + \frac{\xi R_c V_c}{k(h^*)^2} + \frac{\xi\xi_s R_c V_c}{(\xi + \xi_s)kr^2} \left[2 - \log\left(\frac{R_T}{r}\right) \right] + \frac{18\eta_2 R_c V_c}{k r^4} \right\} \\ & + \delta h'' \left\{ 2 + \frac{\bar{\lambda}^2}{r^2} - \frac{\xi\xi_s R_c V_c}{(\xi + \xi_s)kr^2} \left[2 - \log\left(\frac{R_T}{r}\right) \right] - \frac{18\eta_2 R_c V_c}{k r^4} \right\} \\ & - \frac{2\delta h^{(3)}}{r} \left\{ \bar{\lambda}^2 + \frac{\xi\xi_s R_c V_c}{(\xi + \xi_s)k} \left[1 + \log\left(\frac{R_T}{r}\right) \right] - \frac{4\eta_2 R_c V_c}{k r^2} \right\} \\ & - \delta h^{(4)} \left\{ \bar{\lambda}^2 + \frac{\xi\xi_s R_c V_c}{(\xi + \xi_s)k} \log\left(\frac{R_T}{r}\right) + \frac{2\eta_2 R_c V_c}{k r^2} \right\} \end{aligned} \quad (3.19)$$

Again, the growth PDE Eq. 3.19 converges to the equivalent one on the free region (Eq. 3.11) when $\xi, \gamma_{\infty}, \eta_2 \rightarrow 0$.

3.3.3 Boundary conditions

The evolution of the CC heigh profile is controlled by two PDEs over the CAF-covered and CAF-free regions, designated by "adh" and "free" indices respectively, with order 1 in time and 4 in space. The problem is technically complex because both domains evolve in time, either the CC peripheral radius $R_T(t)$ or the CAF ring radius $R_c(t)$, such that this system belongs to the class of boundary-value problems. For later convenience on the numerics, we express fields in eulerian configuration so that the CAF-free and CAF-covered domains are respectively defined as $r \in [0; R_c(t)]$ and $r \in [R_c(t); R_T(t)]$ for any time¹¹.

In total, one needs 8 spatial boundary conditions for the height field, the time initiation $h(r, t =$

¹¹In principle, one also needs $z \in [0; h(r)]$ for consistency but the system has already been reduced to a planar formulation, such that the lagrangian convention $z \in [0; h^*]$ used on the previous section remains valid for a linear expansion theory in the CC height perturbation field $\delta h(r) = h(r) - h^*$.

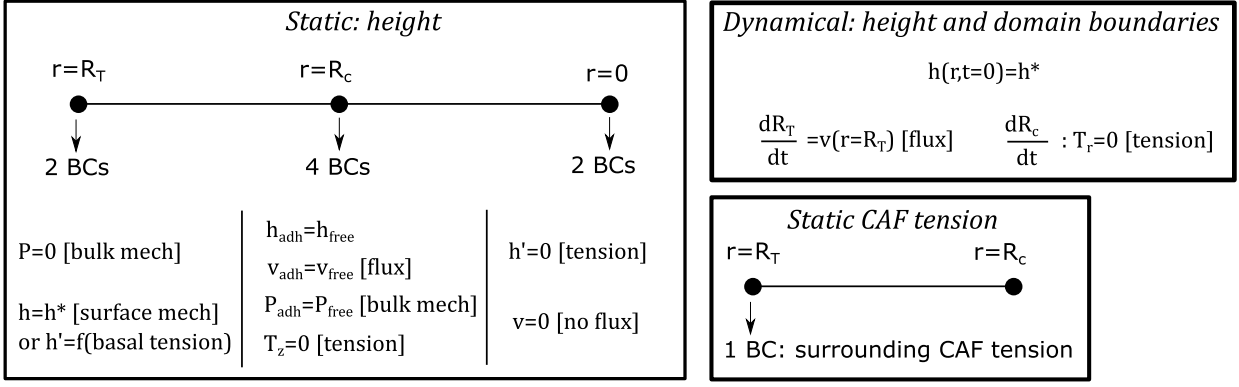


Figure 3.12: Sketch representing the Boundary Conditions (BCs) for the spatio-temporal resolution of the CC height profile, controlled by PDEs on the CAF-covered region ($R_T > r > R_c$) [adh] and CAF-free region ($r < R_c$) [free]. Here one assumes zero line friction and pressure is continuous at the ring position $r = R_c$. Those PDEs for the height field $h(r)$ are at 4th order in space and one needs 8 BCs for the two domains (left): they are either mechanical or geometrical. The PDEs are also at 1st order in time and one adds the initial height profile $h(r) = h^*$, whereas two additional BCs are needed for the domain dynamics $R_T(t)$ and $R_c(t)$ (right, top). Note that the tension balance at the CAF ring is split into a vertical component that enters as a static BC ($T_z = 0$), whereas the horizontal component ($T_r = 0$) enters into the CAF ring dynamics because velocity appears from line friction term and CAF tension term (dependent on surface friction). Finally, the CAF tension gradient requires a last BC which is the CAF tension from the surrounding tissue γ_{rr}^c at $r = R_T$.

$0) = h^*$, two dynamical equations for the temporal evolution of $R_c(t)$ and $R_T(t)$, and finally the value of the surrounding CAF tissue tension at $r = R_T$: this is summarized on Fig. 3.12 in the case of vanishing ring line friction ($\zeta = 0$). On the opposite, a non-zero line friction can be associated with a surface friction $\xi_r \equiv \zeta/w$ over the ring width w and builds a pressure jump

$$\Delta P \simeq \frac{\zeta}{h^*} V_c \quad (3.20)$$

in the limit $w \rightarrow 0$ with $\xi_r w = \zeta$ finite.

Using the notation $v_{\text{CAF}} \equiv -V_c$ at $r = R_c$ and ignoring possible 2nd order terms, the boundary conditions are

- at $r = R_T(t)$: $P_{\text{adh}} = 0$ in absence of peripheral CAF-CC interaction [mechanical balance], $v_{\text{adh}} = dR_T/dt$ [flux balance], and $h_{\text{adh}} = h^*$ that replaces tension balance at a contact line to not deal with the local shape heterogeneity and consider a uniform reference state [tension balance]¹²,
- at $r = R_c$, continuity of $h \equiv h_c$, pressure discontinuity¹³ $P_{\text{adh}} + \Delta P = P_{\text{free}}$ [mechanical balance], $J_{\text{adh}} = J_{\text{free}}$ [flux balance], the two components of tension balance at the ring $\gamma_{rr} + 2\eta_1 V_c/R_c^2 + \zeta(V_c + v_{\text{adh}}) \simeq \Gamma/R_c$ [tension balance (Or)] and $[\gamma_{rr} + \gamma + \zeta(V_c + v_{\text{adh}})]h'_{\text{adh}} \simeq \gamma h'_{\text{free}}$ [tension balance (Oz)],
- at $r = 0$, $h'_{\text{free}} = 0$ [tension] and $v_{\text{free}} = 0$ [flux balance].

The flux balance at the ring $J_{\text{adh}} = J_{\text{free}}$ is explicitly written

$$v_{\text{adh}}(R_c) - \frac{\xi V_c}{\xi + \xi_s} \left(\frac{h_c}{h^*} - 1 \right) = v_{\text{free}}(R_c) \quad (3.21)$$

¹²Strictly speaking, the mechanical balance should be $\sigma_{rr} = 0$ or $P = kh^* \partial_r u_r$. The other condition $h = h^*$ with local incompressibility implies $\partial_r u_r = -u_r/r$ at $r = R_T$. To not have to compute the displacement field u_r from the height field h obtained from growth PDEs, we transform $P = -kh^* u_r/r$ into $P = 0$.

¹³Strictly speaking, mechanical balance corresponds to the continuity of radial stress $\sigma_{rr} = -P + kh^* \partial_r u_r$, but 2D incompressibility gives $h^* \partial_r u_r = -h^* u_r/r - \delta h$. Since both u_r and δh are continuous at $r = R_c$, mechanical balance is indeed equivalent to pressure discontinuity.

The flux balance at $r = R_T$ and radial tension balance at $r = R_c$ give the dynamical equations for the evolution of boundaries, whereas the CAF tension $\gamma_{rr} = \gamma_{\text{CAF}} + 2\eta_2\partial_r v_{\text{CAF}}$ has a boundary tension $\gamma_{\text{CAF}} = \gamma_\infty$ at $r = R_T$ if one neglects CAF-substrate interactions on the surroundings ($\partial_r \gamma_{\text{CAF}} = 0$).

3.3.4 Numerical scheme for the boundary value problem

The spatio-temporal evolution of the CC monolayer height corresponds to a boundary value problem with growth PDEs Eq. 3.11 and Eq. 3.19 defined on the two evolving domains $0 < r < R_c(t)$ [CAF-free region] and $R_c(t) < r < R_T(t)$ [CAF-covered region]. We transform the linear PDEs Eq. 3.11 and Eq. 3.19 into finite difference equations using a central scheme at least order, and implement boundary conditions using the method of ghost points. An evolving spatial grid is defined with approximately constant width Δr_0 , such that the number of points changes with time according to $N_c(t) = E[(R_T - R_c)/\Delta r_0]$ on the CAF-covered region and $N_f(t) = E[R_c/\Delta r_0]$ on the CAF-free region¹⁴. The total number of spatial points is $N(t) = N_c(t) + N_f(t) + 1$. A constant number of points would be less convenient because the CAF-covered region is small at the beginning whereas the CAF-free region vanishes at the end, introducing artificial differences in terms of spatial resolution.

One is dealing with growth PDEs and explicit scheme (Euler) in time $\delta h_j^{(t+1)} - \delta h_j^{(t)} = \Delta t \cdot f([\delta h^{(t)}])$ is unable to start the evolution since $\delta h_j(t = 0) = 0$, where $j(t)$ is a spatial (temporal) index. Thus, one uses an implicit scheme in time such that

$$\delta h_j^{(t+1)} - \delta h_j^{(t)} = \Delta t \cdot [[A]] \cdot [\delta h^{(t+1)}] \quad (3.22)$$

where $[[A]]$ is a $N \times N$ matrix that contains the finite difference coefficients associated to each linear PDE. Since boundary conditions are also linearized with respect to δh , one can explicitly relate ghost points and real points¹⁵ and eliminate the former. The discrete set of height values at time t is interpolated to compensate for the spatial shift of the grid from t to $t + 1$ and define the partial derivative $\Delta t \partial_t h_j = \delta h_j^{(t+1)} - \delta h_j^{(t)}$ for any j .

The condition of CC cluster volume conservation appears numerically unstable when implemented in local flux balance conditions, a well-known issue for conservative equations [254] that is also sensitive to the evolving grid with $N(t)$. One needs to replace the local out-flux condition $v_{\text{adh}} = dR_T/dt$ by a global constraint on volume conservation, with shooting method on the external boundary $R_T(t + \Delta t)$ to select the updated value that minimizes $|1 - V(t + \Delta t)/V_0|$, whereas the internal boundary R_c is explicitly updated as $R_c(t + \Delta t) = R_c(t) - V_c(t)\Delta t$.

3.3.5 CAF closure limit

Independently from the dynamical conditions associated to CAF closure, the deformation should reach a maximum inducing an outward flux driven by the high level of pressure in center compared to periphery. However, the numerical results are constrained by a finite grid on the CAF-free region when $R_c \rightarrow 0$ and a pseudo-divergence is often observed because the reflux is too localized temporally (see next part). Thus, it is instructive to apply a polynomial expansion for the free shape to investigate the deformation limit when $R_c \rightarrow 0$.

When the CAF leading edge has a sufficiently small radius R_c , one can approximate the shape on the free region as $h_{\text{free}}(r) \simeq h_0 - Cr^2/2$, with $h_c = h_0 - CR_c^2/2$ and $h'_{\text{free}}(R_c) = -CR_c$. For a negative slope (positive deformation), $C > 0$ which implies an outward velocity field $v_{\text{free}}(r) = Cr/s$. The volume in the free region reads $V_{\text{free}} = \pi R_c^2(h_0 - CR_c^2/4)$. The pressure field is $P_{\text{free}}(r) =$

¹⁴The function $E[.]$ takes the integer part of the argument.

¹⁵For example, the spatial derivative $\delta h'(r)$ vanishes at $r = 0$, with definition $2\delta h'(0) \mapsto (\delta h_1 - \delta h_{-1})/\Delta r_0$ at $j = 0$. This corresponds to the finite difference equation $\delta h_1 = \delta h_{-1}$ relating the ghost point $j = -1$ to the real point $j = 1$.

$$h_0 - 1 + 2\gamma C - Cr^2/2.$$

BCs of zero velocity and zero slope should be ensured at center when $R_c \rightarrow 0$: to preserve field continuity, one asks for $v_{\text{free}}(R_c) \rightarrow 0$ and $h'_{\text{free}}(R_c) \rightarrow 0$, equivalent to the non-trivial limit $CR_c \rightarrow 0$. Consequently, $CR_c^2 \rightarrow 0$ which implies $h_c \rightarrow h_0$, $P_c \rightarrow h_0 - 1 + 2\gamma C$, and $V_{\text{free}} \rightarrow \pi R_c^2 h_0$.

If the limit $R_c \rightarrow 0$ was associated to a divergence of central height ($h_0 \rightarrow \infty$), volume conservation would require the cluster periphery to reach the center ($R_T \rightarrow 0$) such that the shape on the CAF-covered part can be expressed as a polynomial expansion $h_{\text{adh}}(r) \simeq a(r - R_T) + b(r - R_T)^2/2$. For dissipation dominated by ring viscosity η_1 ($V_c \propto R_c$), continuity of pressure and height as well as tension discontinuity lead to $h'_{\text{adh}}(R_c) \propto CR_c$, $h''_{\text{adh}}(R_c) \propto C$ and $\delta h_c \propto C$. A higher expansion order shows that flux balance at $r = R_c$ is only compatible with $C \rightarrow 0$ to ensure $v_{\text{free}}(R_c) \rightarrow 0$, and volume conservation forces $R_T \rightarrow R_0$.

For dissipation dominated by tissue viscosity η_2 ($V_c \propto 1$), one gets $h'_{\text{adh}}(R_c) \propto C(R_c)^2$, $h''_{\text{adh}}(R_c) \propto CR_c$ and $\delta h_c \propto CR_c$. This comes for viscous term in the CAF stress $2\eta_2 V_c/R_c$ that dominates in the limit $R_c \rightarrow 0$. Because $CR_c \rightarrow 0$, one directly finds $\delta h(r) \rightarrow 0$ and $R_T \rightarrow R_0$ by incompressibility.

For dissipation dominated by line friction ζ , or tissue viscosity η_2 and line tension feed-back ($V_c \propto 1/R_c$), boundary conditions lead to $h'_{\text{adh}}(R_c) \propto C(R_c)^3$, $h''_{\text{adh}}(R_c) \propto C(R_c)^2$ and $\delta h_c \propto C(R_c)^2$. Again, the deformation is released and CAF closure occurs on a flat CC monolayer.

Note that the polynomial shape expansion on the CAF-covered part is strictly valid only when $R_T \rightarrow 0$: the above derivation is able to exclude this case but a finite deformation may be allowed at CAF closure. If some deformation could remain at $R_c = 0$ and in absence of static friction source, the pressure gradient would be released after CAF closure, in a transition not captured by the model because no explicit mechanism describes the finite relaxation of tension Γ/R_c when $R_c \rightarrow 0$.

3.4 Model: vertex framework for CC monolayer deformation

To justify a posteriori the mechanical equations introduced in the previous chapter, we consider an extension of the 2D vertex model from chapter 2 to compare the equivalent continuous equations that emerge. This is performed through the establishment of cortical gradients that balance the frictional shear stress, exerted either by the substrate on the basal interface or by CAFs on the apical interface (see Fig. 3.13). We make the important assumption that both apical and basal tensions are controlled by homeostatic processes, and claim that their average value over the cell interface can be fixed according to the unperturbed state. Therefore, the application of frictional shear stress makes tension differences between adjacent cells that modify apical and vertex force balances, as shown on Fig. 3.13.

In this discrete formalism, quantities associated to vertices are denoted by lower case (i) whereas quantities associated to cells use a capital letter (I).

3.4.1 Basal tension gradient

Calling $v_i \equiv \dot{x}_i$ the material velocity of the basal vertex indexed by i , linear interpolation gives a basal velocity along cell $I \equiv (i, i + 1)$

$$V_{\text{CC}}^{\text{b}}(x) = v_i + \frac{v_{i+1} - v_i}{x_{i+1} - x_i} (x - x_i) \quad (3.23)$$

The substrate friction builds a cortical gradient $\partial_x \gamma_{\text{CC}}^{\text{b}}(x) \simeq \xi_{\text{s}} V_{\text{CC}}^{\text{b}}(x)$ that makes basal tension spatially quadratic. With the homeostatic constraint

$$\langle \gamma_{\text{CC}}^{\text{b}} \rangle = \frac{1}{x_{i+1} - x_i} \int_{x_i}^{x_{i+1}} dx \gamma_{\text{CC}}^{\text{b}}(x), \quad (3.24)$$

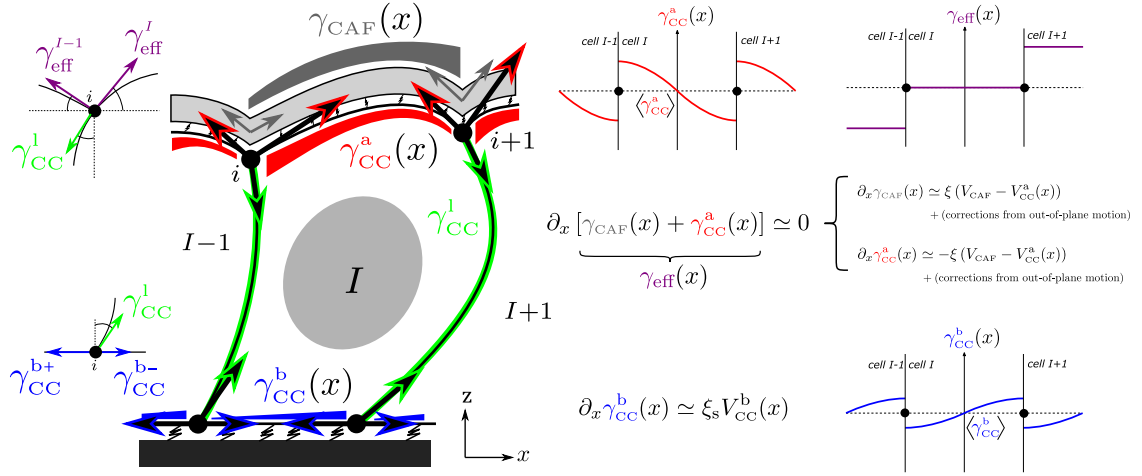


Figure 3.13: Extension of the 2D vertex model in the presence of frictional shear stress applied on apical and basal interfaces. CAFs are slowed by a stress $\xi(V_{CAF} - V_{CC}^a)$, approximately equal to $\partial_x \gamma_{CAF}(x)$ for a flat monolayer. By Newton third law, this stress builds an apical tension gradient such that the effective tension $\gamma_{eff} \equiv \gamma_{CAF} + \gamma_{CC}^a$ remains constant along a cell interface. However, continuity of CAF tension and apical tension homeostasis forces a tension difference for apical vertex force balance. The same description is used for the basal interface where translocation at velocity V_{CC}^b build a frictional shear stress $\xi_s V_{CC}^b$ with the substrate, forcing a tension difference for basal vertex force balance.

one can easily compute the basal tension difference at position i

$$\Delta_i^b \equiv \gamma_{CC}^b(I-1, i) - \gamma_{CC}^b(I, i) = \frac{\xi_s}{6} [(2v_i + v_{i-1})(x_i - x_{i-1}) + (2v_i + v_{i+1})(x_{i+1} - x_i)] \quad (3.25)$$

For a uniform cell translocation speed V without deformation ($x_i = x_{i-1} + l^* \quad \forall i$), this reduces to $\Delta^b = \xi_s l^* V$.

3.4.2 Apical tension gradient

Contrarily to the basal case where the interface remains flat, the apical region can undergo out-of-plane deformations with $h_i \neq h_{i+1}$. Calling $u_i \equiv \dot{X}_i$ and $w_i \equiv \dot{h}_i$ the horizontal and vertical apical vertex velocities, linear interpolation provides the cellular velocities at $I \equiv (i, i+1)$

$$V_{CC}^a(x) = u_i + \frac{u_{i+1} - u_i}{X_{i+1} - X_i} (x - X_i), \quad W_{CC}^a(x) = w_i + \frac{w_{i+1} - w_i}{X_{i+1} - X_i} (x - X_i) \quad (3.26)$$

To simplify the description, we consider the cortical gradients along the lines joining the vertices without next order contributions associated to the apical curvature, calling φ_I the horizontal tilt angle between points (X_i, h_i) and (X_{i+1}, h_{i+1}) . With curvilinear abscissa s (related to x coordinate by $\cos \varphi_I ds = dx$), one gets the apical tension force balance along the tangent direction $\vec{t}_I = (\cos \varphi_I, \sin \varphi_I)$:

$$\cos \varphi_I \partial_x \gamma_{CC}^a(x) = -\xi \left[V_{CAF}^{\parallel} - V_{CC}^a(x) \cos \varphi_I - W_{CC}^a(x) \sin \varphi_I \right] \quad (3.27)$$

Note that line incompressibility for this 2D side system on CAFs requires $\partial_s V_{CAF}^{\parallel}(s) = 0$, where V_{CAF}^{\parallel} is the CAF velocity along \vec{t}_I . Again, the homeostatic constraint on average apical tension can be used to compute the apical tension difference $\Delta_i^a \equiv \gamma_{CC}^a(I, i) - \gamma_{CC}^a(I-1, i)$ at position i

$$\Delta_i^a = \xi V_{CAF}^{\parallel} \left(\frac{X_i - X_{i-1}}{2 \cos \varphi_{I-1}} + \frac{X_{i+1} - X_i}{2 \cos \varphi_I} \right) - \frac{\xi}{6} [2u_i + u_{i-1} + (2w_i + w_{i-1}) \tan \varphi_{I-1}] (X_i - X_{i-1}) \\ - \frac{\xi}{6} [2u_i + u_{i+1} + (2w_i + w_{i+1}) \tan \varphi_I] (X_{i+1} - X_i) \quad (3.28)$$

For a uniform cell translocation speed V without deformation ($x_i = x_{i-1} + l^*$ and $h_i = h^* \quad \forall i$), this reduces to $\Delta^a = \xi l^*(V_{\text{CAF}} - V)$. The CAF tension and CC apical tension add up into an effective tension γ_{eff}^I that remains spatially independent on cell domain I whereas $\gamma_{\text{eff}}^I \neq \gamma_{\text{eff}}^{I+1}$ (see Fig. 3.13). One gets

$$\gamma_{\text{eff}}^I = \langle \gamma_{\text{CC}}^a \rangle + \gamma_{\text{CAF}}(X_i) + \frac{\xi}{6}(X_{i+1} - X_i) \left[\frac{3V_{\text{CAF}}^{\prime\prime}}{\cos \varphi_I} - (2u_i + u_{i+1}) - (2w_i + w_{i+1}) \tan \varphi_I \right] \quad (3.29)$$

with CAF tension on domain $x \in [X_i; X_{i+1}]$

$$\begin{aligned} \gamma_{\text{CAF}}(x) = \gamma_{\text{CAF}}(X_i) + \xi(x - X_i) \left[\frac{V_{\text{CAF}}^{\prime\prime}}{\cos \varphi_I} - u_i - w_i \tan \varphi_I \right] \\ - \frac{\xi}{2} \frac{(x - X_i)^2}{X_{i+1} - X_i} [u_{i+1} - u_i - (w_{i+1} - w_i) \tan \varphi_I] \end{aligned} \quad (3.30)$$

The hypothesis of homeostatic tension along CC interfaces appears justified by the very short relaxation of cortical processes (~ 1 min) compared to the experimental time (~ 10 h) for CAF closure and CC cluster deformations.

In fact, if apical and basal tensions were continuous at vertices, γ_{eff} would be uniform with apical tension decrease and basal tension increase towards center on the covered part. A large CAF covering could generate negative apical tensions near the ring position for relatively small CAF-CC friction ξ , and strong tension discontinuities compared to the free region. Moreover, the tension balance on apical vertices with constant γ_{eff} is hardly compatible with an increase of pressure and height towards center in terms of geometry, because the tilt of the tension axis would favour a decrease of height for an increase of pressure.

Therefore, the chosen hypothesis of homeostatic tensions seems reasonable, contrarily to the tension continuity hypothesis.

3.4.3 Linear perturbation of the vertex model

Formally speaking, the tension differences computed in the previous section can be coupled to vertex and interfacial force balance equations, to solve for the dynamics of the cell monolayer and CAF edge advance (given an initial state). However practically speaking, those non-linear coupled equations involving variables and their time derivative require heavy numerical algorithms and fail to take into account the third dimension of the CC cluster in the transverse direction. Therefore, we only consider a linear perturbation theory similar to the static case of chapter 2. We ignore the inessential complexity present when CAFs initiate their closure dynamics at the periphery of the CC cluster, and only describe system states for which the region covered by CAFs extends over a large number of CCs. Finally, a choice has to be made regarding the zero-th order state of the linear perturbation model. Since we chose to consider sufficiently long times to ignore the effects at CC periphery and let CAFs develop a large covering region, the free equilibrium state of the CC monolayer as defined in chapter 2 only applies to free region (see Fig. 3.14a). On the covered region, one needs to consider a state for which both CAFs and CCs are at rest but a static CAF tension applies an additional pressure on cell cytoplasm¹⁶. In this unperturbed state, since the CC monolayer contains two regions with different apical tensions, it is easy to realize that local height and pressure variations near the contact interface must exist to compensate for the deviation from a uniform equilibrium (with vertical lateral interfaces, uniform height and pressure), as shown on Fig. 3.14a. As a consequence, we choose to only study the response mechanics far from this contact interface to not cumulate technical complexity from zero-th and first order, which requires a large number of cells on both regions. Then, the uniform tissue state is taken as the unperturbed state, with pure apical tension in the region free of CAFs, and effective tension comprising the CAF tension in the covered region (Fig. 3.14a).

¹⁶Here, the effective tension $\gamma_{\text{eff}} \equiv \gamma_{\text{CAF}} + \gamma_{\text{CC}}^a$ that builds a Laplace pressure $\gamma_{\text{eff}} C_a$ would remain spatially independent in the absence of frictional shear stress, contrarily to the previous section (see Fig. 3.13).

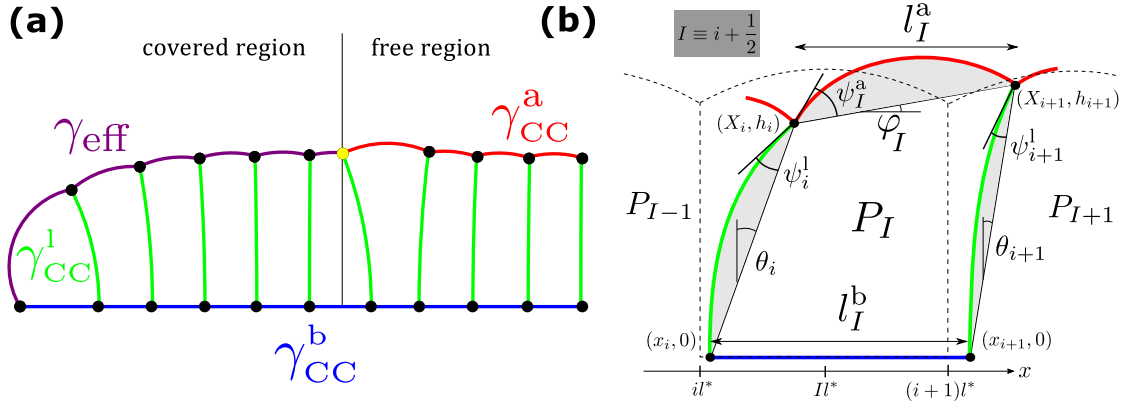


Figure 3.14: **(a)**: Static vertex equilibrium in absence of apical or basal shear stress ($\xi = \xi_s = 0$), with an apical tension $\bar{\alpha} \equiv \gamma_{\text{eff}}/\gamma_{\text{CC}}^1 = 2$ on the covered region (purple) and $\alpha \equiv \gamma_{\text{CC}}^a/\gamma_{\text{CC}}^1 = 1.8$ on the free region (red). Pressure deviation from uniform values exists near the contact point (yellow) separating the two regions, with fast relaxation towards uniformity. There are $N = 10$ cells with $\beta = 1$. **(b)**: Sketch of a perturbed cell with respect to a uniform state.

In addition to cell variables already encountered for the static case¹⁷ (chapter ? and Fig. 3.14b), one needs to expand $v_i = 0 + \delta v_i$, $u_i = 0 + \delta u_i$ with $\delta u_i = \delta v_i + h^* \frac{d}{dt} \delta \theta_i$, $V_{\text{CAF}}^{\prime\prime} = 0 + \delta V_{\text{CAF}}^{\prime\prime}$, and $\gamma_{\text{eff}} = \bar{\gamma} + \delta \gamma_{\text{eff}}$ where $\bar{\gamma} \equiv (\gamma_{\text{CAF}} + \gamma_{\text{CC}}^a)_0$. Since velocities always appear in connexion with friction coefficients, one way to ensure the validity of this linear expansion is to assume a weak frictional coupling on both interfaces.

3.4.4 Cluster region free of CAFs

One starts with the CC cluster region free of CAFs as indicated on Fig. 3.14a that shows the static case. Now, external shear stress is introduced through substrate friction generating a basal tension gradient whereas apical tension remains uniform on this region. The basal tension difference becomes at first order $\gamma_{\text{CC}}^b(I-1, i) - \gamma_{\text{CC}}^b(I, i) = \xi_s l^* (\delta v_{i+1} + 4\delta v_i + \delta v_{i-1})/6$. Here the subscript CC is superfluous and will be ignored for this section. The uniform cell equilibrium introduced in chapter 2 defines a cell height h^* , a cell width l^* and an apical angle ψ^* associated to the bumped apical interface. At linear order, the three vertex force balance equations and the two pressure equations give:

$$\left\{ \begin{array}{l} 6\gamma_l(\delta\theta_i - \delta\psi_i^l) = \xi_s l^* (\delta v_{i+1} + 4\delta v_i + \delta v_{i-1}) \quad [\text{basal vertex}] \\ \delta\psi_{I-1}^a - \delta\psi_I^a - \delta\varphi_{I-1} - \delta\varphi_I = 2(\delta\theta_i + \delta\psi_i^l) \quad [\text{apical vertex Ox}] \\ \delta\psi_I^a + \delta\psi_{I-1}^a + \delta\varphi_I - \delta\varphi_{I-1} = 0 \quad [\text{apical vertex Oz}] \\ (l^*)^2 \delta P_I = -\gamma_l(\delta l_I^a - l^* \cot \psi^* \delta\psi_I^a) \quad [\text{apical interface}] \\ h^*(\delta P_I - \delta P_{I-1}) = 2\gamma_l \delta\psi_i^l \quad [\text{lateral interface}] \end{array} \right. \quad (3.31)$$

whereas the area incompressibility closes the system of equations

$$\left[\frac{2A_0}{l^*} - h^* \right] \delta l_I^a + \frac{l^*}{2} (\delta h_i + \delta h_{i+1}) + (l^*)^2 \frac{1 - \psi^* \cot \psi^*}{2(\sin \psi^*)^2} \delta\psi_I^a - \frac{(h^*)^2}{2} (\delta\theta_{i+1} - \delta\theta_i) - \frac{(h^*)^2}{6} (\delta\psi_{i+1}^l - \delta\psi_i^l) = 0, \quad (3.32)$$

where the term in brackets is called $\tilde{h} \equiv -h^* + 2A_0/l^*$ for later convenience. Because geometry imposes $\delta\varphi_I = (\delta h_{i+1} - \delta h_i)/l^*$, one has six equations for the seven variables $\{h, \theta, P, \psi^l, \psi^a, l^a, v\}$. The last equation used to close the system comes from the evolution of basal size l^b : $\frac{d}{dt} l^b = \delta v_{i+1} - \delta v_i$. Thus, using $\delta l_I^b = \delta l_I^a - h^*(\delta\theta_{i+1} - \delta\theta_i)$, an independent equation mixing both spatial

¹⁷For a uniform equilibrium state with height h^* , width l^* , cell pressure P^* and apical angle ψ^* , one has $h_i = h^* + \delta h_i$, $\theta_i = 0 + \delta\theta_i$, $P_I = P^* + \delta P_I$, $\psi_i^a = \psi^* + \delta\psi_i^a$, $x_{i+1} - x_i = l^* + \delta l_I^b$, $X_{i+1} - X_i = l^* + \delta l_I^a$ with $\delta l_I^a = \delta l_I^b + h^*(\delta\theta_{i+1} - \theta_i)$, $\psi_i^l = 0 + \delta\psi_i^l$ and $\varphi_I = 0 + \delta\varphi_I$ with $\delta\varphi_I = (\delta h_{i+1} - \delta h_i)/l^*$.

and temporal variations of one variable can be found in principle. This differs from the static case (chapter 2), where an independent equation could be obtained for each variable with only spatial variations. Here for this dynamical problem, one can also get equations involving purely spatial variations but they can be simplified up to two variable-coupled equations.

The two apical vertex equations in Eq. 3.31 can be independently manipulated to get:

$$\delta\psi_I^a = \frac{1}{2} \left(\delta\psi_{i+1}^l - \delta\psi_i^l + \delta\theta_{i+1} - \delta\theta_i \right), \quad \delta\varphi_I = -\frac{1}{2} \left(\delta\psi_{i+1}^l + \delta\psi_i^l + \delta\theta_{i+1} + \delta\theta_i \right) \quad (3.33)$$

Those equations are centred at I and it will be more convenient to use a mid-point average $\cdot_I \rightarrow (\cdot_I + \cdot_{I-1})/2$ translating δP , $\delta\psi^a$ and δl_I^a from the cell grid at I to the vertex grid such that all expressions will be centred at i . Indeed, since $\delta\varphi_{I-1} + \delta\varphi_I = (\delta h_{i+1} - \delta h_{i-1})/l^*$ and $\delta\varphi_I - \delta\varphi_{I-1} = (\delta h_{i+1} - 2\delta h_i + \delta h_{i-1})/l^*$, one can obtain two independent equations coupling δh , $\delta\theta$ and δv at point i .

The system Eq. 3.31 and area incompressibility can be further manipulated to isolate important couples of variables. For the couple $\{h, \theta\}$, one gets the equation:

$$\frac{(h^*)^2}{\tilde{h}(l^*)^2} \left[\alpha \cos \psi^* - \frac{h^*}{6l^*} \right] \delta h_i^{(4)} - \frac{1}{l^*} \left[2 + \frac{h^*}{\tilde{h}} \right] \delta h_i^{(2)} = 2\delta\theta_i^{(1)} - \frac{(h^*)^3}{3\tilde{h}(l^*)^2} \delta\theta_i^{(3)} \quad (3.34)$$

where $\alpha \equiv \gamma_a/\gamma_l$ as before and the notation $\cdot_i^{(\cdot)}$ stands for finite difference with central scheme at least accuracy¹⁸. Calling the average lateral pressure $\delta P_i \equiv (\delta P_I + \delta P_{I-1})/2$, one can also obtain an equation for the couple $\{P, h\}$

$$\frac{(h^*)^3}{6\tilde{h}(l^*)^2} \delta P_i^{(2)} - \delta P_i = \frac{\gamma_l h^*}{\tilde{h}(l^*)^2} \left[\alpha \cos \psi^* - \frac{h^*}{2l^*} \right] \delta h_i^{(2)} - \frac{\gamma_l}{\tilde{h}l^*} \delta h_i \quad (3.35)$$

and the couple $\{\theta, v\}$

$$\frac{(h^*)^2}{\tilde{h}l^*} \left[\alpha \cos \psi^* - \frac{h^*}{3l^*} \right] \delta\theta_i^{(2)} - \left[1 + \frac{h^*}{\tilde{h}} \right] \delta\theta_i = \frac{\xi_s (h^*)^2}{12\gamma_l \tilde{h}} \left[\alpha \cos \psi^* - \frac{h^*}{6l^*} \right] \delta v_i^{(4)} - \frac{\xi_s l^*}{6\gamma_l} \left(\delta v_i^{(2)} + 6\delta v_i \right) \quad (3.36)$$

which has a slightly more complicated expression due to the dispersion of substrate friction to neighbouring points $i-1$ and $i+1$ for basal vertex force balance at i Eq. 3.31. Similarly, the couple $\{P, v\}$ leads to:

$$\begin{aligned} & -\frac{(h^*)^2}{\tilde{h}l^*} \left[\alpha \cos \psi^* - \frac{h^*}{3l^*} \right] \delta P_i^{(4)} + \left[1 + \frac{h^*}{\tilde{h}} \right] \delta P_i^{(2)} \\ & = \frac{\xi_s h^*}{6\tilde{h}} \left[\alpha \cos \psi^* - \frac{h^*}{2l^*} \right] \delta v_i^{(5)} + \frac{\xi_s h^*}{\tilde{h}} \left[\alpha \cos \psi^* - \frac{h^*}{2l^*} - \frac{l^*}{6h^*} \right] \delta v_i^{(3)} - \frac{\xi_s l^*}{\tilde{h}} \delta v_i^{(1)} \end{aligned} \quad (3.37)$$

Finally, the use of the dynamical constraint $\frac{d}{dt} \delta l_I^a = \delta v_{i+1} - \delta v_i + h^* \frac{d}{dt} (\delta\theta_{i+1} - \delta\theta_i)$ can be used to express the spatio-temporal evolution of one variable, for example the height variation δh . However, the equation Eq. 3.34 cannot be explicitly inverted to express $\delta\theta$ as a function of δh , and one remains with the couple $\{h, \theta\}$:

$$\frac{d}{dt} \left\{ \delta h_i + \left[\frac{A_0 - h^* l^*}{(l^*)^2} \cot \psi^* + \frac{(h^*)^2}{6(l^*)^2} \right] \delta h_i^{(2)} - \frac{(h^*)^2}{3l^*} \left[1 - \frac{3\tilde{h}}{h^*} \right] \delta\theta_i^{(1)} \right\} = -\frac{\gamma_l \tilde{h}}{\xi_s (l^*)^3} \left(\delta h_i^{(2)} + 2l^* \delta\theta_i^{(1)} \right) \quad (3.38)$$

In the same spirit, it is not possible to express δP as a function of δh only but one can write

$$\delta P_i = \frac{\gamma_l}{\tilde{h}l^*} \delta h_i - \frac{\gamma_l h^*}{\tilde{h}(l^*)^2} \left[\alpha \cos \psi^* - \frac{h^*}{6l^*} \right] \delta h_i^{(2)} - \frac{\gamma_l (h^*)^2}{3\tilde{h}(l^*)^2} \delta\theta_i^{(1)} \quad (3.39)$$

¹⁸For instance, $\cdot_i^{(1)} \equiv (\cdot_{i+1} - \cdot_{i-1})/2$, $\cdot_i^{(2)} \equiv \cdot_{i+1} - 2\cdot_i + \cdot_{i-1}$, $\cdot_i^{(3)} \equiv (\cdot_{i+2} - 2\cdot_{i+1} + 2\cdot_{i-1} - \cdot_{i-2})/2$, $\cdot_i^{(4)} \equiv \cdot_{i+2} - 4\cdot_{i+1} + 6\cdot_i - 4\cdot_{i-1} + \cdot_{i-2}$ and $\cdot_i^{(5)} \equiv (\cdot_{i+3} - 4\cdot_{i+2} + 5\cdot_{i+1} - 5\cdot_{i-1} + 4\cdot_{i-2} - \cdot_{i-3})/2$.

3.4.5 Continuous limit in the free region

The continuous limit becomes valid when the relaxation length scales for fields are much higher than the discrete length step l^* , which corresponds to the unperturbed cell width. When looking at Eq. 3.34, with similar procedure applied to Eq. 3.35, Eq. 3.36 and Eq. 3.37, one gets two parametric (adimensional) scales by separately comparing h and θ terms:

$$\Lambda_h \equiv \frac{(h^*)^2}{l^*(2\tilde{h} + h^*)} \left[\alpha \cos \psi^* - \frac{h^*}{6l^*} \right], \quad \Lambda_\theta \equiv \frac{(h^*)^3}{6\tilde{h}(l^*)^2} \quad (3.40)$$

Both factors depend only on model parameters α and β through the uniform equilibrium state. Calling the field relaxation scales L_h and L_θ , much higher than l^* by hypothesis, one has a scaling $\delta h^{(2)} \sim \delta h(l^*/L_h)^2$ and $\delta h^{(4)} \sim \delta h(l^*/L_h)^4$. The term-by-term comparison gives at the scaling level

$$\Lambda_h \delta h^{(4)} - \delta h^{(2)} \sim \delta h \left(\frac{l^*}{L_h} \right)^2 \left[\Lambda_h \left(\frac{l^*}{L_h} \right)^2 - 1 \right], \quad \Lambda_\theta \delta \theta^{(3)} - \delta \theta^{(1)} \sim \delta \theta \frac{l^*}{L_\theta} \left[\Lambda_\theta \left(\frac{l^*}{L_\theta} \right)^2 - 1 \right] \quad (3.41)$$

If the adimensional scale Λ is of order 1 (dimensionally of order l^*), the higher derivatives can be neglected as long as $L \gg l^*$, but may be kept if $\Lambda \gg 1$.

In the static case (chapter 2), it was possible to have independent equations with purely spatial variations for each variable, and one had $L_{\text{static}} = l^* \Lambda_{\text{static}}$. Then, there was an equivalence between the continuous limit $L \gg l^*$ and the parametric condition $\Lambda_{\text{static}} \gg 1$. It was shown to be valid only if $\alpha \gg 1$, with $\Lambda_{\text{static}} \sim \alpha^2$ for $\beta = \alpha + o(1)$ or $\beta = o(1)$ and $\Lambda_{\text{static}} \sim \alpha$ when $\beta = -\alpha + o(1)$. Here on the dynamical case, one has to distinguish the field relaxation scale L and the parametric scale $l^* \Lambda$. Since an independent equation involves temporal and spatial derivatives, it is likely that L is time-dependent. When one assumes $\alpha \gg 1$ and $\beta = \alpha + o(1)$ or $\beta = o(1)$, it is easy to see that both Λ_h and Λ_θ scale like α^2 , whereas $\beta = -\alpha + o(1)$ leads to $\Lambda_h \sim \alpha$ and $\Lambda_\theta = o(1)$. Indeed, the later limit allows to neglect $\delta \theta^{(3)}$ compared to $\delta \theta^{(1)}$ because $\Lambda_\theta = o(1)$ whereas one needs $L_\theta \gg l^*$ by hypothesis.

Thus, only the parametric limit $\alpha \gg 1$ and $\beta = -\alpha + o(1)$ allows to make a simplification without extra assumption on L_h or L_θ . Note that this parametric corresponds to a finite cell aspect ratio $h^*/l^* = o(1)$, contrarily to cases $\beta = \alpha + o(1)$ or $\beta = o(1)$ that are associated to thin and elongated cells when $\alpha \gg 1$ ($h^*/l^* \propto \alpha$).

We then place ourselves in the parametric conditions $\alpha \gg 1$ and $\beta = -\alpha + o(1)$ and neglect the term $\delta \theta^{(3)}$ in Eq. 3.34 and obtain an explicit function for $\delta \theta$ of δh :

$$\delta \theta_i^{(1)} \simeq \frac{h^*}{2(l^*)^2} \alpha \delta h_i^{(4)} - \frac{3}{2l^*} \delta h_i^{(2)} \quad (3.42)$$

The limit $\alpha \gg 1$ implies $\psi^* \ll 1$, $\tilde{h} \simeq h^* \simeq A_0/l^*$ and greatly simplify the parametric coefficients. Importantly, the incompressibility equation (Eq. 3.38) can now be translated into an independent one for the spatio-temporal evolution of δh :

$$\frac{d}{dt} \left\{ \delta h_i + \frac{1}{6} \left[1 - 5 \left(\frac{h^*}{l^*} \right)^2 \right] \delta h_i^{(2)} + \frac{1}{3} \left(\frac{h^*}{l^*} \right)^3 \alpha \delta h_i^{(4)} \right\} \simeq \frac{2\gamma_l h^*}{\xi_s (l^*)^3} \left(\delta h_i^{(2)} - \frac{h^*}{2l^*} \alpha \delta h_i^{(4)} \right) \quad (3.43)$$

Performing a new term-by-term comparison on the left-hand side Eq. 3.43 in the limit previously considered of $\alpha \gg 1$ and $\beta = -\alpha + o(1)$, it is easy to see that the terms $\delta h^{(2)}$ can be neglected with respect to δh . The term $\delta h^{(4)}$ can be ignored only if $(l^*/L_h)^4$ decreases faster than $1/\alpha$, which is valid if $L_h \sim l^* \sqrt{\Lambda_{\text{static}}}$. The terms of the right-hand side cannot be simplified and the final equation for the height incompressibility reads in continuous language

$$\boxed{\frac{d}{dt} \delta h(x, t) \simeq \frac{(h^*)^2}{\xi_s} \left(\frac{2\gamma_l}{A_0} \delta h^{(2)}(x, t) - \gamma_\alpha \delta h^{(4)}(x, t) \right)} \quad (3.44)$$

with $\delta h_i \equiv \delta h(x, t)$, $\delta h_i^{(2)} \equiv (l^*)^2 \delta h^{(2)}(x, t)$ and $\delta h_i^{(4)} \equiv (l^*)^4 \delta h^{(4)}(x, t)$. One also gets the "constitutive equation" for pressure field as a function of height, either from Eq. 3.39 by neglecting $\delta h^{(4)}$ with respect to $\delta h^{(2)}$ or from Eq. 3.35 by neglecting $\delta P^{(2)}$ with respect to δP :

$$\boxed{\delta P(x) \simeq \frac{\gamma_l}{A_0} \delta h(x) - \gamma_a \delta h^{(2)}(x)} \quad (3.45)$$

Similarly, Eq. 3.36 becomes

$$\delta \theta_i \simeq \frac{h^*}{2l^*} \alpha \delta \theta_i^{(2)} + \frac{\xi_s l^*}{2\gamma_l} \delta v_i \quad (3.46)$$

because $\delta v^{(2)}$ is negligible compared to δv , and $\alpha \delta v^{(4)}$ can be ignored only if $L_v \sim l^* \sqrt{\Lambda_{\text{static}}}$ as for the incompressibility equation Eq. 3.43. Finally contrarily to previous equations, Eq. 3.37 cannot be reduced. Although $\delta v^{(5)}$ is negligible compared with the $\delta v^{(3)}$ term, the equation remains coupled with non-compatible coefficients on left and right hand sides:

$$-\frac{h^*}{l^*} \alpha \delta P_i^{(4)} + 2\delta P_i^{(2)} \simeq \alpha \xi_s \delta v_i^{(3)} - \frac{l^*}{h^*} \xi_s \delta v_i^{(1)} \quad (3.47)$$

If the vertex model was reducible to a 2D-incompressible inviscid fluid with the constitutive law Eq. 3.45, horizontal force balance should provide at least order $h^* \delta P^{(1)}(x) \simeq -\xi_s \delta v(x)$, contradicting the continuity equation Eq. 3.44 because of the factor $2\gamma_l$.

As already explained in chapter 2, this discrepancy comes from an elastic component in the horizontal stress, such that horizontal force balance becomes at least order $h^* \delta \sigma_{xx}^{(1)}(x) \simeq \xi_s \delta v(x)$ with $\delta \sigma_{xx} = -\delta P + \gamma_l \delta h / A_0$. The later equation defines δv as a function of $\delta P^{(1)}$ and $\delta h^{(1)}$, and one can use Eq. 3.45 inside Eq. 3.47 on both sides. Indeed, it is found that the left-hand side is equal to the right-hand side when applying derivation operators on δP and δv , such that Eq. 3.47 corresponds to the continuous version of the horizontal force balance $h^* \delta \sigma_{xx}^{(1)}(x) \simeq \xi_s \delta v(x)$.

This section shows that both approaches from vertex model and continuum mechanics give physically equivalent equations on the free region, and confirms the assumed tissue rheology with incompressible elasticity and surface tension. It also justifies that the introduction of another field (the lateral tilt θ) is not required thanks to Eq. 3.34.

Finally, it will be useful to compute the mid-point average of the basal width perturbation δl_I^b . Using the continuum limit and the expression of tilt angle as a function of height (Eq. 3.42), it can be approximated at least order by:

$$\frac{1}{2} (\delta l_{I-1}^b + \delta l_I^b) \simeq -\frac{l^*}{h^*} \delta h_i - \frac{\xi_s h^* l^*}{12\gamma_l} \delta v_i \quad (3.48)$$

A shrinkage of the basal interface up to 100% deformation ($\delta l^b = -l^*$) leads to the height and velocity condition at point i

$$\boxed{\frac{\delta h_i}{h^*} + \left(\frac{h^*}{l^*}\right)^2 \frac{l^* \delta v_i}{6D_s} = 1} \quad (3.49)$$

where $D_s \equiv (2\gamma_l h^*) / (\xi_s l^*)$ is the effective diffusion coefficient appearing in the local incompressibility Eq. 3.44. At acquisition time $t \simeq 20$ h, high resolution images (Fig. 3.10c) show a rim with typical width $\Delta \sim 50$ μm . Because rim growth is diffusive (Eq. 3.44), the relation $\Delta \sim \sqrt{D_s t}$ leads to $D_s \sim 10^{-14}$ m^2/s . With CC velocities below 1 nm/s and cell scale $l^* \sim 10$ μm , the velocity term in Eq. 3.49 has an order of magnitude below 10^{-1} . Thus, the condition for basal shrinkage is weakly dependent on velocity and is primarily determined by the cell deformation δh . This justifies the introduction of a multilayering criterion according to maximal height h_m , not necessarily at 100% strain because cells fluctuations and heterogeneities may trigger basal shrinkage for smaller strain and connects h_m to a cut-off interfacial length.

3.4.6 Cluster region covered by CAFs

Next, one has to consider the CC cluster region covered by CAFs as indicated on Fig. 3.14a, which contains both basal and apical tension gradients. The basal tension difference remains at first order $\gamma_{\text{CC}}^{\text{b}}(I-1, i) - \gamma_{\text{CC}}^{\text{b}}(I, i) = \xi_s \bar{l} (\delta v_{i+1} + 4\delta v_i + \delta v_{i-1})/6$. Contrarily to the free region, the unperturbed configuration contains a CAF pre-stress γ_∞ such that $\gamma_{\text{eff}} = \bar{\gamma} + \delta\gamma_{\text{eff}}$. Equilibrium cell height, width an apical angle will therefore be respectively noted \bar{h} , \bar{l} and $\bar{\psi}$. The linear perturbation of the effective tension noted $\delta\gamma_I$, spatially constant over the cell width indexed by I , becomes at first order

$$\delta\gamma_I = \delta\gamma_{\text{CAF}}(X_i) + \frac{1}{6}\xi_s \bar{l} \left[3\delta V_{\text{CAF}} - (\delta u_{i+1} + 2\delta u_i) \right] \quad (3.50)$$

with δu_i expressed as a function of δv and $d\delta\theta/dt$ as $\delta u_i = \delta v_i + \bar{h} \frac{d}{dt} \delta\theta_i$.

Compared to the set of equations in the free region (Eq. 3.31), apical equations on vertex and interface contain extra terms related to apical tension gradients $\delta\gamma$. One gets at linear order:

$$\left\{ \begin{array}{l} 6\gamma_l(\delta\theta_i - \delta\psi_i^l) = \xi_s \bar{l} (\delta v_{i+1} + 4\delta v_i + \delta v_{i-1}) \quad [\text{basal vertex}] \\ \gamma_l(\delta\psi_{I-1}^a - \delta\psi_I^a - \delta\varphi_{I-1} - \delta\varphi_I) = 2\gamma_l(\delta\theta_i + \delta\psi_i^l) - 2\cos\bar{\psi}(\delta\gamma_I - \delta\gamma_{I-1}) \quad [\text{apical vertex 1}] \\ \bar{\gamma}(\delta\psi_I^a + \delta\psi_{I-1}^a + \delta\varphi_I - \delta\varphi_{I-1}) = -\tan\bar{\psi}(\delta\gamma_{I-1} + \delta\gamma_I) \quad [\text{apical vertex 2}] \\ \bar{\gamma}\bar{l}^2\delta P_I = \gamma_l\bar{l}\delta\gamma_I - \gamma_l\bar{\gamma}(\delta l_I^a - \bar{l}\cot\bar{\psi}\delta\psi_I^a) \quad [\text{apical interface}] \\ \bar{h}(\delta P_I - \delta P_{I-1}) = 2\gamma_l\delta\psi_i^l \quad [\text{lateral interface}] \end{array} \right. \quad (3.51)$$

Of course, the condition of area incompressibility remains unchanged compared to the free region (Eq. 3.32) with an appropriate shift of equilibrium properties:

$$\left[\bar{h} + 2\left(\frac{A_0}{\bar{l}} - \bar{h}\right) \right] \delta l_I^a + \frac{\bar{l}}{2}(\delta h_i + \delta h_{i+1}) + \bar{l}^2 \frac{1 - \bar{\psi}\cot\bar{\psi}}{2(\sin\bar{\psi})^2} \delta\psi_I^a - \frac{\bar{h}^2}{2}(\delta\theta_{i+1} - \delta\theta_i) - \frac{\bar{h}^2}{6}(\delta\psi_{i+1}^l - \delta\psi_i^l) = 0 \quad (3.52)$$

The terms $\delta\gamma_I$ will affect all the equations found for the free region (see previous sections), in the sense that they will explicitly depend on the variable δu . Although the dynamical condition relating δu to δv and $d\delta\theta/dt$ still allows (in principle) the existence of an independent equation for one variable, it is no longer possible to find static equations relating couples of variables (Eq. 3.35, Eq. 3.34, Eq. 3.36 and Eq. 3.37). The best one can do is to replace the new terms in δu by δv and $d\delta\theta/dt$ in the equation equivalent to the free one with the couple $\{\theta, v\}$ (Eq. 3.36).

As an illustration, the two apical vertex equations in Eq. 3.51 can be independently manipulated to get:

$$\delta\psi_I^a = \frac{1}{2}(\delta\psi_{i+1}^l - \delta\psi_i^l + \delta\theta_{i+1} - \delta\theta_i) - \tan\bar{\psi} \frac{\delta\gamma_I}{\bar{\gamma}} - \frac{1}{4\bar{\gamma}} \left[\cot\bar{\psi} + \tan\bar{\psi} \right] (\delta\gamma_{I+1} - 2\delta\gamma_I + \delta\gamma_{I-1}) \quad (3.53)$$

$$\delta\varphi_I = -\frac{1}{2}(\delta\psi_{i+1}^l + \delta\psi_i^l + \delta\theta_{i+1} + \delta\theta_i) + \frac{1}{4\bar{\gamma}} \left[\cot\bar{\psi} + \tan\bar{\psi} \right] (\delta\gamma_{I+1} - \delta\gamma_{I-1}) \quad (3.54)$$

As for the free region case, the second equation can use the relation between $\delta\varphi$ and δh to get two equations for the four variables $\{h, \theta, v, u\}$. Since the equations derived from the system Eq. 3.51 remain similar to the previous direction, we directly jump to the continuous limit with the same parametric conditions: $\bar{\alpha} \gg 1$ ($\bar{\alpha} \equiv \bar{\gamma}/\gamma_l$) and $\beta = -\bar{\alpha} + o(1)$. At least order, one the two $\{h, \theta, v, u\}$ equations gives

$$\delta h_i^{(2)} + 2\bar{l}\delta\theta_i^{(1)} \simeq \frac{\bar{l}^2}{\gamma_l} \left(\xi_s \delta v_i^{(1)} - \xi \delta u_i^{(1)} \right) \quad (3.55)$$

Another equation coupling $\{h, v, u\}$, obtained by elimination of pressure P from the apical and lateral interfacial equations, reads at first order

$$2\delta h_i^{(2)} - \frac{\bar{h}}{\bar{l}} \bar{\alpha} \delta h_i^{(4)} \simeq -\frac{\bar{l}^2}{\gamma_l} \left(\xi \delta u_i^{(1)} + \xi_s \delta v_i^{(1)} \right) \quad (3.56)$$

Those two equations can be combined to obtain apical and basal velocities as a function of h and θ . Moreover, the addition of the dynamic constraint relating δu , δv and $d\delta\theta/dt$ generates a new equation involving only h and θ :

$$\frac{\xi \bar{h} \bar{l}}{\gamma_l} \frac{d}{dt} \delta \theta_i^{(1)} + \left(1 + \frac{\xi}{\xi_s} \right) \delta \theta_i^{(1)} \simeq \frac{\bar{h}}{2\bar{l}^2} \left(1 - \frac{\xi}{\xi_s} \right) \bar{\alpha} \delta h_i^{(4)} - \frac{3}{2\bar{l}} \left(1 - \frac{\xi}{3\xi_s} \right) \delta h_i^{(2)} \quad (3.57)$$

It is equivalent to Eq. 3.42 for the free region in the limit $\xi \rightarrow 0$, as expected. The major difference with the previous section is the impossibility to express $\delta\theta$ as a function of δh , meaning that contrarily to one independent equation for height equation (Eq. 3.44), one can only obtain a system of two coupled equations for the dynamics of height and tilt angle. Indeed, the second equation containing the evolution rate for height, coming from area incompressibility, can be expressed as a function of h and θ spatial derivatives if one neglects $d\delta h^{(2)}/dt$ and $\bar{\alpha} d\delta h^{(4)}/dt$ with respect to $d\delta h/dt$ (same arguments as for last section). Written in continuous language, one has

$$\begin{aligned} \frac{d}{dt} \left[\delta h(x, t) + \frac{\gamma_l \bar{l}}{12(\bar{\gamma})^2} \delta \gamma_{\text{CAF}}(X_i) \right] \simeq & -\frac{1}{4} \bar{\gamma} \bar{h}^2 \left(\frac{1}{\xi} + \frac{1}{\xi_s} \right) \delta h^{(4)}(x, t) + \frac{\gamma_l \bar{h}}{4\bar{l}} \left(\frac{3}{\xi} + \frac{1}{\xi_s} \right) \delta h^{(2)}(x, t) \\ & - \frac{\gamma_l \bar{h}}{2\bar{l}} \left(\frac{1}{\xi} - \frac{1}{\xi_s} \right) \delta \theta^{(1)}(x, t) \end{aligned} \quad (3.58)$$

whereas the evolution equation for the tilt angle becomes

$$\frac{d}{dt} \delta \theta^{(1)}(x, t) \simeq \frac{1}{2} \bar{\gamma} \bar{l} \left(\frac{1}{\xi} - \frac{1}{\xi_s} \right) \delta h^{(4)}(x, t) - \frac{\gamma_l}{2\bar{h}} \left(\frac{3}{\xi} - \frac{1}{\xi_s} \right) \delta h^{(2)}(x, t) - \frac{\gamma_l}{\bar{h}} \left(\frac{1}{\xi} + \frac{1}{\xi_s} \right) \delta \theta^{(1)}(x, t) \quad (3.59)$$

The limit $\xi \rightarrow 0$ requires some care because of factors $1/\xi$ in Eq. 3.58. A Taylor expansion of Eq. 3.59 at order 1 in ξ will give back Eq. 3.44 at order 0, as expected, up to an extra term $\propto d\delta\theta^{(1)}/dt$ that can be ignored thanks to the zero-th order of Eq. 3.59 and the previous simplifications neglecting $d\delta h^{(2)}/dt$ and $\bar{\alpha} d\delta h^{(4)}/dt$ with respect to $d\delta h/dt$.

3.5 Results: free CAFs pulled by contractile ring

3.5.1 CAF closure or stable equilibrium

The system under study is a monolayer of CAFs with a central hole on which an actomyosin contractile ring exerts a pulling force defined by a line tension Γ . The CAF tissue is described as thin elastic material with active pre-stress γ_∞ , thickness h_c , Young' modulus E_c and Poisson ratio ν . One assumes angular symmetry along the hole center and defines the reference configuration (initial hole radius R_0) with respect to an absence of pre-stress. The external tissue boundary ($r = R_\infty$) is under free stress conditions. The stress tensor then reads

$$\gamma_{rr} = \gamma_\infty + \frac{E_c h_c}{1 - \nu^2} [\epsilon_{rr} + \nu \epsilon_{\theta\theta}] \quad (3.60)$$

$$\gamma_{\theta\theta} = \gamma_\infty + \frac{E_c h_c}{1 - \nu^2} [\epsilon_{\theta\theta} + \nu \epsilon_{rr}] \quad (3.61)$$

where $\epsilon_{rr} = \partial_r u_r$ and $\epsilon_{\theta\theta} = u_r/r$ under the small strain approximation. Here, the displacement is u_r is independent of z at least order (thin film approximation). The z -integrated radial Stokes' force balance is

$$\partial_r \gamma_{rr} + \frac{1}{r} (\gamma_{rr} - \gamma_{\theta\theta}) = \sigma_{rz}|_{z=0} - \sigma_{rz}|_{z=h}$$

with the top surface under free stress ($\sigma_{rz}|_{z=h} = 0$) whereas substrate tractions are $\sigma_{rz}|_{z=0} = T_r$. To be compatible with the existence of steady-state traction forces in the CAF-CC system, the traction stress is considered elastic at small strain: $T_r = Y_s u_r$ and saturates above a yield stress $\sigma_y \equiv f^*$ at $|T_r| = f^*$. If the line tension is high enough, the induced displacements will be above the threshold amplitude f^*/Y_s on a spatial range $[R_0; R_0 + \Delta^*]$ with saturated tractions $T_r = -f^*$, and elastic tractions $T_r = Y_s u_r$ will remain for $r > R_0 + \Delta^*$. This tissue-substrate elastic coupling defines an intrinsic length scale $\lambda_s \equiv \sqrt{E_c h_c / [Y_s (1 - \nu^2)]}$ and the radial force balance becomes (when $|T_r| < f^*$)

$$r^2 \partial_r^2 u_r + r \partial_r u_r - \left(1 + \frac{r^2}{\lambda_s^2}\right) u_r = 0 \quad (3.62)$$

The system is closed with no-stress condition at $r = R_\infty$ equivalent to zero displacement when $R_\infty \gg \lambda_s$, tension balance at the tissue inner edge $\gamma_{rr}|_{r=R_0} = \Gamma/R$ and definition $u_r(R_0) = R - R_0$. Depending on the active line tension Γ , the elastic resistance ($E_c h_c, \nu, Y_s$) and CAF tension γ_∞ , the system can be in stable/unstable mechanical equilibrium or undergo gap closure because the 2D pressure Γ/R introduces a positive feed-back towards small radii. The dimensionless version of the problem uses length $[L] = R_0$ such that $\bar{R} \equiv R/R_0$ and tension $[\gamma] = E_c h_c$ with parameters $g \equiv \gamma_\infty / E_c h_c$, $y_s \equiv Y_s R_0^2 / E_c h_c$, $\bar{\Gamma} \equiv \Gamma / (E_c h_c R_0)$ and $f^* \equiv f^* R_0 / E_c h_c$, or $\lambda_s / R_0 = [y_s (1 - \nu^2)]^{-1/2}$.

Below yield stress, the tension balance at the inner edge of the CAF monolayer becomes in dimensionless format

$$c\bar{R} + \bar{R}(1 - \bar{R}) \left[\frac{1}{1 + \nu} + \sqrt{\frac{y_s}{1 - \nu^2}} \frac{K_0(\sqrt{y_s(1 - \nu^2)})}{K_1(\sqrt{y_s(1 - \nu^2)})} \right] = \bar{\Gamma} \quad (3.63)$$

where K_0, K_1 are modified Bessel functions and $\bar{R} \equiv R/R_0$ the unknown (dimensionless) radius. Written in the format "line tension=elastic resistance", one obtains Fig. 3.15a. For $g > 0$, two local equilibria exist, a stable one at larger R and an unstable one at smaller R leading to gap closure. A negative pre-stress ($g < 0$) would tend to push the tissue inwards and make equilibrium states disappear for sufficiently high amplitude, but we consider those conditions to be unphysical. A phase diagram represents the critical line tension necessary for closure, when the stable equilibrium disappears, as a function of substrate stiffness y_s on Fig. 3.15b. It shows an increase of stability when the reduced elastic parameter y_s increases, whereas a line tension increase triggers gap closure. Similar calculations can be made when a finite yield stress f^* prevents infinitely large tissue-substrate displacements. This leads to a phase diagram on Fig. 3.15c with zero pre-stress ($g = 0$): with yield stress, the critical line tension is reduced and saturates for large substrate stiffness y_s because the unyielded region is sent to infinity and cannot influence the inner tension balance anymore.

This elementary equilibrium study illustrates the natural closure instability coming from the 2D Laplace law $\Delta\gamma_{rr} = \Gamma/R$, which defines a mechanically stable state only for sufficiently high elastic resistance. The introduction of tissue pre-stress γ_∞ , traction yield-stress f^* or elastic tissue-substrate coupling Y_s only add minor quantitative changes to this picture.

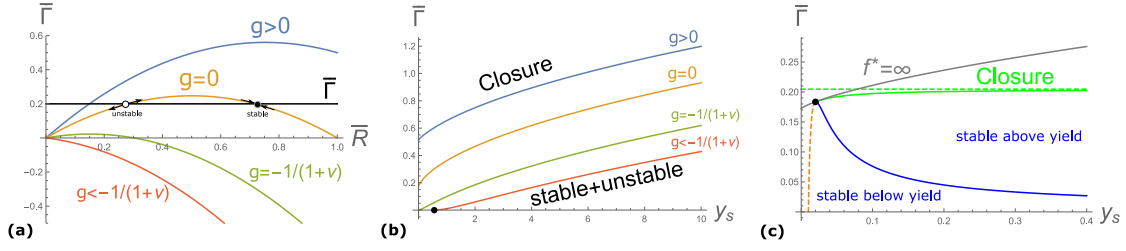


Figure 3.15: **(a)**: Radial force balance at the inner CAF edge between ring line tension $\bar{\Gamma} = 0.2$ and elastic resistance, varying CAF contractility g . Equilibrium is either stable (black dot) or unstable (white dot). It disappears when line tension is too high ($g < 0$ is considered unphysical) and the tissue closes the gap $\bar{R} \rightarrow 0$. $y_s = 0.25$ and $f^* = \infty$. **(b)**: Phase diagram associated to equilibrium (a), as a function of y_s and $\bar{\Gamma}$, showing the contours of critical line tension for different values of g . $f^* = \infty$. **(c)**: Similar phase diagram as a function of line tension $\bar{\Gamma}$ and substrate strength y_s for finite yield stress $f^* = 0.01$ and vanishing contractility $g = 0$. For small y_s , the situation is identical to (b), when tractions are below yield (critical line tension in gray). For $y_s > 2f^*$, the stable equilibrium region contains a spatial range at yield if $\bar{\Gamma}$ is high enough (blue), and similarly for the unstable one (dashed orange). The critical line with yield (green) saturates when $y_s \rightarrow \infty$ (dashed green): a yield stress reduces the system' stability. For all graphs, $\nu = 0.45$.

3.5.2 Constraints on the parameters

Experimentally, the phenotype where the CAF leading edge would be blocked at the cluster periphery has never been observed in normal conditions. Note however that anisotropic CAF climbing has been observed on many clusters when a fraction of the ring remains blocked by the CC periphery, more likely associated to generic heterogeneities in the actomyosin activity and the CC cluster resistance that prevents spontaneous climbing. In conditions of fibronectin knock-down, the line tension decreases because the CAF ring loses its supracellular integration, and the CAFs remain blocked at the cluster periphery. This roughly illustrates the two theoretical states discussed on the last section (stable mechanical equilibrium or dynamical gap closure) and gives quantitative constraints on some modelling parameters. Since the elastic resistance applied by the CC cluster when CAFs remain at the periphery is not sufficient to prevent CAF closure in normal conditions, we consider that this term can be ignored to quantify the parametric constraints on tissue elasticity.

To assign reasonable values to parameters of the CAF tissue, one has to respect the following constraints:

- inward force balance (line tension dominates CAF elastic resistance): since the presence of yield decreases the critical line tension and only occurs after an initial regime of purely elastic traction, a conservative estimate considers a critical line tension value in the "below yield stress" case, with the experimental constraint that $\Gamma \sim 100 - 1000$ nN.
- the yield stress should correspond to a reasonable spring extension δ^* , according to $f^* = Y_s \times \delta^*$, in the broad range $0.1 - 10 \mu\text{m}$ depending on the structures involved in tissue-substrate coupling (CAF fibronectin or focal adhesions).
- if one considers the correlation between yield stress f^* and the asymptotic radial traction stress observed in experiments, this leads to $f^* \simeq 50 - 100$ Pa (see the introduction).
- the traction force localization requires a relaxation length $\lambda_s \propto \sqrt{E_c h_c / Y_s}$ of the order of $10 - 100 \mu\text{m}$.

To fulfil those requirements and get values for $\{h_c, R_0, E_c, Y_s, \Gamma\}$ ($\nu = 0.45$), one uses the dimensional expression for critical line tension

$$\bar{\Gamma}_{\text{crit}} = \frac{E_c h_c R_0}{4(1+\nu)} \left[1 + \frac{1}{1-\nu} \frac{R_0 K_0 (R_0/\lambda_s)}{\lambda_s K_1 (R_0/\lambda_s)} \right] \quad (3.64)$$

and the standard units $L_0 = 10 \mu\text{m}$, $P_0 = 100 \text{ Pa}$, $F_0 = 10 \text{ nN}$ and $Y_{s0} = 10^8 \text{ Pa/m}$. Since R_0 varies between $100 \mu\text{m}$ and $200 \mu\text{m}$ with monotonic increase of $\bar{\Gamma}_{\text{crit}}$, the requirement $\bar{\Gamma} > \bar{\Gamma}_{\text{crit}}$ can be studied at $R_0 = 200 \mu\text{m}$. It appears difficult to validate all the prescribed conditions: for $h = 3 \mu\text{m}$ and $\Gamma = 400 \text{ nN}$, one gets for the parameter plane $(E_c/P_0, Y_s/Y_{s0})$ the figure 3.16a,b. Importantly, the tissue elasticity $E_c \sim 100 \text{ Pa}$ is much smaller than epithelial monolayers [189], a substrate stiffness $Y_s \lesssim 10^7 \text{ Pa/m}$, and the critical tissue displacement is necessarily of the order of $10 \mu\text{m}$ as shown on Fig. 3.16c.

3.5.3 Yield stress nature

The low values of elastic parameters E_c and Y_s give interesting consequences. When discussing rim size, we already mentioned that elastic substrate stiffness coming from molecular adhesive bonds provides too large values $Y_s = k_b n_b \lesssim 10^{10} - 10^{11} \text{ Pa/m}$, using $k_b \sim 0.1 - 1 \text{ pN/nm}$ and $n_b \sim 1/(100 \text{ nm})^2$. Note that a yield stress associated to maximal bond extension before breakage $\delta \sim 10 \text{ nm}$ gives $f^* \sim 0.1 - 1 \text{ kPa}$, which is closer to the experimental value. Rather than single bonds, fibroblasts assemble Focal Adhesions (FAs) which are known to grow under an optimal stress load of the order of $\sim 5 \text{ kPa}$ [111]. The existence of a critical load above which FAs disassemble is predicted theoretically to be $\sim 40 \text{ kPa}$ ([251]), which is clearly too high for the observed tractions. In fact, FA rupture may not be required to justify the generic yield transition we propose: since FA translocation can occur for very small directed forces, (0.1 nN per FA in [252]), one can imagine a scenario where force-dependent FA growth is stimulated by tissue deformation through cytoskeleton stress transmission, and may eventually be captured by $f_s = Y_s u$. For a threshold load probably close to the optimal stress $\sim 5 \text{ kPa}$, FAs stabilize and could exert saturated traction forces on the substrate, captured phenomenologically by the yield stress parameter f^* . The optimal stress may differ for CAFs but one remains at a rather too large value $f^* \sim 1 \text{ kPa}$.

A completely different scenario involves the ECM CAF deposition. Experimentally, our collaborators already showed the requirement of fibronectin to integrate mechanically single cell contractility into a supracellular ring: under fibronectin knock-down conditions, CAFs are unable to significantly compress pillars or clusters, and to climb on top of CCs. In addition, the network assembly of fibronectin fibres observed experimentally over the full tissue of CAFs, already proposed to act as transient cell-cell junctions named stitch adhesions [244], may control both CAF tissue elasticity (E_c) and CAF-substrate elasticity (Y_s). Using a characteristic fibre stiffness [255] $k_f \sim 10^{-3} \text{ N/m}$, this is integrated at the network level with a cell-scale mesh-size $a \sim 10 \mu\text{m}$ as $E_c \simeq k_f/a$ and $Y_s \simeq k_f n_s$ where $n_s \simeq 1/a^2$. Thus, one finds $E_c \sim 100 \text{ Pa}$ and $Y_s \sim 10^7 \text{ Pa/m}$ which is remarkably accurate considering the previous estimates based on cell adhesion response. A yield stress occurs for a typical network deformation of $10 \mu\text{m}$ such that $f^* \sim 100 \text{ Pa}$. Physically, we interpret the yield transition as transient ruptures in the fibronectin-substrate link, later healed by spontaneous reassembly or new CAF deposition of fibronectin (see Fig. 3.16d). Note that under this scenario, it is likely that an additional yield transition may affect the inner CAF elasticity (modulus E_c) but we did not consider this feature and only focused on the CAF-substrate plasticity. However, the relevance of matrix-dependent tissue-substrate gripping may be restricted to our system. Localized inward tractions are also observed at steady-state on gap closure experiments for epithelial monolayers around circular non-adhesive patches [229], an observation which still lacks a structural and mechanical explanation.

3.6 Results: CAF closure and tractions for N-cadh KD

We next study the CAF closure phenotype in the N-cadherin knock-down conditions, in particular the theoretical model compatibility with experimental data on the CAF ring dynamics and substrate tractions (Fig. 3.17). Experimental kymographs for radial CAF velocity field are ignored because they do not contain any clear feature distinguishable from "noise", except some inward

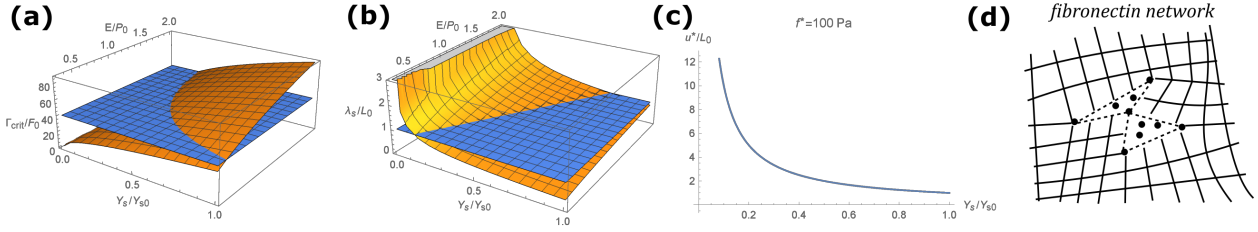


Figure 3.16: **(a)**: Critical line tension $\bar{\Gamma}_{\text{crit}}$ (yellow) and assigned value (blue) $\Gamma = 400$ nN in units of 10 nN, for the parameter plane $(E_c/P_0, Y_s/Y_{s0})$. One is searching for the region $\bar{\Gamma} > \bar{\Gamma}_{\text{crit}}$. **(b)**: Relaxation length (yellow) λ_s in units of 10 μm (blue) for the parameter plane $(E_c/P_0, Y_s/Y_{s0})$. **(c)**: Critical displacement $u^* \equiv f^*/Y_s$ as a function of reduced substrate elasticity Y_s/Y_{s0} . For all graphs, $\nu = 0.45$. **(d)**: Sketch of the fibronectin network in the substrate plane. Network stretching originating from the pulling actomyosin ring generates local fractures in the fibronectin-substrate connexion, later healed by spontaneous reassembly or new fibronectin deposition by CAFs.

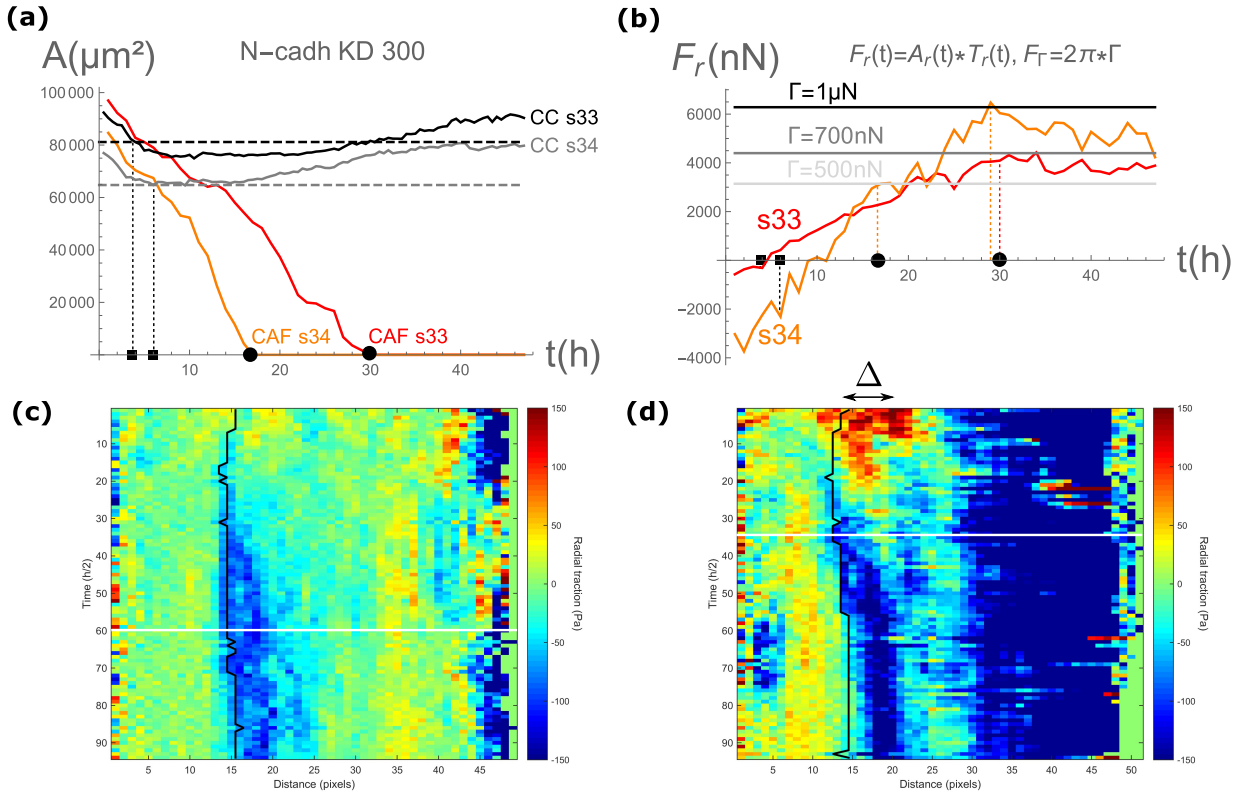


Figure 3.17: **(a)**: CAF closure area dynamics for clusters s33 (red) and s34 (orange), as well as CC cluster area dynamics for s33 (black) and s34 (gray). The dashed lines indicate the cluster areas used to initiate the dynamics when the CAF area is approximately equal (indicated by black squares). Black dots indicate CAF closure. **(b)**: Radial traction force F_r over time obtained by integrating the radial traction stress T_r over the averaging ring surface $A_r = \pi\Delta(2R_0 + \Delta)$ as indicated on (d) for clusters s33 (red) and s34 (orange). The saturated values of traction forces indicate a lower bound for the total force associated to line tension, $2\pi\Gamma$ (light gray, gray, black). Note that contrarily to s33, s34 does not saturate when CAF closes (black circle points). **(c-d)**: Radial traction heat map for cluster s33 (c) and s34 (d) in N-cadh KD conditions. Blue (red) tractions mean inward (outward). A white line indicates the time of CAF closure on top of CC cluster: 30h for s33 and 17h for s34. 1 pixel = 10.32 μm . For s34, tractions at distances higher than 30 pixels are unphysical (numerical error?).

oscillations that may be associated to actomyosin ring pulses. Those pulses are quite generic in cell actomyosin systems [163] but we chose to not take them into account for our modelling procedure. The CAF tissue is described as presented in the previous chapter, with parameters γ_∞ , E_c , $h_c \simeq 4 \mu\text{m}$ (assumes a CAF monolayer), $\nu = 0.45$, Y_s and f^* . The elasto-plastic CAF-substrate mechanics corresponds to radial tractions $T_r = Y_s u_r$ if $|u_r| < f^*/Y_s$ and saturates above the yield stress at $|T_r| = f^*$.

Again, the supracellular actomyosin ring is modelled as a constant line tension Γ generating an inward 2D pressure $\Gamma/R_c(t)$ driving CAF closure with ring radius $R_c(t)$, and dissipation is dominated by a ring line friction ζ . To simplify the description in those N-cadh KD conditions, we assume that surface friction between CAFs and CCs is negligible as well as cluster deformations, so that the peripheral cluster radius R_T remains fixed at its initial value R_0 . Experimentally, the CC cluster area changes significantly in time but we average out those variations (see Fig. 3.17a). Finally, we consider that the configuration for which the CAF tissue is next to the CC cluster corresponds to the elastic reference state, so that the initial CAF edge radius R_0 (zero displacement) corresponds to this average cluster size.

Traction stresses are integrated over a ring surface such that $r \in [R_0; R_0 + \Delta]$ with $\Delta = 41.28 \mu\text{m}$ as indicated on Fig. 3.17d, giving the traction force on Fig. 3.17b. The initial CAF edge radius R_0 and yield stress f^* can be inferred from experimental data: CC cluster area at which CAFs jump on cluster top surface for R_0 (Fig. 3.17a), and saturation value of integrated traction stress for f^* (Fig. 3.17b). Since the CAF tissue displacements induced by ring closure should be sufficiently high to trigger a yield transition, one expects the region surrounding the cluster to apply a constant stress f^* on the substrate: the average over the integration region should be equal to f^* . Finally, the pillar compression experiments give the range 100 – 1000 nN for the line tension Γ , whereas total traction forces (Fig. 3.17b) can be used to estimate a lower bound for each cluster. Therefore, only the elastic coefficients E_c , Y_s , γ_∞ and line friction ζ remain as a priori unknown parameters.

1. the spatially defined width of inward traction forces observed on heat maps (Fig. 3.17c,d) implies an elastic length $\lambda_s = \sqrt{E_c h_c / Y_s}$ of few tens of microns which constrains the ratio E_c / Y_s .
2. ζ will control the CAF edge velocity $V_c = \Gamma / (\zeta R_c)$ to match the experimental closure time.
3. Initially, the integration traction slope (Fig. 3.17b) scales like $Y_s \lambda_s V_0 \propto \sqrt{E_c Y_s} / \zeta$ and can be used in combination with the previous constraints to determine independently an order of magnitude of E_c , Y_s and ζ .
4. To maintain a minimal amount of free parameters, it is ignored: $\gamma_\infty = 0$.

Cluster s34 differs from s33 on one important aspect: whereas radial tractions almost vanish at the initiation point for s33, radial traction is clearly negative for s34 (Fig. 3.17b). Since the elastic tractions scale like $u(r)$ and must start at zero by the previous choice of reference state, there is an issue on cluster s34. There are different ways to treat the problem:

1. change the reference state to the point of vanishing tractions by the use of contractile tension γ_∞ leading to negative displacement when it dominates over the assembling actomyosin ring,
2. add a negative source of traction (expected from CAF crawling), but it has to be maintained for the entire dynamics,
3. maintain the reference state choice but rescale the elastic traction stress from $f_s = Y_s u$ to $f_s = Y_s (u - u_0)$ where u_0 is adjusted to match the traction at the square point.

Overall, this asks for an understanding of the mechanism generating negative traction forces (outward), if it occurs only when the CAF tissue approaches the CC cluster, disappears after CAF jump on top of cluster top surface or stays for the entire dynamics.

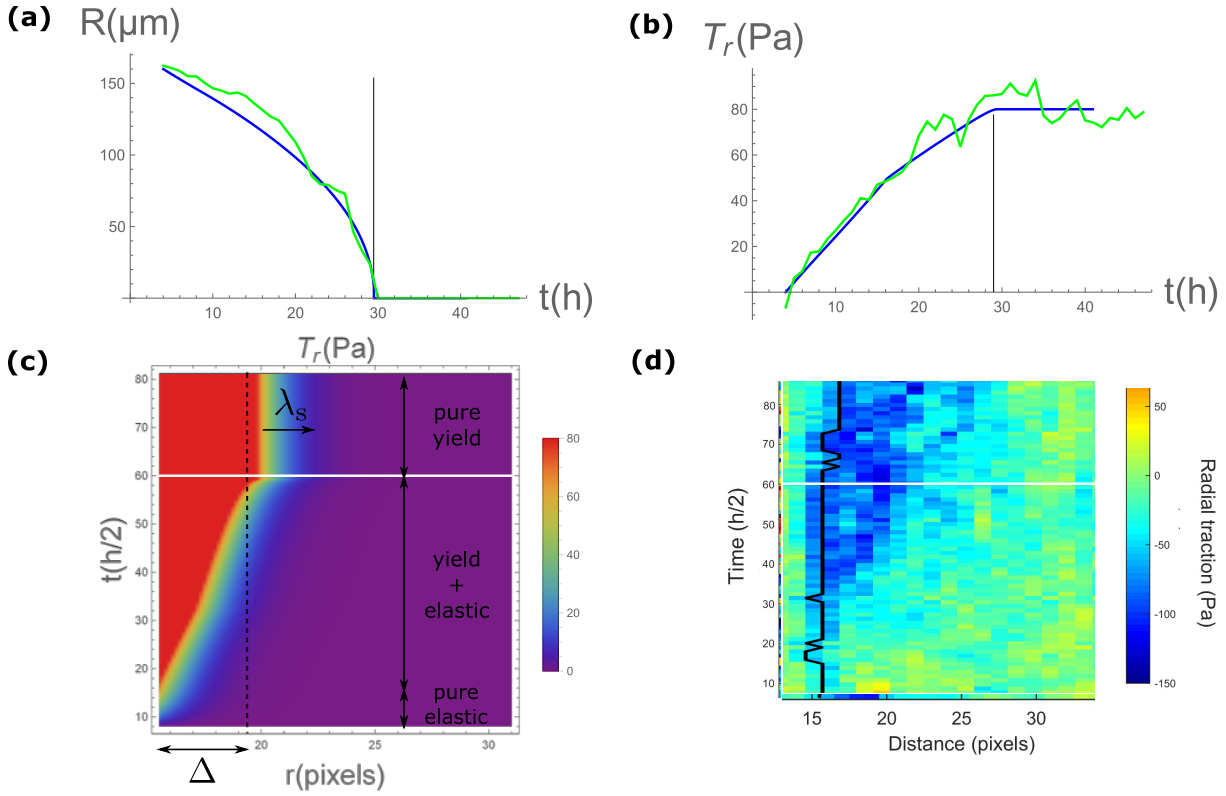


Figure 3.18: (a): CAF edge radius dynamics (starting from $R = R_0$) for cluster s33 (N-cadh KD) with the hypothesis of constant line tension Γ . Theoretical curve is in blue and experimental data in green. (b): Averaged radial traction dynamics for cluster s33 (N-cadh KD). Theoretical curve is in blue and experimental data in green. (c): Theoretical radial traction heat map for cluster s33 (N-cadh KD), centred at the CC cluster periphery, with the hypothesis of constant line tension Γ . The blue region indicates the exponential traction decay over size $\lambda_s \sim \sqrt{E_c h_c / Y_s}$. The red region corresponds to a yield regime for the CAF-substrate interaction. (d): Experimental radial traction heat map for cluster s33 (N-cadh KD), centred similarly to the theoretical graph (c) to facilitate visual comparison. On graphs (c,d), a white line indicates the time of CAF closure on top of CC cluster.

Another crucial issue regarding the cluster s34 is the absence of correlation between CAF closure and radial traction saturation, seen from Fig. 3.17a,b at black circle points. It is tempting to connect these two problems, which is possible if a negative (outward) source of traction exists during CAF dynamics and "hides" the full magnitude of elastic tractions until closure. The protrusive activity of CAFs should be oriented radially at the periphery of the CC cluster thanks to the centripetal tissue flux, such that directionality may be lost when CAF closure ends. As a consequence, the negative tractions could disappear after closure and only the elastic tractions remain.

3.6.1 cluster s33

The initial radius for CAF dynamics is $R_0 = 161 \mu\text{m}$ and corresponds to a time of four hours. Saturation of averaged radial traction (see Fig. 3.18b) indicates that $f^* = 80 \text{ Pa}$. The lower bound value for Γ is 700 nN according to Fig. 3.18a.

First, one takes $E_c = 100 \text{ Pa}$ and $\Gamma = 700 \text{ nN}$. From the knowledge of the initial averaged radial traction slope, one finds $Y_s = 5.10^6 \text{ Pa/m}$, which corresponds to $\lambda_s \simeq 10 \mu\text{m}$. The best value for the line friction is $\zeta = 4.4 \times 10^6 \text{ Pa s}$. The results of the fitting procedure are indicated on Fig. 3.18.

The fact that the initial traction slope is proportional to $\sqrt{E_c Y_s}$ means that an increase of E_c should be compensated by an equivalent decrease of Y_s to maintain the slope at its experimental value. Since $\lambda_s \propto \sqrt{E_c / Y_s}$, the elastic correlation length will increase with E_c . Indeed, one finds

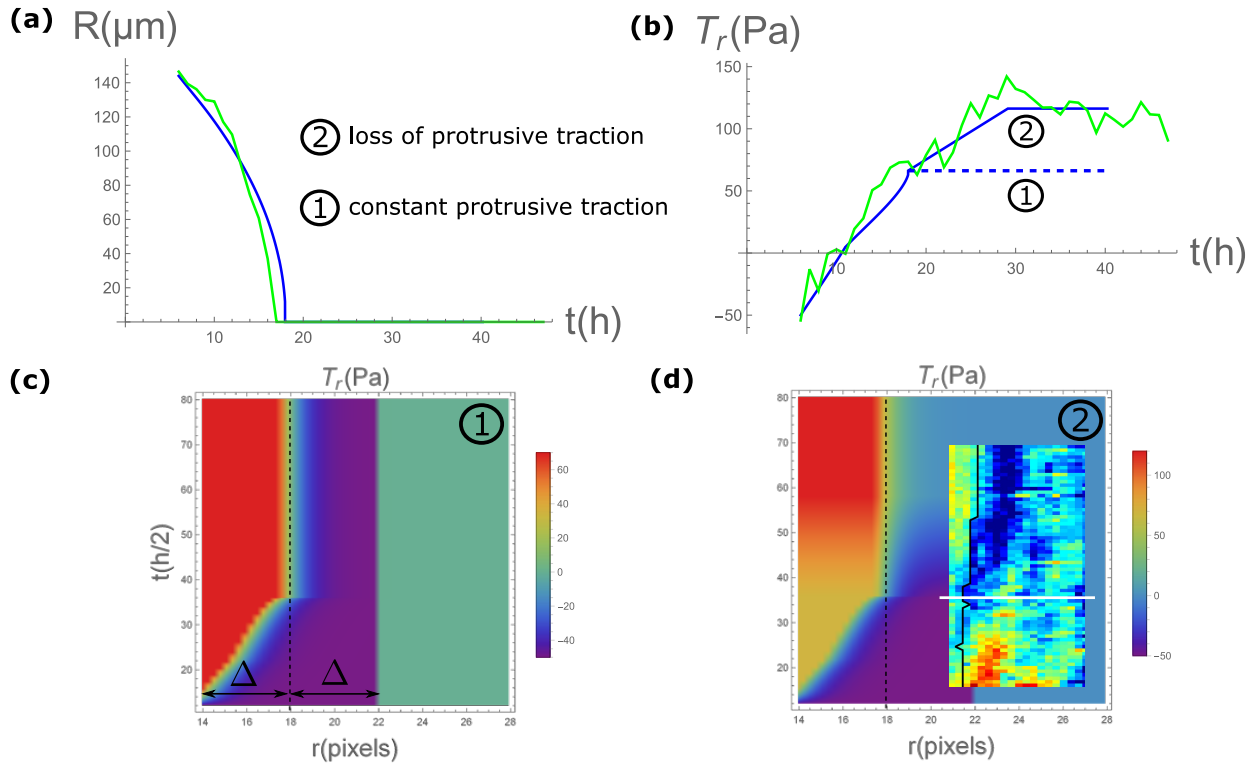


Figure 3.19: (a): CAF edge radius dynamics (starting from $R = R_0$) for cluster s34 (N-cadh KD) with the hypothesis of constant line tension Γ (infinite velocity at closure time). Theoretical curve is in blue and experimental data in green. (b): Averaged radial traction dynamics for cluster s34 (N-cadh KD). Theoretical curve is in blue and experimental data in green. The dashed blue line corresponds to the first scenario where negative tractions are maintained after CAF closure whereas the full blue line represents a linear decrease of directed protrusive activity over time (second scenario). (c,d): Theoretical radial traction heat map for cluster s34 (N-cadh KD) with the hypothesis of constant line tension Γ . Note that the yield region does not fully cover the integration region at the end of CAF closure contrarily to Fig. 3.18c. The negative tractions are assumed to be constant (-50 Pa) for a distance less than 2Δ away from CC cluster and 0 above.

- $E_c = 100$ Pa: $Y_s = 5.10^6$ Pa/m ($\lambda_s = 10$ μm), $\zeta = 4.4 \times 10^6$ Pa s,
- $E_c = 200$ Pa: $Y_s = 4.10^6$ Pa/m ($\lambda_s = 16$ μm), $\zeta = 4 \times 10^6$ Pa s,
- $E_c = 300$ Pa: $Y_s = 2.6.10^6$ Pa/m ($\lambda_s = 24$ μm), $\zeta = 3.6 \times 10^6$ Pa s,

The appropriate value of E_c is chosen from the comparison of traction spatial extension for theoretical and experimental heat maps (Fig. 3.18c,d). Since λ_s increases with E_c , it is equivalent to a choice of the elastic correlation length.

3.6.2 cluster s34

The initial radius for CAF dynamics $R_0 = 144$ μm at a time of six hours. Saturation of averaged radial traction (Fig. 3.19b) occurs around $T_r = 120$ Pa, but the value at which CAFs close on top of CC cluster is $T_r = 70$ Pa. As explained before, we propose to add a permanent source of negative tractions of the order of -50 Pa, originating from CAF protrusive activity at the CC cluster periphery. Then the saturation stress corresponds to the total difference so that $f^* = 120$ Pa ($70 - (-50) = 120$). One gets $\Gamma = 1$ μN from figure Fig. 3.17b.

Again, one takes $E_c = 100$ Pa: the initial traction slope gives $Y_s = 10^7$ Pa/m ($\lambda_s = 7$ μm) and the closure time is obtained for a line friction $\zeta = 3.8 \times 10^6$ Pa s. The results are indicated on Fig. 3.19 for a constant line tension. Contrarily to the situation of s33, CAF closure is so fast that the yield does not cover entirely the integration region so that the elastic component of traction stresses remains until CAF closure.

If the negative tractions are maintained after CAF closure (first scenario), one follows the dashed line of Fig. 3.19b and the traction heat map (Fig. 3.19c). Quite arbitrarily since nothing in the model can explain the spatial distribution of protrusive tractions, a step function has been used over width 2Δ . Therefore, the substrate region far away from cluster is under no stress: this is identical with the previous results and "zero" implicitly corresponds to "noise" level. However, if the negative tractions decrease after CAF closure because of a loss of protrusive directionality (second scenario), the tractions can reach the saturation level of $\simeq 120$ Pa (Fig. 3.19d). The comparison with the region of interest on the experimental radial traction heat map indicates that E_c should be higher because λ_s seems higher, and the appropriate negative traction width (red) is of the order of elastic traction width (blue).

3.7 Results: CC bud stability at steady-state

After the previous focus on the mechanics of the surrounding CAF tissue, we now look more precisely at the CC mechanics induced by CAF-shear stress. One of the most striking features of this CAF-CC *in vitro* co-culture is the observation of strong CC rearrangements into a 3D bud, compressed by the CAF actomyosin ring [190]. Surprisingly, despite sufficiently large experimental times to allow for fluid cell reorganization inside the CC cluster, those buds can remain mechanically stable for tens of hours with an "apparent" steady-state. This chapter deals with a generic analysis of experimental substrate tractions showing a signature of bud compression, and proposes a minimal model for the mechanical stability of buds. It extends the theoretical supplementary note available in [190].

3.7.1 Experimental traction analysis and bud compression

Thin film model

A sketch of the model system is presented in Fig. 3.20a. At the CAF leading edge, the contractile activity of the supracellular ring-like structure is modelled as a constant line tension Γ that pulls the CAF tissue inwards with 2D pressure Γ/R_c for CAF edge radius $R_c(t)$. This tension is resisted by CAF tissue elasticity, function of the plane modulus $E_c h_c$. Prior to budding, the CC cluster constitutes a cell monolayer with peripheral radius $R_T(t)$ which evolves thanks to the shear-driven stress f between the two tissues. This mechanical interaction is assumed to drive the CC rearrangements ultimately responsible for the budding phenotype, and can either be localized at the ring [222] or extend over the CAF-CC contact surface. We concentrate on the dynamics characterized by inward traction forces, for which CAF migration may be disregarded as the outward-inward transition suggests Fig. 3.20b. We further assume rotational invariance, which, although not particularly accurate for the studied experimental situation [190], is a prerequisite for an analytically tractable model. Finally, we adopt a thin sheet approximation for the mechanical description of both CAF tissue and CC cluster, for which we only consider the integrated stress tensors: $h\sigma_{ij} \equiv \int_0^h dz \sigma_{ij}$ for the CC cluster with thickness h and $h_c\sigma_{ij}^c \equiv \gamma_{ij}$ for CAFs.

- For $r > R_T$, the CAFs are in direct contact with the substrate and experience a substrate force density T_r . The local force balance in this region reads [245]:

$$\partial_r \gamma_{rr}(r) + \frac{\gamma_{rr}(r) - \gamma_{\theta\theta}(r)}{r} = T_r(r) \quad (3.65)$$

where γ_{rr} and $\gamma_{\theta\theta}$ are the radial and orthoradial components of the CAF stress tensor and r is the radial coordinate.

- For $R_c + w < r < R_T$, where w is the width of the actomyosin ring, the CAFs are in contact with the CC cluster. The sliding of the CAFs on top of the CC cluster creates a shear stress $f(r)$ which acts as a source of tension gradient in both CAFs and CC cluster:

$$\partial_r \gamma_{rr}(r) + \frac{\gamma_{rr}(r) - \gamma_{\theta\theta}(r)}{r} = f(r), \quad \partial_r h\sigma_{rr}(r) + \frac{h\sigma_{rr}(r) - h\sigma_{\theta\theta}(r)}{r} = -f(r) + T_r(r) \quad (3.66)$$

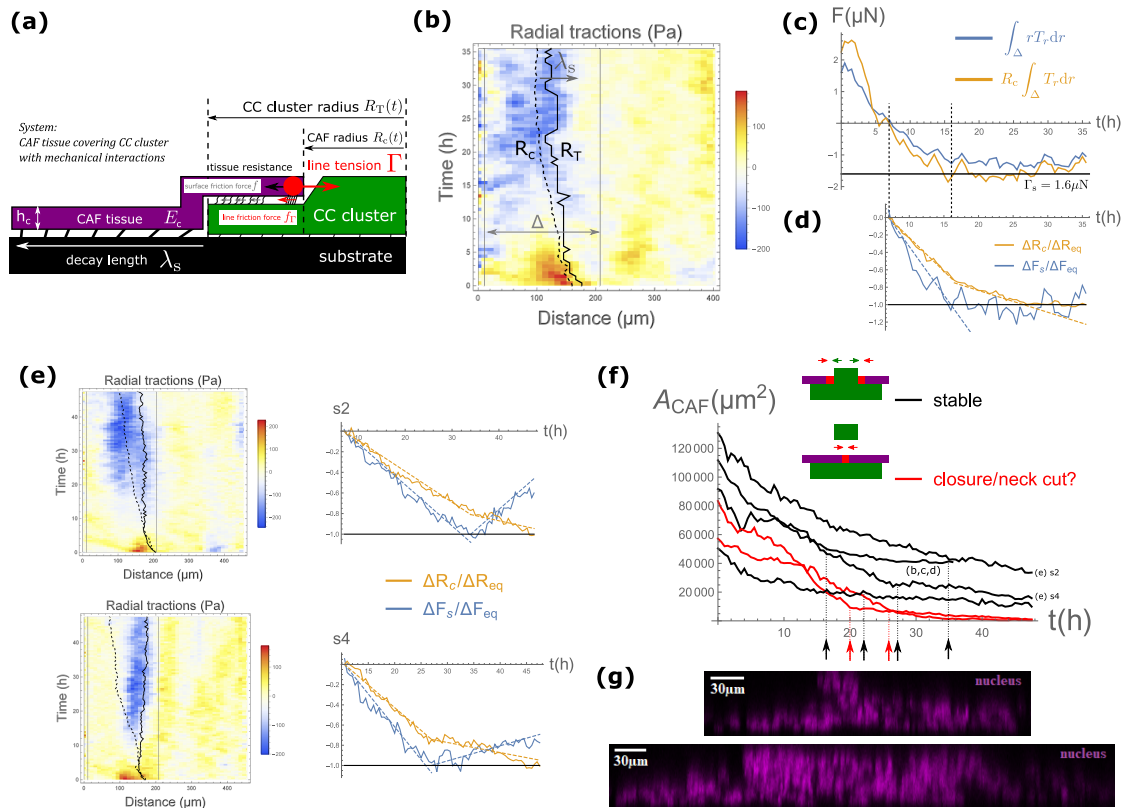


Figure 3.20: **(a)**: Sketch of the model: a CAF monolayer (purple) closes on top of a cluster of cancer cells (green), driven by the line tension provided by a dense actomyosin ring (red). The CAFs exert a surface friction force on the CC cluster – which may include a line friction force f_T at the location of the ring – that creates cluster compression. The movement of both the CAFs and the CC cluster generate traction forces on the substrate. Within an elastic model, the traction stress below the CAF layer is localized within a decay length λ_s . **(b)**: Experimental kymograph of substrate tractions T_r in time and space, with spatial localization for inward stress (blue). Black lines represent the CAF ring radius R_c (dashed) and CC peripheral radius R_T (full). We only focus on times for which tractions are inward (blue) and define a spatial range Δ (gray lines). Outside this range, numerical ($r \simeq 0$) or biological ($r > 200 \mu\text{m}$) fluctuations are dominant. **(c)**: The computed total traction force over Δ , as defined in (b), through a surface integral $\int_{\Delta} r T_r(r) dr \equiv F_s / (2\pi)$ (blue) or a line integral $R_c \int_{\Delta} T_r(r) dr$ (orange). Inward tractions (negative) start after $t = 7$ h and reach a saturation value Γ_s between 1.2 and 1.6 μN for $t > 16$ h. Γ_s defines a lower bound for the ring line tension Γ . **(d)**: Relative variation of the total traction force $F_s = 2\pi F$ as in (c) and the ring radius R_c from their value at $t = 7$ h, normalised by their saturation value at long time. A striking feature is the apparent saturation of traction force before CAF ring radius saturation, that we interpret as an indication of bud compression. **(e)**: Two other clusters with raw traction kymograph and relative variation of traction force and ring radius, similarly to (b,c,d). For all studied clusters with stabilized buds, abrupt changes in ring and traction dynamics coincide. **(f)**: Evolution of the gap area defined by the CAF actomyosin ring over time. Some buds stabilize by resisting ring compression (black), whereas others cannot and presumably let CAFs close with a bud neck cut (red). Abrupt change in ring dynamics (arrows) indicates bud compression prior to closure: the CC cluster is unlikely to remain in monolayer configuration here. Clusters associated to figures (b,c,d) and (e) are indicated. **(g)**: Confocal microscopy images showing CC nuclei for clusters at steady state, with spherical-like shape for small buds (top) and cylindrical-like shape with only 2 – 3 layers for large buds (bottom).

- For $R_c < r < R_c + w$, the balance between the inward force from the ring tension Γ/R_c and the CAF radial tension γ_{rr} may also involve a particular line friction force f_Γ proportional to ring velocity, which in turn causes a discontinuity $\delta(h\sigma_{rr})$ in the CC cluster stress when $w \rightarrow 0$:

$$\gamma_{rr}(R_c) - \frac{\Gamma}{R_c} = f_\Gamma, \quad \delta(h\sigma_{rr}) = -f_\Gamma + T_r(R_c)w \simeq -f_\Gamma \quad (3.67)$$

- For $r < R_c$, the central part of the CC cluster is not covered by the CAFs. Prior to bud formation, the central cluster is weakly deformed and does not directly exert stress on the actomyosin ring. The force balance in the CC cluster simply reads

$$\partial_r h\sigma_{rr}(r) + \frac{h\sigma_{rr}(r) - h\sigma_{\theta\theta}(r)}{r} = T_r(r) \quad (3.68)$$

The persistence of inward pointing traction forces after the ring has reached a stationary position (Fig. 3.20b) suggests an elastic description for the mechanics of CAFs and CC cluster, and an elastic-like interaction with the substrate[245]. For a 3D-incompressible elastic description of the CAF tissue characterised by a 2D elastic modulus $K_c \equiv E_c h_c$, the components of the stress tensor are related to the radial displacement $u_c(r)$ in the CAF layer according to:

$$\gamma_{rr}(r) = \gamma_\infty + \frac{2}{3}K_c \left[2\partial_r u_c(r) + \frac{u_c(r)}{r} \right], \quad \gamma_{\theta\theta}(r) = \gamma_\infty + \frac{2}{3}K_c \left[2\frac{u_c(r)}{r} + \partial_r u_c(r) \right] \quad (3.69)$$

where γ_∞ is the homeostatic contractile tension in the CAF tissue surrounding the cluster, far from the actomyosin ring. Further assuming an elastic interaction with the substrate: $T_r(r) = Y_s u_c(r)$ where Y_s is a static friction coefficient, the solution of Eq. 3.65 for the CAF displacement in the region $r > R_T$ is $u_c(r) \propto K_1(r/\lambda_s)$ where K_1 is a modified Bessel function, which leads to a spatial localisation of the substrate stress over a characteristic length scale $\lambda_s \equiv \sqrt{4K_c/(3Y_s)}$ [245]. This analytic solution is likely to be of limited validity in the present context, regarding the importance of spatial noise (Fig. 3.20b). However, the localisation of the traction forces outside the CC cluster is indeed observed with $\lambda_s \simeq 50 \mu\text{m}$, which suggests that the spatial derivative of the stress dominates the RHS of Eq. 3.65, Eq. 3.66, Eq. 3.68 (quasi 1D approximation). Similarly, a 3D-incompressible elastic description for the CC cluster with radial displacement $u(r)$ reads

$$h\sigma_{rr}(r) = \frac{2}{3}Eh^* \left[2\partial_r u(r) + \frac{u(r)}{r} \right], \quad h\sigma_{\theta\theta}(r) = \frac{2}{3}Eh^* \left[2\frac{u(r)}{r} + \partial_r u(r) \right] \quad (3.70)$$

This rheological choice seems appropriate when the CC cluster is a weakly deformed monolayer and builds a similar length scale $\propto \sqrt{Eh^*/Y_s}$. Note that a more advanced description would be required to include cellular rearrangements, especially during bud formation.

For the chosen CAF and CC constitutive equations, it is easy to prove that the horizontal stress gradient $\partial_r \gamma_{rr} + (\gamma_{rr} - \gamma_{\theta\theta})/r$ can be re-expressed as a total derivative $\frac{2}{3}\partial_r(\gamma_{rr} + \gamma_{\theta\theta})$. This "total" stress is written $\frac{2}{3}(\gamma_{rr} + \gamma_{\theta\theta}) \equiv \gamma_{\text{tot}}$ to simplify the notation. Thus, integration of Eqs. 3.65-3.68 gives a traction integral along a radial line, a measurable quantity, as a function of boundary stresses

$$\int_0^\infty dr T_r(r) = -h\sigma_{\text{tot}}[0] + h\sigma_{\text{tot}}[R_c|\text{free}] - h\sigma_{\text{tot}}[R_c|\text{covered}] + h\sigma_{\text{tot}}[R_T] - \gamma_{\text{tot}}[R_c] + \gamma_{\text{tot}}[\infty] \quad (3.71)$$

with the CAF pre-stress $\gamma_{\text{tot}}[\infty] = \frac{4}{3}\gamma_\infty$. To remain generic and simple, since we don't intend to solve the full set of spatio-temporal equations, one can further assume $\gamma_{rr} \simeq 2\gamma_{\theta\theta}$ or $\gamma_{\text{tot}} \simeq \gamma_{rr}$. This is formally valid when the length scale ratio R/λ becomes large¹⁹.

¹⁹The general solution for the deformation field $u(r)$ is a linear combination of Bessel functions $I_1(r/\lambda)$ and $K_1(r/\lambda)$, where $\lambda \propto \sqrt{Eh^*/Y}$ is the characteristic elastic length. Only the term $I_1(r/\lambda)$ is allowed on a convergent domain (disc) to ensure $u(r \rightarrow 0) \rightarrow 0$ whereas $K_1(r/\lambda)$ is used on a divergent one to get $u(r \rightarrow \infty) \rightarrow 0$. For inner radius R_0 delimiting the two domains, one can show that the strain ratio $\epsilon_r/\epsilon_\theta = (r/u)\partial_r u$ converges to r/λ on inner region and $-r/\lambda$ on outer region when $r \gg \lambda$. If $R_0 \gg \lambda$, this allows to ignore the $\epsilon_\theta = u/r$ contribution compared to $\epsilon_r = \partial_r u$ in the rheological equations Eq. 3.69 and Eq. 3.70. This finally leads to the stress equation $\gamma_{rr} \simeq 2\gamma_{\theta\theta}$ and $\gamma_{\text{tot}} \simeq \gamma_{rr}$.

Injecting the previous equation inside ring force balance equation (Eq. 3.67), with additional boundary condition $h\sigma_{rr}[R_T] = 0$ corresponding to an absence of CAF-CC interaction at the CC cluster periphery, and $\delta(h\sigma_{rr}) = h\sigma_{rr}[R_c|\text{covered}] - h\sigma_{rr}[R_c|\text{free}]$, one finally obtains the global force balance

$$\frac{\Gamma}{R_c} = \frac{4}{3}\gamma_\infty - \int_0^\infty dr T_r(r) - \gamma_b \quad \gamma_b = h\sigma_{rr}|_{r=0} \quad (3.72)$$

The LHS of this equation represents the force (per unit length) driving CAF closure and the RHS the forces resisting closure, which includes the CAF homeostatic tension γ_∞ , integrated traction stress, and the compression of the CC cluster on the central region. Since CAF are always able to climb on top of the cluster, one expects $\gamma_\infty \ll \Gamma/R_c \sim 10^{-2}$ N/m for $\Gamma \sim 1$ μ N and $R_c \lesssim 100$ μ m. The expression given for γ_b corresponds to the low deformation limit of Eqs.3.65-3.68. However, Eq. 3.72 remains valid when a cancerous bud forms in the central region of the CC cluster, provided the bud compressive stress $-\gamma_b$ is calculated by taking into account cellular rearrangement in the bud (see next section). Equivalently, one can multiply on both sides by the ring radius R_c to get $\Gamma = \Gamma_s + \Gamma_b$, expressing that a fraction of the total ring force Γ is sustained by substrate load (Γ_s) whereas the rest builds compression on the cancerous bud (Γ_b).

Traction force and closure dynamics

Eq. 3.72 may be seen as a dynamical equation for the evolution of the ring radius $R_c(t)$ as all the terms (apart from γ_∞) depend on time. The LHS of Eq. 3.72 clearly increases with time as the radius shrinks, so must the RHS. We may assume that the CAF tension far from the cluster γ_∞ remains constant over time, so the increase of the closure force must be compensated by either an increase of traction force or by an increase of the bud resistance to compression or by both. Fig. 3.20c shows the temporal evolution of the total traction force²⁰ with initial outward regime likely associated to CAF migration towards the CC cluster, outward-inward transition at $t = 7$ h, and clear saturation after $t = 16$ h around the value called $\Gamma_s \simeq 1.2 - 1.6$ μ N. Since $\Gamma = \Gamma_s + \Gamma_b$, this gives a lower bound for the ring line tension Γ .

In parallel to tractions, it is instructive to show the ring radius dynamics (Fig. 3.20d) where both quantities are normalized by their steady-state value. From the moment where the total traction force points inward at $t = 7$ h, two dynamical regimes can be distinguished. At earlier time (from 7 to 16 h), the closure dynamics is fast ($dR_c/dt = -3.3$ μ m/h) and corresponds to a linear increase of the inward traction force with time. At later time (16 to 27 h), the closure dynamics is slower ($dR_c/dt = -1$ μ m/h) and the traction force saturates to the value Γ_s .

The linear increase of inward traction force at short time is consistent with the increase of the driving force from the line tension Γ/R_c as the ring closes, although part of the increase of inward traction force must probably also be attributed to the decrease of active outward traction force from CAF migration. The fact that the traction force saturates while the ring is still closing is remarkable, and indicates a build-up of stress in the central cluster region that is eventually driving bud formation. In this regime, only a fraction of the driving force is compensated by the traction forces. The remaining driving force, the ring contractile force reduced by substrate load, must be equilibrated by the compression of the CC cluster: $\Gamma_b = \Gamma - \Gamma_s$. Thus, the CC cluster budding has a signature both in the closure dynamics and in the evolution of the traction force.

The saturation of traction force is weakly conserved among the full population of studied clusters ($N = 8$) as seen on Fig. 3.20e, but all of them have a simultaneous rupture of traction and ring dynamics indicative of bud compression. In fact, although the majority of CC buds remain mechanically stable over time as shown on Fig. 3.20f, with typical radius above 100 μ m or equivalent projected area above 30000 μ m², some buds seem unable to exert sufficient mechanical resistance and the CAF ring shrinks (Fig. 3.20f). The appearance of cell rearrangements and bud formation

²⁰The two alternative definitions $\int dr r T_r$ or $R_c \int dr T_r$ give similar results, which supports the approximation of localised tractions made to obtain Eq. 3.72.

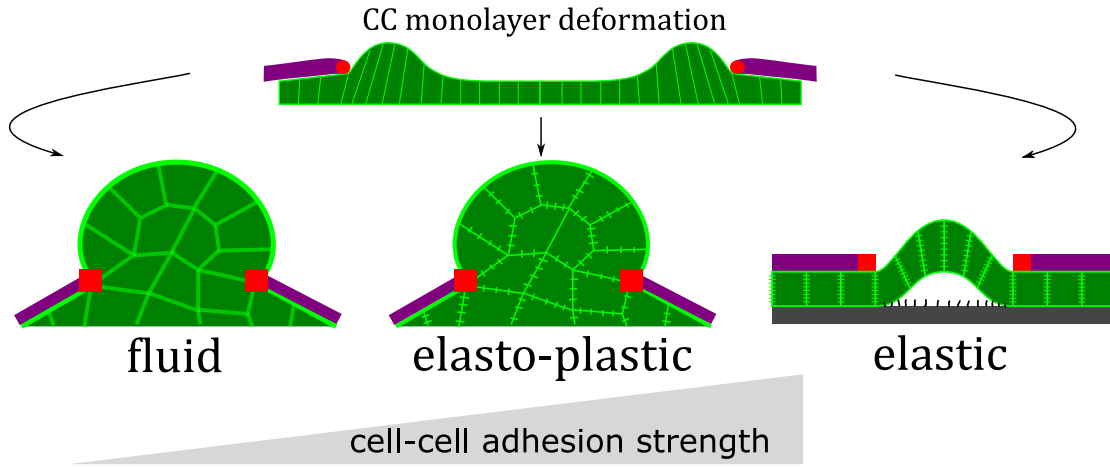


Figure 3.21: From early times, the picture of CAF-induced shear stress applied over a deformed CC monolayer (top) must account for the existence of a stable collective bud. As sketched here, the mechanics of cell-cell adhesion is an essential quantity of interest that can be captured by three limit regimes: fluid at long times with low penalty for cell-cell rearrangements (left), elasto-plastic if cell transitions are allowed only above a critical stress (center), and elastic if cell-cell adhesions cannot be broken (right). The third regime is not compatible with experimental observations since one does not observe CC cluster detachment from the substrate but multilayering transitions. The fluid regime provides only weak bud metastability and we have to incorporate elasto-plastic tissue rheology to account for bud mechanical stability at long times.

can be identified on those clusters with a clear rupture on ring dynamics as discussed before (red arrows on Fig. 3.20f), such that one expects a bud neck to form and be cut by CAFs at closure. In agreement with the biological phenomenon of tumour budding, one can talk about a full budding transition in that case where the bud detaches from the cluster body, the *in vitro* "primary tumour site". Of course, the later state is more likely to occur for small buds as the one imaged on Fig. 3.20g. On the contrary, large buds look like cylinders with small aspect ratio (large surface and small thickness) as seen on Fig. 3.20g, which appears to have higher mechanical stability. This stability is discussed in the next section.

3.7.2 Permeation model with yield pressure

Most cancerous buds remain stable over time (Fig. 3.20b,f) when directly compressed by the CAF ring, but this experimental observation is not straightforward from a theoretical perspective. Cancer cells cannot be considered to be rigidly connected as an elastic sheet because multilayering transitions are observed, resulting in a bud (Fig. 3.21). If cancer cells were fluid - allowed to exchange neighbours easily through 3D T1-like cell rearrangements - large buds would adopt a spherical shape because of apical surface tension, whereas experimental observations show that cylindrical geometry with small height-to-diameter ratio is more accurate. Even for small buds that look closer to a spherical shape, we checked that a fluid spherical cap with apical surface tension, compressed by a contractile ring, is marginally stable for both ensembles of constant bud volume and constant bud pressure as shown on Fig. 3.22a. The feed-back introduced by the curvature-sensitive ring compression tends to destabilize the tension balance at contact point and drive closure on top of the bud, with CC apical tension γ and CAF tissue tension γ_∞ dominated by CAF ring tension Γ/R_c . Therefore, a metastable state exists only for a reduced tension $\bar{g} \equiv \Gamma/(\gamma R) \lesssim 5$ with a weak stability range $\Delta\bar{g} \sim 1$. With CC apical tension $\gamma \sim 10^{-3}$ N/m and small bud radius $R_b \gtrsim 10$ μm , this requires a characteristic ring line tension $\Gamma \sim 0.01 - 0.1$ μN whereas it has been shown to be of the order of 1 μN . Lower apical tension makes it worse and larger buds cannot be assumed to have a spherical shape.

Finally, a last consequence of CC cluster fluidity would be the possibility of outward cell flow driven by the difference between the central bud pressure and the vanishing pressure at cluster periphery to empty the bud. Thus, even the weak metastability coming from tension balance could be non

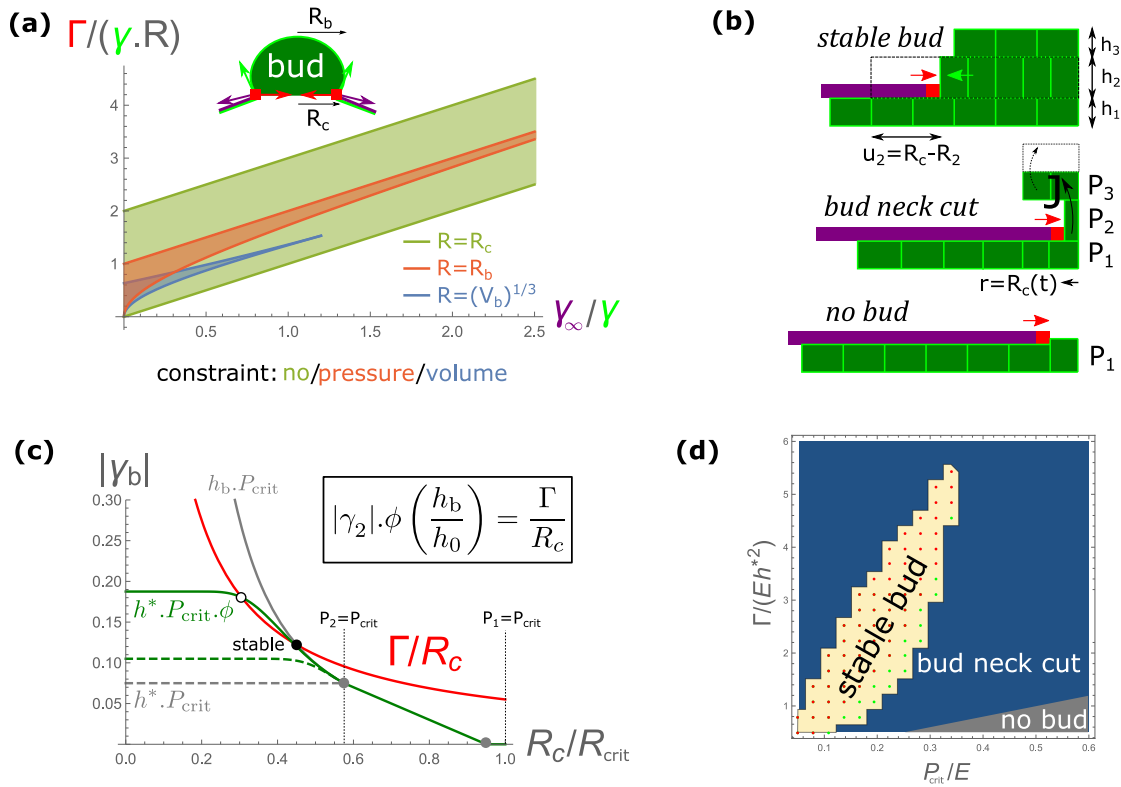


Figure 3.22: **(a)**: Stability range for different values of line tension Γ and CAF tissue tension γ_∞ . The green region corresponds to local tension balance between CC apical tension γ , CAF tension γ_∞ and ring tension Γ/R_c . Ensembles of constant bud pressure $P_b = \gamma/R_b$ (red) or constant bud volume V_b (blue) adds an extra constraint that fixes the range of the leading edge radius R_c over which tension equilibrium is metastable. **(b)**: Sketch of the system in the picture of a multi-layered permeation model, where pressure difference $P_i - P_j$ controls the transfer of cells between layers. Those multilayering transitions are assumed to be activated above a critical pressure P_{crit} with surface flux $J_{i \rightarrow j} = \alpha(|P_i - P_j| - P_{crit})$. The CC pressure comes from the centripetal shear exerted by CAFs through line friction ζ and induces tissue compression, triggering new layers formation at $P_1 > P_{crit}$. The second layer directly resists CAF ring tension and can stabilize the bud (top) or transfer cells to adjacent layers, eventually leading to the cut of the bud neck by CAFs (middle). CAF closure on top of the CC monolayer occurs when the second layer cannot form and no bud appears (bottom). **(c)**: Tension balance at the CAF-CC contact point between the CAF-induced compression (red) and the bud elastic resistance (green), as a function of CAF edge radius R_c . The shear-transmitted resistance from the adjacent layers to the second layer is captured by a shape factor $\phi = 1 + b \tanh[(h_b/h^* - 1)/b]$ (see text). At the beginning ($R_c = R_0$), no direct compression resists CAF closure, then second layer builds at $P_1 = P_{crit}$, is compressed up to $P_2 = P_{crit}$ and eventually builds more layers. The system can either stabilize at steady-state (green) or let CAFs close (green,dashed) if bud resistance is too weak. The parameter b contains cell-cell linker stiffness, which cannot resist CAF closure when vanishing (gray,dashed) whereas the infinite limit ensures global stress transmission and bud stability with $\phi = h_b/h^*$ (gray). **(d)**: Phase diagram as a function of reduced yield pressure P_{crit}/E and reduced line tension $\Gamma/(Eh^*2)$. A stable bud occurs only for small values of both parameters (yellow region) and can contain two layers (green dots) or more than two (red dots). Otherwise, CAF compression triggers cell flow out-of-second layer and cut the bud neck (blue region), or CAF closure occurs on top of the CC monolayer when multilayering is triggered too late (gray region). This phase diagram is dependent on the choice of line friction ζ for the mode of CAF-induced shear stress, compared to a CAF-CC surface friction ξ . Parameters used are $E_c = 0$, $b = 1.5$, $\alpha = 0.5h^*/\zeta$ and $l^* = 20 \mu\text{m}$.

sufficient to ensure bud stability. CAF or CC induced static shear stress, identified experimentally by tractions below the CC cluster Fig. 3.20b, could (or not) build a sufficient pressure gradient to eliminate this flow. This indicates that tissue fluidity may be a key component of the budding fate, and is naturally expected to depend on E-cadherin mechanosensitivity with either strengthened or weakened cell-cell adhesions under mechanical stress (Fig. 3.21).

In addition to CC budding, one also observes a phenotype where CAFs close on top of the CC cluster (data not shown), associated to weak shape variations of the CC tissue. Compared to the initial monolayer state of the CC cluster, those weak perturbations are expected to be a purely elastic response to the mechanical stress exerted by the closing CAFs. Nonetheless, if not fluid, the CC cluster cannot be reduced to an elastic rheology because the generation of the bud relies on discrete cell rearrangements. A solid material that can either respond elastically or undergo structural re-organisation depending on the external applied stress is plastic. To account for both experimental phenotypes, CAF closure and CC budding, we introduce a yield pressure P_{crit} that describes phenomenologically the amount of compressive stress necessary to trigger multilayering events. This corresponds to an elasto-plastic rheology (see Fig. 3.21).

Dynamically, we assume the following picture: CAFs first climb on top of a CC monolayer and exert a shear stress upon gap closure, which induces indirect CC cluster compression later followed by bud initiation above the yield pressure, and finishes on a mechanical equilibrium between ring compressive force and bud resistive force (Fig. 3.22b,top). Interestingly, only a fraction of the bud is in direct compression, and the pressure exerted by the ring could induce cell rearrangements away from this region if above the yield value. With the geometric feed-back of ring tension Γ/R_c , it is easy to imagine an unstable mechanical equilibrium leading to bud neck cut (Fig. 3.22b,middle). If one attenuates the shear stress between the two tissues by making them mechanically disengaged, CAFs would just close the gap (Fig. 3.22b,bottom) as if the substrate was non-adherent [229]. Hence, the CAF-induced shear stress acts as a mechanical source of compression that drives plastic tissue reorganization through a yield effect, which leads to the generation of a bud through transverse plastic flow. Thus despite a curvature-sensitive CAF ring tension, the observation of bud mechanical stability makes the tissue inherently solid, with elastic behaviour as long as cell rearrangement costs remain below the plastic threshold.

To highlight the main features, we perform a number of simplifying assumptions that can easily be removed to get better quantitative accuracy, which is not our target here. First, we use the previously defined CC elastic rheology Eq. 3.70 but describe implicitly the mechanical transmission of compression from layer 2 to other layers²¹, in analogy with the standard problem of elastic pillar deformation induced by a collar pressure [256]. Second, we neglect substrate tractions observed on the bottom layer since they tend to decrease or even vanish at steady state and should not be essential for the equilibrium properties (Fig. 3.20b). Third, we also neglect the CAF elasticity defined through Eq. 3.60 because the contractile ring necessarily overcomes the CAF tissue resistance in control conditions, and our previous analysis is consistent with a leading edge arrest coming from bud elastic resistance to compression. Fourth, we ignore the apical tension that induces local shape variations on a characteristic length scale $\lambda \equiv \sqrt{\gamma h^*/E} \sim 1 - 10 \mu\text{m}$ for a CC elastic modulus $E \sim 0.1 - 10 \text{ kPa}$ [253].

All those neglected features may contribute secondarily to the extent of budding stability but are unlikely to be the main component. This allows us to focus only on the solid bud resistance and the constraints imposed by the yield pressure mechanism.

To remain generic, we neglect the complexity of the cell organization inside the bud and assume that cells stack on discrete layers (see Fig. 3.22b). In agreement with the previous section, we

²¹More explicitly, one could add a shear stress condition $\sigma_{rz} = Y_{CC}(u_i - u_j)$ between layers i and j where Y_{CC} is an effective stiffness quantifying the cell-cell adhesion strength under shear. Other boundary conditions for each layer would be $u_i = 0$ at $r = 0$ by rotational invariance and $\sigma_{rr} = 0$ at the periphery of top layers, whereas the second layer verifies $h\sigma_{rr}^{(2)} = \Gamma/R_c$. This expression couples the deformation mechanics of different layers and analytical solutions are only available for a thin film theory in 2D (rectangle geometry) but not in 3D (cylinder geometry).

assume for convenience that the mechanical coupling between the CAFs and the first CC layer is dominantly localized at the ring through a dynamical friction with coefficient ζ . Upon closure and before multilayering, the dynamics is set by force balance between the driving ring tension Γ/R_c , the CAF tissue tension γ_∞ and the dissipation ζV_c with $V_c \equiv -dR_c/dt > 0$: $\zeta V_c = \Gamma/R_c - \gamma_\infty$. Since dissipation corresponds to a CAF-CC mechanical interaction, CAFs apply a frictional shear stress $\sigma_{rz} = \zeta V_c$ on top of the CC cluster near the ring, responsible for mechanical pressure P_1 in the CC monolayer. The time increase of CAF velocity amplifies the CC monolayer compression, up to the point where the pressure P_1 reaches the yield value P_{crit} that triggers multilayering. The second layer first freely develops on the uncovered CC region but rapidly encounters the CAF leading edge to apply direct elastic resistance on the ring (see Fig. 3.22c). The force balance at contact point $r = R_c$ becomes

$$\zeta(V_c - v_1) = \frac{\Gamma}{R_c} - \gamma_\infty + \gamma_2 \quad (3.73)$$

where $v_1 > 0$ is the inward velocity of the bottom layer resulting from the out-flux of cells, and $\gamma_2 < 0$ the compressive radial tension exerted by the second layer.

Cells can transversely flow between layers according to the pressure difference as long as it reaches the yield pressure P_{crit} , and we assume for simplicity that the threshold value for layer-to-layer or layer-to-medium transitions are the same. This permeation model is inspired from a previous work on the spreading of aggregates [257], at the difference that a yield stress parameter is introduced to phenomenologically account for the energy barrier associated to the layer-to-layer transition. With individual cells assumed to be incompressible, each layer's volume can change only through the transverse velocity flux (volume/surface of contact/time)

$$J_{i \rightarrow j} = -J_{j \rightarrow i} = \alpha (|P_i - P_j| - P_{\text{crit}}) \quad \text{if} \quad |P_i - P_j| \geq P_{\text{crit}} \quad (3.74)$$

expressing that cells will be transferred from layer i to layer $i - 1$ or $i + 1$ if the pressure difference $|P_i - P_j|$ is above the threshold value P_{crit} with $P_i > P_j$. For a cylindrical layer i of thickness h_i and radius R_i , its volume $V_i = \pi h_i R_i^2$ changes according to the in-flux from layer $i - 1$ and out-flux from layer $i + 1$, and reads $d_t V_i = \pi R_i^2 (-J[i \rightarrow i + 1] + J[i - 1 \rightarrow i])$ with the assumption of identical surface of contact πR_i^2 between layers $\{i - 1, i, i + 1\}$ for simplicity.

For a unique monolayer or the top layer under pressure P , bottom-up directed flow also occurs with $P_i = P$ and $P_j = 0$ in Eq. 3.74. Because a pressure increase to P_{crit} at layer i induces an out-flux in a relaxed environment, the number of cells (volume) of that layer is decreased, followed by a pressure release. If the compressive source remains on that layer, the pressure will oscillate around $P = P_{\text{crit}}$ with characteristic time h^*/J where h^* is the layer thickness, with a loss of cells that could end into layer disappearance. For the CC cluster, the second layer is under direct compression by the actomyosin ring and can either sustain the CAF pressure by combination of multilayering events and elastic resistance, or transfer all its cells to adjacent layers and let the CAFs cut the bud neck and close (see Fig. 3.22b,c).

Although the second layer is directly compressed by CAFs, its mechanical connexion to adjacent layers adds a supplementary resistance that modifies the γ_2 term in Eq. 3.73. To quantify this stress propagation effect, we introduce a generic shape factor ϕ depending on the ratio between the total bud thickness h_b and the free monolayer height h^* . The total bud tension γ_b resisting ring compression is written as $\gamma_b = \gamma_2 \phi(h_b/h^*)$, where $\gamma_2 \equiv h^* \sigma_{rr}^{(2)}$ is the tension associated to an "isolated" layer ($h_b = h^*$). Indeed, we checked using finite-element method that the stress response of an elastic pillar (radius R and height h) to an imposed radial displacement δR over a size $\Delta z = h^*$ has a shape factor which can be approximated as $\phi(h/h^*) = 1 + b \tanh[(h/h^* - 1)/b]$ with $b \simeq 0.3$. It equals 1 when pillar deformation is uniform along monolayer height ($h = h^*$) and induces a supplementary resistance through the multiplicative factor $1 + b$ when the pillar is much taller than the compressed region ($h \gg h^*$). Contrarily to a uniform elastic material, the uniaxial elastic stiffness of a CC monolayer (cytoskeleton) may differ from the shear resistance between adjacent layers (cell-cell adhesion), and the propagation factor b can be considered as a free parameter. Indeed, if the stiffness of cell-cell linkers was infinite ($b \rightarrow \infty$), all layers would be

forced to follow the displacement of the compressed layer 2, such that in this limit case $\phi = h_b/h^*$: the total resistive tension is integrated along z and tension balance would read $h_b\sigma_{rr}^{(2)} = -\Gamma/R_c$ at steady-state.

When plastic flow modifies the number of cells on one layer from N_i to N_f , the reference configuration used to define elastic displacements evolves from $(R_i \simeq l^*\sqrt{N_i}, h^*)$ to $(R_f \simeq l^*\sqrt{N_f}, h^*)$, because individual cells keep their preferred height h^* and preferred width l^* . Calling $R_2(t)$ the instantaneous reference radius of the second layer, its compression by the CAF ring defines a radial displacement $u_2(t) = R_c(t) - R_2(t) < 0$ as shown on Fig. 3.22b,top. The linear rheology defined on Eq. 3.70 remains valid because high pressure is relaxed by a decrease of R_2 thanks to the yield mechanism. Thus, the second layer alternates between phases of direct elastic compression and plastic cell rearrangements that release the stress. Since the stress gradients associated to the mechanical coupling between adjacent layers are already captured effectively by the shape factor ϕ , we can consider uniform compression with radial elastic stress

$$\sigma_{rr}^{(2)}(t) = \frac{2E}{R_2(t)} [R_c(t) - R_2(t)] \quad (3.75)$$

If the plastic flows can be considered instantaneous with respect to the CAF closure time scale²², one has the quasi-static equation $\gamma_2 \simeq -h^*P_{\text{crit}}$ relating linearly $R_2(t)$ to $R_c(t)$ thanks to Eq. 3.75. In parallel, the addition of $n(t)$ new layers transforms the preferred bud height to $h_b(t) \equiv [n(t)+1]h^*$ and relates to R_2 by volume incompressibility. For example, n layers with reference radius R_2 give $h_b \propto 1/(R_2)^2 \propto 1/(R_c)^2$.

As a consequence, the tension balance $\gamma_\infty - \gamma_b = \Gamma/R_c$ defines a unique stable equilibrium for the limit case where the load is shared on all layers (infinite cell-cell linker stiffness: $b \rightarrow \infty$) as indicated on Fig. 3.22c (gray). On the opposite, if the cell plastic flows in the second layer were followed by a loss of layer-to-layer cell attachment ($b \rightarrow 0$) as in the phenomenon of cell extrusion [188], tension balance would be reduced to $\gamma_\infty + h^*P_{\text{crit}} = \Gamma/R_c$. Since the quantity h^*P_{crit} is also the bottom layer tension that triggers the creation of the (still uncompressed) second layer, the monotonic ring tension Γ/R_c should dominate bud resistance for any R_c as shown on Fig. 3.22c (gray dashed): CAFs undergo closure with CCs eliminated in the medium. In this limit case $b \rightarrow 0$, one also expects the yield pressure P_{crit} to be associated to basal cell attachments rather than cell-cell adhesion, such that $P_{\text{crit}} \simeq P_{\text{crit}}[\text{basal}]$ and $P_{\text{crit}}[\text{cell-cell}] \simeq 0$. In fact, this behaviour is the opposite of what is believed to happen for the experimental CAF-CC system, where basal cell detachment can be triggered without apparent cell-cell ruptures: $P_{\text{crit}}[\text{cell-cell}] \gg P_{\text{crit}}[\text{basal}]$.

Under a more realistic situation, a shape factor $\phi = 1 + b \tanh[(h_b/h^* - 1)/b]$ limits bud resistive tension $|\gamma_b| = -\gamma_2\phi$ to a maximal value $h^*P_{\text{crit}}(1 + b)$ that defines three phenotypes according to the parameter values (Fig. 3.22c): bud neck cut, stable bud with two or more layers, and CAF closure over a monolayer (no bud). This is summarized on Fig. 3.22d with a phase diagram as a function of reduced yield pressure P_{crit}/E and reduced line tension $\Gamma/(Eh^2)$.

If Γ is larger than the critical value $h^*R_0P_{\text{crit}}(1 + b)$, the ring tension is above the maximal bud resistive tension at the beginning of CAF closure when $R_c = R_0$ and any forming bud will be cut by CAFs. The line tension threshold at which a stable bud is possible can be found numerically and is necessarily below the critical value $h^*R_0P_{\text{crit}}(1 + b)$. If P_{crit} is too small for given Γ , the multilayering transition is rapidly triggered but the bud does not apply a sufficiently high resistance to equilibrates the ring compression; the second layer loses its cells until the neck is cut by the CAF ring. If P_{crit} is too large for given Γ , the multilayering transition occurs too late to build

²²The permeation coefficient α in Eq. 3.74 corresponds to the dissipation coming from the shear stress between the permeating cell and its neighbours, and can be related to a transverse viscosity η_t such that $\alpha \equiv h^*/\eta_t$. With CAF closure time scale $\tau_c \equiv \zeta(R_0)^2/\Gamma$ and plastic flow time scale $\tau_p \equiv \eta_t/P_{\text{crit}}$, the quasi-static approximation relies on $\tau_p \ll \tau_c$ or $\eta_t \ll \zeta.P_{\text{crit}}(R_0)^2/\Gamma$. For ring line friction $\zeta \sim 10^7$ Pa s, yield pressure $P_{\text{crit}} \sim 1 - 10$ kPa, initial CC cluster radius $R_0 \sim 100$ μm , and ring line tension $\Gamma \sim 1$ μN , one gets the inequality $\eta_t \ll 10^8 - 10^9$ Pa s. Equivalently in terms of transverse friction coefficient $\xi_t \equiv \eta_t/h^* \ll 10^{13} - 10^{14}$ Pa s/m, the inequality is compatible with values found for tissue-tissue friction [240] or tissue-substrate friction [242].

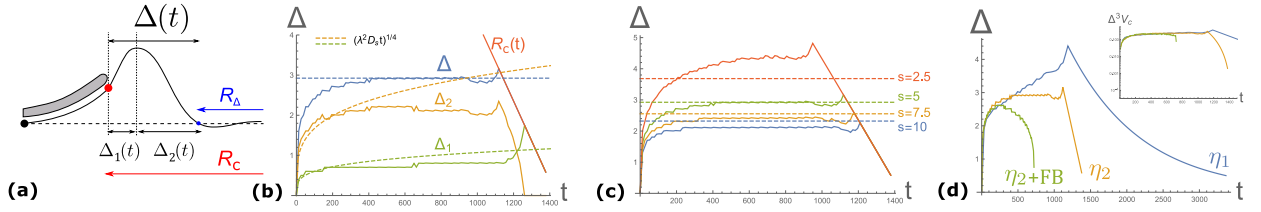


Figure 3.23: **(a)**: Sketch of the rim induced by CAF-shear stress that drives the convergent flow of the CC cluster periphery (black dot), with left width $\Delta_1(t)$ close to the CAF ring (red dot) and right width $\Delta_2(t)$. The total rim width $\Delta(t)$ is defined with the condition $h(R_c - \Delta) = 1$ (blue dot) and is the sum of those two contributions. **(b)**: Evolution of the rim width Δ as a function of time, showing the left width Δ_1 and the right width Δ_2 , both scaling like $(\lambda^2 D_s t)^{1/4}$ at early times with a different pre-factor. Both Δ_1 and Δ_2 saturate around the value $\propto (\lambda^2 D_s / V_c)^{1/3}$ with different pre-factor (blue dashed for Δ). Finally, the deformation reaches the center and $\Delta(t) = R_c(t)$ (red). Here, V_c is approximately constant (η_2 dominant scenario), $c = 0.1$ and $s = 5$. **(c)**: Evolution of the rim width Δ as a function of time, for different values of reduced substrate friction s . The dashed lines correspond to the scaling $\Delta \propto (\lambda^2 D_s / V_c)^{1/3} \propto s^{-1/3}$ at steady-state, where $s = 5$ (b) is used as a reference for the pre-factor. Here, V_c is approximately constant (η_2 dominant scenario) and $c = 0.1$. **(d)**: Evolution of the rim width for CAF closure dynamical regimes showing inverse correlation between Δ and V_c : $V_c \propto R_c$ (η_1 dominant scenario), constant V_c (η_2 dominant scenario) or $V_c \propto 1/R_c$ (η_2 dominant scenario) and line tension Feed-Back (FB) scenario). The factor $\Delta^3 V_c$ is shown to test the scaling $\Delta \propto (\lambda^2 D_s / V_c)^{1/3}$ for different CAF closure dynamics laws in log-linear scale (inset). For all graphs, the flat covered limit has been used (see below), $k = \gamma = 0.01$, $\gamma_\infty = 0$, and $R_0 = 15$.

sufficient bud resistance: the CAF edge curvature is so high that the rate of ring tension ($\propto 1/R_c^2$) increases too fast and overcomes the high resistive pressure $h^* P_{\text{crit}}(1 + b)$. In addition, although the multilayering transition always exists for $R_{\text{crit}} = \Gamma / (h^* P_{\text{crit}})$, it is natural to introduce a length cut-off $l^* \sim 10 - 20 \mu\text{m}$ such that CAFs close on top of a CC monolayer when $R_{\text{crit}} < l^*$ or $P_{\text{crit}} > \Gamma / (h^* l^*)$ (gray region on Fig. 3.22d). Thus, bud stability occurs only on a parametric region where both ring line tension and yield pressure are sufficiently small, and can be enhanced with an increase of CC elastic modulus E or effective parameter b . Depending on the respective values of those two parameters for fixed Γ and P_{crit} , the bud can stabilize with only 2 layers or build other ones as shown on Fig. 3.22c.

From the estimation $\Gamma \sim 1 \mu\text{N}$ obtained in the previous part and $h^* \sim 10 \mu\text{m}$, one can evaluate a stability range for the reduced parameters on the phase diagram (Fig. 3.22d) to extract orders of magnitude for CC elastic modulus and yield pressure: one gets $E \sim 2 - 10 \text{ kPa}$, a reasonable range of values for cancer cells [253], and $P_{\text{crit}} \sim 500 - 2000 \text{ Pa}$. Moreover, the steady-state tension balance $|\gamma_b| = \Gamma / R_c$ gives a typical bud size $R_c \sim 10 - 50 \mu\text{m}$ if one takes $|\gamma_b| \sim E h^* \epsilon_2$ with typical strain $\epsilon_2 \sim 0.1$, and $R_c \sim 20 - 50 \mu\text{m}$ with $|\gamma_b| \sim h^* P_{\text{crit}}$.

One key biophysical structure affecting the budding fate appears to be cell-cell adhesion. When one is allowed to model it with elastic linkers, an increase of their stiffness is expected to affect both model parameters b and P_{crit} and could favour or inhibit bud stability. Thus, under this framework of elasto-plastic response to external stress, a more detailed modelling would be necessary to understand how cell-cell adhesion mechanics modulate the bud response to CAF compression. Note that this modelling approach is sensitive to the curvature-dependent hypothesis for the ring tension, and the dissipative factors that physically prevent an infinite tension when the edge radius closes may also help bud stability.

3.8 Results: CC cluster deformation dynamics

3.8.1 Rim width scaling

On the CAF-free region, the growth PDE for height deformation field δh contains diffusive terms that dictate the spatial propagation of deformation from a given position, with diffusion coefficient $D_s \equiv k h^{*2} / \xi_s$, and tension-dependent terms that build additional localization of deformation over

the scale $\lambda \equiv \sqrt{\gamma/k}$ because of surface tension γ . It reads

$$\partial_t \delta h \simeq D_s \left\{ \left[2 - \frac{\lambda^2}{r^2} \right] \frac{\delta h'}{r} + \left[2 + \frac{\lambda^2}{r^2} \right] \delta h'' - \lambda^2 \left[\frac{2\delta h^{(3)}}{r} + \delta h^{(4)} \right] \right\} \quad (3.76)$$

If the substrate friction ξ_s contained in D_s is non-zero, the rim is localized in space over a finite width Δ as sketched on Fig. 3.23a. The maximal deformation separates the rim into a left part with width Δ_1 and a right part with width Δ_2 , such that $\Delta = \Delta_1 + \Delta_2$. For given parameters, the rim width typically evolves in three distinct phases according to Fig. 3.23b. First, an initiation phase with sub-diffusive growth for Δ_1 and Δ_2 . Then, the rim width saturates into a steady-state regime and finally, the deformation propagates to the center and the rim width simply converges to the CAF ring radius $R_c(t)$. To quantify the rim width, note that there is some arbitrariness in the definition of the size Δ : we consider the point R_Δ at which $h = 1$ (see Fig. 3.23a), starting from the CAF ring radius R_c with deformation $\delta h_c \geq 0$.

Ignoring the transverse curvature ($|\delta h''| \gg |\delta h'|/r$), formally valid when $r \rightarrow \infty$, the growth equation on the CAF-free region Eq. 3.76 reduces to

$$\partial_t \delta h \simeq D_s \left[2\delta h'' - \lambda^2 \delta h^{(4)} \right] \quad (3.77)$$

At early times, one writes $\partial_t \delta h \sim \delta h/t$ with $\delta h \sim \exp(-qr)$, leading to the characteristic equation²³

$$D_s t q^2 (\lambda^2 q^2 - 2) \simeq 1 \quad (3.78)$$

For $\sqrt{D_s t} \ll \lambda$, the second term on the left-hand side is negligible and one gets a sub-diffusive regime $q^{-1} \sim (\lambda^2 D_s t)^{1/4}$. This matches well the early evolution for rim width Δ (Fig. 3.23b).

For $\sqrt{D_s t} \gg \lambda$, the first term on the left-hand side is negligible and one gets a diffusive regime $q^{-1} \sim \sqrt{D_s t}$. In fact, this only matches the right rim width Δ_2 on a small time interval, and $q^{-1} \sim (\lambda^2 D_s t)^{1/4}$ with a different pre-factor appears equally valid as shown on Fig. 3.23b.

At longer times, one can assume a quasi-static approximation in the moving frame of velocity $\dot{R}_c(t) \equiv -V_c$ and coordinate $z = r - R_c(t)$, where $\delta h(r, t) \equiv H(z, t)$. Assuming $\partial_t H \simeq 0$ such that $H \sim \exp(qz)$, the characteristic equation reads

$$V_c q \simeq D_s q^2 (2 - \lambda^2 q^2) \quad (3.79)$$

Without boundary transport ($V_c = 0$), the deformation spreads over the entire CAF-free region with shape relaxation over the characteristic length $q^{-1} = \pm \lambda/\sqrt{2}$. If V_c remains small compared to D_s/λ , one gets $q^{-1} \simeq \{2D_s/V_c, \pm \lambda/\sqrt{2}\}$ with $\lambda \ll D_s/V_c$.

On the contrary for larger V_c ($V_c \gg D_s/\lambda$), one gets

$$q \simeq \left(\frac{V_c}{D_s \lambda^2} \right)^{1/3} \left\{ -1, \frac{1}{2} (1 \pm i\sqrt{3}) \right\}, \quad \text{with} \quad \Delta_c \equiv \left(\lambda^2 \frac{D_s}{V_c} \right)^{1/3} \quad (3.80)$$

The convergent CAF-free region prevents the exponential term $\exp(+z/\Delta_c)$ and one gets damped oscillations over the characteristic length Δ_c . Indeed, the rim width Δ seems to saturate around this value (see Fig. 3.23b). Similarly, an independent variation of reduced substrate friction $s \equiv \xi_s/\xi_0$ for given V_c and R_0 (Fig. 3.23c) shows compatibility with $\Delta \sim \Delta_c$ since values at steady-state scale like $\propto s^{-1/3}$. Finally, different CAF closure laws $V_c(R_c)$ also affect the steady-state value of the rim width for given s and R_0 (Fig. 3.23d): $\Delta \sim \Delta_c$ predicts $\Delta^3 V_c$ to be independent from the chosen law, which is indeed observed in the saturation phase.

²³It is formally equivalent to a Laplace transform of variable s where $\phi(r, s) \equiv \int_0^t \delta h(r, t) \exp(-st)$ is applied on Eq. 3.76. This defines a characteristic equation for $\phi(r, s) \sim \exp(-qr)$ parametrized by s , which is converted to the real time space by the reverse mapping $s \mapsto 1/t$.

Dimensional parameters	geometric= (h^*, R_0) mechanical= $(k, \gamma, \Gamma, \gamma_\infty)$ dissipative= $(\eta_1, \eta_2, \xi, \xi_s)$
Adimensional scaling	length $[L] = h^*$, force $[F] = \Gamma$, time $[t] = \xi_0 h^{*3} / \Gamma$
Dimensionless parameters	same symbol $(R_0, k, \gamma, \gamma_\infty, \eta_1, \eta_2)$ and $c \equiv \xi / \xi_0$ and $s \equiv \xi_s / \xi_0$

Table 3.2: Summary of the dimensional and dimensionless parameters.

A more detailed analysis shows that the rim width Δ slightly increases with k in the plateau phase, whereas the product $\lambda^2 D_s$ in Δ_c should not. Indeed, it appears that a rim width $\Delta \sim \sqrt{\lambda D_s / V_c}$ with scaling $\propto \sqrt{k/s}$ gives equally good results compared to Fig. 3.23b,c,d. This deviation is likely related to a small error introduced by the quasi-static approximation, the choice for numerical estimation (Fig. 3.23a), and the difference between left ($h = h_c$) and right height ($h = 1$) that affects Δ_1 and Δ_2 differently. However, it is hard to derive $\Delta \sim \sqrt{\lambda D_s / V_c}$ from the growth equation Eq. 3.76. Since both choices give similar results except for this slight k dependency and the former $\Delta = \Delta_c$ can be explicitly derived, we focused on this first choice. For the substrate friction dependency, all the arguments presented below remain valid for $s^{-1/3}$ or $s^{-1/2}$.

To summarize, the parameters used on Fig. 3.23, representative of the results discussed in this chapter, are compatible with steady-state scaling values $\Delta_1 \sim \lambda$ and $\Delta_2 \sim \Delta_c$ for rim width. Despite its limitations, this primitive analysis is able to determine the appropriate rim behaviour as shown by Fig. 3.23b,c,d.

3.8.2 Results on CC shape dynamics

We now solve the full set of equations over the two evolving domains $0 < r < R_c(t)$ (CAF-free region) and $R_c(t) < r < R_T(t)$ (CAF-covered region). We assume that a critical deformation of CCs is necessary to trigger the multilayering transitions responsible for the budding phenotype. Then, we search for the maximal height $h_{\max} = \text{Max}[h(r, t), r]$ on the CAF-free region, and how it evolves over time. One striking experimental feature is the correlation of budding frequency and size with initial cluster size R_0 . Our goal is to identify the theoretical properties necessary to reproduce this feature. We place ourselves in the scenario where multilayering is causally related to budding such that budding likelihood is directly related to the value of h_{\max} . For a critical height h_{crit} , we expect budding to occur if $h_{\max}(t) \geq h_{\text{crit}}$ exists for a given time $t = t_{\text{crit}}$. For the rest of this chapter, only dimensionless quantities are used, with normalization based on the CC natural height h^* for length, the line tension Γ for force and a generic friction coefficient ξ_0 that builds a time scale $\xi_0 h^{*3} / \Gamma$, as shown on table 3.2.

As shown in the previous section, several parameters can influence rim geometry and hence the maximal height h_{\max} , notably the substrate friction with reduced value s or CC mechanical parameters through the length λ . In addition, the CAF velocity V_c influences both the source of deformation - the CAF-induced frictional shear stress applied on the top CC surface $\sigma_{rz}(r) = c[v_c(r) - v_r(r)]$ - and the rim localization through the CAF radius-dependent width $\Delta(R_c)$. Therefore, the choice of the dominant dissipation mechanism and the possibility of feed-back on line tension $\Gamma = \Gamma_0(R_c/R_0)^x$ will affect the mechanical response of the CC monolayer, in particular through the correlation between maximal height h_{\max} and cluster size R_0 . In line with a previous analysis in the model section on CAF closure dynamics, we distinguish 3 "CAF dynamics scenarios":

- constant line tension with dominant ring viscosity, such that $2\eta_1 V_c = R_c(1 - \gamma_\infty R_c)$ in absence of CAF-CC interaction whereas tissue viscosity is ignored ($\eta_2 = 0$); CAF closure occurs with exponential relaxation for negligible CAF rest tension (Fig. 3.24a),
- constant line tension with dominant CAF tissue viscosity, such that $2\eta_2 V_c = 1 - \gamma_\infty R_c$ in absence of CAF-CC interaction whereas ring viscosity is ignored ($\eta_1 = 0$); CAFs close linearly in time for negligible CAF rest tension (Fig. 3.25a),

- a positive Feed-Back (FB) on line tension ($\Gamma = R_0/R_c$) with dominant CAF tissue viscosity, such that $2\eta_2 R_c V_c = R_0 - \gamma_\infty (R_c)^2$ in absence of CAF-CC interaction whereas ring viscosity is ignored ($\eta_1 = 0$); CAFs close with constant areal velocity for negligible CAF rest tension (Fig. 3.26a)

In all cases, viscous parameters are chosen so that the initial CAF velocity is the same. In particular for the FB case, the initial line tension is identical to the other scenarios ($\Gamma_0 = 1$). Although the FB on line tension seems artificial, it has already been suggested for epithelial closure on non-adhesive patches [229]. In fact, it is clearly required to reproduce the experimental CAF closure dynamics in N-cadh KD conditions, showing a constant decrease of gap area.

We first consider that CAF rest tension can be neglected ($\gamma_\infty = 0$) and study the evolution of various quantities to characterise the CAF closure dynamics and the CC monolayer deformation. The evolution of CC height profile in time and space on Fig. 3.24a, Fig. 3.25a and Fig. 3.26a with CC peripheral radius R_T and CAF ring position ($r = R_c, z = h_c$). A rim does not exist with ring viscosity (Fig. 3.24a) because the surface tension is the same on CAF-free and CAF-covered regions. On the contrary, the surface viscosity increases the CAF tension by adding the term $\gamma_{rr} = 2\eta_2 V_c / R_c$, such that the slope discontinuity induces a localized rim as seen on Fig. 3.25a and Fig. 3.26a. Whereas CAFs close on top, the CAF-induced shear stress applied on the CAF-covered region ($R_c < r < R_T$) drives convergent flow of the CC monolayer with transport of the peripheral radius R_T , leading to an out-of-plane deformation due to incompressibility.

For relatively high CAF-CC friction $c = 0.5$, closure dynamics significantly deviates from the case where CAF-CC interaction is absent ($c = 0$) in all scenarios (Fig. 3.24b, Fig. 3.25b, Fig. 3.26b). Initial CAF velocity is the same but CAF closure takes longer for ring viscosity (Fig. 3.24b and is shorter for line tension FB (Fig. 3.26b).

More interesting is the evolution of the maximal height h_{\max} : whereas $V_c \propto R_c$ generates a positive correlation between the deformation amplitude and cluster size (Fig. 3.24c), it becomes anti-correlated when CAF tissue viscosity dominates, for either constant line tension ($V_c \propto 1$) on Fig. 3.25c) or with FB ($V_c \propto 1/R_c$) on Fig. 3.26c. For a deformation criterion based on a critical height h^* that triggers a multilayering transition, one can see that the correlation between h_{\max} and R_0 is necessary to reproduce the experimental observations that budding frequency increases with cluster size. Hence, for negligible CAF rest tension, only the first case with ring viscosity seems compatible (Fig. 3.24c).

A rim is characterised by its height $h_{\text{rim}} \equiv h_{\max} - h_c$ where h_c is the CC height below the CAF ring at $r = R_c$, as shown on Fig. 3.24a. In all cases, the assumption of negligible CAF rest tension allows large deformations on the CAF-covered region and one has h_c close to h_{\max} . One can detect the rim localization with the late transmission of deformation to the CC cluster center of height h_0 , remaining fixed to 1 until the rim propagates to the central cells at $r = 0$, as shown by Fig. 3.25a,c or Fig. 3.26a,c. Note that with the same initial velocity in all cases, the stationary rim width will increase for lower CAF velocity ($\Delta \propto V_c^{-1/3}$) such that deformation reaches the center ($r = 0$) for larger ring radius R_c with ring viscosity compared to line tension FB.

For a given cluster size, an increase of the CAF-CC mechanical strength through the friction parameter c reinforces the shear stress transmission and leads to an increase of CC deformation. Hence, the maximal height h_{\max} monotonically increases with c , for all cases as shown on Fig. 3.24d, Fig. 3.25d and Fig. 3.26d. Moreover, the surface friction associated to c builds higher tension gradient on the CAF layer, and the rim height $h_{\max} - h_c$ also increases with c in all scenarios (Fig. 3.24d, Fig. 3.25d and Fig. 3.26d).

To understand qualitatively what controls the correlation between deformation and cluster size, one needs to quantify the deformation magnitude and how the scaling on CAF closure dynamics affects its evolution.

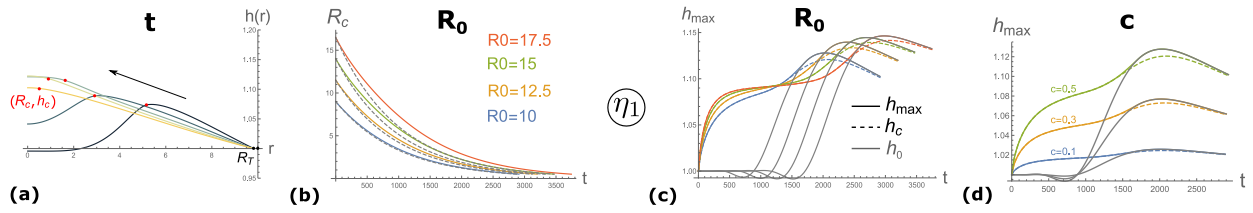


Figure 3.24: *Ring viscosity and constant line tension.* (a): Evolution of the CC height field $h(r,t)$ at $R_0 = 10$ and $c = 0.5$, with CC peripheral radius R_T (black points) and CAF ring position ($r = R_c, z = h_c$) (red points). (b): Evolution of CAF ring radius R_c for different cluster sizes (R_0), at $c = 0.5$ (full) or $c = 0$ (dashed gray). (c,d): Evolution of maximal height h_{\max} for different cluster sizes R_0 at $c = 0.5$ (c), or for different CAF-CC friction strength c at $R_0 = 10$ (d). Next to h_{\max} , the CC height at the ring position h_c (dashed) and at center h_0 (gray) are represented. For all graphs, one uses $k = \gamma = 0.01$, $\eta_1 = 500$, $\gamma_\infty = 0$ and $s = 5$.

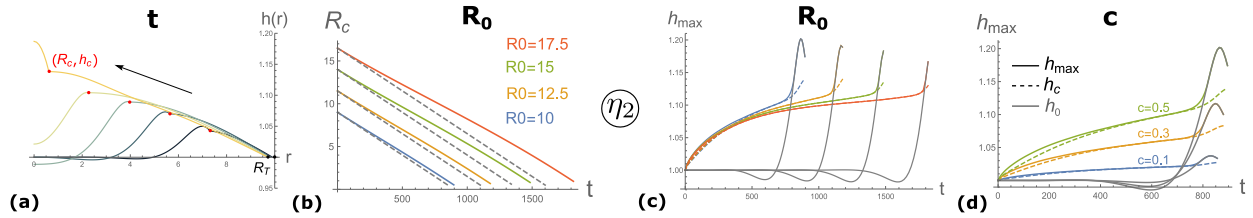


Figure 3.25: *CAF tissue viscosity and constant line tension.* (a): Evolution of the CC height field $h(r,t)$ at $R_0 = 10$ and $c = 0.5$, with CC peripheral radius R_T (black points) and CAF ring position ($r = R_c, z = h_c$) (red points). (b): Evolution of CAF ring radius R_c for different cluster sizes (R_0), at $c = 0.5$ (full) or $c = 0$ (dashed gray). (c,d): Evolution of maximal height h_{\max} for different cluster sizes R_0 at $c = 0.5$ (c), or for different CAF-CC friction strength c at $R_0 = 10$ (d). Next to h_{\max} , the CC height at the ring position h_c (dashed) and at center h_0 (gray) are represented. For all graphs, one uses $k = \gamma = 0.01$, $\eta_2 = 50$, $\gamma_\infty = 0$ and $s = 5$.

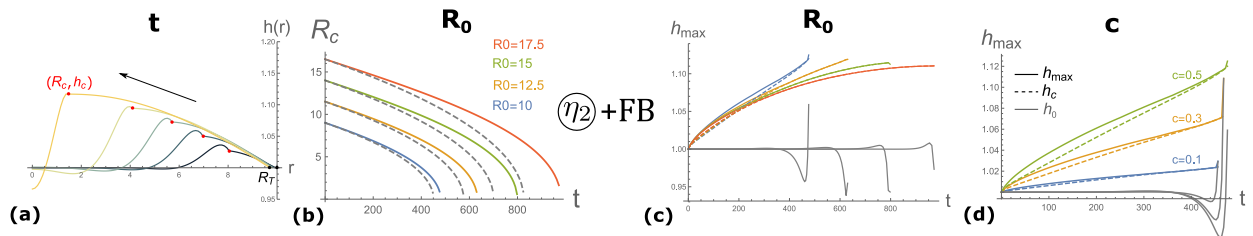


Figure 3.26: *CAF tissue viscosity and line tension Feed-Back (FB).* (a): Evolution of the CC height field $h(r,t)$ at $R_0 = 10$ and $c = 0.5$, with CC peripheral radius R_T (black points) and CAF ring position ($r = R_c, z = h_c$) (red points). (b): Evolution of CAF ring radius R_c for different cluster sizes (R_0), at $c = 0.5$ (full) or $c = 0$ (dashed gray). (c,d): Evolution of maximal height h_{\max} for different cluster sizes R_0 at $c = 0.5$ (c), or for different CAF-CC friction strength c at $R_0 = 10$ (d). Next to h_{\max} , the CC height at the ring position h_c (dashed) and at center h_0 (gray) are represented. For all graphs, one uses $k = \gamma = 0.01$, $\eta_2 = 50$, $\gamma_\infty = 0$ and $s = 5$.

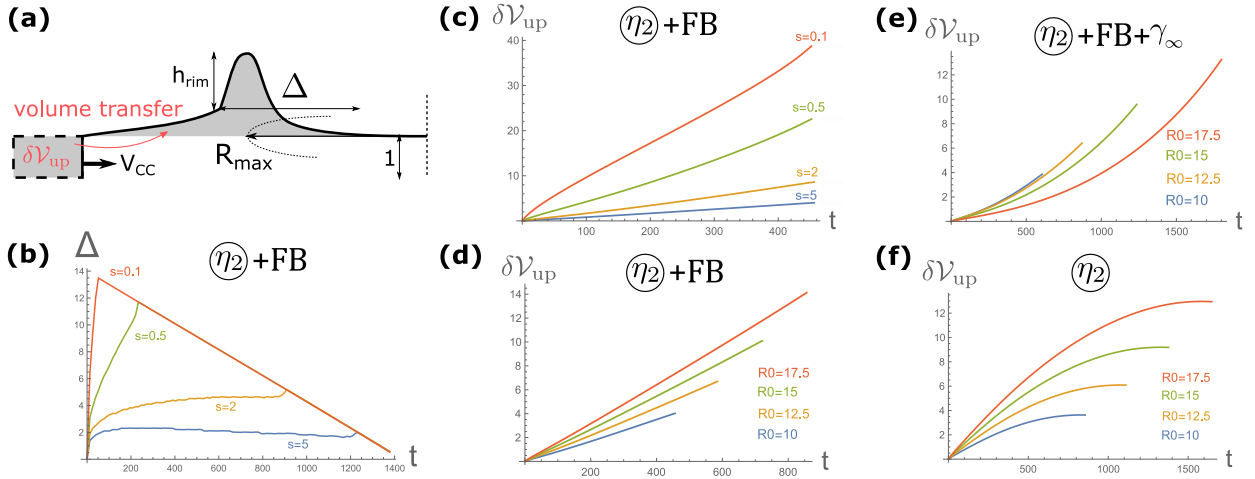


Figure 3.27: Volume transfer from peripheral displacement as a source of deformation on CAF-covered and CAF-free regions. **(a)**: Sketch of out-of-plane volume transfer $\delta\mathcal{V}_{\text{up}}$ due to peripheral inward flow at rate $2\pi R_T V_T$. With rim width Δ , the addition of volume on the CAF-free region corresponds to $\delta\mathcal{V}_{\text{free}} \sim 2\pi R_{\text{max}} h_{\text{rim}} \Delta$. If one can neglect the fraction deforming the CAF-covered region, one has $\delta\mathcal{V}_{\text{up}} \simeq \delta\mathcal{V}_{\text{free}}$. **(b)**: Rim width Δ for different values of substrate friction s at $R_0 = 10$. **(c)**: Evolution of transferred volume $\delta\mathcal{V}_{\text{up}}$ (a) for different values of s , in the scenario with η_2 and line tension Feed-Back (FB) at $R_0 = 10$. **(d)**: Evolution of transferred volume $\delta\mathcal{V}_{\text{up}}$ for different R_0 in the scenario with η_2 and line tension FB. **(e)**: Evolution of transferred volume $\delta\mathcal{V}_{\text{up}}$ for different R_0 in the scenario with η_2 , line tension FB and non-zero CAF rest tension $\gamma_\infty = 0.05$. **(f)**: Evolution of transferred volume $\delta\mathcal{V}_{\text{up}}$ for different R_0 in the scenario with η_2 and constant line tension. For all graphs, $c = 0.1$, $k = \gamma = 0.01$, $\eta_1 = 0/500$, $\eta_2 = 0/50$. $\gamma_\infty = 0$ for (b,c,d,e).

3.8.3 Early volume transfer

Due to the CAF-shear driving, the outer CC boundary $r = R_T$ flows inwards and generates a volume transfer $\delta\mathcal{V}_{\text{up}} = \pi(R_0^2 - R_T^2)$, corresponding to the volume fraction associated to CC out-of-plane deformations (Fig. 3.27a). The rate of volume transfer then reads $d_t \delta\mathcal{V}_{\text{up}} = 2\pi R_T V_T$. Neglecting the deformation on the CAF-covered region compared to the CAF-free region at the beginning, one can assume $\delta\mathcal{V}_{\text{up}} \simeq \delta\mathcal{V}_{\text{free}}$. As shown on Fig. 3.27a, this volume corresponds to $\delta\mathcal{V}_{\text{free}} \sim 2\pi R_{\text{max}} \Delta \delta h_{\text{rim}}$. At early times, the pressure gradient on the covered part can be ignored so that a shear balance is established between the CAF and substrate stresses: one has

$$R_T V_T \simeq \frac{c R_c V_c}{c + s} \quad (3.81)$$

so that the rate of volume transfer follows $d_t \delta\mathcal{V}_{\text{up}} \propto R_c V_c$. Depending on the CAF velocity scaling $V_c(R_c)$ and rim localization over width Δ , different regimes of deformation growth exist.

- CAF velocity scaling depends on the dominant dissipation mechanism. With constant line tension, $V_c \propto R_c$ for ring line viscosity η_1 or $V_c \propto 1$ for CAF tissue viscosity η_2 . $V_c \propto 1/R_c$ if one adds a positive FB on line tension next to CAF tissue viscosity.
- Rim localization is essentially controlled by the substrate friction s through the diffusion coefficient D_s at short times (Fig. 3.27b), with sharp spatial localization when $s \rightarrow \infty$. On the contrary, deformation spreads over the full CAF-free region in the large diffusion limit ($s \gg 1$) such that $\Delta \sim R_c$.
- the outer boundary flow is resisted by substrate friction s such that $d_t \delta\mathcal{V}_{\text{up}} \rightarrow 0$ when $s \rightarrow \infty$ according to Eq. 3.81, as shown on Fig. 3.27c.

If $V_c \propto 1/R_c$ (Fig. 3.27d), the volume transfer $\delta\mathcal{V}_{\text{up}} \propto (R_c V_c)t$ grows linearly in time with correlation to cluster size R_0 and one gets

$$\delta h_{\text{rim}}(t) \propto \frac{V_c}{\Delta} t \quad (3.82)$$

with $R_{\max} \simeq R_c$. If the rim is localized (s/c large), Δ is independent from cluster size R_0 whereas V_c scales like $1/R_0$: δh_{rim} grows faster for smaller clusters. This property is indeed observed and preserved at long times on h_{\max} with line tension FB (see Fig. 3.26c at $s = 5$). In the large diffusion limit where $\Delta = R_c$, one expects a consolidation of the anti-correlation with $(R_0)^{-2}$ scaling.

A priori, a large CAF pre-stress could reduce the fraction of volume transfer on the CAF-covered region and hence favours deformation on the CAF-free region. However, the CAF pre-stress γ_∞ also biases the volume transfer by penalizing large clusters (Fig. 3.27e), because $V_c \propto 1 - \gamma_\infty R_c$. Thus, with those two ambivalent effects in competition (see next section), CAF rest tension alone do not eliminate the anti-correlation between deformation and initial cluster size.

If the CAF ring radius decreases linearly in time, with V_c independent from R_c (Fig. 3.25 and Fig. 3.27f), the volume transfer $\delta \mathcal{V}_{\text{up}} \propto R_c(V_c t)$ now scales linearly with R_0 . For a localized rim, δh_{rim} is independent from cluster size, whereas the large diffusion limit gives an anti-correlation with scaling $1/R_0$. This is compatible with early deformation dynamics (see Fig. 3.25c with $s = 5$). Finally, if CAF closure dynamics follows an exponential relaxation with $V_c \propto R_c$ (Fig. 3.24), $\delta \mathcal{V}_{\text{up}}$ scales like $(R_0)^2$, such that rim growth becomes linearly correlated to cluster size when localized, as observed on Fig. 3.24c ($s = 5$) for early times, and independent from cluster size in the large diffusion limit.

Naively, an extrapolation of those scalings to the full evolution predicts a correlation between h_{\max} and R_0 for the η_1 scenario, which is observed (Fig. 3.24c). Similarly, an anti-correlation occurs for the $\eta_2 + \text{FB}$ scenario (Fig. 3.26c). However, whereas one expects no correlation in the η_2 scenario, a weak anti-correlation occurs (Fig. 3.25c). The quantitative difference is of course associated to the fact that this derivation only considers early evolution whereas the maximal deformation amplitude occurs at longer times, as well as the impossibility to validate the assumption $\delta h_{\text{rim}} \simeq \delta h_{\max}$ because deformation on the CAF-covered region is important as shown on Fig. 3.24a, Fig. 3.25a and Fig. 3.26a.

3.8.4 Rim disappearance and central amplification

For the model to be coherent with the experimental observations on budding frequency, we search for a correlation between maximal deformation and initial cluster size. This feature only occurs in the η_1 scenario (Fig. 3.24c), but the experimental CAF closure dynamics does not follow an exponential relaxation. Thus, we focus on the η_2 scenario to understand why this weak anti-correlation appears (Fig. 3.25c). The previous calculation on early volume transfer is strictly valid at early times, and extrapolation of this simple analysis to a prediction on maximal deformation is not valid. Indeed, the maximal height only appears after the rim have reached the center of the CC cluster (finite size effect $h_0 \neq 1$) and merged into a single bump, as can be verified on Fig. 3.24, Fig. 3.25 and Fig. 3.26 (c,d).

Although one expects rim localization to favour a concentration of deformation at early times ($\delta h_{\text{rim}} \propto 1/\Delta$ in Eq. 3.82), which can be obtained when s is sufficiently large to get weak spatial diffusion, the rim is observed to quickly disappear with deformation absorbed by the CAF-covered region (Fig. 3.28a,d). In fact, a decrease of s to increase spatial diffusion is sufficient to avoid rim disappearance (Fig. 3.28b,c). Those two antagonist effects of rim localization and finite size effect have a striking consequence: as shown on Fig. 3.28d,e,f, the weak anti-correlation between maximal deformation and initial cluster size is reversed when s decreases! In addition, the CC-substrate friction s also influences the convergent CC flow through the shear balance $(c + s)R_T V_T \simeq cR_c V_c$ with more volume transferred into deformation for small s (Fig. 3.27c).

This change of behaviour is intimately related to the deformation absorbed by the CAF-covered region, which is essentially controlled by the CAF tension. The later is sensitive to the CAF rest tension γ_∞ that we neglect here, the CAF-CC friction c (through the induced tension gradient) and the surface viscosity η_2 (through the viscous term $2\eta_2 \partial_r v_c$), which are both fixed on Fig. 3.28. When the CAF-covered region deforms because of the CC pressure generated by the CAF-induced shear stress, the volume transfer can either amplify this response and contribute to rim disappearance

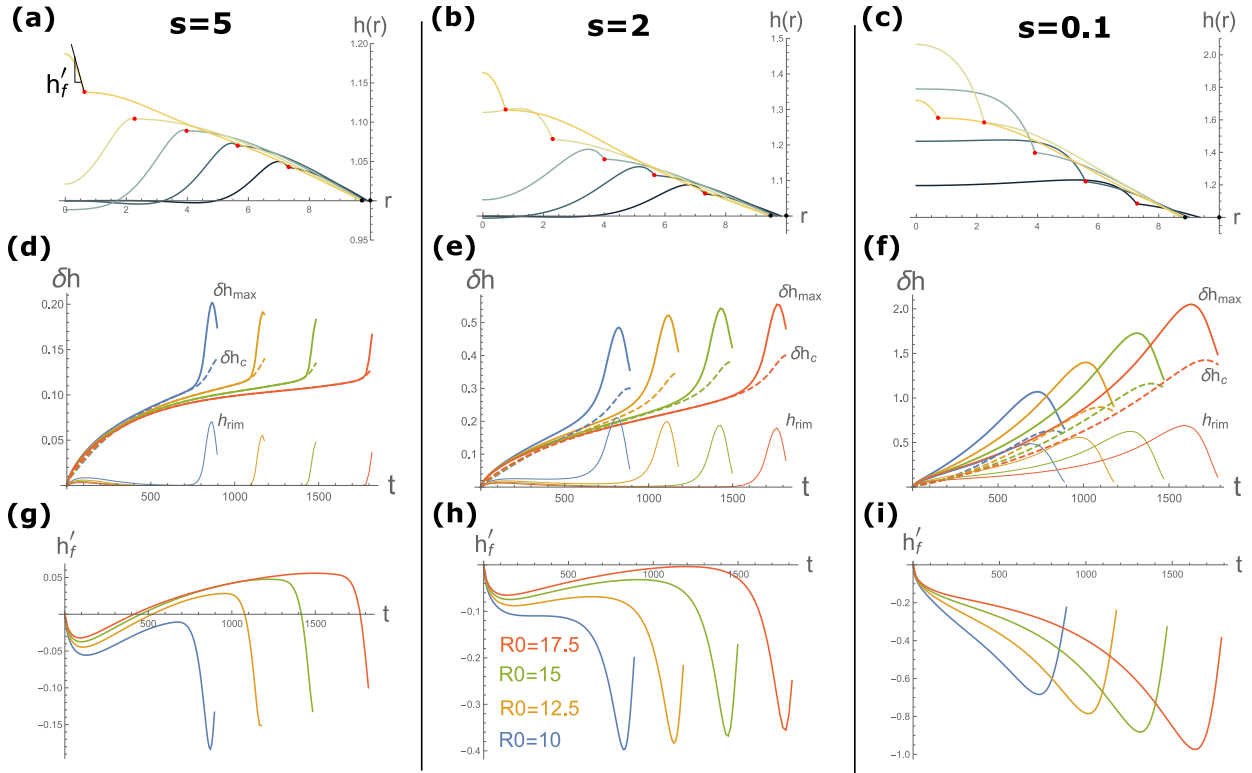


Figure 3.28: *Correlation inversion associated to CC-substrate friction s in the η_2 scenario.* (a,b,c): Evolution of the CC height field $h(r, t)$ at $R_0 = 10$ for $s = 5$ (a), $s = 2$ (b) and $s = 0.1$ (c), with CC peripheral radius R_T (black points) and CAF ring position ($r = R_c, z = h_c$) (red points). (d,e,f): Evolution of deformation for $s = 5$ (d), $s = 2$ (e) and $s = 0.1$ (f) and different cluster sizes (R_0), at maximum δh_{\max} , at ring position δh_c or their difference $h_{\text{rim}} \equiv \delta h_{\max} - \delta h_c$. (g,h,i): The rim slope h'_f at $r = R_c$, as defined in (a), is also represented for $s = 5$ (g), $s = 2$ (h) and $s = 0.1$ (i) and different cluster sizes (R_0). $h'_f > 0$ means indicates rim disappearance: CAFs have climbed on top of the rim. For all graphs, one uses $k = \gamma = 0.01$, $\eta_2 = 50$, $\gamma_\infty = 0$ and $c = 0.5$.

(Fig. 3.28d), or sustain the deformation of the CAF-free region (Fig. 3.28f). When looking at shape profiles on Fig. 3.28 (a,b,c), it is clear that the mechanical cost associated to a deformation near the center of the CAF-free region is higher for large s . Hence, a weak diffusion (large s) concentrates CC pressure near $r = R_c$ to favour the growth of ring height h_c and rim disappearance, whereas a large diffusion (small s) transmits CC pressure to the center and feeds deformation over the full CAF-free region.

This can be quantitatively characterized by the slope at the ring position $r = R_c$ from the CAF-free side h'_f as defined in Fig. 3.28a. The transition from anti-correlation at high s to correlation at small s corresponds to a shift from positive to negative values of h'_f as shown on Fig. 3.28g, Fig. 3.28h and Fig. 3.28i. The rim exists as long as $h'_f < 0$ and persists more for small clusters.

For a given transferred volume, the CAF-covered region extends over time upon CAF closure, with size $\sim R_T - R_c$ correlated to R_0 when $R_c \rightarrow 0$. Hence for a given volume transfer, the deformation is attenuated by diffusion on the CAF-covered region compared to the CAF-free region. Such a diffused deformation leads to a pseudo-plateau phase that prevents accumulation for large clusters and leads to an anti-correlation (Fig. 3.28d). The diffusion in the CAF-covered region is associated with the CC pressure concentration near $r = R_c$ which eliminates the rim (Fig. 3.28d,g). On the contrary, in the CAF-free region which shrinks upon CAF closure when $R_c \rightarrow 0$, the rim is sustained by a diffusion of CC pressure thanks to the finite size effect ($h_0 \neq 1$). Thus, deformation gets amplified (Fig. 3.28f). Hence, this simple accumulation effect leads to a correlation between maximal height and initial cluster size.

3.8.5 Towards undeformed CAF-covered region?

Without precise knowledge of CAF-CC or CC-substrate friction coefficients, it is hard to estimate if the assumption $c \sim s \sim 0.1 - 0.5$ shown to be relevant in the last section is likely to occur. Another strategy to correlate deformation with cluster size is to minimize the deformation on the CAF-covered region so that it accumulates on the CAF-free side similarly to Fig. 3.28c.

A first idea is to apply significant CAF rest tension γ_∞ on the CAF-covered region as shown in Fig. 3.29a,b for the deformation and the transferred volume. As expected, an increase of γ_∞ decreases the CAF-covered deformation (δh_c). It also increases the free slope $|h'_f|$ thanks to the tension balance $\gamma h'_f \simeq (\gamma + \gamma_\infty + \dots) h'_a$ which slightly enhances the rim size h_{rim} . As a consequence, the maximal deformation $\delta h_{\text{max}} = \delta h_c + h_{\text{rim}}$ necessarily increases with γ_∞ . This is confirmed by the relative decrease of covered transferred volume compared to free transferred volume Fig. 3.29b. However as noted before, the addition of CAF rest tension biases negatively the volume transfer for large clusters because the CAF closure dynamics is altered: $V_c \propto 1 - \gamma_\infty R_c$. Hence, γ_∞ can be increased only on a tiny range of values to preserve CAF closure, and it can be checked that the parameter γ_∞ alone is of no help for the (R_0, h_{max}) correlation.

Nonetheless, it is possible to increase the allowed range of values for γ_∞ if the dimensional line tension (1 here in these units) is increased in parallel. To make comparison easier, one also increases viscosity so that CAF velocity remains the same. With dimensions, one applies the transformation $\Gamma = z\Gamma_0$, $\gamma_\infty = z(\gamma_\infty)_0$ and $\eta_2 = z(\eta_2)_0$ where z is a control parameter. $z = 1$ corresponds to Fig. 3.29a,b with dimensionless $(\gamma_\infty)_0 = 0.05$ so that CAF velocity is slightly non constant in time as seen on Fig. 3.29c, but appears independent from z as required.

Whereas an increase of z correctly decreases the transferred volume on the CAF-covered region in favour of the CAF-free region (Fig. 3.29d), the covered deformation captured by height h_c decreases slowly with z (Fig. 3.29e). The low convergence of the limit $h_c \rightarrow 1$ when $z \rightarrow \infty$ preserves anti-correlation between deformation and initial cluster size even at $z = 16$. Again, the CAF pre-stress has ambivalent effects since it biases negatively the volume transfer for large clusters but attenuates CAF-covered deformation, and a change of $(\gamma_\infty)_0$ do not eliminate anti-correlation at $z = 16$.

Thus, even if the maximal height is increased and the rim sustained by the large CAF tension, one needs to reach higher values of z to observe a positive correlation, which indeed occurs for $z = 96$ as shown on Fig. 3.29f. Inversion from anti-correlation to positive correlation around $z \sim 50$. In principle, in the formal limit where $z \rightarrow \infty$ (see next section), one expects a sustained rim with vanishing CAF-covered deformation and an accumulation effect similar to Fig. 3.28f. As a consequence, one should obtain a robust correlation (R_0, h_{max}) marginally dependent on parameters.

Finally, a last possible strategy to reduce deformations on the CAF-covered region is to replace the CAF-CC surface friction $c\Delta v$ by a line friction $\zeta\Delta v$ localised at the interface between the CC cluster and the CAF ring. This is expected to limit covered deformations because the CAF-shear driving is localized at the ring and should reduce diffusion of pressure in the CAF-covered region. One other advantage of ring line friction is the existence of an analytical solution for the η_1 scenario and large diffusion limit $s = 0$. When $c = \eta_2 = 0$, there is no source of CAF tension gradient and CAF tension is simply equal to γ_∞ . Calling $\bar{\lambda}^2 \equiv (\gamma + \gamma_\infty)/k$, the horizontal stress gradient vanishes and one needs to solve the static shape equation on the CAF-covered region

$$\left[2 + \frac{\bar{\lambda}^2}{r^2} \right] \delta h' - \bar{\lambda}^2 \left(\delta h^{(3)} + \frac{\delta h''}{r} \right) = 0 \quad (3.83)$$

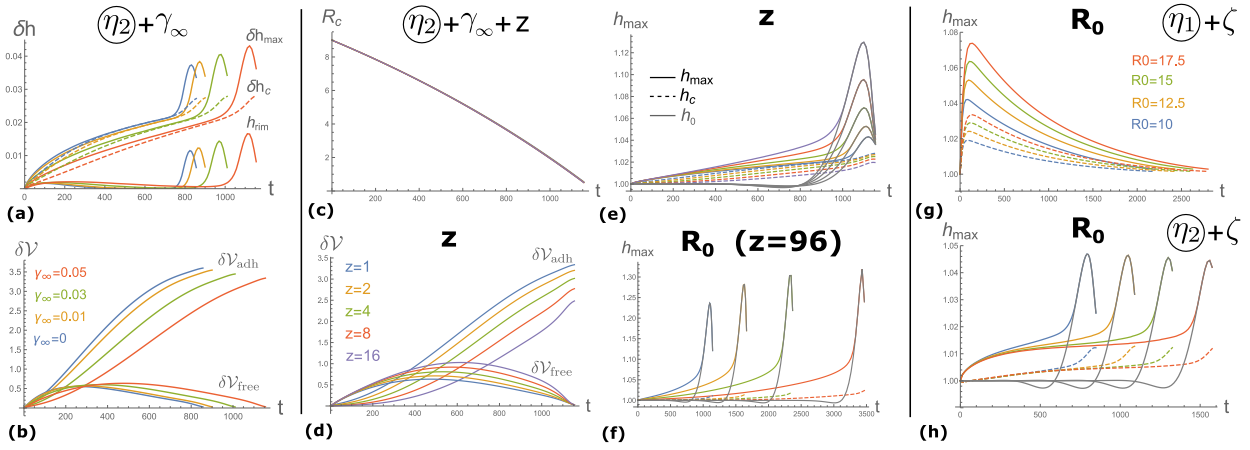


Figure 3.29: **(a,b)**: Evolution of deformation (a) and volume transfer (b) within the η_2 scenario when CAF rest tension γ_∞ is increased. **(c,d,e,f)**: Conjoint increase of line tension and CAF rest tension with $\Gamma = z\Gamma_0$ and $\gamma_\infty = z(\gamma_\infty)_0$ and time rescaling $t = t_0/z$, such that V_c remains constant as in (c) where all curves (z) collapse. Increasing with z , volume transfer is reduced on the CAF-covered region to favour CAF-free region (d). This induces more deformation with h_{\max} increasing and h_c decreasing with z (e). For $z = 96$, anti-correlation between deformation and initial cluster R_0 is reversed (f). **(g,h)**: Evolution of deformation for different R_0 when CAF-CC surface friction c is replaced by line friction ζ , within the η_1 scenario and $s = 0$ (g) or within the η_2 scenario (h). For all graphs, one uses $k = \gamma = 0.01$, $\eta_1 = 500$ or $\eta_2 = 50$, $c = 0.1$ or $\zeta = 0.1$ and $s = 5$ if the contrary is not mentioned.

with $\bar{\lambda}^2 \mapsto \gamma/k$ for the CAF-free region. The solution²⁴ is a combination of modified Bessel functions with deformation maximum in center and one gets the maximal height $h_{\max} = h_0$ as a function of initial cluster size: within the η_1 scenario, it is of no surprise that a correlation appears (Fig. 3.29g).

More interesting is the numerical resolution for η_2 scenario. Using the same parameters as in Fig. 3.25 except for c, ζ that are independent, one can see as expected that the CAF-covered deformation is strongly reduced with a sustained rim (Fig. 3.29h). However, despite a slight improvement, the maximal deformation is still weakly anti-correlated with initial cluster size. Hence, ring line friction alone is generally not sufficient to make the model predictions compatible (in a robust manner) with experimental observations on budding frequency.

3.8.6 Flat covered limit

Shape expansion

The last sections have shown that within this modelling framework, the observed positive correlation between deformation and CC cluster size is hard to obtain, and it is not straightforward to identify optimal features that can maximize the fraction of volume transfer on the CAF-free region to sustain rim growth. Indeed, since the decrease of CAF-covered deformation is slow in $z = \gamma_\infty/(\gamma_\infty)_0$, we consider here the formal limit where $\gamma_\infty, \Gamma, \eta \rightarrow \infty$, where η can be ring or tissue viscosity. This ensures that the CC cluster shape remains flat on the CAF-covered region (Fig. 3.30a,top) whereas CAF velocity V_c , ratio of tension $\Gamma - \gamma_\infty R_c$ and viscosity η , is "finite" as well as the CAF shear stress cV_c . CC Pressure is also "finite" since it is driven by the CAF-induced shear stress, so that the limit $\gamma_\infty \rightarrow \infty$ implies $\gamma_{rr} \rightarrow \infty$ and $r\delta h''(r) + \delta h'(r) \rightarrow 0$. This provides an asymptotic shape

$$\delta h_{\text{adh}}(r) = \delta h_c \frac{\log(R_T/r)}{\log(R_T/R_c)} \quad \text{and} \quad \delta h'_{\text{adh}}(r) = \frac{-\delta h_c}{r \log(R_T/R_c)} \quad (3.84)$$

²⁴Since line friction builds a pressure discontinuity $\Delta P = \zeta(V_c - v_r)$ at $r = R_c$ that acts as a source of deformation even at the beginning when the CC cluster is supposed undeformed, one needs to self-consistently identify the initial shape profile compatible with the boundary conditions. The simple flat state would not be consistent with the non-zero pressure discontinuity $\Delta P = \zeta V_c$.

However, the vertical balance of tensions at the ring position $r = R_c$ asks for $(\gamma + \gamma_{rr})\delta h'_{\text{adh}} \simeq \gamma\delta h'_{\text{free}}$. Since the right-hand side associated to rim deformation should also be "finite", the limit $\gamma_{rr} \rightarrow \infty$ asks for $\delta h'_{\text{adh}}(R_c) \rightarrow 0$. This corresponds to the flat covered part limit with $\delta h_c \rightarrow 0$ and $\delta h_{\text{adh}}(r) \rightarrow 0$.

To account for the formal limit $\gamma_\infty, \Gamma, \eta \rightarrow \infty$, the dimensional force unit Γ used previously in table 3.2 is replaced by the quantity $F_0 \equiv kh^*{}^3$ because the height stiffness k is "neutral" in this derivation contrarily to line tension, and all quantities are written with this rule (same notation). Writing $\gamma_\infty \equiv \bar{\gamma}/\epsilon$, $\Gamma \equiv \bar{\Gamma}/\epsilon$ and $\eta \equiv \bar{\eta}/\epsilon$ with $\epsilon \rightarrow 0$, one can use a perturbation expansion for the different fields (CC height, CC pressure, CC velocity, CAF velocity and CAF tension):

$$\delta h_{\text{adh}} = 0 + \epsilon \delta h_{a1}, \quad \delta h_{\text{free}} = \delta h_{f0} + \epsilon \delta h_{f1}, \quad P = P_0 + \epsilon P_1, \quad v_r = v_0 + \epsilon v_1, \quad v_c = v_{c0} + \epsilon v_{c1}, \quad \gamma_{rr} = \gamma_{-1}/\epsilon + \gamma_0 \quad (3.85)$$

Note that the least order terms ask for $\delta h_{\text{adh}} = 0$ whereas $\delta h_{\text{free}} \neq 0$ and $\gamma_{rr} \rightarrow \infty$.

On the CAF-covered region, expansion of force balance equations in ϵ give at 0th order CC incompressibility $\partial_r(rv_{a0}) = 0$, CAF tension $\gamma_{-1} = \bar{\gamma}$, CC pressure $P_{a0} = -\gamma_{-1}(\delta h''_{a1} + \delta h'_{a1}/r)$ and force balance $\partial_r P_{a0} = cv_{c0} - (c+s)v_{a0}$. Ring tension balance becomes $\bar{\gamma}\delta h'_{a1}(R_c) = \gamma\delta h'_{f0}(R_c)$ and $V_c(2\bar{\eta}_1 + 2\bar{\eta}_2 R_c) = R_c(\bar{\Gamma} - \bar{\gamma}R_c)$. Thus, the pressure field is only controlled by the shear stress difference $cv_c - (c+s)v_{\text{adh}}$ and depends on shape only at higher orders. At 0th order, CC velocity can be written $v_{\text{adh}}(r) = -V_T R_T/r$ whereas $v_c(r) = -V_c R_c/r$, such that $P_{\text{adh}}(r) = [cR_c V_c - (c+s)R_T V_T] \log(R_T/r)$.

The relation between pressure and height in the constitutive equation defines a shape equation for the 1st order height term δh_{a1} that can be ignored if one deals only with 0th order. Similarly, the vertical tension balance on the ring enters as a boundary condition for δh_{a1} , which lets $\delta h'_{\text{free}}(R_c)$ undetermined at least order. The equations remain identical on the CAF-free region with usual boundary conditions $\delta h'_{\text{free}} = v_{\text{free}} = 0$ at $r = 0$, whereas pressure and shape continuity become $\delta P_{\text{free}} = [cR_c V_c - (c+s)R_T V_T] \log(R_T/R_c)$, $\delta h_{\text{free}} = 0$ at $r = R_c$. Finally, flux balance $J_{\text{adh}} = J_{\text{free}}$ at $r = R_c$ is combined with pressure continuity to define a spatial boundary condition for the growth PDE and a dynamical equation for the CC cluster boundary $R_T(t)$.

Accumulation effect and CC-substrate friction dependency

This formal limit is interesting because the volume transfer on the free region is maximized for a given CAF-shear driving (c, s, V_c fixed) since no deformation is "lost" on the covered part (Fig. 3.30a,top). Indeed, it also seems justified experimentally according to few high resolution images showing weak to no height deformation of the CC cluster on the CAF-covered region (Fig. 3.30a,bottom). Hence, the rim cannot disappear ($h_{\text{max}} > h_c$) and deformation tends to accumulate for both scenarios of ring or tissue viscosity, as shown on Fig. 3.30b,c. Again, monolayer deformation saturates when pressure becomes sufficiently high to overcome the CAF shear stress cV_c , which reverses the CC flow with $V_T < 0$. This can be directly understood from the expression of CC pressure at the ring position $P_c = [cR_c V_c - (c+s)R_T V_T] \log(R_T/R_c)$: for a given $cR_c V_c$ that decays over time in the considered scenarios, the increase of P_c caused by higher deformations necessarily triggers the reversal of CC flow ($V_T < 0$) at some time.

Here for both viscosity scenarios (Fig. 3.30b,c), maximal deformation is positively correlated with cluster size. Although a positive correlation was already observed with ring viscosity for the full problem (Fig. 3.24c), the opposite situation occurs for tissue viscosity (Fig. 3.25c). The explanation simply relies on a straightforward accumulation effect that results from the absence of deformation on the CAF-covered region, such that all the volume transfer contributes to an increase of deformation through h_{max} ; even if the rate of increase is smaller for larger clusters as in the case of tissue viscosity (Fig. 3.30c), CAF closure takes longer and those clusters have more time to accumulate deformation. This is similar to Fig. 3.28f except that here, the absence of deformation on the CAF-covered region allows an accumulation effect even for large s .

Note that one uses $\gamma_\infty = 0$ on Fig. 3.30: although one needs $\gamma_\infty \gg \gamma$ for the flat covered limit,

here the CAF pre-stress only enters in the CAF tension balance that fixes dynamics, and the convenient choice $\gamma_\infty = 0$ just corresponds to $\Gamma \gg \gamma_\infty h^*$ (dimensional). A larger value would not affect qualitatively the results except for some shift in CAF closure dynamics, with pre-stress value necessarily bounded by the closure phenotype constraint $\gamma_\infty h^* < 0.1\Gamma$ (dimensional), equivalent to $V_c > 0$.

Another interesting feature is the non-monotonic dependency of maximal deformation with CC-substrate friction s (Fig. 3.30d,e,f). This results from an antagonism between a volume transfer rate $d_t \delta \mathcal{V}_{\text{free}} = 2\pi R_T V_T$ decreasing with s , and rim localization increasing with s because the rim width Δ decreases with s . As shown on Fig. 3.30d, this effect is recapitulated with a toy model combining a simplified geometry (rectangular shape), a full CAF-shear driving with $(c+s)R_T V_T = cR_c V_c$ (no pressure gradient), and a given scaling for rim growth (for example $\Delta = \sqrt{D_s t}$). It naturally reproduces the non-monotonicity between h_{max} and s observed for both ring and tissue viscosity (Fig. 3.30e,f).

At large s , the CAF-shear driving implies $\delta \mathcal{V}_{\text{free}} \propto 1/s$ whereas the rim localization distributes the transferred volume with maximal height $h_{\text{max}} \propto \delta \mathcal{V}_{\text{free}}/\Delta$. For $\Delta^{(4)} = (\lambda^2 D_s t)^{1/4} \propto s^{-1/4}$, $\Delta^{(3)} = (\lambda^2 D_s/V_c)^{1/3} \propto s^{-1/3}$ or $\Delta^{(2)} = \sqrt{D_s t} \propto s^{-1/2}$, one gets a decrease of h_{max} with increasing s as in Fig. 3.30d,e,f. Only a rim width scaling $\Delta^{(1)} = D_s/V_c$ could make the deformation amplitude independent from substrate friction at large s , but this scaling only appears in the saturation phase whereas the growing phase necessarily involves $\Delta^{(4)}$ or $\Delta^{(2)}$. Therefore, h_{max} also decreases with s for early evolution at least and the accumulated deformation will follow the same trend.

At small s , the CAF-shear driving makes the volume transfer independent from s with $R_T V_T \simeq R_c V_c$. If the deformation remains spatially localized, for slow rim growth and/or large cluster size, one gets $h_{\text{max}} \propto 1/\Delta$ and h_{max} now increases with s (Fig. 3.30d,e,f).

Thus, an intermediate value of substrate friction exists at which the deformation amplitude is maximal. The toy model of Fig. 3.30d is limited by the absence of pressure gradient, which couples the peripheral CC flow (volume transfer) and the deformation on the CAF-free region (rim localization) in a non-trivial manner. Nevertheless, it provides a simple argument to understand the non-monotonic dependency of maximal deformation with CC-substrate friction s as shown on Fig. 3.30e,f. Interestingly, the equivalent deformations to Fig. 3.30e,f for the full problem with deformed CAF-covered region do not exhibit this non-monotonic behaviour with CAF-CC surface friction c , whereas the opposite is observed when surface friction is replaced by ring line friction ζ . This indicates that non-monotonicity only occurs for weakly deformed monolayer on the CAF-covered region.

Phase diagrams and budding frequency

A key experimental result is the observation of positive correlation between budding frequency and cluster size. This can be recapitulated on two phase diagrams as a function of initial cluster radius R_0 and either CAF-CC friction c (Fig. 3.31a) or CC-substrate friction s (Fig. 3.31b). Using a critical deformation for the multilayering criterion reached at height h_{crit} , this separates the parameter space in two regions: **budding** when $h_{\text{max}} > h_{\text{crit}}$ occurs before CAF closure and **no budding** when $h_{\text{max}} < h_{\text{crit}}$ at all times, as shown on Fig. 3.31 for the tissue viscosity scenario. For a given friction value, the accumulation effect specific to the flat covered limit ensures the absence of multilayering transition for small clusters that are not sufficiently deformed whereas larger ones can trigger budding. Note that close to the critical line $h_{\text{max}} = h_{\text{crit}}$ (Fig. 3.31a), multilayering events are activated when the rims have merged into a central bump, whereas at larger distances in the budding region, cell rearrangements occur when the rim is still localized spatially.

With parametric noise on both cluster radius and friction parameter, one can compute an equivalent budding frequency as a surface fraction on the "budding" region, as indicated on Fig. 3.31a. To illustrate the reasoning with critical deformation at 30%, noise amplitude around 10–20% and CAF-CC friction $\xi \sim 10^{10}$ Pa s/m, one gets a budding frequency of the order of 20% for clusters of radius $R_0 \simeq 110 \mu\text{m}$, 90% for $R_0 \simeq 150 \mu\text{m}$ and 100% for $R_0 \simeq 190 \mu\text{m}$ (Fig. 3.31a). Experimentally, budding frequency is found to be around 25% for adhesive patches of radius $R_p = 100 \mu\text{m}$,

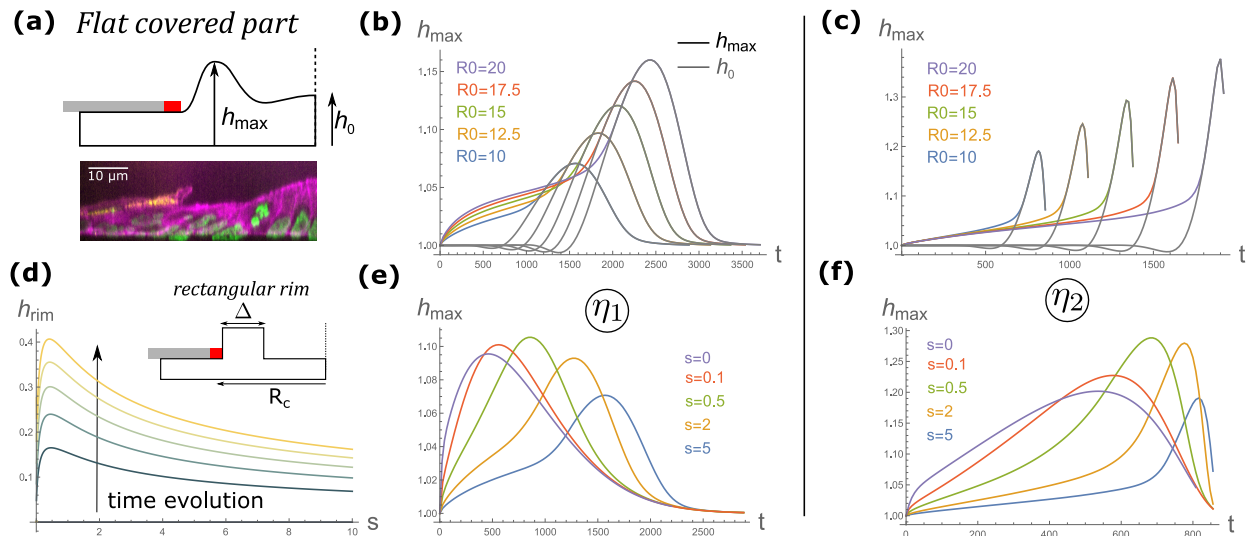


Figure 3.30: *The flat covered limit.* (a): Sketch of the deformed CC monolayer (top) with the assumption that the cluster shape on the CAF-covered region remains flat. The behaviour of the system is modified because the rim is always present since $h_{\max} > h_c = 1$. At late times, rim merging still occurs at the central boundary ($r = 0$) when $h_0 \neq 1$. High resolution image (bottom) of a deformed cluster at $t = 24$ h where one sees weak to no height deformation on the CAF-covered region. (b): Evolution of maximal height h_{\max} for different cluster sizes (R_0), at $s = 5$ under the η_1 scenario as in Fig. 3.24c. With same parameters, deformation is much more significant because no volume fraction is transferred to the covered region. The center height h_0 (gray) indicates the rim merging time. (c): Evolution of maximal height h_{\max} for different cluster sizes (R_0), at $s = 5$ under the η_2 scenario as in Fig. 3.25c. (d): Illustrative evolution of rim height $h_{\text{rim}} \equiv h_{\max} - 1$ as a function of substrate friction s , for a toy model where the covered part is flat ($h_a = 1$) and the rim has a rectangular shape over width Δ such that $h_f(R_c - \Delta < r < R_c) = h_{\max}$ and $h_f(r < R_c - \Delta) = 1$. Pressure gradient is ignored for simplicity ($(c + s)R_T V_T = cR_c V_c$), CAF velocity is constant (η_2 scenario) and rim growth is diffusive: $\Delta = \sqrt{D_s t}$. (e,f): Evolution of maximal height h_{\max} for different substrate friction values s , at $R_0 = 10$ under the η_1 (e) or η_2 (f) scenario. In both cases, the relation between h_{\max} and s is non-monotonic with maximal deformation reached for $s \sim 1$. For all graphs, one uses $k = \gamma = 0.01$, $\gamma_\infty = 0$, $\eta_1 = 500$ or $\eta_2 = 50$ and $c = 0.1$.

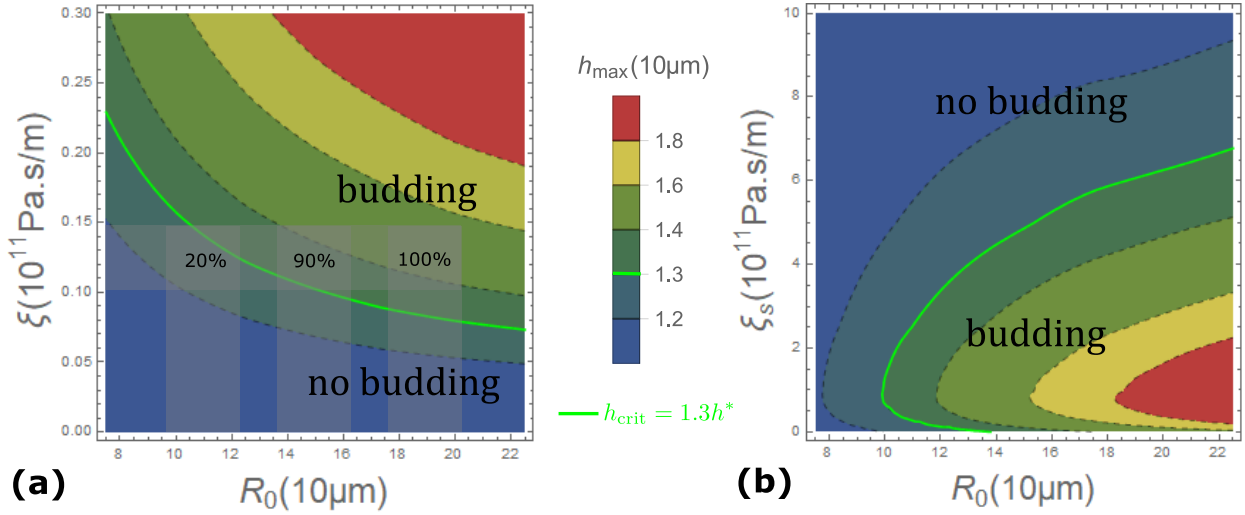


Figure 3.31: *Phase diagrams for the flat covered limit in the η_2 scenario.* (a,b): Phase diagrams for the maximal height h_{\max} in the parameter space (R_0, c) at $s = 5$ (a) and (R_0, s) at $c = 0.1$ (b). Here, the multilayering criterion on critical height h_{crit} is chosen at 30% strain (green line). For given c (ξ) and s (ξ_s), it shows that small clusters are unlikely to trigger multilayering transitions (no budding) whereas larger ones should build multicellular buds (budding). For both graphs, one uses $k = \gamma = 0.01$, $\gamma_\infty = 0$ and $\eta_2 = 50$.

60% for radius $R_p = 150 \mu\text{m}$ and 100% for adhesive patches of radius $R_p = 200 \mu\text{m}$.

For a given cluster size R_0 , the first phase diagram naturally indicates an increase of deformation with CAF-CC friction coefficient c . However as discussed before, the CC-substrate friction coefficient s has a less straightforward dependency on cluster deformation: as explained on Fig. 3.30d, the antagonist effects associated to CAF-shear driving and rim localization lead to a maximized deformation at an intermediate friction value around $s \sim 1$ which is confirmed by Fig. 3.31b.

Large diffusion limit: analytics

A last interest of the flat covered limit is its combination with the hypothesis of large diffusion coefficient ($D_s \rightarrow \infty/s \rightarrow 0$). Contrarily to the full problem where an analytical solution is only possible on the CAF-free region, whereas a growth PDE with evolving boundaries still asks for a full numerical procedure on the CAF-covered region, here the later part is trivially determined and one has access to full analytics.

With CC height at ring position $h_c = 1$ and deformation at center $\delta h(r = 0) \equiv \delta h_0$, the absence of stress gradient on the CAF-free region leads to the height field and free pressure

$$\delta h_f(r) = \delta h_0 \frac{I_0(R_c/\lambda) - I_0(r/\lambda)}{I_0(R_c/\lambda) - 1}, \quad \delta P_f(R_c) = 2k\delta h_0 \frac{I_0(R_c/\lambda)}{I_0(R_c/\lambda) - 1} \quad (3.86)$$

with $\lambda \equiv \sqrt{\gamma/(2k)}$ fixing the relaxation length from $\delta h(R_c) = 0$ to δh_0 as shown on Fig. 3.32a. The appearance of the modified Bessel function I introduces inessential complexity and we consider the limit $\lambda \rightarrow 0$ for simplicity: one gets $\delta h_f(r) \simeq \delta h_0$ and $\delta P_f \simeq 2k\delta h_0$ (Fig. 3.32a). This rectangular shape simplifies the expression of volume conservation since one has $\delta \mathcal{V}_{\text{free}} = \pi R_c^2 \delta h_0$ for the fraction transferred into deformation. The convergent flow of the CC cluster periphery with radius R_T and inward velocity V_T transfers volume in the CAF-free region at rate $d_t \delta \mathcal{V}_{\text{free}} = 2\pi R_T V_T$. Moreover, pressure continuity between CAF-covered and CAF-free regions fixes the peripheral cluster dynamics

$$V_T = \frac{R_c}{R_T} V_c - \frac{2k\delta h_0}{c R_T \log(R_T/R_c)} \quad (3.87)$$

Finally, the CAF closure dynamics is determined by the balance between viscous dissipation, ring line tension, CAF rest tension and CAF-CC friction resistance, such that the dynamical system is closed with

$$(2\eta_1 + 2\eta_2 R_c) \frac{V_c}{R_c^2} = \frac{1}{R_c} - \gamma_\infty - 2k\delta h_0 \quad (3.88)$$

A two-variable closed dynamics is obtained from volume rate equation $d_t \delta \mathcal{V}_{\text{free}} = 2\pi R_T V_T$ and volume $\pi(R_0^2 - R_T^2) = \pi R_c^2 \delta h_0$ to eliminate R_T , in terms of central height perturbation for the two variables $(R_c, \delta h_0)$

$$d_t \delta h_0 = \frac{2V_c}{R_c} + 2\delta h_0 \left[\frac{V_c}{R_c} - \frac{2k}{cR_c^2 \log(R_T/R_c)} \right] \quad (3.89)$$

or in terms of free volume transfer with couple $(R_c, \delta \mathcal{V}_{\text{free}})$

$$d_t \delta \mathcal{V}_{\text{free}} = 2\pi R_c V_c - \frac{4k \delta \mathcal{V}_{\text{free}}}{cR_c^2 \log(R_T/R_c)} \quad (3.90)$$

An evolution profile for central height h_0 , solution of the later equations, is represented on Fig. 3.32b in the η_2 scenario. As before for the flat covered limit, it starts with an usual growing phase and ends on a retraction phase with $h_0 \rightarrow 1$ at closure. The retraction can be understood from the CC peripheral velocity (Eq. 3.87): the first term on the right-hand side represents the source of convergent flow coming from the CAF-shear driving whereas the second one is associated to outward flow from the pressure generated by deformation (δh_0). As δh_0 grows by CAF-shear driving, it increases pressure until the second term compensates for the first one and reverses the CC flow (Fig. 3.32c).

The two dynamical equations Eq. 3.89 and Eq. 3.90 exhibit two transition times t^* and t^\dagger at which $d_t \delta \mathcal{V}_{\text{free}}|_{t^*} = 0$ and $d_t \delta h_0|_{t^\dagger} = 0$, respectively. They are associated to critical heights

$$\delta h_0^* = \frac{c}{2k} R_c V_c \log \left[\frac{R_T}{R_c} \right], \quad \delta h_0^\dagger = \frac{c R_c V_c \log[R_T/R_c]}{2k - c R_c V_c \log[R_T/R_c]} \quad (3.91)$$

and equivalent quantities for volume transfer with $\delta \mathcal{V}_{\text{free}} = \pi R_c^2 \delta h_0$. Since the rate of volume transfer is proportional to V_T , $d_t \delta \mathcal{V}_{\text{free}}|_{t^*} = 0$ is simultaneous to $V_T = 0$ as can be checked on Fig. 3.32c,d. The quantities δh_0^* , δh_0^\dagger defined on Eq. 3.91 can be computed at any time as shown on Fig. 3.32b, where $\delta h_0^* = \delta h_0$ only at $t = t^*$ and $\delta h_0^\dagger = \delta h_0$ only at $t = t^\dagger$. Similar quantities $\delta \mathcal{V}_{\text{free}}^*$, $\delta \mathcal{V}_{\text{free}}^\dagger$ for volume transfer are shown on Fig. 3.32d. The pressure is sufficiently high to reverse the CC flow for $t > t^*$ such that $d_t \delta \mathcal{V}_{\text{free}} < 0$, but deformation still accumulates (Fig. 3.32b) because there is still sufficient volume available to distribute upwards on the CAF-free region (thanks to the CAF boundary convergent drift $d_t R_c < 0$). However, this increase in deformation builds more pressure to drive the outward CC flow and reduces the available volume, until $t = t^\dagger$ at which outward (V_T) and upward ($d_t \delta h_0$) flows compensate to fix a maximal deformation.

Following a linearisation of equations Eq. 3.87 and Eq. 3.88 with expansion parameter c , where $c = 0$ corresponds to CAF closure on undeformed CC cluster, one gets at least order

$$V_c = \frac{R_c(1 - \gamma_\infty R_c)}{2\eta_1 + 2\eta_2 R_c}, \quad R_0 - R_T = \frac{c R_c^3}{4k R_0} V_c \log \left[\frac{R_0}{R_c} \right], \quad \delta h_0 = \frac{2R_0}{R_c^2} (R_0 - R_T) \quad (3.92)$$

For $\gamma_\infty = 0$, the problem contains an exact dynamical solution in the scenarios investigated so far:

- for the η_1 scenario following CAF closure dynamics $R_c(t) = R_0 e^{-t/(2\eta_1)}$, the exact solution for the central deformation reads

$$\delta h_0(t) = \frac{c}{2k} \left(\frac{R_0}{2\eta_1} \right)^2 t e^{-t/\eta_1}, \quad \text{with} \quad \delta h_{\text{max}} = \frac{c \eta_1}{2k e} \left(\frac{R_0}{2\eta_1} \right)^2 \quad \text{at} \quad t_{\text{max}} = \eta_1 \quad (3.93)$$

whereas the initial growth rate $d_t h_0|_{t=0} = c R_0^2 / (8k \eta_1^2)$ is proportional to the square of initial cluster radius, as well as the maximal deformation δh_{max} (see Fig. 3.32e). This agrees with the simple scaling argument on the section discussing early volume transfer 3.8.3. The solution of the full non-linear system (Eq. 3.89) is also indicated for comparison.

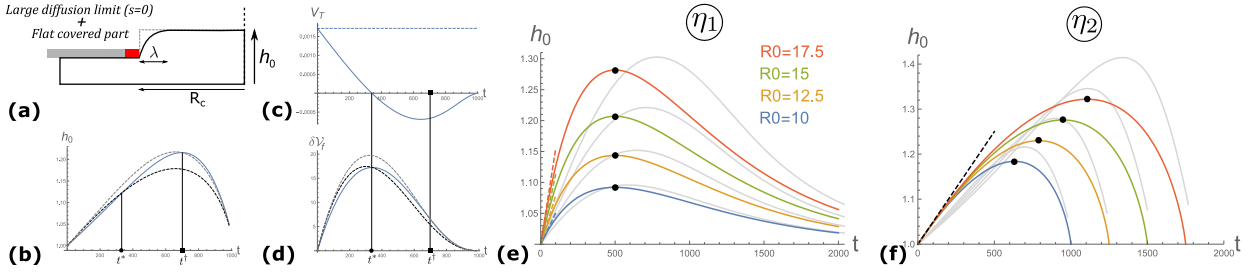


Figure 3.32: *Flat covered and large diffusion limits.* (a): Sketch of the deformed CC monolayer (black) with local shape relaxation near the CAF ring over length $\lambda \equiv \sqrt{\gamma/(2k)}$ and maximal height at center h_0 . The limit $\gamma \rightarrow 0$ corresponds to a rectangular shape with shape discontinuity at $r = R_c$ (dashed). (b,c,d): Quantification of CC deformation evolution through central height h_0 (b), CC peripheral velocity V_T (c) and volume transfer $\delta\mathcal{V}_{\text{free}}$ (d) in the η_2 scenario at $R_0 = 10$. The quantities defined in Eq. 3.91 δh_0^* (dashed gray) and δh_0^\dagger (dashed black) are represented on (b) and equivalent expressions for volume transfer $\delta\mathcal{V}_{\text{free}}^*$ and $\delta\mathcal{V}_{\text{free}}^\dagger$ on (d). $d_t\delta\mathcal{V}_{\text{free}} = 0$ and $V_T = 0$ occur at t^* (square) and $d_t\delta h_0 = 0$ at t^\dagger (circle). (e,f): Evolution of central height for different cluster sizes R_0 , for the linear approximation (color) and the full non linear system (gray). In η_1 scenario (e), initial slope $d_t h_0|_{t=0}$ (dashed) increases with initial cluster radius R_0 . In the η_2 scenario, initial slope $d_t h_0|_{t=0}$ (dashed) is independent from cluster size. For all graphs, one uses $k = 0.01$, $\gamma = 0$, $\gamma_\infty = 0$, $\eta_1 = 500$ or $\eta_2 = 50$ and $c = 0.1$.

- for the η_2 scenario following CAF closure dynamics $R_c(t) = R_0 - t/(2\eta_2)$, the exact solution for the central deformation reads

$$\delta h_0(t) = \frac{c(2\eta_2 R_0 - t)}{2k(2\eta_2)^2} \log \left[\frac{2\eta_2 R_0}{2\eta_2 R_0 - t} \right], \quad \text{with} \quad \delta h_{\text{max}} = \frac{cR_0}{4k\eta_2 e} \quad \text{at} \quad t_{\text{max}} = 2\eta_2 R_0 \left(1 - \frac{1}{e}\right) \quad (3.94)$$

whereas the initial growth rate $d_t h_0|_{t=0} = c/(8k\eta_2^2)$ is independent from initial cluster radius (see Fig. 3.32f). Nonetheless, the maximal deformation δh_{max} remains proportional to cluster size²⁵ as in section 3.8.3 and again, one gets positive correlation $(R_0, \delta h_{\text{max}})$.

3.8.7 Bud final area

In addition to the experimental observation correlating budding frequency and initial cluster size R_0 , the final projected area of buds (in the xy plane) is also measured to increase with R_0 Fig. 3.33d. However, unlike the first experimental constraint which is only satisfied for specific scenarios, the second one is compatible with all scenarios as long as the critical height h_{crit} for multilayering transition is not too high.

For given conditions, the evolution of the CC cluster maximal height $h_{\text{max}}(t)$, spatially transported by the CC flow along the trajectory $r = R_{\text{max}}(t)$, reaches h_{crit} at a time t_{crit} and localizes at a radius $R_{\text{max}}(t_{\text{crit}}) \equiv R_{\text{crit}}$ as shown on Fig. 3.33a. At $t = t_{\text{crit}}$, we assume for simplicity that the volume contained in the CAF-free region approximately corresponds to the final bud volume, through accumulation of multilayering events²⁶. Then, one can write the bud volume as $V_b \simeq \pi h^*(R_{\text{crit}})^2$ if deformations remain small on the CAF-free region: calling $\epsilon_{\text{crit}} \equiv (h_{\text{crit}} - h^*)/h^*$, this asks for $\epsilon_{\text{crit}} \ll 1$. As can be seen on Fig. 3.33a for ring viscosity, Fig. 3.33b for tissue viscosity and Fig. 3.33c for line tension FB with, there is a straightforward correlation between bud size and initial cluster size which is weakly dependent on the chosen scenario for $\epsilon_{\text{crit}} = 5\%$. The scaling of CAF closure dynamics starts to affect the correlation only for $\epsilon_{\text{crit}} \gtrsim 10\%$, with this threshold value dependent on the amplitude of the CAF-induced shear stress, controlled by the parameter c . For the flat covered limit, the higher amplitude of h_{max} coming from the absence of CAF-covered deformation

²⁵For the $\eta_2 + \text{FB}$ scenario where $V_c \propto 1/R_c$, following CAF closure dynamics $R_c(t) = \sqrt{R_0^2 - R_0 t/\eta_2}$, one can show that deformation diverges when $t \rightarrow R_0 \eta_2 \equiv t_{\text{closure}}$, with initial growth rate identical to the η_2 scenario. The growth rate then evolves in favour of small clusters (anti-correlated with R_0) but no maximal deformation exists.

²⁶This is expected to be valid when multilayering occurs on top of a localized rim ($\Delta < R_c$), such that the second layer will apply mechanical resistance on the CAF ring and transmit the pressure to the surroundings to trigger a cascade of multilayering events.

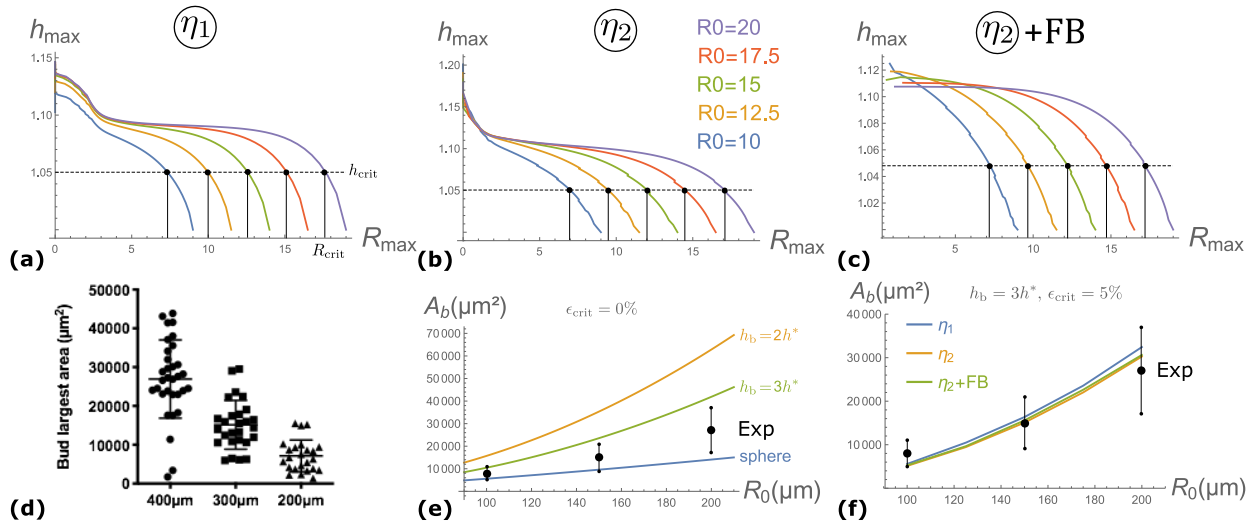


Figure 3.33: Comparison between experimental and theoretical bud final area A_b . (a,b,c): Maximal height h_{\max} as a function of R_{\max} defined such that $h = h_{\max}$ at $r = R_{\max}$, for η_1 (a), η_2 (b) and $\eta_2 + \text{FB}$ (c) scenarios. The critical height parameter h_{crit} at which multilayering occurs is chosen at the value $1.05h^*$. It corresponds to a strain $\epsilon_{\text{crit}} \equiv (h_{\text{crit}} - h^*)/h^* = 5\%$. The equation $h_{\max} = h_{\text{crit}}$ defines an equivalent radius R_{crit} at which budding occurs, indicated for $R_0 = 20$ here (a). For all graphs, one uses $k = 0.01$, $\gamma = 0.01$, $\gamma_\infty = 0$, $\eta_1 = 500$ or $\eta_2 = 50$ and $c = 0.5$. (d): Experimental measurements of bud projected area (from the top view) at steady-state for CC clusters on adhesive patches of 200, 300 and 400 μm diameter. (e): Bud area A_b (see text) as a function of initial cluster radius R_0 with different assumptions for bud final shape: a sphere, a cylinder with 2 or 3 layers. It assumes spontaneous budding ($\epsilon_{\text{crit}} = 0\%$) to show that even in this "optimal" situation, a spherical shape is not compatible with experimental data. (f): Bud area A_b as a function of initial cluster radius R_0 , comparison between experimental (black) and theoretical values (color). It corresponds to graphics (a,b,c) with $\epsilon_{\text{crit}} = 5\%$. Here one chooses $h_b = 3h^*$ but another number can be chosen if ϵ_{crit} is adjusted in parallel. One expects $h_b/h^* \simeq 2 - 4$ for large buds based on experiments.

(Fig. 3.30b,c) increases the threshold strain value at which the correlation is lost.

The fact that criticality weakly depends on the chosen scenario can be understood by considering the rate of increase $\omega \equiv |dh_{\max}/dR_{\max}|$ in the space (R_{\max}, h_{\max}) . At the beginning and following a previous calculation where one neglects volume transfer on the CAF-covered region (Eq. 3.82), one can write $\omega = |d_t h_{\max}/d_t R_{\max}|$ with $d_t h_{\max} \simeq d_t h_{\text{rim}}$ and $d_t R_{\max} \simeq d_t R_c = -V_c$. Using Eq. 3.82 with $h_{\text{rim}} \propto V_c t / \Delta$ and rim width independent from V_c at early times, one gets the same ω for all scenarios. Hence, if ϵ_{crit} remains small, the critical radius R_{crit} should be approximately the same on Fig. 3.33a,b,c as observed.

Since the experimental quantification of final bud size involves projected bud area A_b , one needs an extra assumption to relate the total bud volume V_b to A_b . This corresponds to an hypothesis on final bud shape, and we consider the possibilities of either a sphere or a cylinder with n layers. For example, a sphere of radius R_b has a projected area $A_b = \pi^{1/3}(3V_b/4)^{2/3}$. Interestingly as shown on Fig. 3.33e, even if multilayering was spontaneous with $\epsilon_{\text{crit}} = 0\%$ such that $V_b = \pi h^*(R_0)^2$, the experimentally measured values for A_b (Fig. 3.33d) are not compatible with the spherical assumption. Indeed, independent arguments on steady-state cluster rheology discussed in the previous chapter and experimental observation of small height-to-size ratio for large buds indicate that a cylindrical shape is more appropriate. Nonetheless, the number of layers n remains undetermined and we only expect $n \lesssim 2 - 4$ with $A_b = V_b/(nh^*)$. Assuming $n = 3$ for simplicity, we obtain for the final bud area $A_b = \frac{\pi}{3}(R_{\text{crit}})^2$ where the critical radius R_{crit} is determined as a function of initial cluster radius R_0 as indicated on Fig. 3.33a. With the conditions used on Fig. 3.33a,b,c for which $\epsilon_{\text{crit}} = 5\%$, one can plot the theoretical final bud area to find a good agreement with the experimentally measured values as can be checked on Fig. 3.33f. In terms of viscosity and line tension, the different scenarios should marginally affect the final value when $\epsilon \ll 1$ as explained before, which is indeed the case Fig. 3.33f.

Chapter 4

Cell extrusion

"Vivre de mort, mourir de vie."

Héraclite

The aim of this theoretical project is to propose a minimal description of cell extrusion mechanics in epithelial monolayers, and how external tissue compression could change its likelihood. The modelling framework uses a 2D vertex model in transverse plane with curved interfaces, already presented in part II. A first chapter presents the biological context of the phenomenon. The second and third chapter show the results obtained. These results are only preliminary and the project remains to be finished.

The phenomenon of cell extrusion is assumed to be the consequence of two consecutive transitions, as sketched on Fig. 4.1. The first step is the loss of basal cell contact, leaving only cell-cell and cell-lumen interfaces for the extruding cell. Then, the loss of cell-cell interface corresponds to an extrusion event. In a chemical reaction setting, extrusion occurs through the conversion reactions *basal* \rightarrow *lateral* and *lateral* \rightarrow *apical* for interfaces. With a focus on cell shape, a normal epithelial cell is represented by the symbol U , whereas a V corresponds to the first transition, a Y is associated to the new equilibrium shape and O is the suspended-like extruding cell. If one can assume the irreversibility of these transitions, extrusion is represented as the two mechanical "reactions" $U \rightarrow V \rightarrow Y$ and $Y \rightarrow O$. Our goal is to find the conditions under which these transitions are likely to occur. The interest of such a minimal description is to give some robustness to the phenomenon in the sense that it "hides" fine biochemical effects behind effective parameters, and can give a first picture which could be specialized later to more specific situations. Therefore, based

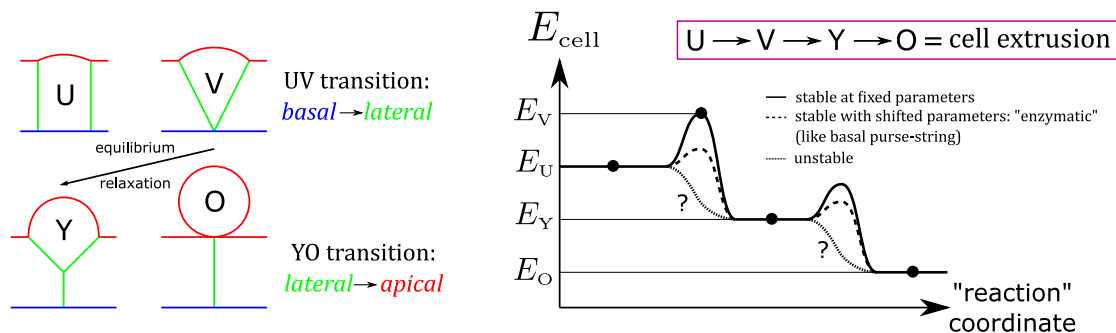


Figure 4.1: Single cell extrusion is seen as a two-step irreversible transition. Starting from uniform state (U), the target cell first loses its basal interface (V), relaxes to state (Y) where forces equilibrate on the central lateral vertex, and exit the tissue monolayer (O) by transition to total apical interface. In terms of energy landscape, the $U \rightarrow V$ and $Y \rightarrow O$ transitions can be prevented by the mechanical stability of U and Y states (full line), be favoured under an "enzymatic" shift of some mechanical parameters (dashed line), or occur spontaneously through an instability (pointed line).

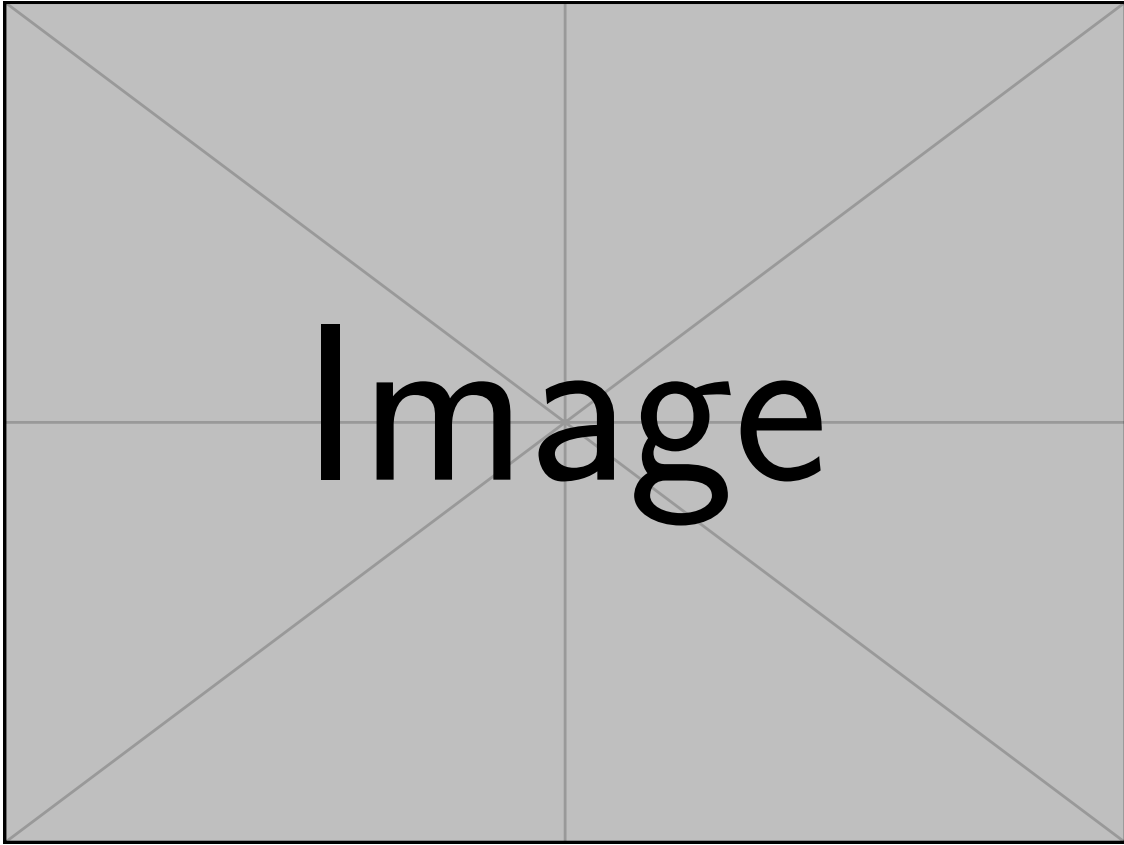


Figure 4.2: *Cell extrusion in biology.* **(a)**: Top view of live-cell extrusion (left) versus apoptotic extrusion (right), where the later activates caspases (green). In both cases, a contractile actomyosin ring assembles to eliminate the target cell from the tissue. From review [258]. **(b)**: Transverse view of the amniosera tissue in *Drosophila* embryo, showing myosin intensity at two different times (~ 1 min intervall). An apical enrichment of actomyosin leads to basal cell extrusion. From [259]. **(c)**: Side view of a transformed MDCK cell expressing a constitutively active form of CDC42 (green). It is eliminated from the tissue through apical cell extrusion. From [260]. **(d)**: Top view of an intestinal villi from rabbit, showing tight junctions (red), nuclei (blue), and bacteria *Listeria monocytogenes* (green). The white arrow indicates an extruding cell. From [261].

on generic mechanical properties of cells (cortical tension, cell-cell adhesion, contractile ring), we try to identify those able to control the two transitions responsible for extrusion.

In particular, the mechanical stability of those states up to small shape perturbations is expected to be central, as any instability regime may be found to spontaneously drive the cell extrusion process. As depicted on Fig. 4.1, one distinguishes three regimes for those transitions: stability of U and Y states, either at fixed parameters (high activation barrier) or with modified properties (low activation barrier), as well as a mechanical instability (spontaneous extrusion). A straightforward example for an "enzymatic" shift of cell properties is the assembly of a contractile ring at the base of apoptotic cells [230] that would naturally drive the $U \rightarrow V$ transition.

To reduce the technical complexity coming from the stress propagation away from the target cell, we considered that only first neighbours are perturbed and included in a uniform tissue when studying enzymatic shifts. Similarly for the study of shape instabilities, we choose to consider a three-cell system rather than a full tissue under confinement (external compression). This allows for a full non-linear description and we expect the main results to be qualitatively preserved.

4.1 Introduction to cell extrusion

4.1.1 The biological context

Cell extrusion is a highly conserved mechanism in metazoan organisms: it consists in the elimination of a target cell from the tissue (generally an epithelial monolayer), whereas neighbours converge to close any residual gap and preserve the barrier function [230]. This phenomenon is essential to regulate cell density and defend epithelial tissues against oncogenic transformations, pathogenic infections and generic cell damages inducing programmed cell-death (reviews [262, 263]).

As shown on Fig. 4.2a, cells can extrude before any programmed cell death or during apoptosis with activated caspases. Live-cell extrusion is then followed by a special programmed cell death called anoikis, associated to the loss of cell-cell and cell-matrix adhesion (review [258]). Whether cell death is a cause or a consequence of cell extrusion remains controversial: whereas some observations suggest that over-crowding is sufficient to active live-cell extrusion [188, 264], other reports on similar *in vitro* or *in vivo* biological systems reach opposite conclusions [265, 266]. In addition, the *in vivo* observation of extruded cells showing features of programmed cell death on mutants lacking caspase genes adds even more complexity [267].

Nonetheless, the canonical picture of the phenomenon associates cell extrusion to the assembly of a contractile actomyosin ring on the basal side which leads to its removal (Fig. 4.2a). This structure is not cell-autonomous but an initial actomyosin enrichment is observed at the apex of apoptotic cell [268], a first step that could build a rosette-like structure for neighbours to efficiently eliminate the target cell [261]. Actomyosin enrichment is believed to be controlled by sphingosine-1-phosphate (S1P) signalling [269], but how it localizes on the basal side and which upstream factors trigger the extrusion process remain poorly understood. Indeed, some apoptotic cells are not observed to extrude apically but in the basal direction as shown on Fig. 4.2b, with frequency dependent on the perturbation of the microtubule network [270]. The polarity reversal of cell extrusion may be important for the dissemination of pre-cancerous cells ([270, 271] and reviews [262, 263]). Cell extrusion also constitutes a protective mechanism against neoplasia, in a process called Epithelial Defense Against Cancer (EDAC) to eliminate transformed cells in the lumen (reviews [263, 272]). As shown on Fig. 4.2c, extrusion of transformed cells [273, 260] can be seen as a limit case of EDAC in the context of cell competition [169, 265].

More generally, various biological phenomena designated with a variety of different names share strong similarities with cell extrusion: ingression [274] or delamination [259, 264] during development with basal polarity (Fig. 4.2b), cell competition and elimination with apical polarity [273, 265, 169] or intestinal cell shedding for tissue renewal [275, 188]. For the later case, cell extrusion can also be hijacked by pathogens to infect the organism, illustrating its ambivalent effect with a role on several diseases (review [263]). As shown on Fig. 4.2d, *Listeria monocytogenes* is able to bind E-cadherins of extruding cells at the tip of villi and cross the epithelial barrier [261]. Finally, some reports have recently accumulated to identify some sub-cellular processes controlling cell extrusion: the recruitment of polarized neighbour cells through a calcium wave [276], the re-assembly of desmosomal junctions to control the actomyosin ring positioning [277], an E-cadherin dependent mechanotransduction posterior to S1P activation [278], a potential link between pulsatile actomyosin contractions and cells selected for extrusion [279], or DNA replication stress [280].

4.1.2 Crowding-induced cell extrusion

Beyond biochemical properties and biological context, a canonical picture of epithelial tissue homeostasis emerged recently with sensitivity to the mechanical pressure induced by over-crowding ([188, 264], review [258]). Indeed, *in vitro* experiments showed that a compressed epithelium have a higher extrusion rate (Fig. 4.3a), whereas cell stretching promotes cell division [281]. Interestingly, the fraction of non-apoptotic versus apoptotic extrusion events increases with tissue compression

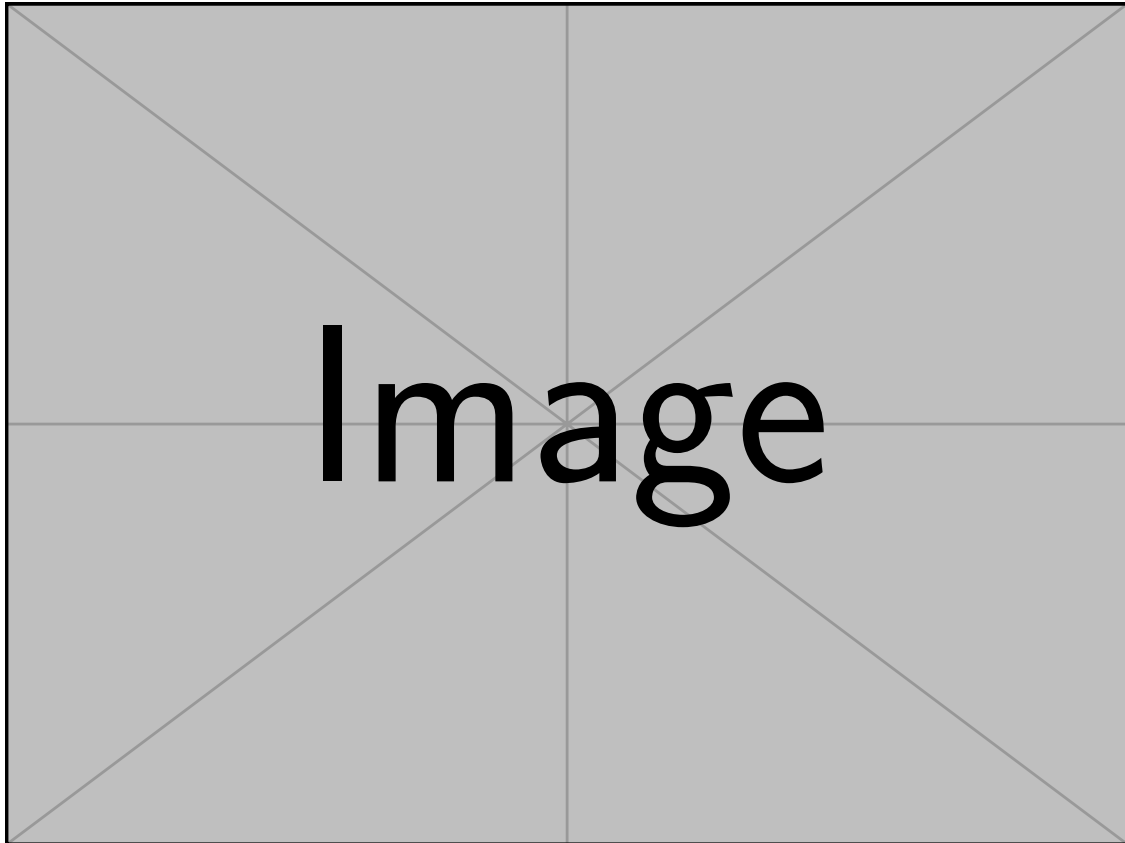


Figure 4.3: *Cell extrusion under growth-induced compression.* **(a)**: Cell extrusion rate over an MDCK monolayer that grows over a stretchable elastic membrane. Prior membrane stretching is applied and released after tissue confluence to apply a controlled compression strain (% of stretch). From [188]. **(b)**: Sketch of epithelial tissue homeostasis: low density promotes cell division through stretching (top left) whereas high density triggers extrusion events (bottom left). Those feed-back mechanisms stabilize the confluent monolayer state (right). Modified from review [258]. **(c)**: Sketch of the live-cell extrusion pathway induced by sphingosine-1-phosphate (S1P), itself activated by the mechano-sensitive channel Piezo1 that responds to the tissue crowding state. Cell extrusion is followed by anoikis-type of death by loss of cell-matrix adhesion. From review [262]. **(d)**: Apoptotic extrusion of MDCK monolayers is generated by a contractile actomyosin ring for high tissue density (right) and lamellipodial protrusions for small tissue density (left). This is reminiscent of epithelial gap closure. From [231]. **(e)**: Probability density for the number of $+1/2$ defects at a given distance r_e from the different extrusion sites. It shows a positive correlation between extrusion and $+1/2$ defect positions, which is robust to a change of cell type. From [266].

amplitude as shown on Fig. 4.3a. Moreover, a global density threshold around 30% compression strain appears to significantly increase the extrusion rate on *in vitro* measurements [188]. Another threshold appears when measuring the local density increase between proliferating regions and extrusion sites, found to be around 80% for human intestine, zebrafish epidermis or MDCK cell culture ([188] and review [258]).

This density dependency is summarized on Fig. 4.3b where a low density generates cell spreading and stretching to activate cell division whereas over-crowding leads to cell extrusion: therefore, those feed-back mechanisms ensure tissue homeostasis with a confluent monolayer state.

In both cases of compressed or stretched monolayer, the mechano-transduction appears to be controlled by the mechano-sensitive channel Piezo1 [188, 281]. Then, Piezo1 appears upstream in the live-cell extrusion pathway, to activate S1P and trigger cell elimination (Fig. 4.3c). Thus, tissue cell density appears as an important variable for the localization of cell extrusion, this is exemplified by the localization of cell shedding at the tip of villi where proliferating cells born at the crypts accumulate ([275, 188], review [258]).

Similarly, other *in vitro* experiments showed that a contractile actomyosin ring is not the only possible mechanism to eliminate apoptotic cells: lamellipodial protrusions are observed to trigger cell extrusion through neighbour-to-neighbour contact at low density whereas a ring assembles for highly-packed tissues (Fig. 4.3d). This draws a beautiful analogy with the phenomenon of epithelial wound healing where those two modes are also observed [226], seeing the extruding site as a tissue gap of one cell-width.

Finally, the local cell alignment (in the horizontal plane) also appears as an important property for cell extrusion in epithelial monolayers. A non-polar alignment can be assigned to individual cells on confluent monolayers with image analysis of their shape, and averaged into a mesoscopic field that exhibits topological defects in orientation with $+1/2$ or $-1/2$ topological charge in the plane. Interestingly, [266] observed for different cell types a clear correlation between apoptotic extrusion sites and $+1/2$ nematic defects (Fig. 4.3e). Indeed, $+1/2$ nematic defects co-localize with regions of highest compressive stresses whereas cells at $-1/2$ defects are stretched, and could justify mechanically the experimental correlation. Note that contrarily to previous expectations, no clear correlation has been observed between regions highest cell density and extrusion rate [266].

Hence, all those experimental features converge towards a positive correlation between cell extrusion likelihood and tissue compression in the neighbourhood, either in terms of deformation or mechanical pressure exerted by the surroundings on the target cell.

4.2 Results: weakly perturbed tissue around target cell

In normal conditions, since cell extrusion is crucial for the physiological integrity of epithelial tissues *in vivo*, one expects specific biochemical elements (S1P, Piezo1) to regulate its activation or inhibition based on the mechanical tissue state. Therefore, a purely mechanical modelling without integration of essential pathways is unlikely to be relevant for this situation. However, oncogenic transformations on individual cells are known to affect their shape and mechanics [273, 260]: we then target the phenomenology of epithelia under local hyperplasia with single transformed cells surrounded by a normal tissue to apply our generic description.

A previous model [282] used a clever quantification to map continuously the U , V and Y configurations on a single geometric variable: crowding-dependency was then investigated based on pure energetics within a 3D polygonal framework. Here, we try to identify a full configurational path from the U state to cell extrusion. In that picture, a spontaneous transition would correspond to an absence of activation barrier (Fig. 4.1).

4.2.1 Extrusion and multilayering 'rule of thumb'

The simplest way to approach single cell extrusion is to compute the energy difference between a uniform monolayer of N cells and that with $N - 1$ cells where one cell gets extruded and converts its baso-lateral interface into apical type, with circular shape of radius R as shown on Fig. 4.4a.

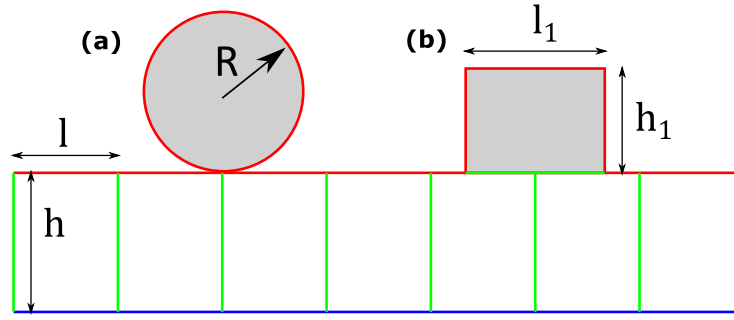


Figure 4.4: **(a)**: One cell is extruded from the monolayer going from N to $N - 1$ cells. The baso-lateral interface is converted into apical type (cell-lumen). **(b)**: One cell builds a new layer on top of a monolayer (multilayering transition). In principle, the apical interface should be a circular arc but we force a rectangular geometry for simplicity.

For high apical tension, the uniform tissue configuration has an energy $E_{\text{unif}} = N [(\alpha + \beta)l + 1/l]$ (with $N \gg 1$). Area conservation imposes $R = 1/\sqrt{\pi}$ to the central cell and the total energy of the new configuration is

$$E_{\text{extr}} = (N - 1) \left[(\alpha + \beta)l + \frac{1}{l} \right] + 2\alpha\sqrt{\pi} \quad (4.1)$$

This energy is minimal with respect to l when $l = l^* \equiv 1/\sqrt{\alpha + \beta}$. Then the new configuration will be energetically favourable only if $E_{\text{extr}}^* < E_{\text{unif}}^*$, or

$$\beta > \alpha(\pi\alpha - 1) \quad (4.2)$$

The factor $\pi\alpha - 1$ should be positive because this derivation assumes flat apical interfaces ($\alpha \gg 1$). It is clear that spontaneous extrusion is unfavoured when $\beta < 0$, for a well-spread tissue. However, even if $\beta \lesssim \alpha$, this criterion allows extrusion only for values of apical tension that are not compatible with the apical constraint $\alpha \gg 1$ and spontaneous extrusion is unlikely.

One can show that this qualitative behaviour is preserved when the uniform tissue is assumed to have curved apical interfaces, and extrusion is favoured only when $\alpha \lesssim 1$ and $\beta \sim \alpha$ or $\beta > \alpha$. Note that for uniform polar tensions, the later condition is incompatible with the basal vertex equilibrium at the tissue periphery that asks for $\beta < \alpha$, and the tissue state is ill-defined. Thus, this simple energetic analysis shows that extrusion is likely to occur when $\alpha \lesssim 1$ and $\beta \sim \alpha$: the costs to convert interfaces from basal-to-lateral or lateral-to-apical are equivalent and one needs to increase lateral tension. This is hard to achieve because of the strict apical force balance constraint $\alpha > 1/2$, whereas the different sources of interfacial tensions (see part II) argue for $\Gamma_1 < \Gamma_a$ ($\alpha > 1$) due to the adhesion energy density $w_{\text{cadherins}}$.

Of course, this doesn't take into account the different intermediate states that cells must reach to end in the extruded configuration, whose would be energetically disfavoured in general since the uniform state is stable. An activation barrier needs to be overpassed, thanks to spontaneous fluctuations, internal active processes or change of tissue environment like an external compression (see below).

For a multilayering transition where the extruded cell does not lose its lateral interface with neighbours. Ignoring the local shape perturbations necessary to reach a new mechanical equilibrium and simplifying the top cell shape¹ as in Fig. 4.4b, the energetic cost of the process is

$$\Delta E_{\text{multi}} \simeq -\beta l - h - \alpha l + l_1 + 2\alpha h_1 \quad (4.3)$$

The top cell minimizes its energy $E_1 = 2\alpha/l_1 + (2\alpha + 1)l_1/2$ for $l_1^* = \sqrt{4\alpha/(2\alpha + 1)}$. Since the rectangular shape assumption requires $\alpha \gg 1$, one gets $l_1^* \simeq \sqrt{2}$, and the condition for spontaneous

¹A correct tension balance on vertices and curved apical interfaces would deform the cells near the top cell, with spatial stress propagation to neighbours that goes beyond the simple approach of this section.

multilayering transition ($\Delta E_{\text{multi}}^* < 0$) becomes

$$\beta > \frac{1}{2}\alpha^2 \quad (4.4)$$

with weakly perturbed monolayer ($l \simeq l^*$). The criterion is qualitatively equivalent to full extrusion: again, a spreading tissue with negative basal tension remains as a monolayer whereas a sufficient basal enrichment of actomyosin is necessary (not sufficient) for the creation of new layers.

If one now considers a tissue monolayer of N cells to be under compression, one can ask in which conditions it would be favourable to get n extruded cells and release the tissue pressure.

To achieve this, a fixed deformation is applied on a monolayer of N cells, from a total undeformed length $L^* = Nl^*$ to $L = Nl$, with an horizontal strain $\epsilon = (L^* - L)/L^*$. The energy increase associated to compression is $\Delta E_{\text{comp}}^* = N\sqrt{\alpha + \beta}\epsilon^2/(1 - \epsilon)$ and it corresponds to an applied force (per unit length) $F_\epsilon = (\alpha + \beta)\epsilon(2 - \epsilon)(1 - \epsilon)^{-2}$. The compressed cell has a width $l = l^*(1 - \epsilon) = 1/\sqrt{\alpha + \beta + F_\epsilon}$ which obviously decreases if the deformation ϵ increases.

Using the expressions of the first paragraph and the compressive constraint $Nl^*(1 - \epsilon) = (N - n)l_n$, where l_n is the cell width on the bottom layer when n cells have been extruded ($l_0 \equiv l$), one gets the energy difference

$$\Delta E_n = n \left[2\alpha\sqrt{\pi} + \frac{\sqrt{\alpha + \beta}}{1 - \epsilon} \left(\frac{n}{N} - 2 \right) \right] \quad (4.5)$$

The condition $\Delta E_n < 0$ is independent from n if $n \ll N$ and one obtains a deformation threshold in that case

$$\epsilon > \epsilon_{\text{crit}}, \quad \text{with} \quad \epsilon_{\text{crit}} \equiv 1 - \frac{\sqrt{\alpha + \beta}}{\sqrt{\pi\alpha}} \quad (4.6)$$

One recovers the spontaneous criterion if $\epsilon = 0$ whereas extrusion can be triggered for a sufficient compression amplitude. The critical strain $\epsilon_{\text{crit}} \propto \sqrt{\alpha}$ for $\alpha \gg 1$ and $\beta \lesssim \alpha$: columnar cells are unlikely to increase. If $\beta > 0$ with $\beta \lesssim \alpha$, one has $\epsilon_{\text{crit}} \propto 1 - 1/\sqrt{\alpha}$ and the transition is unfavoured when α is too large.

4.2.2 Enzymatic shift of model parameters

As explained above, the first transition corresponding to a loss of basal interface ($U \rightarrow V$) can occur either spontaneously through an instability or appear for a critical change of cell parameters. Here in 2D, a contractile actomyosin ring on the basal side [230] corresponds to inward forces on basal vertices, and appears equivalent to an increase of basal (line) tension: $\Gamma_b \mapsto \Gamma_b^p$. In addition, more general cell transformations that are observed to affect cell shape and mechanical properties [273] could be mapped to a shift of lateral ($\Gamma_l \mapsto \Gamma_l^p$) or apical tension ($\Gamma_a \mapsto \Gamma_a^p$). Since the 2D side vertex model only contains polar tensions $\Gamma_b, \Gamma_l, \Gamma_a$ and target area A_0 as parameters, some specific transformation applied on an individual cell could also affect its size ($A_0 \mapsto A_0^p$). All possibilities are shown on Fig. 4.5a. Dimensionless perturbed tensions are called $\beta_p \equiv \Gamma_b^p/\Gamma_b$, $\lambda \equiv \Gamma_l^p/\Gamma_l$ and $\alpha_p \equiv \Gamma_a^p/\Gamma_a$, whereas $a_p \equiv A_0^p/A_0$.

In principle, one should compute the equilibrium state associated to a monolayer with homogeneous properties, centred on a target cell with different parameters (see Fig. 4.5a). However, this local perturbation causes a mechanical relaxation in the neighbourhood, on a length $l^*\Lambda$ with the characteristic factor $\Lambda(\alpha, \beta)$ that increases with α . Here the periphery is sent to infinity but, for exact (non-linear) deformations, the computation requires the resolution of a boundary-value problem to match the perturbed shape of the target cell and the homogeneous equilibrium state at infinity ($h = h^*$). It requires a double-shooting method on the central cell variables but convergence to $h = h^*$ at infinity is sensitive to the initial shooting point. Although achievable for specific parametric conditions (α, β) , a more systematic exploration of the parameter space is numerically demanding and has not been done yet. Another strategy could be to use the continuous approximation for the surrounding tissue, valid when $\alpha \gg 1$, and keep discretization on the target and its

first neighbours.

A simplifying assumption can be made to reduce the technical complexity and illustrate the expected results: it assumes a cell-scale size for the tissue relaxation away from the target cell such that the second neighbours have an homogeneous equilibrium state as shown on Fig. 4.5a. Then, the 2D monolayer can effectively be described as a 3-cell system with modified apical and basal vertex force balances when tensions differ on the central cell. Formally speaking, this limit is valid when the shape relaxation occurs over one cell-size when the continuous limit is unvalid ($\Lambda \lesssim 1$): this occurs when $\alpha \lesssim 1$ and $|\beta| \lesssim \alpha$. With this model, one searches the necessary conditions for an equilibrium state with vanishing basal interface on the central cell, representing the "enzymatic-driven" $U \rightarrow V$ transition associated to oncogenic-like cell transformations.

One studies the perturbation response of the central cell to four independent parametric shifts (apical tension, lateral tension, basal tension and area), keeping other parameters at their standard value. The results are given on Fig. 4.5b,c and Fig. 4.6a as density plots in the plane (α, β) , representing critical shifts at which interfacial loss occurs². As expected, basal detachment of the central cell is associated to an increase of basal tension β_p (Fig. 4.5b), phenomenologically related to a contractile ring in cell extrusion [230]. The density plot shows that higher basal tension in the surrounding tissue reduces the enzymatic shift amplitude needed for the $U \rightarrow V$ transition. To eliminate the basal interface, a reduction of apical tension α_p is also effective since it decreases the energetic cost for more apical interface (Fig. 4.5c, inset). On the opposite, a change of central area a_p does not lead to a loss of basal interface because a positive shift weakly affects the basal width, whereas a decrease tends to reduce the apical interface. It comes from the vertical slope of the lateral interface on the basal plane, whereas the apical vertex force balance is tilted towards center through apical area decrease and induces interfacial loss for a critical reduction. Then, the density plot in Fig. 4.6a represents the critical central area at which the apical size vanishes.

Compared to a full monolayer response, the accuracy of this 3-cell system (Fig. 4.5a) can be captured by the difference between hydrostatic pressure P_1 in the first neighbours to central cell and the uniform value P^* . Whereas a pressure difference between central cell and first neighbour is equilibrated by lateral curvature, the 3-cell system cannot account for the pressure difference with second neighbours. With boundary pressure imposed at uniform value P^* , the quantity $\Delta P_1 \equiv (P_1 - P^*)/P^*$ can account for the "error" introduced by the 3-cell system. It is shown for the case of an areal shift in a density plot (Fig. 4.6b). Note that the error is reduced when α and β decrease: this is expected because it corresponds to the region of higher stress localization (small factor Λ). Thus, the results from the 3-cell system are equivalent to the full monolayer response when $\alpha \lesssim 1$ and $|\beta| \lesssim \alpha$.

Finally, a perturbation of the lateral tension, with a factor λ between the central cell and first neighbour value (Fig. 4.6c,d) does not lead to any interfacial disappearance. Again, the 3-cell system reproduces accurately the full monolayer response only when λ weakly deviates from 1, as shown by the error on Fig. 4.6d.

For each perturbation scenario (Fig. 4.5b,c and Fig. 4.6a), one should search for the density plot region associated to lowest critical shift: it corresponds to high apical α and basal β tensions for apical, basal and area shift. Of course, the link between α , β amplitudes and equilibrium tissue shape means that too high values are not expected to account for reasonable height-to-width cell aspect ratios measured experimentally³. In all cases, the criticality (interface loss) occurs at large relative perturbations and a scenario where fluctuations could drive this interfacial transition is unlikely: this enzymatic shift then needs to be associated to biochemical-dependent expression of acto-myosin levels as observed on transformed cells [273, 170].

²In principle, an epithelial-to-mesenchymal transition at the tissue periphery could generate a basal tension gradient so that the tension constraint $|\beta| < \alpha$ on the peripheral basal vertex is not mandatory. Nonetheless, the constraint $|\beta| < \alpha$ is assumed on Fig. 4.5 and Fig. 4.6 to keep coherence with other chapters.

³The aspect ratio h^*/l^* is of the order of 2α for large α and $\beta \lesssim \alpha$ such that a reasonable limit may be $\alpha < 5$.

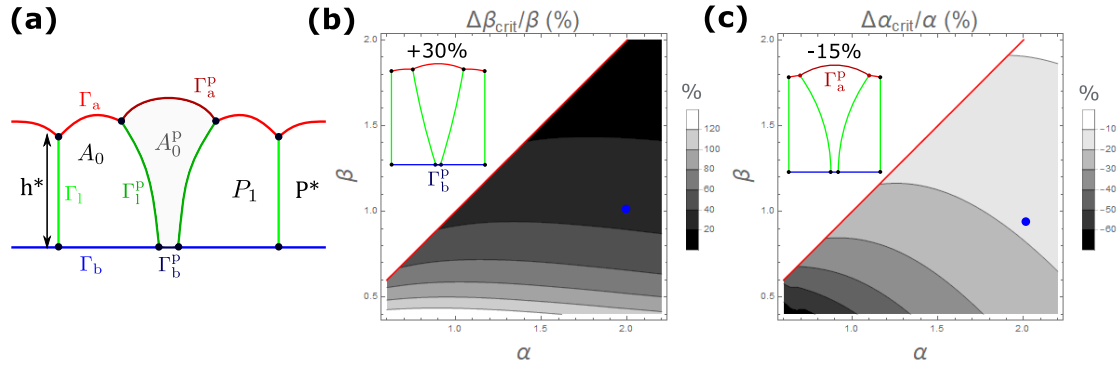


Figure 4.5: **(a)**: Sketch of three cells included in a large monolayer where the central cell has perturbed properties with respect to normal tensions Γ_b , Γ_1 , Γ_a and area A_0 : basal tension Γ_b^p , lateral tension Γ_1^p , apical tension Γ_a^p and area A_0^p . Shape perturbation is assumed to occur over one cell size such that second neighbours are in the standard equilibrium state (h^* , l^* , P^*). **(b)**: Density plot in parameter space (α, β) for basal detachment of the central cell in the case of basal tension perturbation, with $\Delta\beta \equiv \beta_p - \beta$. The inset represents the equilibrium state associated to the blue point before basal disappearance, for $\alpha = 2$, $\beta = 1$ and $\Delta\beta/\beta = +30\%$ (disappearance at $\sim +40\%$). Red line represents $\beta = \alpha$. **(c)**: Density plot for basal detachment of the central cell in the case of apical tension perturbation, with $\Delta\alpha \equiv \alpha_p - \alpha$. The inset represents the equilibrium state associated to the blue point before basal disappearance, for $\alpha = 2$, $\beta = 1$ and $\Delta\alpha/\alpha = -15\%$ (disappearance at $\sim -20\%$). Red line represents $\beta = \alpha$.

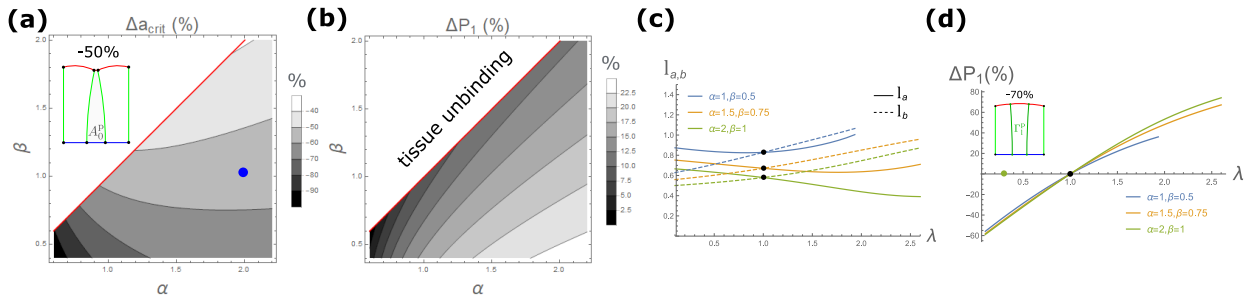


Figure 4.6: **(a)**: Density plot in the case of surface area perturbation, with $\Delta a \equiv a_p - 1$. Central area reduction leads to apical disappearance. This is illustrated by the inset representing the equilibrium state of the blue point before apical disappearance, for $\alpha = 2$, $\beta = 1$ and $\Delta a = -50\%$ (disappearance at $\sim -60\%$). Red line represents $\beta = \alpha$. **(b)**: Density plot for the error induced by the assumption of one cell relaxation, measured in terms of pressure difference $\Delta P_1 \equiv (P_1 - P^*)/P^*$. Red line represents $\beta = \alpha$. **(c,d)**: Plot of central cell widths (c) and pressure deviation (d) when lateral tension is perturbed with $\lambda \equiv \Gamma_1^p/\Gamma_1$ and chosen values of α and β . No criticality exists either for positive ($\lambda > 1$) or negative deformation ($\lambda < 1$), as shown by the inset representing the equilibrium state for the green point (d): $\alpha = 2$, $\beta = 1$ and $\lambda - 1 = -70\%$. Black dots corresponds to the uniform state with $\lambda = 1$.

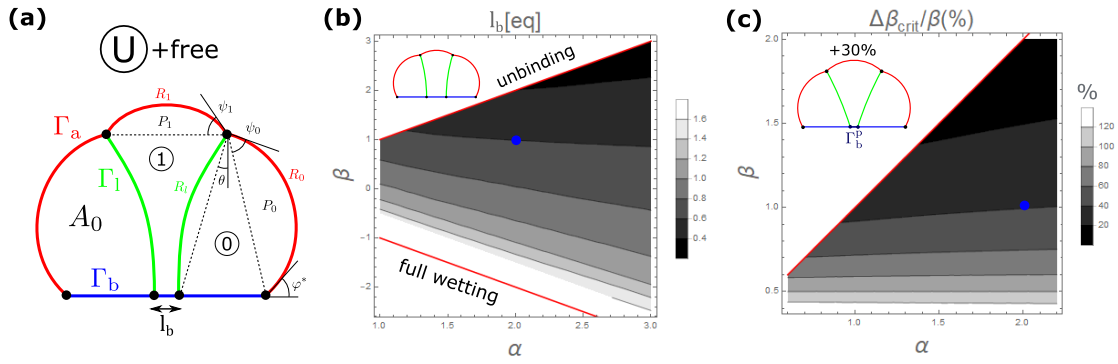


Figure 4.7: **(a)**: Sketch of the free 3-cell system in the U configuration, where the central cell keeps a finite basal interface with $\beta > 0$. **(b)**: Density plot in the parametric space (α, β) , for the basal width l_b of the central cell at equilibrium. An equilibrium shape is shown for the blue dot at $\alpha = 2$ and $\beta = 1$ (inset). Red lines represent $\beta = \pm\alpha$, with $|\beta| > \alpha$ not captured by the model. One has full wetting when $\beta \rightarrow -\alpha$ and substrate unbinding if $\beta > \alpha$, by force balance on peripheral basal vertices. **(c)**: Density plot for the critical basal tension shift $\Delta\beta_{\text{crit}}/\beta(\%)$ at which basal disappearance occurs on the central cell. An equilibrium shape prior to criticality is shown for the blue dot at $\alpha = 2$, $\beta = 1$ and $\beta_p = 1.3\beta$ (inset). Red line represents $\beta = \alpha$.

4.3 Results: three-cell system and spontaneous instability

As explained in the previous chapter, the identification of mechanical equilibrium for a non-uniform epithelial monolayer is already challenging technically. Rather than enzymatic shift of polar tensions on a target cell, we now search for a generic instability that could trigger the two extrusion-like transitions $U \rightarrow V$ and $Y \rightarrow O$ (see Fig. 4.1) when external compression is applied on tissue boundaries. Since intermediate configurations where the basal interface of the target cell has been lost (represented by symbol Y) cannot be captured by a simple linear expansion, we ask for a minimal description able to capture non-linear shape transformations.

For that, we consider a 3-cell system which differs from the previous chapter by the absence of any surrounding monolayer (Fig. 4.7a). This is a minimal system to study central cell extrusion and its simplicity allows the description of non-linear shape transformations. One drawback is the over-sensitivity to tissue boundaries, at only one cell width from the target cell, but since we search for the existence of shape transitions $U \rightarrow V$ and $Y \rightarrow O$, we claim that this 3-cell system gives necessary (not sufficient) conditions on them.

We first study the equilibrium state of this minimal system and then apply external compression to search for generic shape instabilities.

4.3.1 Free conditions

The equilibrium state of three incompressible cells with polar tensions looks as the sketch of Fig. 4.7a. It deviates from the spherical cap of a liquid droplet by the existence of lateral tensions that pull on the apical vertices with apical tension balance $2\alpha \sin \psi^* = 1$. The uniformity of tensions for all cells impose a vertical slope on the lateral interface at the basal plane, but a pressure difference exists and curves the lateral interface. Then compared to a uniform tissue, the apical tension balance is tilted and the central cell makes an angle $\psi \neq \psi^*$ with the horizontal line (Fig. 4.7a).

At the "tissue" boundary, equilibrium between basal and apical tension is ensured with a contact angle φ^* such that $\alpha \cos \varphi^* = \beta$. Thus the parametric constraint $|\beta| < \alpha$ is mandatory here, contrarily to the previous chapter where the existence of a surrounding tissue could implicitly allow for some basal tension gradient at the periphery. In addition, apical tension balance requires $\alpha > 1/2$ to be defined. Hence, the density plot for the equilibrium basal width l_b (Fig. 4.7b) is restricted to the parametric sub-space $|\beta| < \alpha$ and $\alpha > 1/2$. Again to prevent unrealistic height-to-width cell aspect ratios, we also restrict values of apical tension to $\alpha \lesssim 4$. Finally, the limit $\beta \rightarrow -\alpha$ corresponds to a full wetting regime ($\varphi^* \rightarrow \pi$) with vanishing tissue height and infinite

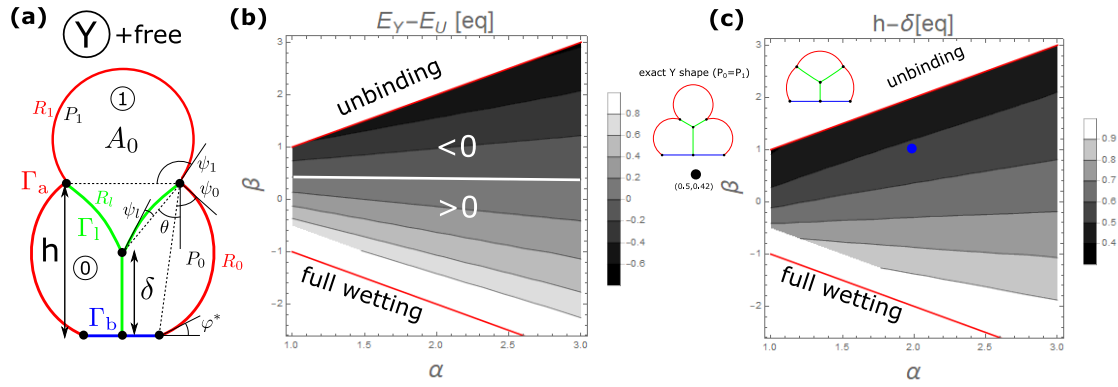


Figure 4.8: **a)** Sketch of the free 3-cell system in the Y configuration, when the central cell has lost its basal interface. **(b)**: Density plot of the equilibrium energy differences between Y and U configurations. The first one is favoured when $\beta > 0$ as expected. Red lines represent $\beta = \pm\alpha$. **(c)**: Density plot of the lateral height difference $h - \delta$ as defined in (a). An equilibrium shape is shown for the blue dot at $\alpha = 2$, $\beta = 1$ (inset). A special case is represented at $\alpha = 1/2$ for the black dot, when pressure difference $P_1 - P_0$ vanishes (outset). Red lines represent $\beta = \pm\alpha$.

planar extension: on Fig. 4.7b and below, one ignores this limit with the additional constraint $\beta > -\alpha + 0.5$. In such conditions, the mechanical equilibrium is well defined and the basal width of the central cell remains finite. Although not captured by this model, one expects basal tissue detachment when $\beta > \alpha$ as indicated on Fig. 4.7b.

For one central cell 1 and two identical neighbour cells 0, the energy of the system can be written in dimensionless form as

$$E_{\text{tot}} = \beta L_b + L_l + \alpha L_a - 2P_0(A_0 - 1) - P_1(A_1 - 1) \quad (4.7)$$

where L_b , L_l and L_a are, respectively, the total length associated to basal, lateral and apical interfaces. Areal incompressibility is introduced through Lagrange multipliers (pressures) P_0 and P_1 . The minimization of this energy (with constraints $A_0 = A_1 = 1$) gives at equilibrium: tension balance on vertices, Laplace relations $P_0 = \alpha/R_0$, $P_1 = \alpha/R_1$ and $P_0 - P_1 = 1/R_l$ for radii of curvature R_0, R_1 (apical) and R_l (lateral) (see Fig. 4.7a). Apical interfaces are characterized by "bump" angles ψ_0 and ψ_1 whereas the lateral "bump" angle ψ_l is equal to the angular tilt θ at equilibrium by basal tension balance. Then, apical tension balance can be shown to be equivalent to

$$\psi_0[\text{eq}] = \frac{1}{2} \left(\frac{\pi}{2} + \psi^* - 2\theta_{\text{eq}} \right), \quad \psi_1[\text{eq}] = \psi^* + 2\theta_{\text{eq}}, \quad \psi_l[\text{eq}] = \theta_{\text{eq}} \quad (4.8)$$

Similarly to the last chapter, an enzymatic shift of basal tension on the central cell is also able to trigger a $U \rightarrow V$ transition from a purely equilibrium reconfiguration (Fig. 4.7c). However, the present result is exact: the fact that critical percentages have a similar order of magnitude on both Fig. 4.5b and Fig. 4.7c indicates *a posteriori* the qualitative robustness of last chapter results, much beyond few percents error in ΔP_1 (Fig. 4.6b). Again, one observes a relative decrease of critical enzymatic shift when basal tension increases, making the $U \rightarrow V$ more likely through biochemical perturbations [273, 170].

Assuming basal disappearance to have occurred, the system needs to reorganize to ensure lateral tension balance on a tri-cellular junction (Y profile) as shown on Fig. 4.8a: at equilibrium, interfaces with identical tensions are separated through an angle of $2\pi/3$. Then, the equilibrium interfacial angles are modified according to

$$\psi_0[\text{eq}] = \frac{1}{2} \left(\frac{5\pi}{6} + \psi^* - 2\theta_{\text{eq}} \right), \quad \psi_1[\text{eq}] = \psi^* + 2\theta_{\text{eq}} - \frac{\pi}{3}, \quad \psi_l[\text{eq}] = \theta_{\text{eq}} - \frac{\pi}{3} \quad (4.9)$$

For given values of α and β , one can compare the system's energy for this Y configuration ($l_b[1] = 0$) with the U configuration ($l_b[1] \neq 0$): in agreement with intuition, a large basal tension makes the Y

configuration energetically favourable whereas the opposite occurs when $\beta < 0$ (Fig. 4.8b). Thus, if a mechanical instability can happen to trigger spontaneously a $U \rightarrow Y$ transition, it has to be in the parametric sub-space where basal tension is positive ($\beta > 0$). Note that a geometric incompatibility ($\delta < 0$) occurs for highly negative β , between the tissue spreading tendency and the tension balance at the tri-cellular junction.

For the central cell to reach a $Y \rightarrow O$ transition, one wants to minimize the size of its lateral interface, captured by the quantity $h - \delta$ as defined in Fig. 4.8a. Fig. 4.8c shows that the relevant region of parameter space that is more likely for extrusion corresponds to $\beta \lesssim \alpha$ and $\alpha \lesssim 1$. Indeed, the special case that minimizes $h - \delta$ appears at $\alpha = 1/2$ and $\beta \simeq 0.42$ as shown on Fig. 4.8c (inset): it corresponds to a state where the pressure difference $P_1 - P_0$ vanishes such that lateral interfaces are straight (Fig. 4.8c). Formally speaking, within this modelling framework with constant polar tensions and uniform pressure, the state symbolically represented by O (Fig. 4.1) cannot exist at mechanical equilibrium because it does not follow the constraints of shape circularity and tension balance at vertices.

4.3.2 External compression

We now move to the stability analysis of equilibrium configurations when external compression is applied, through a stiff device with untreated walls such that cell-wall interface does not affect the apical tension value. Starting from a tissue size L_0 , one applies a compressive strain ϵ with new tissue size L such that $\epsilon \equiv (L_0 - L)/L_0$. Phenomenologically, this external compression originates from over-crowding induced by cell divisions in the neighbourhood of a target cell.

We study separately the cases of negative or positive basal tension, for both $U \rightarrow Y$ transition from U configuration and $Y \rightarrow O$ transition from Y configuration.

Negative basal tension

As discussed previously, a negative basal tension makes energetically unfavourable the $U \rightarrow Y$ transition. Nonetheless, it is useful to introduce the compression procedure and to check that the stability analysis is compatible with expectations. As can be seen on Fig. 4.9a for the U configuration and Fig. 4.9d for the Y configuration, we describe external compression as two rigid walls forcing the system to extend over a tissue size L . To ensure that compression is applied for any value of (α, β) , we measure deformation with respect to the free tissue size $L_0(\alpha, \beta)$ which can be derived according to the previous section. For given parameters (α, β) , the free equilibrium size L_0 is first computed and one then applies the deformation constraint on tissue size $L = L_0(1 - \epsilon)$ for given compression strain ϵ . Thus, the external strain ϵ enters as a new parameter that can be replaced by tissue length $L(\alpha, \beta, \epsilon)$.

To adapt to the rigid wall constraints, cells must reorganize their apical interfaces as shown Fig. 4.9a,d: cells and walls form interfaces over the contact height d and the free apical interface connects with continuous slope such that $\psi_0 + \phi_0 = \pi/2$. Indeed, an increase of compressive strength increases the contact height in both U and Y configurations (Fig. 4.9b,f). As expected, external compression also reduces the basal width l_b of the central cell in the U configuration and induces more lateral tilt through angle θ (Fig. 4.9b).

For the Y configuration only, the lateral central height $h - \delta$ as defined in Fig. 4.9e decreases with ϵ . Indeed, since one asks for $h - \delta \rightarrow 0$ for a "complete" extrusion to occur with $Y \rightarrow O$ transition, compression has a positive influence. At higher strain, the central cell would also need to adapt its shape to the walls.

Note that for both U and Y configurations, a geometric incompatibility occurs when β is too negative, between the spreading tendency and the shape constraint from the wall leading to negative contact height d (Fig. 4.9c,g). Contrarily to the previous incompatibility for the free case ($\delta < 0$ when β too negative), this is artificial in the sense that the degree of freedom d is not required anymore and one has to remove the constraint $\psi_0 + \phi_0 = \pi/2$. In this situation, tensions on basal vertices at the tissue periphery are not equilibrated because of the stiff wall.

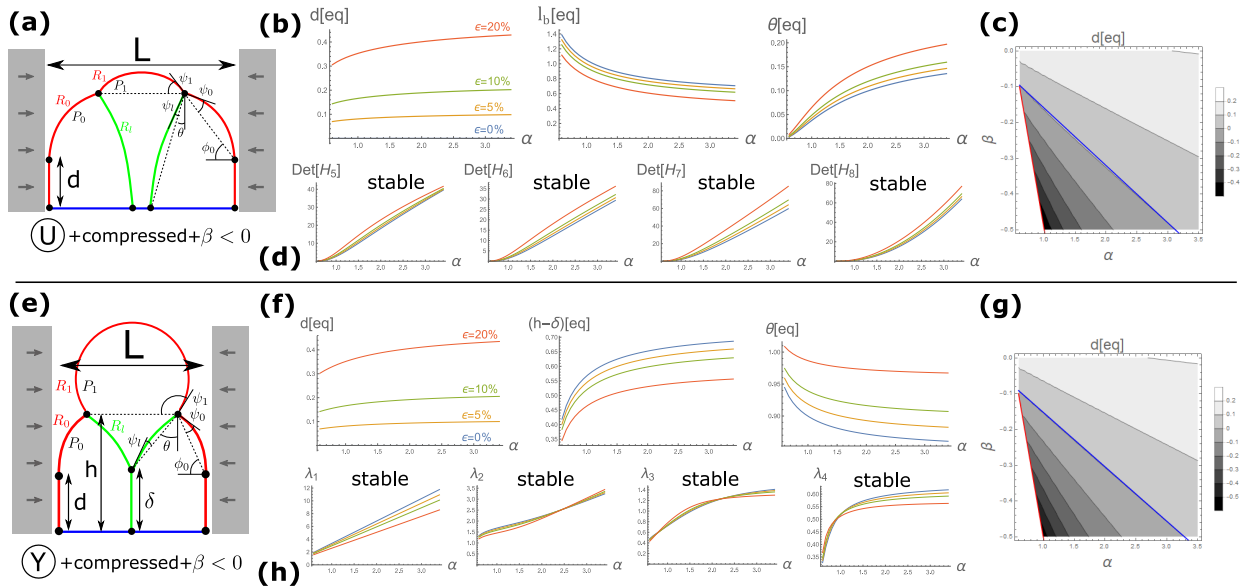


Figure 4.9: (a): Sketch of the compressed 3-cell system in the U configuration for $\beta < 0$. (b): Equilibrium quantities as a function of α along the parametric line $\beta = 0$ for U configuration: contact height d (left), central basal width l_b (middle) and tilt angle θ (right). The different lines correspond to different compression amplitudes for strain $\epsilon = 0, 5, 10, 20\%$. (c): Density plot of the contact height d in parametric space, for $\epsilon = 10\%$ and U configuration. The blue line indicates the limit of geometric compatibility under compression ($d = 0$). The red line corresponds to $\beta = -\alpha + 0.5$. (d): Determinants of Hessian matrix minors as a function of α along the parametric line $\beta = 0$, for U configuration and different compression amplitudes as in (b). (e): Sketch of the compressed 3-cell system in the Y configuration for $\beta < 0$. (f): Equilibrium quantities as a function of α along the parametric line $\beta = 0$ for Y configuration: contact height d (left), central lateral height $h - \delta$ (middle) and tilt angle θ (right). The different lines correspond to different compression amplitudes for strain $\epsilon = 0, 5, 10, 20\%$. (g): Density plot of the contact height d in parametric space for $\epsilon = 10\%$ and Y configuration. The blue line indicates the limit of geometric compatibility under compression ($d = 0$). The red line corresponds to $\beta = -\alpha + 0.5$. (h): Eigenvalues of the Hessian matrix as a function of α along the parametric line $\beta = 0$, for Y configuration and different compression amplitudes as in (f).

To study the stability of those equilibrium points, one needs to study the proximal energy landscape for out-of-equilibrium states. For the U case, one needs variables $\{P_0, P_1, R_0, R_l, R_1, d, \psi_0, \psi_l, \theta, \psi_1\}$ (Fig. 4.9a). In addition to incompressibility, there are two geometric constraints for tissue size and tissue height:

$$L = 4R_0 \sin^2 \psi_0 + 2R_1 \sin \psi_1, \quad 2R_0 \sin \psi_0 \cos \psi_0 + d = 2R_l \sin \psi_l \cos \theta \quad (4.10)$$

Those equations are used to eliminate d and R_1 but the two areal constraints $A_0 = A_1 = 1$ cannot be used explicitly to reduce the number of variables more and one has 8 independent variables $\{P_0, P_1, R_0, R_l, \psi_0, \psi_l, \theta, \psi_1\}$. This constrained optimization problem is associated to the computation of a bordered Hessian matrix and the determinants of its largest minors: $\text{Det}[H_5]$, $\text{Det}[H_6]$, $\text{Det}[H_7]$ and $\text{Det}[H_8]$. For given parameters (α, β, L) , the equilibrium state is

- a local minimum (stable) if all determinants are positive,
- a local maximum (unstable) if $(-1)^j \text{Det}[H_j] > 0$ for $5 \leq j \leq 8$,
- a saddle-point otherwise

Along the parametric line $\beta = 0$ as shown on Fig. 4.9d, one can compute those determinants for different compression values. The equilibrium is indeed stable for any α and ϵ , except when $\alpha \rightarrow 1/2$ where it looks marginal.

The stability analysis differs for the Y case because lateral height δ appears as a new variable and an additional geometric constraint exists (Fig. 4.9e), such that

$$L = 4R_0 \sin^2 \psi_0 + 2R_1 \sin \psi_1, \quad 2R_0 \sin \psi_0 \cos \psi_0 + d = 2R_l \sin \psi_l \cos \theta + \delta, \quad 2R_l \sin \psi_l \sin \theta = R_1 \sin \psi_1 \quad (4.11)$$

Now the two areal constraints $A_0 = A_1 = 1$ can be used explicitly to eliminate the five variables: d, δ, R_0, R_l and R_1 . Remains the four angular variables $\{\psi_0, \psi_l, \theta, \psi_1\}$. Here the problem becomes unconstrained and only depends on the eigenvalues of the Hessian matrix λ_j for $1 \leq j \leq 4$. The equilibrium state is stable (unstable) if eigenvalues are positive (negative), and corresponds to a saddle-point if they do not have the same sign. Again along the parametric line $\beta = 0$ as shown on Fig. 4.9h, one can compute those eigenvalues for different compression values, and see that the equilibrium is indeed stable for any α as expected.

Positive basal tension

For positive basal tension, the cells must adapt differently to the wall constraint because of the peripheral vertex force balance and one needs a new degree of freedom: the contact angle φ_0 (Fig. 4.10a and Fig. 4.11a). When uncompressed, the equilibrium state has already been determined (Fig. 4.7 and Fig. 4.8) with $\varphi_0[\text{eq}] = \varphi^*$. The addition of compression do not add any qualitative difference with the equilibrium quantities shown in the case of negative basal tension (Fig. 4.9b,f). The stability analysis follows the same trend but the new variable φ appears because of the freedom on the peripheral contact point when considering out-of-equilibrium states.

For the U configuration (Fig. 4.10), one gets 9 independent variables $\{P_0, P_1, R_0, R_l, \psi_0, \varphi_0, \psi_l, \theta, \psi_1\}$ with modified geometric constraint on tissue height

$$2R_0 \sin \psi_0 \cos \psi_0 + R_0 \cos \varphi_0 + d = 2R_l \sin \psi_l \cos \theta \quad (4.12)$$

The relevant determinants of the bordered Hessian matrix are: $\text{Det}[H_5]$, $\text{Det}[H_6]$, $\text{Det}[H_7]$, $\text{Det}[H_8]$ and $\text{Det}[H_9]$. The rules defined before are preserved and one needs $\text{Det}[H_j] > 0$ for any $5 \leq j \leq 9$ for mechanical stability. Density plots for those determinants show apparent stability over a large region of parametric space (α, β) but they all decrease near 0 when close to the parametric line $\beta = 0$ (Fig. 4.10b). Indeed, one finds $\text{Det}[H_5] \neq 0$ but $\text{Det}[H_6] = \text{Det}[H_7] = \text{Det}[H_8] = \text{Det}[H_9] = 0$

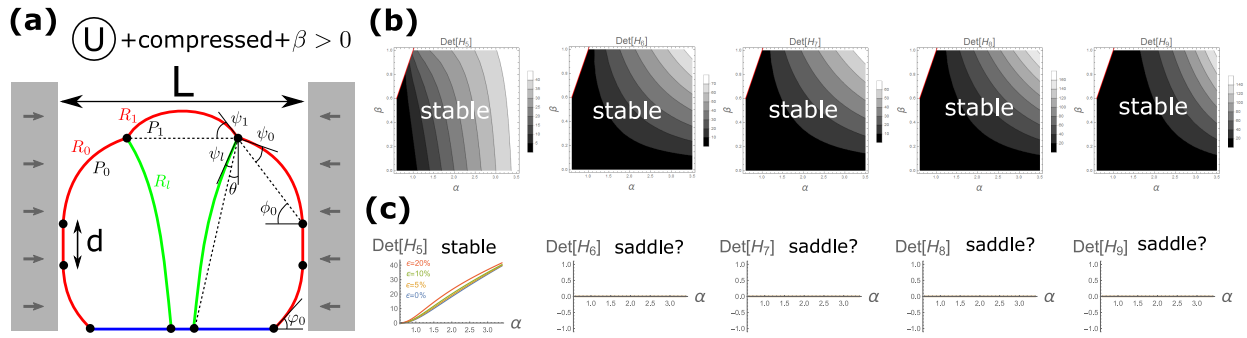


Figure 4.10: (a): Sketch of the compressed 3-cell system in the U configuration for $\beta > 0$. (b): Density plots of the determinants of Hessian matrix minors in parametric space, for $\epsilon = 10\%$. The red line corresponds to $\beta = \alpha$. (c): Determinants of Hessian matrix minors as a function of α along the parametric line $\beta = 0$, for different compression amplitudes with strain $\epsilon = 0, 5, 10, 20\%$.

along this line, which indicates marginal stability (Fig. 4.10c). However, the fact that this loss of stability is independent from compression strain ϵ or apical tension α makes it look like an artefact. Note that despite the same parameter values and hence identical equilibrium states, the stability analysis differs for negative (Fig. 4.9d) and positive basal tensions because the degrees of freedom are different: in the case of positive basal tension, a contact angle φ_0 adds another degree of freedom.

For the Y configuration (Fig. 4.11), the geometric constraint on tissue height is also modified as

$$2R_0 \sin \psi_0 \cos \psi_0 + R_0 \cos \varphi_0 + d = 2R_l \sin \psi_l \cos \theta + \delta \quad (4.13)$$

such that the five angles $\{\psi_0, \varphi_0, \psi_l, \theta, \psi_1\}$ remain as independent variables. Hence, there are now five eigenvalues λ_j associated to the Hessian matrix. Following again the parametric line $\beta = 0$ (Fig. 4.11b,c), another marginal stability appears and differs from the clear stability observed for negative basal tension for the same parameters (Fig. 4.9h). Density plots for those eigenvalues in the parametric space (α, β) show strict positivity for the first four eigenvalues (Fig. 4.11d). However, λ_5 is more interesting since it becomes slightly negative near the parametric line $\beta = \alpha$ (Fig. 4.11e), in addition to the marginal stability along the line $\beta = 0$ as in Fig. 4.11c.

To conclude from both equilibrium and stability analysis, minimization of central lateral height $h - \delta$ occurs when $\alpha \lesssim 1$ and $\beta \lesssim 1$ at equilibrium, whereas a spontaneous mechanical instability may trigger the $Y \rightarrow O$ transition necessary for a complete cell extrusion, as shown on Fig. 4.11e. However, no clear signature of mechanical instability has been identified for the $U \rightarrow Y$ transition, which may only rely on an enzymatic shift of either apical or basal tension.

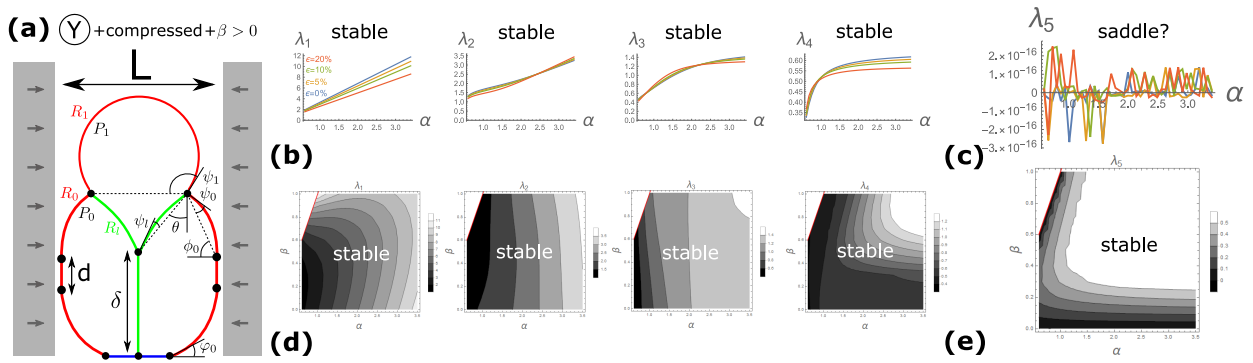


Figure 4.11: (a): Sketch of the compressed 3-cell system in the Y configuration for $\beta > 0$. (b,c): Eigenvalues of the Hessian matrix as a function of α along the parametric line $\beta = 0$, for different compression amplitudes with strain $\epsilon = 0, 5, 10, 20\%$. The first four eigenvalues (b) are positive but the last one λ_5 is zero (c). (d,e): Density plots of the eigenvalues associated to the Hessian matrix in parametric space, for $\epsilon = 10\%$. The last eigenvalue λ_5 is close to 0 along the parametric lines $\beta = 0$ and $\beta = \alpha$ (e). The red line corresponds to $\beta = \alpha$.

Chapter 5

General conclusion and perspectives

The theoretical work performed during this PhD have dealt with *in vitro* cell and tissue mechanics on solid substrates, in three different contexts: single cell spreading, collective rearrangements of cancer cells monolayers into 3D buds, and single cell elimination within epithelial monolayers. Whereas the first project can be considered independent, the two others share similarities: the initial state of those systems is an epithelial monolayer which undergoes cell rearrangements driven by external mechanical stress. For the second one, cells undergo multilayering transitions with a detachment from the substrate (basal-to-lateral), but remain in contact with neighbours. For the third one, a target cell starts with the same transition and loses its basal interface (basal-to-lateral), but also detaches from neighbours (lateral-to-apical) to exit the tissue. The major difference comes from the mechanical stress applied on both tissues: the source that triggers rearrangements is a frictional shear stress on the second project, but cell extrusion is driven by global tissue compression on the third project.

5.1 Lamellipodial initiation

The first project was purely theoretical, interested in the emergence of thin sheet protrusions called lamellipodia at the leading edge of spreading cells. The central idea of the model was to consider a generic coupling between membrane curvature (from a side view) and actin filament orientation in the cortex, which tends to align normally to the membrane plane. The localization of polymerization factors at the membrane establishes a natural cytoplasm-to-membrane polarity that defines a mesoscopic vector for the filamentous network polarization, and indicates the direction of actin retrograde flow. A deviation from the normal orientation adds an energetic cost described through a 2D liquid crystal framework, that favours alignment under high membrane curvature. On the ventral part of the cell, the interaction between the horizontal projection of the retrograde flow the adhesion receptors bound to the substrate generates frictional tractions.

Using a minimal ensemble with constant surface tension/2D volume/adhesion energy density, we described the quasi-static equilibrium similarly to liquid droplet wetting. The traction force adds an effective adhesion term that can trigger a «full wetting» transition thanks to a positive feedback loop between membrane edge curvature, actin reorientation and traction force generation. It occurs when actin filaments can follow the cell shape with minor energetic cost. We interpreted this asymptotic state as an emerging lamellipodium, which can also be nucleated in an anisotropic manner thanks to a bi-stability for intermediate values of actin-substrate coupling.

A direct extension of this model would be to treat axi-symmetric cells to check that nucleation of protrusions can also occur along the cell contour, a feature that would be reminiscent of the experimental distinction between isotropic and anisotropic cell spreading. After that, non axi-symmetric perturbations could be introduced to study the possibility of spontaneous symmetry-breaking and the establishment of cell polarization.

5.2 Cancerous budding and cell extrusion

The second project was made in collaboration with experimentalists, who studied the *in vitro* mechanics of circular Cancer Cell (CC) monolayers surrounded by a tissue of Cancer-Associated Fibroblasts (CAFs). Our collaborators wanted to investigate if CAFs could actively remodel tumours and generate invasive buds as it is observed *in vivo* for colo-rectal cancer. *In vitro*, CAFs assemble a contractile actomyosin ring along the CC cluster periphery and end up on top of CCs, undergoing gap closure.

CAFs eventually cover the CC cluster and exhibit a robust localization of inward tractions on substrate near the cluster periphery, that remain at steady-state. This is a signature of the pulling force applied by the contractile ring on the surrounding tissue. To account for those features, we described theoretically the CAF tissue as an elastic material whereas the CAF-substrate interaction was seen as elasto-plastic with a yield transition. A joined quantitative comparison with experimental CAF closure dynamics and traction kymographs has been made to validate the theoretical assumptions.

Rather than full CAF closure over a CC monolayer, CAF convergent motion can trigger out-of-plane CC rearrangements that accumulate into a bud-like structure. We claimed that a frictional shear stress between closing CAFs and CCs applies compression on the CC cluster to activate multilayering events at a critical monolayer deformation. We used a combination of a 2D side vertex model and continuum mechanics with elasticity and surface tension to describe how the CC shape evolves. Experimentally, budding frequency and final bud size are correlated with initial cluster size. This observation does not appear straightforward in our model, and seems robust only in a limit of high CAF tissue tension so that the CC cluster covered by CAFs remains approximately flat.

Finally, we described in a minimal model how a combination of elastic resistance and plastic cell rearrangements, triggered by a yield stress, can justify the experimental observation of mechanically stable buds compressed by CAF contractile rings. Bud compression has been quantitatively identified as a rupture in dynamics, that appears simultaneously on CAF ring radius and integrated tractions through a discontinuity of slopes.

The last project was purely theoretical and dealt with the mechanics of single cell extrusion, within epithelial monolayers under compression. This pressure is associated with tissue crowding, a property believed to promote elimination of target cells to establish an homeostatic cell density. We saw extrusion as a 2-step transition where the basal interface is first converted into lateral interface, followed by complete extrusion when it becomes entirely apical.

Using a 2D side vertex model with curved interfaces, constant polar tensions and incompressibility, we first considered «enzymatic» reactions where transformed mechanical properties around a target cell can drive the system into the basal-lateral or lateral-apical transition. To reduce the technical complexity, we needed to assume a cell-size localization of neighbour shape relaxation around a transformed cell. Then, we searched for spontaneous mechanical instabilities for uniform tissue mechanics under external compression, focusing on a minimal 3-cell system to consider the full state space. Although this thesis only reports some preliminary results, we could identify a region of parameter space for which extrusion is more likely to occur. A more detailed analysis of the energetic landscape in this parametric region of interest, with identification of the "reaction coordinate" that optimizes the path towards the extrusion state, remains to be done.

Despite the proximity between the two last projects, it has been hard to make a proper convergence and extract significant results from the 2D side bubbly vertex model that could have been directly applied to budding generation. Even if the extrusion project has been considered as the main PhD subject for a while and was the perfect starting point in terms of framework to describe the cancerous cell rearrangements, a real synergy never appeared because of blocking moments in both projects. Still, we had applied for an ARC grant to fund a 4th year on the integration of those projects but it has not been accepted. Then facing the richness and complexity of our experimental collaboration for this second project, the main extrusion project became only a side project.

Indeed, when this experimental collaboration started in the middle of my PhD, the extrusion project was still embryonic with unclear directionality despite the demanding technical complexity. In addition, six months have been lost on the budding project with a theoretical description making the (false) assumption that cancerous clusters could remain as monolayers when out-of-plane deformations were observed. Through the indirect compression applied by the CAF frictional shear stress, the monolayer could detach from the substrate and bend similarly to a buckling transition. Although not compatible with experimental observations, initial results were both simple and robust when neglecting the basal detachment cost. We tried with difficulty to take into account this cost (that removes a proper buckling instability), without much success regarding the ratio between the invested time and the improvement of the results. In fact, this model is a limit case of our recent elasto-plastic model used to describe the mechanical stability of compressed buds: when the strength of cell-cell adhesions becomes infinite and cell-substrate adhesions are weak. With accumulation of data on dynamics, tractions and images showing 3D cell rearrangements, we moved to a different description with analogy to liquid rim dewetting.

One major draw-back of our theoretical analysis describing the shape evolution of cancerous monolayers is the discrepancy between the heavy technical problem of a double boundary-value problem and the small time window on which we are able to describe the system. Whereas interesting things occur after the first multilayering events, our dynamical model only look at early deformations and needs the introduction of an ad-hoc criterion to trigger 3D cell rearrangements. This shows the most natural project extension of this work, to be able to connect early monolayer deformations to the mechanics of well-formed buds, that we captured with a different model. Indeed, since multilayering events intrinsically at the cell scale, it is natural to use a theoretical framework that contains this spatial resolution: a vertex model. However, some raw arguments based on the 2D side model show that a critical transition where some cells could lose their basal interface in a finite time is not straightforward. Thus, a dynamical simulation of the 2D side vertex model may not be so useful and could reproduce the draw-back identified above for the continuous framework; a high technical complexity with poor physical insight on the mechanisms behind the multilayering events. Another extension concerns the use of a 3D axi-symmetric geometry rather than a projective plane, with a 3D vertex model.

5.3 Outlook

More generally, the main difficulty throughout this PhD have been the search for a correct balance between the large amount of biological results which has been accumulating in the literature during the last decades (in cell and tissue biomechanics) and the requirement of simplicity in the modelling process. This subtle equilibrium between "biophysics" and "physics inspired by biology" is the main challenge of the theoretical physicist to successfully describe complex living systems. Indeed, it has been quite hard to select the relevant biochemical/biophysical discoveries that should be exposed in the thesis, without creating an unpleasant asymmetry between a large amount of sophisticated biological results and the rather simplistic approach used to model these systems theoretically. This is especially true for the actin-based structures like the lamellipodium, a famous structure which has been substantially studied in the last decades.

One one hand, generic assumptions and a minimal set of elements to define the system allows to highlight the key mechanisms without adding inessential details, but on the other hand, it takes the risk of artificiality and abstraction to loose any relevance for the understanding of the real phenomenology. Moreover, it is rarely straightforward to convert some results obtained through pharmacological, genetic or mechanical perturbations into a generic description able to synthesize faithfully the observed behaviours: one has to choose a description level to describe implicitly or explicitly the key elements, identify the correct variables (concentration, tension, surface, etc...), couple them according to reasonable mathematical assumptions (constitutive laws, dynamics), and check that the theoretical behaviour does not lead to "massive" contradictions when compared with the real system.

From a biological perspective accustomed to unreproducible or sensitive cell behaviours, a web of hints obtained by different methods is the only way to extract scientific robustness. The most enlightening example seems to be the long quest for the understanding of suspended cell rheology, where very different frameworks tried to provide some robustness to a mass of poorly coherent/comparable observations. Of course in the end, an exhaustive analysis can be considered hopeless in biology, but some modelling assumptions can still be strongly weakened by specific observations and severely damage the interest of a given modelling description.

As an example, the rheology of filamentous biological networks often emphasizes the importance of non-linearity in the gel response to perturbation, but theoretical descriptions of the actin cortex (among other cell mechanical structures) tend to use linear theories at the mesoscopic scale: it is unclear if the effects described so far in the literature are weakly dependent on potential nonlinearities, if those could be cancelled by different modelling approaches, or if new mechanisms can be expected. Generally speaking, this highlights the huge dimensionality of the modelling "space" and asks for the limit at which we can reduce it for such complicated phenomena. Can several models reproduce the observations with completely different insights for the driving mechanisms? Is it possible to distinguish their predictions experimentally?

Probably the most intense challenge of such a PhD in biomechanics is the huge amount of scattered informations, going in many directions and layers of complexity. This can be hard to follow for physicists lacking an appropriate background on the various biochemical elements at play, or on the contrary for biologists lacking a good intuition of mechanical interactions.

To finish on a positive note, despite this natural desire for a better understanding of the elemental machinery behind the mesoscopic phenomena, it is interesting to realize that it would not have shifted qualitatively the orientation of our modelling approach, since most biological results are very hard to translate into a theoretical framework with precise statements. Thus, I consider that a significant improvement of the scientific robustness of this PhD work tends to go beyond the practical conditions in which it has been developed. Indeed in the current research environment, a state of scientific maturation often just needs some time to select the works able to become a standard knowledge and eliminate the irrelevant trials. Some "research noise" at the knowledge frontier necessarily generates infertile directions, and it is far from obvious that an obsession for exhaustiveness and over-precision is the right mental frame for successful research. The impressive achievements and the amount of technical sophistication reached in some fields can sometimes give an illusion of completeness, which could hide serious inabilities in the attempt to solve fundamental scientific questions. Despite the limitations that have been emphasized here (among many others), I hope that the work achieved during those years reasonably reaches the scientific standards and will integrate the web of research in biophysics. It could even modestly contribute to the exploration of new fertile directions, towards the inaccessible but attractive target of understanding the living world.

Appendix A

French report

A.1 Initiation d'un lamellipode

Le but de ce projet est de proposer un modèle minimal de la transition entre l'actine corticale (sous la membrane plasmique) d'une cellule suspendue et la protrusion lamellipodiale de cette cellule lorsqu'elle s'étale sur un substrat plat *in vitro*. On se focalise sur le couplage mécanique entre l'orientation des filaments d'actine et la courbure (moyennée sur les fluctuations) de la membrane plasmique à la périphérie de la cellule.

A.1.1 Modèle: la vésicule corticale adhérente 2D

Partant d'une forme sphérique en suspension, une cellule s'étalant sur un substrat solide subit un changement important de sa courbure entre la surface adhérente et la surface libre. Cela devrait affecter l'organisation du cortex d'actine, connu pour être un important régulateur des formes cellulaires [ref]. Après quelques minutes d'étalement, de nombreuses cellules développent une ou plusieurs protrusions plates de membrane le long de leur ligne de contact, appelées lamellipodes. Elles contiennent un réseau branché d'actine dont les filaments sont principalement orientés horizontalement. On s'attend à une transition "continue" entre le cortex d'actine et le lamellipode, dont la différence majeure se situe au niveau de l'orientation des filaments d'actine, plutôt orientés parallèlement à la membrane dans le cortex [27]. Comme l'architecture d'un réseau d'actine est influencé par la géométrie de la membrane de laquelle il croît [8], on s'attend à un couplage entre l'évolution de la forme de la cellule durant l'étalement et l'organisation du cytosquelette d'actine. On propose donc un modèle minimal avec un mécanisme de l'initiation de lamellipodes qui repose sur cette interaction entre forme cellulaire et orientation du cortex d'actine (Fig. A.1).

Pour cela, on introduit un champ de polarisation \vec{p} qui consiste en la moyenne mésoscopique de filaments individuels, orientés selon des vecteurs \vec{p}_f dans le plan cortical en vue de côté (voir Fig. A.1a). Comme la polymérisation d'actine est induite par des nucléateurs activés sur la membrane (review [123]), cela définit une polarisation naturelle des filaments avec le côté branché (polymérise) du côté de la membrane et le côté pointu (dépolymérise) du côté du cytoplasme. Cela induit un mouvement rétrograde ("treadmilling") dont le flux mésoscopique suit l'orientation moyenne définie par le vecteur \vec{p} . Sans orientation privilégiée des filaments dans le plan de la membrane [27], le vecteur mésoscopique de polarisation \vec{p} est orienté normalement au plan de la membrane (Fig. A.1a).

Lorsque la courbure membranaire est importante (en vue de côté), les flux normaux adjacents sont contraints à s'aligner pour limiter les contraintes internes au gel d'actine. Par ailleurs, cet alignement local rentre en conflit avec l'orientation du flux dans la zone voisine de courbure plus faible, ce qui peut être décrit par une résistance à la déviation de l'orientation normale $\vec{p} = \vec{n}$ qui émerge naturellement par symétrie (Fig. A.1b). Pour capturer ces deux effets, on utilise une énergie effective pour la surface cellulaire moyenne, inspirée de l'énergie de Frank des cristaux liquides [126, 127]. Elle se décompose en un terme de résistance normale $\propto |\vec{p} - \vec{p} \cdot \vec{n}|^2 \equiv |\vec{p}_t|^2$

et un terme d'alignement local $\propto (\nabla_S \vec{p})^2$ où ∇_S représente le gradient surfacique dans le plan membranaire. Pour réduire la complexité technique, on se limite à un système 2D en vue de côté avec symétrie miroir comme indiqué en Fig. A.1. On néglige aussi les couplages associés à une variation d'amplitude du vecteur de polarisation ($\vec{p} = 1$) comme pour la théorie des cristaux liquides nématiques avec vecteur directeur [126]. La surface membranaire devient une ligne paramétrée par l'abscisse curviligne s , tandis que le vecteur de polarisation peut être remplacé par l'angle $\theta(s)$ qu'il fait avec le vecteur normal $\vec{n}(s)$, tel que $\vec{p} \cdot \vec{n} = \cos \theta$ (voir Fig. A.1b). Le gradient ∇_S devient la simple dérivée ∂_s et on montre que le terme d'alignement vérifie $|\partial_s \vec{p}|^2 = [C(s) - \partial_s \theta(s)]^2$, montrant explicitement le couplage entre l'orientation d'actine décrite par l'angle θ et la forme cellulaire décrite par la courbure C . Le terme de résistance suit $|\vec{p}_t|^2 = [\sin \theta(s)]^2 \simeq \theta^2(s)$ en limitant l'expansion énergétique à l'ordre quadratique. L'énergie corticale s'écrit alors:

$$E_{\text{cortex 2D}} \simeq \frac{1}{2} \oint ds \left\{ k_\alpha \theta^2(s) + \kappa_c [C(s) - \partial_s \theta(s)]^2 \right\} \quad (\text{A.1})$$

où k_α est la rigidité d'ancrage et κ_c est un coefficient d'alignement qui peut être interprété comme une rigidité de courbure pour le cortex. Cela induit une localisation de la réorientation ($\theta \neq 0$) sur une longueur caractéristique $\lambda_c \equiv \sqrt{\kappa_c/k_\alpha}$. On fixe la rigidité corticale à $\kappa_c = 100\kappa$ car cette quantité est relativement bien connue, alors que la rigidité d'ancrage k_α est laissée indéterminée.

On suppose ensuite que la mécanique de l'étalement cellulaire peut être décrite de manière quasi-statique en utilisant un ensemble où le volume (aire projetée en 2D) A_0 , la tension de surface (projetée) γ et la densité d'énergie d'adhésion ϵ sont constants. Contrairement à une vésicle simple dont la surface est approximativement constant par conservation du nombre de lipides, une cellule en étalement utilise des réservoirs et des ajouts de membrane pour réguler sa tension [75]. L'énergie d'adhésion est supposée constante par simplicité mais joue pas de rôle actif dans le modèle.

Sans cortex, cela revient à décrire une goutte liquide dont l'étalement dépend de l'équilibre horizontal des tensions au point de contact $\gamma(1 + \cos \phi) = \epsilon$ (loi de Young-Dupré [128]). Selon le ratio ϵ/γ , la goutte peut être en démoillage ($\epsilon = 0$, $\phi = \pi$), en mouillage total ($\epsilon \geq 2\gamma$, $\phi = 0$), ou en mouillage partiel ($0 < \epsilon < 2\gamma$, $0 < \phi < \pi$). La membrane plasmique entourant la cellule contient une rigidité de courbure κ en plus de la tension de surface qui induit une longueur de relaxation mécanique $\lambda \equiv \sqrt{\kappa/\gamma}$, de sorte que l'énergie totale du système s'écrit comme la somme de l'énergie corticale et de l'énergie de membrane

$$E_{\text{tot}} = \frac{1}{2} \oint ds \left\{ \kappa [C(s)]^2 + 2\gamma + k_\alpha \theta^2(s) + \kappa_c [C(s) - \partial_s \theta(s)]^2 \right\} - 2\epsilon L - \Delta P (A - A_0) \quad (\text{A.2})$$

avec ΔP la différence de pression avec le milieu extérieur qui assure l'incompressibilité. On retrouve la goutte liquide 2D quand $\kappa = \kappa_c = k_\alpha = 0$.

Finalement, le dernier ingrédient du modèle est l'interaction entre le flux cortical d'actine et les récepteurs d'adhésion attachés au substrat sur la partie ventrale de la cellule (voir Fig. A.1c), qui sont directement connectés de manière transitoire par des protéines d'adaptation comme la taline ou la vinculine [109]. La projection horizontale du flux rétrograde de vitesse est supposée interagir de manière frictionnelle avec le substrat aux temps longs (plusieurs minutes) de l'étalement, de sorte que la densité de force est proportionnelle à la vitesse rétrograde v_r . La projection horizontale de la vitesse est proportionnelle à $\sin \theta(s)$, linéarisée pour des petites déviations, et on obtient la force totale (projetée) sur le substrat f_s allant du centre en $s = 0$ au point de contact à $s = L$ (Fig. A.1c):

$$f_s \simeq 2\xi v_r \int_0^L ds \theta(s) \equiv 2\epsilon_s \quad (\text{A.3})$$

Le coefficient de friction ξ quantifie l'intensité du couplage actine-substrat. Cette force sur le substrat crée des gradients de tension dans la couche corticale en contact $\partial_s \gamma_{ss} \simeq \xi v_r \theta(s)$. On s'attend à ce que la tension relaxe à sa valeur naturelle γ loin de la zone de contact où les changements d'orientation sont localisés (sur une longueur λ_c), alors que la friction génère une chute de tension

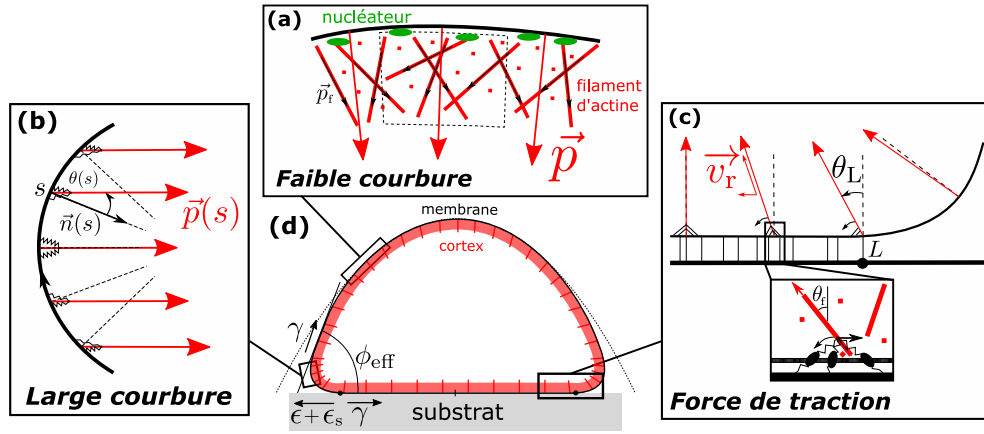


Figure A.1: *Modèle de la vésicule corticale en 2D (vue de côté)*. (a): Le cortex d'actine sous la membrane plasmique est décrit à l'aide d'un champ de polarisation \vec{p} comme la moyenne mésoscopique de la polarisation de filaments individuels \vec{p}_f sur le volume V_m . A l'échelle du réseau filamentueux, la polymérisation permanente d'actine induite par des activateurs sur la membrane plasmique favorise la proximité des bouts barbés, alors que l'absence d'orientation privilégiée dans le plan tangent oriente \vec{p} le long de la direction normale à la membrane \vec{n} quand la courbure reste faible. (b): Dans les régions de grande courbure comme le bout d'une cellule étalée, l'orientation du champ de polarisation $\vec{p}(s)$ (à l'abscisse curviligne s) dévie du vecteur normal de la membrane $\vec{n}(s)$ d'un angle $\theta(s)$, pour dissiper les contraintes mécaniques associées aux gradients du flot rétrograde d'actine. La forme de la cellule est décrite par la mécanique des membranes, et doit donc être couplée à l'architecture corticale. Le champ de polarisation $\vec{p}(s)$ est représenté par des filaments "mésoscopiques" (flèches rouges) qui capturent l'orientation corticale le long de la surface cellulaire. Une déviation de l'orientation normale crée une force de réaction représentée par les attaches du cortex à la membrane (ressorts noirs). (c): Les effets antagonistes entre l'alignement du flot et l'ancrage normal propagent la déviation angulaire θ_L de la région de plus grande courbure à la région adhérente qui est plate (séparées par le point L). L'interaction du flot rétrograde d'actine (vitesse v_r) avec les complexes d'adhésion attachés au substrat génère une force de traction, proportionnelle à la projection horizontale du flot. (d): Schéma d'une cellule étalée sur un substrat rigide, faite d'une membrane, d'un noyau et d'un cortex d'actine avec des filaments "mésoscopiques" représentant le champ de polarisation \vec{p} le long du contour cellulaire (projection 2D). L'orientation à large échelle des filaments d'actine est normale à la membrane (a) au-dessus et en dessous du noyau, alors que la grande courbure de la ligne de contact facilite l'alignement du flot (b). En analogie avec le mouillage liquide, le contour de la cellule fait un angle ϕ_{eff} avec le substrat, ce qui définit une balance des tensions analogue à l'équation de Young-Dupré pour la tension cellulaire γ , l'adhésion ϵ et la densité de force de traction ϵ_s . La cellule a une longueur de contact (2D) notée $2L$.

$\gamma_{ss}(L) - \gamma = \epsilon_s$ au point de contact en $s = L$. Cela conduit à écrire un équilibre horizontal des tensions au point de contact, équivalent à une équation de Young-Dupré pour les liquides simples, où la friction joue le rôle d'un terme d'adhésion supplémentaire¹:

$$\partial_L E_{\text{tot}}^* = \epsilon - \epsilon_f \int_0^L \frac{ds}{L_0} \theta(s) \quad (\text{A.4})$$

avec $\theta < 0$ par convention et le paramètre d'adhésion frictionnelle $\epsilon_f \equiv \xi v_r L_0$. Le terme de résistance $\partial_L E_{\text{tot}}^*$ généralise la projection horizontale des tensions ($1 + \cos \phi_{\text{eff}}$) comme montré au centre de la Fig. A.1c. E_{tot}^* est la moitié de l'énergie de l'Eq. A.2 privée du terme d'adhésion qui se trouve sur le côté droit de l'Eq. A.4.

A.1.2 Résultats: transitions d'étalement

Pour obtenir l'état d'équilibre du système, on devrait minimiser les équations locales pour la forme et le champ d'orientation sur laquelle il est défini. Pour réduire la complexité de ces équations, on utilise une forme paramétrée avec des branches de courbure constante: une courbure centrale

¹On peut montrer avec une description visqueuse que la chute de tension au point de contact reste de l'ordre de ϵ_s si la dissipation est localisée près du point de contact et si $k_\alpha \ll \gamma$. On verra plus bas que cette dernière condition correspond à la région de l'espace des paramètres où les choses intéressantes se passent.

C_0 ($s_e \leq s \leq s_c$), une courbure de bord C_e ($L \leq s \leq s_e$) et une courbure nulle sur la partie adhérente ($s \leq L$). s_e est l'abscisse curviligne séparant les régions courbées et s_c correspond au point symétrique sur la surface au-dessus du noyau. Dans la limite où $\kappa, \kappa_c \rightarrow 0$, la vésicule corticale se réduit à une simple goutte liquide et l'énergie Eq. A.2 est minimisée pour une surface libre de courbure constante $C_0 = \Delta P/\gamma$ qui est connectée à la partie plate par $C_e \rightarrow \infty$. La rigidité de courbure introduite par la membrane et/ou le cortex introduit une courbure de bord localisée C_e de l'ordre de $\lambda = \sqrt{\kappa/\gamma}$ ou $\sqrt{(\kappa + \kappa_c)/\gamma}$, où on s'attend à $\lambda \ll \sqrt{A_0}$. Lorsque la cellule commence à s'étaler, la courbure de bord C_e part d'une valeur identique à C_0 correspondant à un cercle et augmente à mesure que la région adhérente se développe, jusqu'à saturer autour d'une des valeurs caractéristiques λ ou $\sqrt{(\kappa + \kappa_c)/\gamma}$. On minimise alors le champ d'orientation le long de ces domaines de courbure constante pour obtenir l'équation locale $\lambda_c^2 \partial_s^2 \theta(s) = \theta(s)$, qui conduit à une relaxation exponentielle sur la longueur caractéristique $\lambda_c = \sqrt{\kappa_c/k_\alpha}$.

Puisque la rigidité du cortex κ_c est bien connue contrairement à la rigidité d'ancrage k_α , la réorientation peut se localiser à la périphérie de la cellule si $\alpha \equiv k_\alpha/\gamma \gg 1$ (limite d'ancrage fort), mais aussi se propager jusqu'au centre de la cellule lorsque $\alpha \lesssim 1$ (limite d'ancrage faible). En cas d'ancrage fort, la localisation de la réorientation autour de la région de grande courbure induit une dépendance faible à l'étalement cellulaire paramétrée par la longueur L , avec une déviation angulaire asymptotique $|\theta_L| \propto 1/\sqrt{\alpha}$ quand $\alpha \gg 1$. Au contraire en cas d'ancrage faible, la réorientation induite par la grande courbure au bord peut atteindre $\pi/2$ lorsque la cellule étalée prend la forme d'un "pancake" plat (orientation du cortex parallèle au substrat).

La solution de l'équation locale d'orientation est alors paramétrée par la forme en étant fonction de L , C_e et C_0 . En injectant dans l'énergie Eq. A.2, on obtient une fonction de L , C_e , C_0 et ΔP qu'on minimise pour les trois dernières variables et exprimer l'énergie en fonction de L uniquement. Enfin, on injecte la force de résistance membrano-corticale $\partial_L E_{\text{tot}}^* \equiv F_{m\oplus c}$ (sans le terme d'adhésion) dans l'équation de balance des tensions Eq. A.4 en $s = L$.

Cette force de résistance $F_{m\oplus c}$, qui se réduit à 2γ pour une goutte liquide, est équilibrée par la densité d'énergie d'adhésion ϵ et la force de traction frictionnelle ϵ_s comme représentée graphiquement (Fig. A.2a).

Pour une vésicule sans cortex, la force d'adhésion ϵ est indépendante de L tandis que la force de résistance croît jusqu'à la valeur limite d'une goutte complètement étalée 2γ . Le mouillage total a lieu si $\epsilon > 2\gamma$ (lorsque $\lambda \ll \sqrt{A_0}$), où l'état d'équilibre est $L \rightarrow \infty$.

Avec le cortex, la force de résistance $F_{m\oplus c}$ est faiblement modifiée comme on peut le voir sur la Fig. A.2a dans les deux limites d'ancrage faible ($\alpha \lesssim 1$) ou d'ancrage fort ($\alpha \gg 1$). Cependant, la force de traction $\propto \epsilon_f |\theta_L|$ augmente avec L jusqu'à une valeur correspondant à la réorientation maximale du cortex, d'ordre $1/\sqrt{\alpha}$ en limite d'ancrage fort ($\alpha \gg 1$) et d'ordre 1 pour un ancrage faible ($\alpha \lesssim 1$). Sur la Fig. A.2a, le paramètre d'adhésion frictionnelle ϵ_f est choisi de sorte que la valeur de la force de traction quand $L \rightarrow \infty$ est similaire pour les deux limites d'ancrage. Quand $L \gg \lambda_c$ (ancrage fort), la force de traction vaut approximativement $f_f \sim \epsilon_f \lambda_c |\theta_L|$ est devient proportionnelle à $1/\alpha$ quand $L \rightarrow \infty$.

Ainsi, une transition de mouillage total est possible quand l'adhésion frictionnelle ϵ_f dépasse le seuil de résistance $\epsilon + f_f^\infty \gtrsim 2\gamma$, avec les comportements asymptotiques suivant pour les deux limites d'ancrage

$$\epsilon_f = \sqrt{\frac{\kappa}{\kappa_c}} (2\gamma - \epsilon) g(\alpha) \quad , \quad g(\alpha) \sim \begin{cases} \sqrt{\alpha}, & \text{if } \alpha \ll 1 \\ \alpha, & \text{if } \alpha \gg 1 \end{cases} . \quad (\text{A.5})$$

La transition d'étalement total est résumée sur le diagramme de phase (Fig. A.2b) reliant les valeurs seuils d'amplitude de la force de traction (adhésion frictionnelle réduite $\bar{\epsilon}_f$) et de résistance corticale (rigidité d'ancrage réduite α), en excellent accord avec les relations d'échelle de l'Eq. A.5.

Une propriété importante de la force de traction est la manière dont elle atteint la valeur de saturation quand $L \rightarrow \infty$. Pour un ancrage fort, la réorientation se propage faiblement sur une distance

$\lambda_c \ll \sqrt{A_0}$ du bord de la cellule, et la force de traction sature avec la courbure périphérique C_e lorsque $L \sim \sqrt{A_0}$ (Fig. A.2a, rouge). Pour l'ancrage faible, la réorientation corticale se propage sur toute la partie adhérente tant que $L < \lambda_c$, et la force de traction augmente linéairement avec L : $f_f \sim \frac{\pi}{4}\epsilon_f L$ pour une réorientation totale ($|\theta_L| \simeq \pi/2$). La balance des forces peut donc admettre deux solutions stationnaires dont l'une stable et l'autre instable (Fig. A.2a, bleu) si la force de traction augmente plus faiblement avec L que la force de résistance. On s'attend donc à une région de bi-stabilité pour le diagramme de phase dans la limite d'ancrage faible comme observé (Fig. A.2b), où un état d'étalement partiel (L fini) coexiste avec l'étalement total ($L \rightarrow \infty$).

Finalement, une dernière spécificité de ce couplage entre orientation, forme et traction est la présence de deux régimes d'orientation: une réorientation corticale faible (forte) en cas d'ancrage α fort (faible) comme indiqué sur le diagramme de phase (Fig. A.2b). On prétend que l'émergence d'un lamellipode correspond dans ce modèle à un étalement total, avec réorientation des filaments parallèlement au substrat près de la ligne de front. Ces critères sont remplis dans la région où les paramètres ont des valeurs physiologiquement accessibles (cadre rose de la Fig. A.2b).

A.1.3 Conclusion

En résumé, on propose qu'il existe une boucle de rétro-action positive entre la courbure membranaire, l'orientation du cytosquelette et la force de traction à la périphérie de cellule étalées. Une grande courbure induit une orientation des filaments d'actine qui est parallèle au substrat, ce qui augmente la force de traction, augmente l'étalement cellulaire et donc la courbure au bord. Cela correspondrait à l'initiation d'un lamellipode, la fine protrusion plate de filaments d'actine observée à la périphérie de cellules étalées ou en migration.

Notre transition est principalement contrôlée par deux paramètres (voir Fig. A.2b): le rapport de l'amplitude de la force de tension d'un cortex orienté et de la tension cellulaire $\bar{\epsilon}_f = \epsilon_f \sqrt{A_0} / \gamma$, et le rapport de la rigidité d'ancrage du cortex et de la tension $\alpha = k_\alpha / \gamma$. Les valeurs attendues pour ces paramètres correspondent à la région du diagramme de phase où les choses intéressantes ont lieu, comme une grande réorientation corticale ou la transition entre étalement partiel et total, avec la coexistence possible de deux états où l'initiation du lamellipode est une nucléation. Cela pourrait constituer un mécanisme de brisure spontanée de symétrie en établissant une polarité front-arrière suivie de migration cellulaire, comme observée le long de bandes adhésives en 1D [91].

Concernant l'initiation des lamellipodes, l'importance de la courbure au bord de la cellule a déjà été confirmée expérimentalement [118]: des cellules s'étalant sur des zones d'adhésion de forme carrée génèrent des protrusions aux coins (régions de plus grande courbure). Contrairement à notre modèle qui ne traite que la courbure en vue de côté, ce résultat expérimental est associé à la courbure dans la direction orthoradiale. Cependant, l'aspect générique de cette boucle de rétro-action théorique suggère qu'une instabilité similaire pourrait avoir lieu dans cette direction. Avant une future extension du modèle aux cellules 3D axi-symétriques, pour montrer que des fluctuations de courbure le long de la ligne de contact peuvent nucléer des protrusions locales (transition analogue à la bi-stabilité), une extrapolation de nos résultats 2D semble naturelle. Cette extension pourrait justifier l'observation expérimentale des modes d'étalement isotrope et anisotrope [80]. En fait, l'extrapolation des résultats 2D suggère qu'une diminution de l'amplitude de l'adhésion frictionnelle ϵ_f devrait induire une transition d'un étalement isotrope (étalement total) à un étalement anisotrope (bi-stabilité) (Fig. A.2b). Ceci a bien été observé pour des cellules endothéliales après réduction de la densité de ligands sur le substrat [140].

A.2 Modèle de "vertex" 2D en vue de côté

Les deux projets suivants impliquent la description théorique de la mécanique de monocouches épithéliales: ce chapitre est dédié à un cadre théorique décrivant les cellules de manière discrète. Il consiste en un modèle de "vertex" à 2D projeté dans le plan transverse (xz), contrairement à la majorité des modèles qui s'intéressent au plan horizontal (xy) plus facilement accessible au microscope. Bien que de nombreux modèles supposent des interfaces plates, il est à la fois plus consistant théoriquement et nécessaire expérimentalement de considérer la courbure interfaciale

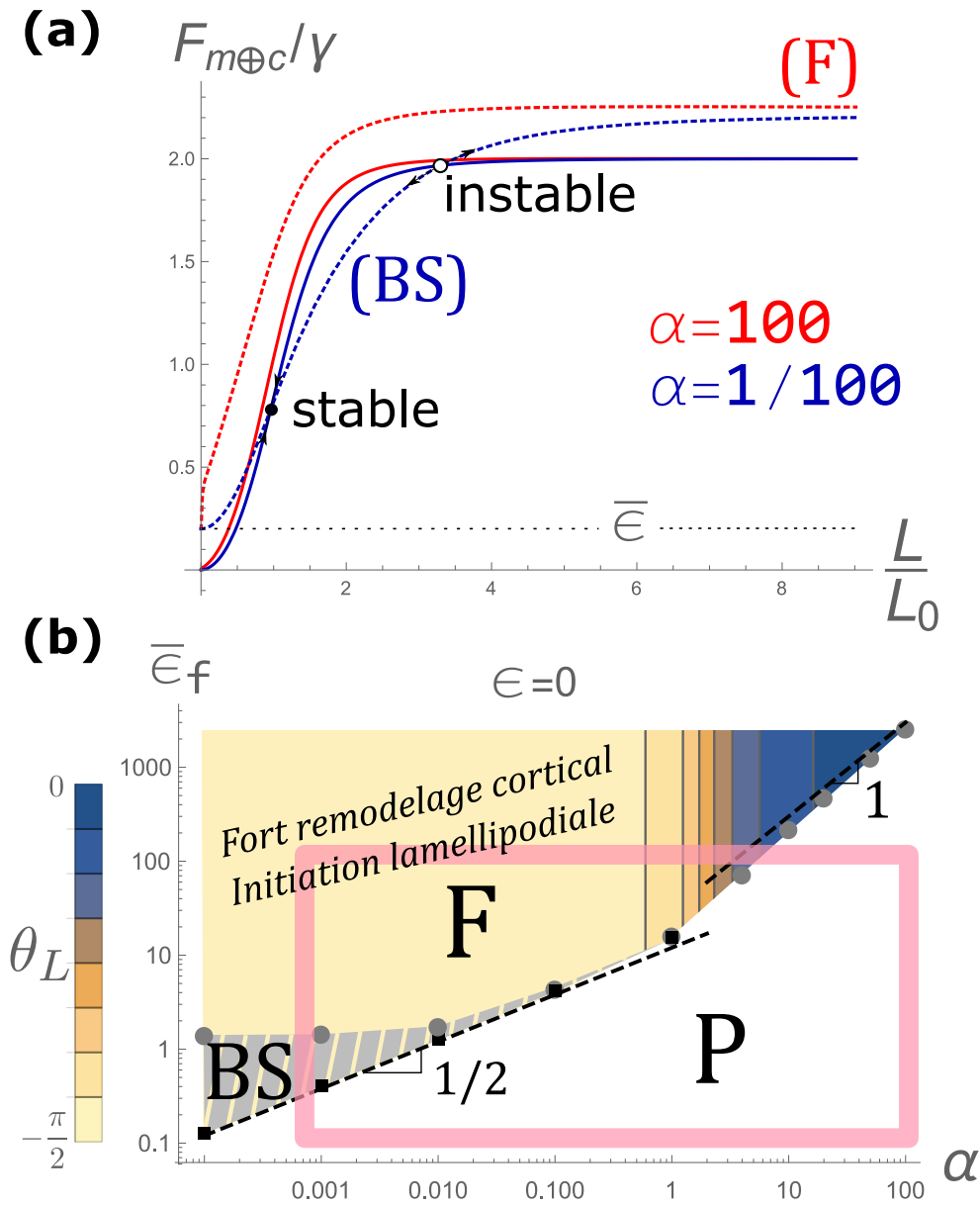


Figure A.2: **(a)**: Résolution graphique de l'équation de balance des forces (par unité de longueur transverse) Eq. A.4. La force de résistance (lignes pleines), la force d'adhésion passive seule (ligne pointillée) et l'adhésion totale avec adhésion frictionnelle (lignes avec tirets) sont montrées en fonction de la longueur adhérente réduite L/L_0 où $L_0 \equiv \sqrt{A_0}$, pour l'ancrage faible (bleu) ou fort (rouge). Les limites d'ancrage sont quantifiées par la rigidité corticale d'ancrage "réduite" $\alpha \equiv k_\alpha/\gamma$. L'état d'équilibre partiel (P) apparaît lorsque les forces d'adhésion et de résistance se compensent, et l'étalement total (F) a lieu lorsque l'adhésion domine la résistance comme montré pour l'ancrage fort ($\bar{\epsilon}_f = 2750$). Pour l'ancrage faible, une bi-stabilité (BS) peut apparaître avec deux solutions (méta)stable et instable, conduisant à l'étalement total ($\bar{\epsilon}_f = 1.3$). Les valeurs des paramètres sont: $\bar{\lambda} = 0.01$, $\kappa_c = 100\kappa$ and $\bar{\epsilon} = 0.2$. **(b)**: Diagramme de phase dans l'espace des paramètres ($\alpha, \bar{\epsilon}_f$) où $\bar{\epsilon}_f (= \epsilon_f \sqrt{A_0}/\gamma)$ en négligeant l'adhésion passive ($\epsilon = 0$). Cela délimite trois régimes en blanc (partiel P), gris (bi-stable BS) and beige-bleu (étalement total F). La région d'étalement total contient une quantification de la réorientation angulaire du cortex au bord de la cellule θ_L . Elle est maximale pour une limite d'ancrage faible (orientation parallèle au substrat) ce qui indique l'initiation d'un lamellipode. Les relations d'échelle de l'Eq. A.5 sont confirmées par les lignes avec tirets. Le cadre rose délimite les valeurs physiologiques attendues des paramètres.

dans certains cas [182, 162] comme le montre la Fig. A.3a.

On considère des tensions constantes sur chaque interface cellulaire et supposons qu'une différence de pression hydrostatique est équilibrée par une courbure de l'interface (loi de Laplace): on parle de modèle de "vertex" 2D à bulles (Fig. A.3b). On distingue la tension apicale Γ_a (cellule-lumen), la tension latérale Γ_l (cellule-cellule) et la tension basale Γ_b (cellule-substrat). Par ailleurs, le volume cellulaire est supposé constant, ce qui correspond à l'aire projetée dans le plan transverse A_0 pour ce modèle 2D. Ainsi, ce modèle contient seulement quatre paramètres pour décrire la forme des cellules d'une monocouche reposant sur un substrat solide.

Pour un tissu uniforme, la pression est équilibrée entre les cellules et seules les interfaces sont courbées, avec un angle de déviation ψ et un rayon de courbure R (voir Fig. A.3b). Avec une largeur cellulaire $l = 2R \sin \psi$ et une hauteur h , l'énergie d'une cellule peut alors s'écrire

$$E_{\text{cell}} = \Gamma_a 2R\psi + \Gamma_b 2R \sin \psi + \Gamma_l h - \Delta P (2Rh \sin \psi + R^2 [\psi - \cos \psi \sin \psi] - A_0) \quad (\text{A.6})$$

où la pression ΔP est un multiplicateur de Lagrange qui assure la conservation de l'aire. On peut obtenir l'état d'équilibre qui minimise cette énergie et on obtient la forme de la cellule en fonction des paramètres

$$\left\{ \begin{array}{l} \psi^* = \arcsin\left(\frac{\Gamma_l}{2\Gamma_a}\right) \\ l^* = \sqrt{A_0} \frac{2\Gamma_l}{\sqrt{\Gamma_l \left(4\Gamma_b + \sqrt{4\Gamma_a^2 - \Gamma_l^2}\right) + 4\Gamma_a^2 \arcsin\left(\frac{\Gamma_l}{2\Gamma_a}\right)}} \\ h^* = \sqrt{A_0} \frac{2\Gamma_b + \sqrt{4\Gamma_a^2 - \Gamma_l^2}}{\sqrt{\Gamma_l \left(4\Gamma_b + \sqrt{4\Gamma_a^2 - \Gamma_l^2}\right) + 4\Gamma_a^2 \arcsin\left(\frac{\Gamma_l}{2\Gamma_a}\right)}} \\ R^* = \Gamma_a l^* / \Gamma_l \\ P^* = \Gamma_a / R^* \end{array} \right. \quad (\text{A.7})$$

La région de l'espace des paramètres pour laquelle l'équilibre mécanique est bien défini impose $2\Gamma_a > \Gamma_l$ (balance des tensions apicales) et $2\Gamma_b + \sqrt{4\Gamma_a^2 - \Gamma_l^2} > 0$ (hauteur positive) comme le montre la Fig. A.3c. Il est intéressant de noter qu'en terme de balance des tensions, le paramètre basal n'apparaît qu'en considérant la frontière du tissu: l'équilibre mécanique n'est donc pas autonome pour les cellules individuelles. La tension apicale Γ_a correspond à une tension corticale et reste positive, tout comme Γ_l pour assurer la stabilité mécanique, mais Γ_b peut être positive ou négative. Ces restrictions de paramètres permettent d'utiliser $\sqrt{A_0}$ comme unité de longueur et Γ_l comme unité de tension, introduisant les tensions réduites $\alpha \equiv \Gamma_a / \Gamma_l$ et $\beta \equiv \Gamma_b / \Gamma_l$.

On peut retrouver la limite du modèle de vertex polygonal [171] lorsque $\Gamma_a \gg \Gamma_l$ et l'interface apicale s'aplatit ($\psi^* \rightarrow 0$). L'énergie cellulaire (adimensionnelle) se réduit à $E_{\text{cell}} = (\alpha + \beta)l + h - P(hl)$, de sorte que $l^* / \sqrt{A_0} = (\alpha + \beta)^{-1/2}$ et $h^* / \sqrt{A_0} = (\alpha + \beta)^{1/2}$.

Lorsque une perturbation induit un changement de forme de certaines cellules, comme avec une transformation oncogénique qui modifie la hauteur d'une cellule [273]. Cela propage horizontalement des contraintes mécaniques aux cellules voisines qui doivent adapter leur forme. En faisant une théorie linéaire de perturbation d'un tissu hétérogène autour de l'état uniforme, on obtient une équation discrète de réponse mécanique pour la hauteur h_i des différentes cellules:

$$\left(3\alpha \cos \psi^* - \frac{h^*}{l^*}\right) (\delta h_{i+2} - 4\delta h_{i+1} + 6\delta h_i - 4\delta h_{i-1} + \delta h_{i-2}) = \frac{6}{(h^*)^2} (\delta h_{i+1} - 2\delta h_i + \delta h_{i-1}) \quad (\text{A.8})$$

Cette équation contient une longueur caractéristique λ fonction des paramètres α et β sur laquelle la déformation est localisée. On montre que λ devient proche de la largeur d'une cellule l^* quand α et β sont proches de l'unité, alors que la limite polygonale $\alpha \gg 1$ conduit à une relaxation à l'échelle tissulaire. Cela permet de construire une approximation continue lorsque $\lambda \gg l^*$, et remplacer l'équation discrète Eq. A.8 par $(h^* l^*)^2 \left(3\alpha \cos \psi^* - \frac{h^*}{l^*}\right) \delta h^{(4)}(x) \simeq 6\delta h''(x)$.

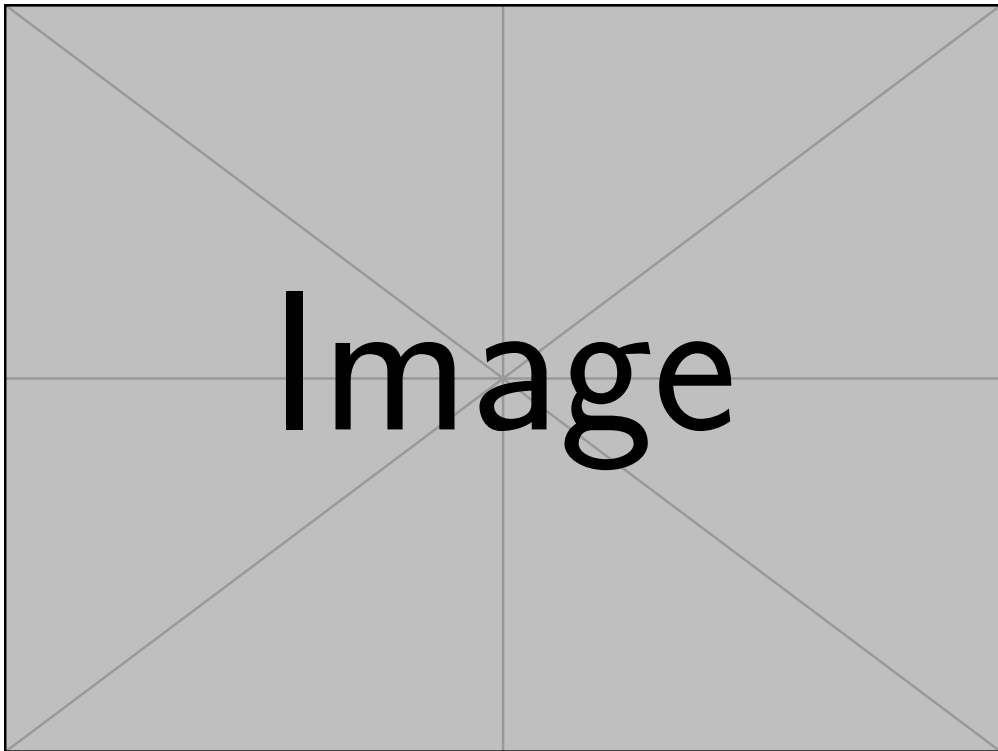


Figure A.3: **(a)**: Image fluorescente de cellules MDCK en vue de côté, montrant une courbure nette des interfaces apicales. Tiré de la thèse [162]. **(b)**: Cellule 2D au sein d'une monocouche uniforme avec une interface apicale courbée. Sa géométrie est paramétrée selon un squelette polygonal défini par des points à la hauteur h sur une largeur l , alors que la courbure est capturée par un angle ψ et un rayon de courbure R . Une variable peut être éliminée par $l = 2R \sin \psi$. **(c)**: Région des paramètres pour laquelle l'état uniforme existe, dans le plan ($\alpha \equiv \Gamma_a/\Gamma_1, \beta \equiv \Gamma_b/\Gamma_1$). La limite du modèle polygonal ($\Gamma_a \gg \Gamma_1$) est indiquée par une ligne avec tirets.

A.3 Bourgeonnement cancéreux

A.3.1 Présentation du système expérimental

Ce projet est une collaboration avec la cheffe d'équipe Danijela Matic Vignjevic (UMR 144, institut Curie) and ses post-doctorants Jorge Barbazán et Carlos Pérez-González, pour ajouter une compréhension théorique à un projet expérimental en cours. Dans le contexte de l'invasion cancéreuse, ils ont créé un dispositif expérimental *in vitro* pour étudier l'influence mécanique de cellules conjonctives dans la générations d'amas cancéreux. Ces cellules conjonctives sont spécialement reliées au cancer: on parle de Fibroblastes-Associés au Cancer (FACs). Ce système expérimental essaye de mimer sur un substrat plat la formation *in vivo* de bourgeons cancéreux depuis la tumeur primaire, et confirme l'hypothèse d'un rôle actif joué par les FACs dans ce processus associé à un diagnostic peu favorable chez les patients. Une pré-publication se focalisant sur les aspects expérimentaux du projet est disponible sur la plateforme en ligne bioRxiv [190].

Des cellules cancéreuses sont déposées sur des couches adhésives circulaires de taille contrôlable (diamètre de 100 à 400 microns) et prolifèrent jusqu'à confluence. Ensuite, des FACs sont ajoutés autour de l'amas sur la partie non-adhésive (Fig. A.4a), proliférant et déposant des composants de matrice extra-cellulaire comme du collagène ou de la fibronectine (Fig. A.4b). Un aspect clé apparaît après quelques heures de co-culture: l'assemblage spontané d'un anneau supra-cellulaire d'acto-myosine (Fig. A.4c) dans les FACs à l'interface avec les cellules cancéreuses. Initialement, l'anneau comprime l'amas cancéreux mais il grimpe rapidement au-dessus en entraînant le tissu de FACs dans un processus de fermeture de trou, qui est analogue au mécanisme de constriction observé pendant la guérison des plaies épithéliales [229]. Cet anneau contractile est contrôlé par l'activité des moteurs myosines, mais aussi par les fibres de fibronectine qui intègrent les câbles cellulaires en une structure tissulaire.

Une fraction des amas cancéreux se réorganisent massivement en un bourgeon 3D de cellules cancéreuses (Fig. A.4d), tandis que d'autres amas sont faiblement perturbés et laissent les FACs se fermer au-dessus (Fig. A.4e,f) grâce à la contractilité de l'anneau. Dans les deux cas, des variations localisées d'épaisseur sont souvent observées lorsque l'amas cancéreux est encore une monocouche (Fig. A.4d,e). Cette tension générée au front du tissu de FACs se propage aux régions environnantes, ce qui est détecté par des tractions convergentes appliquées sur le substrat (Fig. A.4f). Dans le premier cas, l'anneau peut éventuellement couper le bourgeon du corps cancéreux, mais la plupart atteignent un équilibre mécanique équilibrant la résistance élastique des couches supérieurs et la tension de l'anneau de FACs (Fig. A.4g).

Des expériences préliminaires ont montré une réduction significative du bourgeonnement cancéreux après inhibition des N-cadhérines exprimées par les FACs. Des travaux récents [214] suggèrent l'existence d'une interaction spécifique de ces cadhérines avec les E-cadhérines des CCs. Cela incite à penser qu'une force de friction entre FACs et CCs, spécifique à cette interaction N/E-cadhérine, pourrait contrôler la fréquence d'apparition de bourgeons au sein d'une population d'amas de CCs. Ce phénotype observé avec des cellules humaines apparaît moins robuste avec des cellules de souris.

De toute façon, des sources non-spécifiques de friction entre les deux tissus (glycocalyx, matrice extra-cellulaire, adhésions) pourraient agir comme source de déformation des CCs et induire le bourgeonnement. Ainsi, l'hypothèse centrale de notre modèle est que la contractilité des FACs dans l'anneau du front, qui induit un glissement convergent des FACs, génère aussi des contraintes de cisaillement sur les CCs qu'on suppose responsable des réarrangements cellulaires conduisant au bourgeonnement.

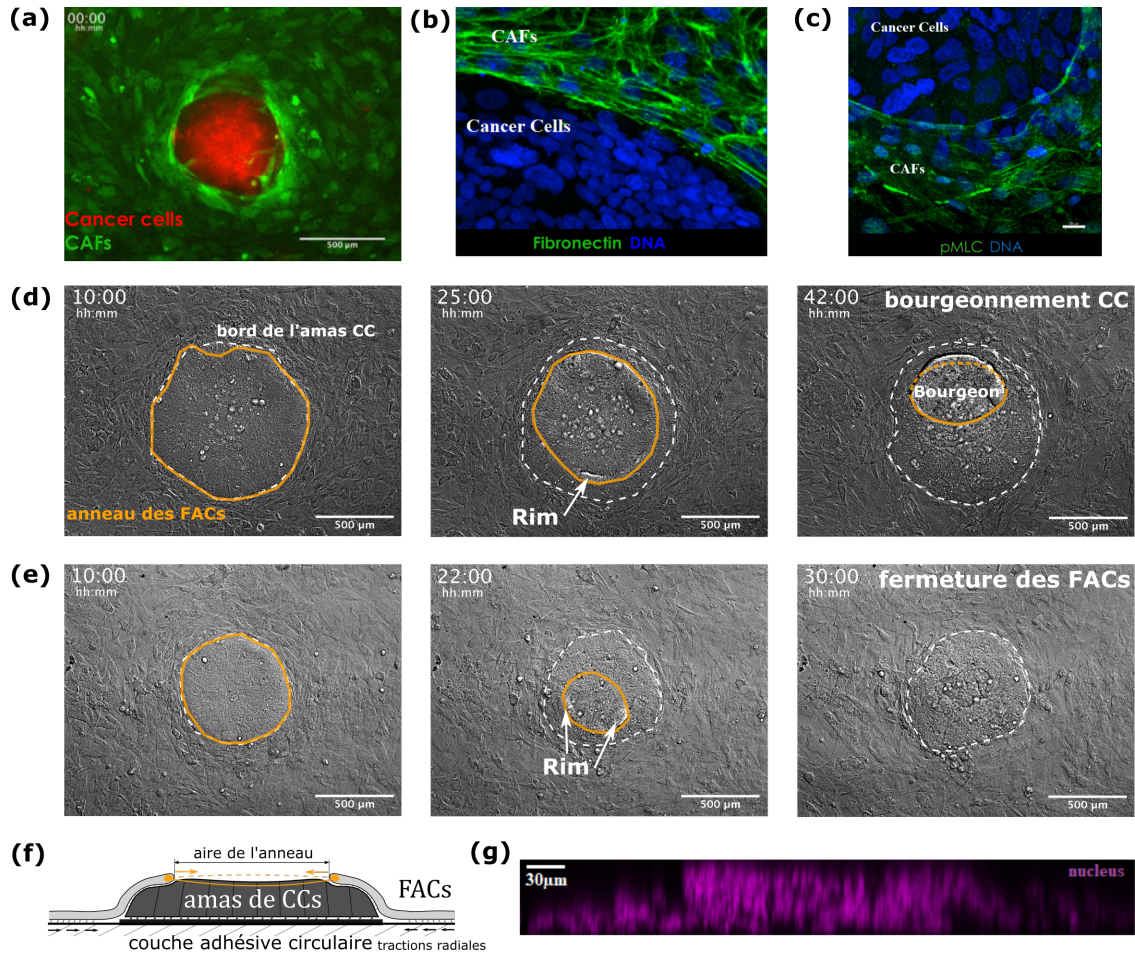


Figure A.4: (a): Image fluorescente d'un amas de Cellules Cancéreuses (CCs) en rouge, entourées d'un tissu de Fibroblastes-Associés au Cancer (FACs) en vert. Ici, la couche adhésive sur laquelle les CCs sont déposées à un diamètre de 400 microns. (b): Image fluorescente de haute résolution de tissus de FACs et de CCs avant l'évènement de montée des FACs, avec l'ADN (noyau) en bleu et la fibronectine (fibres matricielles) produite par les FACs en vert. La région libre de fibronectine indique l'amas de CCs. Ce réseau de matrice hétérogène semble stabiliser l'anneau d'actomyosine (c) assemblé à l'interface FAC-CC. (c): Image fluorescente de haute résolution de FACs et de CCs avec l'ADN (noyau) en bleu et la myosine (pMLC) en vert, indiquant certains câbles d'actomyosine autour du front de FACs. L'intégrité de l'anneau supra-cellulaire semble dépendre de l'expression de fibronectine (b). Les FACs sont déjà en train de fermer le trou au-dessus de l'amas cancéreux, qu'on peut distinguer sur la région libre de myosine au-dessus. (d,e): Séquence temporelle de l'amas cancéreux (délimité par une ligne avec tirets) par microscopie à contraste de phase, entouré de FACs avec un anneau supracellulaire (ligne orange) assemblé au front du tissu. Les FACs initient la fermeture du trou au-dessus des CCs après 10 h, induisant des déformations localisées ("rim") qu'on peut distinguer à 25 h (d) ou 22 h (e). L'anneau peut se stabiliser autour d'un bourgeon 3D en multicouche (d) ou terminer la fermeture du trou au-dessus d'un amas faiblement perturbé (e). (f): Schéma du système FAC-CC vu de côté, aux premières étapes avant le passage en multicouche. La tension venant du câble d'actomyosine (orange) déforme les CCs et tire sur le tissu de FACs environnant, confirmé par l'observation de tractions radiales convergentes sur le substrat. (g): Image au microscope confocal de noyaux de CCs à l'état stationnaire, montrant un large bourgeon avec une forme cylindrique à partir d'un amas développé sur une couche adhésive avec un diamètre de 400 microns. [Courtoisie de D. Vignjevic, J. Barbazán and C. Pérez-González]

A.3.2 Modèle: contraintes expérimentales et mécanique des tissus

A partir de ces contraintes de cisaillements exercées par les FACs sur la monocouche de CCs, on suppose simplement qu'il existe une déformation critique au-delà de laquelle les cellules perdent leur contact basal. On s'inspire pour cela du phénomène de démouillage de films liquides [234] où une déformation localisée appelée "rim" est observée comme en Fig. A.4d,e. Ces transitions dites "en multicouche" s'accumulent jusqu'à ce bourgeon 3D, mais on ne considère que la première phase pour décrire les conditions d'apparition du seuil critique.

Pour décrire la réponse mécanique de la monocouche de CCs, on utilise le cadre de la mécanique des milieux continus en s'aidant du modèle de "vertex" en vue de côté (chapitre 2) qui doit être adapté aux contraintes exercées par les FACs sur la surface apicale. Le tissu de FACs est également décrit dans le formalisme des milieux continus.

Contraintes expérimentales et FACs

Nos collaborateurs ont également créé un système de piliers cylindriques dont l'élasticité peut quantifier l'intensité de la contractilité exercée par l'anneau des FACs. En particulier, ils mesurent un taux de déformation radial plus faible pour des piliers plus large, ce qui est compatible avec la modélisation de l'anneau comme une tension de ligne Γ . Par application de la loi de Laplace (2D), l'anneau d'épaisseur h applique une pression $\Gamma/(hR)$ sur un de rayon R . Connaissant la taille et le module élastique du pilier, on trouve alors une tension de ligne $\Gamma \simeq 600 \pm 400$ nN.

Après la montée des FACs sur l'amas cancéreux, on a tendance à observer une fermeture complète du front avec de faibles déformations des CCs dans les conditions d'inhibition des N-cadhérines. La dynamique de fermeture, décrite par le rayon instantané du front FACs $R_c(t)$, repose sur la force convergente de l'anneau, la résistance du tissu de FACs et différentes sources de dissipation (Fig. A.5a). Expérimentalement, on observe que l'aire du trou de FACs diminue de façon approximativement linéaire avec le temps (Fig. A.5b), soit une augmentation de la vitesse radiale $dR_c(t)/dt \equiv -V_c$ au cours du temps (Fig. A.5c). Par ailleurs, la vitesse initiale de fermeture semble indépendante des conditions expérimentales et du phénotype final (Fig. A.5d). Puisque la fréquence de bourgeonnement est affectée par l'inhibition des N-cadhérines qui affecte l'interaction spécifique N/E-cadh, on s'attend à une dissipation non-spécifique mais une source de friction FAC-CC spécifique.

Pour un amas de rayon initial R_0 , les différents mécanismes de la Fig. A.5a mènent à une dynamique

$$V_c = \frac{\Gamma(R_c|R_0)/R_c - \gamma_\infty - E_c h_c (R_0 - R_c)/R_c}{2\eta_1/(R_c)^2 + 2\eta_2/R_c + \zeta + \xi_{sc} R_c \log[R_\infty/R_0] + \xi R_c \log[R_0/R_c]} \quad (\text{A.9})$$

Puisque la dynamique de fermeture intrinsèque des FACs montre une augmentation de vitesse à mesure que la courbure du trou augmente, on peut considérer

- soit une dissipation dominée par l'une des viscosités η_1 ou η_2 , avec une interaction FAC-CC spécifique par friction de surface ζ ou friction de ligne ξ ,
- soit des viscosités négligeables $\eta_1 = \eta_2 = 0$ mais une dissipation dominée par une friction de ligne non-spécifique ζ , alors que l'interaction FAC-CC dépend uniquement d'une friction de surface spécifique ξ .

En fait, on a supposé que la résistance du tissu de FACs était de nature élastique parce qu'on observe des tractions convergentes sur le substrat à l'état stationnaire. Même si on s'attend à une fluidité du tissu de FACs sur l'échelle temporelle des expériences (dizaines d'heures), la matrice extra-cellulaire déposée par les FACs pourrait agir comme une matrice élastique reliant les cellules entre elles et les attachant au substrat. Comme les tractions sont en plus localisées spatialement, l'idée la plus simple est de supposer une rhéologie élastique pour le tissu de FACs (module plan $E_c h_c$) et pour l'interaction FAC-substrat (module Y_s). Cela localise les tractions sur une longueur

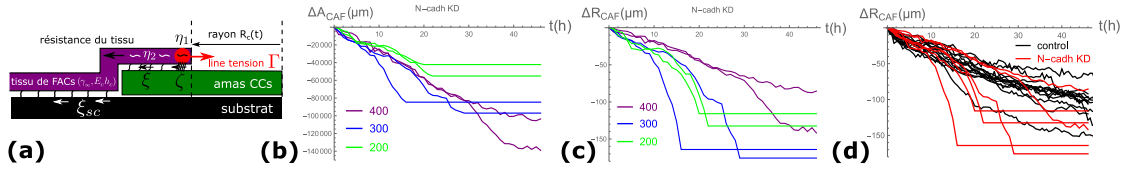


Figure A.5: **(a)**: Schéma du tissu de FACs montant au-dessus des CCs avec une fermeture de trou contrôlée par la tension de ligne de l'anneau Γ (rouge). Une pré-tension γ_∞ ou une élasticité de module $E_c h_c$ peut y résister. La dissipation peut être dominée par une viscosité de ligne η_1 au niveau de l'anneau, une viscosité du tissu de FACs η_2 , des frictions 2D avec coefficients ξ_{sc} (FAC-substrat), ξ (FAC-CC) ou une friction de ligne ζ sur l'anneau. **(b,c)**: Dynamique expérimentale de fermeture des FACs, en terme de l'aire du trou (b) ou de son rayon (c) pour différents diamètres d'amas et dans des conditions d'inhibition des N-cadhérines. Les amas d'un diamètre de 400 microns forment un bourgeons alors que les autres se font recouvrir par le tissu de FACs (fermeture complète). **(d)**: Dynamique du rayon du front de FACs dans des conditions normales (noir) ou avec l'inhibition des N-cadhérines (rouge). La vitesse initiale semble indépendante des conditions expérimentales.

caractéristique $\lambda_s \sim \sqrt{E_c h_c / Y_s}$.

La rhéologie plan peut alors s'écrire

$$\begin{aligned}\gamma_{rr} &= \gamma_\infty + \frac{E_c h_c}{1 - \nu^2} [\epsilon_{rr} + \nu \epsilon_{\theta\theta}] \\ \gamma_{\theta\theta} &= \gamma_\infty + \frac{E_c h_c}{1 - \nu^2} [\epsilon_{\theta\theta} + \nu \epsilon_{rr}]\end{aligned}\quad (\text{A.10})$$

où γ_∞ est une pré-tension constante, $\epsilon_{rr} = \partial_r u_r$ et $\epsilon_{\theta\theta} = u_r / r$ sont les composantes du taux de déformation associé au champ de déplacement radial u_r en supposant une invariance ortho-radiale du système.

Pour limiter l'amplitude de déformation des liens FAC-substrat, on introduit une contrainte de rupture f^* [229], de sorte que

$$T_r = Y_s u_r \quad \text{if} \quad |T_r| < f^*, \quad T_r = -f^* \quad \text{otherwise} \quad (\text{A.11})$$

Pour ne pas augmenter la complexité de la description avec une rhéologie visco-élastique de type Kelvin-Voigt, on suppose que les termes visqueux proportionnels à η_2 sont négligeables par rapport aux termes élastiques dans la région qui entoure les amas cancéreux. Au contraire, on considère cette viscosité η_2 pour le front du tissu au-dessus des CCs et assumons une incompressibilité plan.

Mécanique de la monocouche de CCs

On passe maintenant à la description mécanique du tissu cancéreux, au stade où les CCs sont toujours organisées en mono-couches. En s'inspirant du modèle de "vertex" en vue de côté du précédent chapitre, qui décrit un matériau solide puisqu'aucune dissipation interne n'est décrite, on utilise une rhéologie élastique avec une tension de surface apicale pour la déformation verticale. Dans une approximation de faible épaisseur telle que le rayon initial de l'amas R_0 soit grand par rapport à l'épaisseur de référence h^* , cela revient à écrire une équation "constitutive" pour le champ de pression $P(r)$ en fonction du champ de déformation verticale $\delta h(r) \equiv h(r) - h^*$

$$P(r) \simeq k \delta h(r) - \gamma \left[\delta h''(r) + \frac{\delta h'(r)}{r} \right] \quad (\text{A.12})$$

où k est la rigidité élastique verticale et γ la tension de surface (le second terme est l'équation de Laplace). On suppose également que les divisions cellulaires sont suffisamment lentes pour assumer une incompressibilité 3D.

Il reste à décrire l'interaction substrat-CC. On observe expérimentalement une localisation spatiale des déformations verticales, qu'on peut rapprocher des "rims" présents à la périphérie de films liquides en démouillage. Cependant, alors que la largeur Δ de ces derniers dépend de la viscosité

η_2 et de la friction avec le substrat ξ_s selon la relation paramétrique $\Delta \sim \sqrt{\eta_2/\xi_s}$ [234], on a supposé que la rhéologie de la monocouche était élastique. On peut soit obtenir une localisation spatiale constante $\Delta \sim \sqrt{k h^{*2}/Y_s}$ avec une interaction substrat-CC élastique, soit une localisation dynamique $\Delta(t)$ avec une rhéologie frictionnelle de coefficient ξ_s . Des tractions convergentes sont observées sous l'amas cancéreux mais leur maintien à l'état stationnaire n'est pas concluant: ainsi, on privilégie la rhéologie frictionnelle ξ_s pour l'interaction substrat-CC.

On peut montrer que l'Eq. A.12 pour la partie libre est compatible avec le modèle de "vertex" 2D en supposant que les contraintes de cisaillement conduisent à des gradients corticaux pour les interfaces apicales et basales autour d'une valeur homéostatique, de sorte que des sauts de tension apparaissent entre cellules voisines. En faisant une théorie perturbative autour de l'état uniforme et en considérant une limite continue, on retrouve l'équation constitutive de l'Eq. A.12 avec $k = \Gamma_l/A_0$ et $\gamma = \Gamma_a$ pour un système plan. On obtient alors la correspondance 3D entre les deux modèles avec $k \sim \gamma_l/V_0^2/3$ et $\gamma \sim \gamma_a$.

Dans ces conditions, la balance radiale des contraintes devient alors

$$-h^* [P'(r) + k\delta h'(r)] \simeq \xi_s v_r(r) \quad (\text{A.13})$$

où $v_r = \partial_t u_r$. Comme le champ de pression P est relié au champ de déformation δh (Eq. A.12), on peut obtenir une Equation aux Dérivées Partielles (EDP) en combinant l'Eq. A.13 avec l'incompressibilité locale: $\partial_t \delta h + (h^*/r)\partial_r[r v_r] \simeq 0$. Utilisant le coefficient de diffusion $D_s \equiv k h^{*2}/\xi_s$ et la longueur mécanique $\lambda \equiv \sqrt{\gamma/k}$, on obtient une EDP de croissance pour la déformation verticale de l'amas cancéreux sur la partie libre de FACs

$$\partial_t \delta h \simeq D_s \frac{1}{r} \partial_r \left[2r \delta h' - \lambda^2 \left(r \delta h^{(3)} + \delta h'' - \frac{\delta h'}{r} \right) \right] \quad (\text{A.14})$$

Une équation similaire est obtenue sur la partie couverte par les FACs, avec des termes supplémentaires associés à la friction FAC-CC, la viscosité η_2 et la pré-tension γ_∞ du tissu de FACs. Appelant la longueur mécanique effective de l'interface $\bar{\lambda}^2 \equiv (\gamma + \gamma_\infty)/k$ et le coefficient de diffusion de cette région $D \equiv k(h^*)^2/(\xi + \xi_s)$, on obtient une EDP de croissance sur la partie couverte par les FACs

$$\begin{aligned} \frac{\partial_t \delta h}{D} \simeq & \frac{\delta h'}{r} \left\{ 2 - \frac{\bar{\lambda}^2}{r^2} + \frac{\xi R_c V_c}{k(h^*)^2} + \frac{\xi \xi_s R_c V_c}{(\xi + \xi_s) k r^2} \left[2 - \log \left(\frac{R_T}{r} \right) \right] + \frac{18 \eta_2 R_c V_c}{k r^4} \right\} \\ & + \delta h'' \left\{ 2 + \frac{\bar{\lambda}^2}{r^2} - \frac{\xi \xi_s R_c V_c}{(\xi + \xi_s) k r^2} \left[2 - \log \left(\frac{R_T}{r} \right) \right] - \frac{18 \eta_2 R_c V_c}{k r^4} \right\} \\ & - \frac{2 \delta h^{(3)}}{r} \left\{ \bar{\lambda}^2 + \frac{\xi \xi_s R_c V_c}{(\xi + \xi_s) k} \left[1 + \log \left(\frac{R_T}{r} \right) \right] - \frac{4 \eta_2 R_c V_c}{k r^2} \right\} \\ & - \delta h^{(4)} \left\{ \bar{\lambda}^2 + \frac{\xi \xi_s R_c V_c}{(\xi + \xi_s) k} \log \left(\frac{R_T}{r} \right) + \frac{2 \eta_2 R_c V_c}{k r^2} \right\} \end{aligned} \quad (\text{A.15})$$

qui est obtenue à partir d'une généralisation de l'équation "constitutive" pour la pression sur la partie couverte

$$P(r) \simeq k \delta h(r) - [\gamma + \gamma_{\text{FAC}}(r)] \left\{ \delta h''(r) + \frac{\delta h'(r)}{r} \right\} + 2 \eta_2 \frac{R_c V_c}{r^2} \left\{ \delta h''(r) - \frac{\delta h'(r)}{r} \right\} \quad (\text{A.16})$$

Contrairement à la région libre de FACs, la théorie perturbative du modèle de "vertex" ne permet pas d'obtenir une EDP unique pour δh , et la limite continue génère deux EDPs couplées pour les champs $\theta(x, t)$ (angle de déviation de l'interface latérale) et $h(x, t)$. On abandonne ici le modèle de vertex et considérons uniquement la version continue avec l'Eq. A.16 pour la pression sur la région de l'amas couverte de FACs, menant à une EDP unique pour le champ de déformation verticale δh (Eq. A.15).

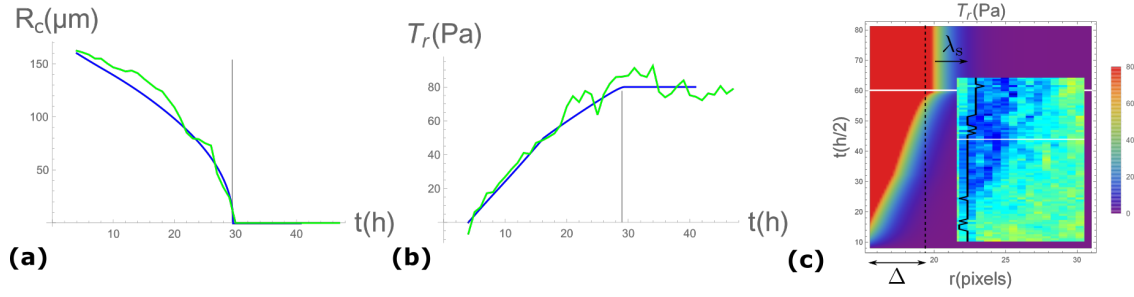


Figure A.6: (a): Dynamique du rayon de front des FACs (commençant à $R_c = R_0$) pour l'amas s33 sous les conditions d'inhibition des N-cadhérines. La courbe théorique (expérimentale) est en bleu (vert). (b): Dynamique des tractions radiales pour l'amas s33, moyennées autour de l'amas sur une largeur de 40 microns (c). La courbe théorique (expérimentale) est en bleu (vert). (c): Kymographe théorique des tractions radiales pour l'amas s33, centré sur sa périphérie. La courbe théorique de (b) est obtenue en moyennant sur la largeur Δ . La région bleue indique la décroissance exponentielle des tractions sur une taille $\lambda_s \sim \sqrt{E_c h_c / Y_s}$. La région rouge correspond au régime de rupture $|T_r| = f^*$ pour l'interaction substrat-FACs. Kymographe expérimental où le bleu correspond à $T_r < 0$, le vert à $T_r = 0$ et le jaune à $T_r > 0$ (encart). Une ligne blanche indique le temps de fermeture des FACs au-dessus de l'amas.

Concernant la mécanique de déformation de l'amas cancéreux, on obtient un système qui évolue sur deux domaines spatiaux: une région libre de FACs ($r < R_c$) et une région couverte par le tissu de FACs ($R_T > r > R_c$). On compte alors trois classes de paramètres

- géométrique: hauteur de référence des CCs h^* , rayon initial de l'amas de CCs R_0 ,
- mécanique: rigidité verticale des CCs k , tension de surface des CCs γ , pré-tension des FACs γ_∞ , tension de ligne de l'anneau Γ ,
- dissipatif: coefficient de friction FAC-CC ξ , coefficient de friction substrat-CC ξ_s , coefficient de friction de ligne ζ , viscosité tissulaire des FACs η_2 , et/ou viscosité de l'anneau η_1 .

L'évolution du profil de hauteur des CCs est contrôlé par les deux EDPs (Eq. A.14 et Eq. A.15) avec les deux frontières du système, le rayon de l'anneau $R_c(t)$ et le rayon périphérique de l'amas $R_T(t)$. Le système mathématique se ferme avec 8 conditions aux bords spatiales, l'initialisation temporelle $h(r, t = 0) = h^*$ et $R_c(t = 0) = R_T(t = 0) = R_0$, deux équations dynamiques pour $R_c(t)$ et $R_T(t)$, et la tension du tissu environnant de FACs appliquée sur le front en $r = R_T$. Notons qu'une friction de ligne de coefficient ζ crée une discontinuité de pression $\Delta P \simeq \zeta V_c / h^*$ en $r = R_c$. A l'ordre linéaire, les conditions aux bords sont

- en $r = R_T(t)$: $P_{\text{adh}} = 0$ [mécanique], $v_{\text{adh}} = dR_T/dt$ [flux], et $h_{\text{adh}} = h^*$ qui remplace la balance des tensions pour ne pas traiter un état initial hétérogène [tension], $\gamma_{\text{FAC}} = \gamma_\infty$ [tension],
- en $r = R_c$, continuité de $h \equiv h_c$, discontinuité de pression $P_{\text{adh}} + \Delta P = P_{\text{free}}$ [mécanique], $J_{\text{adh}} = J_{\text{free}}$ [flux], les deux composantes de la balance des tensions sur l'anneau $\gamma_{rr} + 2\eta_1 V_c / R_c^2 + \zeta(V_c + v_{\text{adh}}) \simeq \Gamma / R_c$ [tension (Or)] et $[\gamma_{rr} + \gamma + \zeta(V_c + v_{\text{adh}})]h'_{\text{adh}} \simeq \gamma h'_{\text{free}}$ [tension (Oz)],
- en $r = 0$, $h'_{\text{free}} = 0$ [tension] et $v_{\text{free}} = 0$ [flux].

La balance des flux en $r = R_T$ et la balance des tensions radiales en $r = R_c$ donnent les équations dynamiques pour l'évolution des domaines spatiaux.

A.3.3 Résultats: fermeture des FACs et tractions sans N-cadhérines

On étudie maintenant le phénotype de fermeture des FACs lorsque l'expression des N-cadhérines est inhibée. On utilise la description élastique pour le tissu de FACs, de paramètres $E_c h_c$, $\nu = 0.45$,

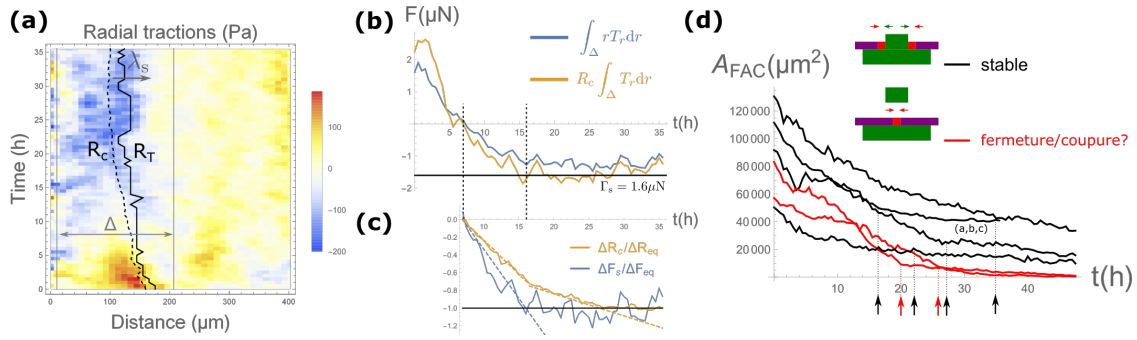


Figure A.7: **(a)**: Kymographe expérimental des tractions radiales T_r , avec une localisation spatiale lorsqu'elles sont convergentes (bleu), avec le rayon de l'anneau R_c (ligne avec tirets) et le rayon de l'amas R_T (ligne pleine). Les tractions sont intégrées sur la largeur Δ en **(b)**. **(b)**: Force de traction totale F intégrée suivant Δ (a), avec une intégrale surfacique (bleu) ou linéique (orange). Les tractions convergentes apparaissent à $t = 7$ h et atteignent une valeur de saturation $-\Gamma_s$ pour $t > 16$ h. **(c)**: Variation relative de la force de traction $F_s = 2\pi F$ (b) et du rayon de l'anneau R_c à partir de $t = 7$ h, en normalisant par leur valeur à temps long. La saturation des tractions coïncide avec une rupture de pente dans la dynamique de fermeture, qu'on voit comme un signe de résistance mécanique du bourgeon. **(d)**: Évolution de l'aire du trou défini par l'anneau des FACs au cours du temps. Certains bourgeons se stabilisent par résistance élastique à la compression de l'anneau (noir), tandis que d'autres semblent se détacher du corps de l'amas (rouge). Les ruptures de pente sont indiquées par des flèches.

Y_s, f^* , qui permet la localisation des forces de tractions appliquées au substrat comme observé expérimentalement. On suppose ici que les déformations de l'amas cancéreux peuvent être négligées de sorte que les FACs se ferment sur un matériau considéré rigide avec $R_T(t) \simeq R_0$, et on néglige la pré-tension $\gamma_\infty = 0$ qui joue un rôle secondaire. La fermeture est générée par la contractilité de l'anneau supracellulaire d'actomyosine, paramétrée par une tension de ligne Γ , et on suppose par simplicité qu'une friction de ligne ζ domine la dissipation pour reproduire la dynamique expérimentale telle que $V_c \propto 1/R_c$ (Fig. A.5b,c et Fig. A.6a). Les tractions radiales sont d'abord moyennées sur une petite largeur Δ (Fig. A.6c) pour quantifier leur évolution temporelle (Fig. A.6b). Pour comparer les résultats théoriques et expérimentaux, on fixe les paramètres en utilisant la tension de ligne obtenue par compression des piliers (Γ), la longueur de localisation $\lambda_s \propto \sqrt{E_c/Y_s}$, la dynamique de fermeture (Γ/ζ) et le taux de croissance des tractions moyennées ($\propto \sqrt{E_c Y_s}/\zeta$). La saturation des tractions à l'état stationnaire (Fig. A.6b) fixe la valeur du paramètre f^* , puisque la région délimitée par Δ est intégralement convertie au régime de rupture $|T_r| = f^*$ (Fig. A.6c). Même si la contrainte de rupture f^* n'est pas indispensable, le kymographe expérimental (Fig. A.6c, encart) indique une région où les tractions convergentes semblent relativement homogènes autour de l'amas.

On prend $\Gamma = 700$ nN, avec $R_0 = 161$ μm , $f^* = 80$ Pa et $h_c = 4$ μm . La comparaison entre théorie et expérience donne $E_c = 300$ Pa, $Y_s = 2.6 \cdot 10^6$ Pa/m ($\lambda_s = 24$ μm) et $\zeta = 3.6 \times 10^6$ Pa s.

A.3.4 Résultats: stabilité des bourgeons cancéreux

On s'intéresse maintenant à l'autre phénotype ou des réarrangements cellulaires mènent à l'observation de bourgeons cancéreux en 3D, compressés par l'anneau des FACs [190]. Ces réarrangements proviennent de contraintes frictionnelles entre FACs et CCs, soit par leur surface de contact avec un coefficient ξ , soit par une interaction localisée au niveau de l'anneau de coefficient ζ . Même si on pourrait s'attendre à une relaxation fluide à cause de la large durée des expériences (dizaines d'heures), cette configuration semble mécaniquement stable comme on peut le voir sur la Fig. A.7a.

Une première analyse comparative montre que la dynamique des tractions intégrées et du rayon de l'anneau possèdent des propriétés communes: alors que les tractions radiales deviennent convergentes autour de $t = 7$ h pour l'amas de la Fig. A.7a et saturent après $t = 16$ h (Fig. A.7b), on observe une rupture de pente simultanée pour la dynamique de fermeture (Fig. A.7c). Cette caractéristique apparaît de manière robuste pour différents amas, et on l'interprète comme l'apparition

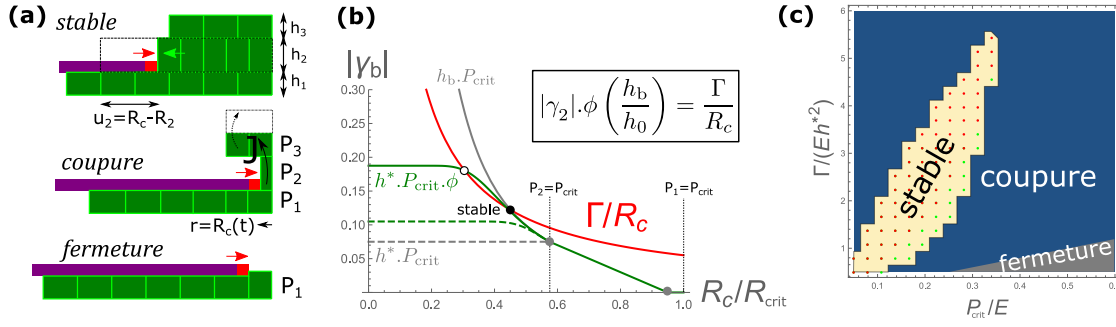


Figure A.8: **(a)**: Schéma du système pour le modèle en multicouches, où la différence de pression $P_i - P_j$ contrôle le transfert de cellules entre les couches par l'intermédiaire d'une pression critique P_{crit} . Le flux vertical s'écrit alors $J_{i \rightarrow j} = \alpha(|P_i - P_j| - P_{crit})$. Le bourgeon central peut résister la compression de l'anneau de manière stable (dessus), être séparé du corps de l'amas (milieu) où ne pas apparaître si le détachement basal n'a pas encore eu lieu quand $R_{crit} < l^*$ (bas). **(b)**: Balance des tensions entre la compression de l'anneau (rouge) et la résistance élastique du bourgeon (vert), en fonction du rayon de l'anneau R_c . La deuxième couche apparaît quand $R_c = R_{crit}$, applique une résistance élastique sur l'anneau qui dépend du nombre de couches par un facteur effectif de propagation des contraintes $\phi = 1 + b \tanh[(h_b/h^* - 1)/b]$. **(c)**: Diagramme de phase en fonction de la pression critique réduite P_{crit}/E et la tension de ligne réduite $\Gamma/(Eh^2)$. Un bourgeon stable existe seulement pour des valeurs faibles de ces paramètres (région jaune) et peut contenir deux couches (points verts) ou davantage (points rouges). Sinon, la compression des FACs activent le flot des CCs en dehors de la deuxième couche jusqu'à coupure du bourgeon (région bleue), ou la fermeture des FACs a lieu car le détachement basal ne peut plus avoir lieu quand $R_{crit} < l^*$ (région grise).

d'une résistance élastique sur l'anneau venant du bourgeon 3D. Cela revient à une équation effective de balance des forces $\Gamma = \Gamma_s + \Gamma_b$, où une fraction Γ_s de la tension de ligne de l'anneau est transmise au substrat (Fig. A.7b) tandis que la fraction restante Γ_b s'applique sur le bourgeon. En fait, même si une majorité de bourgeons sont mécaniquement stables, certains ne semblent pas exercer de résistance suffisante et on s'attend à une coupure de l'anneau les séparant du corps de l'amas (Fig. A.7d). On parle alors de bourgeonnement total par analogie avec la physiologie des bourgeons tumoraux [190].

On s'attend naturellement à ce que de larges bourgeons soient plus susceptibles de rester stables, et on utilise un modèle minimal pour décrire la transition en multicouche et étudier la stabilité des bourgeons formés. Si les réarrangements cellulaires pouvaient avoir lieu de manière fluide au sein d'un bourgeon, on peut montrer que la stabilité mécanique aurait tendance à être marginale et les FACs se fermentaient au-dessus. Pour justifier les observations expérimentales, on doit considérer une résistance élastique des CCs (module $E \equiv kh^*$) avec une plasticité autorisant les réarrangements en multicouche comme indiqué sur la Fig. A.8a. Les contraintes de cisaillement FAC-CC génèrent une pression au sein de la monocouche de CCs, jusqu'à une valeur critique P_{crit} qui active le détachement basal pour former une deuxième couche pendant que l'anneau se ferme. A partir d'un rayon de l'anneau R_{crit} , la deuxième couche s'étend sur toute la partie libre et applique une force de résistance (Fig. A.8b). Comme les cellules gardent d'importantes interactions avec leurs voisines, on introduit un facteur de propagation $\phi(h/h^*) = 1 + b \tanh[(h/h^* - 1)/b]$ qui capture la contribution des couches adjacentes à la force de résistance. Ainsi, le bourgeon de CCs peut soit être séparé du corps de l'amas par coupure de l'anneau, soit se stabiliser avec deux couches ou davantage (Fig. A.8c). Dans cette description élasto-plastique, l'équilibre mécanique du système n'existe que pour une région limitée de l'espace des paramètres. Connaissant expérimentalement les tailles typiques des bourgeons, on peut estimer le module élastique des CCs $E \sim 2 - 10$ kPa et la pression critique $P_{crit} \sim 500 - 2000$ Pa. Il est naturel de supposer qu'aucun bourgeon ne se forme si le rayon critique de l'anneau auquel $P = P_{crit}$ est inférieur à une taille cellulaire, ce qui définit une région du diagramme de phase où les FACs se ferment au-dessus d'une simple monocouche de CCs (Fig. A.8c).

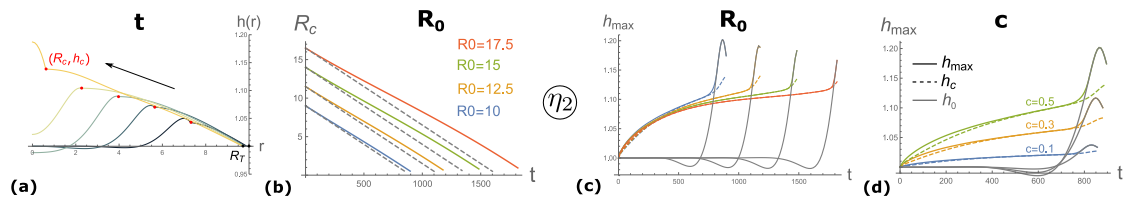


Figure A.9: *scénario avec viscosité de surface η_2 et tension de ligne Γ constante.* (a): Evolution de du champ de hauteur $h(r, t)$ à $R_0 = 10$ et $c = 0.5$, avec un rayon périphérique de l'amas R_T (points noirs) et la position de l'anneau ($r = R_c, z = h_c$) (points rouges). (b): Evolution du rayon de l'anneau R_c pour différents rayons d'amas R_0 , à $c = 0.5$ (lignes pleines) ou $c = 0$ (lignes pointillées). (c,d): Evolution de la hauteur maximale h_{\max} pour différentes tailles d'amas à $c = 0.5$ (c) ou pour différentes amplitudes de friction FAC-CC à $R_0 = 10$ (d). La hauteur de l'anneau h_c (lignes pointillées) et la hauteur au centre de l'amas h_0 (lignes grises) sont représentées.

A.3.5 Résultats: dynamique de déformation des amas de CCs

Anti-corrélation entre déformation et taille de l'amas

On résout maintenant le système complet d'équations sur les deux domaines $0 < r < R_c(t)$ (libre de FACs) et $R_c(t) < r < R_T(t)$ (couvert de FACs). On suppose qu'une hauteur critique des CCs est nécessaire pour activer le détachement basal responsable du bourgeonnement. On cherche donc la hauteur maximale $h_{\max}(t) = \text{Max}[h(r, t), r]$ de la partie libre et comment elle évolue en fonction des paramètres. Une observation expérimentale clé est la corrélation entre fréquence de bourgeonnement et taille initiale des amas. On veut donc identifier les propriétés nécessaires pour la reproduction théorique de cette propriété. On suppose également que le premier évènement de passage en multicouche induit une accumulation de sorte qu'un lien causal existe entre une valeur critique de la hauteur h_{crit} et l'apparition d'un bourgeon à l'état final.

On utilisera ici des quantités sans dimensions avec la hauteur de référence des CCs (h^*) comme unité de longueur, la tension de ligne Γ comme unité de force et une unité arbitraire ξ_0 pour les coefficients de friction, de sorte que $c \equiv \xi/\xi_0$ et $s \equiv \xi_s/\xi_0$. Les autres paramètres sans dimension gardent la même notation.

Comme discuté précédemment pour la dynamique de fermeture, différents mécanismes de dissipation peuvent être supposés en supposant soit une tension de ligne constante soit une sensibilité à la courbure de l'anneau [229]. On s'intéresse ici au scénario où la viscosité surfacique du tissu de CAFs domine la dissipation de sorte que la vitesse de fermeture $V_c(t) \simeq \Gamma/(2\eta_2)$ est approximativement constante. On obtient alors l'évolution du profil de hauteur de la monocouche de CCs (Fig. A.9a) avec une fermeture du trou de rayon $R_c(t)$ après un temps $t_f \simeq 2\eta_2 R_0/\Gamma$ (Fig. A.9b). Un "rim" apparaît au début puis disparaît à cause de la trop grande déformation sur la partie couverte (Fig. A.9a), car on a pris $\gamma_\infty = 0$. En fait dans ces conditions, la déformation est anti-corrélée avec la taille initiale de l'amas comme on peut le voir sur la Fig. A.9c, ce qui est opposé aux résultats expérimentaux. Par contre comme attendu, l'amplitude de déformation augmente avec la friction de surface FAC-CC c (Fig. A.9d).

Si on avait considéré le scénario où la viscosité de l'anneau était dominante, on aurait eu une vitesse radiale de fermeture $V_c(t) = \Gamma R_c(t)/(2\eta_1)$ et cette fois il y aurait bien corrélation entre h_{\max} et R_0 . Cela montre que la dynamique de fermeture influence l'évolution de la déformation, mais une vitesse $V_c \propto 1/R_c$ montre également une anti-corrélation. En fait pour le scénario η_2 avec vitesse constante, on peut montrer qu'une diminution suffisante de la friction substrat-CC s mène à une corrélation positive entre h_{\max} et R_0 . Cette inversion est associée à l'étalement spatial du "rim" dont la largeur Δ est proportionnelle à $(\lambda^2 D_s/V_c)^{1/3}$ en phase stationnaire, soit une augmentation de l'étalement quand s diminue. Lorsque s est suffisamment petit, la déformation se propage sur toute la partie libre par diffusion ce qui empêche la disparition du "rim" comme sur la Fig. A.9a. Malgré une croissance plus faible, cela permet une accumulation de déformation pour les grands

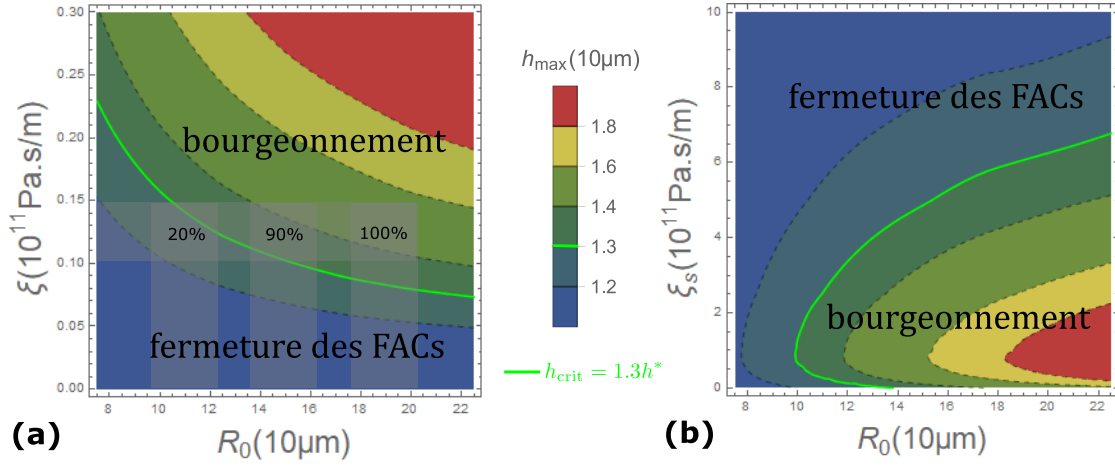


Figure A.10: Diagrammes de phase pour la limite de partie couverte plate dans le scénario η_2 . (a,b): Diagrammes de phase pour la hauteur maximale h_{\max} dans l'espace des paramètres (R_0, c) à $s = 5$ (a) et (R_0, s) à $c = 0.1$ (b). Ici, on prend une hauteur critique $h_{\text{crit}} = 1.3h^*$ (ligne verte). Pour c (ξ) et s (ξ_s) donnés, la déformation augmente avec R_0 ce qui favorise le détachement basal.

amas où la fermeture est plus longue et on obtient une corrélation entre h_{\max} et R_0 .

Lorsque s est trop grand, la faible diffusion de la déformation dans la partie libre concentre la pression au niveau de l'anneau et déforme davantage la partie couverte. Comme les grands amas ont une plus grande partie couverte, la fraction de volume transférée en déformation (associée au déplacement convergent de la périphérie de l'amas) est relativement plus faible sur la partie libre de sorte qu'une anti-corrélation apparaît entre h_{\max} et R_0 (Fig. A.9c). En fait, on peut retrouver une corrélation dans la limite où la déformation de la partie couverte est négligeable. Comme la vitesse de fermeture suit $V_c \propto \Gamma - \gamma_\infty R_c$, on ne peut pas juste supposer $\gamma_\infty \rightarrow \infty$ et on doit cumuler les limites $\Gamma, \gamma_\infty, \eta_2 \rightarrow \infty$ pour que la vitesse de fermeture soit inchangée tout en supprimant la déformation de la partie couverte. Dans cette limite où $h_{\text{couv}} = 1$, le "rim" ne peut pas disparaître et l'effet d'accumulation permet d'observer une corrélation entre h_{\max} et R_0 quelle que soit la valeur de s (Fig. A.10b).

Diagrammes de phase et fréquence de bourgeonnement

Un résultat expérimental clé est l'observation d'une corrélation positive entre la fréquence d'observation de bourgeons et la taille initiale des amas. Cet aspect est compatible avec le modèle dans la limite où la partie couverte reste plate, que l'on peut représenter avec des diagrammes de phases fonction du rayon initial R_0 et des paramètres de friction FAC-CC c (Fig. A.10a) ou substrat-CC s (Fig. A.10b). En utilisant une déformation critique pour le critère de passage en multicouche, correspondant à une hauteur cellulaire h_{crit} , cela sépare l'espace des paramètres en une région de bourgeonnement lorsque $h_{\max} > h_{\text{crit}}$ a lieu avant la fermeture des FACs, et une région sans bourgeonnement lorsque $h_{\max} < h_{\text{crit}}$ (Fig. A.10).

Avec un bruit paramétrique sur le rayon initial et le coefficient de friction, on peut construire une fréquence de bourgeonnement équivalente comme une fraction surfacique (voir Fig. A.10a): on obtient une fréquence théorique de 20% pour $R_0 \simeq 110 \mu\text{m}$, 90% pour $R_0 \simeq 150 \mu\text{m}$ et 100% pour $R_0 \simeq 190 \mu\text{m}$. Expérimentalement, on a plutôt 25% pour des couches adhésives de rayon $R_p = 100 \mu\text{m}$, 60% pour $R_p = 150 \mu\text{m}$ et 100% pour $R_p = 200 \mu\text{m}$.

On voit en Fig. A.10b les effets antagonistes introduits par la friction substrat-CC s (localisation spatiale du "rim" et entraînement convergent de la périphérie de l'amas avec $V_T \propto cV_c/(c+s)$), de sorte que la déformation est maximisée pour des valeurs intermédiaires autour de $s \sim 1$.

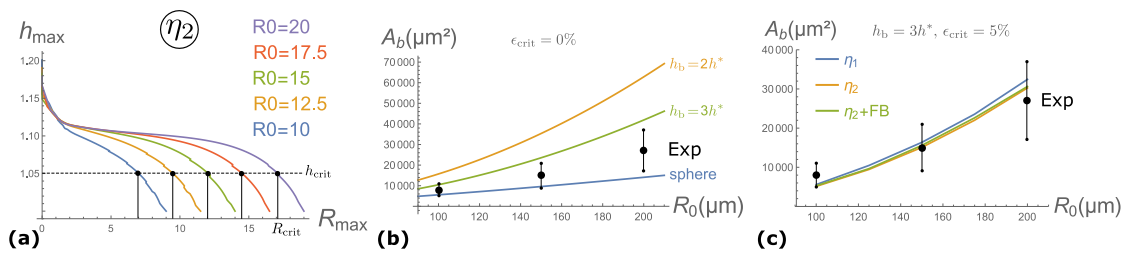


Figure A.11: *Comparaison entre théorie et expérience pour l'aire finale des bourgeons A_b .* (a): Hauteur maximale h_{\max} en fonction de R_{\max} pour le scénario η_2 , avec une hauteur critique $h_{\text{crit}} = 1.05h^*$ ou un taux de déformation $\epsilon_{\text{crit}} \equiv (h_{\text{crit}} - h^*)/h^* = 5\%$. L'équation $h_{\max} = h_{\text{crit}}$ définit un rayon équivalent R_{crit} auquel le bourgeonnement apparaît. (b): Aire des bourgeons A_b (voir texte) en fonction du rayon initial des amas R_0 avec $\epsilon_{\text{crit}} = 0\%$ et différentes hypothèses sur la forme finale: une sphère, un cylindre avec 2 ou 3 couches. (c): Aire des bourgeons A_b en fonction du rayon initial des amas R_0 , en comparant expérience (noir) et théorie (couleur). Cela correspond à (a) avec $\epsilon_{\text{crit}} = 5\%$. On choisit $h_b = 3h^*$ mais un autre nombre peut être pris si ϵ_{crit} est ajusté en parallèle.

Aire projetée des bourgeons

En plus des mesures expérimentales corrélant la fréquence des bourgeons à la taille initiales des amas, l'aire projetée (en vue de dessus) des bourgeons à l'état stationnaire augmente également avec le rayon R_0 Fig. A.11b,c. Pour des conditions données, l'évolution de la hauteur maximale $h_{\max}(t)$ qui est transportée spatialement selon la trajectoire $r = R_{\max}(t)$, atteint h_{crit} au temps t_{crit} à un rayon $R_{\max}(t_{\text{crit}}) \equiv R_{\text{crit}}$ (Fig. A.11a). A $t = t_{\text{crit}}$, on suppose que le volume de la région libre de FACs correspond approximativement au volume final du bourgeon par accumulation des événements de passage en multicouche. Ainsi, on écrit le volume du bourgeon comme $V_b \simeq \pi h^* (R_{\text{crit}})^2$ tant que les déformations restent faibles: avec un taux de déformation $\epsilon_{\text{crit}} \equiv (h_{\text{crit}} - h^*)/h^*$, cela revient à $\epsilon_{\text{crit}} \ll 1$. La Fig. A.11a montre une corrélation évidente entre taille du bourgeon et taille initiale de l'amas, ce qui reste indépendant du scénario dissipatif tant que ϵ_{crit} reste faible.

Pour relier le volume du bourgeon V_b à la mesure expérimentale d'aire projetée A_b , on doit faire une hypothèse sur la forme: la Fig. A.11b montre qu'une sphère est incompatible avec les données expérimentales même en cas de transition spontanée ($\epsilon_{\text{crit}} = 0\%$), contrairement à un cylindre de quelques couches comme on peut le confirmer par observation directe en microscopie confocale. Le nombre de couches n reste cependant indéterminé avec $A_b \simeq V_b/(nh^*)$. En supposant $n = 3$ avec $\epsilon_{\text{crit}} = 5\%$ (Fig. A.11a), on obtient un bon accord entre les valeurs théoriques et expérimentales de A_b comme le montre la Fig. A.11c.

A.4 Extrusion cellulaire

Le but de ce projet théorique est de proposer une description minimale de la mécanique de l'extrusion cellulaire dans les monocouches épithéliales, et comment une compression externe sur le tissu peut changer son occurrence. Le cadre théorique utilise un modèle de "vertex" à 2D en vue de côté avec des interfaces courbées. Les résultats sont encore préliminaires et le projet doit être terminé.

Le phénomène d'extrusion cellulaire est supposé être la conséquence de deux transitions consécutives, comme représenté sur la Fig. A.12. La première étape est la perte de contact basal de la cellule, suivie par la perte de l'interface latérale correspondant à l'évènement d'extrusion lui-même. Dans un langage de réaction chimique, l'extrusion a lieu à travers les réactions de conversion des interfaces *basal* \rightarrow *lateral* et *lateral* \rightarrow *apical*. En se focalisant sur la forme cellulaire, une cellule épithéliale normale est représentée par le symbole U , alors que V correspond à la première transition, Y est associé au nouvel état d'équilibre et O est la cellule extrudée en suspension. L'extrusion est alors représentée comme la combinaison des deux "réactions mécaniques" irréversibles $U \rightarrow V \rightarrow Y$ et $Y \rightarrow O$. Notre but est de trouver les conditions pour lesquelles ces transitions sont susceptibles

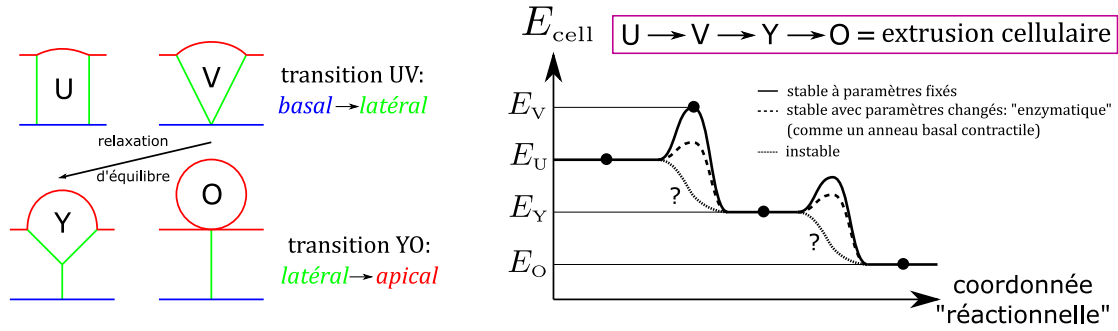


Figure A.12: L'extrusion cellulaire est vue comme une transition irréversible en deux étapes. Partant d'un état uniforme (U), la cellule cible perd d'abord son interface basale (V), relaxe vers l'état (Y) où les forces du vertex latéral central s'équilibrent, et quitte la monocouche (O) par transition vers une interface complètement apicale. En terme de paysage énergétique, les transitions $U \rightarrow V$ et $Y \rightarrow O$ peuvent être empêchées par la stabilité mécanique des états U et Y (ligne pleine), être favorisées par un décalage "enzymatique" de certains paramètres mécaniques (ligne avec tiret), ou avoir lieu spontanément à travers une instabilité (ligne pointillée).

d'apparaître. L'intérêt d'une telle description minimale est de donner une certaine robustesse au phénomène dans le sens que les effets biochimiques spécifiques sont "cachés" derrière des paramètres effectifs, et donne donc une première image qui pourra être spécialisée plus tard.

Comme montré en Fig. A.12, on distingue trois régimes pour ces transitions: la stabilité des états U et Y , soit à paramètres fixés (barrière d'activation haute) soit en modifiant ces propriétés (barrière d'activation basse), ainsi qu'une instabilité mécanique (extrusion spontanée). Un exemple évident pour le décalage "enzymatique" des propriétés mécaniques est l'assemblage d'un anneau contractile à la base des cellules apoptotiques [230] qui conduirait naturellement à la transition $U \rightarrow V$.

A.4.1 Résultats: critère énergétique naïf

Dans des conditions normales, comme l'extrusion cellulaire est cruciale pour l'intégrité physiologique des tissu épithéliaux *in vivo*, des éléments biochimiques spécifiques à l'extrusion (S1P, Piezo1) devraient réguler son activation en étant sensibles à l'état mécanique du tissu. Ainsi, une description purement mécanique ne prenant pas en compte ces circuits essentiels n'est pas pertinente dans cette situation, Cependant, des transformations oncogéniques de cellules individuelles sont connus pour affecter leur forme et mécanique [273, 260]. Pour notre description générique, on cible donc la phénoménologie d'épithélia avec hyperplasie locale, avec des cellules uniques transformées et entourées d'un tissu normal.

Un modèle précédent [282] a utilisé une quantification maligne pour cartographier continument les configurations U , V et Y sur une seule variable géométrique: l'impact d'une sur-densité a ensuite été étudiée avec une approche purement énergétique dans le cadre d'un modèle de "vertex" polygonal à 3D. Ici, on essaye d'identifier le chemin de configurations complet depuis l'état U jusqu'à l'extrusion cellulaire. Dans ce cadre, une transition spontanée correspondrait à l'absence d'une barrière d'activation (Fig. A.12).

La manière la plus simple d'approcher l'extrusion est de calculer la différence d'énergie entre l'état uniforme d'une monocouche à N cellules et $N - 1$ cellules avec une autre extrudée ayant converti son interface baso-latérale en type apical, avec une forme circulaire de rayon R . Pour une grande tension apicale, la configuration uniforme du tissu a une énergie $E_{\text{unif}} = N [(\alpha + \beta)l + 1/l]$ (avec $N \gg 1$). Pour rappel, on utilise $\sqrt{A_0}$ comme unité de longueur et Γ_1 comme unité de tension de sorte que $\alpha \equiv \Gamma_a/\Gamma_1$ et $\beta \equiv \Gamma_b/\Gamma_1$. La conservation de l'aire impose $R = 1/\sqrt{\pi}$ à la cellule cible et l'énergie totale de la nouvelle configuration est $E_{\text{extr}} = (N - 1) [(\alpha + \beta)l + \frac{1}{l}] + 2\alpha\sqrt{\pi}$. L'énergie est minimale par rapport à l lorsque $l = l^* \equiv 1/\sqrt{\alpha + \beta}$. La nouvelle configuration devient énergétiquement favorable si $E_{\text{extr}}^* < E_{\text{unif}}^*$, ou $\beta > \alpha(\pi\alpha - 1)$. Le facteur $\pi\alpha - 1$ devrait être positif parce qu'on a supposé des interfaces apicales plates ($\alpha \gg 1$). Il est clair qu'une extrusion spontanée

n'est pas attendue quand $\beta < 0$ pour un tissu bien étalé. Cependant, même si $\beta \lesssim \alpha$, ce critère n'autorise l'extrusion que pour des valeurs de tension apicale qui ne sont pas compatibles avec notre hypothèse initiale $\alpha \gg 1$, où l'extrusion n'est pas attendue.

On peut montrer que ce comportement est préservé lorsqu'on prend en compte la courbure des interfaces apicales, et l'extrusion n'est favorable que si $\alpha \lesssim 1$ et $\beta \sim \alpha$ ou $\beta > \alpha$. Cela montre que les coûts de conversion d'interfaces basal-latéral et latéral-apical sont équivalents et on doit augmenter la tension latérale. Ces conditions sont difficiles à atteindre parce que la contrainte de balance des tensions apicales impose $\alpha > 1/2$, alors que les différentes sources de tension donneraient $\Gamma_1 < \Gamma_a$ ($\alpha > 1$) à cause de l'énergie d'adhésion des cadhérines.

Si on applique une compression externe sur le tissu avec un taux de déformation fixé ϵ , le même analyse énergétique sur l'extrusion de n cellules ($n \ll N$) montre qu'il existe un taux de déformation critique $\epsilon_{\text{crit}} \equiv 1 - \sqrt{\alpha + \beta}/(\sqrt{\pi}\alpha)$ tel que l'extrusion devient favorable si $\epsilon > \epsilon_{\text{crit}}$. On retrouve le critère d'extrusion spontanée si $\epsilon = 0$, alors qu'une compression suffisante du tissu devrait déclencher l'extrusion. Pour $\alpha \gg 1$ et $\beta \lesssim \alpha$, le taux de déformation critique devient proportionnel à $\sqrt{\alpha}$: les cellules hautes et fines ne devraient pas extruder. Si $\beta > 0$ avec $\beta \lesssim \alpha$, on a $\epsilon_{\text{crit}} \propto 1 - 1/\sqrt{\alpha}$ et la transition n'est pas favorable quand α est trop grand.

A.4.2 Résultats: décalage enzymatique des paramètres

Comme expliqué plus haut, la première transition correspond à une perte d'interface basale ($U \rightarrow V$) qui peut avoir lieu par une modification des paramètres cellulaires. Ici en 2D, un anneau contractile sur la face basale [230] applique des forces convergentes sur les points basaux et devient équivalent à une augmentation de la tension basale (linéique) $\Gamma_b \mapsto \Gamma_b^p$. Plus généralement, comme le modèle de "vertex" à 2D en vue de côté ne contient que les tensions polarisées $\Gamma_b, \Gamma_1, \Gamma_a$ et l'aire projetée A_0 comme paramètres, des variations appliquées sur une cellule individuelle peuvent être appliquées sur chacun d'eux comme montré en Fig. A.13a. Cette cellule cible modifiée applique des contraintes sur ses voisines, et on suppose que ces contraintes sont relaxées sur la taille d'une cellule de sorte que les secondes voisines gardent l'état uniforme du tissu environnant.

On donne les résultats pour une variation de tension basale ou apicale en Fig. A.13b,c en gardant les autres à leur valeur standard. On représente le décalage critique auquel la perte d'interface basale a lieu, dans le plan paramétrique (α, β) qui caractérise l'état du tissu uniforme. Comme attendu, le détachement basal de la cellule centrale est associé à une augmentation de la tension basale Γ_b^p (Fig. A.13b) qui peut être reliée phénoménologiquement à l'anneau contractile de l'extrusion apoptotique [230]. Une plus grande tension basale dans le tissu environnant réduit l'amplitude du décalage enzymatique nécessaire pour la transition $U \rightarrow V$.

Pour éliminer l'interface basale, une réduction de la tension apicale Γ_a^p est également efficace puisqu'elle décroît le coût énergétique associé à davantage d'interface apicale (Fig. A.13c, encart). On peut montrer qu'un changement de l'aire de la cellule cible ne mène pas à une perte d'interface basale mais peut éliminer l'interface apicale pour une diminution d'aire critique. Enfin, une variation de la tension latérale n'amène aucune transition de forme.

Comparée à la réponse exacte d'une monocouche à la perturbation d'une cellule cible, la justesse de ce système à trois cellules (Fig. A.13a) peut être estimée en regardant la différence entre la pression hydrostatique des premières voisines et la valeur uniforme P^* . Alors qu'une différence de pression devrait être équilibrée par la courbure de l'interface latérale entre premières et secondes voisines, la quantité $\Delta P_1 \equiv (P_1 - P^*)/P^*$ quantifie l'erreur associée à l'hypothèse que cette interface reste verticale. On montre que l'erreur est minimale lorsque α et β sont faibles: ceci est relié à la longueur caractéristique de propagation des contraintes mécaniques au sein du tissu, qui atteint la taille d'une cellule pour cette région de l'espace des paramètres.

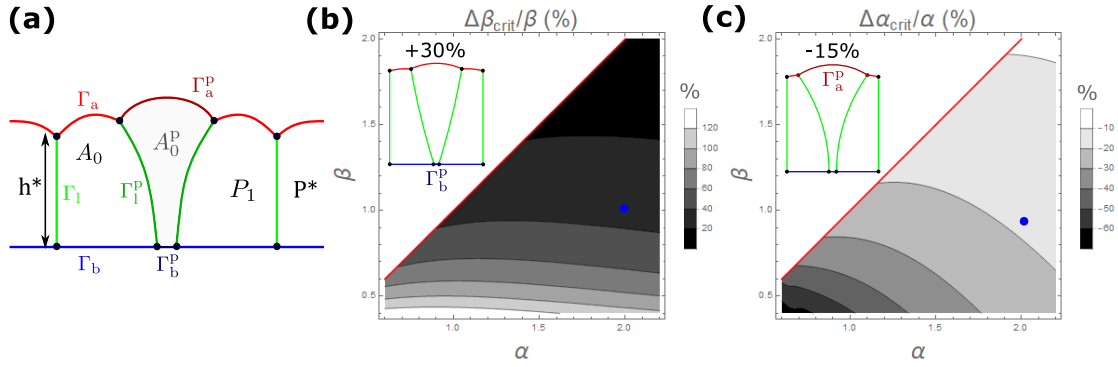


Figure A.13: **(a)**: Schéma de trois cellules incluses dans une monocouche "infinie" où la cellule centrale a des propriétés perturbées par rapport aux tensions Γ_b , Γ_l , Γ_a et l'aire A_0 des cellules autour. La perturbation de forme est supposée se propager sur la taille d'une cellule de sorte que les secondes voisines restent à l'état d'équilibre du tissu uniforme (h^* , l^* , P^*). **(b)**: Graphique quantifiant la tension basale critique (relative) pour un détachement basal de la cellule centrale, dans l'espace des paramètres (α, β) avec $\Delta\beta \equiv \beta_p - \beta$. L'encart représente l'état d'équilibre associé au point bleu avant la disparition basale, pour $\alpha = 2$, $\beta = 1$ et $\Delta\beta/\beta = +30\%$ (disparition à $\sim +40\%$). La ligne rouge représente $\beta = \alpha$. **(c)**: Graphique quantifiant la tension apicale critique (relative) pour un détachement basal de la cellule centrale, dans l'espace des paramètres (α, β) avec $\Delta\alpha \equiv \alpha_p - \alpha$. L'encart représente l'état d'équilibre associé au point bleu avant la disparition basale, pour $\alpha = 2$, $\beta = 1$ et $\Delta\alpha/\alpha = -15\%$ (disparition à $\sim -20\%$). La ligne rouge représente $\beta = \alpha$.

A.4.3 Résultats: système à trois cellules sous compression et instabilités

Au lieu d'un décalage enzymatique des tensions d'une cellule cible, on cherche ici une instabilité générique qui pourrait activer spontanément les deux transitions $U \rightarrow V$ et $Y \rightarrow O$ (voir Fig. A.12) quand une compression externe est appliquée à la frontière du tissu. On utilise un système à trois cellules qui permet de décrire la forme de manière complètement non-linéaire (Fig. A.14a), ce qui est nécessaire pour la configuration intermédiaire (Y) car la transition topologique ne peut pas être capturée par une simple perturbation linéaire. Cela représente un système minimal pour décrire l'extrusion de la cellule centrale, dont l'inconvénient majeur est la sensibilité aux bords qui disparaît pour une large monocouche. On regarde d'abord l'état d'équilibre en frontières libres pour la configuration Y et appliquons ensuite une compression externe, à la recherche d'instabilités de forme.

Pour respecter les contraintes imposées par les balances de tensions basale et apicale, on doit imposer $|\beta| < \alpha$ et $\alpha > 1/2$. La limite $\beta \rightarrow -\alpha$ correspond à un régime de "mouillage total" pour le tissu avec une hauteur évanescende and une extension plane infinie: on ignore cette limite en imposant $\beta > -\alpha + 0.5$. Pour les deux configurations topologiques U et Y , l'énergie réduite du système s'écrit

$$E_{\text{tot}} = \beta L_b + L_l + \alpha L_a - 2P_0(A_0 - 1) - P_1(A_1 - 1) \quad (\text{A.17})$$

où L_b , L_l et L_a sont, respectivement, la longueur totale associées aux interfaces basale, latérale et apicale. L'incompressibilité plan est introduite par des multiplicateurs de Lagrange (pressions) P_0 et P_1 . La minimisation de l'énergie donne à l'équilibre: balance des tensions sur les points, relations de Laplace $P_0 = \alpha/R_0$, $P_1 = \alpha/R_1$ et $P_0 - P_1 = 1/R_l$ pour des rayons de courbure R_0 , R_1 (apical) et R_l (latéral) (voir Fig. A.14a). Les interfaces apicales sont caractérisées par des angles de "gonflement" ψ_0 et ψ_1 alors que l'angle latéral ψ_l est égal à l'inclinaison angulaire θ à l'équilibre par balance des tensions basales. La balance des tensions apicales est équivalente à

$$\psi_0[\text{eq}] = \frac{1}{2} \left(\frac{5\pi}{6} + \psi^* - 2\theta_{\text{eq}} \right), \quad \psi_1[\text{eq}] = \psi^* + 2\theta_{\text{eq}} - \frac{\pi}{3}, \quad \psi_l[\text{eq}] = \theta_{\text{eq}} - \frac{\pi}{3} \quad (\text{A.18})$$

dans la configuration Y (similaire pour U). Le point latéral central est à l'équilibre lorsque les interfaces sont séparées par un angle $2\pi/3$.

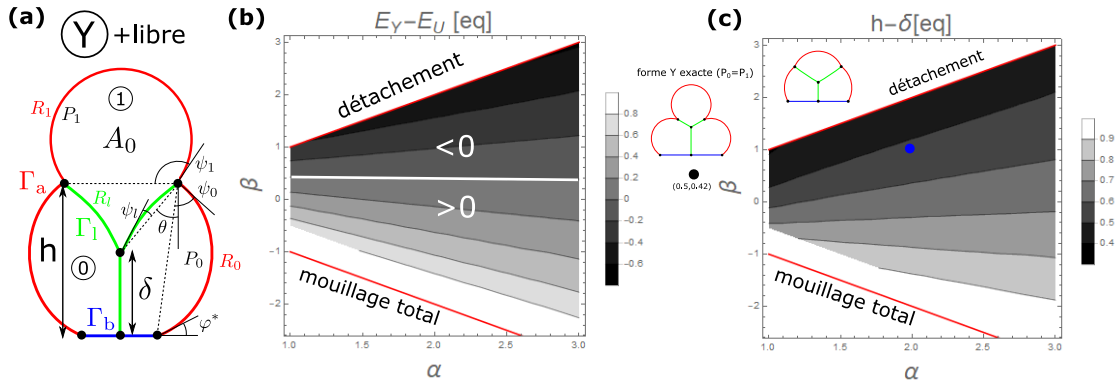


Figure A.14: **(a)**: Schéma du système à trois cellules libre dans la configuration Y , où la cellule centrale a perdu son interface basale. **(b)**: Graphique de la différence d'énergie à l'équilibre entre les configurations Y et U . La première est favorisée quand $\beta > 0$ comme attendu. Les lignes rouges représentent $\beta = \pm\alpha$. **(c)**: Graphique de la différence de hauteur latérale $h - \delta$ comme définie en (a). Une forme d'équilibre est montrée pour le point bleu à $\alpha = 2$, $\beta = 1$ (encart interne). Un cas spécial est représenté à $\alpha = 1/2$ pour le point noir, où la différence de pression $P_1 - P_0$ s'annule (encart externe). Les lignes rouges représentent $\beta = \pm\alpha$.

Pour des valeurs données de α et β , on peut comparer l'énergie du système pour les deux configurations Y (Fig. A.14a) et U (non représenté). En accord avec l'intuition, une grande tension basale rend la configuration Y plus favorable alors que l'opposé a lieu quand $\beta < 0$ (Fig. A.14b). Ainsi, si une instabilité mécanique peut activer la transition $U \rightarrow Y$, cela doit avoir lieu dans le sous-espace paramétrique où $\beta > 0$. Pour que la cellule centrale atteigne la transition $Y \rightarrow O$, on veut minimiser la taille de son interface latérale, ce qui peut être capturé par la quantité $h - \delta$ comme définie en Fig. A.14a. Fig. A.14c montre que la région pertinente de l'espace des paramètres correspond à $\beta \lesssim \alpha$ et $\alpha \lesssim 1$. En fait, le cas spécial qui minimise $h - \delta$ apparaît quand $\alpha = 1/2$ et $\beta \simeq 0.42$ comme on le voit dans l'encart externe de la Fig. A.14c: cet état à une différence de pression $P_1 - P_0$ nulle de sorte que les interfaces latérales sont plates. Formellement, ce cadre théorique avec tensions constantes et pressions uniformes ne permet pas d'obtenir l'état symboliquement représenté par O (Fig. A.12) à l'équilibre mécanique, parce que les contraintes de circularité et de balance des tensions sont incompatibles pour ce cas limite.

On s'intéresse maintenant à la stabilité de l'équilibre mécanique lorsqu'une compression externe est appliquée comme schématisé en Fig. A.15, à travers des murs rigides (dont la surface de contact est neutre pour les cellules) qui appliquent un taux de déformation $\epsilon \equiv (L_0 - L)/L_0$ de la taille initiale L_0 à la taille finale L . La longueur initiale $L_0(\alpha, \beta)$ correspond à l'extension latérale maximale du tissu et dépend des paramètres mécaniques. Pour un taux de déformation ϵ donné, on peut utiliser la contrainte $L = L_0(1 - \epsilon)$ qui dépendra de α et β . Comme attendu, une tension basale négative n'amène pas d'instabilité pour les deux transitions $U \rightarrow Y$ et $Y \rightarrow O$. De même, il n'y a pas d'instabilité pour la configuration U lorsque la tension basale devient positive lorsqu'on applique un taux de déformation de $\epsilon = +10\%$. On s'intéresse donc uniquement au cas d'une tension basale positive dans la configuration Y , pour la seconde transition $Y \rightarrow O$.

Pour étudier la stabilité des états d'équilibre sous compression (similaires à la Fig. A.14), on s'intéresse au paysage énergétique des états locaux hors-équilibre. Pour cela, on a besoin des variables $\{P_0, P_1, R_0, R_l, R_1, d, \psi_0, \varphi_0, \psi_1, \theta, \psi_1\}$ (Fig. A.15a). En plus de l'incompressibilité des aires projetées, il y a trois contraintes géométriques sur la taille comprimée du tissu, l'extension latérale de la cellule centrale et la hauteur:

$$L = 4R_0 \sin^2 \psi_0 + 2R_1 \sin \psi_1, \quad 2R_l \sin \psi_1 \sin \theta = R_1 \sin \psi_1, \quad 2R_0 \sin \psi_0 \cos \psi_0 + R_0 \cos \varphi_0 + d = 2R_l \sin \psi_1 \cos \theta + \delta \quad (\text{A.19})$$

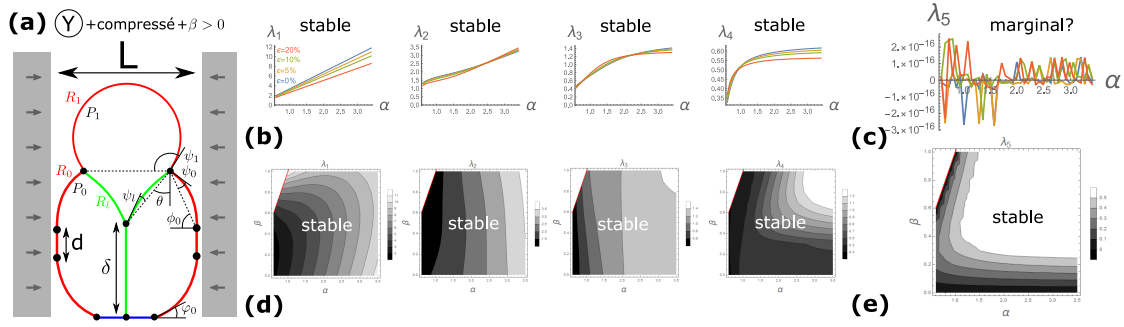


Figure A.15: **(a)**: Schéma du système de trois cellules sous compression, dans la configuration Y pour $\beta > 0$. **(b,c)**: Valeurs propres de la matrice hessienne en fonction de α le long de la ligne paramétrique $\beta = 0$, pour des amplitudes de compression où $\epsilon = 0, 5, 10, 20\%$. Les quatre premières valeurs propres **(b)** sont positives mais la dernière λ_5 est nulle **(c)**. **(d,e)**: Graphique des valeurs propres associées à la matrice hessienne dans l'espace paramétrique (α, β) , pour $\epsilon = 10\%$. La dernière valeur propre λ_5 est proche de 0 pour les lignes paramétriques $\beta = 0$ et $\beta = \alpha$ **(e)**. La ligne rouge correspond à $\beta = \alpha$.

Ces équations sont utilisées pour éliminer les longueurs de sorte que les cinq angles $\{\psi_0, \varphi_0, \psi_1, \theta, \psi_1\}$ restent comme variables indépendantes².

Il y a donc cinq valeurs propres λ_j associée à la matrice hessienne. Si on suit la ligne paramétrique $\beta = 0$ (Fig. A.15b,c), une stabilité marginale apparaît tandis qu'une stabilité nette existe pour $\beta > 0$ (Fig. A.15d). On considère cette stabilité marginale comme un artefact lié à la transition entre des valeurs positives et négatives de la tension basale, qui n'amène pas de mécanisme physique pour une transition de forme $Y \rightarrow O$. Cependant, bien que les quatre premières valeurs propres soient strictement positives dans l'espace paramétrique (α, β) , λ_5 est intéressante puisqu'elle devient légèrement négative le long de la ligne paramétrique $\beta = \alpha$ (Fig. A.15e). Il resterait à analyser le paysage énergétique dans cette région paramétrique et voir si le chemin des configurations mène bien à la transition escomptée.

Par ces deux analyses d'équilibre et de stabilité, la minimisation de la hauteur latérale centrale $h - \delta$ apparaît quand $\alpha \lesssim 1$ et $\beta \lesssim 1$ à l'équilibre, alors qu'une instabilité mécanique pourrait activer la transition finale $Y \rightarrow O$ comme montré sur la Fig. A.15e pour $\beta = \alpha$. Cependant, aucune signature d'instabilité mécanique n'a été identifiée pour la transition $U \rightarrow Y$, qui pourrait reposer sur un décalage enzymatique des tensions apicale ou basale.

²Cette situation est spécifique à la configuration Y . Pour la configuration U , la contrainte sur l'extension latérale disparaît et les contraintes d'incompressibilité ne peuvent plus être inversées. Il faut alors utiliser l'optimisation sous contrainte pour étudier, fonction du signe des déterminants des mineurs principaux de la matrice hessienne ("bordered").

Bibliography

- [1] D'Arcy Thompson. *On Growth and Form*. Cambridge University Press, Cambridge, first edition, 1917.
- [2] E. Schrödinger. *What is Life? The Physical Aspect of the Living Cell*. Cambridge University Press, first edition, 1944.
- [3] A. Yeung and E. Evans. Cortical shell-liquid core model for passive flow of liquid-like spherical cells into micropipets. *Biophysical Journal*, 56(1), 1989.
- [4] T. Frisch and O. Thoumine. Predicting the kinetics of cell spreading. *Journal of Biomechanics*, 35(8), 2002.
- [5] C.S. Peskin, G.M. Odell, and G.F. Oster. Cellular motions and thermal fluctuations: the Brownian ratchet. *Biophysical Journal*, 65(1), 1993.
- [6] J. A. Theriot. The Polymerization Motor. *Traffic*, 1(1), 2000.
- [7] A. Mogilner. On the edge: modeling protrusion. *Current Opinion in Cell Biology*, 18(1), 2006.
- [8] V. Noireaux, R.M. Golsteyn, E. Friederich, J. Prost, C. Antony, D. Louvard, and C. Sykes. Growing an Actin Gel on Spherical Surfaces. *Biophysical Journal*, 78(3), 2000.
- [9] T. P. Loisel, R. Boujemaa, D. Pantaloni, and M.-F. Carrier. Reconstitution of actin-based motility of *Listeria* and *Shigella* using pure proteins. *Nature*, 401(6753), 1999.
- [10] T. D. Pollard. Theory from the Oster Laboratory Leaps Ahead of Experiment in Understanding Actin-Based Cellular Motility. *Biophysical Journal*, 111(8), 2016.
- [11] A. E. Carlsson. Growth Velocities of Branched Actin Networks. *Biophysical Journal*, 84(5), 2003.
- [12] D. R. Kovar and T. D. Pollard. Insertional assembly of actin filament barbed ends in association with formins produces piconewton forces. *Proceedings of the National Academy of Sciences*, 101(41), 2004.
- [13] R. B. Dickinson, L. Caro, and D. L. Purich. Force Generation by Cytoskeletal Filament End-Tracking Proteins. *Biophysical Journal*, 87(4), 2004.
- [14] M. K. Driscoll, E. S. Welf, A. R. Jamieson, K. M. Dean, T. Isogai, R. Fiolka, and G. Danuser. Robust and automated detection of subcellular morphological motifs in 3D microscopy images. *Nature Methods*, 16(10), 2019.
- [15] J. Sedzinski, M. Biro, A. Oswald, J.-Y. Tinevez, G. Salbreux, and E. Paluch. Polar actomyosin contractility destabilizes the position of the cytokinetic furrow. *Nature*, 476(7361), 2011.
- [16] C. P. Caridi, M. Plessner, R. Grosse, and I. Chiolo. Nuclear actin filaments in DNA repair dynamics. *Nature Cell Biology*, 21(9), 2019.
- [17] B. Alberts, A. Johnson, J. Lewis, D. Morgan, M. Raff, K. Roberts, and P. Walter. *Molecular Biology of the Cell*. Garland Science, sixth edition, 2014.

- [18] B. L. Goode, J. A. Eskin, and B. Wendland. Actin and Endocytosis in Budding Yeast. *Genetics*, 199(2), 2015.
- [19] G. Salbreux, G. Charras, and E. Paluch. Actin cortex mechanics and cellular morphogenesis. *Trends in Cell Biology*, 22(10), 2012.
- [20] P. Chugh and E. K. Paluch. The actin cortex at a glance. *Journal of Cell Science*, 131(14), 2018.
- [21] M. Kelkar, P. Bohec, and G. Charras. Mechanics of the cellular actin cortex: From signalling to shape change. *Current Opinion in Cell Biology*, 66, 2020.
- [22] A. G. Clark, K. Dierkes, and E. K. Paluch. Monitoring Actin Cortex Thickness in Live Cells. *Biophysical Journal*, 105(3), 2013.
- [23] E. Evans and A. Yeung. Apparent viscosity and cortical tension of blood granulocytes determined by micropipet aspiration. *Biophysical Journal*, 56(1), 1989.
- [24] T. M. Svitkina. Actin Cell Cortex: Structure and Molecular Organization. *Trends in Cell Biology*, 30(7), 2020.
- [25] M. Fritzsche, A. Lewalle, T. Duke, K. Kruse, and G. Charras. Analysis of turnover dynamics of the submembranous actin cortex. *Molecular Biology of the Cell*, 24(6), 2013.
- [26] M. Bovellan, Y. Romeo, M. Biro, A. Boden, P. Chugh, A. Yonis, M. Vaghela, M. Fritzsche, D. Moulding, R. Thorogate, A. Jégou, A. J. Thrasher, G. Romet-Lemonne, P. P. Roux, E. K. Paluch, and G. Charras. Cellular Control of Cortical Actin Nucleation. *Current Biology*, 24(14), 2014.
- [27] N. Morone, T. Fujiwara, K. Murase, R. S. Kasai, H. Ike, S. Yuasa, J. Usukura, and A. Kusumi. Three-dimensional reconstruction of the membrane skeleton at the plasma membrane interface by electron tomography. *The Journal of Cell Biology*, 174(6), 2006.
- [28] S. Suetsugu. Activation of nucleation promoting factors for directional actin filament elongation: Allosteric regulation and multimerization on the membrane. *Seminars in Cell & Developmental Biology*, 24(4), 2013.
- [29] A. Ponti, M. Machacek, S. L. Gupton, C. M. Waterman-Storer, and G. Danuser. Two Distinct Actin Networks Drive the Protrusion of Migrating Cells. *Science*, 305(5691), 2004.
- [30] J. R. Glenney and P. Glenney. Fodrin is the general spectrin-like protein found in most cells whereas spectrin and the TW protein have a restricted distribution. *Cell*, 34(2), 1983.
- [31] G. Wiche. Role of plectin in cytoskeleton organization and dynamics. *Journal of Cell Science*, 111(17), 1998.
- [32] M. Mayer, M. Depken, J. S. Bois, F. Jülicher, and S. W. Grill. Anisotropies in cortical tension reveal the physical basis of polarizing cortical flows. *Nature*, 467(7315), 2010.
- [33] M. Kapustina, T. C. Elston, and K. Jacobson. Compression and dilation of the membrane-cortex layer generates rapid changes in cell shape. *The Journal of Cell Biology*, 200(1), 2013.
- [34] J.-Y. Tinevez, U. Schulze, G. Salbreux, J. Roensch, J.-F. Joanny, and E. Paluch. Role of cortical tension in bleb growth. *Proceedings of the National Academy of Sciences*, 106(44), 2009.
- [35] P. Chugh, A. G. Clark, M. B. Smith, D. A. D. Cassani, K. Dierkes, A. Ragab, P. P. Roux, G. Charras, G. Salbreux, and E. K. Paluch. Actin cortex architecture regulates cell surface tension. *Nature Cell Biology*, 19(6), 2017.

- [36] J. Dai and M. P. Sheetz. Membrane Tether Formation from Blebbing Cells. *Biophysical Journal*, 77(6), 1999.
- [37] P. Sens and J. Plastino. Membrane tension and cytoskeleton organization in cell motility. *Journal of Physics: Condensed Matter*, 27(27), 2015.
- [38] J. Dai, H. P. Ting-Beall, R. M. Hochmuth, M. P. Sheetz, and M. A. Titus. Myosin I Contributes to the Generation of Resting Cortical Tension. *Biophysical Journal*, 77(2), 1999.
- [39] M. Fritzsche, D. Li, H. Colin-York, V. T. Chang, E. Moeendarbary, J. H. Felce, E. Sezgin, G. Charras, E. Betzig, and C. Eggeling. Self-organizing actin patterns shape membrane architecture but not cell mechanics. *Nature Communications*, 8(1), 2017.
- [40] R. Nambiar, R. E. McConnell, and M. J. Tyska. Control of cell membrane tension by myosin-I. *Proceedings of the National Academy of Sciences*, 106(29), 2009.
- [41] B. Rouven Brückner, A. Pietuch, S. Nehls, J. Rother, and A. Janshoff. Ezrin is a Major Regulator of Membrane Tension in Epithelial Cells. *Scientific Reports*, 5(1), 2015.
- [42] F. Eghiaian, A. Rigato, and S. Scheuring. Structural, Mechanical, and Dynamical Variability of the Actin Cortex in Living Cells. *Biophysical Journal*, 108(6), 2015.
- [43] M. Fritzsche, C. Erlenkämper, E. Moeendarbary, G. Charras, and K. Kruse. Actin kinetics shapes cortical network structure and mechanics. *Science Advances*, 2(4), 2016.
- [44] S. Sadegh, J. L. Higgins, P. C. Mannion, M. M. Tamkun, and D. Krapf. Plasma Membrane is Compartmentalized by a Self-Similar Cortical Actin Meshwork. *Physical Review X*, 7(1), 2017.
- [45] O. Chaudhuri, S. H. Parekh, and D. A. Fletcher. Reversible stress softening of actin networks. *Nature*, 445(7125), 2007.
- [46] D. Humphrey, C. Duggan, D. Saha, D. Smith, and J. Käs. Active fluidization of polymer networks through molecular motors. *Nature*, 416(6879), 2002.
- [47] G. H. Koenderink, Z. Dogic, F. Nakamura, P. M. Bendix, F. C. MacKintosh, J. H. Hartwig, T. P. Stossel, and D. A. Weitz. An active biopolymer network controlled by molecular motors. *Proceedings of the National Academy of Sciences*, 106(36), 2009.
- [48] Y. Tseng, K. M. An, O. Esue, and D. Wirtz. The Bimodal Role of Filamin in Controlling the Architecture and Mechanics of F-actin Networks. *The Journal of Biological Chemistry*, 279(3), 2004.
- [49] M. L. Gardel, F. Nakamura, J. H. Hartwig, J. C. Crocker, T. P. Stossel, and D. A. Weitz. Prestressed F-actin networks cross-linked by hinged filamins replicate mechanical properties of cells. *Proceedings of the National Academy of Sciences*, 103(6), 2006.
- [50] P. M. Bendix, G. H. Koenderink, D. Cuvelier, Z. Dogic, B. N. Koeleman, W. M. Briehner, C. M. Field, L. Mahadevan, and D. A. Weitz. A Quantitative Analysis of Contractility in Active Cytoskeletal Protein Networks. *Biophysical Journal*, 94(8), 2008.
- [51] A. P. Liu, D. L. Richmond, L. Maibaum, S. Pronk, P. L. Geissler, and D. A. Fletcher. Membrane-induced bundling of actin filaments. *Nature Physics*, 4(10), 2008.
- [52] K. Carvalho, J. Lemièrre, F. Faqir, J. Manzi, L. Blanchoin, J. Plastino, T. Betz, and C. Sykes. Actin polymerization or myosin contraction: two ways to build up cortical tension for symmetry breaking. *Philosophical Transactions of the Royal Society B: Biological Sciences*, 368(1629), 2013.

- [53] K. Dürre, F. C. Keber, P. Bleicher, F. Brauns, C. J. Cyron, J. Faix, and A. R. Bausch. Capping protein-controlled actin polymerization shapes lipid membranes. *Nature Communications*, 9(1), 2018.
- [54] E. Abu Shah and K. Keren. Symmetry breaking in reconstituted actin cortices. *eLife*, 3, 2014.
- [55] E. Fischer-Friedrich, Y. Toyoda, C. J. Cattin, D. J. Müller, A. A. Hyman, and F. Jülicher. Rheology of the Active Cell Cortex in Mitosis. *Biophysical Journal*, 111(3), 2016.
- [56] Y. Ideses, V. Erukhimovitch, R. Brand, D. Jourdain, J. Salmeron Hernandez, U. R. Gabinet, S. A. Safran, K. Kruse, and A. Bernheim-Groswasser. Spontaneous buckling of contractile poroelastic actomyosin sheets. *Nature Communications*, 9(1), 2018.
- [57] G. Salbreux, J. Prost, and J.-F. Joanny. Hydrodynamics of Cellular Cortical Flows and the Formation of Contractile Rings. *Physical Review Letters*, 103(5), 2009.
- [58] H. Turlier, B. Audoly, J. Prost, and J.-F. Joanny. Furrow Constriction in Animal Cell Cytokinesis. *Biophysical Journal*, 106(1), 2014.
- [59] A. Mietke, F. Jülicher, and I. F. Sbalzarini. Self-organized shape dynamics of active surfaces. *Proceedings of the National Academy of Sciences*, 116(1), 2019.
- [60] M. Fošnarič, S. Penič, A. Iglič, V. Kralj-Iglič, M. Drab, and N. S. Gov. Theoretical study of vesicle shapes driven by coupling curved proteins and active cytoskeletal forces. *Soft Matter*, 15(26), 2019.
- [61] J. Prost, F. Jülicher, and J.-F. Joanny. Active gel physics. *Nature Physics*, 11(2), 2015.
- [62] H. Berthoumieux, J.-L. Maître, C.-P. Heisenberg, E. K. Paluch, F. Jülicher, and G. Salbreux. Active elastic thin shell theory for cellular deformations. *New Journal of Physics*, 16(6), 2014.
- [63] N. Levernier and K. Kruse. Spontaneous formation of chaotic protrusions in a polymerizing active gel layer. *New Journal of Physics*, 22(1), 2020.
- [64] T. E. Schaus, E. W. Taylor, and G. G. Borisy. Self-organization of actin filament orientation in the dendritic-nucleation/array-treadmilling model. *Proceedings of the National Academy of Sciences*, 104(17), 2007.
- [65] W. M. McFadden, P. M. McCall, M. L. Gardel, and E. M. Munro. Filament turnover tunes both force generation and dissipation to control long-range flows in a model actomyosin cortex. *PLOS Computational Biology*, 13(12), 2017.
- [66] A. G. Clark and E. Paluch. Mechanics and Regulation of Cell Shape During the Cell Cycle. In Jacek Z. Kubiak, editor, *Cell Cycle in Development*, Results and Problems in Cell Differentiation. Springer, Berlin, Heidelberg, 2011.
- [67] S. Carreno, I. Kouranti, E. S. Glusman, M. T. Fuller, A. Echard, and F. Payre. Moesin and its activating kinase Slik are required for cortical stability and microtubule organization in mitotic cells. *The Journal of Cell Biology*, 180(4), 2008.
- [68] A. C. Taylor. Attachment and spreading of cells in culture. *Experimental Cell Research*, 8, 1961.
- [69] S. B. Carter. Haptotaxis and the Mechanism of Cell Motility. *Nature*, 213(5073), 1967.
- [70] K. Lam Hui, C. Wang, B. Grooman, J. Wayt, and A. Upadhyaya. Membrane Dynamics Correlate with Formation of Signaling Clusters during Cell Spreading. *Biophysical Journal*, 102(7), 2012.
- [71] J. A. Witkowski and W. D. Brighton. Stages of spreading of human diploid cells on glass surfaces. *Experimental Cell Research*, 68(2), 1971.

- [72] B. J. Dubin-Thaler, J. M. Hofman, Y. Cai, H. Xenias, I. Spielman, A. V. Shneidman, L. A. David, H.-G. Döbereiner, C. H. Wiggins, and M. P. Sheetz. Quantification of Cell Edge Velocities and Traction Forces Reveals Distinct Motility Modules during Cell Spreading. *PLOS ONE*, 3(11), 2008.
- [73] C. A. Erickson and J. P. Trinkaus. Microvilli and blebs as sources of reserve surface membrane during cell spreading. *Experimental Cell Research*, 99(2), 1976.
- [74] D. Raucher and M. P. Sheetz. Characteristics of a Membrane Reservoir Buffering Membrane Tension. *Biophysical Journal*, 77(4), 1999.
- [75] N. C. Gauthier, M. A. Fardin, P. Roca-Cusachs, and M. P. Sheetz. Temporary increase in plasma membrane tension coordinates the activation of exocytosis and contraction during cell spreading. *Proceedings of the National Academy of Sciences*, 108(35), 2011.
- [76] A. D. Lieber, S. Yehudai-Resheff, E. L. Barnhart, J. A. Theriot, and K. Keren. Membrane Tension in Rapidly Moving Cells Is Determined by Cytoskeletal Forces. *Current Biology*, 23(15), 2013.
- [77] C.E. Morris and U. Homann. Cell Surface Area Regulation and Membrane Tension. *The Journal of Membrane Biology*, 179(2), 2001.
- [78] A. J. Kosmalska, L. Casares, A. Elosegui-Artola, J. J. Thottacherry, R. Moreno-Vicente, V. González-Tarragó, M. Á. del Pozo, S. Mayor, M. Arroyo, D. Navajas, X. Trepát, N. C. Gauthier, and P. Roca-Cusachs. Physical principles of membrane remodelling during cell mechanoadaptation. *Nature Communications*, 6(1), 2015.
- [79] D. Cuvelier, M. Théry, Y.-S. Chu, S. Dufour, J.-P. Thiéry, M. Bornens, P. Nassoy, and L. Mahadevan. The Universal Dynamics of Cell Spreading. *Current Biology*, 17(8), 2007.
- [80] B. J. Dubin-Thaler, G. Giannone, H.-G. Döbereiner, and M. P. Sheetz. Nanometer Analysis of Cell Spreading on Matrix-Coated Surfaces Reveals Two Distinct Cell States and STEPs. *Biophysical Journal*, 86(3), 2004.
- [81] G. Giannone, B. J. Dubin-Thaler, H.-G. Döbereiner, N. Kieffer, A. R. Bresnick, and M. P. Sheetz. Periodic Lamellipodial Contractions Correlate with Rearward Actin Waves. *Cell*, 116(3), 2004.
- [82] P. T. Yam, C. A. Wilson, L. Ji, B. Hebert, E. L. Barnhart, N. A. Dye, P. W. Wiseman, G. Danuser, and J. A. Theriot. Actin–myosin network reorganization breaks symmetry at the cell rear to spontaneously initiate polarized cell motility. *The Journal of Cell Biology*, 178(7), 2007.
- [83] B. Geiger, J. P. Spatz, and A. D. Bershadsky. Environmental sensing through focal adhesions. *Nature Reviews Molecular Cell Biology*, 10(1), 2009.
- [84] P. W. Oakes and M. L. Gardel. Stressing the limits of focal adhesion mechanosensitivity. *Current Opinion in Cell Biology*, 30, 2014.
- [85] F. Chamaroux, S. Fache, F. Bruckert, and B. Fourcade. Kinetics of Cell Spreading. *Physical Review Letters*, 94(15), 2005.
- [86] M. A. Fardin, O. M. Rossier, P. Rangamani, P. D. Avigan, N. C. Gauthier, W. Vonnegut, A. Mathur, J. Hone, R. Iyengar, and M. P. Sheetz. Cell spreading as a hydrodynamic process. *Soft Matter*, 6(19), 2010.
- [87] A. B. Verkhovskiy, T. M. Svitkina, and G. G. Borisy. Self-polarization and directional motility of cytoplasm. *Current Biology*, 9(1), 1999.
- [88] N. Ofer, A. Mogilner, and K. Keren. Actin disassembly clock determines shape and speed of lamellipodial fragments. *Proceedings of the National Academy of Sciences*, 108(51), 2011.

- [89] M. M. Kozlov and A. Mogilner. Model of Polarization and Bistability of Cell Fragments. *Biophysical Journal*, 93(11), 2007.
- [90] L. P. Cramer. Forming the cell rear first: breaking cell symmetry to trigger directed cell migration. *Nature Cell Biology*, 12(7), 2010.
- [91] K. Hennig, I. Wang, P. Moreau, L. Valon, S. DeBeco, M. Coppey, Y. A. Miroshnikova, C. Albiges-Rizo, C. Favard, R. Voituriez, and M. Balland. Stick-slip dynamics of cell adhesion triggers spontaneous symmetry breaking and directional migration of mesenchymal cells on one-dimensional lines. *Science Advances*, 6(1), 2020.
- [92] C. Brangwynne, S. Huang, K. K. Parker, and D. E. Ingber. Symmetry breaking in cultured mammalian cells. *In Vitro Cellular & Developmental Biology-Animal*, 36(9), 2000.
- [93] G. Maheshwari, G. Brown, D. A. Lauffenburger, A. Wells, and L. G. Griffith. Cell adhesion and motility depend on nanoscale RGD clustering. *Journal of Cell Science*, 113(10), 2000.
- [94] J. Bereiter-Hahn, M. Luck, T. Miebach, H. K. Stelzer, and M. Voth. Spreading of trypsinized cells: cytoskeletal dynamics and energy requirements. *Journal of Cell Science*, 96(1), 1990.
- [95] J. Étienne and A. Duperray. Initial Dynamics of Cell Spreading Are Governed by Dissipation in the Actin Cortex. *Biophysical Journal*, 101(3), 2011.
- [96] D. J. Mooney, R. Langer, and D. E. Ingber. Cytoskeletal filament assembly and the control of cell spreading and function by extracellular matrix. *Journal of Cell Science*, 108(6), 1995.
- [97] Y. Cai, N. Biais, G. Giannone, M. Tanase, G. Jiang, J. M. Hofman, C. H. Wiggins, P. Silberzan, A. Buguin, B. Ladoux, and M. P. Sheetz. Nonmuscle Myosin IIA-Dependent Force Inhibits Cell Spreading and Drives F-Actin Flow. *Biophysical Journal*, 91(10), 2006.
- [98] E. E. Bragina, Ju. M. Vasiliev, and I. M. Gelfand. Formation of bundles of microfilaments during spreading of fibroblasts on the substrate. *Experimental Cell Research*, 97(2), 1976.
- [99] C. Yang, L. Czech, S. Gerboth, S. Kojima, G. Scita, and T. Svitkina. Novel Roles of Formin mDia2 in Lamellipodia and Filopodia Formation in Motile Cells. *PLOS Biology*, 5(11), 2007.
- [100] E. Atilgan, D. Wirtz, and S. X. Sun. Morphology of the Lamellipodium and Organization of Actin Filaments at the Leading Edge of Crawling Cells. *Biophysical Journal*, 89(5), 2005.
- [101] U. S. Schwarz and M. L. Gardel. United we stand – integrating the actin cytoskeleton and cell–matrix adhesions in cellular mechanotransduction. *Journal of Cell Science*, 125(13), 2012.
- [102] L. B. Case and C. M. Waterman. Integration of actin dynamics and cell adhesion by a three-dimensional, mechanosensitive molecular clutch. *Nature Cell Biology*, 17(8), 2015.
- [103] D. Raucher and M. P. Sheetz. Cell Spreading and Lamellipodial Extension Rate Is Regulated by Membrane Tension. *The Journal of Cell Biology*, 148(1), 2000.
- [104] B. Sabass and U. S. Schwarz. Modeling cytoskeletal flow over adhesion sites: competition between stochastic bond dynamics and intracellular relaxation. *Journal of Physics: Condensed Matter*, 22(19), 2010.
- [105] P. Dillard, R. Varma, K. Sengupta, and L. Limozin. Ligand-Mediated Friction Determines Morphodynamics of Spreading T Cells. *Biophysical Journal*, 107(11), 2014.
- [106] M. L. Gardel, B. Sabass, L. Ji, G. Danuser, U. S. Schwarz, and C. M. Waterman. Traction stress in focal adhesions correlates biphasically with actin retrograde flow speed. *The Journal of Cell Biology*, 183(6), 2008.

- [107] C. E. Chan and D. J. Odde. Traction Dynamics of Filopodia on Compliant Substrates. *Science*, 322(5908), 2008.
- [108] A. del Rio, R. Perez-Jimenez, R. Liu, P. Roca-Cusachs, J. M. Fernandez, and M. P. Sheetz. Stretching Single Talin Rod Molecules Activates Vinculin Binding. *Science*, 323(5914), 2009.
- [109] G. Jiang, G. Giannone, D. R. Critchley, E. Fukumoto, and M. P. Sheetz. Two-piconewton slip bond between fibronectin and the cytoskeleton depends on talin. *Nature*, 424(6946), 2003.
- [110] V. Swaminathan, R. S. Fischer, and C. M. Waterman. The FAK–Arp2/3 interaction promotes leading edge advance and haptosensing by coupling nascent adhesions to lamellipodia actin. *Molecular Biology of the Cell*, 27(7), 2016.
- [111] N. Q. Balaban, U. S. Schwarz, D. Riveline, P. Goichberg, G. Tzur, I. Sabanay, D. Mahalu, S. Safran, A. Bershadsky, L. Addadi, and B. Geiger. Force and focal adhesion assembly: a close relationship studied using elastic micropatterned substrates. *Nature Cell Biology*, 3(5), 2001.
- [112] W. R. Legant, C. K. Choi, J. S. Miller, L. Shao, L. Gao, E. Betzig, and C. S. Chen. Multidimensional traction force microscopy reveals out-of-plane rotational moments about focal adhesions. *Proceedings of the National Academy of Sciences*, 110(3), 2013.
- [113] M. Sheetz. MBIInfo | Defining Mechanobiology, 2020. web: www.mechanobio.info.
- [114] C. Ciobanasu, B. Faivre, and C. Le Clainche. Actin Dynamics Associated with Focal Adhesions. *International Journal of Cell Biology*, 2012.
- [115] E. Urban, S. Jacob, M. Nemethova, G. P. Resch, and J. V. Small. Electron tomography reveals unbranched networks of actin filaments in lamellipodia. *Nature Cell Biology*, 12(5), 2010.
- [116] C. Schmeiser and C. Winkler. The flatness of Lamellipodia explained by the interaction between actin dynamics and membrane deformation. *Journal of Theoretical Biology*, 380, 2015.
- [117] H. Boukellal, O. Campás, J.-F. Joanny, J. Prost, and C. Sykes. Soft Listeria: Actin-based propulsion of liquid drops. *Physical Review E*, 69(6), 2004.
- [118] K. K. Parker, A. L. Brock, C. Brangwynne, R. J. Mannix, N. Wang, E. Ostuni, N. A. Geisse, J. C. Adams, G. M. Whitesides, and D. E. Ingber. Directional control of lamellipodia extension by constraining cell shape and orienting cell tractional forces. *The FASEB Journal*, 16(10), 2002.
- [119] S. Bohnet, R. Ananthakrishnan, A. Mogilner, J.-J. Meister, and A. B. Verkhovsky. Weak Force Stalls Protrusion at the Leading Edge of the Lamellipodium. *Biophysical Journal*, 90(5), 2006.
- [120] J. Mueller, G. Szep, M. Nemethova, I. de Vries, A. D. Lieber, C. Winkler, K. Kruse, J. V. Small, C. Schmeiser, K. Keren, R. Hauschild, and M. Sixt. Load Adaptation of Lamellipodial Actin Networks. *Cell*, 171(1), 2017.
- [121] P. W. Oakes, T. C. Bidone, Y. Beckham, A. V. Skeeters, G. R. Ramirez-San Juan, S. P. Winter, G. A. Voth, and M. L. Gardel. Lamellipodium is a myosin-independent mechanosensor. *Proceedings of the National Academy of Sciences*, 115(11), 2018.
- [122] L. M. Machesky and R. H. Insall. Signaling to Actin Dynamics. *The Journal of Cell Biology*, 146(2), 1999.
- [123] C. Le Clainche and M.-F. Carrier. Regulation of Actin Assembly Associated With Protrusion and Adhesion in Cell Migration. *Physiological Reviews*, 88(2), 2008.
- [124] L. G. Tilney, D. J. DeRosier, A. Weber, and M. S. Tilney. How Listeria exploits host cell actin to form its own cytoskeleton. II. Nucleation, actin filament polarity, filament assembly, and evidence for a pointed end capper. *The Journal of Cell Biology*, 118(1), 1992.

- [125] F. Julicher, K. Kruse, J. Prost, and J.-F. Joanny. Active behavior of the Cytoskeleton. *Physics Reports*, 449(1-3), 2007.
- [126] P. G. de Gennes and J. Prost. *The Physics of Liquid Crystals (2nd edition)*. Oxford science publication edition, 1995.
- [127] G. Napoli and L. Vergori. Surface free energies for nematic shells. *Physical Review E*, 85(6), 2012.
- [128] P. G. de Gennes. Wetting: statics and dynamics. *Reviews of Modern Physics*, 57(3), 1985.
- [129] W. Helfrich. Elastic properties of lipid bilayers: theory and possible experiments. *Z Naturforsch C*, 28(11), 1973.
- [130] B. Sinha, D. Köster, R. Ruez, P. Gonnord, M. Bastiani, D. Abankwa, R. V. Stan, G. Butler-Browne, B. Védie, L. Johannes, N. Morone, R. G. Parton, G. Raposo, P. Sens, C. Lamaze, and P. Nassoy. Cells Respond to Mechanical Stress by Rapid Disassembly of Caveolae. *Cell*, 144(3), 2011.
- [131] G. Salbreux, J.-F. Joanny, J. Prost, and P. Pullarkat. Shape oscillations of non-adhering fibroblast cells. *Physical Biology*, 4(4), 2007.
- [132] J. Tao and S. X. Sun. Active Biochemical Regulation of Cell Volume and a Simple Model of Cell Tension Response. *Biophysical Journal*, 109(8), 2015.
- [133] E. Sackmann and R. F. Bruinsma. Cell Adhesion as Wetting Transition? *ChemPhysChem*, 3(3), 2002.
- [134] A.-S. Smith and U. Seifert. Effective adhesion strength of specifically bound vesicles. *Physical Review E*, 71(6), 2005.
- [135] M. Guo, A. F. Pegoraro, A. Mao, E. H. Zhou, P. R. Arany, Y. Han, D. T. Burnette, M. H. Jensen, K. E. Kasza, J. R. Moore, F. C. Mackintosh, J. J. Fredberg, D. J. Mooney, J. Lippincott-Schwartz, and D. A. Weitz. Cell volume change through water efflux impacts cell stiffness and stem cell fate. *Proceedings of the National Academy of Sciences*, 114(41), 2017.
- [136] K. Xie, Y. Yang, and H. Jiang. Controlling Cellular Volume via Mechanical and Physical Properties of Substrate. *Biophysical Journal*, 114(3), 2018.
- [137] U. Seifert and R. Lipowsky. Adhesion of vesicles. *Physical Review A*, 42(8), 1990.
- [138] R. Lipowsky and U. Seifert. Adhesion of membranes: a theoretical perspective. *Langmuir*, 7(9), 1991.
- [139] U. Seifert. Adhesion of vesicles in two dimensions. *Physical Review A*, 43(12), 1991.
- [140] C. A. Reinhart-King, M. Dembo, and D. A. Hammer. The Dynamics and Mechanics of Endothelial Cell Spreading. *Biophysical Journal*, 89(1), 2005.
- [141] X. Zhang, G. Jiang, Y. Cai, S. J. Monkley, D. R. Critchley, and M. P. Sheetz. Talin depletion reveals independence of initial cell spreading from integrin activation and traction. *Nature Cell Biology*, 10(9), 2008.
- [142] P. Sens. Rigidity sensing by stochastic sliding friction. *EPL (Europhysics Letters)*, 104(3), 2013.
- [143] Y. Li, D. Lovett, Q. Zhang, S. Neelam, R. A. Kuchibhotla, R. Zhu, G. G. Gundersen, T. P. Lele, and R. B. Dickinson. Moving Cell Boundaries Drive Nuclear Shaping during Cell Spreading. *Biophysical Journal*, 109(4), 2015.
- [144] D.V. Zhelev, D. Needham, and R.M. Hochmuth. A novel micropipet method for measuring the bending modulus of vesicle membranes. *Biophysical Journal*, 67(2), 1994.

- [145] R. Simson, E. Wallraff, J. Faix, J. Niewöhner, G. Gerisch, and E. Sackmann. Membrane Bending Modulus and Adhesion Energy of Wild-Type and Mutant Cells of Dictyostelium Lacking Talin or Cortexillins. *Biophysical Journal*, 74(1), 1998.
- [146] M. Bouaouina, Y. Lad, and D. A. Calderwood. The N-terminal Domains of Talin Cooperate with the Phosphotyrosine Binding-like Domain to Activate beta1 and beta3 Integrins *. *Journal of Biological Chemistry*, 283(10), 2008.
- [147] C. K. Choi, M. Vicente-Manzanares, J. Zareno, L. A. Whitmore, A. Mogilner, and A. R. Horwitz. Actin and a-actinin orchestrate the assembly and maturation of nascent adhesions in a myosin II motor-independent manner. *Nature Cell Biology*, 10(9), 2008.
- [148] Y. Xiong, P. Rangamani, M.-A. Fardin, A. Lipshtat, B. Dubin-Thaler, O. Rossier, M. P. Sheetz, and R. Iyengar. Mechanisms Controlling Cell Size and Shape during Isotropic Cell Spreading. *Biophysical Journal*, 98(10), 2010.
- [149] A. Hall. Rho GTPases and the Actin Cytoskeleton. *Science*, 279(5350), 1998.
- [150] A. Steffen, M. Ladwein, G. A. Dimchev, A. Hein, L. Schwenkmezger, S. Arens, K. I. Ladwein, J. M. Holleboom, F. Schur, J. V. Small, J. Schwarz, R. Gerhard, J. Faix, T. E. B. Stradal, C. Brakebusch, and K. Rottner. Rac function is crucial for cell migration but is not required for spreading and focal adhesion formation. *Journal of Cell Science*, 126(20), 2013.
- [151] K. Rottner, A. Hall, and J. V. Small. Interplay between Rac and Rho in the control of substrate contact dynamics. *Current Biology*, 9(12), 1999.
- [152] M. R. Mejillano, S. Kojima, D. A. Applewhite, F. B. Gertler, T. M. Svitkina, and G. G. Borisy. Lamellipodial Versus Filopodial Mode of the Actin Nanomachinery: Pivotal Role of the Filament Barbed End. *Cell*, 118(3), 2004.
- [153] J. Renkawitz, K. Schumann, M. Weber, T. Lämmermann, H. Pflücke, M. Piel, J. Polleux, J. P. Spatz, and M. Sixt. Adaptive force transmission in amoeboid cell migration. *Nature Cell Biology*, 11(12), 2009.
- [154] K. A. DeMali, C. A. Barlow, and K. Burridge. Recruitment of the Arp2/3 complex to vinculin : coupling membrane protrusion to matrix adhesion. *The Journal of Cell Biology*, 159(5), 2002.
- [155] R. M. Ezzell, Wolfgang H. Goldmann, N. Wang, N. Parasharama, and Donald E. Ingber. Vinculin Promotes Cell Spreading by Mechanically Coupling Integrins to the Cytoskeleton. *Experimental Cell Research*, 231(1), 1997.
- [156] J. D. Humphries, P. Wang, C. Streuli, B. Geiger, M. J. Humphries, and C. Ballestrem. Vinculin controls focal adhesion formation by direct interactions with talin and actin. *The Journal of Cell Biology*, 179(5), 2007.
- [157] D. A. Potter, J. S. Tirnauer, R. Janssen, D. E. Croall, C. N. Hughes, K. A. Fiacco, J. W. Mier, M. Maki, and I. M. Herman. Calpain Regulates Actin Remodeling during Cell Spreading. *The Journal of Cell Biology*, 141(3), 1998.
- [158] O. M. Rossier, N. Gauthier, N. Biais, W. Vonnegut, M.-A. Fardin, P. Avigan, E. R. Heller, A. Mathur, S. Ghassemi, M. S. Koeckert, J. C. Hone, and M. P. Sheetz. Force generated by actomyosin contraction builds bridges between adhesive contacts. *The EMBO Journal*, 29(6), 2010.
- [159] M. Megias Pacheco, P. Molist Garcia, and M. A. Pombal Diego. Animal Tissues - Covering epithelium, 2020. web: mmegias.webs.uvigo.es.
- [160] Lu.qianhe. Cell junctions types shown on epithelial cells including cell-cell and cell-matrix junctions, 2020. web: commons.wikimedia.org.

- [161] D. Krndija, F. El Marjou, B. Guirao, S. Richon, O. Leroy, Y. Bellaiche, E. Hannezo, and D. M. Vignjevic. Active cell migration is critical for steady-state epithelial turnover in the gut. *Science*, 365(6454), 2019.
- [162] N. Harmand. *Pertinence et limites des tensions de surface et de ligne pour rendre compte des formes de cellules épithéliales*. PhD thesis, Université de Paris, Paris, 2019.
- [163] A. C. Martin, M. Kaschube, and E. F. Wieschaus. Pulsed contractions of an actin–myosin network drive apical constriction. *Nature*, 457(7228), 2009.
- [164] G. Walko, M. J. Castañón, and G. Wiche. Molecular architecture and function of the hemidesmosome. *Cell and Tissue Research*, 360(2), 2015.
- [165] S. Tlili, C. Gay, F. Graner, P. Marcq, F. Molino, and P. Saramito. Colloquium: Mechanical formalisms for tissue dynamics. *The European Physical Journal E*, 38(5), 2015.
- [166] R. Farhadifar, J.-C. Röper, B. Aigouy, S. Eaton, and F. Jülicher. The Influence of Cell Mechanics, Cell-Cell Interactions, and Proliferation on Epithelial Packing. *Current Biology*, 17(24), 2007.
- [167] S. Alt, P. Ganguly, and G. Salbreux. Vertex models: from cell mechanics to tissue morphogenesis. *Philosophical Transactions of the Royal Society B: Biological Sciences*, 372(1720), 2017.
- [168] E. Hannezo, J. Prost, and J.-F. Joanny. Theory of epithelial sheet morphology in three dimensions. *Proceedings of the National Academy of Sciences*, 111(1), 2014.
- [169] C. Bielmeier, S. Alt, V. Weichselberger, M. La Fortezza, H. Harz, F. Jülicher, G. Salbreux, and A.-K. Classen. Interface Contractility between Differently Fated Cells Drives Cell Elimination and Cyst Formation. *Current Biology*, 26(5), 2016.
- [170] H. A. Messal, S. Alt, R. M. M. Ferreira, C. Gribben, V. M.-Y. Wang, C. G. Cotoi, G. Salbreux, and A. Behrens. Tissue curvature and apicobasal mechanical tension imbalance instruct cancer morphogenesis. *Nature*, 566(7742), 2019.
- [171] O. Polyakov, B. He, M. Swan, J. W. Shaevitz, M. Kaschube, and E. Wieschaus. Passive Mechanical Forces Control Cell-Shape Change during Drosophila Ventral Furrow Formation. *Biophysical Journal*, 107(4), 2014.
- [172] M. Krajnc. *Mechanics of epithelial tissues*. PhD thesis, University of Ljubljana, Ljubljana, 2017.
- [173] G. Salbreux and F. Jülicher. Mechanics of active surfaces. *Physical Review E*, 96(3), 2017.
- [174] N. Murisic, V. Hakim, I. G. Kevrekidis, S. Y. Shvartsman, and B. Audoly. From Discrete to Continuum Models of Three-Dimensional Deformations in Epithelial Sheets. *Biophysical Journal*, 109(1), 2015.
- [175] X. Serra-Picamal, V. Conte, R. Vincent, E. Anon, D. T. Tambe, E. Bazellieres, J. P. Butler, J. J. Fredberg, and X. Trepat. Mechanical waves during tissue expansion. *Nature Physics*, 8(8), 2012.
- [176] G. Duclos, C. Blanch-Mercader, V. Yashunsky, G. Salbreux, J.-F. Joanny, J. Prost, and P. Silberzan. Spontaneous shear flow in confined cellular nematics. *Nature Physics*, 14(7), 2018.
- [177] C. Pérez-González, R. Alert, C. Blanch-Mercader, M. Gómez-González, T. Kolodziej, E. Bazellieres, J. Casademunt, and X. Trepat. Active wetting of epithelial tissues. *Nature Physics*, 15(1), 2019.
- [178] S. Yabunaka and P. Marcq. Emergence of epithelial cell density waves. *Soft Matter*, 13(39), 2017.

- [179] M. Basan, T. Risler, J.-F. Joanny, X. Sastre-Garau, and J. Prost. Homeostatic competition drives tumor growth and metastasis nucleation. *HFSP Journal*, 3(4), 2009.
- [180] E. Hannezo, J. Prost, and J.-F. Joanny. Instabilities of Monolayered Epithelia: Shape and Structure of Villi and Crypts. *Physical Review Letters*, 107(7), 2011.
- [181] D. Bi, J. H. Lopez, J. M. Schwarz, and M. L. Manning. A density-independent rigidity transition in biological tissues. *Nature Physics*, 11(12), 2015.
- [182] Y. Ishimoto and Y. Morishita. Bubbly vertex dynamics: A dynamical and geometrical model for epithelial tissues with curved cell shapes. *Physical Review E*, 90(5), 2014.
- [183] B. Li and Sean X. Sun. Coherent Motions in Confluent Cell Monolayer Sheets. *Biophysical Journal*, 107(7), 2014.
- [184] D. Bi, X. Yang, M. C. Marchetti, and M. L. Manning. Motility-Driven Glass and Jamming Transitions in Biological Tissues. *Physical Review X*, 6(2), 2016.
- [185] S. Henkes, Y. Fily, and M. C. Marchetti. Active jamming: Self-propelled soft particles at high density. *Physical Review E*, 84(4), 2011.
- [186] A. H. Brezavšek, M. Rauzi, M. Leptin, and P. Ziherl. A Model of Epithelial Invagination Driven by Collective Mechanics of Identical Cells. *Biophysical Journal*, 103(5), 2012.
- [187] F. Graner and D. Riveline. ‘The Forms of Tissues, or Cell-aggregates’: D’Arcy Thompson’s influence and its limits. *Development*, 144(23), 2017.
- [188] G. T. Eisenhoffer, P. D. Loftus, M. Yoshigi, H. Otsuna, C.-B. Chien, P. A. Morcos, and J. Rosenblatt. Crowding induces live cell extrusion to maintain homeostatic cell numbers in epithelia. *Nature*, 484(7395), 2012.
- [189] A. R. Harris, L. Peter, J. Bellis, B. Baum, A. J. Kabla, and G. T. Charras. Characterizing the mechanics of cultured cell monolayers. *Proceedings of the National Academy of Sciences*, 109(41), 2012.
- [190] J. Barbazan, C. Perez-Gonzalez, M. Gomez-Gonzalez, M. Dedenon, S. Richon, E. Latorre, M. Serra, P. Mariani, S. Descroix, P. Sens, X. Trepast, and D. Matic-Vignjevic. Cancer-associated fibroblasts actively compress cancer cells and modulate mechanotransduction. *bioRxiv*, 2021.
- [191] P. Friedl and K. Wolf. Tumour-cell invasion and migration: diversity and escape mechanisms. *Nature Reviews Cancer*, 3(5), 2003.
- [192] J. Sleeman and P. S. Steeg. Cancer metastasis as a therapeutic target. *European Journal of Cancer*, 46(7), 2010.
- [193] C. A. Klein. Parallel progression of primary tumours and metastases. *Nature Reviews Cancer*, 9(4), 2009.
- [194] K. R. Fischer, A. Durrans, S. Lee, J. Sheng, F. Li, S. T. C. Wong, H. Choi, T. El Rayes, S. Ryu, J. Troeger, R. F. Schwabe, L. T. Vahdat, N. K. Altorki, V. Mittal, and D. Gao. Epithelial-to-mesenchymal transition is not required for lung metastasis but contributes to chemoresistance. *Nature*, 527(7579), 2015.
- [195] X. Zheng, J. L. Carstens, J. Kim, M. Scheible, J. Kaye, H. Sugimoto, C.-C. Wu, V. S. LeBleu, and R. Kalluri. Epithelial-to-mesenchymal transition is dispensable for metastasis but induces chemoresistance in pancreatic cancer. *Nature*, 527(7579), 2015.
- [196] A. Glentis, P. Oertle, P. Mariani, A. Chikina, F. El Marjou, Y. Attieh, F. Zaccarini, M. Lae, D. Loew, F. Dingli, P. Sirven, M. Schoumacher, B. G. Gurchenkov, M. Plodinec, and D. M. Vignjevic. Cancer-associated fibroblasts induce metalloprotease-independent cancer cell invasion of the basement membrane. *Nature Communications*, 8(1), 2017.

- [197] V. Padmanaban, I. Krol, Y. Suhail, B. M. Szczerba, N. Aceto, J. S. Bader, and A. J. Ewald. E-cadherin is required for metastasis in multiple models of breast cancer. *Nature*, 573(7774), 2019.
- [198] J.-P. Thiery. Epithelial–mesenchymal transitions in tumour progression. *Nature Reviews Cancer*, 2(6), 2002.
- [199] M. Yu, A. Bardia, B. S. Wittner, S. L. Stott, M. E. Smas, D. T. Ting, S. J. Isakoff, J. C. Ciciliano, M. N. Wells, A. M. Shah, K. F. Concannon, M. C. Donaldson, L. V. Sequist, E. Brachtel, D. Sgroi, J. Baselga, S. Ramaswamy, M. Toner, D. A. Haber, and S. Maheswaran. Circulating Breast Tumor Cells Exhibit Dynamic Changes in Epithelial and Mesenchymal Composition. *Science*, 339(6119), 2013.
- [200] M. A. Nieto, R. Y.-J. Huang, R. A. Jackson, and J.-P. Thiery. EMT: 2016. *Cell*, 166(1), 2016.
- [201] M. Teeuwssen and R. Fodde. Cell Heterogeneity and Phenotypic Plasticity in Metastasis Formation: The Case of Colon Cancer. *Cancers*, 11(9), 2019.
- [202] A. T. Plygawko, S. Kan, and K. Campbell. Epithelial–mesenchymal plasticity: emerging parallels between tissue morphogenesis and cancer metastasis. *Philosophical Transactions of the Royal Society B: Biological Sciences*, 375(1809), 2020.
- [203] N. Aceto, A. Bardia, D. T. Miyamoto, M. C. Donaldson, B. S. Wittner, J. A. Spencer, M. Yu, A. Pely, A. Engstrom, H. Zhu, B. W. Brannigan, R. Kapur, S. L. Stott, T. Shioda, S. Ramaswamy, D. T. Ting, C. P. Lin, M. Toner, D. A. Haber, and S. Maheswaran. Circulating Tumor Cell Clusters Are Oligoclonal Precursors of Breast Cancer Metastasis. *Cell*, 158(5), 2014.
- [204] K. J. Cheung, V. Padmanaban, V. Silvestri, K. Schipper, J. D. Cohen, A. N. Fairchild, M. A. Gorin, J. E. Verdone, K. J. Pienta, J. S. Bader, and A. J. Ewald. Polyclonal breast cancer metastases arise from collective dissemination of keratin 14-expressing tumor cell clusters. *Proceedings of the National Academy of Sciences*, 113(7), 2016.
- [205] J. A. Galván, I. Zlobec, M. Wartenberg, A. Lugli, B. Gloor, A. Perren, and E. Karamitopoulou. Expression of E-cadherin repressors SNAIL, ZEB1 and ZEB2 by tumour and stromal cells influences tumour-budding phenotype and suggests heterogeneity of stromal cells in pancreatic cancer. *British Journal of Cancer*, 112(12), 2015.
- [206] D. G. Duda, A. M. M. J. Duyverman, M. Kohno, M. Snuderl, E. J. A. Steller, D. Fukumura, and R. K. Jain. Malignant cells facilitate lung metastasis by bringing their own soil. *Proceedings of the National Academy of Sciences*, 107(50), 2010.
- [207] F. R. Balkwill, M. Capasso, and T. Hagemann. The tumor microenvironment at a glance. *Journal of Cell Science*, 125(23), 2012.
- [208] J. Tommelein, L. Verset, T. Boterberg, P. Demetter, M. Bracke, and O. De Wever. Cancer-Associated Fibroblasts Connect Metastasis-Promoting Communication in Colorectal Cancer. *Frontiers in Oncology*, 5, 2015.
- [209] J. Barbazán and D. Matic Vignjevic. Cancer associated fibroblasts: is the force the path to the dark side? *Current Opinion in Cell Biology*, 56, 2019.
- [210] A. F. Olumi, G. D. Grossfeld, S. W. Hayward, P. R. Carroll, T. D. Tlsty, and G. R. Cunha. Carcinoma-associated Fibroblasts Direct Tumor Progression of Initiated Human Prostatic Epithelium. *Cancer Research*, 59(19), 1999.
- [211] B. Erdogan, M. Ao, L. M. White, A. L. Means, B. M. Brewer, L. Yang, M. K. Washington, C. Shi, O. E. Franco, A. M. Weaver, S. W. Hayward, D. Li, and D. J. Webb. Cancer-associated fibroblasts promote directional cancer cell migration by aligning fibronectin/CAFs direct cancer cell migration via fibronectin. *The Journal of Cell Biology*, 216(11), 2017.

- [212] Y. Attieh, A. G. Clark, C. Grass, S. Richon, M. Pocard, P. Mariani, N. Elkhatib, T. Betz, B. Gurchenkov, and D. M. Vignjevic. Cancer-associated fibroblasts lead tumor invasion through integrin-beta3-dependent fibronectin assembly. *The Journal of Cell Biology*, 216(11), 2017.
- [213] C. Gaggioli, S. Hooper, C. Hidalgo-Carcedo, R. Grosse, J. F. Marshall, K. Harrington, and E. Sahai. Fibroblast-led collective invasion of carcinoma cells with differing roles for RhoGTPases in leading and following cells. *Nature Cell Biology*, 9(12), 2007.
- [214] A. Labernadie, T. Kato, A. Brugués, X. Serra-Picamal, S. Derzsi, E. Arwert, A. Weston, V. González-Tarragó, A. Elosegui-Artola, L. Albertazzi, J. Alcaraz, P. Roca-Cusachs, E. Sahai, and X. Trepat. A mechanically active heterotypic E-cadherin/N-cadherin adhesion enables fibroblasts to drive cancer cell invasion. *Nature Cell Biology*, 19(3), 2017.
- [215] B. C. Özdemir, T. Pentcheva-Hoang, J. L. Carstens, X. Zheng, C.-C. Wu, T. R. Simpson, H. Laklai, H. Sugimoto, C. Kahlert, S. V. Novitskiy, A. De Jesus-Acosta, P. Sharma, P. Heidari, U. Mahmood, L. Chin, H. L. Moses, V. M. Weaver, A. Maitra, J. P. Allison, V. S. LeBleu, and R. Kalluri. Depletion of Carcinoma-Associated Fibroblasts and Fibrosis Induces Immunosuppression and Accelerates Pancreas Cancer with Reduced Survival. *Cancer Cell*, 25(6), 2014.
- [216] A. C. Rogers, D. C. Winter, A. Heeney, D. Gibbons, A. Lugli, G. Puppa, and K. Sheahan. Systematic review and meta-analysis of the impact of tumour budding in colorectal cancer. *British Journal of Cancer*, 115(7), 2016.
- [217] L. S. Lino-Silva, R. A. Salcedo-Hernández, and A. Gamboa-Domínguez. Tumour budding in rectal cancer. A comprehensive review. *Contemporary Oncology*, 22(2), 2018.
- [218] J. Ferlay, E. Steliarova-Foucher, J. Lortet-Tieulent, S. Rosso, J. W. W. Coebergh, H. Comber, D. Forman, and F. Bray. Cancer incidence and mortality patterns in Europe: Estimates for 40 countries in 2012. *European Journal of Cancer*, 49(6), 2013.
- [219] N. Erez, M. Truitt, P. Olson, and D. Hanahan. Cancer-Associated Fibroblasts Are Activated in Incipient Neoplasia to Orchestrate Tumor-Promoting Inflammation in an NF-kappaB-Dependent Manner. *Cancer Cell*, 17(2), 2010.
- [220] D. Vignjevic, M. Schoumacher, N. Gavert, K.-P. Janssen, G. Jih, M. Laé, D. Louvard, A. Ben-Ze'ev, and S. Robine. Fascin, a Novel Target of beta-Catenin-TCF Signaling, Is Expressed at the Invasive Front of Human Colon Cancer. *Cancer Research*, 67(14), 2007.
- [221] S. Begnaud, T. Chen, D. Delacour, R.-M. Mège, and B. Ladoux. Mechanics of epithelial tissues during gap closure. *Current Opinion in Cell Biology*, 42, 2016.
- [222] A. Brugués, E. Anon, V. Conte, J. H. Veldhuis, M. Gupta, J. Colombelli, J. J. Muñoz, G. W. Brodland, B. Ladoux, and X. Trepat. Forces driving epithelial wound healing. *Nature Physics*, 10(9), 2014.
- [223] M. S. Sakar, J. Eyckmans, R. Pieters, D. Eberli, B. J. Nelson, and C. S. Chen. Cellular forces and matrix assembly coordinate fibrous tissue repair. *Nature Communications*, 7(1), 2016.
- [224] E. Anon, X. Serra-Picamal, P. Hersen, N. C. Gauthier, M. P. Sheetz, X. Trepat, and B. Ladoux. Cell crawling mediates collective cell migration to close undamaged epithelial gaps. *Proceedings of the National Academy of Sciences*, 109(27), 2012.
- [225] O. Cochet-Escartin, J. Ranft, P. Silberzan, and P. Marcq. Border Forces and Friction Control Epithelial Closure Dynamics. *Biophysical Journal*, 106(1), 2014.
- [226] A. Ravasio, I. Cheddadi, T. Chen, T. Pereira, H. T. Ong, C. Bertocchi, A. Bragues, A. Jacinto, A. J. Kabla, Y. Toyama, X. Trepat, N. Gov, L. Neves de Almeida, and B. Ladoux. Gap geometry dictates epithelial closure efficiency. *Nature Communications*, 6(1), 2015.

- [227] J. H. Kim, X. Serra-Picamal, D. T. Tambe, E. H. Zhou, C. Y. Park, M. Sadati, J.-A. Park, R. Krishnan, B. Gweon, E. Millet, J. P. Butler, X. Trepata, and J. J. Fredberg. Propulsion and navigation within the advancing monolayer sheet. *Nature Materials*, 12(9), 2013.
- [228] V. Nier, M. Deforet, G. Duclos, H. G. Yevick, O. Cochet-Escartin, P. Marcq, and P. Silberzan. Tissue fusion over nonadhering surfaces. *Proceedings of the National Academy of Sciences*, 112(31), 2015.
- [229] S. R. K. Vedula, G. Peyret, I. Cheddadi, T. Chen, A. Brugués, H. Hirata, H. Lopez-Menendez, Y. Toyama, L. N. de Almeida, X. Trepata, C. T. Lim, and B. Ladoux. Mechanics of epithelial closure over non-adherent environments. *Nature Communications*, 6(1), 2015.
- [230] J. Rosenblatt, M. C. Raff, and L. P. Cramer. An epithelial cell destined for apoptosis signals its neighbors to extrude it by an actin- and myosin-dependent mechanism. *Current Biology*, 11(23), 2001.
- [231] L. Kocgozlu, T. B. Saw, A. P. Le, I. Yow, M. Shagirov, E. Wong, R.-M. Mège, C. T. Lim, Y. Toyama, and B. Ladoux. Epithelial Cell Packing Induces Distinct Modes of Cell Extrusions. *Current Biology*, 26(21), 2016.
- [232] X. Trepata, M. R. Wasserman, T. E. Angelini, E. Millet, D. A. Weitz, J. P. Butler, and J. J. Fredberg. Physical forces during collective cell migration. *Nature Physics*, 5(6), 2009.
- [233] Y. Maroudas-Sacks and A. Zemel. Theoretical Analysis of Stress Distribution and Cell Polarization Surrounding a Model Wound. *Biophysical Journal*, 115(2), 2018.
- [234] C. Redon, F. Brochard-Wyart, and F. Rondelez. Dynamics of dewetting. *Physical Review Letters*, 66(6), 1991.
- [235] F. Brochard-Wyart, G. Debregeas, R. Fondécave, and P. Martin. Dewetting of supported viscoelastic polymer films: birth of rims. *Macromolecules*, 30(4), 1997.
- [236] T. Vilmin and E. Raphaël. Dewetting of thin polymer films. *The European Physical Journal E*, 21(2), 2006.
- [237] S. Deguchi, T. Ohashi, and M. Sato. Tensile properties of single stress fibers isolated from cultured vascular smooth muscle cells. *Journal of Biomechanics*, 39(14), 2006.
- [238] C. Blanch-Mercader, R. Vincent, E. Bazellères, X. Serra-Picamal, X. Trepata, and J. Casademunt. Effective viscosity and dynamics of spreading epithelia: a solvable model. *Soft Matter*, 13(6), 2017.
- [239] N. Yoshinaga and P. Marcq. Contraction of cross-linked actomyosin bundles. *Physical Biology*, 9(4), 2012.
- [240] M. Smutny, Z. Ákos, S. Grigolon, Sh. Shamipour, V. Ruprecht, D. Čapek, M. Behrndt, E. Papushcheva, M. Tada, B. Hof, T. Vicsek, G. Salbreux, and C.-P. Heisenberg. Friction forces position the neural anlage. *Nature Cell Biology*, 19(4), 2017.
- [241] S. Tlili, J. Yin, J.-F. Rupprecht, M. A. Mendieta-Serrano, G. Weissbart, N. Verma, X. Teng, Y. Toyama, J. Prost, and T. E. Saunders. Shaping the zebrafish myotome by intertissue friction and active stress. *Proceedings of the National Academy of Sciences*, 116(51), 2019.
- [242] C. Blanch-Mercader, P. Guillamat, A. Roux, and K. Kruse. Quantifying Material Properties of Cell Monolayers by Analyzing Integer Topological Defects. *Physical Review Letters*, 126(2), 2021.
- [243] P. Lee and C. W. Wolgemuth. Crawling Cells Can Close Wounds without Purse Strings or Signaling. *PLOS Computational Biology*, 7(3), 2011.

- [244] R. Pankov, A. Momchilova, N. Stefanova, and K. M. Yamada. Characterization of stitch adhesions: Fibronectin-containing cell-cell contacts formed by fibroblasts. *Experimental Cell Research*, 384(1), 2019.
- [245] C. M. Edwards and U. S. Schwarz. Force Localization in Contracting Cell Layers. *Physical Review Letters*, 107(12), 2011.
- [246] A. F. Mertz, Y. Che, S. Banerjee, J. M. Goldstein, K. A. Rosowski, S. F. Revilla, C. M. Niessen, M. Cr. Marchetti, E. R. Dufresne, and V. Horsley. Cadherin-based intercellular adhesions organize epithelial cell-matrix traction forces. *Proceedings of the National Academy of Sciences*, 110(3), 2013.
- [247] A. Münch, B. A. Wagner, and T. P. Witelski. Lubrication Models with Small to Large Slip Lengths. *Journal of Engineering Mathematics*, 53(3), 2005.
- [248] J. G. Oldroyd. A rational formulation of the equations of plastic flow for a Bingham solid. *Mathematical Proceedings of the Cambridge Philosophical Society*, 43(1), 1947.
- [249] H. J. Lee, M. F. Diaz, K. M. Price, J. A. Ozuna, S. Zhang, E. M. Sevick-Muraca, J. P. Hagan, and P. L. Wenzel. Fluid shear stress activates YAP1 to promote cancer cell motility. *Nature Communications*, 8(1), 2017.
- [250] A. M. J. Edwards, R. Ledesma-Aguilar, M. I. Newton, C. V. Brown, and G. McHale. Not spreading in reverse: The dewetting of a liquid film into a single drop. *Science Advances*, 2(9), 2016.
- [251] D. Kong, B. Ji, and L. Dai. Stability of Adhesion Clusters and Cell Reorientation under Lateral Cyclic Tension. *Biophysical Journal*, 95(8), 2008.
- [252] P. J. Mack, M. R. Kaazempur-Mofrad, H. Karcher, R. T. Lee, and R. D. Kamm. Force-induced focal adhesion translocation: effects of force amplitude and frequency. *American Journal of Physiology-Cell Physiology*, 287(4), 2004.
- [253] C. Alibert, B. Goud, and J.-B. Manneville. Are cancer cells really softer than normal cells? *Biology of the Cell*, 109(5), 2017.
- [254] T. Y. Hou and P. G. Le Floch. Why Nonconservative Schemes Converge to Wrong Solutions: Error Analysis. *Mathematics of Computation*, 62(206), 1994.
- [255] J. Ulmer, B. Geiger, and J. P. Spatz. Force-induced fibronectin fibrillogenesis in vitro. *Soft Matter*, 4(10), 2008.
- [256] V. V. Meleshko and Yu. V. Tokovyy. Equilibrium of an elastic finite cylinder under axisymmetric discontinuous normal loadings. *Journal of Engineering Mathematics*, 78(1), 2013.
- [257] G. Beaune, T. V. Stirbat, N. Khalifat, O. Cochet-Escartin, S. Garcia, V. V. Gurchenkov, M. P. Murrell, S. Dufour, D. Cuvelier, and F. Brochard-Wyart. How cells flow in the spreading of cellular aggregates. *Proceedings of the National Academy of Sciences*, 111(22), 2014.
- [258] G. T. Eisenhoffer and J. Rosenblatt. Bringing balance by force: live cell extrusion controls epithelial cell numbers. *Trends in Cell Biology*, 23(4), 2013.
- [259] C. Meghana, N. Ramdas, F. M. Hameed, M. Rao, G. V. Shivashankar, and M. Narasimha. Integrin adhesion drives the emergent polarization of active cytoskeletal stresses to pattern cell delamination. *Proceedings of the National Academy of Sciences*, 108(22), 2011.
- [260] A. G. Grieve and C. Rabouille. Extracellular cleavage of E-cadherin promotes epithelial cell extrusion. *Journal of Cell Science*, 127(15), 2014.

- [261] M. Pentecost, G. Otto, J. A. Theriot, and M. R. Amieva. *Listeria monocytogenes* Invades the Epithelial Junctions at Sites of Cell Extrusion. *PLOS Pathogens*, 2(1), 2006.
- [262] S. A. Gudipaty and J. Rosenblatt. Epithelial cell extrusion: Pathways and pathologies. *Seminars in Cell & Developmental Biology*, 67, 2017.
- [263] S. Ohsawa, J. Vaughen, and T. Igaki. Cell Extrusion: A Stress-Responsive Force for Good or Evil in Epithelial Homeostasis. *Developmental Cell*, 44(3), 2018.
- [264] E. Marinari, A. Mehonic, S. Curran, J. Gale, T. Duke, and B. Baum. Live-cell delamination counterbalances epithelial growth to limit tissue overcrowding. *Nature*, 484(7395), 2012.
- [265] R. Levayer, C. Dupont, and E. Moreno. Tissue Crowding Induces Caspase-Dependent Competition for Space. *Current Biology*, 26(5), 2016.
- [266] T. B. Saw, A. Doostmohammadi, V. Nier, L. Kocgozlu, S. Thampi, Y. Toyama, P. Marcq, C. T. Lim, J. M. Yeomans, and B. Ladoux. Topological defects in epithelia govern cell death and extrusion. *Nature*, 544(7649), 2017.
- [267] D. P. Denning, V. Hatch, and H. R. Horvitz. Programmed elimination of cells by caspase-independent cell extrusion in *C. elegans*. *Nature*, 488(7410), 2012.
- [268] D. Kuipers, A. Mehonic, M. Kajita, L. Peter, Y. Fujita, T. Duke, G. Charras, and J. E. Gale. Epithelial repair is a two-stage process driven first by dying cells and then by their neighbours. *Journal of Cell Science*, 127(6), 2014.
- [269] Y. Gu, T. Forostyan, R. Sabbadini, and J. Rosenblatt. Epithelial cell extrusion requires the sphingosine-1-phosphate receptor 2 pathway. *The Journal of Cell Biology*, 193(4), 2011.
- [270] G. Slattum, K. M. McGee, and J. Rosenblatt. P115 RhoGEF and microtubules decide the direction apoptotic cells extrude from an epithelium. *The Journal of Cell Biology*, 186(5), 2009.
- [271] C. Villeneuve, E. Lagoutte, L. de Plater, S. Mathieu, J.-B. Manneville, J.-L. Maître, P. Chavrier, and C. Rossé. aPKC α triggers basal extrusion of luminal mammary epithelial cells by tuning contractility and vinculin localization at cell junctions. *Proceedings of the National Academy of Sciences*, 116(48), 2019.
- [272] N. Tanimura and Y. Fujita. Epithelial defense against cancer (EDAC). *Seminars in Cancer Biology*, 63, 2020.
- [273] C. Hogan, S. Dupré-Crochet, M. Norman, M. Kajita, C. Zimmermann, A. E. Pelling, E. Piddini, L. A. Baena-López, J.-P. Vincent, Y. Itoh, H. Hosoya, F. Pichaud, and Y. Fujita. Characterization of the interface between normal and transformed epithelial cells. *Nature Cell Biology*, 11(4), 2009.
- [274] M. van der Sande, Y. Kraus, E. Houliston, and J. Kaandorp. A cell-based boundary model of gastrulation by unipolar ingression in the hydrozoan cnidarian *Clytia hemisphaerica*. *Developmental Biology*, 460(2), 2020.
- [275] T. F. Bullen, S. Forrest, F. Campbell, A. R. Dodson, M. J. Hershman, D. M. Pritchard, J. R. Turner, M. H. Montrose, and A. J. M. Watson. Characterization of epithelial cell shedding from human small intestine. *Laboratory Investigation*, 86(10), 2006.
- [276] Y. Takeuchi, R. Narumi, R. Akiyama, E. Vitiello, T. Shirai, N. Tanimura, K. Kuromiya, S. Ishikawa, M. Kajita, M. Tada, Y. Haraoka, Y. Akieda, T. Ishitani, Y. Fujioka, Y. Ohba, S. Yamada, Y. Hosokawa, Y. Toyama, T. Matsui, and Y. Fujita. Calcium Wave Promotes Cell Extrusion. *Current Biology*, 30(4), 2020.
- [277] M. Thomas, B. Ladoux, and Y. Toyama. Desmosomal Junctions Govern Tissue Integrity and Actomyosin Contractility in Apoptotic Cell Extrusion. *Current Biology*, 30(4), 2020.

- [278] K. Duszyc, G. A. Gomez, A. K. Legendijk, M.-K. Yau, B. N. Nanavati, B. L. Gliddon, T. E. Hall, S. Verma, B. M. Hogan, S. M. Pitson, D. P. Fairlie, R. G. Parton, and A. S. Yap. Mechanotransduction activates RhoA in the neighbors of apoptotic epithelial cells to engage apical extrusion. *Current Biology*, 31(6), 2021.
- [279] Y. Atieh, T. Wyatt, A. M. Zaske, and G. T. Eisenhoffer. Pulsatile contractions promote apoptotic cell extrusion in epithelial tissues. *Current Biology*, 31(6), 2021.
- [280] V. K. Dwivedi, C. Pardo-Pastor, R. Droste, J. N. Kong, N. Tucker, D. P. Denning, J. Rosenblatt, and H. R. Horvitz. Replication stress promotes cell elimination by extrusion. *Nature*, 2021.
- [281] S. A. Gudipaty, J. Lindblom, P. D. Loftus, M. J. Redd, K. Edes, C. F. Davey, V. Krishnegowda, and J. Rosenblatt. Mechanical stretch triggers rapid epithelial cell division through Piezo1. *Nature*, 543(7643), 2017.
- [282] S. Okuda and K. Fujimoto. A Mechanical Instability in Planar Epithelial Monolayers Leads to Cell Extrusion. *Biophysical Journal*, 118(10), 2020.

Sujet : Description physique de mécanique cellulaire et tissulaire appliquée à l'étalement de cellules uniques, le bourgeonnement cancéreux et l'extrusion cellulaire

Résumé : Durant ce doctorat, j'ai étudié différents phénomènes liés à la mécanique de cellules et tissus. Le premier projet décrit l'initiation lamellipodiale durant l'étalement cellulaire. Le modèle introduit un couplage entre la courbure membranaire et l'orientation d'actine corticale, qui génère des tractions sur le substrat par friction. Une transition de mouillage total existe quand la courbure du bord, l'orientation d'actine et les tractions entrent dans une boucle rétro-active positive. Une transition bi-stable autorise une nucléation polarisée. Le second projet est une collaboration expérimentale qui étudie comment des Fibroblastes-Associés au Cancer (FACs) pourraient remodeler des tumeurs. Des FACs entourant un amas de Cellules Cancéreuses (CCs) assemblent un anneau contractile pour finir au-dessus des CCs, et génèrent parfois un bourgeon 3D par contrainte de cisaillement. On utilise un modèle élasto-plastique pour les FACs, comparé à la dynamique de fermeture des FACs et les tractions. On combine des modèles mécaniques à «vertex» et continu pour décrire la forme de la monocouche de CCs, jusqu'à l'apparition des réarrangements. Finalement, on décrit la stabilité mécanique des bourgeons en combinant élasticité et réarrangements plastiques. Le dernier projet rapporte des résultats préliminaires sur la mécanique de l'extrusion cellulaire dans une monocouche épithéliale sous compression. Utilisant le même modèle de vertex, on regarde les propriétés mécaniques capables de générer les transitions basal-latéral et latéral-apical. Ensuite, on cherche une instabilité mécanique pour un système minimal à trois cellules, identifiant les conditions qui favorisent l'extrusion.

Mots clés : lamellipode, cortex d'actine, extrusion cellulaire, mécanique épithéliale, modèle de vertex, bourgeonnement cancéreux

Subject : Physical modelling of cell and tissue mechanics applied to single cell spreading, cancerous budding and cell extrusion

Abstract: During this PhD, I studied different phenomena pertaining to the mechanics of cells and tissues. The first project describes lamellipodial initiation during cell spreading. The model introduces a coupling between membrane curvature and cortical actin orientation, that generates substrate tractions by friction. A full wetting transition exists when edge curvature, actin orientation and tractions enter into a positive feed-back loop. A bi-stable transition allows a polar nucleation. The second project is an experimental collaboration that studies the way Cancer-Associated Fibroblasts (CAFs) cells could reshape tumours. CAFs surrounding a cluster of Cancer Cells (CCs) assemble a contractile ring to end up on top of CCs, and sometimes build a 3D bud through a shear stress. We use an elasto-plastic model for CAFs, compared with CAF closure dynamics and tractions. We combine vertex and continuous mechanical models to describe the CC monolayer shape, until the appearance of rearrangements. Finally, we describe the mechanical stability of buds by combining elasticity with plastic rearrangements. The last project reports preliminary results on the mechanics of cell extrusion in an epithelial monolayer under compression. Using the same vertex model, we look at the mechanical properties able to drive the basal-to-lateral and lateral-to-apical transitions. Then, we search for a mechanical instability on a minimal 3-cell system, and identify conditions that favour extrusion.

Keywords : lamellipodium, actin cortex, cell extrusion, epithelial mechanics, vertex model, cancerous budding